RESEARCH ARTICLE

Cobalt-Containing Oxide Catalysts Obtained by The Sol-Gel Method with Auto-Combustion in The Reaction of Low-Temperature Oxidation of Carbon Monoxide

S. M. Zulfugarova[1*] (iD) **, G. R. Azimova**[1] (iD) **, Z. F. Aleskerova**[1] (iD) **, D. B. Tagiev**[1] (iD)

[1]Institute of Catalysis and Inorganic Chemistry of the Ministry of Science and Education of Azerbaijan, Baku, AZ 1143, Azerbaijan.

Abstract: The reaction of low-temperature oxidation of carbon monoxide is important in the context of air purification and reduction of automotive emissions. Along with the search for active catalytic systems for carbon monoxide oxidation, the development of new energy-saving methods of catalyst synthesis also seems important. Cobalt-iron-, cobalt-manganese, cobalt-chromium, cobalt-copper binary and cobalt-manganese-iron, cobalt-copper-iron-containing triple oxide systems for low-temperature oxidation of carbon monoxide into carbon dioxide were synthesized by the sol-gel method with auto-combustion. The samples were analyzed by X-ray diffraction, IR spectral and derivatographic methods of analysis, their specific surface area was measured by the BET method, micro-photographs were taken on a scanning electron microscope. It was established that the resulting binary and ternary cobalt-containing oxide systems are multiphase systems containing ferrites, manganites, and oxides of cobalt, copper, manganese, and iron. The resulting catalysts are active in the low-temperature oxidation of carbon monoxide at 145-180 °C. The activation energy of the CO oxidation reaction on the analyzed oxide systems was revealed by the Arrhenius equation is placed in the range of 17-33 kJ/mol. In the systems, an intensifying effect of the influence of its components on the catalytic activity is observed in the oxide and spinel phases. The Co-Cr=2:1 system, which, along with chromite, also contains cobalt oxide, which is active at a much lower temperature – 145 °C than systems with a Co-Cr=1:1 and 1:2 ratios. A similar dependence was obtained in the Co-Fe=2:1 system, i.e. in a sample that, along with cobalt ferrite, also contains cobalt oxide. On this catalyst, 100% conversion of CO to CO_2 occurs at a temperature of 200 °C, and a Co-Fe = 1: 2 sample with a stoichiometric ratio of metals, in which the ferritization reaction completely occurs, as experiments have shown, is active only at temperatures above 300 °C. The intensifying effect of the influence of the components on its activity is also observed in three-component systems, in which the complete conversion of CO occurs at a temperature of 145-160 °C. The appearance of various structural defects during short-term combustion of the gel without additional heat treatment, which can potentially be considered as catalytically active centers, on the one hand, and the presence of oxide and spinel phases in the composition of catalysts, which exhibit a mutual reinforcing effect, on the other hand, is demonstrative advantage of this method for the synthesis of active catalysts for low-temperature oxidation of carbon monoxide to dioxide.

1. INTRODUCTION

The problem of utilization of carbon monoxide, which makes a significant contribution to environmental pollution, is relevant to this day. CO emissions are mostly the result of anthropogenic impact on the biosphere. It is known, that most often CO is formed in the process of incomplete combustion of various carbon-containing materials during the operation of internal combustion engines used in various types of

land, water and air transport. In addition to transport, CO is a by-product of a number of large-scale production of the chemical industry. Also, the release of significant amounts of CO accompanies the work of metallurgical and a number of other industries. Among the many gas cleaning systems on the market today, the most promising are catalytic conversion systems containing an active monocatalyst or their mechanical mixture, introduced into the carrier by impregnation or deposition. Catalysts used to oxidize carbon monoxide to carbon dioxide can be divided into three classes:

The first class includes noble metals, such as Pt, Pd and Rh on various carriers (CeO, ZrO_2, Al_2O_3, TiO_2, etc.), which have a high catalytic activity in CO oxidation in the temperature range of 150-250 °C and widely used in the disinfection of exhaust gases (1-8). The second class of catalysts includes nanosized gold catalysts used at very low temperatures of CO oxidation to CO_2 (9-13). These catalysts can work under normal conditions, especially in air purification systems, breathing apparatus.

The catalysts of the third class include metal oxides of Fe, Ni, Mn, Cu, Co, Cr, Ni, Ce, etc. Oxides can be used separately or in various combinations of oxides, including ferrites (14-29). In recent years, there are also many works in the literature devoted to the oxidation of CO on catalysts of the spinel structure (30-38).

Currently, the most advanced catalysts for the neutralization of waste and waste gases are catalysts containing noble metals (Pt, Pd, Rh) (1). However, for industrial catalysts containing platinoids, a cost-effective technology for extracting an expensive active phase for reuse has not yet been proposed. From the point of view of the efficiency of the CO oxidation process, it is especially important to carry out the oxidation process at the lowest possible temperatures, i.e., in an energy-saving mode. Therefore, the search for active and stable catalysts for the low-temperature oxidation of CO instead of expensive catalysts containing noble metals remains a priority in research.

From this point of view, many works are devoted to cobalt-containing catalysts, both oxide and more complex (39-48).

Catalysts for the oxidation of carbon monoxide are obtained by various methods - co-precipitation, thermal decomposition of salts, sol-gel method, ceramic, combustion of solutions in a high-temperature stream, plasma-chemical, etc. In all available methods, the formation of the catalyst structure proceeds at high temperature during sintering, which is a solid-phase process and requires long-term heat treatment. Mechanochemistry (49-50), microwave radiation (27, 36, 51-52) are often used to accelerate solid-phase processes.

Along with the search for active catalytic systems, the development of new energy-saving synthesis methods also seems important for heterogeneous catalysis.

To date, among the methods for obtaining highly dispersed catalysts, much attention is paid to the sol-gel method, the main advantage of which is the high homogenization of the initial components with the production of sol and its transformation into gel due to the processes of hydrolysis and condensation, followed by aging, drying and heat treatment.

A variation of the sol-gel method is the sol-gel with auto-combustion. The process of drying and heat treatment in this method occurs in one stage. The method includes an exothermic and self-sustaining redox reaction of a xerogel, which is obtained from an aqueous solution containing metal salts (oxidizing agent) and an organic component (reducing agent), which is also "combustible". The organic component forms complexes with metal ions, which prevents the precipitation of metal salts and thereby improves gelation conditions. In addition to these advantages, as a result of the combustion of the organic component, a large amount of gaseous products is formed, which prevents the solid phase crystallites from sintering - it is obtained in the form of ash or a fine powder. The reaction proceeds quickly and at a sufficiently low temperature. The method is quite simple for practical implementation and economical in terms of time and energy.

Based on the foregoing, this paper presents the results of a study of the reaction of carbon monoxide oxidation on cobalt-containing oxide catalysts obtained by the sol-gel method with auto-combustion, as well as using microwave treatment.

2. EXPERIMENTAL PART

Double cobalt-iron-, cobalt-manganese, cobalt-chromium, cobalt-copper and triple cobalt-manganese-iron, cobalt-copper-iron-containing oxide systems were synthesized by the sol-gel method with auto-combustion.

Precursors for the synthesis of these systems were nitrates of salts of the appropriate metals – $Co(NO_3)_2 \cdot 6H_2O$, $Fe(NO_3)_3 \cdot 9H_2O$, $Cu(NO_3)_2 \cdot 3H_2O$, $Mn(NO_3)_2 \cdot 4H_2O$ and citric acid, glycine, urea as organic reagents. Two-component cobalt-iron oxide systems were synthesized with a ratio of Co:Fe = 1:1, 1:2 and 2:1, cobalt-manganese oxide systems with a ratio of Co-Mn = 1:1, cobalt-copper oxide systems with a ratio of Co-Cu=1:1 and three-component cobalt-manganese-iron-containing oxide compositions with ratio Co:Mn:Fe= 1:1:1, 2:1:1, 1:2:1. Aqueous solutions of the calculated amounts of salts and the organic reagent were mixed on a magnetic stirrer with heating until a gel formed. The resulting gel was placed in an oven heated to 175-190 °C, in which it completely dried and then ignited. Microwave technology has also been used in the synthesis of some catalytic systems.

Microwave sol-gel synthesis was carried out in two ways:

- Gel was subjected to microwave treatment until complete cessation of combustion with the formation of powder within a few minutes.

- Microwave treatment of the gel was stopped at the moment of ignition, i.e. microwave energy was used to ignite the gel without further prolonged irradiation, and even at low magnetron power; this took several seconds.

X-ray phase diffraction analysis of the products was carried out on a Bruker D 2Phazer automatic diffractometer with a CuKα radiation source. IR spectra were recorded on a Bruker FTIR Alfa spectrometer. Measurement of the specific surface of the samples was determined by low-temperature nitrogen adsorption according to the multipoint BET method on SORBI-MS (Russia) device.

Derivatographic analysis was performed on a NETZCH STA 449F3 instrument. Micrographs were taken on a Hitachi TM 3000 electron microscope.
The obtained powders of oxide systems in the amount of 1 gram were mixed with a binder - alumogel, formed into granules, dried in air, further heat treatment was carried out in a drying cabinet and a muffle furnace at a temperature of 135 and 500 °C, respectively.

CO oxidation was carried out by the flow method at a ratio of CO: air = 1:(3-5), a volumetric rate of

6000-12000 h^{-1}. The analysis was carried out on an LKhM chromatograph, in two columns with sorbents CaA and porapak Q. The measure of activity was the temperature of 100% conversion of CO into CO_2.

$$X_{CO} = 100 \frac{C_{input} - C_{output}}{C_{input}}$$

Where;
C_{input} is the concentration of CO in the gas mixture at the inlet to the reactor,
C_{output} is the concentration of CO in the gas mixture at the outlet of the reactor,
X_{CO} - CO conversion (%).

3. RESULTS

3.1. Catalytic activity of double cobalt-containing oxide systems in the oxidation of carbon monoxide.
3.1.1. Co-Fe system
X-ray diffraction analysis of the resulting two-component Co-Fe system with a ratio of 1:2 showed the formation of cobalt ferrite $CoFe_2O_4$, as well as a small amount of double iron oxide Fe_3O_4 (Fig. 1, a). In the IR spectrum, a band characteristic of ferrites was also observed at 547.56 cm^{-1}. The phase composition of the sample with the ratio Co-Fe = 1: 1 consists of oxides of cobalt, iron and ferrite, and the sample with the ratio Co-Fe = 2: 1 - from cobalt oxide and ferrite.
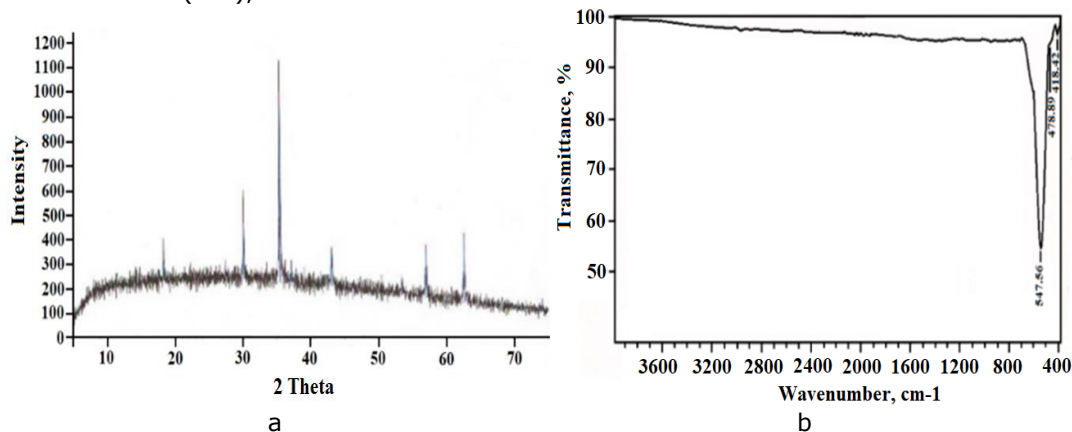
Figure 1: Diffraction pattern (a) and IR spectrum (b) of the Co-Fe=1:2 sample obtained by the sol-gel method with auto-combustion.

Previously, we carried out the microwave synthesis of cobalt ferrite using a ceramic method from cobalt oxide and magnetite (53). To compare the catalytic activity of cobalt ferrite obtained by various methods, we carried out a microwave sol-gel synthesis; burning the gel in a microwave oven. The diffraction pattern of the resulting sample was identical to the diffraction pattern of the sample obtained by conventional gel combustion.

To elucidate the processes occurring during the combustion of a xerogel during the synthesis of a two-component Co-Fe system by the sol-gel method with combustion, a differential thermal analysis was carried out of a xerogel prepared from metal nitrates and citric acid by heating it to a temperature of 900 °C (Fig. 2).
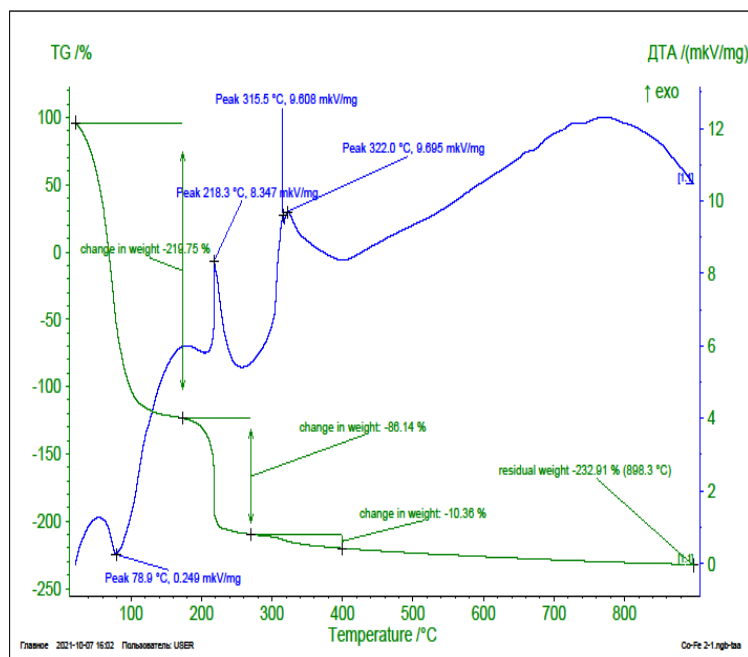
Figure 2: Derivatogram of Co-Fe system

The DTA curve shows an endothermic peak at 80 °C and two exothermic peaks at 218 and 322 °C. C is about 64% due to water evaporation. In the range of 180-280 °C, a chemical reaction occurs between metal nitrates and citric acid due to the ignition of the latter. The weight loss in this case is about 25%. Note that the onset of combustion, i.e., the reaction initiation temperature, was previously recorded during the synthesis of ferrite. The drying of the gel took place in an oven at a temperature of 175-180 °C. Under these conditions, ignition and further combustion of the gel occurred. The exothermic band between 280 and 400 °C with a maximum at 322 °C complies with the combustion of residual amounts of the organic component and the weight loss in this temperature range is 2.7%. With a further increase in temperature, the mass loss is very small.

The catalytic activity of Co-Fe systems prepared by various methods with different ratios of metals was studied in the reaction of oxidation of carbon monoxide to dioxide. The measure of activity was the temperature of 100% conversion of CO to CO_2. The experimental results are shown in Fig.3.

It can be seen from the Fig. 3 that for all the synthesized samples, the complete conversion of carbon monoxide is achieved in the temperature range above 350 °C. The exception is a sample with a ratio of Co-Fe=2:1, on which 100% conversion of CO to CO_2 occurs at a temperature of 200 °C. According to elemental analysis, the content of cobalt in this catalyst is 71, and iron is 29%. It is likely that the presence of Co_3O_4 in samples with a higher ratio of cobalt to iron favors the occurrence of the oxidation reaction as compared to the Co-Fe=1:2 sample with a stoichiometric ratio of metals, in which the ferritization reaction occurs almost completely. On the samples obtained by the microwave sol-gel method and microwave synthesis from oxides, the conversion at 500 °C is 64 and 16%, respectively, so

carrying out the reaction on these samples at higher temperatures was of no interest. Samples obtained by "igniting" the gel in a microwave show the same activity as samples obtained by the conventional sol-gel method with combustion. The specific surface area of the samples is shown in Table 1, according to which a relatively long microwave treatment leads to a decrease in the specific surface area, which affects the catalytic activity.
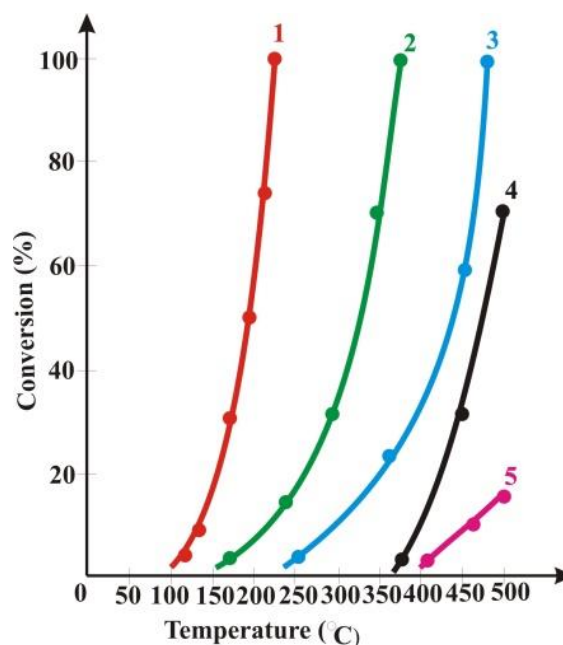
Figure 3: Dependence of carbon monoxide conversion on temperature on the Co-Fe catalytic system synthesized by various methods: sol-gel method with combustion (1 - Co-Fe=2:1; 2 - Co-Fe=1:1; 3 - Co- Fe=1:2), gel combustion in a microwave field (4-Co-Fe=1:2) and microwave synthesis from oxides (5-Co-Fe=1:2).

Table 1: Specific surface area values of synthesized catalysts samples

Catalyst and synthesis method	Specific surface, m^2/g
Co-Fe=1:2, solid phase microwave synthesis from oxides	0.2
Co-Fe=1:2, microwave sol-gel synthesis	1.5
Co-Fe=1:2, sol-gel synthesis with auto-combustion	12
Co-Fe=1:1, « ----------------------------------»	26
Co-Fe=2:1, « --------------------------------- »	28
Co-Mn-Fe, sol-gel synthesis with auto-combustion	28
Co-Mn-Fe, microwave sol-gel synthesis	1.8
Co-Cu-Fe, sol-gel synthesis with auto-combustion	26
Co-Cu-Fe, microwave sol-gel synthesis	2.2

a　　　　　　　　　　　　　　　　　　b
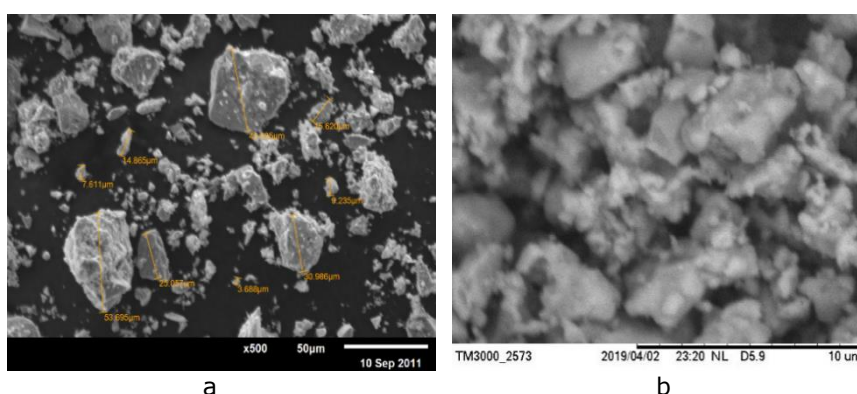
Figure 4: Micrographs of a Co-Fe=2:1 sample obtained by microwave treatment from oxides (a) and microwave sol-gel synthesis (b).

Fig. 4 shows the data of an electron microscopic study of samples using microwave exposure, from which rather large crystallites are visible, the dimensions of which vary within 500 nm -2 µm. When samples are obtained by solid-phase microwave synthesis from oxides, the time of microwave treatment as compared to gel combustion is rather long and is measured in minutes, since microwave treatment alternates with grinding the initial mixture of oxides. Owing to the high ability of the initial oxides to absorb microwave radiation, a strong rise in temperature occurs which leads to aggregation of the formed particles. This occurs both during the microwave sol-gel synthesis of samples and during additional microwave treatment of the powder obtained after burning the gel. These samples are also characterized by low specific surface area, which is 0.2–1.8 m^2/g, respectively.

In the synthesis of the sol-gel method with combustion, as a result of the release of a large amount of gas, a bulk mass of ash is formed, which, when rubbed, produces a fine powder (Fig. 5). The burning of the gel occurs within a few seconds. The specific surface of the samples obtained by the sol-gel method with combustion is 12–28 m^2/g.

Figure 5: A sample of the catalyst Co-Fe=1:2 obtained sol-gel method with auto-burning.

3.1.2. Co-Mn, Co-Cu and Co-Cr systems
According X-ray diffraction analysis, along with the binary spinel-type oxide, cobalt manganite $CoMn_2O_4$, cobalt and manganese oxides are also formed in the Co-Mn system ($CoMn_2O_4$ - 48%, Mn_3O_4 - 29.5%, Co_3O_4 - 22.5%) (Fig. 6, a). The IR spectrum shows an absorption band at 665 cm^{-1}, which characterizes the Me-O bonds of tetrahedrally coordinated ions in spinels. The absorption bands in the range 900–1400 cm^{-1} (1168.97, 1276.97, 1458.85) are related to Me–OH bending vibrations (19, 30).
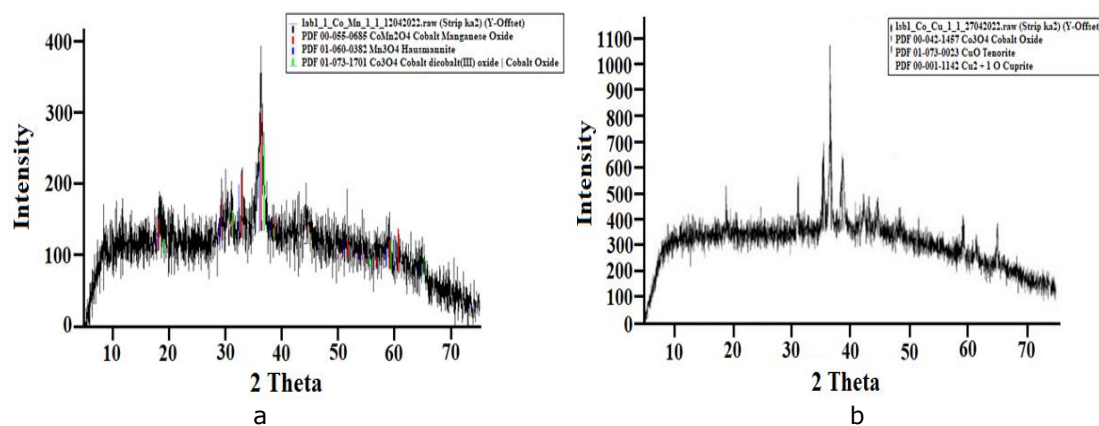
Figure 6: X-ray diffraction patterns of Co-Mn=1:1 (a) and Co-Cu=1:1 (b) samples

In the Co-Cu (1:1) system, only oxides Co_3O_4, CuO, Cu_2O are formed while in the Co-Cr system there are formed cobalt chromite Co_2CrO_4. The phase composition of double oxide systems is given in Table 2.

Table 2 shows that the complete conversion of carbon monoxide on these systems is achieved within 7-11 minutes of the reaction. The nature of the dependence of the degree of conversion on time at different temperatures for these samples is shown in Fig. 7, from which it can be seen that the relatively higher the reaction temperature, the shorter the time to achieve complete conversion of carbon monoxide.

Table 2: Phase composition of binary oxide system

Catalyst	Reaction temperature,^{0}C	Time to reach 100% conversion, min
Co-Mn=1:1	200	9
Co-Mn=2:1	180	10
Co-Cu=1:1	150	8-9
Co-Cr=1:1	300	9-10
Co-Cr=1:2	280	7-8
Co-Cr=2:1	145	11
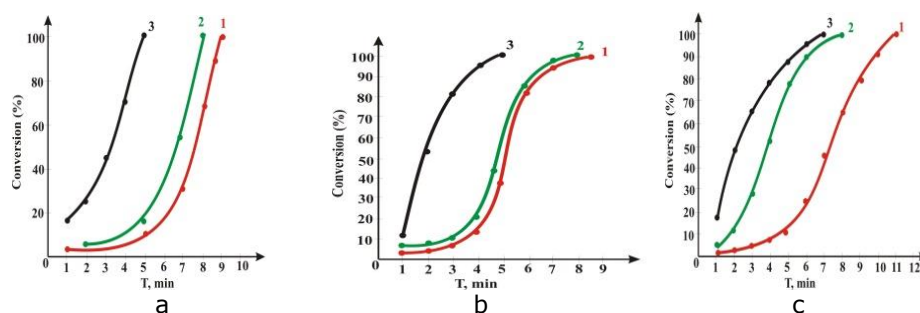
Figure 7: Dependence of the degree of conversion of carbon monoxide on time in oxide catalytic systems at different temperatures: a) Co-Mn (1-185^{0}C, 2-215 ^{0}C, 3-245^{0}C); b) Co-Cu (1-140^{0}C, 2-150 ^{0}C, 3 - 180^{0}C) and c) Co-Cr (1 - 145^{0}C, 2 - 160 ^{0}C, 3 - 180^{0}C).

3.1.3. Three-component systems Co-Mn-Fe and Co-Cu-Fe

The composition of three-component systems obtained by the sol-gel method with combustion is more complex. Reflections of $CoFe_2O_4$, $CoFe_{0.8}Mn_{1.2}O_4$, Mn_3O_4, Fe_3O_4 are observed in the diffraction pattern of the Co-Mn-Fe-oxide system (Fig. 8,a). Reflections of the following phases are observed on the diffraction pattern of the Co-Cu-Fe-oxide system: $CuFe_2O_4$, $CoFe_2O_4$, $CoCu_2O_3$, CuO (Fig. 8,b). Thus, we see that in the studied 3-component

systems obtained by the sol-gel method with auto-combustion, in addition to copper, iron and manganese oxides, the formation of spinels - cobalt ferrite, as in the case of a two-component Co-Fe system, and copper ferrite is observed. These systems can be considered as solid solutions in the same way as binary compositions. And as the composition becomes more complex, various combinations of mixed oxides are possible.
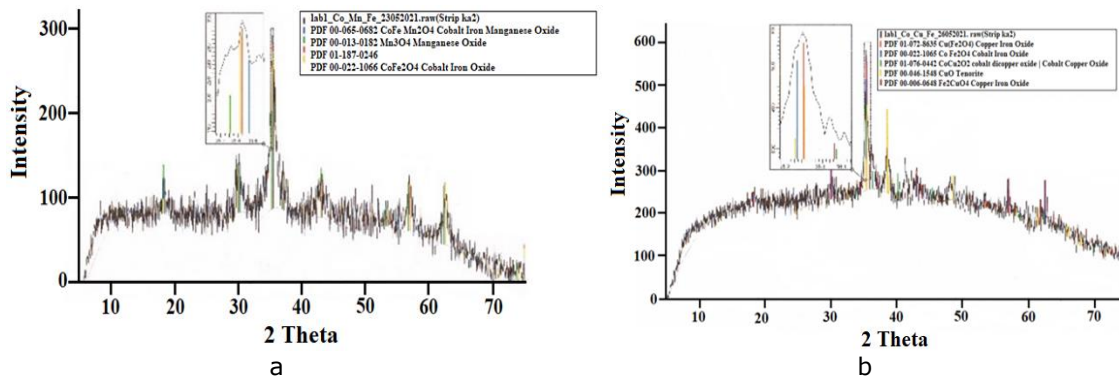
Figure 8: Diffractograms of X-ray diffraction patterns of Co-Mn-Fe (a) and Co-Cu-Fe (b) systems

Thermogravimetric analysis of the Co-Mn-Fe system (Fig. 9) showed that there are 3 exothermic peaks on the DTA curve of the system, one is pronounced at a temperature of 209 °C, the other two at 401 and 486 °C are less pronounced. In the domain of the first exothermic peak at 209 °C, a sharp weight loss occurs, which corresponds to the ignition of the nitrate-citrate gel, followed by combustion. The weight loss in this case is about 70%. Further, in the range of 350-500 °C, the residual amounts of the organic component burn out, which complies with a

weight loss of 12%. The difference in the weight loss between samples of two-component Co-Fe and three-component Co-Mn-Fe systems in the temperature range before ignition of the gel can be related to different moisture content of the initial samples.

The dependence of the degree of conversion of carbon monoxide on time for three-component oxide catalytic systems is shown in Fig.10.
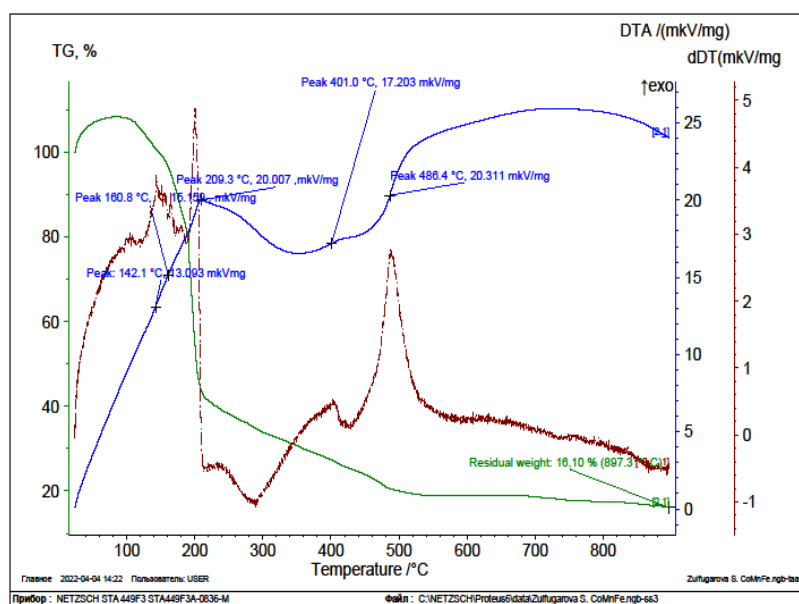
Figure 9: Thermogravimetric analysis of the Co-Mn-Fe system
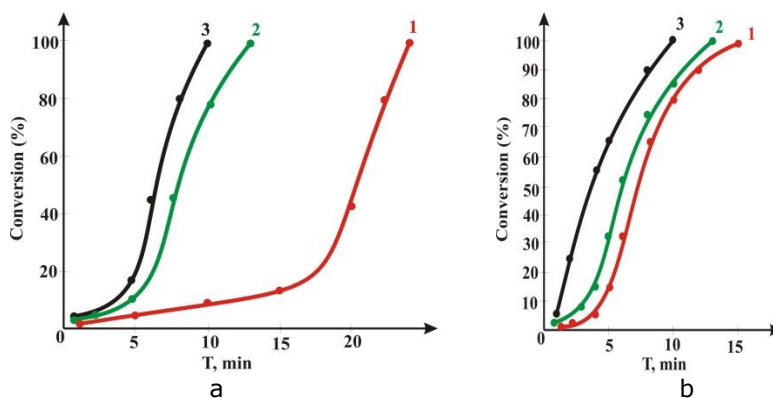
Figure 10: Dependence of the degree of conversion of carbon monoxide on three-component oxide systems at different temperatures:
a) Co-Mn-Fe (1 – 145 °C, 2 – 165 °C, 3 – 180 °C); b) Co-Cu-Fe (1 – 160 °C, 2 – 170 °C, 3 – 215 °C)

Fig. 10 shows that these ternary systems are also active in the low-temperature oxidation of carbon monoxide. The lower temperature of their activity, at which complete conversion of carbon monoxide is achieved, is 145-160 °C. However, unlike two-component cobalt-containing systems, for which the time to achieve complete CO conversion is 7-11 minutes (Table 2), complete CO conversion on three-component systems is achieved within 15-20 minutes. At higher temperatures, this time is reduced to 10-13 minutes.

The activation energy of the CO oxidation reaction on the studied oxide systems found by the Arrhenius equation lies in the range of 17-33 kJ/mol (Table 3). The CO oxidation reaction proceeds with the lowest activation energy on two-component systems Co-Cu and Co-Cr.

Table 3: Activation energy of the CO oxidation reaction on oxide catalysts

Catalyst	E, kJ/mol
Co-Mn=1:1	33
Co-Mn=2:1	31
Co-Cu=1:1	17
Co-Cr= 2:1	25
Co-Mn-Fe=1:1:1	31
Co-Cu-Fe= 1:1:1	30

4. DISCUSSION

As is known, solids with a defective surface have a higher catalytic and adsorption activity as compared to the structure of the perfect crystal. Therefore, using various synthesis methods, it is possible to increase the defectiveness of the outer surface of crystals. From this point of view, the sol-gel method with combustion is the most suitable. It can be seen as a variation of the SHS (Self-Propagating High Temperature Synthesis) method but at lower temperatures. Combustion occurs with a short-term thermal effect on the system, in which an exothermic reaction is initiated and further combustion occurs due to its own heat release. In this case, various physicochemical transformations occur: melting (due to crystallization water of salts), chemical reaction (decomposition of salts with the formation of the appropriate oxides and further interaction of oxides due to mutual diffusion). All these processes occur within a very short time, which affects the formation of the composition and structure, textural parameters of the system. It should be noted that in most works devoted to the synthesis of complex oxide systems, including ferrites of transition metals, for example, cobalt, nickel, by the sol-gel method with combustion, additional heat treatment is carried out at a temperature of 600-700 °C of the powder obtained after combustion. This is due to the requirements of their area of application. These compounds are used as fuel cell electrodes, oxygen membranes, sensitive components of gas sensors, in microelectronics, where the high purity and crystallinity of the resulting compound plays an important role. In catalysis, a similar picture is not always observed. For example, in (53), we synthesized cobalt, nickel, and copper ferrites from oxides of these metals by microwave treatment. Prolonged microwave processing led to a decrease in the content of individual oxides and an increase in the corresponding ferrite, which occurs due to an increase in the degree of conversion of the initial oxides. An increase in the degree of crystallinity was also observed. However, these samples, when tested in the CO oxidation reaction, showed low catalytic activity. Conversely, two- and three-component systems obtained by the sol-gel method with auto-combustion without additional heat treatment showed high activity in low-temperature CO oxidation.

As follows from Table 1, the specific surface area of systems obtained by this method is significantly higher than similar samples obtained using long-term microwave irradiation, measured in minutes, at which a powerful temperature rise occurs throughout the entire volume, leading to intense aggregation of particles of the resulting substances. However, as noted above, if microwave irradiation is used only to "ignite" the gel, then systems with a similar catalytic activity are obtained as the samples obtained with conventional combustion. Incidentally, the authors of (54) also note that the catalyst synthesized at 550 °C with the Cu/Mn = 1/2 ratio in the precursor exhibits the highest catalytic activity with respect to CO oxidation due to the formation of the $CuMn_2O_4$ phase with poor crystallinity.

As noted above, the catalytic systems obtained by us through the use of the sol–gel method with auto-combustion are mainly a combination of simple oxides and spinels. They can be considered as solid solutions, and as the composition becomes more complex, various combinations of mixed oxides are possible. During a very short combustion, crystallites of various sizes are formed in the systems, and along with nanosized agglomerates, there are also larger agglomerates, as can be seen from Fig. 11, which shows micrographs of two and three-component cobalt-containing catalytic systems.

The binary and ternary catalysts synthesized by us are multiphase oxide systems of variable composition; therefore, they may have all types of defects in solids, including point defects, extended defects (dislocations), electronic defects representing local disturbances in the charge distribution (38). On the one hand, the presence of defects that can potentially be considered as catalytically active centers, on the other hand, the presence of oxide and spinel phases in the composition of the synthesized catalysts favors the coordination of surface oxygen with different metal atoms of the structure, thereby exhibiting different

reactivity. Spinels in an ideal structure are crystallized in the cubic space group Fd-3m. In a close-packed lattice, two types of voids are distinguished: tetrahedral, limited by four oxygen anions, and octahedral, limited by six oxygen anions. The unit cell of spinel contains 32 oxygen anions, forming 64 tetrahedral positions (8 are occupied by metal cations) and 32 octahedral positions (16 are occupied by metal cations). In spinels, transition metals can be placed in tetrahedral and octahedral positions. Based on a large number of theoretical and experimental works, cations are arranged in the following row according to their tendency to occupy octa-pores (at T = 0): Cr^{3+}, Ni^{2+}, Mn^{3+}, Cu^{2+}, Al^{3+}, Cu^+, Fe^{2+}, Co^{2+}, Fe^{3+}, Mn^{2+}. The cations on the left up to Al^{3+} are more inclined to occupy octahedral pores, while the cations from Al^{3+} to Fe^{2+} can occupy both tetra- and octa-pores (55). The placement of transition metal ions in octahedral vacancies leads to a decrease in the Me–O bond energy, which contributes to an easier electronic transition and thereby an increase in the rate of the oxidation reaction, which, apparently, can also be associated with a higher activity of the synthesized double and ternary systems as compared to individual oxides.
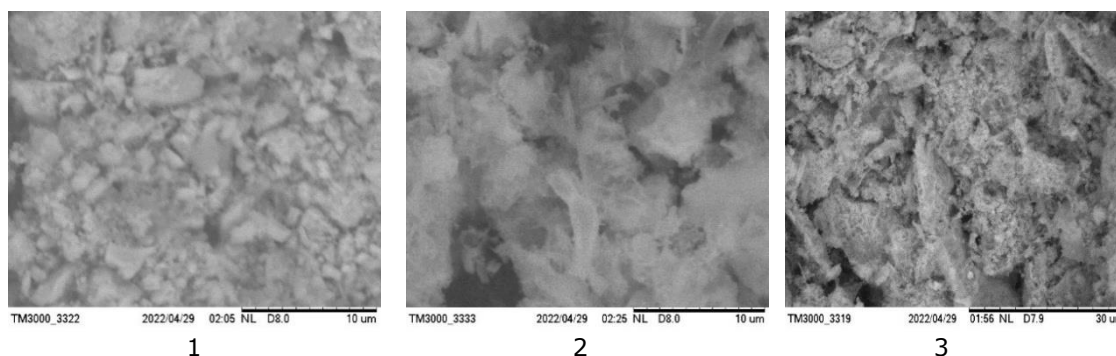
Figure 11: Micrographs of cobalt-containing oxide systems obtained by the sol-gel method with combustion: 1-Co-Mn; 2 - Co-Mn-Fe; 3-Co-Cu-Fe

The mutual influence of the oxide and spinel phases on the catalytic activity was established in (38). The authors synthesized the sol-gel method using citric acid copper-manganese oxide catalyst with different initial ratios of metals. One of the components of the resulting catalyst was spinel $Cu_{1.5}Mn_{1.5}O_4$; the other component, depending on the ratio, was either copper oxide CuO or Mn_3O_4. The study of the catalytic activity of the obtained systems showed that the $CuO-Cu_{1.5}Mn_{1.5}O_4$ system manifested the best performance in the temperature range of 80-170 °C than the $Cu_{1.5}Mn_{1.5}O_4$ and $Mn_3O_4-Cu_{1.5}Mn_{1.5}O_4$ systems. The authors opine that there is a synergistic effect between CuO and $Cu_{1.5}Mn_{1.5}O_4$, since individual copper and manganese oxides exhibit low activity in low-temperature CO oxidation, and only the presence of copper oxide in the system (the authors call this modification) makes it active.

The systems synthesized by us also contain spinel phases and oxides. But not all of these systems can demonstrate the effect of mutual influence. Individual oxides Co_3O_4 and Mn_3O_4, obtained by us by means of the sol-gel method with combustion, as well as two-component systems based on them containing spinel (cobalt manganite), are active in the oxidation of CO in the temperature range of 180-190 °C, i.e. in this case, there is no synergistic effect. However, the Co-Cr=2:1 system, which, along with chromite, also contains cobalt oxide, is active already at a much lower temperature – 145 °C, than systems with a ratio of Co-Cr=1:1 and 1:2 (Table 3). A similar dependence was obtained in the Co-Fe=2:1 system, i.e. in a sample that, along with cobalt ferrite, also contains cobalt oxide. On this catalyst, 100% conversion of CO to CO_2 occurs at a temperature of 200 °C. A Co-Fe=1:2 sample with a stoichiometric ratio of metals, in which the ferritization reaction almost completely occurs, as experiments have shown, are active only at temperatures above 300 °C. Only Co_3O_4, CuO and a small amount of Cu_2O were found in the Co-Cu=1:1 system, but it is active at 150 °C (Table 3). That is, in these two systems, there is an intensifying effect of the influence of the components on its activity The effect of synergy can also be observed in the obtained three-component systems, on which the complete conversion of CO occurs at a temperature of 145-160 °C. In these systems, along with spinels - ferrites of cobalt, copper, there are oxides of copper, cobalt, and iron.

The authors of (41) also associated the high catalytic activity in low-temperature CO oxidation of the Cu-Mn-O catalyst with a synergistic effect. They found that the Cu-Mn-O spinel has a higher catalytic activity as compared to the activity of pure copper or manganese CO. The Cu1Mn2-550 sample (550 - catalyst synthesis temperature) not only provides more defects and vacancies to create more active sites, but also generates more highly active Cu (II), which promotes CO oxidation. On the contrary, a decrease in the amount of Cu(II) and a higher degree of crystallinity as a result of a higher synthesis temperature lead to a deterioration in catalytic activity.

In the catalysts under study, both lattice oxygen and oxygen adsorbed on the surface of a metal or oxide in atomic or molecular form can serve as the so-called active oxo center. Depending on this, the reaction can proceed both in one stage (the Langmuir-Hinshelwood mechanism) and in two stages (the Mars-van-Krevelen mechanism) (33). In the first case, carbon monoxide adsorbed on the catalyst reacts with adsorbed oxygen (fusion

mechanism). According to the Mars–van Crevelen mechanism, CO is initially oxidized by the oxygen of the catalyst outer lattice, resulting in the formation of an oxygen vacancy; then, the spinel is re-oxidized by oxygen from the gas phase; the active form of oxygen is lattice oxygen, and during the reaction, alternating reduction and oxidation of the catalyst occurs.

To clarify this issue, special experiments were carried out on Co-Mn and Co-Mn-Fe catalysts. First, the oxidation reaction of CO on the catalyst was carried out in the absence of air; then, the surface of the catalyst was preliminarily cleaned with an inert gas at the reaction temperature, after which the reaction was carried out without access to air. In the third version of the experiments, after cleaning the catalyst surface with an inert gas, the reaction was carried out in an inert gas atmosphere by adding carbon monoxide to the reaction medium. The results showed that in all experiments there was a slight conversion of carbon monoxide, as evidenced by the increase in the reaction temperature by 12-15 °C during the first 3 minutes. The temperature then drops very slowly to the initial temperature, indicating the termination of the reaction. Only when air is introduced into the reaction medium, the reaction begins to proceed intensively, and within a few minutes the monoxide conversion reaches 100%. These experiments confirm the assumption that the reaction proceeds according to the Langmuir-Hinshelwood mechanism.

Summarizing the above, we can say that the use of a technologically simple sol-gel method with auto-combustion in the synthesis of active multicomponent oxide catalysts based on transition metals is promising.

The formation of multiphase systems, including oxide and spinel phases during gel combustion without additional heat treatment, is a proven advantage of this method in the synthesis of active catalysts for the low-temperature oxidation of carbon monoxide to dioxide.

5. CONCLUSION

1. Two- and three-component cobalt-containing oxide catalytic systems were synthesized by the sol-gel method with auto-combustion.

2. It found that the synthesized cobalt-containing oxide systems are active in the low-temperature oxidation of carbon monoxide in the temperature range of 145-180 °C.

3. The synthesized binary and three-component catalysts are multiphase oxide systems of variable composition. X-ray phase analysis established that they contain ferrites, manganites and individual oxides of cobalt, copper, manganese and iron.

4. The use of a technologically simple sol-gel method with auto-combustion for the synthesis of oxide cobalt-containing catalysts based on transition metals contributes to the formation of multiphase

systems during gel combustion, including oxide and spinel phases, which provide catalytic activity. Needlessness for additional thermal treatment of the synthesized catalysts is an advantage of this method for the synthesis of active catalysts in terms of the low-temperature oxidation of carbon monoxide to dioxide.

6. CONFLICT OF INTEREST

The authors confirm that this article's content has no conflict of interest.

7. REFERENCES

1. Gandhi HS, Graham GW, McCabe RW. Automotive exhaust catalysis. J Catal [Internet]. 2003 May 1;216(1–2):433–42. Available from: <URL>.

2. Bekyarova E, Fornasiero P, Kašpar J, Graziani M. CO oxidation on Pd/CeO$_2$–ZrO$_2$ catalysts. Catal Today [Internet]. 1998 Oct 19;45(1–4):179–83. Available from: <URL>.

3. Bratan V, Munteanu C, Hornoiu C, Vasile A, Papa F, State R, et al. CO oxidation over Pd supported catalysts —In situ study of the electric and catalytic properties. Appl Catal B Environ [Internet]. 2017 Jun 15;207:166–73. Available from: <URL>.

4. Carlsson P-A, Skoglundh M. Low-temperature oxidation of carbon monoxide and methane over alumina and ceria supported platinum catalysts. Appl Catal B Environ [Internet]. 2011 Jan 14;101(3–4):669–75. Available from: <URL>.

5. Deng Y, Wang T, Zhu L, Jia A-P, Lu J-Q, Luo M-F. Enhanced performance of CO oxidation over Pt/CuCrO$_x$ catalyst in the presence of CO$_2$ and H$_2$O. Appl Surf Sci [Internet]. 2018 Jun 1;442:613–21. Available from: <URL>.

6. Elazab HA, Moussa S, Brinkley KW, Gupton BF, El-Shall MS. The continuous synthesis of Pd supported on Fe$_3$O$_4$ nanoparticles: a highly effective and magnetic catalyst for CO oxidation. Green Process Synth [Internet]. 2017 Jan 28;6(4):413–24. Available from: <URL>.

7. Mandapaka R, Madras G. Aluminium and rhodium co-doped ceria for water gas shift reaction and CO oxidation. Mol Catal [Internet]. 2018 May 1;451:4–12. Available from: <URL>.

8. Zou Z-Q, Meng M, Zha Y-Q. Surfactant-Assisted Synthesis, Characterizations, and Catalytic Oxidation Mechanisms of the Mesoporous MnOx−CeO$_2$ and Pd/MnOx−CeO$_2$ Catalysts Used for CO and C$_3$H$_8$ Oxidation. J Phys Chem C [Internet]. 2010 Jan 14;114(1):468–77. Available from: <URL>.

9. Arenz M, Mayrhofer KJJ, Stamenkovic V, Blizanac BB, Tomoyuki T, Ross PN, et al. The Effect of the Particle Size on the Kinetics of CO Electrooxidation on High Surface Area Pt Catalysts. J Am Chem Soc [Internet]. 2005 May 1;127(18):6819–29. Available from: <URL>.

10. Du M, Sun D, Yang H, Huang J, Jing X, Odoom-

Wubah T, et al. Influence of Au Particle Size on Au/TiO$_2$ Catalysts for CO Oxidation. J Phys Chem C [Internet]. 2014 Aug 21;118(33):19150–7. Available from: <URL>.

11. Joo SH, Park JY, Renzas JR, Butcher DR, Huang W, Somorjai GA. Size Effect of Ruthenium Nanoparticles in Catalytic Carbon Monoxide Oxidation. Nano Lett [Internet]. 2010 Jul 14;10(7):2709–13. Available from: <URL>.

12. Raphulu M, McPherson J, Pattrick G, Ntho T, Mokoena L, Moma J, et al. CO oxidation: Deactivation of Au/TiO$_2$ catalysts during storage. Gold Bull [Internet]. 2009 Dec;42(4):328–36. Available from: <URL>.

13. Tana, Wang F, Li H, Shen W. Influence of Au particle size on Au/CeO$_2$ catalysts for CO oxidation. Catal Today [Internet]. 2011 Oct 25;175(1):541–5. Available from: <URL>.

14. Royer S, Duprez D. Catalytic Oxidation of Carbon Monoxide over Transition Metal Oxides. ChemCatChem [Internet]. 2011 Jan 10;3(1):24–65. Available from: <URL>.

15. Xanthopouloua GG, Novikova VA, Knysha YA, Amosova AP. Nanocatalysts for Low-Temperature Oxidation of CO: Review. Eurasian Chem J [Internet]. 2014 Dec 19;17(1):17–32. Available from: <URL>.

16. Soliman NK. Factors affecting CO oxidation reaction over nanosized materials: A review. J Mater Res Technol [Internet]. 2019 Apr 1;8(2):2395–407. Available from: <URL>.

17. Dey S, Mehta NS. Selection of Manganese oxide catalysts for catalytic oxidation of Carbon monoxide at ambient conditions. Resour Environ Sustain [Internet]. 2020 Sep 1;1:100003. Available from: <URL>.

18. Mahammadunnisa S, Manoj Kumar Reddy P, Lingaiah N, Subrahmanyam C. NiO/Ce$_{1−x}$Ni$_x$O$_{2−δ}$ as an alternative to noble metal catalysts for CO oxidation. Catal Sci Technol [Internet]. 2013 Feb 12;3(3):730–6. Available from: <URL>.

19. Dey S, Mohan D, Dhal GC, Prasad R. Copper based mixed oxide catalysts (CuMnCe, CuMnCo and CuCeZr) for the oxidation of CO at low temperature. Mater Discov [Internet]. 2017 Dec 1;10:1–14. Available from: <URL>.

20. Dey S, Dhal GC, Mohan D, Prasad R. Low-temperature complete oxidation of CO over various manganese oxide catalysts. Atmos Pollut Res [Internet]. 2018 Jul 1;9(4):755–63. Available from: <URL>.

21. Dasireddy VDBC, Valand J, Likozar B. PROX reaction of CO in H$_2$/H$_2$O/CO$_2$ Water–Gas Shift (WGS) feedstocks over Cu–Mn/Al$_2$O$_3$ and Cu–Ni/Al$_2$O$_3$ catalysts for fuel cell applications. Renew Energy [Internet]. 2018 Feb 1;116:75–87. Available from: <URL>.

22. Dasireddy VDBC, Bharuth-Ram K, Hanzel D, Likozar B. Heterogeneous Cu–Fe oxide catalysts for preferential CO oxidation (PROX) in H$_2$ -rich process streams. RSC Adv [Internet]. 2020 Sep 28;10(59):35792–802. Available from: <URL>.

23. Al Soubaihi RM, Saoud KM, Dutta J. Critical Review of Low-Temperature CO Oxidation and Hysteresis Phenomenon on Heterogeneous Catalysts. Catalysts [Internet]. 2018 Dec 14;8(12):660. Available from: <URL>.

24. Li X-N, Wang L-N, Mou L-H, He S-G. Catalytic CO Oxidation by Gas-Phase Metal Oxide Clusters. J Phys Chem A [Internet]. 2019 Oct 31;123(43):9257–67. Available from: <URL>.

25. Zulfugarova SM, Azimova GR, Aleskerova ZF, Qasimov RJ, Bayramov MA, Ismailov EH, et al. Effect of preparation method of iron-, copper-containing oxide catalysts on their activity in the reaction of oxidation of carbon monoxide to carbon dioxide. Chem Probl [Internet]. 2022;20(1):82–94. Available from: <URL>.

26. Azimova GR. Study of low-temperature oxidation of carbon monooxide on Cu-Mn-Fe catalytic oxide systems obtained by the sol-gel combustion method. Azerbaijan Chem J [Internet]. 2022 Jun 22;2:93–9. Available from: <URL>.

27. Zulfugarova SM, Ramiz AG, Fikret AZ, Humbat IE, Nikolayevich LY, Babir TD. Microwave Sol-gel Synthesis of Co, Ni, Cu, Mn Ferrites and the Investigation of Their Activity in the Oxidation Reaction of Carbon Monoxide. Curr Microw Chem [Internet]. 2022 Apr 4;9(1):37–46. Available from: <URL>.

28. Njagi EC, Chen C-H, Genuino H, Galindo H, Huang H, Suib SL. Total oxidation of CO at ambient temperature using copper manganese oxide catalysts prepared by a redox method. Appl Catal B Environ [Internet]. 2010 Aug;99(1–2):103–10. Available from: <URL>.

29. Jones C, Cole KJ, Taylor SH, Crudace MJ, Hutchings GJ. Copper manganese oxide catalysts for ambient temperature carbon monoxide oxidation: Effect of calcination on activity. J Mol Catal A Chem [Internet]. 2009 Jun 15;305(1–2):121–4. Available from: <URL>.

30. Dey S, Dhal GC. Catalytic conversion of carbon monoxide into carbon dioxide over spinel catalysts: An overview. Mater Sci Energy Technol [Internet]. 2019 Dec 1;2(3):575–88. Available from: <URL>.

31. Aniz CU, Radhakrishnan Nair TD. A Study on Catalysis by Ferrospinels for Preventing Atmospheric Pollution from Carbon Monoxide. Open J Phys Chem [Internet]. 2011;1(3):124–30. Available from: <URL>.

32. Prasad R, Singh P. A Review on CO Oxidation Over Copper Chromite Catalyst. Catal Rev [Internet]. 2012 Apr 1;54(2):224–79. Available from: <URL>.

33. Bhagwat VR, Humbe A V., More SD, Jadhav KM.

Sol-gel auto combustion synthesis and characterizations of cobalt ferrite nanoparticles: Different fuels approach. Mater Sci Eng B [Internet]. 2019 Sep 1;248:114388. Available from: <URL>.

34. Kaufmann Junior CG, Zampiva RYS, Alves AK, Bergmann CP, Giorgini L. Synthesis of cobalt ferrite ($CoFe_2O_4$) by combustion with different concentrations of glycine. IOP Conf Ser Mater Sci Eng [Internet]. 2019 Oct 1;659(1):012079. Available from: <URL>.

35. Amini M, Kafshdouzsani MH, Akbari A, Gautam S, Shim C-H, Chae KH. Spinel copper ferrite nanoparticles: Preparation, characterization and catalytic activity. Appl Organomet Chem [Internet]. 2018 Sep 1;32(9):e4470. Available from: <URL>.

36. Azimova GR, Zulfugarova SM, Aleskerova ZF, Ismailov EH. Catalytic activity of copper ferrite synthesized with the using of microwave treatment in the oxidation reaction of carbon monoxide. AJCN. 2020;2(2):29–35.

37. Tang Z-R, Kondrat SA, Dickinson C, Bartley JK, Carley AF, Taylor SH, et al. Synthesis of high surface area $CuMn_2O_4$ by supercritical anti-solvent precipitation for the oxidation of CO at ambient temperature. Catal Sci Technol [Internet]. 2011 Jul 18;1(5):740–6. Available from: <URL>.

38. Sun R, Zhang S, An K, Song P, Liu Y. $Cu_{1.5}Mn_{1.5}O_4$ spinel type composite oxide modified with CuO for synergistic catalysis of CO oxidation. J Fuel Chem Technol [Internet]. 2021 Jun 1;49(6):799–808. Available from: <URL>.

39. Grillo F, Natile MM, Glisenti A. Low temperature oxidation of carbon monoxide: the influence of water and oxygen on the reactivity of a Co_3O_4 powder surface. Appl Catal B Environ [Internet]. 2004 Apr 8;48(4):267–74. Available from: <URL>.

40. Han SW, Kim DH, Jeong M-G, Park KJ, Kim YD. CO oxidation catalyzed by NiO supported on mesoporous Al_2O_3 at room temperature. Chem Eng J [Internet]. 2016 Jan 1;283:992–8. Available from: <URL>.

41. Xie X, Li Y, Liu Z-Q, Haruta M, Shen W. Low-temperature oxidation of CO catalysed by Co_3O_4 nanorods. Nature [Internet]. 2009 Apr 9;458:746–9. Available from: <URL>.

42. Singh SA, Madras G. Detailed mechanism and kinetic study of CO oxidation on cobalt oxide surfaces. Appl Catal A Gen [Internet]. 2015 Sep 5;504:463–75. Available from: <URL>.

43. Gómez LE, Tiscornia IS, Boix A V., Miró EE. Co/ZrO_2 catalysts coated on cordierite monoliths for CO preferential oxidation. Appl Catal A Gen [Internet]. 2011 Jul 15;401(1–2):124–33. Available from: <URL>.

44. Alvarez A, Ivanova S, Centeno MA, Odriozola JA. Sub-ambient CO oxidation over mesoporous Co_3O_4:

Effect of morphology on its reduction behavior and catalytic performance. Appl Catal A Gen [Internet]. 2012 Jul 26;431–432:9–17. Available from: <URL>.

45. Jansson J. Low-Temperature CO Oxidation over Co_3O_4/Al_2O_3. J Catal [Internet]. 2000 Aug 15;194(1):55–60. Available from: <URL>.

46. Lima TM, Castelblanco WN, Rodrigues AD, Roncolatto RE, Martins L, Urquieta-González EA. CO oxidation over Co-catalysts supported on silica-titania – The effects of the catalyst preparation method and the amount of incorporated Ti on the formation of more active Co^{3+} species. Appl Catal A Gen [Internet]. 2018 Sep 5;565:152–62. Available from: <URL>.

47. Lou Y, Wang L, Zhao Z, Zhang Y, Zhang Z, Lu G, et al. Low-temperature CO oxidation over Co_3O_4-based catalysts: Significant promoting effect of Bi_2O_3 on Co_3O_4 catalyst. Appl Catal B Environ [Internet]. 2014 Mar 1;146:43–9. Available from: <URL>.

48. Ma L, Seo CY, Chen X, Sun K, Schwank JW. Indium-doped Co_3O_4 nanorods for catalytic oxidation of CO and C_3H_6 towards diesel exhaust. Appl Catal B Environ [Internet]. 2018 Mar 1;222:44–58. Available from: <URL>.

49. Molchanov V V., Buyanov RA, Pavlyukhin YT. Effect of Mechanochemical Activation on the Catalytic Properties of Ferrites with the Spinel Structure. Kinet Catal [Internet]. 2003 Nov;44(6):788–92. Available from: <URL>.

50. Manova E, Tsoncheva T, Paneva D, Popova M, Velinov N, Kunev B, et al. Nanosized copper ferrite materials: Mechanochemical synthesis and characterization. J Solid State Chem [Internet]. 2011 May 1;184(5):1153–8. Available from: <URL>.

51. Rakhmankulov DL, Bikbulatov IK, Shulaev NS, Shavshukova SY. Microwave radiation and intensification of chemical processes. Chemistry Puplication. Moscow; 2003. 220 p.

52. Vanetsev AS, Tretyakov YD. Microwave-assisted synthesis of individual and multicomponent oxides. Russ Chem Rev [Internet]. 2007 May 31;76(5):397–413. Available from: <URL>.

53. Litvishkov YN, Zul'fugarova SM, Aleskerova ZF, Gasangulieva NM, Shakunova N V., Aleskerov AG. Microwave Synthesis of Co, Ni, Cu, Zn Ferrites. Russ J Appl Chem [Internet]. 2018 May 25;91(5):793–801. Available from: <URL>.

54. Zhou Y, Liu X, Wang K, Li J, Zhang X, Jin X, et al. Porous Cu-Mn-O catalysts fabricated by spray pyrolysis method for efficient CO oxidation. Results Phys [Internet]. 2019 Mar 1;12:1893–900. Available from: <URL>.

55. Brusentsov YA, Minaev A.M. Fundamentals of physics and technology of oxide semiconductors. Tambov; 2002. 80 p.

Electrochemical Study of 17β-estradiol and its Determination in Pharmaceutical Preparations using Square Wave Voltammetry

Bilal Yilmaz[1]* iD **, Yucel Kadioglu[1]** iD

[1]Ataturk University, Faculty of Pharmacy, Department of Analytical Chemistry, 25240, Erzurum, Turkey

Abstract: In the present study, the electroanalytical behavior of 17β-estradiol was investigated using cyclic voltammetry. The procedure was based on 17β-estradiol being electrochemically oxidized at a platinum electrode in non-aqueous solutions. At 1.47 V, the oxidation peak was noted. It was discovered that 17β-estradiol's oxidation was diffusion-controlled. Additionally, a quick and easy square wave voltammetry method was developed and validated in this work to determine 17β-estradiol in pharmaceutical preparations. The calibration curve was linear at 5 and 30 µg/mL concentrations. The precision was given by relative standard deviation and was less than 3.36%. Accuracy was given with relative error and did not exceed 2.54%. In pharmaceutical preparations, 17β-estradiol had an average recovery of 100.3%. Under the chosen experimental conditions, no interference was found. The suggested method is highly accurate and precise. Therefore, the method applies to measuring 17β-estradiol in pharmaceutical formulations.

1. INTRODUCTION

The most substantial naturally-occurring human estrogen is 17β-estradiol (Figure 1) [1]. This hormone, also known chemically as 1,3,5(10)-estratrien-3,17-diol, is the most potent among endogenous estrogen steroids, including estrone and estriol. 17β-estradiol is primarily responsible for the development of secondary sexual characteristics, the formation of breast and reproductive epithelia, as well as the maturation of long bones.
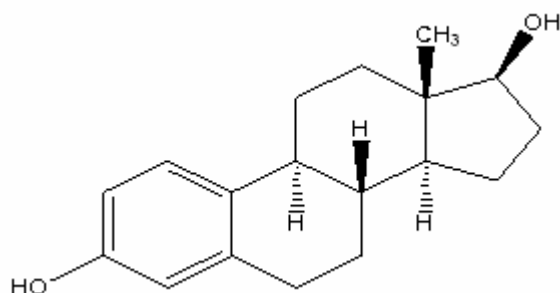
Figure 1: Chemical structure of 17 β-estradiol.

The primary application of 17β-estradiol and its semi-synthetic esters is as menopausal hormone replacement. Additionally, they can serve as alternative treatments for primary ovarian failure or female hypogonadism. When 17β-estradiol levels decline during menopause, it often results in vascular instability, increased incidence of heart disease, and heightened risk of osteoporosis (2). Various techniques for determining 17β-estradiol have been published, including spectrophotometry (3) and high-performance liquid chromatography (4-9). Furthermore, many gas chromatography-mass spectrophotometry (GC-MS) techniques for quantifying 17β-estradiol and its metabolites have been documented (10-16).

A comprehensive literature survey has revealed a broad spectrum of chromatographic techniques for detecting 17β-estradiol in human plasma. However, the reported methods can be hindered by endogenous interference, potential drug loss during re-extraction, labor-intensive and time-consuming processes for preparing and extracting plasma samples, and the requirement of expensive equipment.
Developing a new method for calculating medication dosage in pharmaceutical dosage

forms is vital. Electroanalytical techniques, which often do not require derivatization and are less prone to matrix effects than other analytical techniques, have been utilized to identify numerous medicinal compounds. Another application of electrochemistry involves elucidating electrode mechanisms. The redox properties of drugs can provide insights into their pharmacological potency, in vivo redox activities, or metabolic fate.

Despite the analytical significance of the electrochemical behavior and oxidation mechanism of 17β-estradiol, no research on its voltammetric oxidation in non-aqueous media has been published. Given that experimental and operational parameters directly influence the electrochemical process and the voltammetric response of pharmaceuticals, investigating how 17β-estradiol oxidizes in aprotic environments would be intriguing. However, the voltammetry method has not yet been utilized to assess 17β-estradiol using a platinum electrode quantitatively. The primary objective of this work was to develop a novel square wave voltammetry (SWV) method for swiftly and accurately evaluating 17β-estradiol in pharmaceutical preparations without requiring labor-intensive extraction or evaporation procedures prior to drug testing.

This study describes SWV methods using a platinum disc electrode to determine 17β-estradiol via simple, quick, and selective processes that have been thoroughly validated. Additionally, the technique was effectively applied to evaluate the consistency of formulation content and to quantitate a commercially available 17β-estradiol medication for quality control.

2. EXPERIMENTAL SECTION

2.1. Chemicals
17β-estradiol standard (98≥ purity), lithium perchlorate (LiClO$_4$), and acetonitrile were purchased from Sigma (Germany). Estrofem tablet that included 2 mg 17β-estradiol was purchased from a pharmacy (Erzurum, Turkey).

2.2. Electrochemical Instrumentation
Using the software PHE 200 and PV 220, electrochemical experiments were carried out on a Gamry Potentiostat Interface 1000. The single-compartment electrochemical cell used for all tests has a conventional three-electrode setup. Platinum wire was the counter electrode, and a platinum disk was the working electrode. The reference electrode for each potential was Ag/AgCl/KCl (3.0 M). The SWV was operated at pulse amplitudes of 25 mV, 10 Hz, 4 mV potential step, and 0.1 V/s scan rate.

2.3. Preparation of Standard Solutions
In 0.1 M LiClO$_4$/acetonitrile, the stock standard solution of 17β-estradiol (100 μg/mL) was prepared. This stock solution was used to prepare working standard solutions. The concentrations of the standard solutions were 5, 7.5, 10, 15, 20, 25, and 30 μg/mL. The QC solutions were created at 7.5, 12.5, and 27.5 μg/mL concentrations.

3. RESULTS AND DISCUSSION

3.1. Development and Optimization of the Method
The electrochemical behavior of 17β-estradiol was studied at the Pt disc electrode. An acetonitrile solution with 0.1 M LiClO$_4$ was the supporting electrolyte in cyclic voltammetry. Figure 2 depicts a typical cyclic voltammogram for 100 μg/mL 17β-estradiol at 0.1 V/s scan rate. The oxidation peak was seen in the anodic sweep at 1.47 V.
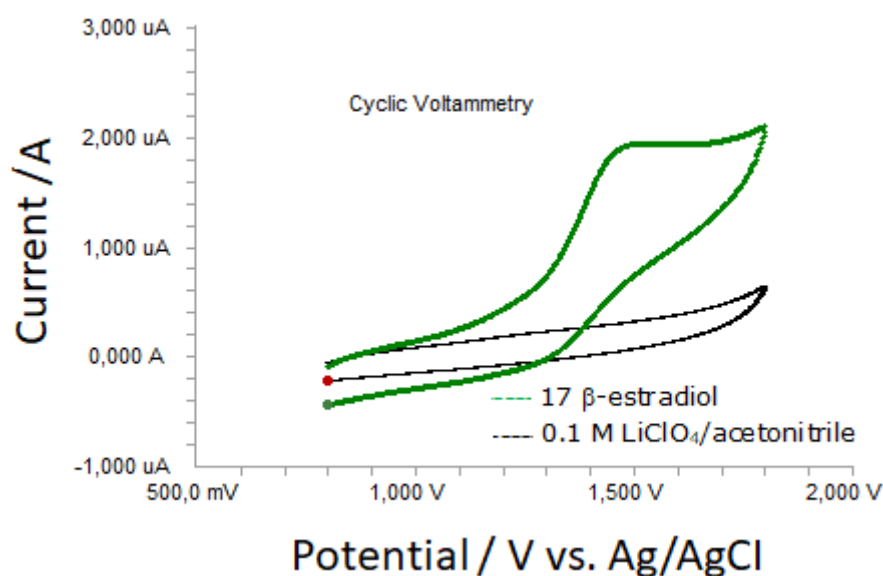
Figure 2: Cyclic voltammogram of 17β-estradiol (30 μg/mL)

The influence of scan rate on the anodic peak currents and peak potentials was investigated in the range of 0.01-1 V/s (Figure 3).
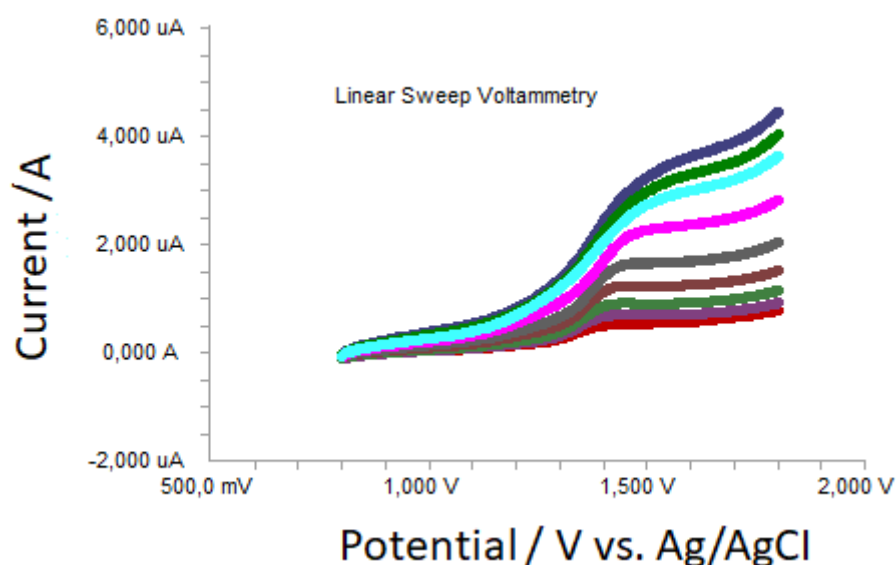
Figure 3: Linear sweep voltammograms of 30 µg/mL 17β-estradiol as a function of scan rate

Figure 4a,b shows the linear sweep voltammograms for 17β-estradiol as a function of scan rate. However, at 17β-estradiol concentrations of 30 µg/mL, the logarithm of peak currents against the logarithm of scan rates graphs display straight lines with a slope of 0.39 (Figure 4c), which is close to the predicted value of 0.5 anticipated for an ideal diffusion-controlled electrode process (17).

In order to accomplish this, the *log I-log v* curve is more suitable; therefore, a diffusional process for the peak should be considered. These findings show that the redox species readily diffuse from the solution instead of precipitating onto the electrode surface. This phenomenon can be brought on by either a lack of product adhesion to the electrode surface or the solubility of the intermediate species in acetonitrile.

$$y = 0{,}0029x + 0{,}7229$$
$$R^2 = 0{,}9902$$
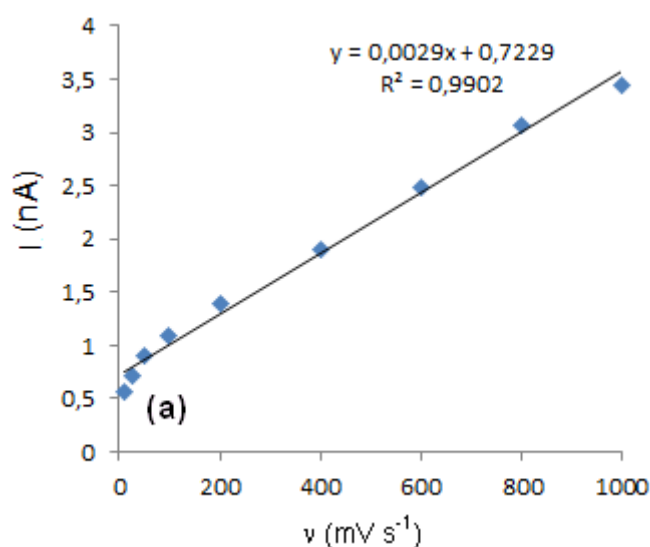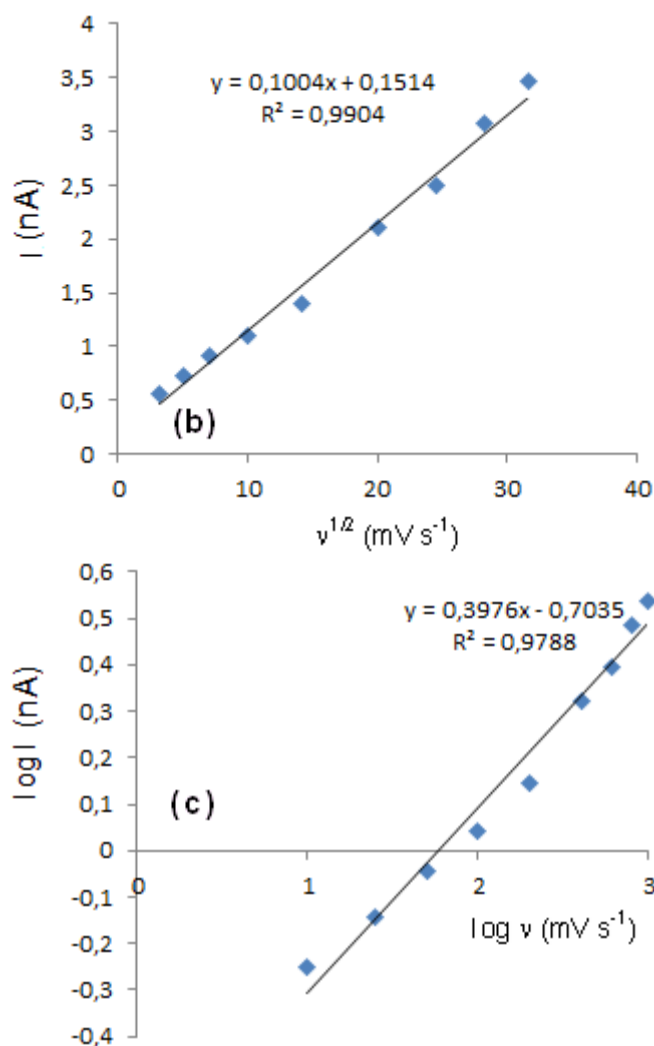
Figure 4(a-c): Peak current dependence on scan rate (30 μg/mL).

Figure 3 shows the oxidation peak potential (Epa) movement for peaks toward higher positive values as the scan rate increases. The equation below (18) describes the relationship between the peak potential and scan rate,

$$E_{pa} = E^{0'} + RT / \left[(1-\alpha) n_a F \right] \left[0.78 + \ln \left(D^{1/2} k_s^{-1} \right) - 0.5 \ln RT / \left[(1-\alpha) n_a F \right] \right] + RT / \left[(1-\alpha) n_a F \right] / 2 \ln v$$

and from the variation of peak potential with scan rate, αn_a can be determined, where α is the transfer coefficient, and n_a is the number of electrons transferred in the rate-determining step. The plots of the oxidation peak potentials against *ln v* demonstrate a linear connection in accordance with this equation (Figure 5).

$$y = 20{,}59x + 1344{,}8$$
$$R^2 = 0{,}9867$$
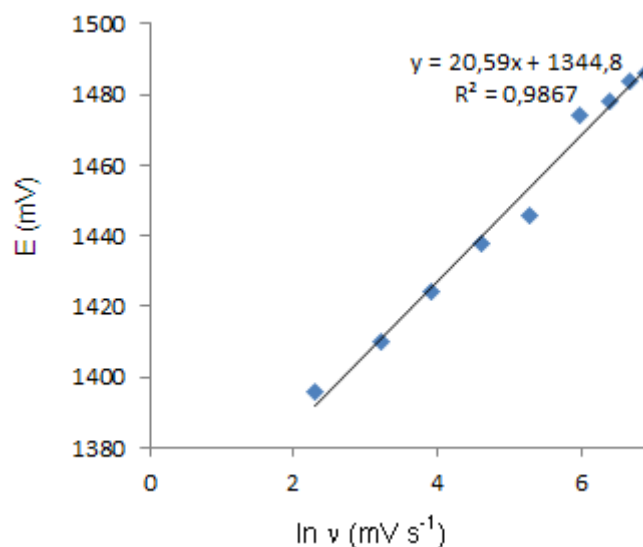
Figure 5: Dependence of the 17β-estradiol anodic peak potentials on the scan rate

The slope indicates that the highest value of αn is 9.41. Additionally, this value shows that the electron transfer processes are entirely irreversible. This outcome demonstrates that the chemical step is a charge transfer and a quick following reaction.

3.2. Validation of the Method
ICH Q2B guidelines were followed while determining the validation parameters (19). These criteria include specificity, linearity, precision, accuracy, recovery, the limit of detection (LOD), limit of quantification (LOQ), ruggedness, and stability.

3.2.1. Specificity
In this study, it was investigated the potential interferences of common excipients and additives. The control samples were prepared and examined. There is no evidence of any interference from these chemicals at the concentrations in dosage forms. The excipient employed in this formulation was one that the pharmaceutical industry employs most frequently. The method's specificity was examined by examining for any interference from common tablet ingredients like talc, lactose, sodium chloride, titanium dioxide, and magnesium stearate. These exceptions had no adverse effects on the suggested method. The procedure might be specific in accordance with the findings of the analysis.

3.2.2. Linearity
Standard solutions at concentrations of 5, 7.5, 10, 15, 20, 25, and 30 µg/mL were prepared for SWV (Figure 6). Plotting the 17β-estradiol concentration versus peak current responses allowed constructing the calibration curve for the 17β-estradiol (Figure 7).
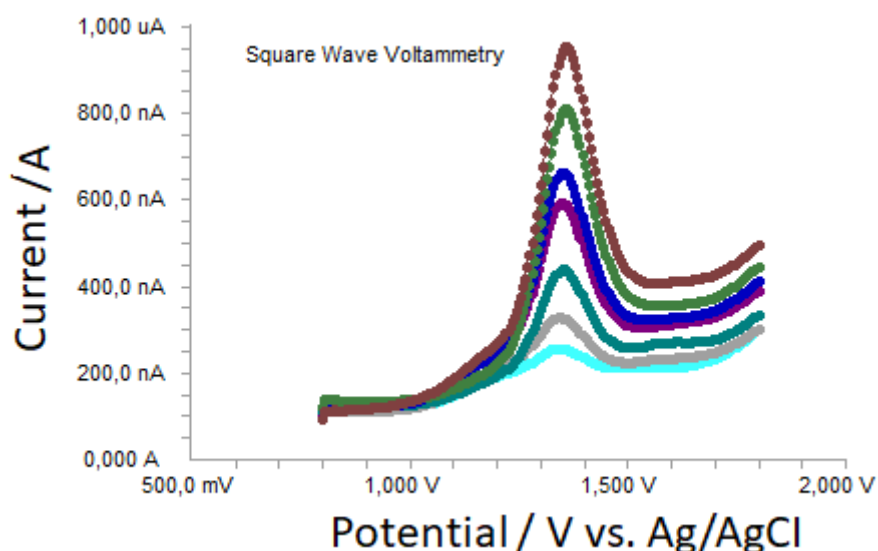
Figure 6: SWV voltammograms of 17 β-estradiol.
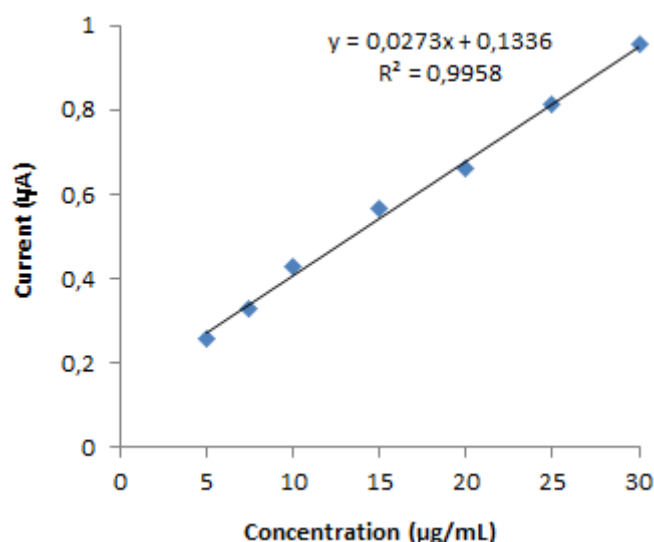
Figure 7: Calibration curve of 17 β-estradiol.

All calibration curves' correlation coefficients (r) were consistently higher than 0.99. Using the least squares method and the Microsoft Excel® application, the linear regression equations were derived and described in Table 1.

Table 1: Linearity of 17 β-estradiol.

Parameters	17β-estradiol
Linearity range (µg/mL)	5-30
Slope	0.0273
Intercept	0.1336
Correlation coefficient	0.9958
LOD (µg/mL)	1.00
LOQ (µg/mL)	3.00

3.2.3. Precision and accuracy
The precision and accuracy of the square wave voltammetry (SWV) method were evaluated for intra-day and inter-day measurements using quality control (QC) samples. Intra-day precision and accuracy were assessed by analyzing the QC samples on the same day. Inter-day precision and accuracy were evaluated by comparing the assays conducted on two different days. The results showed that the intra-day accuracy ranged from 1.09% to 1.33%, and the precision ranged from 0.95% to 3.36% (Table 2). These findings indicate that the SWV method demonstrates good accuracy and precision in this study.

Table 2: Precision and accuracy of 17 β-estradiol.

	Intra-day			Inter-day		
Added (µg/mL)	Found ± SD[a]	Precision % RSD[b]	Accuracy[c]	Found ± SD[a]	Precision % RSD[b]	Accuracy[c]
7.5	7.6 ± 0.205	2.70	1.33	7.4 ± 0.142	1.92	-1.33
12.5	27.2 ± 0.914	3.36	-1.09	26.8 ± 0.821	3.06	-2.54
27.5	44.5 ± 0.424	0.95	-1.11	45.9 ± 0.532	1.16	2.00

3.2.4. Recovery
At three different concentrations, the recovery was examined to investigate the impacts of formulation interference. The recoveries were carried out by mixing pre-analyzed samples of 17β-estradiol tablets with a known quantity of pure medicines. The recoveries were calculated by comparing the amounts extracted from the spiked samples with the actually added concentrations. The results are listed in Table 3.

Table 3: Recovery of 17β-estradiol in tablets (n=6).

Tablet	Added (μg/mL)	Found ± SD	%Recovery	%RSD
Estrofem (10 μg/mL)	5	4.9 ± 0.131	98.0	2.67
	15	14.9 ± 0.312	99.3	2.09
	25	25.3 ± 0.684	101.2	2.70

3.2.5. LOD and LOQ
The suggested technique's LOD and LOQ values were calculated using calibration standards. LOD and LOQ values were calculated as 3.3 /S and 10 /S, respectively (19). In this equation, S is the calibration curve's slope and is the y-intercept's standard deviation (n=6). The results are summarized in Table 1.

3.2.6. Ruggedness
A separate analyst used the same instrument and standard solution in this study to assess the concentration of 17β-estradiol (Table 4). No statistically significant discrepancies between the operators were found in the results, indicating the ruggedness of the developed method.

Table 4: Results of another analyst's studies of 17β-estradiol (n=6).

Method	Added (μg/mL)	Found (μg/mL) (Mean±SD)	% Recovery	% RSD
	5	5.1 ± 0.12	102.0	2.35
SWV	15	14.9 ± 0.21	99.3	1.41
	35	35.1 ± 1.07	100.2	3.04

3.2.7. Stability
The stability of 17β-estradiol stock solution was examined over a period of at least 72 hours. Furthermore, 17β-estradiol standard solutions were stable for 72 hours at 4 and -20 °C refrigeration temperatures and ambient temperature. The 17β-estradiol accuracy is within the acceptable range of 90 to 110% (Table 5). There are no major 17β-estradiol breakdown products under these circumstances.

Table 5: 17 β-estradiol's stability at various temperatures (n = 6).

Added (μg/mL)	Room temperature 24 h (Mean ± SD)	Room temperature 72 h (Mean ± SD)	Refrigeratory +4 °C, 72 h (Mean ± SD)	Frozen -20 °C, 72 h (Mean ± SD)
15	100.7 ± 2.57	100.3 ± 1.71	101.2 ± 1.67	98.6 ± 3.71
30	98.9 ± 1.77	98.9 ± 2.16	100.2 ± 1.96	98.7 ± 2.73
45	99.6 ± 2.19	101.2 ± 2.37	98.8 ± 2.27	101.7 ± 3.09

3.3.   Procedure   for   Pharmaceutical Preparations
Estrofem tablet containing 2 milligrams of 17β-estradiol was precisely weighed and finely powdered. A suitable amount of powder was dissolved in 50 mL of 0.1 M LiClO$_4$/acetonitrile. Then, the final volume was made up to 100 mL in a balloon flask. Whatman filter (paper no 42) was used to filter the tablet solutions after they had been properly diluted in order to provide a final concentration that was within the linearity constraints of the SWV method (Figure 8). The calibration curve determined the drug concentration for 17β-estradiol (Table 6).
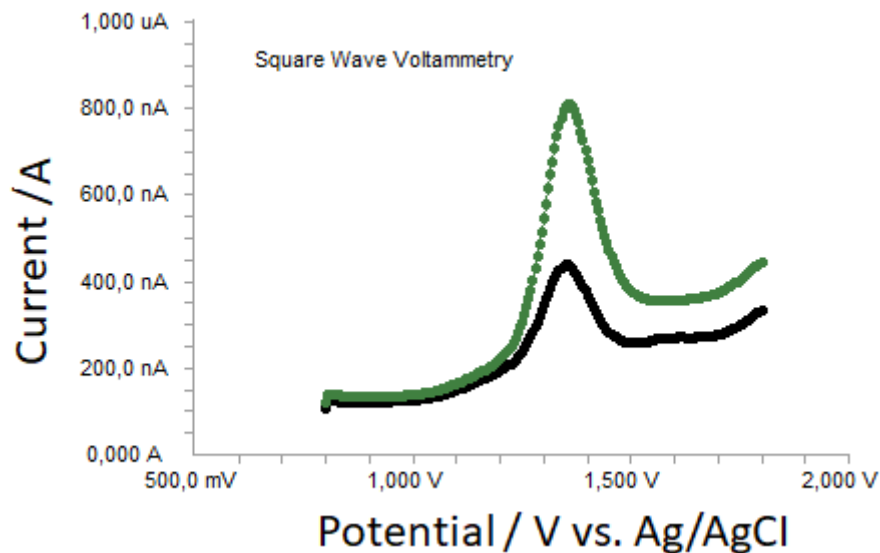
Figure 8: The voltammograms of Estrofem tablet containing 17 β-estradiol.

For the analysis of associated compounds in pure 17β-estradiol and the assay of 17β-estradiol in pharmaceutical dosage form (tablet), the United States Pharmacopoeia (20) has recommended the liquid chromatography (HPLC) method. The method suggested uses a stainless steel column (5 µm, 4.6 mm, 250 mm i.d.) with UV detection (280 nm) and a mobile phase of 2,2,4-trimethylpentane-n-butyl chloride-methanol (45:4:1, v/v) at a flow rate of 2 mL/min. In contrast, the previously described HPLC technique (5) uses methanol as the mobile phase instead of buffered systems.

The proposed SWV approach was relatively quick compared to previously published and authorized methods for estimating 17β-estradiol in pharmaceutical formulations (3,10,11). The sample recoveries in a formulation aligned with the claims made on the corresponding labels. Additionally, the reported methods (3) and the new SWV method were statistically evaluated using the F-test. The computed F-values do not exceed the theoretical values at a 95% confidence level (Table 6).

Table 6. Comparison of the proposed and reported methods for determination of 17 β-estradiol.

Parameters	SWV	Reported Method (3) (Spectrophotometry)	Reported Method (3) (HPLC)
Mean (Recovery %)	100.3	101.6	100.2
SD	1.29	0.038	0.060
%RSD	1.28	0.52	0.60
Variance	1.66	0.270	0.360
F-test	3.07		

SD: Standard deviation, RSD: relative standard deviation, Ho is acceptable (P > 0.05) since there is no statistically significant difference between the three methods.

The analytical findings in this investigation showed that the level of the active ingredient in the medicine is within the pharmacopeia's recommended range. The developed method was practical, accurate, and adaptable to drug dose forms. Therefore, the developed SWV method can be advised for the routine QC analyses of 17β-estradiol in pharmaceutical preparations.

4. CONCLUSION

In the current work, the CV method has been used to examine the electrochemical behavior of 17β-estradiol in non-aqueous media. Additionally, a quick, accurate, specific, and precise SWV method was developed and validated in the Study for detecting 17β-estradiol in pharmaceutical

formulations. Voltammetry runs for one minute. The method enables the speedy analysis of a large number of samples. As a result, the method can regularly examine 17β-estradiol in both its formulations and pure form.

5. CONFLICT OF INTEREST

The authors state that they did not have a conflict of interest.

6. REFERENCES

1. Koga AY, Carletto B, Lipinski LC, Klein T, Farago PV. Development and validation of an high-performance

lıquid chromatography method for the determination of 17 β-estradiol in polymeric nanoparticles. Asian Journal of Pharmaceutical and Clinical Research. 2021;14(5):112-16. Available from: <URL>

2. Schulster M, Bernie AM, Ramasamy R. The role of estradiol in male reproductive function. Asian Journal of Andrology. 2016;18:1-6. Available from: <URL>

3. Yilmaz B, Kadioglu Y. Determination of 17 β-estradiol in pharmaceutical preparation by UV spectrophotometry and high performance liquid chromatography methods, Arabian Journal of Chemistry. 2017;10 (1):S1422-28. Available from: <URL>

4. Lamparczyk H, Zarzycki PK, Nowakowska J, Ochocka RJ. Application of β-cyclodextrin for the analysis of estrogenic steroids in human urine by high-performance liquid chromatography. Chromatographia. 1994;38:168-72. Available from: <URL>

5. Yamada H, Yoshizawa K, Hayase T. Sensitive determination method of estradiol in plasma using high-performance liquid chromatography with electrochemical detection. Journal of Chromatography B. 2002;775:209-13. Available from: <URL>

6. Yan Q, Yang L, Li S. Solid-phase extraction combined with high performance liquid chromatography-diode array detector for rapid determination of estrogens in milk. Tropical Journal of Pharmaceutical Research. 2015;14:2077–82. Available from: <URL>

7. Afifi R, Elnwishy N, Hannora A, Hedström M, Mattiasson B, Omran H, Alharbi OML, Ali I. SPE and HPLC monitoring of 17-β-estradiol in Egyptian aquatic ecosystems. Journal of Liquid Chromatography & Related Technologies. 2016;39:428–34. Available from: <URL>

8. Shahbazi Y, Malekinejad H, Tajik H. Determination of naturally occurring estrogenic hormones in cow's and river buffalo's meat by HPLC-FLD method. Journal of Food and Drug Analysis. 2016;24:457-63. Available from: <URL>

9. Ingrand V, Herry G, Beausse J, De Roubin MR, Analysis of steroid hormones in effluents of wastewater treatment plants by liquid chromatography-tandem mass spectrometry. Journal of Chromatography A. 2003;1020:99-104. Available from: <URL>

10. Zacharia LC, Dubey RK, Jackson EK, A gas chromatography-mass spectrometry assay to measure estradiol, catecholestradiols, and methoxyestradiols in plasma. Steroids. 2004;69:255-61. Available from: <URL>

11. Azzouz A, Jurado-Sánchez B, Souhail B, Ballesteros E. Simultaneous determination of 20 pharmacologically active substances in cow's milk, goat's milk, and human breast milk by gas chromatography-mass spectrometry. Journal of Agricultural and Food Chemistry. 2011;59:5125–32. Available from: <URL>

12. Adlercreutz H, Martin F, Wahlroos O, Soini E. Mass spectrometric and mass fragmentographic determination of natural and synthetic steroids in biological fluids. Journal of Steroid Biochemistry. 1975;6:247-59. Available from: <URL>

13. Stanczyk FZ, Clarke NJ. Advantages and challenges of mass spectrometry assays for steroid hormones. Journal of Steroid Biochemistry and Molecular Biology. 2010;121(3–5):491-95. Available from: <URL>

14. Zuchowska IM, Wozniak B, Posyniak A. Determination of hormones residues in milk by gas chromatography-mass spectrometry. Food Analytical Methods. 2017;10:727-39. Available from: <URL>

15. Castagnetta LA, Granata OM, Arcuri FP, Polito LM, Rosati F, Cartoni GP. Gas chromatography-mass spectrometry of catechol estrogens. Steroids. 1992;57:437-43. Available from: <URL>

16. B.C. Chung, J.-Y. Moon, M.H. Moon, M.H. Choi, K.J. Kim, A novel GC-MS method in urinary estrogen analysis from postmenopausal women with osteoporosis. Journal of Lipid Research. 2011;52:1595-1603. Available from: <URL>

17. Laviron E, Roullier L, Degrand C. A multilayer model for the Study of space distributed redox modified electrodes: Part II. theory and application of linear potential sweep voltammetry for a simple reaction. Journal of Electroanalytical Chemistry. 1980;112:11-23. Available from: <URL>

18. Yilmaz B, Ekinci D. Voltammetric behavior of carvedilol in non-aqueous media and its analytical determination in pharmaceutical preparations. Reviews in Analytical Chemistry. 2011;30:187-93. Available from: <URL>

19. The European Agency for the Evaluation of Medicinal Products. ICH Topic Q2B Note for Guideline on Validation of Analytical Procedures: Methodology GPMP/ICH/281/95, 1996. Available from: <URL>

20. The United States Pharmacopoeia, United States Pharmacopoeial Convention, 24th ed. Rockville, USA, 2000; 676-680. Available from: <URL>

Synthesis of S-(5-aryl-1,3,4-oxadiazol-2-yl) O-alkyl carbonothioate and alkyl 2-((5-aryl-1,3,4-oxadiazol-2-yl)thio) acetate, and their antimicrobial properties

Abdukhakim A. Ziyaev[1] , **Sobirdjan A. Sasmakov[1]*** , **Turdibek T. Toshmurodov[1]** ,

Mavluda A. Ziyaeva[2] , **Jaloliddin M. Abdurakhmanov[1]** , **Shukhrat Sh. Khasanov[1]** ,

Shakhnoz S. Azimova[1]

[1]Acad. S.Yu. Yunusov Institute of the Chemistry of Plant Substances, Academy of Sciences of the Republic of Uzbekistan, Mirzo Ulugbek Str. 77, Tashkent, 100170, Uzbekistan
[2]Tashkent state Technical University named after I. Karimov, Universitetskaya-2 Str., Tashkent, 100095, Uzbekistan

Abstract: The S-(5-aryl-1,3,4-oxadiazol-2-yl) O-alkyl carbonothioate (4-9) and the alkyl 2-((5-aryl-1,3,4-oxadiazol-2-yl)thio) acetate (10-15) were synthesized by interaction of 5-aryl-1,3,4-oxadiazole-2-thiones with alkyl esters of chloroformic acid and chloroacetic acid. The yields of target compounds (7-9) obtained with isobutyl chloroformate were 69-73%, compounds (4-6) with propyl chloroformate - 74-79% and compounds (10-15) with alkyl esters of chloroacetic acid - 86-92%, respectively. The structures of the synthesized compounds were confirmed by IR, UV, ^{1}H and ^{13}C NMR spectra. The antibacterial and antifungal activities of these compounds were investigated. The results of in *vitro* antimicrobial activity tests showed that S-(5-phenyl(2-chlorophenyl)-1,3,4-oxadiazol-2-yl) O-propyl carbonothioate (4-5) and S-(5-phenyl(2-chlorophenyl)-1,3,4-oxadiazol-2-yl) O-isobutyl carbonothioate (7-8) exhibited weak, but selective antibacterial activity against gram-positive bacteria (*Bacillus subtilis* and *Staphylococcus aureus*). At the same time, no activity was shown by compounds with two chlorine atoms in the aromatic ring (13-15) and alkyl 2-((5-aryl-1,3,4-oxadiazol-2-yl) thio) acetate (10-15).

1. INTRODUCTION

A wide interest in the chemistry of derivatives of 5-substituted-1,3,4-oxadiazole-2-thiones is associated with a broad variety of biological and physiological activities exhibited by their derivatives. Recently, numerous works on synthesis and biological activities such as antibacterial, antifungal, antiviral, anticonvulsant, anti-inflammatory, antitumor of 5-substituted-1,3,4-oxadiazole-2-thione derivatives were reported (1-10). A distinctive structural feature of 5-aryl-1,3,4-oxadiazol-2-thiones is the presence of an ambient thioamide group NH-C=S in their molecule, therefore, depending on the nature of the attacking electrophilic agent, derivatives can be obtained at the exocyclic sulfur atom, and on the endocyclic nitrogen atom or simultaneously on both reaction centers (S- or N-). Continuing the research (11-13) on the synthesis of various derivatives of oxadiazole-2-thiones, in this work we have investigated the synthesis of derivatives of S-(5-aryl-1,3,4-oxadiazol-2-yl)O-alkyl carbonothioate and alkyl 2-((5-aryl-1,3,4-oxadiazol-2-yl)thio)acetate, as well as their antimicrobial activity.

2. EXPERIMENTAL SECTION

2.1. General Considerations
UV spectra of the synthesized compounds were recorded on the Perkin Elmer Lambda-16 spectrophotometer in ethanol, IR spectra on the FTIR system-2000 (Perkin Elmer) Fourier spectrometer in KBr tablets. ^{1}H and ^{13}C NMR spectra were recorded on a Unity 400 spectrometer at working frequencies 400 and 100 MHz, respectively, at 20-25°C in CDCl$_3$, with HMDS internal standard. The reaction flow and the individuality of the obtained compounds were controlled by TLC on ALUGRAM® SIL G/UV254 plates in the CHCl3-EtOH system, 24:1, visualization in UV light. Melting points were determined using a Boethius hot-stage microscope.

2.2. General Procedure for the Synthesis of S-(5-aryl-1,3,4-oxadiazol-2-yl) O-alkyl carbonothioate 4-9 and alkyl 2-((5-aryl-1,3,4-oxadiazol-2-yl)thio)acetate (10-15).
5-Aryl-1,3,4-oxadiazole-2-thions (**1-3**) were synthesized according to the method (14).
Equimolar amounts of 5-aryl-1,3,4-oxadiazole-2-thion, corresponding alkyl esters of chloroformic acid (alkyl chloroformates) or chloroacetic acid and K$_2$CO$_3$ were boiled in dry acetone for 5 hours. The reaction was controlled by TLC. Then the solvent was removed from the mixture. The residue was sequentially washed with water, NaOH solution (2-3%) and then again with water until a neutral reaction. After air drying, target products (**4-15**) were obtained.

2.2.1. S-(5-phenyl-1,3,4-oxadiazol-2-yl) O-propyl carbonothioate (4)
White powder, yield 74%, mp 89-90°C (from ethanol); R$_f$ = 0,66; UV (ethanol), λ$_{max}$ (nm): 286. IR (KBr, cm^{-1}) v: 1788 (COOC$_3$H$_7$), 1220 (C-O-C, oxadiazole). ^{1}H NMR (400 MHz, CDCl$_3$, δ, ppm): 1.05 (3H, t, J = 7.4 Hz, CH$_3$), 1.86 (2H, sextet, J = 7.3 Hz, CH$_2$-CH$_3$), 4.44 (2H, t, J = 6.6 Hz, O-CH$_2$), 7.50 (2H, t, J = 7.2 Hz, ArH-3', 5'), 7.59 (1H, t, J = 7.4 Hz, ArH-4'), 7.98 (2H, dd, J = 7.2, 1.4 Hz, ArH-2', 6'). ^{13}C NMR (100 MHz, CDCl$_3$): δ 10.38 (C-11), 21.95 (C-10), 71.15 (C-9), 121.64 (C-1'), 127.21 (C-2', 6'), 129.31 (C-3', 5'), 133.25 (C-4'), 148.19 (C-2), 158.55 (C-5), 174.10 (C-7).

2.2.2. S-(5-(2-chlorophenyl)-1,3,4-oxadiazol-2-yl) O-propyl carbonothioate (5)
White powder, yield 69%, mp 84-85°C (from ethanol); R$_f$ = 0,61; UV (ethanol), λ$_{max}$ (nm): 283; IR (KBr, cm^{-1}) v: 1769(COOC$_3$H$_7$), 1197(C-O-C, oxadiazole). ^{1}H NMR (400 MHz, CDCl$_3$, δ, ppm): 1.05 (3H, t, J = 7.4 Hz, CH$_3$), 1.85 (2H, sextet, J = 7.2 Hz, CH$_2$-CH$_3$), 4.44 (2H, t, J = 6.6 Hz, O-CH$_2$), 7.41 (1H, t, J = 7.1 Hz, ArH-4'), 7.51 (1H, t, J = 7.1 Hz, ArH-3'), 7.55 (1H, dd, J = 8.0, 1.2 Hz, ArH-2'), 7.90 (1H, dd, J = 7.9, 1.3 Hz, ArH-5'). ^{13}C NMR (100 MHz, CDCl$_3$): δ

10.36 (C-11), 21.94 (C-10), 71.17 (C-9), 120.91 (C-1'), 127.29 (C-3'), 131.10 (C-2'), 131.66 (C-5'), 133.66 (C-4'), 133.83 (C-6'), 148.01 (C-2), 156.82 (C-5), 173.62 (C-7).

2.2.3. S-(5-(2,4-dichlorophenyl)-1,3,4-oxadiazol-2-yl) O-propyl carbonothioate (6)
White powder, yield 73%, mp 132-133°C (from ethanol); R$_f$ = 0,63; UV (ethanol), λ$_{max}$ (nm): 284; IR (KBr, cm^{-1}) v: 1778 (COOC$_3$H$_7$), 1195 (C-O-C, oxadiazole). ^{1}H NMR (400 MHz, CDCl$_3$, δ, ppm): 1.05 (3H, t, J = 7.4 Hz, CH$_3$), 1.85 (2H, sextet, J = 7.4 Hz, CH$_2$-CH$_3$), 4.44 (2H, t, J = 6.6 Hz, O-CH$_2$), 7.40 (1H, dd, J = 8.5, 2.0 Hz, ArH-3'), 7.57 (1H, d, J = 2.0 Hz, ArH-5'), 7.86 (1H, d, J = 8.5 Hz, ArH-2'). ^{13}C NMR (100 MHz, CDCl$_3$): δ 10.35 (C-11), 21.94 (C-10), 71.25 (C-9), 119.41 (C-1'), 127.87 (C-3'), 131.73 (C-5', 2'), 134.66 (C-6'), 139.62 (C-4'), 147.92 (C-2), 156.05 (C-5), 173.28 (C-7).

2.2.4. S-(5-phenyl-1,3,4-oxadiazol-2-yl) O-isobutyl carbonothioate (7)
White powder, yield 67%, mp 98-99°C (from ethanol); R$_f$ = 0,63; UV (ethanol), λ$_{max}$ (nm): 286; IR (KBr, cm^{-1}) v: 1765 (COOCH$_2$(CH$_3$)$_2$), 1222 (C-O-C, oxadiazole). ^{1}H NMR (400 MHz, CDCl$_3$, δ, ppm): 1.04 (3H, s, CH$_3$), 1.06 (3H, s, CH$_3$), 2.15 (1H, septet, J = 6.7 Hz, CH(CH$_3$)$_2$), 4.26 (2H, d, J = 6.6 Hz, O-CH$_2$), 7.51 (2H, t, J = 7.8 Hz, ArH-3',5'), 7.59 (1H, t, J = 7.5 Hz, ArH-4'), 7.99 (2H, dd, J = 7.7 and 1.4 Hz, ArH-2', 6'). ^{13}C NMR (100 MHz, CDCl$_3$): δ 19.03 (C-11), 19.04 (C-12), 27.85 (C-10), 75.46 (C-9), 121.67 (C-1') 127.20 (C-2', 6'), 129.30 (C-3', 5'), 133.23 (C-4'), 148.21 (C-2), 158.59 (C-5), 174.11 (C-7).

2.2.5. S-(5-(2-chlorophenyl)-1,3,4-oxadiazol-2-yl) O-isobutyl carbonothioate (8)
White powder, yield 64%, mp 88-89°C (from ethanol); R$_f$ = 0,65; UV (ethanol), λ$_{max}$ (nm): 282; IR (KBr, cm^{-1}) v: 1787(COOCH$_2$(CH$_3$)$_2$), 1226(C-O-C, oxadiazole). ^{1}H NMR (400 MHz, CDCl$_3$, δ, ppm): 1.03 (3H, s, CH$_3$), 1.05 (3H, s, CH$_3$), 2.14 (1H, septet, J = 6.7 Hz, CH(CH$_3$)$_2$), 4.26 (2H, d, J = 6.5 Hz, O-CH$_2$), 7.41 (1H, t, J = 7.8 Hz, ArH-3'), 7.51 (1H, dd, J = 8.1 and 1.4 Hz, ArH-4'), 7.55 (1H, dd, J = 8.0, 1.3 Hz, ArH-2'), 7.90 (1H, dd, J = 7.8, 1.4 Hz, ArH-5'). ^{13}C NMR (100 MHz, CDCl$_3$): δ 18.99 (C-11,12), 27.84 (C-10), 75.44 (C-9), 120.90 (C-1'), 127.29 (C-3'), 131.06 (C-2'), 131.68 (C-5'), 133.64 (C-4'), 133.83 (C-6'), 148.02 (C-2), 156.81 (C-5), 173.61 (C-7).

2.2.6. S-(5-(2,4-dichlorophenyl)-1,3,4-oxadiazol-2-yl) O-isobutyl carbonothioate (9)
White powder, yield 68%, mp 130-131°C (from ethanol); R$_f$ = 0,66; UV (ethanol), λ$_{max}$ (nm): 285; IR (KBr, cm^{-1}) v: 1772(COOCH$_2$(CH$_3$)$_2$), 1211(C-O-C, oxadiazole). ^{1}H NMR (400 MHz, CDCl$_3$, δ, ppm): 1.03 (3H, s, CH$_3$), 1.05 (3H, s, CH$_3$), 2.14 (1H, septet, J = 6.7 Hz, CH(CH$_3$)$_2$), 4.26 (2H, d, J = 6.5 Hz, O-CH$_2$), 7.40 (1H, dd, J

= 8.5, 2.0 Hz, ArH-3'), 7.57 (1H, d, J = 1.9 Hz, ArH-5'), 7.86 (1H, d, J = 8.5 Hz, ArH-2'). ^{13}C NMR (100 MHz, CDCl$_3$): δ 18.99 (C-11,12), 27.84 (C-10), 75.51 (C-9), 119.40 (C-1'), 127.86 (C-3'), 131.70 (C-5', 2'), 134.66 (C-6'), 139.59 (C-4'), 147.92 (C-2), 156.05 (C-5), 173.28 (C-7).

2.2.7. Propyl 2-((5-phenyl-1,3,4-oxadiazol-2-yl)thio)acetate (10)

White powder, yield 89%, mp 67-68°C (from ethanol); R$_f$ = 0,68; UV (ethanol), λ$_{max}$ (nm): 280; IR (KBr, cm^{-1}) v: 1725(CH$_2$COOC$_3$H$_7$), 1176(C-O-C, oxadiazole). ^{1}H NMR (400 MHz, CDCl$_3$, δ, ppm): 0.92 (3H, t, J = 7.4 Hz, CH$_3$), 1.65 (2H, sextet, J = 7.2 Hz, CH$_2$-CH$_3$), 4.10 (2H, s, S-CH$_2$), 4.14 (2H, t, J = 6.7 Hz, O-CH$_2$), 7.45-7.53 (3H, m, ArH-3',5',4'), 7.97 (2H, dd, J = 7.6, 1.1 Hz, ArH-2',6'). ^{13}C NMR (100 MHz, CDCl$_3$): δ 10.37 (C-12), 21.94 (C-11), 34.49 (C-7), 68.04 (C-10), 123.55 (C-1'), 126.80 (C-2', 6'), 129.16 (C-3', 5'), 131.88 (C-4'), 163.02 (C-2), 166.18 (C-5), 167.63 (C-8).

2.2.8. Propyl 2-((5-(2-chlorophenyl)-1,3,4-oxadiazol-2-yl)thio)acetate (11)

White powder, yield 90%, mp 44-45°C (from ethanol), R$_f$ = 0,66; UV (ethanol): λ$_{max}$ (nm): 278; IR (KBr, cm^{-1}) v: 1726 (CH$_2$COOC$_3$H$_7$), 1179(C-O-C, oxadiazole). ^{1}H NMR (400 MHz, CDCl$_3$, δ, ppm): 0.92 (3H, t, J = 7.4 Hz, CH$_3$), 1.67 (2H, sextet, J = 6.8 Hz, CH$_2$-CH$_3$), 4.11 (2H, s, S-CH$_2$), 4.14 (2H, t, J = 6.7 Hz, O-CH$_2$), 7.38 (1H, t, J = 7.7 Hz, ArH-4'), 7.44 (1H, t, J = 7.9 Hz, ArH-3'), 7.52 (1H, dd, J = 8.0, 1.3 Hz, ArH-2'), 7.91 (1H, dd, J = 7.7, 1.8 Hz, ArH-5'). ^{13}C NMR (100 MHz, CDCl$_3$): δ 10.37 (C-12), 21.94 (C-11), 34.46 (C-7), 68.08 (C-10), 122.83 (C-1'), 127.20 (C-3'), 131.07 (C-2'), 131.36 (C-5'), 132.58 (C-4'), 133.15 (C-6'), 163.74 (C-2), 164.47 (C-5), 167.55 (C-8).

2.2.9. Propyl 2-((5-(2,4-dichlorophenyl)-1,3,4-oxadiazol-2-yl)thio)acetate (12)

White powder, yield 87%, mp 62-64°C (from ethanol), R$_f$ = 0,63; UV (ethanol): λ$_{max}$ (nm): 280; IR (KBr, cm^{-1}) v: 1742(CH$_2$COOC$_3$H$_7$), 1177(C-O-C, oxadiazole). ^{1}H NMR (400 MHz, CDCl$_3$, δ, ppm): 0.92 (3H, t, J = 7.4 Hz, CH$_3$), 1.67 (2H, sextet, J = 6.8 Hz, CH$_2$-CH$_3$), 4.11 (2H, s, S-CH$_2$), 4.13 (2H, t, J = 6.7 Hz, O-CH$_2$), 7.36 (1H, dd, J = 8.5, 2.0 Hz, ArH-3'), 7.53 (1H, d, J = 2.0 Hz, ArH-5'), 7.87 (1H, d, J = 8.5 Hz, ArH-2'). ^{13}C NMR (100 MHz, CDCl$_3$): δ 10.37 (C-12), 21.93 (C-11), 34.45 (C-7), 68.10 (C-10), 121.35 (C-1'), 127.74 (C-3'), 131.30 (C-2'), 131.70 (C-5'), 133.88 (C-6'), 138.27 (C-4'), 163.74 (C-2), 163.96 (C-5), 167.46 (C-8).

2.2.10. Isopropyl 2-((5-phenyl-1,3,4-oxadiazol-2-yl)thio)acetate (13)

White powder, yield 92%, mp 76-77°C (from ethanol); R$_f$ = 0,65; UV (ethanol), λ$_{max}$ (nm): 276; IR (KBr, cm^{-1}) v: 1772(CH$_2$COO(CH$_3$)$_2$), 1172(C-O-C, oxadiazole). ^{1}H NMR (400 MHz,

CDCl$_3$, δ, ppm): 1.25 (3H, s, CH$_3$), 1.27 (3H, s, CH$_3$), 4.07 (2H, s, S-CH$_2$), 5.08 (1H, septet, J = 6.3 Hz, O-CH), 7.45-7.54 (3H, m, ArH-3',5',4'), 7.97-8.00 (2H, m, ArH-2',6'). ^{13}C NMR (100 MHz, CDCl$_3$): δ 21.78 (C-11,12), 34.81 (C-7), 70.45 (C-10), 123.58 (C-6'), 126.80 (C-2', 6'), 129.17 (C-3', 5'), 131.87 (C-4'), 163.07 (C-2), 166.16 (C-5), 167.04 (C-8).

2.2.11. Isopropyl 2-((5-(2-chlorophenyl)-1,3,4-oxadiazol-2-yl)thio)acetate (14)

White powder, yield 88%, mp 66-67°C (from ethanol), R$_f$ = 0,63; UV (ethanol): λ$_{max}$ (nm): 279; IR (KBr, cm^{-1}) v: 1736 (CH$_2$COO(CH$_3$)$_2$), 1179(C-O-C, oxadiazole). ^{1}H NMR (400 MHz, CDCl$_3$, δ, ppm): 1.25 (3H, s, CH$_3$), 1.26 (3H, s, CH$_3$), 4.07 (2H, s, S-CH$_2$), 5.07 (1H, septet, J = 6.3 Hz, O-CH), 7.37 (1H, t, J = 7.7 Hz, ArH-4'), 7.44 (1H, t, J = 8.0 Hz, ArH-3'), 7.52 (1H, dd, J = 8.1, 1.2 Hz, ArH-2'), 7.91 (1H, dd, J = 7.7, 1.7 Hz, ArH-5'). ^{13}C NMR (100 MHz, CDCl$_3$): δ 21.78 (C-11,12), 34.78 (C-7), 70.49 (C-10), 122.85 (C-1'), 127.19 (C-3'), 131.06 (C-2'), 131.36 (C-5'), 132.56 (C-4'), 133.13 (C-6'), 163.77 (C-2), 164.43 (C-5), 166.96 (C-8).

2.2.12. Isopropyl 2-((5-(2,4-dichlorophenyl)-1,3,4-oxadiazol-2-yl)thio)acetate (15)

White powder, yield 86%, mp 96-98°C (from ethanol), R$_f$ = 0,62; UV (ethanol): λ$_{max}$ (nm): 276; IR (KBr, cm^{-1}) v: 1737 (CH$_2$COO(CH$_3$)$_2$), 1177(C-O-C, oxadiazole). ^{1}H NMR (400 MHz, CDCl$_3$, δ, ppm): 1.26 (3H, s, CH$_3$), 1.28 (3H, s, CH$_3$), 4.08 (2H, s, S-CH$_2$), 5.08 (1H, septet, J = 6.3 Hz, O-CH), 7.38 (1H, dd, J = 8.5, 2.0 Hz, ArH-3'), 7.56 (1H, d, J = 2.0 Hz ArH-5'), 7.89 (1H, d, J = 8.5 Hz, ArH-2'). ^{13}C NMR (100 MHz, CDCl$_3$): δ 21.79 (C-11,12), 34.78 (C-7), 70.56 (C-10), 121.39 (C-1'), 127.74 (C-3'), 131.32 (C-2'), 131.71 (C-5'), 133.90 (C-6'), 138.28 (C-4'), 163.74 (C-2), 164.02 (C-5), 166.89 (C-8).

2.3. Determination of Antibacterial and Antifungal Activity

Test microorganisms: *Staphylococcus aureus* (ATCC - 25923), *Bacillus subtilis* (RKMUz - 5), *Pseudomonas aeruginosa* (ATCC 27879), *Escherichia coli* (RKMUz - 221) and *Candida albicans* (RKMUz - 247). The RKMUz bacteria and fungi strains were obtained from the microorganism cultures collection of the Institute of Microbiology, Republic of Uzbekistan. The antibacterial and antifungal activity of synthesized compounds were evaluated by modified agar disk diffusion method (15). The average value of inhibition zones was calculated for the three replicates in independent assays.

3. RESULTS AND DISCUSSION

The reactions of 5-aryl-1,3,4-oxadiazole-2-thions (aryl = phenyl; 2-chlorophenyl; 2,4-dichlorophenyl) with such electrophilic reagents as alkyl esters of chloroformic acid (alkyl chloroformates) and chloroacetic acid were

carried out in order to study the influence of the nature (length and branching) of the alkyl radical on the yield and direction of the interaction products. The propyl, iso-propyl and iso-butyl groups were selected as alkyl radicals.

The interaction of thions (**1**-**3**) with alkyl chloroformates and alkyl esters of chloroacetic

acid was carried out in dry acetone (in the presence of K_2CO_3) at the boiling point of the solvent, the ratio of reagents was equimolar (1:1:1, alkyl ether, K_2CO_3, Scheme 1):

R=H (**1, 4, 7, 10, 13**),
2-Cl (**2, 5, 8, 11, 14**),
2,4-Cl (**3, 6, 9, 12, 15**).
i= acetone, 56°C, K_2CO_3.
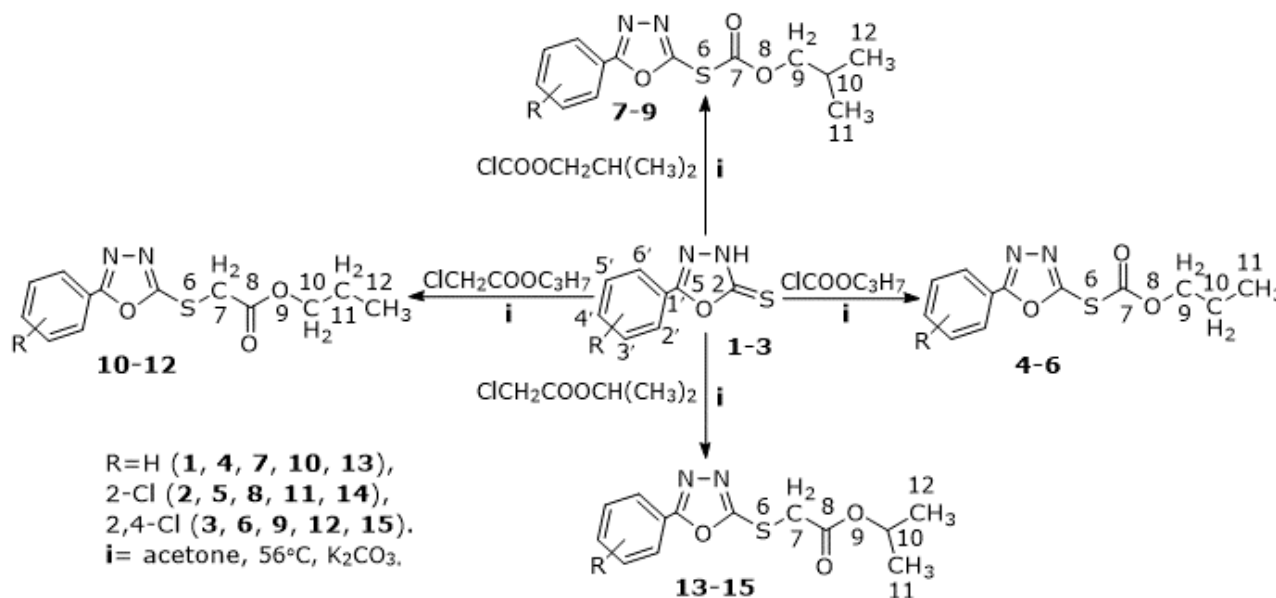
Scheme 1: Synthesis of S-(5-aryl-1,3,4-oxadiazol-2-yl) O-alkyl carbonothioate (**4-9**) and alkyl 2-((5-aryl-1,3,4-oxadiazol-2-yl)thio)acetate (**10-15**).

The course of interaction was controlled by TLC, all synthesized compounds were solids. The obtained data showes higher yield of the corresponding target products in reactions of three oxadiazolthions (**1-3**) with propyl chloroformate (**4-6**) – 74-79% were higher than with iso-butyl chloroformate (**7-9**) – 69-73%. The yields of products of propyl (**10-12**) – 87-90% and iso-propyl esters (**13-15**) - 86-92% of chloroacetic acid with the (**1-3**) thions were very close. However, the yields of products of propyl ester of chloroacetic acid (**10-12**) were significantly higher than products obtained with propyl chloroformate (**4-6**). A significant difference (17-19%) can be observed when comparing the yields of derivatives (**7-9**) and (**13-15**) obtained by reaction with alkyl esters having branched alkyl radicals (iso-propyl and iso-butyl).

The structure of the obtained derivatives was esatblished and characterized by the data of ^{1}H and ^{13}C NMR, IR, and UV spectra. In the IR spectra of compounds (**4-15**) there are characteristic absorption bands of the C(O)OR (R=alkyl) group at 1725-1788 cm^{-1}. The absorption maximum (272-286 nm) of all synthesized compounds (**4-15**) in the UV spectra corresponded to the literature data for S-derivatives (16-18), which shows that the interaction proceeds exclusively in the S-center to obtain S-(5-aryl-1,3,4-oxadiazol-2-yl) O-alkyl

carbonothioate (**4-9**) and alkyl 2-((5-aryl-1,3,4-oxadiazol-2-yl)thio)acetate (**10-15**). The possible N-products were not detected neither by TLC method, nor by spectral data (^{1}H NMR, UV-spectroscopy).

In the ^{1}H NMR spectra of compounds (**4-6**), the proton signals of the propyl fragment were observed in the corresponding regions: 1.05 ppm (3H, t, CH_3), 1.85-1.86 (2H, sextet, $C\underline{H}_2CH_3$), 4.44 (2H, t, $-OCH_2$) and protons of the isobutyl fragment of substances (**7-9**) in the range of 1.03-1.04, 1.05-1.06 ppm (6H, s, $(C\underline{H}_3)_2$), 2.14-2.15 (1H, septet, CH), 4.26 (2H, d, $-OCH_2$). All protons chemical shifts of compounds (**10-15**) fully correspond to their structure: substances (**10-12**), 0.92 ppm (3H, t, CH_3), 1.65-1.67 (2H, sextet, $C\underline{H}_2CH_3$), 4.10-4.11 (2H, s, $S-CH_2$), 4.13-4.14 (2H, t, $-OCH_2$) and substances (**13-15**), 1.25-1.26, 1.26-1.28 ppm (6H, d, $-CH(C\underline{H}_3)_2$), 4.07-4.08 (2H, s, $S-CH_2$), 5.07-5.08 (1H, septet,- $C\underline{H}(CH_3)_2$). At the same time, the signals of protons of aromatic groups in all compounds (**4-15**) were observed in the range of 7.32-8.05 ppm, which are familiar for these groups.

There were in the ^{13}C NMR spectra signals of all carbon atoms of the obtained compounds (**4-15**). The signals of C-7 carbons bound to the S atom in compounds (**10-15**) obtained with chloroacetic acid esters were in a strong field at

34.45-34.81 ppm, while the signals of similar C-7 carbon atoms in the form of C=O in compounds (**4-9**) obtained from the corresponding alkyl formates were shifted to a weaker field and have values of 173.28-174.11 ppm. The opposite situation was observed when comparing the values of C-10 carbon atoms in the form of CH in both series of synthesized compounds. Thus, the C-10 signals in the compounds obtained with alkyl chloroformates (**7-9**) were in a stronger field (2.14-2.15 ppm) than the signals (5.07-5.08 ppm) for the analogous carbon atom of compounds (**13-15**) obtained with alkyl ethers of chloroacetic acid.

Antibacterial activity. All synthesized compounds (**4**-**15**) and initial oxadiazolthions (**1**-**3**) were tested for antibacterial and antifungal activity by a modified disc diffusion method on agar (14). The test results (Table 1) showed that unsubstituted oxadiazoles (**1**-**3**) exhibited significant antibacterial activity, mainly

against gram-positive bacteria *Staphylococcus aureus* and *Bacillus subtilis*. The activity of oxadiazolthione (**1**) without substituents in the phenyl ring was minimal (diameters of the bacterial growth inhibition zone 7-9 mm at the concentration of 0.2 mg/disc), while in compound (**3**) with Cl atoms in positions 2 and 4 the inhibition diameters were largest (13-17 mm). Oxadiazolthione (**2**) with one Cl at position 2 showed an intermediate result (10-12 mm). It should be noted that the introduction of propyl and isobutyloxycarbonyl fragments into 5-(2,4-dichlorophenyl)-1,3,4-oxadiazole-2-thione led to a loss of activity of the observed in unsubstituted oxadiazolthione (**3**). At the same time, these compounds exhibit minimal (6-8 mm) fungicidal activity against *C. albicans.* Compounds (**10**-**15**) obtained by propyl and isopropyl esters of α-chloroacetic acid with three oxadiazolthiones (**1**-**3**) exhibited no antimicrobial activity (Table 1).

Table 1: Antimicrobial activity evaluated by diameter of inhibition zone (mm) for compounds (1-15) using agar disk diffusion test

Compound	Gram-positive bacteria		Gram-negative bacteria		Fungus
	S. aureus	*B. subtilis*	*P. aeruginosa*	*E. coli*	*C. albicans*
1	7.08±0.12	9.04±0.10	na	na	na
2	10.08±0.12	12.04±0.10	6.12±0.13	6.12±0.13	na
3	13.08±0.12	17.04±0.10	8.12±0.13	na	na
4	7.08±0.12	7.04±0.10	na	na	8.04±0.10
5	7.08±0.12	6.04±0.10	na	na	6.04±0.10
6	na*	na	na	na	na
7	7.08±0.12	6.04±0.10	na	na	6.04±0.10
8	7.08±0.12	6.04±0.10	na	na	6.04±0.10
9	na	na	na	na	na
10	na	na	na	na	na
11	na	na	na	na	na
12	na	na	na	na	na
13	na	na	na	na	na
14	na	na	na	na	na
15	na	na	na	na	na
Ampicillin (10µg/disc)	25.08±0.12	26.04±0.10	25.12±0.13	nt	nt
Ceftriaxone (30 µg/disc)	na*	nt	nt	26.12±0.13	nt
Fluconazole (25 µg /disc)	nt	nt	nt	nt	27.04±0.10

na*- not active; nt* – not tested.

4. CONCLUSION

Thus, the reactions of 5-aryl-1,3,4-oxadiazole-2-thiones with propyl(isobutyl)chloroformates and propyl(isopropyl)esters of chloroacetic acid have been studied. Only the corresponding S-derivatives were obtained. It has been established that the yields of target products are much higher when using alkyl esters of chloroacetic acid. The lowest yields were observed in reactions with isobutyl chloroformate having a branched alkyl radical of 69-73% (compounds **7-9**), the highest yields of

86-92% were observed with alkyl esters of chloroacetic acid containing propyl and isopropyl radicals (compounds **10-15**), and propyl chloroformate with normal propyl radical has intermediate values of 74-79% (compounds **4-6**). A relationship has been established between the structure of the synthesized compounds and their antimicrobial activity, which makes further research in this direction interesting.

5. CONFLICT OF INTEREST

The authors declare no conflict of interest.

Ziyaev AA et al. JOTCSA. 2023; 10(3): 599-604.

RESEARCH ARTICLE

7. REFERENCES

1. Glomb T, Świątek P. Antimicrobial Activity of 1,3,4-Oxadiazole Derivatives. Int. J. Mol. Sci. 2021;22:6979. <URL>

2. Glomb T, Szymankiewicz K, Swiatek P. Anti-Cancer Activity of Derivatives of 1,3,4-Oxadiazole. Molecules. 2018;23:3361. <URL>

3. Rubina B, Dharam PP, Garima K, Ravi K, Manni D. Recent Developments on Pharmacological Potential of 1,3,4-Oxadiazole Scaffold. Ind. J. Pharm. Edu. Res. 2019;53(2S):1-16. <DOI>

4. Tantray MA, Khan I, Hamid H, Alam MS, Dhulap A, Kalam A. Synthesis of Benzimidazole-Linked-1,3,4-Oxadiazole Carboxamides as GSK-3β Inhibitors with in Vivo Antidepressant Activity. Bioorg Chem. 2018;77:393-401. <URL>

5. Akram M, Rauf A, Saeed A, Ahmed F, Mubeen S, Ashraf M, Hussain S, Qureshi AM. Synthesis, biological evaluation and molecular docking studies of Mannich bases derived from 1,3,4-oxadiazole-2-thiones as potential urease inhibitors. Trop J Pharm Res. 2018;17(1):127-134. <URL>

6. Kumar D, Kumar V, Marwaha R, Singh G. Oxadiazole-An Important Bioactive Scaffold for Drug Discovery and Development Process Against HIV and Cancer- A Review. Current Bioactive Compounds. 2019;15(3):271-279. <URL>

7. Alam MM. 1,3,4-Oxadiazole as a Potential Anti-Cancer Scaffold: A Review. Biointerface Research in Applied Chemistry. 2022;12(4):5727-5744. <URL>

8. Thakkar SS, Thakor P, Doshi H, Ray A. 1,2,4-Triazole and 1,3,4-oxadiazole analogues: Synthesis, MO studies, in silico molecular docking studies, antimalarial as DHFR inhibitor and antimicrobial activities. Bioorganic & Medicinal Chemistry. 2017;25(15):4064-4075. <URL>

9. Espinosa AV, Costa DS, Tunes LG, do Monte-Neto RL, Grazul RM, de Almeida MV, Silva H. Anticancer and antileishmanial in vitro activity of gold (I) complexes with 1,3,4-oxadiazole-2(3H)-thione ligands derived from δ-D-gluconolactone. Chem Biol Drug Des. 2021;97(1):41-50. <URL>

10. Verma SK, Verma R, Verma S, Vaishnav Y, Tiwari SP, Rakesh KP. Antituberculosis activity and its structure-activity relationship (SAR) studies of oxadiazole derivatives: A key review. Eur J Med Chem. 2021;209:112886. <URL>

11. Ziyaev AA, Galust'yan GG. Reaction of 5-aryl-1,3,4-oxadiazole-2(3H)-thiones with chloromethyl alkyl ethers. Chem Heterocycl Compd. 1999;35:1104-1106. <URL>

12. Tozhiev IF, Ziyaev AA, Shakhidoyatov KhM. Alkylation of 5-aryl-1,3,4-oxadiazol-2(3H)-thions with allyl- and benzylhalogens. Chemistry and chemical technology. 2012;4:17-20.

13. Ziyaev AA, Tozhiev IF, Shakhidoyatov KhM. 5-Aryl-1,3,4-oxadiazolin-2(3H)-thiones in reactions with alkyl haloacetates. Chem Heterocycl Compd. 2012;48:488-491. <URL>

14. Ziyaev AA, Ismailova DS. Synthesis of 5-phenoxymethyl-1,3,4-oxadiazolin-2(3H)-thion and its alkylation. Uzbek Chem J. 2015;1:15-18.

15. Performance Standards for Antimicrobial Disk Susceptibility Tests. CLSI document M02. 13th Edition. Wayne, PA, USA; 2018. ISBN 1-56238-834-7.

16. Koparır M, Çetin A, Cansız A. 5-Furan-2yl[1,3,4]oxadiazole-2-thiol, 5-Furan-2yl-4H [1,2,4] triazole-3-thiol and Their Thiol-Thione Tautomerism. Molecules. 2005;10(2):475-480. <URL>

17. Rozhkova N, Sabirov K, Seytanidi KL. Reaction of benzothiazolin-2-thione with 1-chloro-2,3-epoxypropane. Chem Heterocycl Compd. 1983;11:1170-1173. <URL>

18. Eshimbetov AG, Tojiev IF, Ziyaev AA. DFT and TD-DFT study of isomeric 5-(pyridyl)-1,3,4-oxadiazol-2-thiones and 2-methylthio-5-(pyridyl)-1,3,4-oxadiazoles. Spectrochim Acta A Mol Biomol Spectrosc. 2017 Dec 5;187:191-197. <URL>

Preparation and Characterization of Polyaspartic and a High Solids Acrylic Copolymer Polyol Based Polyurethanes

Cemil DIZMAN [1*] , **Elif CERRAHOĞLU KAÇAKGIL** [1*] ,
Levent BABAYIĞIT [1] , **Caner ARAR** [1]

[1]İzel Kimya Research and Development Center, Kocaeli, 41455, Turkiye

Abstract: In this work, a high solids acrylic copolymer polyol (poly(MMA/BA/HEMA/AA)) was synthesized from the polymerization of methyl methacrylate (MMA), butyl acrylate (BA), hydroxyethyl methacrylate (HEMA) and acrylic acid (AA) and was added to the polyaspartic resin. The polyaspartic-polyol mixtures reacted with polyisocyanates to create hybrid polyurethane-polyaspartic hybrid coatings. Different amounts of synthesized acrylic copolymer (5, 10, and 20% of total resin mixture) were mixed into polyaspartic resin and subsequently reacted with polyisocyanates in a 1:1 molar ratio. The characterization of the polymer was performed with Gel Permeation Chromatography (GPC), Fourier-Transform Infrared-Attenuated Total Reflection (FTIR-ATR) and Differential Scanning Calorimetry (DSC). The determination of physical and mechanical properties of the hybrid coatings was accomplished by hardness, glossiness, abrasion, stress-strain, corrosion, and impact tests. The results indicated that by adding high solids acrylic copolymer (HSAC), the drawbacks of polyaspartic resin (short pot life, hardness and brittleness, and poor adhesiveness) have been largely eliminated without reducing its intrinsic properties. The pot life increased from 16 minutes to 27 minutes and shore D hardness decreased from 60-65 to 52-55 as the polyol content increased in the mixtures. The acrylic polyols and aspartic mixtures may be used in the preparation of paints and varnishes applied on concrete, metal, and wood surfaces.

1. INTRODUCTION

Polyurea coatings have been very popular for their superior properties such as, flexibility, high cure speed, higher mechanical and chemical resistance, and fast drying compared to the epoxies and polyurethanes (1-6). The chemistry of the polyurea is based on the reaction of primary amines with polyisocyanates. There is no need to use catalysts and it is performed without any heat applied. The curing time is too short (under minutes) that needs special machines like spray guns and needed to be

expertise in applications (7-8). Instead of using primary amines, a new technology, polyaspartic ester polyurea, was developed as shown in Scheme 1.

In polyaspartic polyurea system, a secondary amine is reacted with an aliphatic isocyanate in which sterically hindered hydrogens on nitrogen atoms slowly react with isocyanates that increases the pot life of the system (9-10). Polyaspartic resins were initially used as diluents for polyurethane acrylic systems. They decrease the viscosity and increase

the hardness and the curing speed of the polyacrylics to prepare fast cure polyurethane coatings (11). After all, these resins have been favored as more preferable environmentally friendly resins with superior properties such as, low VOC (volatile organic components), more hardness, fast cure, and have been used in many areas such as oil and natural gas piping lines, airports, mineral processing facilities, food facilities and factories, shipyards, marine enterprises, waste centers, walkways and balconies, water and wastewater treatment facilities, industrial production areas and power plants (12-16).

Polyaspartics exhibit superior physical, mechanical and chemical (color fastness, resistance to chemicals, solvents, acids and bases, excellent hardness and mechanical strength) properties compared to two component resins such as epoxies and polyacrylates (17-18). Being expensive as compared to epoxy and polyurethanes, they also suffer from the sensitiveness to the air moisture that makes the reaction with isocyanates faster and prevents adhesion to the substrates acting as a barrier. The shorter pot life of the polyaspartics is also a drawback due to that it prevents the resin from spreading and preventing it from penetrating the floor (20). In order to minimize the moisture effect and to increase the pot life and adhesiveness of the polyaspartic polyurea coatings, several attempts have been conducted by using nano-silica and hydroxyl functional soybean oil (21-22).

High solids acrylic polymers having hydroxyl functional groups react also with aliphatic isocyanates to prepare crosslinking polyurethane networks having superior mechanical properties (excellent clarity, good thermal resistance, high glossiness, and excellent gloss retention, resistance to discoloration by time, well flexibility, not brittle, tunable glass transition temperature, good adhesiveness, etc.) that makes them withstand

chemicals and alkalis, more durable to exterior factors. They may be utilized in a variety of industries, including wood coatings, automotive goods, ships, and storage tanks (23-26). In the last decade, due to the environmental awareness, the polyurethanes have been prepared from bio-based chemicals (27-28).

In this study, a poly(MMA/BA/HEMA/AA) acrylic copolymer with low cost, high yellowing resistance, and high solid value was synthesized and mixed in different proportions with polyaspartic ester (PAE) resins to eliminate the disadvantages of polyaspartic ester (PAE) resins (expensiveness, poor adhesiveness, and short pot life). FTIR, DSC, and GPC were used to characterize the resins.

In addition to determining physical characteristics including color, viscosity, gloss, hardness, drying time, pot life, yellowing resistance, and gloss loss following UV exposure, mechanical characteristics were also assessed using impact, tensile, abrasion, and salt spray tests. A suitable paint formulation was designed to PAE and PAE with acrylic copolymers, and physical and mechanical properties of the paints were also examined and compared.

2. EXPERIMENTAL SECTION

2.1. Materials
Butyl acetate, methyl methacrylate (MMA, 98%, ARKEM), butyl acrylate (BA,>99%, Ataman Chemical), 2-hydroxyethyl methacrylate (2-HEMA, >99%, Prochema Chemical LTD.), acrylic acid (AA, 98%, ARKEM), tert-butylperoxybenzoate (TBPB, Merck) were purchased and used without any further purification. Aliphatic isocyanate (Tolonate HDT-LV2) used for curing studies was purchased from Vencorex. The polyaspartic ester was kindly obtained from İZEL KİMYA SANAYİ VE TİCARET A.Ş. with the code of IZASP 14. All other materials were used without any further purification.
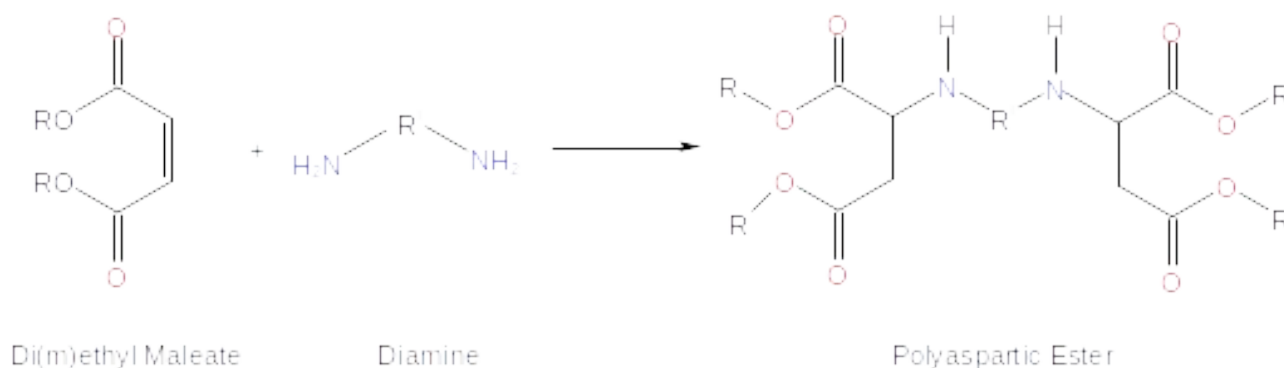
Scheme 1: Polyaspartic ester synthesis.

2.2. Characterizations
FTIR spectra were measured with JASCO FT/IR-4200 with ATR (JASCO Corp., Tokyo, Japan). Spectra were obtained at mid-IR region (ca. 4000–700 cm^{-1}) at a resolution of 4 cm^{-1} with 16 scans (Spectra Manager

II software, JASCO Corp.). Molecular weights and polydispersity indexes of the polymers were measured by gel permeation chromatography (GPC) employing an Agilent 1100 instrument equipped with a differential refractometer by using

tetrahydrofuran (THF) as the eluent at a flow rate of 1 mL/min at 30 ºC. Molecular weights were determined by using polystyrene standards. Brookfield viscosity was measured by Brookfield viscometer (RVDV-I Prime, 25 ºC, spindle SC4-21, 50 rpm). Cross-cut adhesion test kit CC2000 from TQC Sheen B.V. (Capelleaan den IJssel, Netherlands) was used to test the adhesion of dry coatings on their substrate. The brightness of the films was determined using a Novo-Gloss Trio glossmeter. The color controls of the materials were made with LICO 620. TQC Sheen Pendulum Hardness Tester /SP0500 I141 was used to determine the hardness. In the mechanical tests, impact test with TQC Sheen, tensile test with Devotrans (DVT GP/R D NN 10 kN), abrasion test with Taber Rotary Abraser (1700) and corrosion test with Programmable Salt Spray Cabinet (880/S) were used. DSC was performed on a TA-DSC 250 instrument. Approximately 50 mg of sample was placed in a pan and heated to 250 ºC at a rate of 10 ºC min^{-1} in nitrogen atmosphere.

2.3. Synthesis of Acrylic Copolymer
Free radical polymerization was accomplished according to an adapted procedure (Scheme 2) to create acrylic copolymer (poly(MMA/BA/HEMA/AA)) in nitrogen atmosphere

(29). All monomers and the initiator (MMA; 1 mol, BA; 2,5 mol, 2-HEMA; 0,9 mol, AA;0,1 mol, TBPB; 0,1 mol) were put into an additional funnel and added for about 3-4 hours to a reactor with agitation containing butyl acetate pre-heated to 125 ℃. After

monitoring gas chromatography to ensure that all monomers had reacted, the agitation was halted. The final polymer solution was analyzed and the results are as follows: The solid content: 72.6%, acid value: 7.3 mg KOH/g, viscosity: 19.000 cP and the molecular weight (Mw): 2.4934 e^4 g/mol.

2.4. Preparation of Polyaspartic Resins and Acrylic Copolymer Mixtures
Polyaspartic ester resin (PAE) has the following properties: solid content; 96.7 %, viscosity; 1800 cP, amine value; 191 mg KOH/g and the equivalent weight; 290 g/mol. Polyaspartic resin and HSAC were mixed in different percentages as shown in Table 1 and the mixtures were cured with aliphatic isocyanate at a 1:1 ratio.

2.5. Preparation and characterization of paint formulations
A simple paint recipe was applied for mixtures of polyaspartic and polyacrylics resins. From these, white paints were made using the same ratio of resins, pigments, and other components. For mixing all ingredients in the paint, a high–speed mixer was used, and fineness of grinding was followed by using a grindometer. Paints were applied to the glass and metal surfaces by using a film applicator with 90 micrometer thickness. Adhesion, drying time, and gloss properties of the paints were determined by using metal surfaces. Glass panels were used for determination of hard drying times by drying time recorder.

Scheme 2: Synthesis of high solids acrylic copolymer (poly(MMA/BA/HEMA/AA)).

3. RESULTS AND DISCUSSION

3.1. Characterizations of Resins and Cross-linked Polymeric Networks
As mentioned in section 2.3 and 2.4, the synthesis of acrylic copolymer, the chemical analyses of the mixtures of polyaspartics and polyacrylic before and after curing and the final prepared coatings has been carried out by ATR-FTIR, GPC, GC and DSC measurements.

In Figure 1, the synthesis of high solids acrylic copolymer was followed by checking the functional group analysis by ATR-FTIR. At the beginning while all

the monomers were mixed, there were peaks around 1637 cm^{-1} that show us the presence of the acrylic double bonds. After the reaction, the disapperance of this peak proved that all acrylic monomers were reacted. Acrylic copolymer has typical absorption bands corresponding to acrylate and methacrylate units. The peak around 3350 cm^{-1} were assigned to the -OH symmetric stretching vibrations from hydroxyl group. 2950.55 cm^{-1} (C-H bond stretching vibrations), 1727.56 cm^{-1} (C=O absorption peak of the carbonyl ester group), 1238.08 cm^{-1} (C-O stretching modes), 1157.08 cm^{-1} (C-O-C stretching vibrations) (30-31).

The synthesis of HSAC were also followed by using GPC for molecular weight measurements. The GPC showed us that all monomers were reacted and a polymer were existed as shown in Figure 2. The molecular weight: Mw: 2.31 e4 g/mol, Mn: 5.74 e^3 g/mol, PDI: 4.03.

The monomer residue analysis was also conducted by using headspace-GC. Abundance to time graph showed that the signals for acrylic monomers at the time interval between 2-4 minutes was so low after the polymerization. There were almost no identified monomers (below 0.1%) in the final acrylic solution showing that all the monomers were reacted with each other to give a polymer as shown in Figure 3.

After the mixing of the acrylic to polyaspartic resins and then with the isocyanate, the presence of ester and amine groups is observed in the main absorption bands in the FTIR spectrum of the PAEs as shown in Figure 4.

Table 1: The amount of ingredients in weight percentage (wt%) of the PAE-HSAC mixtures.

Sample	Polyaspartic (PAE) (%)	Acrylic Copolymer (HSAC) (%)
Control-F_1	100	0
F_2	95	5
F_3	90	10
F_4	80	20
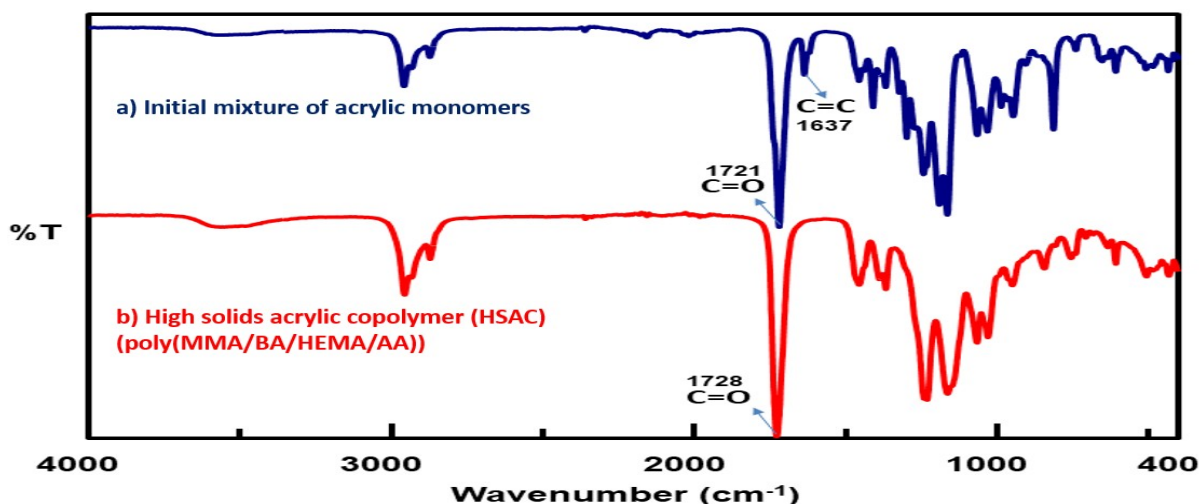
Figure 1: ATR-FTIR spectra of a) Initial mixture of acrylic monomers and b) HSAC (poly(MMA/BA/HEMA/AA)).

The presence of the peak at around 2264 cm^{-1} was related to the –OCN groups. The disappearance of the –OH and –NH groups at around 3350 cm^{-1} proved the existence of the curing process. All isocyanates can be reacted with –OH and –NH groups or sometimes some groups could not react because of the insufficient mixing or there were not enough reactive functional groups reacting with isocyanates (21). As in the case of PAE-20, there were not peaks at around 3300 cm^{-1} and at around 2264 cm^{-1}, that showed us the all functional groups were completely reacted with each other as shown in Figure 5.

After the curing, the –OH and –NH groups reacted with –OCN groups and turned out the cross-linking polymeric networks containing the final polyurea and polyurethane bonds as shown in Scheme 3.

After the coatings were prepared, the glass transition temperatures (Tg) of the coatings were determined by using differential scanning calorimeter (DSC). Measurements were made for the Tg value which is of great importance in obtaining information about the properties of the polymers that whether it will be flexible or hard. The graphs are given in Figure 6 for PAE, poly(MMA/BA/HEMA/AA), PAE-5, PAE-10 and PAE-20.
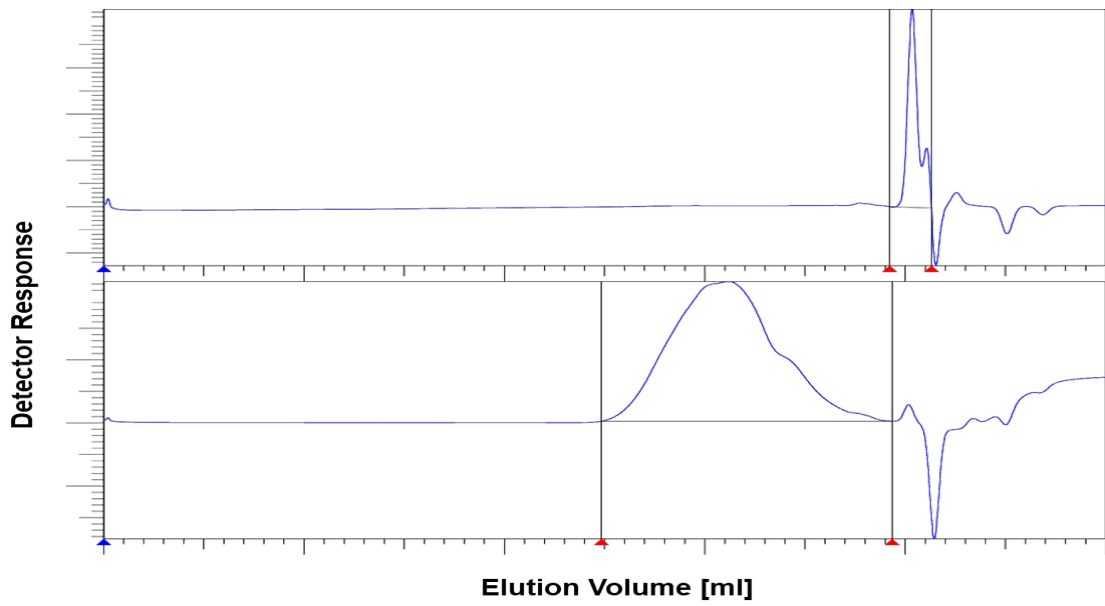
Figure 2: GPC spectra of initial mixture of acrylic monomers and HSAC (poly(MMA/BA/HEMA/AA)).
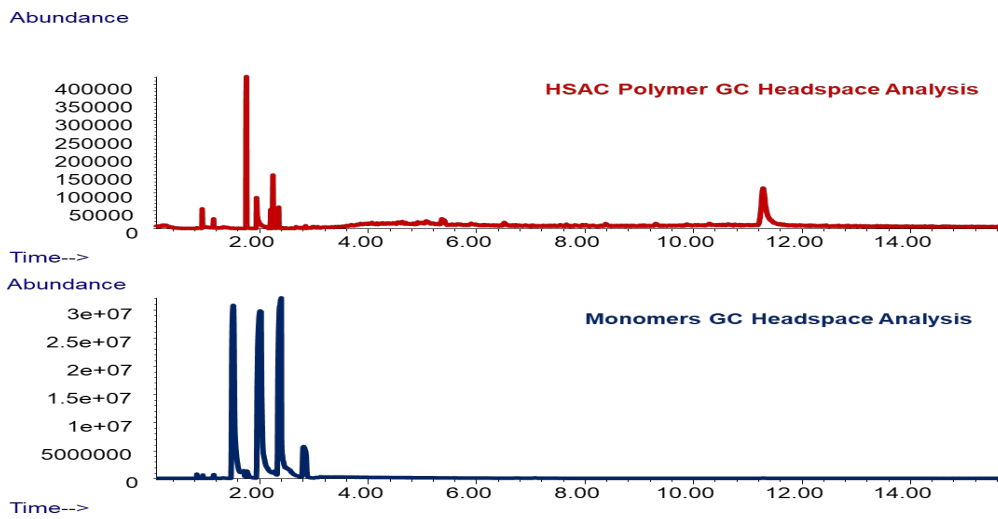
Figure 3: Headspace-GC analyses of initial mixture of acrylic monomers and HSAC (poly(MMA/BA/HEMA/AA)).
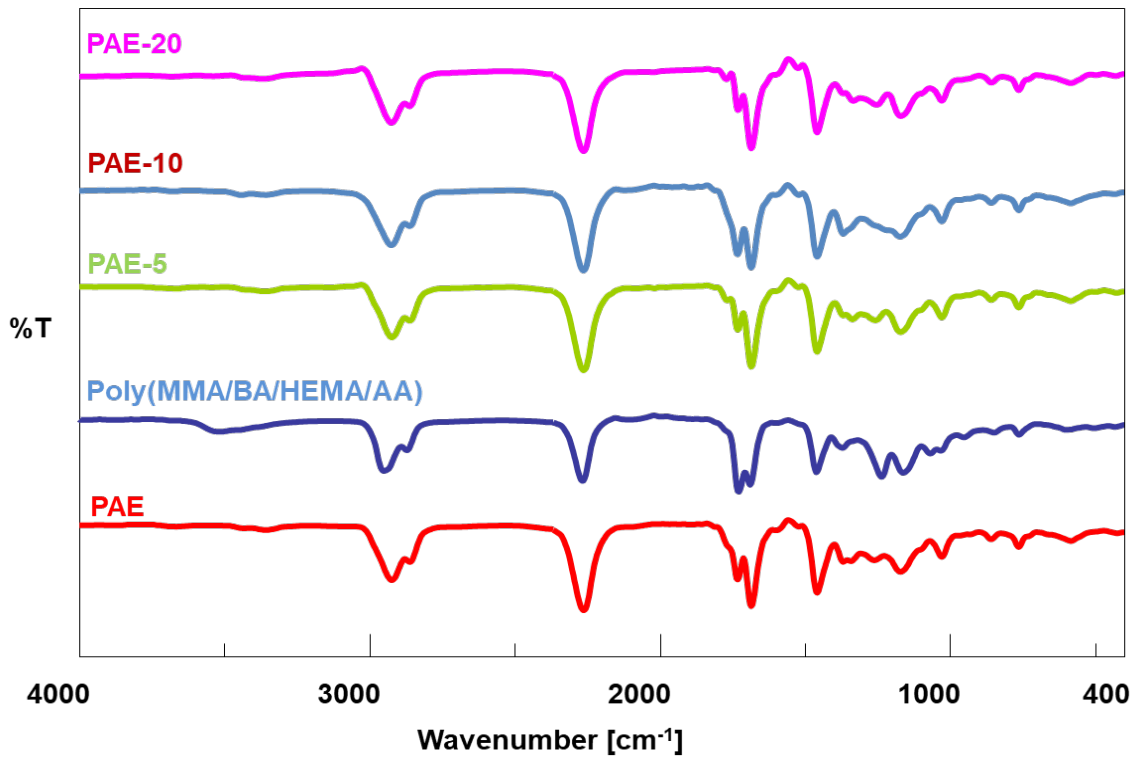
Figure 4: FTIR spectra of materials before curing.
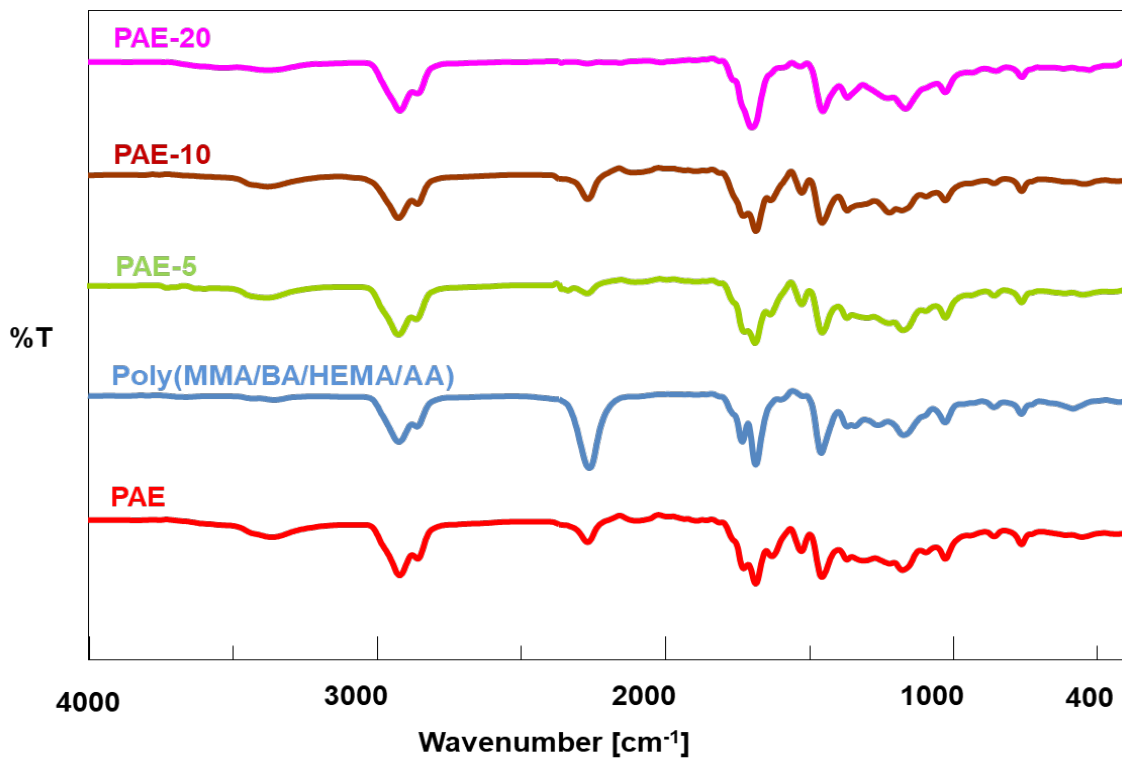
Figure 5: FTIR spectra of materials after curing.

High solids acrylic copolymers (HSAC)

+

Polyaspartic ester

isocyanate

mixing at room temperature

Chemically crosslinked polyurea and polyurethane network
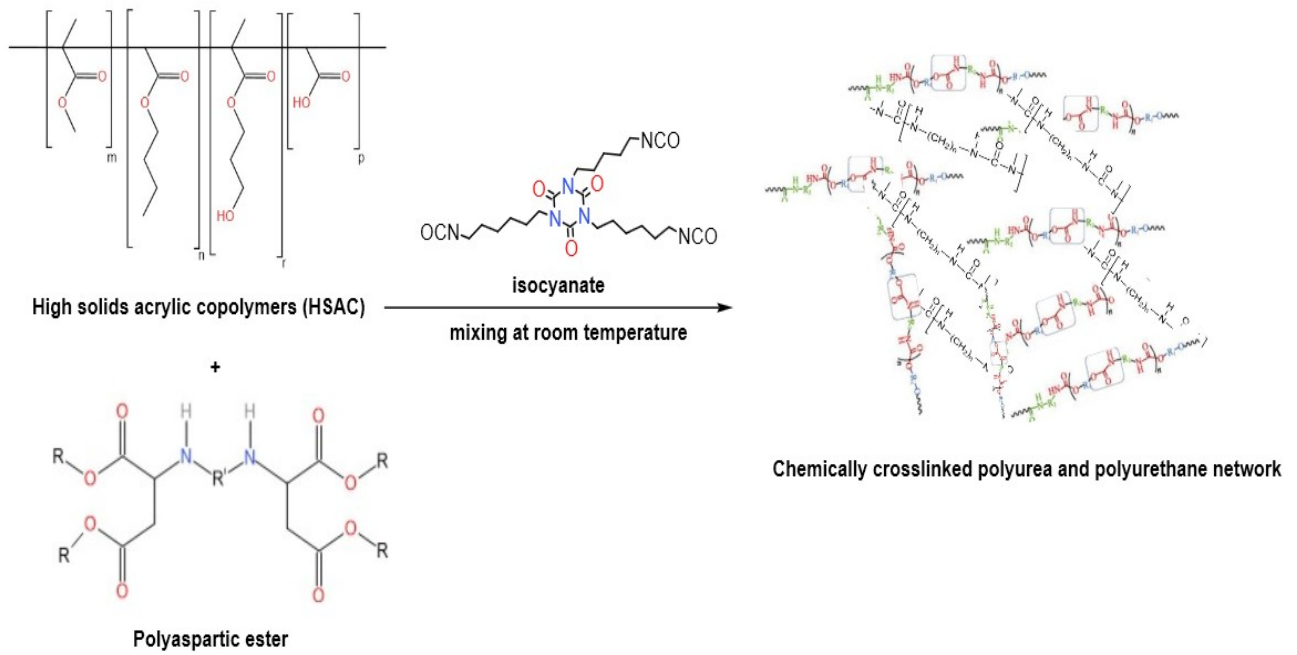
Scheme 3: Preparation of cross-linking networks by the reaction of PAE and polyacrylic polyol (HSAC) with isocyanate.
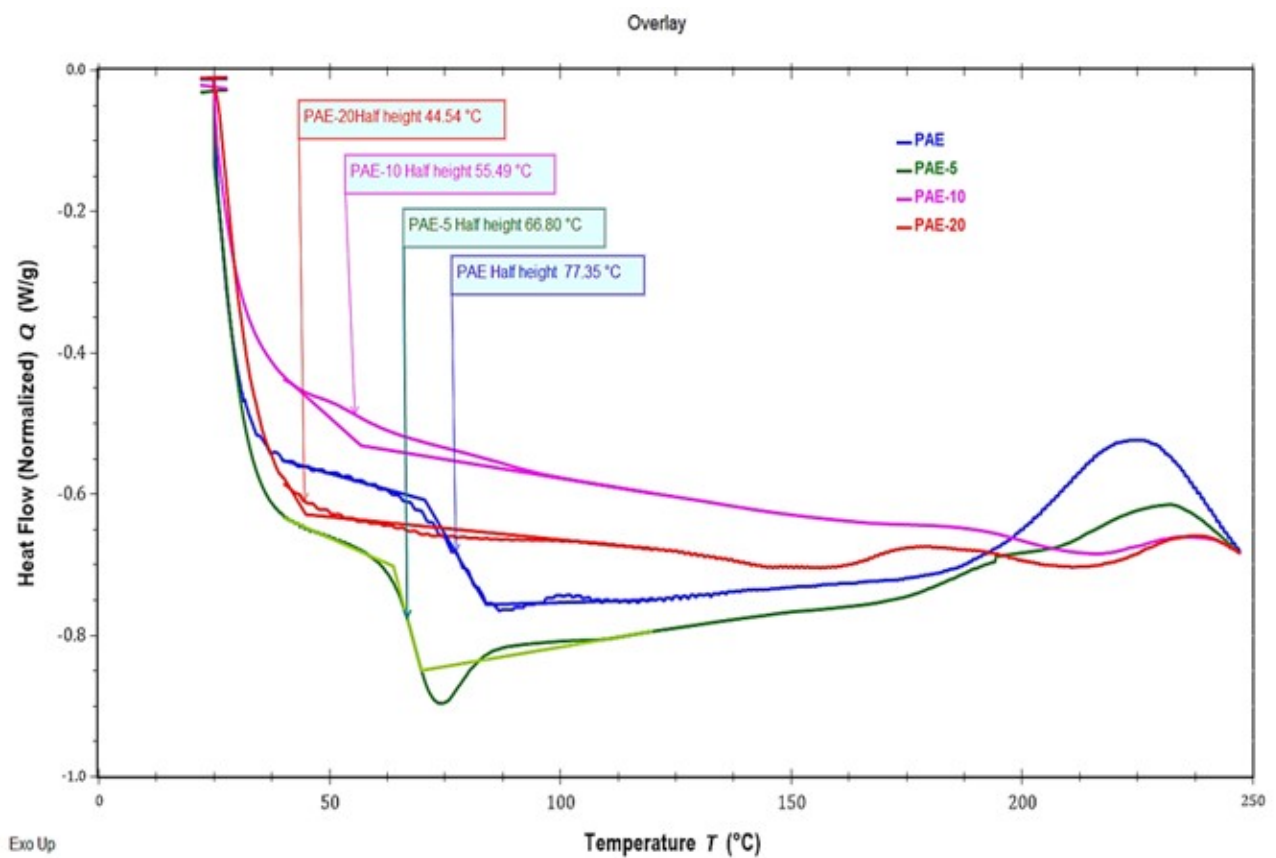
Figure 6: DSC graphs for a) PAE, b) PAE-5, c) PAE-10, and d) PAE-20.

Dizman C et al. JOTCSA. 2023; 10(3): 605–620 .

RESEARCH ARTICLE

The Tg of the neat PAE was measured as 77.35 °C. As the poly(MMA/BA/HEMA/AA) content of the samples increased, their Tg gradually decreased as 66.80, 55.49 and 44.54 °C for the 5, 10 and 20%, respectively. Insufficient amounts of polymerizable groups and more flexible monomers in the backbone or sidechain of polymers were likely to be responsible for the low Tg values, which also led to a poor crosslinking density (32-33). HSAC chemical structure contains flexible butyl acrylate groups that makes it very flexible. Long alkyl chain length groups in acrylic polyols leads to increase the movements of the molecular structure that lowers the Tg. Increasing the acrylic content consumed the isocyanates more fully and all isocyanates reacted as the disappearance of the peak related to isocyanate around 2264 cm^{-1} as shown in the FTIR spectrum of PAE-20. Decrease in Tg resulted more flexibility to the polymeric network and makes enhancements in their adhesion to the substrates.

3.2. Mechanical and Physical Properties of the Mixtures of PAE and HSAC and the coatings

The physical and mechanical properties (color, viscosity, glossiness, hardness, drying time, and pot life) of the resins and coatings were given in the Table 2.

According to the results given, Hazen color value of PAE resin, which is relatively high (171), decreased to 150, 145 and 130, respectively, with the increase of acrylic copolymer ratio in the mixture. These results show that the color status, which is very important for polyaspartic ester resin, can be improved by mixing with acrylic copolymers.

Viscosity values measured as Brookfield at 25 °C, on the other hand, were increased as predicted with the increase in the acrylic copolymer ratio, which has a very high viscosity value. It was determined that there was no loss in the gloss and Persoz hardness values, which are the important features of the polyaspartic ester resin, after mixing and showing that these properties were preserved. Decrease in drying times while increasing the pot life is desirable property for the workability with the resins. The increase in pot life can be because of the isocyanate groups cannot find the hydroxyl groups easily in the polymeric backbone due to the other functional groups that can hinder sterically the hydroxyl groups for the reaction.

The decrease in drying times can be due to more functional hydroxyl groups react with isocyanate groups that increase the number of the reactive crosslink points with increasing the crosslink density. More crosslinking leads to drying faster.

Table 2. Mechanical and physical properties of the resins and coatings.

Tests	PAE	HSAC	PAE-5	PAE-10	PAE-20
Color (Hazen)	171	11	150	145	130
Viscosity (cP, Brookfield, 25℃)	1800	19000	2200	2500	3400
Gloss (20 degree)	87	80	87	87	87
Persoz Hardness (150 micron, 7 days)	300-310	200-210	300-310	300-310	300-310
Shore Hardness (7 days)	65-70	40-45	65-70	60-65	50-55
Drying (hour)	12	12	7.5	6.0	5.5
Pot life (min)	16	71	17	21	27
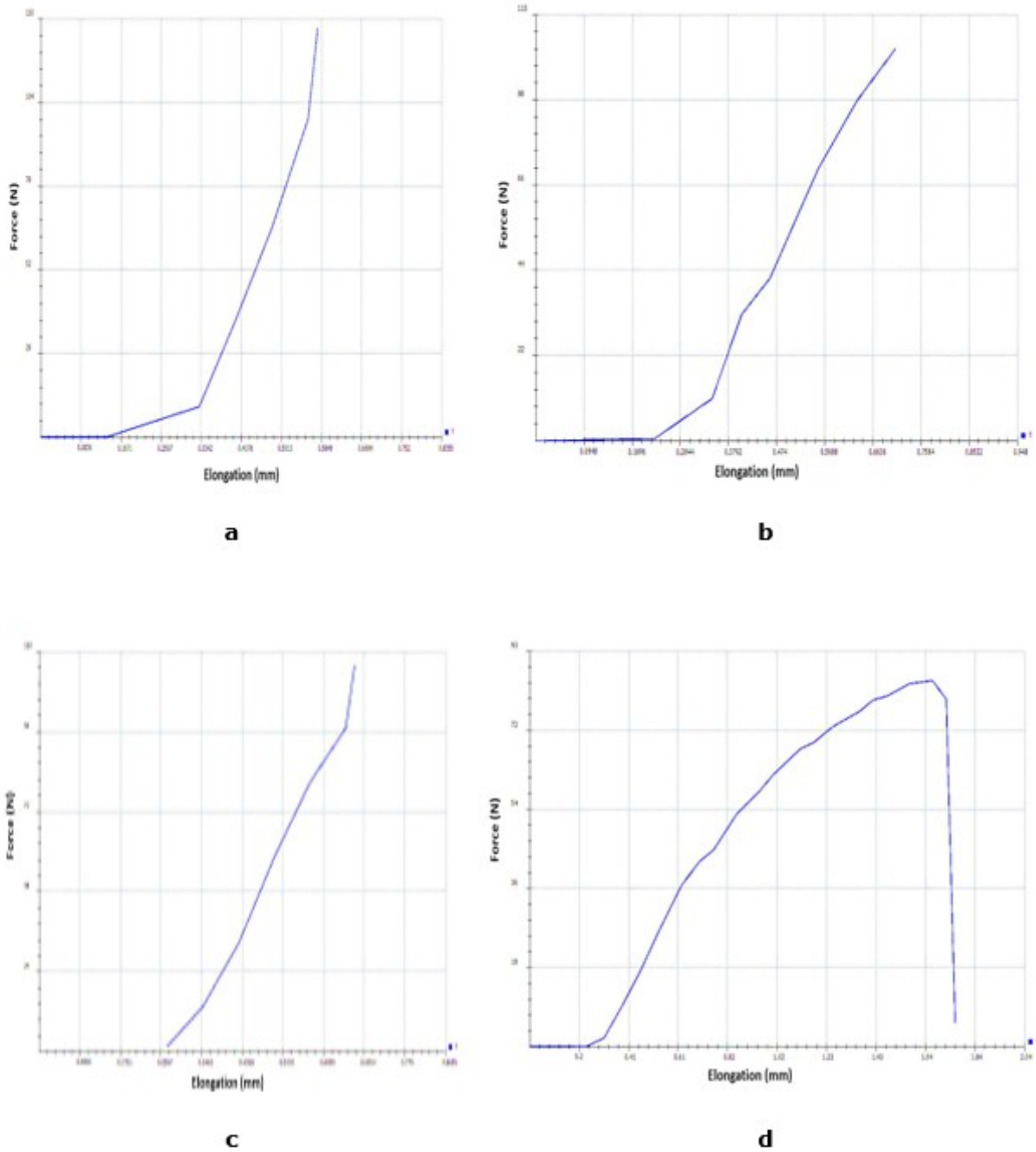
Figure 7: Force (N)-Elongation (mm) graphs of a) PAE, b) PAE-5, c) PAE-10, d) PAE-20.

Tensile testing is a destructive process that provides information about the material's properties such as tensile strength and ductility. It measures the force required to break or rapture the material and how far the sample has stretched to that break or break off point. For this purpose, control was achieved under operating conditions adjusted for 100 mm/min test speed and 100 N target force, and elongation and elastic modulus values were examined. The Force (N)-Elongation (mm) graphs of PAE resin and mixtures and the results are given in Figure 7 and Table 3.

According to the values given in Table 3, the elongation values were approximately 24.5%, 56.1% and 189.5% for the acrylic copolymer ratios added; elasticity modules increased by 2.2, 4.1 and 21.5%. This could be due to flexible acrylic polymer backbone and the flexible functional groups (2-HEMA and butyl acrylate) that made the crosslink networks more flexible. According to tensile test results, the incorporation of more acrylic resins into polyaspartics decreased the tensile strength due to the less strong polyurethane linkages compared to strong polyurea linkages.

Table 3. Elongation and elasticity modules of PAE, PAE-5, PAE-10, and PAE-20.

Product	Elongation at break (mm)	Elasticity Modulus (N/mm²)	Tensile Strength (N/mm)
PAE	0.57	183.70	7.067
PAE-5	0.71	187.24	5.863
PAE-10	0.89	191.26	5.621
PAE-20	1.65	223.15	4.627

In the test applied according to the ASTM D4060 standard and mass loss, the original weight of the sample was measured. The test sample was then placed in the abrasion tester. A load of 500 g was placed on the abrasive wheel and allowed to rotate for 1000 cycle. When the number of cycles was completed, the final weight was measured and the amount of material removed from the surface was determined. The results of the abrasion test performed with this method were given in Figure 8 for PAE, PAE-5, PAE-10 and PAE-20.

The graph given in Figure 8. C was calculated according to the Taber Wear Index given in Equation 1.

$$Taber\,Wear\,Index = (I \times 1000)/C \text{ (Eq. 1)}$$

In Equation 1, I=A-B, A=weight (mass) of specimen before abrasion, B=weight (mass) of specimen after abrasion, n=number of test cycles.

Accordingly, for PAE and PAE-10, with the increase in the number of cycles, the Taber Wear Index decreased, that is, there was less wear. With the increase in the acrylic polymer ratio in the mixture, the abrasion started to increase in the mixture added 10% and it had a high abrasion rate for 20%. For PAE and PAE-5, the decreasing index values with the increase in the number of revolutions can be interpreted as lower hardness in the inner layers after surface wear and therefore lower wear.

3.3. Paint Formulation and Test Results
The paint formulation given in Table 4 was used for the mixture made with polyaspartic ester resin and acrylic copolymer. Some physical properties of the prepared paints and some mechanical properties of the films were investigated.

The test results for the paint mixtures prepared according to the guide formulation given in Table 4 are summarized in Table 5.

The cross-cut test was performed according to ASTM D3359 standard for aluminum, galvanized, and sheet surfaces. The visuals of the test result are given in Figure 9.

The gloss measurements of the samples were made to examine the aesthetic properties for paint mixtures (34).

The gloss measurements of the paint mixtures to which PAE and acrylic copolymer were added at the specified rates at 20 degrees were measured as 85 gloss, and it was determined that there was no decrease in the gloss value as a result of the addition. In addition, when the effect of UV rays on the film was examined, it was determined that there was no decrease in yellowing resistance after a period of 10 days.

Corrosion often causes failures that shorten the life of connections. When exposed to certain conditions such as humidity and salinity, durability and mechanical strength are affected and failures may occur more frequently. The salt spray test is an accelerated test used to determine the ability of surface coatings to resist atmospheric corrosion (35-36).
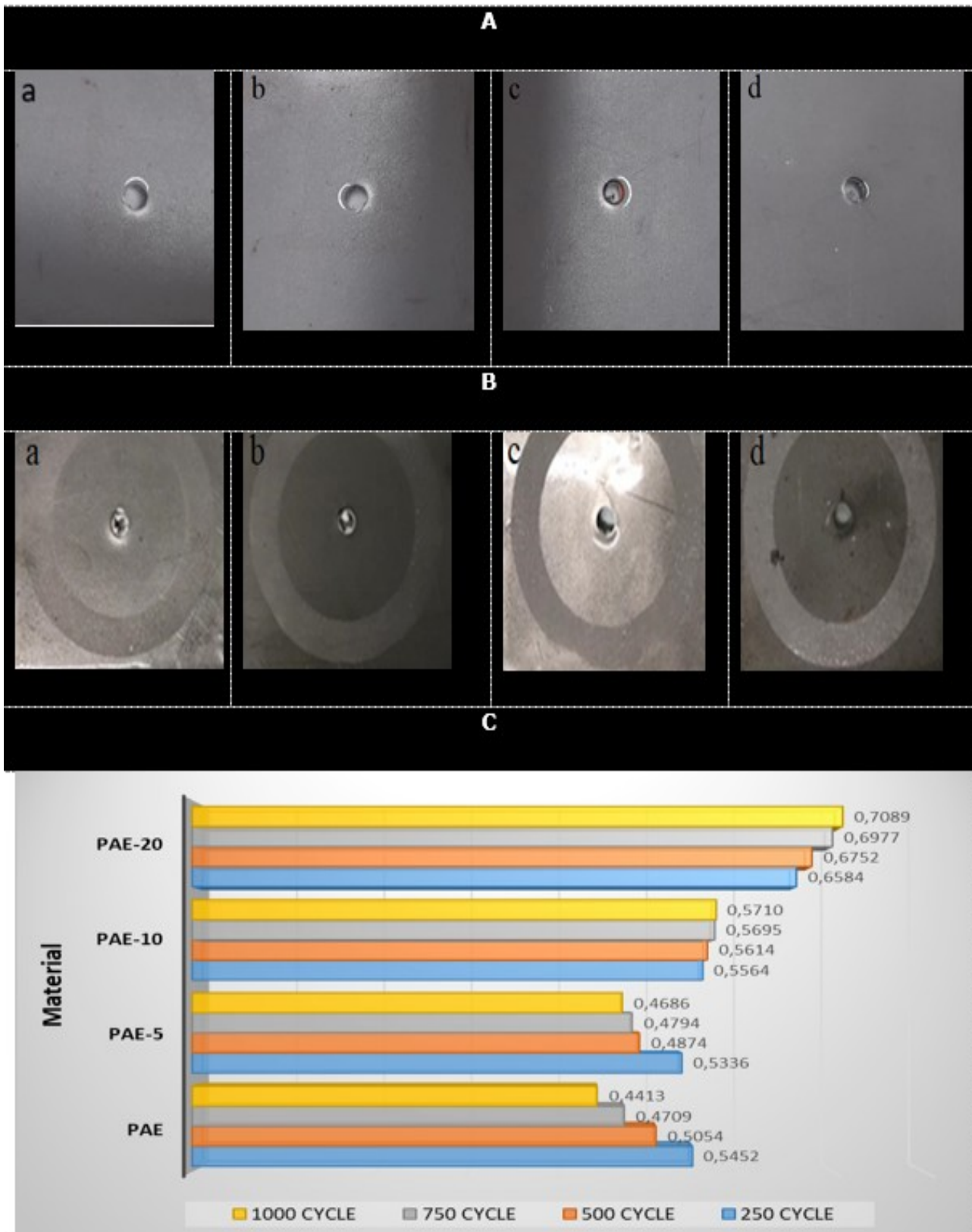
Figure 8: Abrasion test images of A) Before ND, B) After the 1000 cycle a) PAE, b) PAE-5, c) PAE-10, d) PAE-20, and C) Graphical images according to Taber Wear Index.

Table 4. Guide paint formulations.

	PAE	PAE-5	PAE-10	PAE-20
Contents	g	g	g	g
PAE	51.00	48.45	45.90	40.80
poly(MMA/BA/HEMA/AA)	-	2.55	5.10	10.20
Wetting and dispersing additive	0.50	0.50	0.50	0.50
Titan (for cloaking)	25.00	25.00	25.00	25.00
Barite (for filler)	12.50	12.50	12.50	12.50
Dehumidifier	1.60	1.60	1.60	1.60
Defoamer	1.00	1.00	1.00	1.00
Wetting substrates	0.60	0.60	0.60	0.60
UV absorber	0.60	0.60	0.60	0.60
UV absorber	0.60	0.60	0.60	0.60
Butyl Acetate	2.90	2.90	2.90	2.90
Xylene	3.70	3.70	3.70	3.70
Total	100	100	100	100
For 100 g of paint				
Aliphatic isocyanate	35.00	35.00	35.00	35.00
Butyl Acetate	15.00	15.00	15.00	15.00

Table 5. The properties of the paint prepared from PAE, PAE-5, PAE-10 and PAE-20.

Tests	PAE	PAE-5	PAE-10	PAE-20
Viscosity (Brookfield, 25℃)	350 cP	410 cP	460 cP	750 cP
Gloss (20 degree)	85	85	85	85
Persoz Hardness (150 micron, 7 days)	290-300	285-290	270-280	265-275
Shore Hardness (7 days)	65-70	65-70	60-65	52-55
Drying (hour)	7	6	5	4.5
Pot life (hour)	7.5	5.5	4.5	3.5
Gloss after UV (20 degree)*	85	85	85	85
Abrasion Test (mg loss/1000 cycle)*	0.1771	0.2325	0.2487	0.3489
Impact Strength (500 g/30, 50, 70 cm)*	4,4,2	4,4,2	4,4,4	4,4,5
Cross-cut Adhesion Test (aluminum/galvanized/sheet)*	1,1,4	0,0,3	0,0,3	0,0,0
Salt Spray Test (350 hours)*	4	5	5	5

*1 was rated as the worst and 5 as the best.
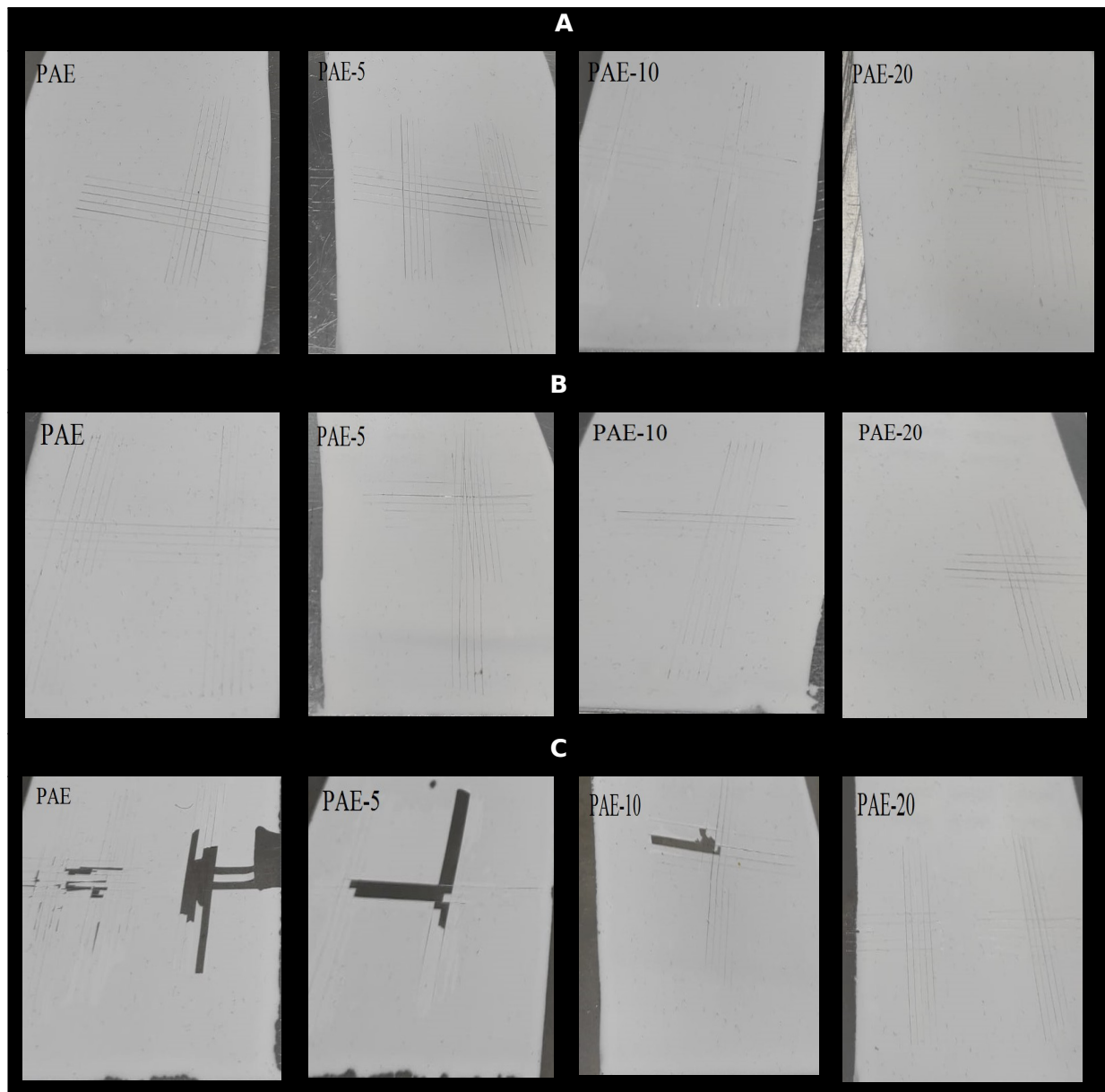
Figure 9. Cross-cut images for A) aluminum, B) galvanized and C) sheet surfaces.

In this study, the panels of paint mixtures prepared at the same film thickness were kept in a salt spray cabinet containing 20% NaCl solution for 250 hours. The images obtained at the end of the period are given in Figure 10. It was observed that the corrosion resistance increased with the increase of the acrylic copolymer ratio in the mixture, this improvement may have been achieved due to increased adhesion to the ground and reduced the amount of areas reached by the salt solution.

In impact testing, which is used to evaluate the toughness, fracture resistance, or impact resistance of the material during an impact, a generally known weight is released from a known height so that it collides with the sample with a sudden force. The layers coated with the paints prepared in this study were subjected to an impact test with a weight of 500 g at 30, 50 and 70 cm heights. Experiment result images are given in Figure 11. There was no difference in impact strengths for 30 and 50 cm heights. When the height of 70 cm was increased, the impact resistance increased especially in mixtures prepared from resins with 10% and 20% acrylic copolymer added.
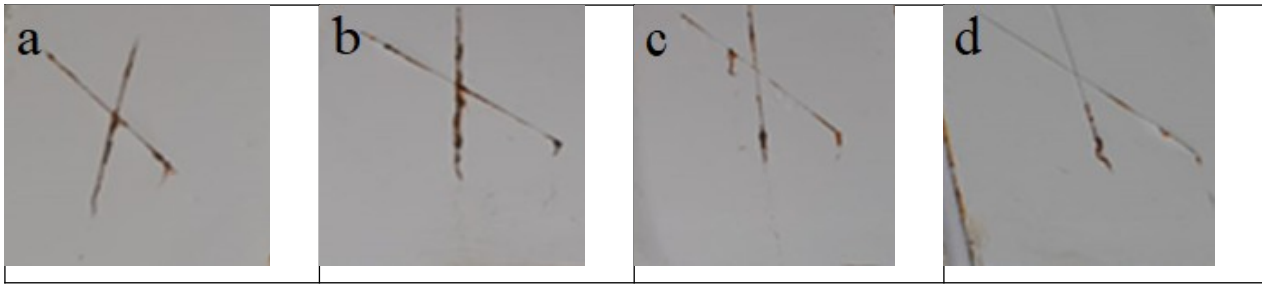
Figure 10. Paint salt spray test results of a) PAE, b) PAE-5, c) PAE-10, d) PAE-20 after 250 h.
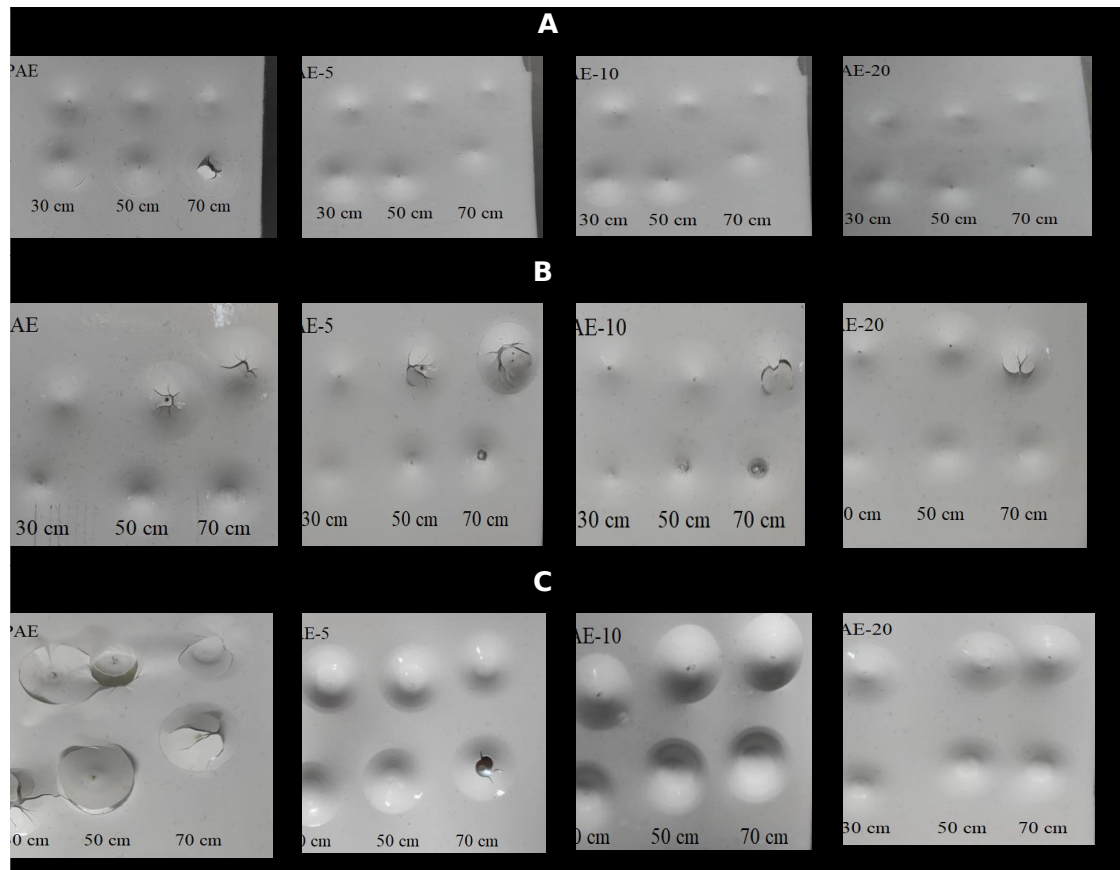
Figure 11. Paint impact test results of A) aluminum, B) galvanized and C) sheet surfaces.

4. CONCLUSION

In this study, besides the prominent and very important properties of polyaspartic ester resin, which is a new generation aliphatic coating system, studies were carried out to improve the properties such as, pot life, flexibility, color, adhesion etc... that can be considered as negative. The properties to be investigated were made by adding an acrylic copolymer with high OH value at 5, 10 and 20% ratios to PAE. The adhesion property was examined by the cross-cut test and increased according to the standard test method. This result was obtained especially for mixtures containing 10 and 20% copolymers. The flexibility of PAE was examined by the tensile-tensile test, and the increase in flexibility with the increase of the acrylic copolymer ratio added to the mixture was evaluated by taking into account the elasticity modules. The improvement of these properties has been achieved in PAE's superior yellowing resistance property and again without decreasing its superior pre- and post-UV gloss properties. These results, which are positive and do not lose the existing properties, also reduced the cost by adding acrylic copolymer to PAE. All results increased the application potential of a new system, polyaspartic ester resin, with new properties. The acrylic polyols and aspartic mixtures may be used in the preparation of paints and varnishes applied on concrete, metal, and wood surfaces.

5. CONFLICT OF INTEREST

There is no conflict of interest.

6. ACKNOWLEDGMENTS

We would like to express our gratitude to İZEL KİMYA SAN TIC A.S. for their financial support under the project (IZL 60) and to Paint Application Chief Technician Rasim AKKOCA, who contributed to the works.

7. REFERENCES

1. Shojaei B, Najafi M, Yazdanbakhsh A, Abtahi M, Zhang C. A review on the applications of polyurea in the construction industry. Polym Adv Technol [Internet]. 2021 Aug 1 [cited 2023 Jun 12];32(8):2797–812. Available from: <URL>

2. Szafran J, Matusiak) A. LIGHTWEIGHT STRUCTURES in CIVIL ENGINEERING POLYUREA COATING SYSTEMS: DEFINITION, RESEARCH, APPLICATIONS. 2016; Available from: <URL>

3. Iqbal N, Tripathi M, Parthasarathy S, Kumar D, Roy PK. Polyurea spray coatings: Tailoring material properties through chemical crosslinking. Prog Org Coat. 2018 Oct 1;123:201–8. Available from: <DOI>

4. T A, M A, Jayaprabakar J, Jeevahan J, Rb D. Study on mechanical properties of polyurea coating with various process parameters. <DOI> [Internet]. 2020 [cited 2023 Jun 12];25(5):257–63. Available from: <URL>

5. Sánchez-Ferrer A, Soprunyuk V, Engelhardt M, Stehle R, Gilg HA, Schranz W, et al. Polyurea Networks from Moisture-Cure, Reaction-Setting, Aliphatic Polyisocyanates with Tunable Mechanical and Thermal Properties. ACS Appl Polym Mater [Internet]. 2021 Aug 13 [cited 2023 Jun 12];3(8):4070–8. Available from: <URL>

6. Editors A, Bhudolia SK, Chandrakant Joshi S, Leong Sing S, Min Huang W, Luo J, et al. Mini-Review of Self-Healing Mechanism and Formulation Optimization of Polyurea Coating. Polymers 2022, Vol 14, Page 2808 [Internet]. 2022 Jul 9 [cited 2023 Jun 12];14(14):2808. Available from: <URL>

7. Sánchez-Ferrer A, Rogez D, Martinoty P. Synthesis and Characterization of New Polyurea Elastomers by Sol/Gel Chemistry. Macromol Chem Phys [Internet]. 2010 Aug 2 [cited 2023 Jun 12];211(15):1712–21. Available from: <URL>

8. Santana JS, Cardoso ES, Triboni ER, Politi MJ. Polyureas Versatile Polymers for New Academic and Technological Applications. Polymers 2021, Vol 13, Page 4393 [Internet]. 2021 Dec 15 [cited 2023 Jun 12];13(24):4393. Available from: <URL>

9. Liu XP, Zheng TL. The Synthesis of a Polyaspartic Acid Ester and Development of the Coatings. Adv Mat Res [Internet]. 2014 [cited 2023 Jun 12];842:297–301. Available from: <URL>

10. Effect of Temperature on Tensile Curve of Polyaspartic Ester Polyurea and Its Activation Energy Analysis -

IOPscience [Internet]. [cited 2023 Jun 12]. Available from: <URL>

11. Bringing Polyaspartic Technology to the Next Level: Low Viscous Solvent-free Floor Coatings. ENVVT 2014 / / Karl H. - PDF Free Download [Internet]. [cited 2023 Jun 12]. Available from: <URL>

12. Feng J, Liao LM, Chen L, Xiao CJ, Wang SF, Li H. Research on the Formula of Polyaspartic Ester Polyurea Concrete Coating and its Application. Applied Mechanics and Materials [Internet]. 2013 [cited 2023 Jun 12];423–426:1159–63. Available from: <URL>

13. Jing F, Wei H, Zhen L, Zai-Qin W. Aliphatic Polyurea Coating Materials Based on Novel Polyaspartic Ester : Preparation and Application. Journal of Yangtze River Scientific Research Institute [Internet]. 2012 Feb 1 [cited 2023 Jun 12];29(2):64. Available from: <URL>

14. Lu P, Huang WB, Ma XQ, Liu XD. Novel Polyaspartic Ester Polyureas Based on Flexible Polyaspartic Ester. Adv Mat Res [Internet]. 2011 [cited 2023 Jun 12];197–198:1294–8. Available from: <URL>

15. Carl Angeloff PE, Edward P. Squiller PhD, and Kurt E. Best, Bayer Corporation. Two-Component Aliphatic Polyurea Coatings for High Productivity Applications [Internet]. [cited 2023 Jun 12]. Available from: <URL>

16. Ii DJP. Polyurea Elastomer Technology: History, Chemistry & Basic Formulating Techniques. Available from: <URL>

17. Dudley J. Primeaux II. Polyurea vs Polyurethane & Polyurethane/Polyurea: What's the Difference? [Internet]. [cited 2023 Jun 12]. Available from: <URL>

18. Golling FE, Pires R, Hecking A, Weikard J, Richter F, Danielmeier K, et al. Polyurethanes for coatings and adhesives – chemistry and applications. Polym Int [Internet]. 2019 May 1 [cited 2023 Jun 12];68(5):848–55. Available from: <URL>

19. Smith[1] A, Eng[2] B. INTERCORR2010_365 Polyaspartic Coatings That Perform as Well as Polyurethane Coatings. 2010; Available from: <URL>

20. Carl Angeloff PE, Edward P. Squiller PhD, and Kurt E. Best, Bayer Corporation. Two-Component Aliphatic Polyurea Coatings for High Productivity Applications [Internet]. [cited 2023 Jun 12]. Available from: <URL>

21. Assarian A, Martinez S. Improving Polyaspartic Anti-Corrosion Coating Protective Properties with the use of Nano-silica. Acta Chim Slov [Internet]. 2018 Sep 17 [cited 2023 Jun 12];65(3):569–77. Available from: <URL>

22. Eco-Friendly Hyperbranched Polyaspartic Polyol and Polyurethane-Urea-Polyurea Hybrid Coatings | 2021-02-11 | PCI Magazine [Internet]. [cited 2023 Jun 12]. Available from: <URL>

23. Petit H, Henry N, Krebs A, Uytterhoeven G, Jong F de. Ambient cure high solids acrylic resins for automotive refinish clear coat applications. Prog Org Coat. 2001 Nov 1;43(1–3):41–9. Available from: <DOI>

24. Ding K, Liu J, Chen H, Wang H. Hyper-branched acrylic resin with high solid contents. <DOI> [Internet]. 2017 Oct 23 [cited 2023 Jun 12];31(9):1149–60. Available from: <URL>

25. Diakournakos CD, Xu Q, Jones FN, Baghdachi J, Wu L. Synthesis of acrylic resins for high-solids coatings by solution and separation polymerization. Journal of Coatings Technology [Internet]. 2000 [cited 2023 Jun 12];72(908):61–70. Available from: <URL>

17. Ii DJP. Polyurea Coatings: That Was Then, This is Now. 2004; Available from: <URL>

26. Kim JW, Lee DC, Choi JS. Synthesis of Eco-Friendly High Solid Acrylic Resins and Curing Properties of Acrylic Urethane Resin Coatings. Korean Chemical Engineering Research [Internet]. 2017 Oct 1 [cited 2023 Jun 12];55(5):586–92. Available from: <DOI>

27. Wendels S, Avérous L. Biobased polyurethanes for biomedical applications. Bioact Mater. 2021 Apr 1;6(4):1083–106. Available from: <DOI>

28. Akay O, Altinkok C, Acik G, Yuce H, Ege GK. A bio-based and non-toxic polyurethane film derived from Luffa cylindrica cellulose and ʟ-Lysine diisocyanate ethyl ester. Eur Polym J. 2021 Dec 5;161:110856. Available from: <DOI>

29. Taheri M, Jahanfar M, Ogino K. Synthesis of acrylic resins for high-solids traffic marking paint by solution polymerization. <DOI> [Internet]. 2019 Jan 1 [cited 2023 Jun 12];22(1):213–25. Available from: <URL>

30. Zheng J, Aziz T, Fan H, Haq F, Ullah Khan F, Ullah R, et al. Synergistic impact of cellulose nanocrystals with multiple resins on thermal and mechanical behavior. Zeitschrift fur Physikalische Chemie [Internet]. 2021 Oct 1 [cited 2023 Jun 12];235(10):1247–62. Available from: <URL>

31. Ulianas A, Heng LY, Ahmad M. A Biosensor for Urea from Succinimide-Modified Acrylic Microspheres Based on Reflectance Transduction. Sensors 2011, Vol 11, Pages 8323-8338 [Internet]. 2011 Aug 26 [cited 2023 Jun 12];11(9):8323–38. Available from: <URL>

32. Lastovickova DN, Toulan FR, Mitchell JR, VanOosten D, Clay AM, Stanzione JF, et al. Resin, cure, and polymer properties of photopolymerizable resins containing bio-derived isosorbide. J Appl Polym Sci [Internet]. 2021 Jul 5 [cited 2023 Jun 12];138(25):app50574. Available from: <URL>

33. Zhang Y, Wang H, Eberhardt TL, Gu Q, Pan H. Preparation of carboxylated lignin-based epoxy resin

with excellent mechanical properties. Eur Polym J. 2021 May 5;150:110389. Available from: <DOI>

34. Çöpoğlu N, Çiçek B. Abrasion resistant glass-ceramic coatings reinforced with WC-nanoparticles. Surf Coat Technol. 2021 Aug 15;419:127275. Available from: <DOI>

35. Calabrese L, Proverbio E, Di Bella G, Galtieri G, Borsellino C. Failure behaviour of SPR joints after salt spray test. Eng Struct. 2015 Jan 1;82:33–43. Available from: <DOI>

36. Fujita S, Mizuno D. Corrosion and corrosion test methods of zinc coated steel sheets on automobiles. Corros Sci. 2007 Jan 1;49(1):211–9. Available from: <DOI>

Synthesis of New Azo Compounds and Their Application for a Simple Spectrophotometric Determination of Methyldopa Drug Using Anthranilic Acid and 2-Aminopyrimidine as Reagents

Ekhlas A. Abdulkareem¹* iD **, Nuha Farhan Abd Al-Karim¹** iD **, Israa I. Mahmoud²**

¹University of Diyala, Collage of Science, Department of Chemistry, Diyala, Iraq.
²Ministry of Education, General Directorate of Education, Muqdadiya, Diyala, Iraq.

Abstract: The goal of the current work is to synthesize methyldopa derivatives. Based on these reactions, two easy, speedy, accurate, inexpensive, and sensitive spectrophotometric approaches have been established for determining methyldopa (MED) in both pure and pharmaceutical forms. The proposed azo-coupling method depends on forming an azo compound between methyldopa drug and 2-AMPY or ANTH to produce two compounds of MED-2AMPY and MED-ANTH in the alkaline medium. The characterization of synthesized compounds utilizing UV-Visible and FT-IR spectra. FT-IR spectra of 2AMPY-MED confirmed the existence of OH, C-H$_{or}$, C-H$_{al}$, NH, N=N, C=O, and C=C vibration at 3455, 3059, 2973, 3100, 1476,1692, and 1560 cm^{-1}, and FT-IR spectra of ANTH-MED confirmed the existence of OH, C-H$_{or}$, NH, C=O and N=N vibration at 3490, 3050, 3100, 1701 and 1462 cm^{-1}, correspondingly. The obtained color of azo compounds was spectrophotometrically measured for the previously mentioned azo compounds at 450 and 455 nm, respectively. Under perfect conditions, the azo compound solutions exhibited molar absorptivities of 1563.0058 and 2091.0285 L.mol^{-1}.cm^{-1}, Sandell's sensitivity of 0.135 and 0.10 μg.cm^{-1}, and Beer-Lambert's law are obeyed over the ranges 6.25- 62.5 mg. L^{-1} for the two developed procedures, respectively.

1. INTRODUCTION

Methyldopa (MED), IUPAC name was α-methyl-3,4-dihydroxyphenylalalnine, whose structure is shown in Scheme 1. Methyldopa is a catecholamine derivative commonly used to treat mild to moderate arterial hypertension. Methyldopa is classified as a pro-drug since it works chiefly due to its metabolism in the central nervous system to α-methyl norepinephrine, an α2-adrenergic agonist(1,2). Several methods for quantifying methyldopa in pharmaceutical formulations have been proposed, including HPLC (3-5), polarography (6), flow injection analysis(7-10), titrimetry(11), potentiometry(12), and spectrophotometry methods(13-19). Aromatic amines were previously identified using the diazotization reaction. It is based on the reaction of a chromogenic reagent with a free primary amine to produce a diazonium salt. The technique includes using sulfamic acid or urea to remove excess nitrous acid, the stability of an intermediate diazonium salt at low temperatures, and the ejection of nitrogen bubbles (20-22). The

need for a simple, fast, low-cost, and selective method for determining methyldopa is evident based on the foregoing considerations. The technique described in this paper is depened on the reaction of methyldopa drug with 2-aminopyrimidine and anthranilic acid to produce orange color azo compounds (λ_{max} = 450 and 455 nm), respectively. Also, the reaction conditions were investigated by experimental design approaches in order to optimize the analytical response. When compared to other publications (23-25), the analytical results obtained by using the proposed

method are reliable.

2. EXPERIMENTAL

2.1. Apparatus
The new approach and the standard method used a portable UV-Vis spectrophotometer single beam (160) that used 1 cm quartz cells to measure absorbance with a wavelength range between 200 and 800 nm. The pH solutions were recorded using a Metlar pH meter. A digital Sartorius balance was used for the weighing process.
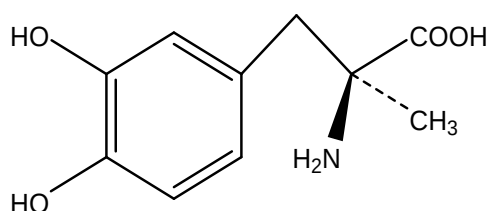
Scheme 1: The structure of methyldopa (26).

2.2. Reagents and Solutions
All of the chemicals utilized were of the highest quality. The purity of methyldopa (99.8%) was obtained from SAMARRA, FT-IR AQ, (SDI), 2-aminopyrimidine, and anthranilic acid from the Sigma-Aldrich company. Stock methyldopa drug solution (250 mg L^{-1}) was prepared by dissolving 25 mg in D.W. and diluting it in the 100 mL volumetric flask to the mark. A stock 2-aminopyrimidine and anthranilic acid solution (250 mg L^{-1}) were prepared by dissolving 25 mg in D.W. and diluting it in the volumetric flask (100 mL). 25% sodium hydroxide, 4% urea solution, and (1.0 %) NaNO$_2$ solution.

2.3. General Procedure for Pharmaceutical Preparations
Tablets 250 mg of Aldomet (Lebanon) and Aldosam (SDI) were carefully weighted, and the average dosage weight was calculated. The distilled water was used to dissolve the entire weight. The solution was then diluted in a volumetric flask (100 mL) and filtered to achieve complete solubility.

2.4. Synthesis of MED Azo Compound (23)
To 2-AMPY or ANTH (3.0 mmol) ice, conc. HCl (1.0 mL), and a (3.3 mmol) solution of NaNO$_2$ in H$_2$O (9 mL) were subsequently added, and the mixture was stirred at 0-10 ^{0}C for 8 minutes to produce a diazonium salt (RN$_3$$^+Cl^-$). To a methyldopa drug (3.0 mmol) solution in D.W (15 mL) 10% aq. sodium hydroxide (3 mL) was added. As well as the diazonium salt solution was subsequently added at 0-10 °C. The orange compound (2AMPY-MED) was produced by filtering the resulting product, washing it with small amounts of cold water, and drying it at 70 °C. Formula: C$_{14}$H$_{15}$N$_5$O$_4$; Mwt: 317.3 g/mol; Yield: 82%; m.p: 243-245 ^{0}C; FTFT-IR (cm^{-1}): OH (3455), CH$_{or}$(3059), CH$_{al}$(2973), NH(3100),C=O(1692), C=C(1560), N=N(1476) and orange compound

(ANTH-MED). Formula: C$_{17}$H$_{17}$N$_3$O$_6$; Mwt: 359.35 g/mol; Yield: 87%; m.p: 221-224 ^{0}C; FT-IR (cm^{-1}): OH (3490), CH$_{or}$(3050), NH(3100),C=O(1701), C=C(1592), N=N(1462). The purity of these compounds were checked by TLC using ethylacetate-n-hexane as eluent (27).

2.5. A General Method of Diazotization
The most efficient method was to produce an azo coupling solution by adding 1 mL of methyldopa 250 mg L^{-1} to a volumetric flask (10 mL) soaked in an ice bath (0-10 ^{0}C), 1 mL of hydrochloric acid (1:1), and 1 mL of (1%) NaNO$_2$ solution step by step. After 20 minutes, the mixture was prepared to use. Also, add (1.25 mL) of 4% urea solution with stirring to remove the excess nitrite, followed by adding 1.5 of 2-aminopyrimidine or 2.0 mL of anthranilic acid 250 mg L^{-1}. For 2AMPY or ANTH, add sodium hydroxide (1.0 or 1.75 mL, 25%), then dilute the mixture to 10 mL with D.W. The azo dye solution appears orange, and the absorption wavelengths for azo-2AMPY and azo-ANTH are 450 nm and 455 nm, respectively (28).

3. RESULTS AND DISCUSSION

2- amino pyrimidine and anthranilic acid has been used as chromogenic reagents to evaluate methyldopa drug. This procedure is based on a reaction between MED drug and reagents using azo-coupling reaction and producing an intensely colored azo dye solution (Scheme 2).

Absorption spectra of azo compounds MED–2AMPY and MED-ANTH system against a blank in an alkaline medium were produced orange-colored products which absorb maximally at 450 and 455 nm, as revealed in Figure 1 and Figure 2.

3.1. Synthesis and Characterization of MED Azo Compounds

By converting 2-AMPY and ANTH reagents to diazonium salt using HCl concentrated solution and sodium nitrate, followed by coupling with methyldopa, we synthesized novel methyldopa azo derivatives. FT-IR spectra of 2AMPY-MED confirm the existence of OH, $C-H_{or}$, $C-H_{al}$, NH, N=N, C=O, and C=C vibration at 3455, 3059, 2973, 3100, 1476,1692 and 1560 cm^{-1}, and FT-IR spectra of ANTH-MED confirm the existence of OH, $C-H_{or}$, NH, C=O and N=N vibration at 3490, 3050, 3110, 1701

and 1462 cm^{-1} (28), respectively.

3.2. Optimization of the Experimental Conditions

Parameters affected the absorption intensity of colored azo compounds, such as volume and type of acid, $NaNO_2$ volume, and reaction time. The influence of various acids was achieved for the formation of the diazonium salt solution, and the results are recorded in Table 1. The perfect acid volume was 1.0 and 0.25 mL for MED-2AMPY and MED-ANTH, respectively (Figure 5).
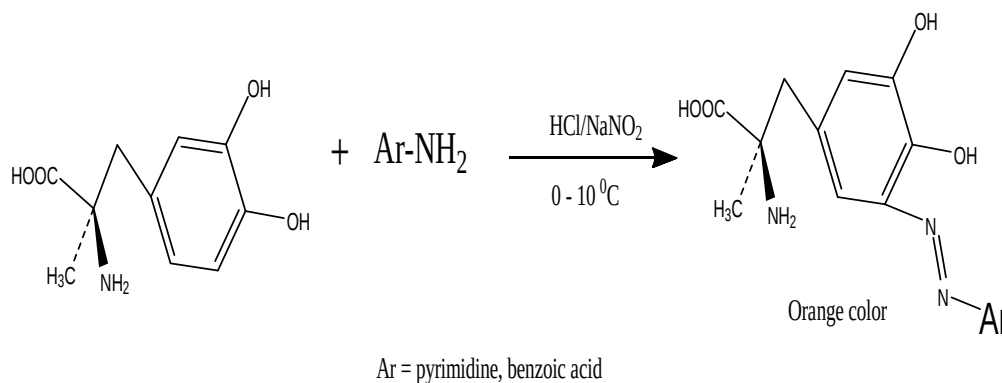
Scheme 2: Azo-coupling reaction (27).
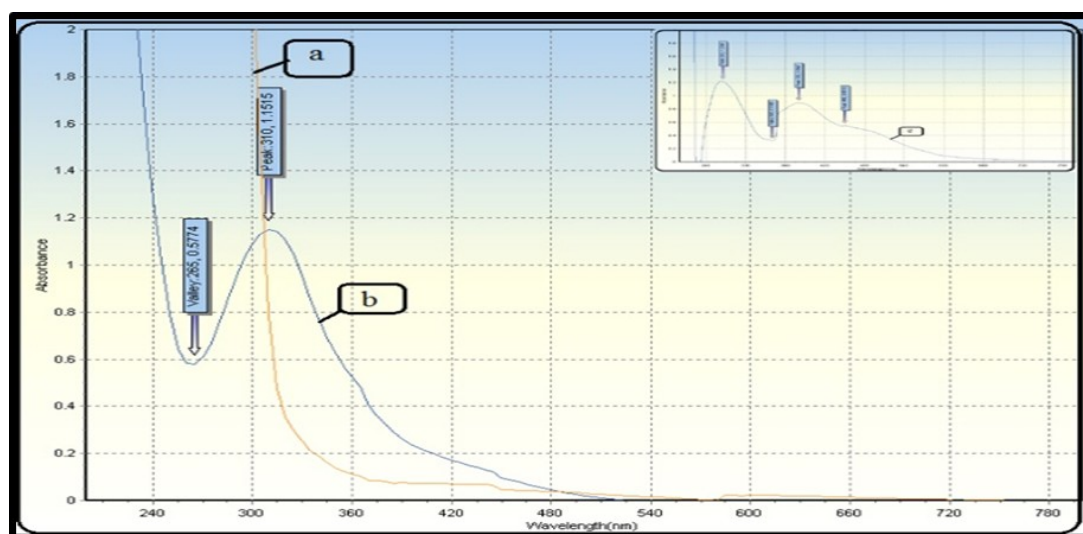
Figure 1: Absorption spectrum of (25µg.mL^{-1}) for (a- 2-Amino. Reag., b-MED drug) versus the blank solution (D.W), and c- MED- 2-Amino. azo comp. versus the blank solution.
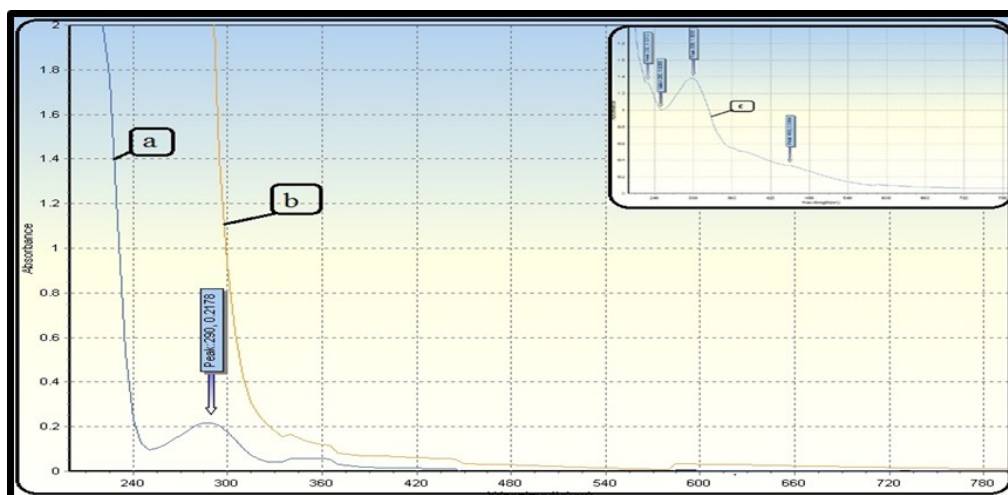
Figure 2: Molecular absorption spectrum of (25 µg/mL) for (a-MED drug, b-Anthranilic acid. Reag.) versus the blank solution (D.W), and c- MED- 2-Amino. azo comp. versus the blank of solution.
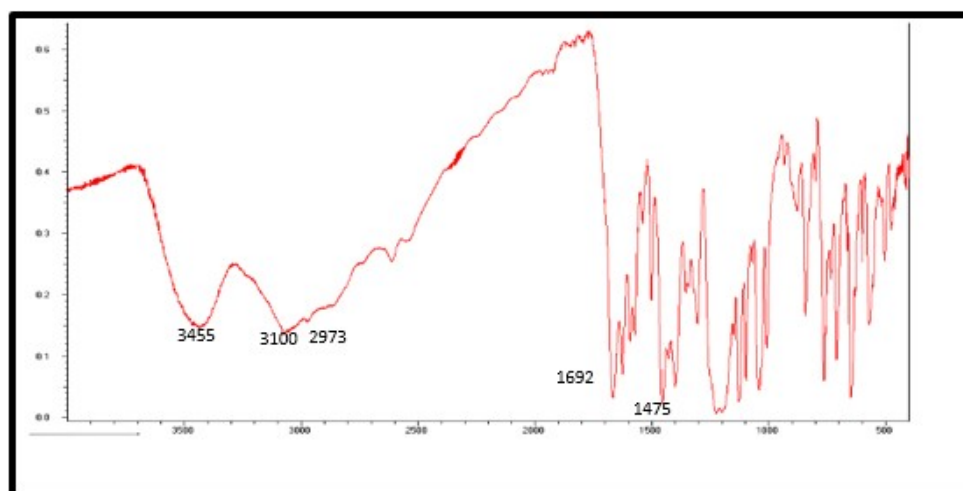
Figure 3: FT-IR of 2AMPY-MED azo compound.
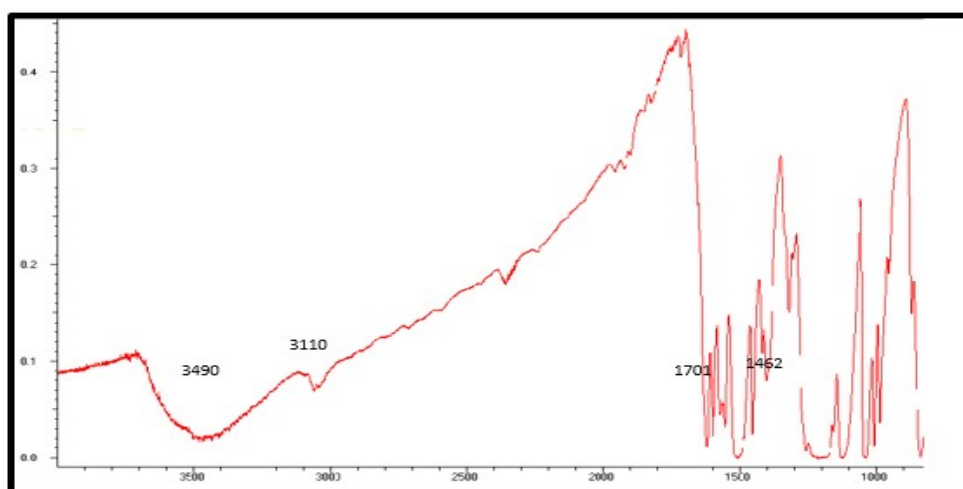
Figure 4: FT-IR of ANTH-MED azo compound.
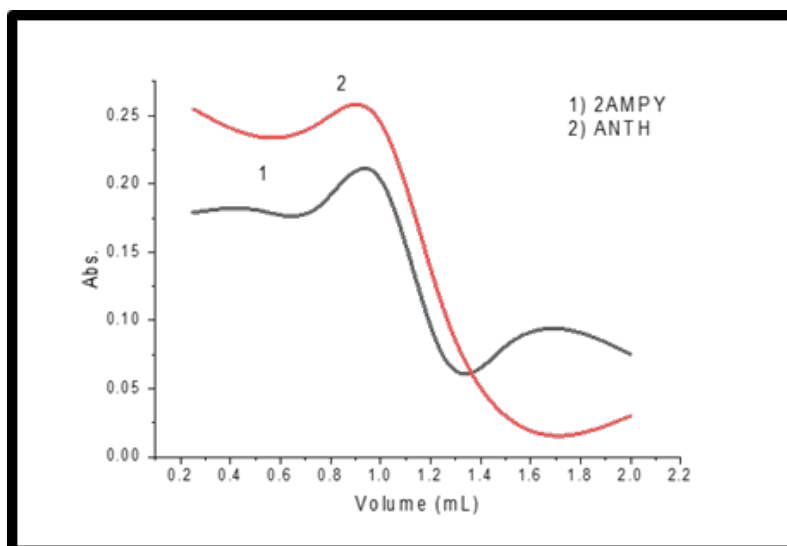
Figure 5: Effect of the volume of acid.

By experimenting with various volumes between the range of (0.2- 2.0 mL), the effect of the volume of sodium nitrite (1.0%) was examined. It showed that 1.0 mL for MED-2AMPY and MED-ANTH produced the best absorption intensity, as shown in Figure 6. To remove and extract the excess nitrous acid, varying volumes (0.25- 2.0 mL) from 4% urea solution were utilized (Figure 7).

Table 2 studied the effect of various bases on forming azo derivative (25%) of NaOH, KOH, and NH3 solution. The findings indicate that the ideal base was NaOH solution. The different volumes of NaOH (25%) from (0.25 to 2.0 mL) were examined. The best absorbance appeared by adding 1.0 mL and 1.7 mL for MED-2AMPY and MED-ANTH, respectively, as in Figure 8.

1.5 and 2.0 mL from reagent (2AMPY or ANTH) gave the greatest absorbance and was formed with high sensitivity, as shown in Figure 11. Under the perfect conditions (type and volume of acid, NaNO2 volume, and type of base), the reaction's stoichiometry between MED and 2-AMPY or ANTH was studied with continuous variation methods (29). The stoichiometric ratio between 2AMPY or ANTH with MED was 1:1, Figures 9 and 10.

3.3. Calibration Curve
The calibration graph for MED pure form through azo-coupling reaction with 2AMPY or ANTH showed excellent linearity at concentration ranges of 6.25 – 62.5 mg L^{-1}. The results are shown in Figure 12.

3.4. Comparison with Literature Studies
The results of the suggested method were contrasted with those of the previously published ones. Table 5 compares the performance of the suggested process with that of other methods in evaluating MED drugs for a variety of samples.

Table 1. Effect of the type of acid.

Type of acid	Abs. of MED-2AMPY (450 nm)	Abs. of MED-ANTH (455 nm)
HCl	0.205	**0.245**
CH$_3$COOH	0.115	**0.175**
HNO$_3$	0.080	**0.080**
H$_2$SO$_4$	0.072	**0.061**
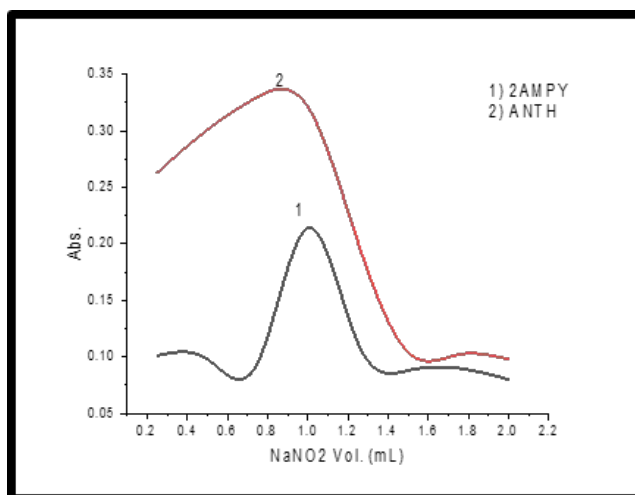
Figure 6: Effect of sodium nitrite (1%).
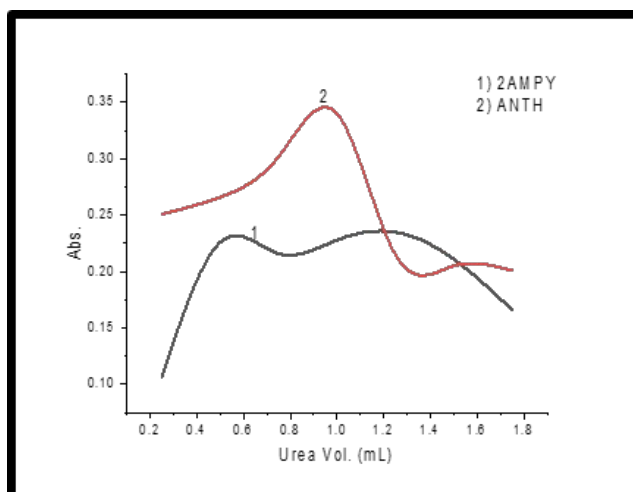
Figure 7: Effect of the volume of urea.
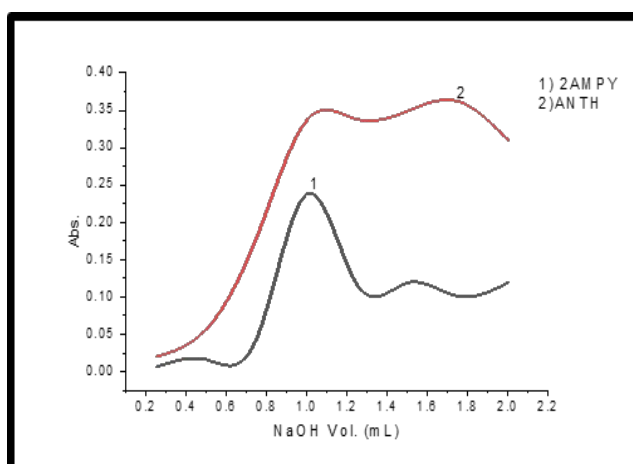
Figure 8: Effect of volume of NaOH.

Table 2: Effect of the type of base.

Type of base	Abs. of MED-2AMPY (450 nm).	Abs. of MED-ANTH (455 nm)
NaOH	0.238	**0.342**
KOH	0.090	**0.173**
NH$_3$	0.084	**0.060**
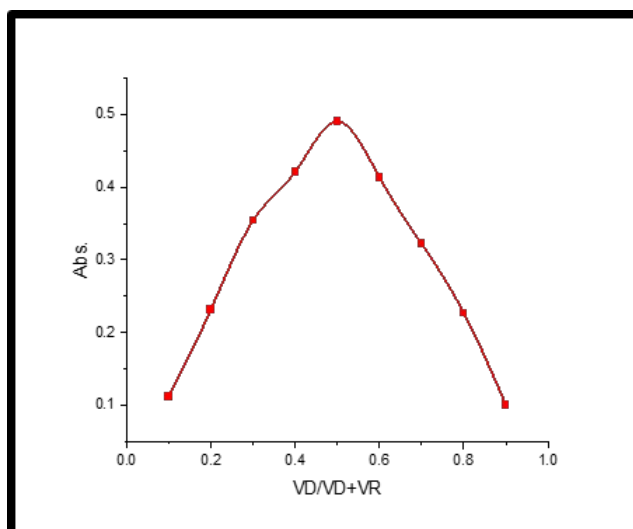
Figure 9: Continuous variation method of 2AMPY-MED azo compound.
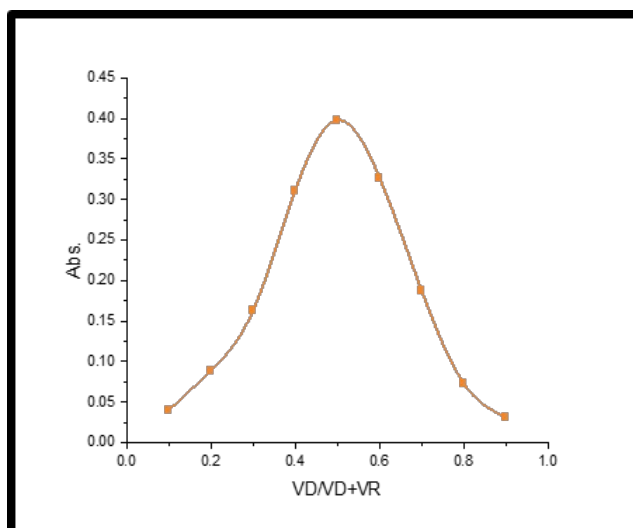
Figure 10: Continuous variation method of ANTH-MED azo compound.
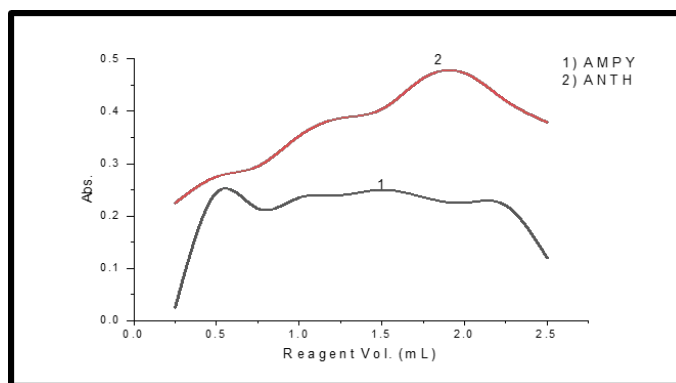
Figure 11: Effect of reagent.
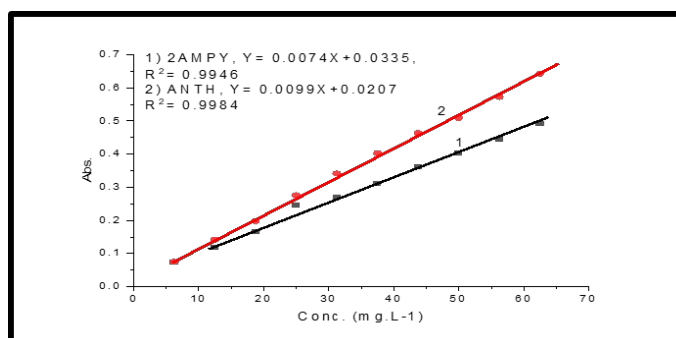
Figure 12: Calibration graph of MED-2AMPY and MED-ANTH (resulting product).

Table 3: Optical characteristics of the calibration graph for determination of MED by 2AMPY and ANTH reagent.

Parameters	MED-2AMPY	MED-ANTH
λ_{max} (nm)	450	455
Color	Orange	
Regression equation	Y=0.0074X+0.0335	Y=0.0099X+0.0207
Linearity range(mg L-1)	6.25-62.5	6.25-62.5
Correlation Cofficient (R^2)	0.9946	0.9984
ε(L.mol^{-1}.cm^{-1})	1563.0058	2091.0285
Sandell's sensivity ,μg . cm^{-2}	0.135	0.10
Slope (b)	0.0074	0.0099
Intercept(a)	0.0335	0.0207
LOD(mg L^{-1})	1.77	1.32
LOQ(mg L^{-1})	5.80	4.37
C.L.for the slope(b$\pm$ts$_b$), 95%	0.0335$\pm$9.25 x10^{-5}	0.0099$\pm$ 2.2 x10^{-3}
C.L.for the intercept(a$\pm$ts$_a$), 95%	0.0074$\pm$ 3.5x10^{-3}	0.0207$\pm$ 6.6x 10^{-5}
Standard error for regression line ,$S_{y/x}$	0.01	0.0088
*C.L for Conc.(X$_1$) mg L^{-1} at 95%	25.31$\pm$ 0.99	24$\pm$0.77
*C.L for Conc.(X$_2$) mg L^{-1} at 95%	35.62$\pm$0.59	35$\pm$0.49
*C.L for Conc.(X$_3$) mg L^{-1} at 95%	48.95$\pm$1.17	51$\pm$1.20

*MED-2AMPY (X$_1$=25, X$_2$=35, X$_3$=50) and MED-ANTH (X$_1$= 25, X$_2$= 35, X$_3$=50)

Table 4. Evaluation of MED drug in commercial tablets by spectrophotometric technique.

Drug	Conc. of drug mg L^{-1}		Relative Error%	Recov. %	Average Recov.%	RSD% (n=3)
	Taken	**Found**				
			MED-2AMPY			
Methyldopa (Aldomet)	12.50	12.13	-3.05	97.04	100.90	5.10
	25.00	25.94	3.76	103.76		4.31
	37.50	38.22	1.92	101.92		2.02
Methyldopa (Aldosam)	12.50	12.80	2.4	102.5	101.66	4.20
	25.00	26.00	4	104		3.62
	37.50	36.92	-1.5	98.5		2.44
			MED-ANTH			
Methyldopa (Aldomet)	12.50	11.93	-4.56	95.44	99.63	4.70
	25.00	26.18	4.72	104.72		3.99
	37.50	37.03	-1.25	98.75		1.92
Methyldopa (Aldosam)	12.50	12.40	-0.8	99.2	97.00	3.83
	25.00	24.01	-3.96	96.04		4.56
	37.50	35.92	-4.21	95.78		1.09

Table 5: Comparing the suggested method's LOD and LOQ values to those of other methyldopa evaluation techniques reported in the literature.

Method	LOD	LOQ	Ref.
HPLC	0.027 mg L^{-1}	-	(30)
Spectrophotometric method	0.152 mg L^{-1}	0.460 mg L^{-1}	(31)
electrochemical sensor	9.0 nM	-	(32)
Flow injection method	0.769 mg L^{-1}	-	(33)
Colorimetric method	0.38 mg L^{-1}	-	(34)
Nanostructured TiO$_2$ Carbon Paste Based Sensor	1μM	-	(35)
Electrochemical method	0.01 mg L^{-1}	-	(36)
Electrochemical method	8 μM	-	(37)
HPLC	-	2 ng/mL	(38)
Spectrophotometric method	1.77 mg L^{-1} 1.32 mg L^{-1}	5.80 mg L^{-1} 4.37 mg L^{-1}	Present work

4. CONCLUSION

The suggested method for evaluating methyldopa in bulk and pharmaceutical dosage forms is straightforward, precise, accurate, and selective. Unlike the chromatographic technique, this one is quick, inexpensive, and requires no expensive tools. As a result, it may be successfully used for routine evaluation of methyldopa medication in bulk and commercial formulation.

5. CONFLICT OF INTEREST

The researchers affirm that there are no conflicts of interest.

6. ACKNOWLEDGMENT

The researchers extend their gratitude to University of Diyala and the College of Science for providing them with the necessary requirements to complete this work.

7. REFERENCES

1. Gotardo MA, Lima LS, Sequinel R, Rufino JL, Pezza L, Pezza HR. A simple spectrophotometric method for the determination of methyldopa using p-chloranil in the presence of hydrogen peroxide. Eclética Química. 2008;33:7-12. Available from: <URL>

2. Al-Abachi MQ, Al-Uzri WA, Abed SS. Batch and Flow-Injection Spectrophotometric Determination of Methyldopa Using Metochlopramide as diazotized Chromogenic Reagent. Iraqi National Journal of Chemistry. 2013;49:12-24. Available from: <URL>

3. Zečević M, Živanović LJ, Agatonovic-Kustrin S, Minic D. The use of a response surface methodology on HPLC analysis of methyldopa, amiloride and hydrochlorothiazide in Tablets. Journal of pharmaceutical and biomedical analysis. 2001 Mar 1;24(5-6):1019-25. Available from: <DOI>

4. Ting S. Liquid chromatographic determination of methyldopa and methyldopa-thiazide combinations in dosage forms. Journal of the Association of Official Analytical Chemists. 1983 Nov 1;66(6):1436-42. Available from: <URL>

5. Susan T, Collaborators: Brown RL Dougherty LA Schepman JB Doucette YH Schneider PJ Perry PJ Rihbany LA Gordon K. Liquid chromatographic determination of methyldopa and methyldopa-thiazide combinations in Tablets: collaborative study. Journal of the Association of Official Analytical Chemists. 1984 Nov 1;67(6):1118-20. Available from: <URL>

6. J. Ballantine and A. D. Woolfson, "Determination of catecholamines in pharmaceutical preparations by differential pulse polarography at the glassy carbon electrode," Int. J. Pharm., vol. 3, no. 4–5, pp. 239–246, 1979. Available from: <DOI>

7. Erdoğdu G, Yağci ŞZ, Savan EK. Investigation of the voltammetric behavior of methyldopa at a poly (p-Aminobenzene Sulfonic Acid) modified sensor. Turkish Journal of Pharmaceutical Sciences. 2019 Dec;16(4):450. Available from: <URL>

8. Berzas Nevado JJ, Lemus Gallego JM, Buitrago Laguna P. Spectrophotometric determination of dopamine and methyldopa with metaperiodate by flow injection analysis. Fresenius' journal of analytical chemistry. 1995 Jan;353(2):221-3. Available from: <DOI>

9. Ribeiro PR, Neto JG, Pezza L, Pezza HR. Flow-injection spectrophotometric determination of methyldopa in pharmaceutical formulations. Talanta. 2005 Jul 15;67(1):240-4. Available from: <DOI>

10. Matthieu T, Junior AR, Vila M. A Simple Flow Injection Spectrophotometric Method for the Determination of α-Methyldopa in Pharmaceutical Preparations Original Paper. Journal of Flow Injection Analysis. 2004;21(2):132. Available from: <URL>

11. Pathak VN, Shukla SR, Shukla IC. Direct titrimetric determination of the antihypertensive drugs methyldopa and propranolol in pharmaceutical preparations. Analyst. 1982;107(1278):1086-7. Available from: <DOI>

12. Badawy SS, Issa YM, Tag-Eldin AS. Potentiometric determination of l-dopa, carbidopa, methyldopa and aspartame using a new trinitrobenzenesulfonate selective electrode. Electroanalysis. 1996 Nov;8(11):1060-4. Available from: <DOI>

13. Sanati AL, Faridbod F. Electrochemical determination of methyldopa by graphene quantum dot/1-butyl-3-methylimidazolium hexafluoro phosphate nanocomposite electrode. Int. J. Electrochem. Sci. 2017 Sep 1;12(9):7997-8005. Available from: <URL>

14. Rashid QN, Bakir MH, Baban SO. Spectrophotometric determination of methyldopa in pure form and in the pharmaceutical preparations. Tikrit Journal of Pharmaceutical Sciences. 2016;11(1):67-77. Available from: <URL>

15. Upadhyay K, Asthana A, Tamrakar RK. Extractive spectrophotometric determination of α-methyldopa in bulk dosage and in its formulations. Research on Chemical Intermediates. 2015 Aug;41(8):5521-8. Available from: <DOI>

16. Bahgat EA. Spectrophotometric Microdetermination of Methyldopa and Etilefrine Hydrochloride using Copper (II)-Neocuproine Reagent in Pure Form and Pharmaceutical Formulations. Scholars Research Library. 2018. Available from: <URL>

17. Sultan MA. New, simple and validated kinetics spectrophotometric method for determination of moxifloxacine in its pharmaceutical formulations. Arabian Journal of Chemistry. 2009 Oct 1;2(2):79-85. Available from: <DOI>

18. Fiaz T, Fatima N, Zaidi SZ, Abbas T, Kazimi MR. Investigation of iron complex formation of anti-hypertensive drug: Methyldopa. American Journal of Analytical Chemistry. 2015 May 5;6(06):551. Available from: <URL>

19. Helaleh MI, Rahman N, Abu-Nameh ES. Use of cerium (IV) nitrate in the spectrophotometric determination of levodopa and methyldopa in the pure form and pharmaceutical preparations. Analytical sciences. 1997 Dec 10;13(6):1007-10. Available from: <DOI>

20. Abdullah AM, Hasson MM, Thani MZ. Synthesis, thermal analysis, spectroscopy and magnetic properties of some transition metals complexes derived from new azo compound. Materials Today: Proceedings. 2020 Jan 1;20:595-8. Available from: <DOI>

21. Thani MZ, Dadoosh SA, Abdullah AM, Fahad AS, Fahad YS, Faraj FL. Evaluation of salbutamol in pure form and pharmaceutical formulations using spectrophotometry and green nonionic surfactant of cloud point extraction. InJournal of Physics: Conference Series 2021 Mar 1 (Vol. 1853, No. 1, p. 012022). IOP Publishing. Available from: <URL>

22. Dadoosh SA, Thani MZ, Abdullah AM, Fahad AS, Fahad YS. Development of an Ecological-friendly Method for Dexamethasone Determination and Cloud Point Extraction in pharmaceutical formulations using Schiff Base Reaction. Egyptian Journal of Chemistry. 2021 Sep 1;64(9):5083-92. Available from: <URL>

23. P. R. S. Ribeiro, J. A. G. Neto, L. Pezza, and H. R. Pezza, "Flow-injection spectrophotometric determination of methyldopa in pharmaceutical formulations," Talanta, vol. 67, no. 1, pp. 240–244, 2005. Available from: <DOI>

24. S. Ashour, "A novel sensitive colorimetric determination of catecholamine drug in dosage form via oxidative coupling reaction with MBTH and potassium ferricyanide," Drug Anal. Res., vol. 5, no. 1, pp. 51–58, 2021. Available from: <DOI>

25. T. Fiaz, N. Fatima, S. Z. A. Zaidi, T. Abbas, and M. R. Kazimi, "Investigation of Iron Complex Formation of Anti-Hypertensive Drug: Methyldopa," Am. J. Anal. Chem., vol. 6, no. 06, p. 551, 2015. Available from: <DOI>

26. S. Emara, T. Masujima, W. Zarad, M. Kamal, M. Fouad, and R. El-Bagary, "A Combination of isocratic and gradient elution modes in HPLC with the aid of time-overlapping process for rapid determination of methyldopa in human urine," J. Liq. Chromatogr. Relat. Technol., vol. 38, no. 2, pp. 153–162, 2015. Available from: <DOI>

27. M. Z. Thani, S. A. Dadoosh, A. S. Fahad, A. M. Abdullah, and Y. S. Fahad, "Synthesis of New Azo Compound and its Application for Spectrophotometric Determination of Sulfamethoxazole and Extraction using Cloud Point Extraction" IJDDT, Volume 12 Issue 3, July - September 2022. Available from: <URL>

28. D. L. Pavia, G. M. Lampman, G. S. Kriz, and J. A. Vyvyan, Introduction to spectroscopy. Cengage learning, 2014. Available from: <URL>

29. Santos LD, Santos QO, Moreno I, Novaes CG, dos Santos MJ, Bezerra MA. Multivariate optimization of a simultaneous cloud point extraction procedure of Cd, Cu and Ni from sediments samples and determination by ICP OES. Journal of the Brazilian Chemical Society. 2016;27:745-52. Available from: <URL>

30. Emara S, Masujima T, Zarad W, Kamal M, Fouad M, El-Bagary R. An eco-friendly direct injection HPLC method for methyldopa determination in serum by mixed-mode chromatography using a single protein-coated column. Journal of chromatographic science. 2015 Sep 1;53(8):1353-60. Available from: <DOI>

31. BICHAN MJ, ABDOON FM. A NOVEL SPECTROPHOTOMETRIC DETERMINATION OF METHYLDOPA THROUGH TERNARY COMPLEXATION PROCEDURE USING FE (III), MN (II), AND CO (II) WITH 2-AMINOPYRIDINE. Asian Journal of pharmaceutical and Clinical Research. 2019;12(3):366-71. Available from: <URL>

32. Mohammadi SZ, Beitollahi H, Jasemi M, Akbari A. Nanomolar determination of methyldopa in the presence of large amounts of hydrochlorothiazide using a carbon paste electrode modified with graphene oxide nanosheets and 3-(4′-amino-3′-hydroxy-biphenyl-4-yl)-acrylic acid. Electroanalysis. 2015 Oct;27(10):2421-30. Available from: <DOI>

33. Al-Abachi MQ, Sinan R, Haddi H. Spectrophotometric determination of methyldopa and dopamine hydrochloride in pharmaceutical preparations using flow injection analysis.

National Journal of Chemistry. 2009;36:597-604. Available from: <URL>

34. AL-Da'amy MA, AL-Moswi RF. Asensitive colorimetric method for the determination of Methyldopa in pharmaceutical preparation via oxidative coupling organic reaction with Thiamine Hydrochloride in the presence of potassium periodate. kerbala journal of pharmaceutical sciences. 2013(6). Available from: <URL>

35. Garcia LF, Cunha CE, Moreno EK, Thomaz DV, Sanz Lobón G, Luque R, Somerset V, de Souza Gil E. Nanostructured TiO2 carbon paste based sensor for determination of methyldopa. Pharmaceuticals. 2018 Oct 5;11(4):99. Available from: <URL>

36. Sanati AL, Faridbod F. Electrochemical determination of methyldopa by graphene quantum dot/1-butyl-3-methylimidazolium hexafluoro phosphate nanocomposite electrode. Int. J. Electrochem. Sci. 2017 Sep 1;12(9):7997-8005. Available from: <URL>

37. Antunes RS, Thomaz DV, Garcia LF, de Souza Gil E, Sommerset VS, Lopes FM. Determination of methyldopa and paracetamol in pharmaceutical samples by a low cost genipa americana l. polyphenol oxidase based biosensor. Advanced Pharmaceutical Bulletin. 2019 Aug;9(3):416. Available from: <URL>

38. Bahrami G, Kiani A, Mirzaeei S. A rapid high performance liquid chromatographic determination of methyldopa in human serum with fluorescence detection and alumina extraction: Application to a bioequivalence study. Journal of Chromatography B. 2006 Mar 7;832(2):197-201. Available from: <URL>

Novel Perylene-Based Antimicrobial PDI Chromophores

Cansu Yılmaz[1] (iD), Pinar Güner[2] (iD), Tülin Aşkun[2] (iD), Funda Yükrük[1]* (iD)

[1]Department of Chemistry, Faculty of Science and Arts, Balikesir University, Balikesir, 10145, Türkiye
[2]Department of Biology, Faculty of Sciences and Arts, Balikesir University, Balikesir, 10145, Türkiye

Abstract: The main goal of the study was to monitor the Antimicrobial activity of two novel perylene diimides which were synthesized and characterized. Antimicrobial activity was investigated against Four *Mycobacterium tuberculosis* strains (MT) (Mt-H$_{37}$Rv, Mt-H$_{37}$Ra and two clinical isolates) and two *Staphylococcus aureus* strains [Methicillin-resistant *Staphylococcus aureus* (MRSA) and *Staphylococcus aureus (SA)*]. Minimum inhibitory concentrations (MICs) and minimum bactericidal activity (MBCs) were determined. Both compounds exhibited bactericidal effects and MICs were found to be changing in the range of 48-96 µg/mL for four MT-strains. Compounds were also effective on *Staphylococcus* strains at MIC = 96 µg/mL.

1. INTRODUCTION

Perylene diimides are reddish dyes with very high quantum yields. Red chromophores based on 3,4:9,10-perylenebis(dicarboximide)s have shown great promise in a variety of applications owing to their outstanding chemical, thermal and photochemical stability. They have been used widely in such as reprographic processes (1-2), organic light-emitting diodes (3-4), molecular switches and wires (5-6), light-harvesting arrays (7), photoreactive thin films (8-11), solar cells (12-13), and dye lasers (14-15) and photosensitizers (16). By single or double amine substitution on the perylene core, the absorption maxima at these dyes can be shifted up to 750 nm with further appropriate modifications, solubility can be improved.

Perylene diimides also became important field of interest for antimicrobial activities of perylene derivatives in addition to their role in the chemical industry (18-19). *Mycobacterium tuberculosis* (MT), is a bacteria, causes "Tuberculosis (TB)", affects the lung. TB causes serious health problems such as multi drug resistance (MDR-TB), and extensive drug resistance (XDR-TB) and leads to many more human deaths than any other microbial disease (20). MDR-TB resistance is a problem of acquired drug resistance and known as tuberculosis whose bacteria are resistant to isoniazid (INH) and rifampin (RIF). Extensive drug resistant TB (XDR-TB) is a form of tuberculosis whose bacteria are resistant to INH and RIF and in addition to any fluoroquinolone (21). Therefore, XDR-TB is much severe then TB and MDR-TB (22). One in three people in the world is infected with dormant TB bacteria. Bacteria might be active and causes disease depend on the several factors such as immunity, poverty and age of a person, and HIV (23). Nowadays, XDR-TB patients can be treated by current drugs, unfortunately reaching the success rate is not high. On the other hand, MRSA is resistant to many beta-lactam antibiotics such as penicillins and cephalosporins. Initially, MRSA was viewed as a hospital-acquired infection, but is now seen as an advanced and community-associated MRSA (24).

Therefore, as mentioned above, It is essential to discover new molecules effective on resistance targets of bacteria. For this aims, two perylene diimide derivatives investigated effects against *M. tuberculosis* strains (Mt-H37Rv, Mt-H37Ra and two clinical isolates) and SA strains. Minimum inhibitory concentrations (MICs) and minimum bactericidal activity (MBCs) were investigated.

2.MATERIALS AND METHODS

2.1.Chemicals and Measurements
All chemicals and solvents obtained from Aldrich and Sigma and used without further purification. Column chromatography of all the products were performed using Merck Silica Gel60 (particle size:0.040-0.063 mm, 230-400 mesh ASTM) penetrated with the eluent. Reactions were monitored by thin layer chromatography using precoated silica gel plates (Merck Silica Gel 60 Kiesel gel F254 TLC Aluminum Sheets 20x20 cm).

^{1}H and ^{13}CN MR spectra were recorded on a Bruker Instruments Avance Series-Spectro spin DPX-400 Ultrashield (400 MHz) High Performance digital FTNMR spectrometer (METU, NMR Laboratory). All chemical shifts are referenced to residual solvent signals previously referenced to TMS and splitting patterns are designated as s (singlet), d (doublet), t (triplet), q (quartet) and m (multiplet). Electrospray Ionization (ESI) mass spectra were recorded on Agilent 6500 Series LC-MS spectrometer, Agilent instruments, Paolo Alto, CA, USA. UV-Visible spectra were performed with Perkin Elmer Lambda 25 UV/Vis Spectrometer.

2.2. Synthesis of *N,N'*-O-*t*-butyl-L-serine *t*-butylester-3,4:9,10-perylene diimide (Compound 1)
A mixture of 0.5 g (1.274x10^{-3} mol) perylene-3,4:9,10-tetracarboxylic acid dianhydride and 0.646 g (2.548x10^{-3}mol) O-*t*-butyl-L-serine *t*-butyl ester hydrochloride in 10 mL H$_2$O, 10 mL n-butanol and 1.5 mL triethylamine was stirred for 48 h at 85°C. The reaction solution was removed by rotary evaporator, and purified by column chromatography (CHCl$_3$:CH$_3$OH - 97:3). After solvent removal by rotary evaporator, the precipitate was dried in vacuo (Yield: 29%).

(1) C$_{47}$H$_{53}$N$_2$O$_{10}$,ESI-MS:m/z805.37(M$^+$ + 1).
(2) ^{1}H-NMR (400 MHz, CDCl$_3$), δ[ppm], 1.10 (s, 18H, -O-C), 1.48 (s, 18H, -C(=O)O-CH$_3$), 4.15-4.20 (m, 4H, -C(=O)O-CH$_3$), 5.88 (t, 2H, N-CH), 7.26 (d, J= 8Hz, 2H, CH-arom), 8.51 (d, J=8.1 Hz,2H, CH-arom), 8.61 (d, J=8Hz, 2H, CH-arom)
(3) ^{13}C-NMR (100 MHz, CDCl$_3$), δ[ppm], 27.43, 27.97, 38.72, 68.14, 76.98, 82.35, 120.83, 121.91, 128.57, 128.77, 130.24, 130.84, 132.43, 138.18, 167.18, 167.73.

2.3. Synthesis of *N,N'*-O-*t*-butyl-L-threonine *t*-butylester-3,4:9,10-perylene diimide (Compound 2)

A mixture of 0.5 g (1.274x10^{-3} mol) perylene-3,4:9,10-tetracarboxylicacid dianhydride and 0.742 g (2.548x10^{-3} mol) O-*tert*-butyl-L-threonine *t*-butyl ester acetate salt in 10 mL H$_2$O, 10 mL n-butanol and 1.5 mL triethylamine was stirred for 48 h at 85 °C. The reaction solution was removed by rotary evaporator, and purified by column chromatography (CHCl$_3$:CH$_3$OH - 97:3). After solvent removal by rotary evaporator, the precipitate was dried in vacuo (Yield 31%).

(1) C$_{49}$H$_{57}$N$_2$O$_{10}$, ESI-MS: m/z 833.40 (M$^+$ + 1).

(2) ^{1}H-NMR (400 MHz, CDCl$_3$), δ[ppm], 1.27 (s, 18H, -O-C), 1.43 (s, 18H, -C(=O)O-CH$_3$), 1.54 (s, 6H, CH$_3$), 4.43-4.47 (m, 4H, -C(=O)O-CH$_3$), 5.44 (t, 2H, N-CH), 7.24 (d, J= 8 Hz, 2H, CH-arom), 8.55 (d, J=8,1 Hz, 2H, CH-arom), 8.66 (d, J=8Hz, 2H, CH-arom)
(3) ^{13}C-NMR (100 MHz, CDCl$_3$), δ[ppm], 23.75, 27.42, 28.448, 29.616, 31.58, 58.78, 59.32, 64.88, 67.38, 73.75, 77.20, 81.68, 122.96, 126.41, 129.07, 131.49, 134.73, 162.84, 167.55. Relative absorption of Compound 1 ''*N,N'*-O-*t*-butyl-L-serine *t*-butyl ester-3,4:9,10-perylene diimide'' and Compound 2 ''*N,N'*-O-*t*-butyl-L-threonine *t*-butyl ester-3,4:9,10-perylene diimide'' was measured using by UV-Vis spectrometer as these articles (25-27) (Fig 2).

Before the biological evaluation of synthesized derivatives, the protective groups were removed upon treatment with CF$_3$COOH:CHCl$_3$ (50:50).

2.4. Antimicrobial Activities
2.4.1. Antistaphylococcal activity
Microorganisms and culture media: Methicillin resistant *S. aureus* (MRSA, ATCC 33592), *S. aureus* (ATTC 6538P) were used for antistaphylococcal assays. Nutrient agar and Nutrient Broth were used as a culture media.

Preparation of samples: The samples (10 mg) were solubilized in DMSO (1 mL) so as to prepare the stock solution. Final solutions of the samples were prepared as two concentration series, 1.5-768 µg/mL to obtain precisely correct MIC and MBC values.

Preparation of Staphylococcus spp. cultures and inocula: Suspensions of microorganism were prepared from the fresh cultures of bacteria (24 hours) on nutrient agar by suspended in sterile saline solution. The turbidities of bacteria were arranged to a 0.5 McFarland standard (10^8 CFU/mL) then diluted at 100 times to reach of 10^6 CFU/mL. Mueller Hinton Agar and Mueller Hinton Broth were used in vitro antistaphylococcal activity assays.

Antistaphylococcal Activity Assays for S. aureus and MRSA: Mueller Hinton Broth was used for microdilution assays for *S. aureus* susceptible and MRSA. We used a 96-well plate in the experiments. Two-fold dilutions were performed from the first well to the next well (100 µL). The

wells were filled with Mueller Hinton Broth (100 µL) then sample (100 µL) was added to the first well, after mixing several times by pipetting, the procedure was repeated for the dilution series except control wells. Afterwards, inoculum (20 µL) was added all the wells except negative control wells. All plates incubated at 37 °C for 24-48 hours for bacteria (28).

Determination of Minimum Inhibitory Concentrations (MICs) and Minimum Bactericidal Activity (MBCs): To determine of the bacterial growth, Thiazolyl Blue Tetrazolium, a dye for cell growth assays (20 µL, Sigma), was used. To determine the MIC values, dye were added into the wells then incubated at 37 °C for 24-48 h. When the dye turned to pink, bacterial growth was indicated. MIC value is accepted the lowest concentration of the compounds that inhibits visibly the growth of the microorganism after 24-48 h incubation.

To determine MBCs, the wells were filled with fresh Mueller Hinton broth (185 µL) except test compounds, then a bacterial suspension (15 µL) were added to the wells starting from MIC concentration and the higher concentrations in the series. After incubating the microplates at 37 °C for 24-48 h, indicator dye was added to the microplates. MBC was described as the lowest concentration of compounds that there is no growth when subculture in an antibiotic-free growth medium. All tests were performed according to National Committee for Clinical Laboratory Standards for bacteria in triplicate (29). Iecilline (Ulagay, TR)(concentration: 79.36 µg/mL) was used as a standard drug for comparison the activity of the compounds. Standard drug concentrations were given in table 1.

2.4.2. Antimycobacterial activity
Microorganisms and culture media: Four bacteria, *M. tuberculosis* $H_{37}Ra$ (ATCC 25177), *M. tuberculosis* $H_{37}Rv$ (ATCC 25618) and two positive clinical isolates of *M. tuberculosis* MT-strain-1 and MT-strain-2, obtained from hospital, were used for antimycobacterial bioassays. Middlebrook 7H9 Broth (Becton & Dickinson, USA) and Middlebrook 7H10 Agar (Becton & Dickinson, USA) was used as *Mycobacterium* culture media.

Preparation of Mycobacterial inocula: All strains were cultured in MGIT Mycobacteria Growth Indicator Tubes, containing 4 mL of modified Middlebrook 7H9 Broth Base at 37 °C for 5-7 days. OADC supplement (0.5 mL) was added to each tube. Inoculum was prepared from a positive BACTEC *Mycobacteria* Growth Indicator Tube (MGIT) according to the manufacturer's (Becton, Dickinson) instructions (30). To prepare inoculum from a positive BACTEC MGIT tube, the tubes which were day-1 and day-2 positive were used for the susceptibility test. Tubes were checked according to consume the oxygen by

actively respiring micro-organisms and allow the fluorescence to be observed using a 365 nm UV transilluminator (31). Positive MGIT 7 mL tubes ranges were changed between 0.8×10^5 to 3.2×10^5 CFU/mL.

Antimycobacterial activity test for MT strains: The activity of all compounds against *M. tuberculosis* strains was tested using the Microplate Presto Blue Assay (MPBA) by the method described (32). 100 µL of compound was transferred in the first column then 100 µL of 7H9 broth was transferred from the column 1 to column 10. Column 11 and 12 were negative and positive control respectively. 100 µL of compound were transferred from column 1 to column 2 then mixed by pipettes three times and go on the same to provide serial 1:2 dilutions. 100 µL of excess medium was discarded from the wells in column 10. Afterwards, of inoculum (20 µL) was added into the wells from 1 to 10 and positive control wells. Negative control wells were not inoculated with bacteria. Positive and negative control columns were compound-free controls (33-28). Fluorometric susceptibility test procedure carried out according to recommended by the manufacturer, Becton, Dickinson and Company (30).

Determination of minimum inhibitory concentrations (MICs) and minimum bactericidal activity (MBCs): Microplates were incubated at 37 °C for 6 days then presto blue (15 µL, Life Technologies) was added to the bacterial growth control wells (without compound) monitoring the growth of *Mycobacterium.* The microplates were incubated at 37 °C for an additional 24 h. When the dye turned from blue to pink in the positive control tubes (indicating positive bacterial growth); Presto blue solution was added to the other wells to determine the MIC values. All tests were performed in triplicate. The minimum inhibitory concentration (MIC) was defined as the lowest concentration of sample that prevents a color change to pink. The minimum bactericidal concentration (MBC) was corresponded to the minimum compound concentration which is not cause a color change in the subcultures when re-incubated in fresh medium (34). Streptomycin (Concentration: 83 µg/mL; STR, BD), ethambutol (Concentration: 415 µg/mL. EMB, BD), rifampin (Concentration: 83 µg/mLRIF, BD), and izoniazid (Concentration: 8.3 µg/mL.INH, BD) were used as standard drugs for comparison the activity of the compounds. All antibiotics were purchased from BD Company, USA as the BD BACTEC™ MGIT™ 960 SIRE Kit for susceptibility testing of *M. tuberculosis*. Standard drug concentrations were given in Table 1.

3. RESULTS and DISCUSSION

In this work, we designed two different perylene diimides which are expected to show antimicrobial activity (Fig1). Target molecules

were synthesized in a few steps from commercially available materials. Relative absorption of Compound 1 and Compound 2 was shown using by uv-vis spectrometer in Figure 2. Then antimicrobial activities both, antimycobacterial and antistaphylococcal, were given in Table 1. Antimycobacterial activity of the compounds as MIC and MBC (μg/mL) were shown against of two novel perylene diimides in Figure 3.

The synthesis was started with double amine substitution by O-*t*- butyl-L-serine *t*-butyl ester hydrochloride and *O*-*t*-butyl-L-threonine-*t*-butyl ester acetate salt on the perylene core to be improved solubility. We synthesized *N,N'*-O-*t*-butyl-L-serine-*t*-butylester-3,4:9,10-perylene diimide and *N,N'*-*(*O-*t*-butyl-L-threonine-*t*-butyl ester**-**3,4:9,10-perylene diimide. The chemical structures of two compounds were verified analytically.

3.1. The Synthesis of Two Novel Compounds
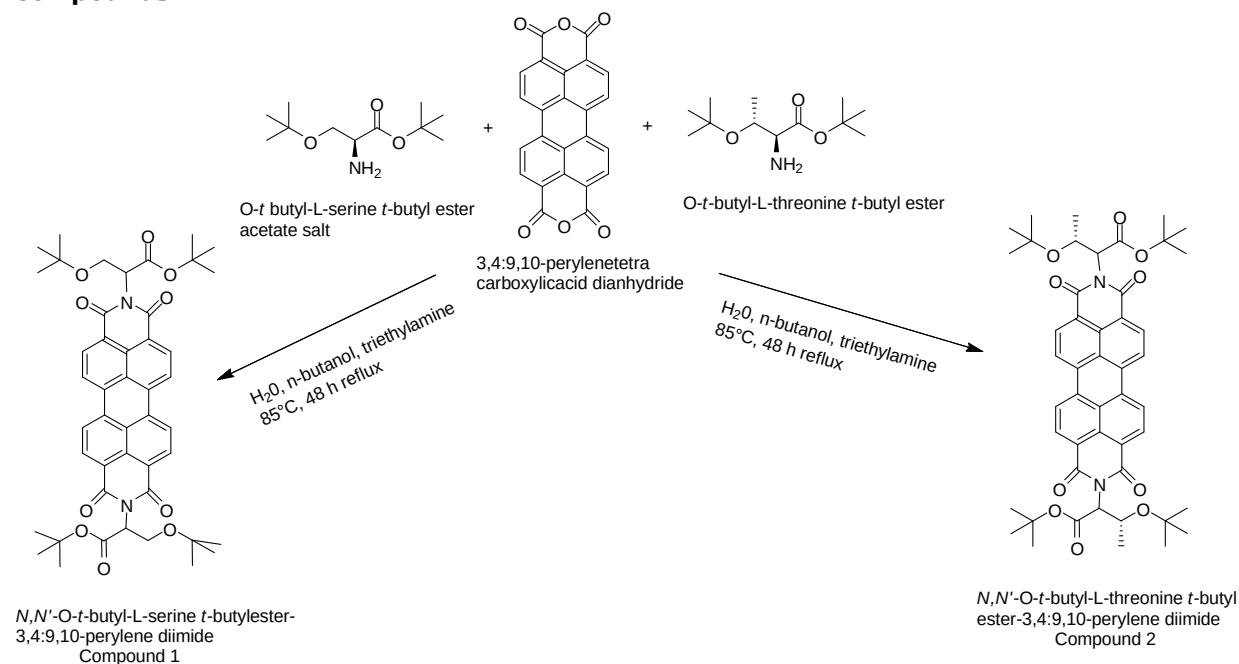
Figure 1: Synthesis of perylene diimide derivatives (*N,N'*-O-*t*-butyl-L-serine *t*-butyl ester-3,4:9,10-perylene diimide and *N,N'*-O-*t*-butyl-L-threonine *t*-butyl ester-3,4:9,10-perylene diimide).
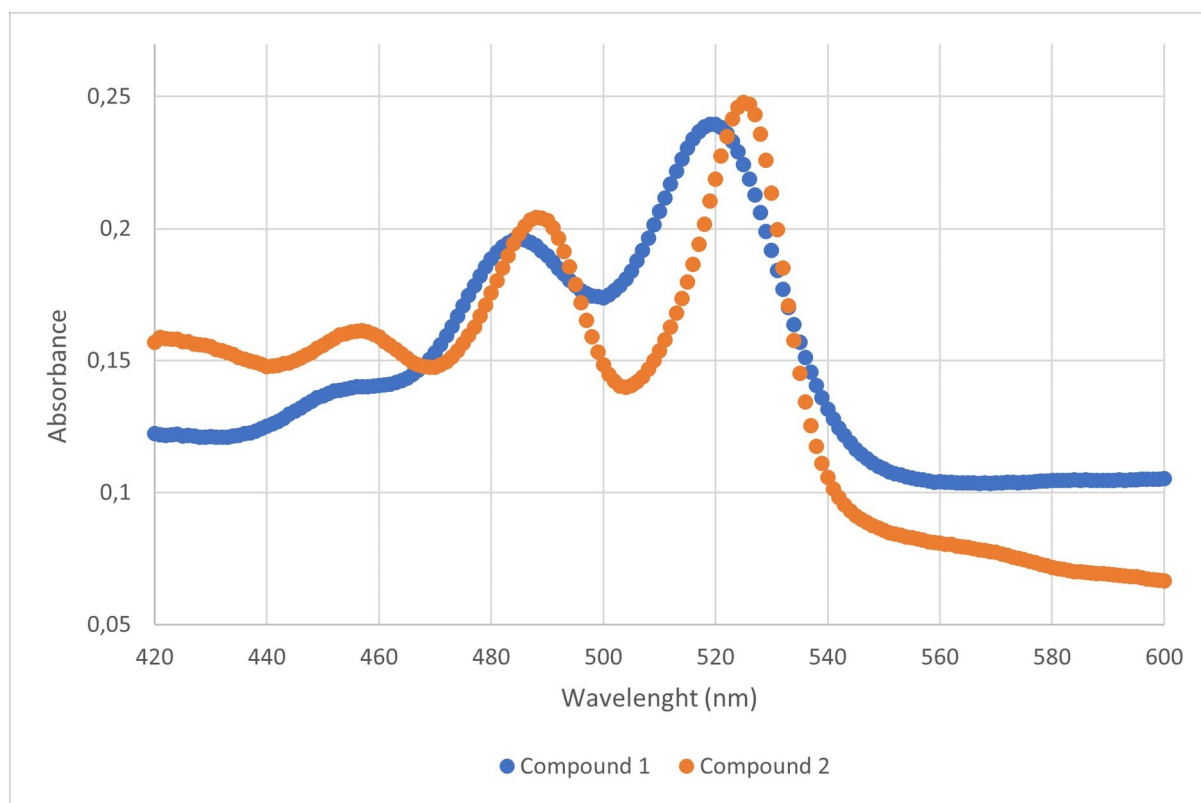
Figure 2: Relative Absorbance Graph of Compound 1 ''*N,N'*-O-*t*-butyl-L-serine *t*-butyl ester-3,4:9,10-perylene diimide'' and Compound 2 ''*N,N'*-O-*t*-butyl-L-threonine *t*-butyl ester-3,4:9,10-perylene diimide''

3.2. Antimycobacterial Activity Assays
All biological activity assays performed for two compounds. Compounds were more effective on all the microorganisms.

Efficacy of the compounds against drug resistant (Mt-H$_{37}$Rv), drug susceptible (Mt-H$_{37}$Ra*)* and clinical isolates showed that the MICs were changing between 48-192 µg/mL. MBC values were a little bit higher than MIC values and changed between 96-384 µg/mL (Table 1). For compound **1**, the lowest MIC values were determined against Mt-H$_{37}$Ra and MT-strain-1 (MIC 48 µg/mL)**,** MBC was 192 and 96 µg/mL respectively. Compound 2 showed the lowest

MIC values (MIC 48 µg/mL) against Mt-H$_{37}$Ra. MBCs were varies between 48-384 µg/mL). The highest MBCs determined in MT- Strain-1 and MT- Strain-2.

3.3. Antistaphylococcal Activity Assays
While, compound **1** and compound **2** exhibited the same MIC and MBC values 96, 192 µg/mL respectively against MRSA. The efficacy of the compound **1** against *S. aureus* was 96 µg/mL (MIC) and 384 µg/mL (MBC) and the compound **2** against *S. aureus* was 96 µg/ mL (MIC) and 192 µg/mL (MBC) (Table 1). As a results, both of the compounds showed bactericidal effects and kill the bacteria depended the concentrations.

Table 1. Minimum inhibitory concentrations (MIC) and minimum bactericidal concentrations (MBC) of the samples (µg/mL),

Compounds	Antimicrobial activity (µg/mL)											
	$Mt-H_{37}Rv$		$Mt-H_{37}Ra$		MT-Strain 1		MT-Strain 2		S. aureus		MRSA	
	MIC	MBC	MIC	MBC	MIC	MBC	MIC	MBC	MIC	MBC	MIC	MBC
Compound **1**	96	384	48	192	48	96	96	192	96	384	96	192
Compound **2**	96	192	48	96	96	384	96	384	96	192	96	192
Standard drugs												
Streptomycin	0.65	0.65	0.65	1.29	2.59	5.18	0.65	**nt**	nt	nt	nt	nt
Izoniazid	0.13	1.03	0.51	1.03	0.10	1.03	0.51	0.51	nt	nt	nt	nt
Rifampin	0.65	5.18	0.32	2.59	0.65	0.65	0.65	5.18	nt	nt	nt	nt
Ethambutol	3.74	7.48	1.87	1.87	3.74	3.74	1.87	nt	nt	nt	nt	nt
Iecilline	nt	nt	nt	nt	nt	nt	nt	**nt**	0.31	0.62	10	20

nt: Not tested;
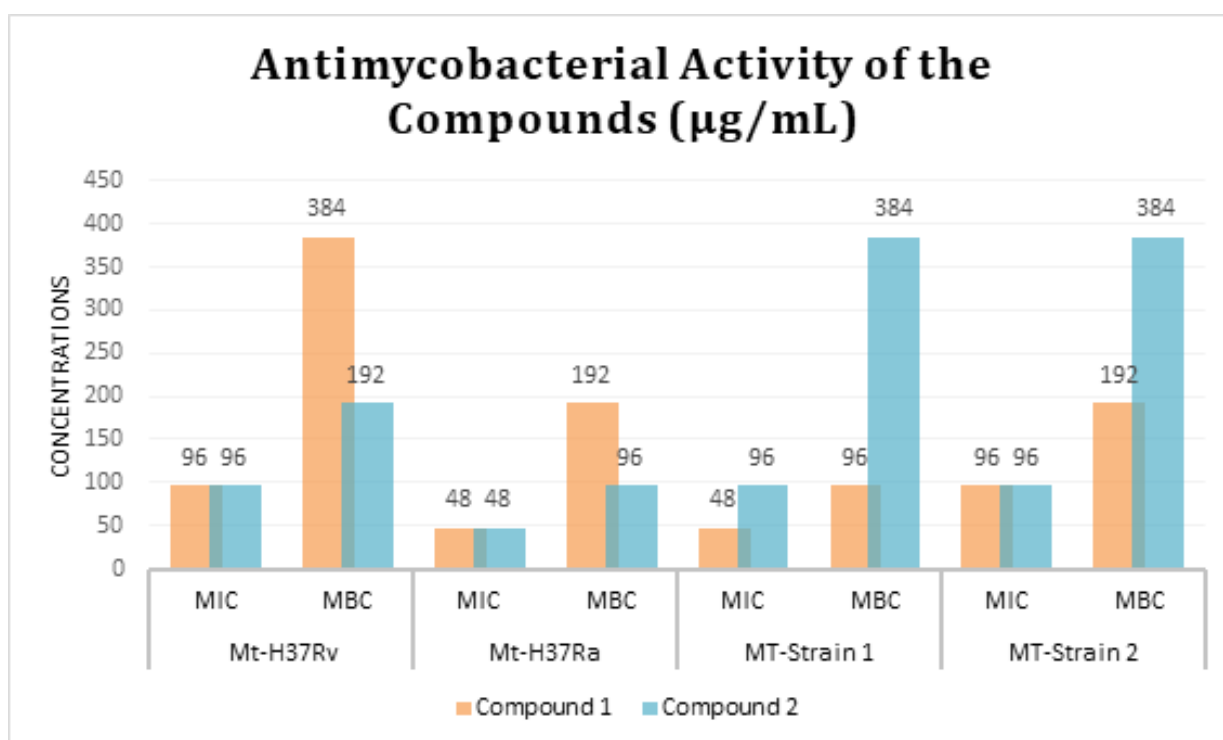
Figure 3: Antimycobacterial activity of the compounds as MIC and MBC (µg/mL).

Recently, perylene diimide derivatives have been attracted great interest and find lots of area to use Yukruk et al, that Minimum inhibitory concentration (MIC) and minimum bactericidal concentration (MBC) of perylene diimides for Staphylococcus aureus were determined respectively (35). Keskin et al. studied potential therapeutic advantages of perylene diimide derivatives on cancer therapy as a drug (36). Liu et al. reported that the potential usege of PDI derivatives as a recyclable specific Hg^{2+} ion

sensor and an efficient DNA delivery transporter (37).

We researched possible antimicrobial activity of two novel perylene diimides. This activity might be occurred from the moiety of serine or threonine part of PDI. A serine/threonine protein kinase enzyme, exist in procaryotes. It works by phosphorylating the OH group of serine or threonine (38). Ohlsen&Donat showed that serine/threonine phosphorylation and dephosphorylation are of great importance for *S. aureus* strains on the cell wall metabolism, cell proliferation, citrate cycle, apoptosis, and translation (38).

The results from this study will be beneficial for further development of new complexes.

4. CONCLUSIONS

In this study, two novel perylene diimides were synthesized and characterized. Accumulating evidence has demonstrated the potential antimicrobial activities of two novel PDI. They displayed a clear, concentrations-depended bactericidal activity against the bacteria resistant to the medicine. More consideration should be given to the research on PDI that could produce more valuable data to expand on their usage area.

5. ACKNOWLEDGEMENTS

6. CONFLICT of INTEREST

The authors have declared no conflict of interest.

7. REFERENCES

1. Sapagovas VJ, Gaidelis V, Kovalevskij V, Undzenos A. Perylenetetracarboxylicacid derivatives and photophysical properties. Dyes Pigm.2016;71:178-187. Available from: <URL> .

2. Cormier RA, Gregg BA. Synthesis and characterization of liquid crystalline perylene diimide. Chem Mater. 1998;10:1309-1319. Available from: <URL>.

3. Angadi MA, Gosztola D, Wasielewski MR. Organic light emitting diodes usig poly (phenylenevinylene) doped with perylenediimide electron acceptors. Mater Sci Eng B. 1999;63:191-194. Available from: <URL>.

4. Ranke P, Bleyl I, Simmerer J, Haarer D, Bacher A, Schmidt HW. Electroluminescence and electron transport in a perylene dye. Appl Phys Lett. 1997;71:1332-1334. Available from: <URL>.

5. Hayes RT, Wasielewski MR, Gosztola DJ. Organic dyes with excited state transformations (electron, charge, and proton transfers). Am Chem Soc. 2000;122:5563-5567. Available from: <URL>.

6.Davis WV, Svec WA, Ratner MA. Wasielewski MR Molecular wire behaviour in p-phenylenevinylene oligomers. Nature.1998;396:60-63. Available from: <URL>.

7. Tornizaki K, Loewe RS, Kirmaier C, Schwartz JK, Retsek JL, Bocian DF, Holten DLindsey JS. Synthesis and Photophysical Properties of Light Harvesting Arrays Comprised of a Porphyrin Bearing Multiple Perylene-Accessory Pigments. J Org Chem. 2002;67:6519-6534. Available from: <URL>.

8. Fuller MJ, Wasielewski M. Photorefractivity in Nematic Liquid Crystals Using a Donor−AcceptorDyadwith a Low Lying Excited Singlet State for Charge Generation. J Phys Chem B.2001;105:7216-7219. Available from: <URL>.

9.Fuller MJ, Walsh CJ, Zhao Y, Wasielewski MR. Hybrid Photorefractive Material Composed of Layered Conjugated Polymer and Dye Doped Liquid Crystal Films. Chem Mater. 2002;14:952-953. Available from: <URL>.

10. Ozcan O, Yukruk F, Akkaya EU, Uner D. Dye sensitized artificial photosynthesis in the gas phase over thin and thick TiO_2 films under UV and visible light irradiation. Appl Catal B Environ. 2006;71:291-297. Available from: <URL>.

11. Acikbas Y, Capan R, Erdogan M, Yukruk F. Thin film characterization and vapor sensing properties of a novel perylene diimide material. Sensor Actuat B-Chem. 2011;160: 65-71. Available from: <URL>.

12. Gregg BA, Cormier RA. Doping Molecular Semiconductors: n-Type Doping of a Liquid Crystal Perylene Diimide. J Am Chem Soc. 2001;123:7959-7960. Available from: <URL>.

13. Breeze AJ, Salomon A, Ginley DS, Gregg BA, Tillmann H, Horhold HH.Polymer perylenediimide heterojunction solar cells. Appl Phys Lett. 2002;81:3085-3087. Available from: <URL>.

14. Sadrai M, Hadel L, Sauers RR, Husain S, Krogh-Jespersen K, Westbrook JD, Bird FR. Lasing action in a family of perylene derivatives: single absorption and emission spectra, triplet absorption and oxygen quenching constants, and molecular mechanics and semiempirical molecular orbital calculations. J Phys Chem. 1992;96:7988-7996. Available from: <URL>.

15. Gvishi R, Reisfeld R, Brushtein Z. Spectroscopy and laser action of the "red Perylimide dye" in various solvents. Chem Phys Lett.1993;213:338-344. Available from: <URL>.

16. Yukruk F, Dogan AL, Canpinar H, Guc D,Akkaya EU. Water soluble green perylene diimide (PDI) dyes as potential sensitizers for photo dynamic therapy. OrgLett. 2005;7(14):2885-2887. Available from: <URL>.

17.Tuna G, Kulaksiz Erkmen G, Dalmizrak O, Dogan A, Ogus IH. Inhibition characteristics of hypericin on rats mallintestine glutathione-Stransferases. N Chem Biol Interact. 2010;188(1):59–65. Available from: <URL>.

18. Ma GY, Khan SI, Jacob MR, Tekwani BL, Li ZQ, Pasco DS, Walker LA, Khan LA. Antimicrobial and

antileishmanial activities of hypocrellins A and B. Antimic Agents Chemother. 2004;48(11):4450-4452. Available from: <URL>.

19. Feyzioglu B, Demircili ME, Ozdemir M, Dogan M, Baykan M, Baysal B. Antibacterial effect of hypericin. Afr J Microbiol Res. 2013;7(11):979-982. Available from: <URL>.

20. WHO, World Health Organization, Guidance on ethics of tuberculosis prevention, care and control. WHO/HTM/TB/2010.16. Geneva, 2010. Available from: <URL>.

21. WHO, World Health Organisation, Multidrug-resistant tuberculosis (MDR-TB). World Health Organization. 2013. Available from: <URL>.

22. WHO, World Health Organization. Tuberculosis MDR-TB & XDR-TB 2011 progress report, WHO Report: Towards universal access to diagnosis and treatment of MDR-TB & XDR-TB by 2015, 23 March 2011, p.2, ISBN 978 92 4 150133 0. 2011. Available from: <URL>.

23. WHO, World Health Organisation, Drug-resistant TB Surveillance &Response, Supplement Global Tuberculosis Report. 2014. Available from: <URL>.

24. Egea AL, Gagetti P, Lamberghini R, Faccone D, Lucero C, Vindel A, Tosoroni D,Garnero A, Saka HA, Galas M, Bocco JL, Corso A, Sola C. New patterns of methicillin-resistant Staphylococcus aureus (MRSA) clones, community-associated MRSA genotypes behave like healthcare-associated MRSA genotypes within hospitals, Argentina. Int J Med Microbiol. 2014; 304:1086–99. Available from: <URL>.

25. Kursunlu A.N, Sahin E, Guler E. Cu (II) chemosensor based on a fluorogenic bodipy-salophen combination: sensitivity and selectivity studies. J. Fluoresc. 2016; 26, 1997-2004. Available from: <URL>.

26. Alizada M, Gul A, Oguz M, Kursunlu A.N., Yilmaz M. Ion sensing of sister sensors based-on calix [4] arene in aqueous medium and their bioimaging applications, Dyes Pigm 2020; 184, 108741. Available from: <URL>.

27. Oguz M., Gul A., Kursunlu A.N., Yilmaz M. A bifunctional and multi-responsive fluorescent sensor for toxic analytes in the aqueous medium: Easy synthesis, NIR-visible effect, imaging in living cells, J. Mol. 2021; 336, 116861. Available from: <URL>.

28. NCCLS National Committee for Clinical Laboratory Standards (NCCLS). Methods for Dilution Antimicrobial Susceptibility Tests for Bacteria That Grow Aerobically; Approved Standard. Seventh Edition NCCLS Document M7-A7., Wayne, Pennsylvania 2006;26(2):1-16. Available from: <URL>.

29. NCCLS Methods for Determining Bactericidal Activity of Antimicrobial Agents; Approved Guideline, NCCLS document M26-A [ISBN 1-56238-384-1]. NCCLS, 940 West Valley Road, Suite 1400, Wayne, Pennsylvania 19087 USA, Agents; Approved Guideline 1999. Available from: <URL>.

30. BD, Becton, Dickinson and Company Newsletter BD Bactec MGIT 960 SIRE kit now FDA-cleared for susceptibility testing of Mycobacterium tuberculosis. Microbiology News &Ideas 2002;13:4-4. Available from: <URL>.

31. Chaudhuri S, Chung SW, Hockney G, Lykken J, Reisner BS, Gatson AM et al. Evaluation of Mycobacteria growth indicator tubes for susceptibility testing of Mycobacterium tuberculosis to isoniazid and rifampin. Diag Microbiol Infect Dis 1995;22(4):325–329. Available from: <URL>

32. Collins L, Franzbla SG Microplate alamar blue assay versus BACTEC 460 system for high-throughput screening of compounds against *Mycobacterium tuberculosis* and *Mycobacterium avium*. Antimicrob Agents Chemother 1997; 41:1004–1009. Available from: <URL>.

33. NCCLS Susceptibility Testing of Mycobacteria, Nocardiae, and Other Aerobic Actinomycetes; Approved Standard. NCCLS document M24-A [ISBN 1-56238-500-3]. NCCLS, 940 West Valley Road, Suite 1400, Wayne, Pennsylvania 19087-1898 USA 2003. Available from: <URL>.

34. Molina-Salinas GM, Ramos-Guerra MC, Vargas-Villarreal J, Mata-Cárdenas BD, Becerril-Montes P, Said-Fernández S.Bactericidal Activity of Organic Extracts from Flourensiacernua DC against Strains of Myco*bacterium tuberculosis.* Archives of Medical Research. 2006;37(1):45-49. Available from: <URL>.

35. Yagan S, Yukruk F, Unlu G.V., Antimicrobial Activities of Four Perylene diimides, Afr J Microbiol Res.; 9(7), 427-432. Available from: <URL>.

36. Keskin T, Isgor BS, Isgor YG, Yukruk F.Evaluation of Perylene diimide Derivatives for Potential Therapeutic Benefits on Cancer Chemotherapy. Chem Biol Drug Des. 2012;80(5):675-681. Available from: <URL>.

37. Liu K, Xu Z, Yin M, Yang W, He B, Wie W, Shen J.Towards rational design of organic electron acceptors for photovoltaics: A study based on perylene diimide derivatives. J Mater Chem. 2014; 2(15):2093-2096. Available from: <URL>.

38. Ohlsen K, Donat S. The impact of serine/threonine phosphorylation in *Staphylococcus aureus*. Int J Med Microbiol. 2010;300:137–141. Available from: <URL>.

Adsorption of the *Meso*-Tetra-*p*-Tolylporphyrin (TTPH$_2$) and *Meso*-Tetra-Naphthylporphyrin (TNPH$_2$) onto Montmorillonite

Jasim Hamadi Hassen[1]* (iD) **, Jack Silver[2]** (iD)

[1]University of Anbar, College of Pharmacy, Department of Pharmaceutical Chemistry, Ramadi, Iraq.
[2]University of Brunel, Wolfson Centre for Material Processing, London, UK.

Abstract: The behavior of two porphyrin compounds, *meso*-tetra-*p*-tolylporphyrin (TTPH$_2$) and *meso*-tetra-naphthylporphyrin (TNPH$_2$) was studied and monitored during their adsorption on cation-exchanged montmorillonite clay (MMT). When these two compounds were reacted with MMT, the visible absorption spectra showed a clear shift of 10 nm higher than that found in the acetic acid solution. This suggests that the two compounds prefer to be more planar on the clay surface and, in the case of TTPH$_2$, in the MMT interlamellar layers. The basal spacing of the MMT was increased by 4.4 Å when the TTPH$_4{}^{2+}$ cations entered the spacers. The metal-exchanged ion in the clay is incorporated into the porphyrin rings when the TTPH$_2$ and TNPH$_2$ molecules react with MMT saturated with the metal ion of an appropriate size to fit in the porphyrin ring, such as Cu(II). The process occurred when executed in a solvent miscible with water that allowed the penetration of the hydrated sphere of the metal ion. Metalloporphyrin complexes are formed as a result of this process. The reactions were monitored using visible absorption spectra, diffuse reflectance spectra, x-ray diffraction, infrared spectra, and electron microscopy.

1. INTRODUCTION

The interaction of porphyrins with clays has been widely studied (1-6) since the late 1970s. The adsorption of two *meso*-substituted porphyrins, TPP and TPyP, on cations exchanged clays revealed that TPP is protonated during adsorption, but TPyP behavior is water-dependent. In the presence of enough water, stable metallocomplexes such as Sn(IV)TPP can be adsorbed without demetallation. While weak complexes like Fe(III)TPP are demetallated (7). The porphyrin compounds *p*-TMPyP and *m*-TMPyP were examined for their adsorption on clay. Depending on the solution used, it was shown that the orientation of both compounds on the clay monolayer was parallel and inclined concerning the clay surface (8). By using a new technique for sample preparation, cationic porphyrin was successfully intercalated onto a transparent clay membrane. When the porphyrin penetration process was carried out with water:ethanol ratio of 1:2, high-density intercalation was accomplished (6). As discussed earlier, porphyrins and other tetrapyrrole macrocycles exhibit a variety of functional qualities. They can achieve and regulate important functions like light harvesting, electron transport, and catalytic reactions when complex with metals (9). The electron-transfer reaction that occurs after light harvesting is described in a unique energy-transfer system utilizing nonaggregated cationic porphyrins adsorbed on an anionic-type clay

surface (10). The *m*-TMPyP and *p*-TMPyP were found to be the most suitable porphyrins for a quantitative energy transfer reaction (11). The photochemical energy transfer reaction was used to investigate the adsorption of two porphyrin compounds on anionic clay. Energy transfer reactions of moderate magnitude were found. The adsorbed chemicals were found to be able to travel on the surface but not from the surface to the sheet (12). The mechanism to deter the quenching of porphyrins on the surface of the clay (used as an optimum solid surface for the transfer of photochemical energy) was investigated using a range of porphyrin derivatives (13). Hydrothermal synthesis was used to produce saponite-type clays with various cation exchange capacities, which were then reacted with tetrakis(1-methylpyridinium-4-yl)porphyrin. It was found that, depending on the charge density of the saponite, the average intermolecular distance between porphyrin molecules on the saponite surface might be adjusted (14). During the adsorption of cationic porphyrin on anionic-type clay, two processes occur: surface adsorption and intercalation (15). The production of clay-porphyrin complexes and the spectrum behavior of metalloporphyrins with divalent, trivalent, and tetravalent central metals with synthetic clay have also been investigated. The complex formation, where the clay sheets were either exfoliated or layered in an aqueous colloidal solution, resulted in a spectral shift of the porphyrin Soret band to higher wavelengths (16). The energy transfer efficiency and quenching efficiency were estimated for excited energy transfer from tetrakis(1-methylpyridinium-2-yl) porphyrin to tetrakis(1-methylpyridinium-4-yl) porphyrin on an anionic clay. It was found that when the dye loadings increased, both the energy transfer efficiency and the quenching efficiency increased (17). Ion exchange was used to intercalate the Cu(II) and Fe(III) complexes of water-soluble tetrakis(*N,N,N*-trimethylanilinium)porphyrin and tetrakis(*N*-methylpyridyl)porphyrin within the interlayers of Ca(II) MMT. Porphyrins in their free base forms were also reacted with Cu(II) and Fe(III) MMT samples. It was found that when the Cu(II) metalloporphyrins contact the acidic MMT support, they do not demetalate. On smectite supports, the Fe(III) porphyrin complexes are also stable. A stable Cu(II)porphyrin-clay complex is formed when a free base porphyrin metalates on the surface of a Cu(II)-exchanged clay (18). It has been found that vanadyl and nickel *meso*-tetraphenylporphyrin are stable toward demetallation, whereas magnesium porphyrin is notably unstable (19). Adsorption studies of Sn(IV)TPyP on sodium hectorite showed that the complex demetallates to the dication TPyP when the clay is dehydrated, and it was found that the procedure is reversible (20). MMT was found to be useful to support the porphyrin complex ions MnTPyP$^+$ on the surface by adsorption (21).

Moreover, the MnTPYP$^+$ ions can penetrate through the clay layers and, by ionic exchange, replace the exchangeable cations (22). Another study reported that when MnTPyP$^+$ ion has been reacted with MMT, the ion was able to intercalate in a horizontal, diagonal, and perpendicular direction (23). The porphyrin complexes Sn(IV)TPPCl$_2$, Sn(IV)TNPCl$_2$, Fe(III)TPPCl, Fe(III)TNPCl, [(Fe(III)TPP)$_2$O], and [(Fe(III)TNP)$_2$O], were all found to be stable on the MMT surface and show no demetallation (24).

The aim of the current research was to study the interactions that take place when two different porphyrins are adsorbed on cation-exchanged MMT clay. Moreover, knowing the new properties of these compounds and complexes when they are present on the MMT surface or between its layers, as this system has many industrial applications. The porphyrins are *meso*-tetra-tolylporphyrin (TTPH$_2$) and *meso*-tetra-napthylporphyrin (TNPH$_2$).

2. MATERIALS AND METHODS

The TTPH$_2$ and TNPH$_2$ compounds were prepared according to the methods described in the literature (25) for TPPH$_2$. The MMT sample was obtained from Podmore and Sons Ltd., England, UK. All other solvents were grade reagents and used without further purification. Diffuse reflectance spectra were recorded on a Unicam SP 700 spectrophotometer. Visible absorption spectra were recorded on Perkin-Elmer Lambda 5 UV/VIS and Beckman Du-7 spectrophotometer. Transmission electron micrographs were obtained on a JEOL 200CX transmission electron microscope at 100 KV. An ultramicrotomic technique was used to prepare the sections, on a Sorvall Porter-Blum MT2 ultramicrotome. Infrared spectra were recorded on a Perkin Elmer 1330 infrared spectrophotometer. X-ray diffraction patterns were recorded on a Philips diffractometer using CuKα radiation.

2.1. Cation-exchanged MMT Preparation
Cation-exchanged MMT samples were prepared by mixing the MMT sample with a 1 M solution of different metal chloride salts on a magnetic stirrer for 24 hours in distilled water. Then the samples were filtered and rinsed with distilled water many times until the AgNO$_3$ test for chloride ions came out negative. The samples were then dried in the air for 24 hours before being crushed into a fine powder.

2.2. Adsorption onto MMT
1 g of the cation-exchanged MMT has added to solutions of 10, 20, and 30 mg of the porphyrin compound in chloroform or acetone. The slurries were stirred for 24 hours at room temperature, then filtered, washed several times with the solvent used, and air-dried.

3. RESULTS AND DISCUSSION

3.1. Characterization of the MMT Sample

The MMT clay sample used for this study has the chemical composition presented in Table 1. The main oxides in the sample are aluminum oxide and silicon oxide, which represent 76.6% of the total composition. The rest of the oxides in the sample are of iron, titanium, calcium, sodium, and potassium.

Table 1: The chemical composition of the MMT sample.

Fe_2O_3 (%)	Al_2O_3 (%)	SiO_2 (%)	TiO_2 (%)	CaO (%)	MgO (%)	Na_2O (%)	K_2O (%)	Loss on ignition (%)	Total (%)
3.5	19.1	57.5	0.2	1.2	2.4	1.7	0.3	13.9	99.8

A limited number of impurities, including quartz, feldspar, and mica, were found in the MMT sample, as determined by X-ray diffraction studies. Figure 1 shows the X-ray diffraction pattern of the sample which showed a basal spacing of 13 Å. Since the thickness and regularity of the water layers vary depending on the exchangeable cation present as well as the conditions under which the sample was prepared, the basal spacing varies from one MMT sample to another (26).
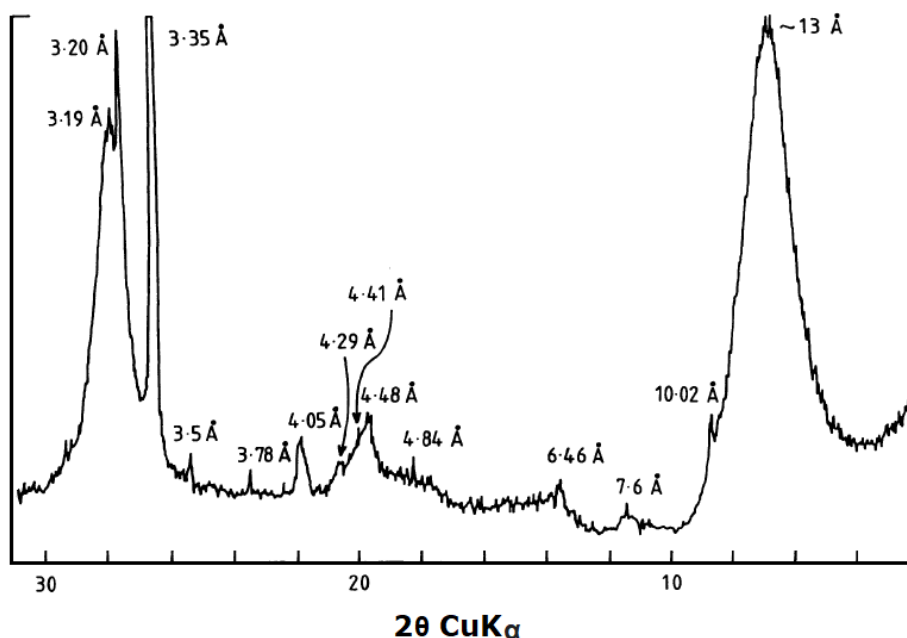
Figure 1: X-ray diffraction pattern of the MMT sample.

Characterization of the sample by IR spectra indicated the presence of Si-O stretching and OH bending, they are the primary characteristics of the MMT in the IR region. The bands have been assigned to Fe^{3+}-OH-Fe^{3+}, Al-OH-Mg, Fe^{3+}-OH-Al, Al-OH-Al, and Si-O at 800, 850, 880, 917, and 1040 cm^{-1}, respectively (27, 28).

3.2. Visible absorption and diffuse reflectance spectra

The visible spectra presented in this work are in Figures 2, 3, 5, and 7, and the diffuse reflectance spectra are shown in Figures 4 and 6. Figure 1 shows the visible absorption spectrum of the free base form of $TTPH_2$, which is identical to the spectra of $TNPH_2$. Only the intensities of the bands are different. They have a strong absorption Soret band at about 420 nm and four additional bands in the 450-700 nm range.

In acetic acid, the protonation of the free base of $TTPH_2$ causes the Soret band to be shifted to a higher wavelength, 441 nm, (Figure 3), due to the formation of the dicationic form $TTPH_4^{+2}$, while $TNPH_2$ shows a resistance toward protonation

(Figure 5). The visible spectrum of TNPH$_2$ in acetic acid indicates a significant proportion of the molecules are still present as TNPH$_2$ with little or no movement in the main Soret band. However, the presence of a smaller band (at a higher wavelength) on the right of the Soret band possibly indicates a very small amount of a dication form is present.

When the free base compounds are adsorbed onto metal cation-exchanged MMT, such as Fe(III) MMT, the spectrum of the TTPH$_2$ compound is similar to that of the dicationic form TTPH$_4^{2+}$ in shape but the position of the bands differ (Figure 3). The Soret band at 417 nm (in the unprotonated state) is shifted to 452 nm in the adsorbed state, and a broad band appears in the red region at 676 nm with a shoulder at 620 nm (Figure 3).The band at 676 nm is 10 nm higher in wavelength than that of the dication in solution.
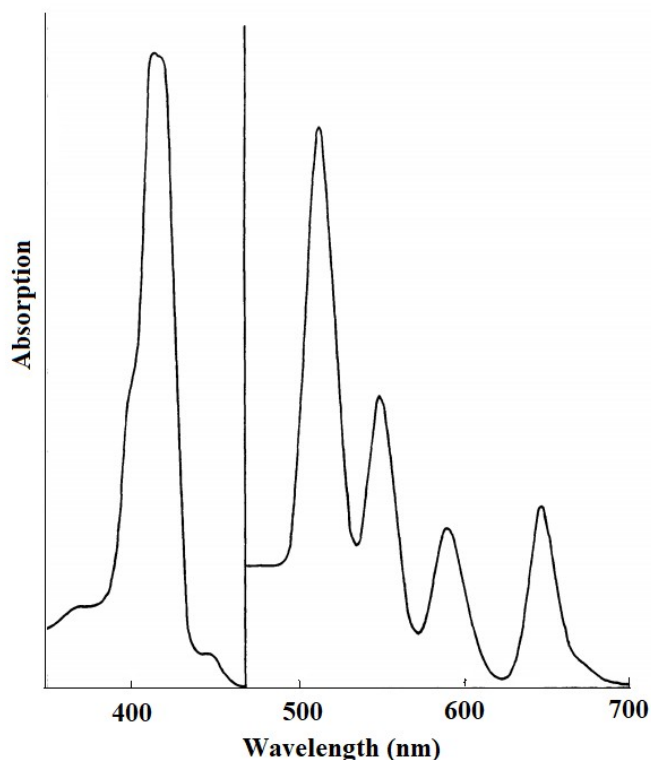
Figure 2: Visible absorption spectrum of TTPH$_2$ in chloroform. For clarity, the y-axis in the region from 470 nm to 700 nm has been magnified by 10 times.
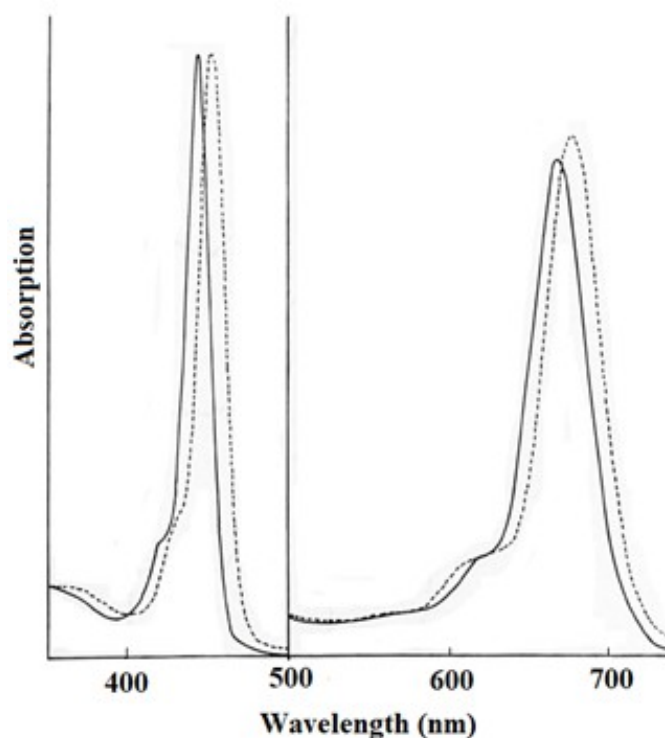
Figure 3: Visible absorption spectra of (_____) $TTPH_4^{2+}$ in glacial acetic acid, (------) $TTPH_4^{2+}$ on Fe(III) MMT after adsorption of $TTPH_2$. For clarity, the y-axis in the region from 500 nm to 700 nm has been magnified by 10 times.

The fact that the visible absorption spectrum of the adsorbed cationic form shows a clear shift of 10 nm higher than that of the cationic form found in acetic acid is evidence that the $TTPH_2$ prefers to be more planar in the MMT interlamellar and on the surface. The width of the Soret band of $TTPH_2$ on Fe(III) MMT (Figure 3) does not appear to be different to that in acid solution, implying that there is only one form of porphyrin present on the clay. The porphyrin would be expected to be restricted to a more planar conformation in the interlayer region. Clearly, some of the $TTPH_2$ must be on the clay surface as well as in the interlamellar spacing. The molecules on the surface also contribute to the absorption spectra, therefore also generating the same shift in the Soret band. The molecules can only be in contact with one surface and held flat by van der Waals forces and hydrogen bonding from the acidic surface of the MMT via surface protons. It is therefore also likely that even the porphyrin molecules in the interlayers are held flat via similar bonding rather than squeezing. Figure 4 shows the diffuse reflectance spectra of the $TTPH_2$ adsorbed on cation-exchanged MMT. The results are in good agreement with visible spectra, as all cation-exchanged MMT cause protonation of the $TTPH_2$ compound.

Figure 5 presents the visible absorption spectrum of $TNPH_2$ in glacial acetic acid on a Fe(III) MMT surface. Adsorption of $TNPH_2$ on Fe(III) MMT causes the Soret band to be shifted to an absorption wavelength higher than that of the free base. The shift of 15 nm when the compound is in the adsorbed state, and the behaviour of the compound in acetic acid, which showed only a small shoulder at a longer wavelength, help to understand how this porphyrin behaves when it's on the clay surface or possibly even in the interlayers.

Clearly, in the acetic acid, almost all the $TNPH_2$ molecules are not protonated. In and on the clay, the surfaces are much more like a strong acid and a large proportion of the $TNPH_2$ molecules are present as the dication, although there is evidence that some of the molecules are still present in the neutral form from the width of the Soret band and the presence of the four weak bands between 500 nm and 700 nm. It can be inferred that because the porphyrin molecule is a non-rigid aromatic system, the planar conformation is favorably affected by both the acidic character of the clay and the van der Waals and H bonds to the clay, hence the dication forms.

The diffuse reflectance spectrum of the $TNPH_2$ adsorbed on Fe(III) MMT sample also shows a shift in the Soret band (Figure 6).
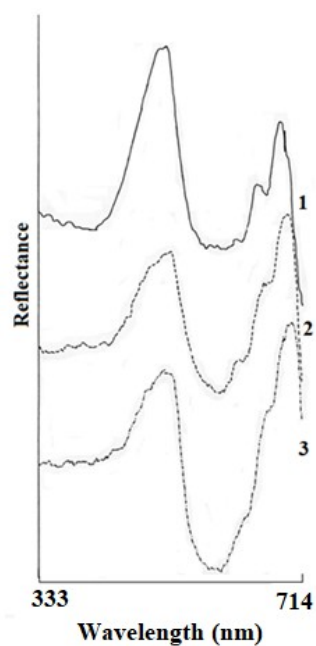
Figure 4: Diffuse reflectance spectra of TTPH$_2$ compound adsorbed on (1) Ni(II) MMT, (2) Fe (III) MMT, (3) Cd(II) MMT.
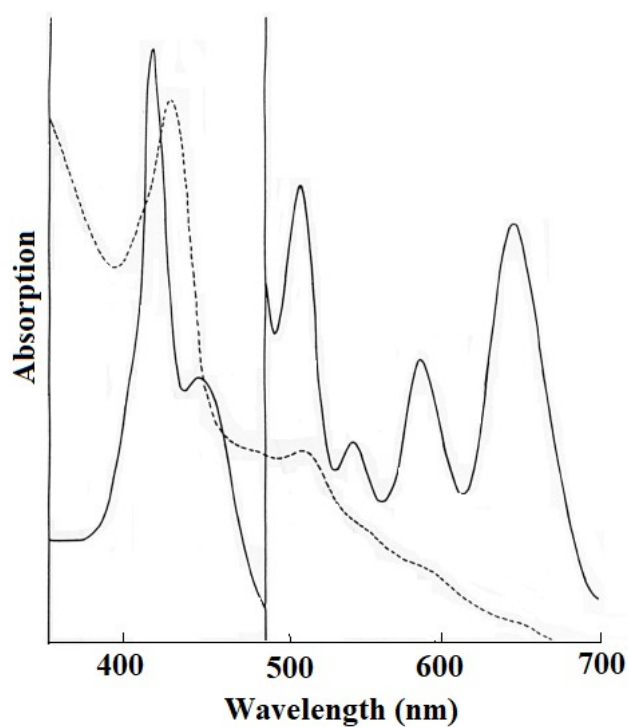
Figure 5: Visible absorption spectra of (_____) TNPH$_2$ in glacial acetic acid, (------) TNPH$_2$ on Fe(III) MMT. For clarity, the y-axis in the region from 500 nm to 700 nm has been magnified by 20 times for the visible absorption spectrum of TNPH$_2$ in acetic acid.
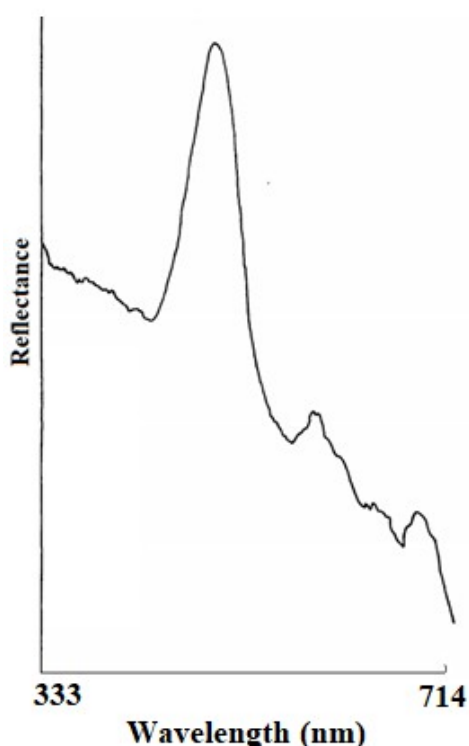
Figure 6: Diffuse reflectance spectrum of TNPH$_2$ compound adsorbed on Fe(III) MMT.

When the two compounds react with MMT saturated with metal ions of a suitable size to fit in the porphyrin ring, such as Cu(II), in a solvent miscible with water that facilitates the penetration of the hydrated sphere of the metal ion, the metal ions are incorporated into the porphyrin rings. This generates metalloporphyrin complexes. Figure 7 shows the visible absorption spectra of the two porphyrin compounds adsorbed onto Cu(II) MMT in acetone, clearly the Soret bands are around 420 nm, with three further bands between 530 nm and 600 nm. The spectra are similar to those reported for a Cu (II) porphyrin complex formed in solution (29) and are typical of porphyrins containing metals (note the absence of the four bands (between 500 nm and 700 nm) found in the unmetallated compounds.

The metal porphyrins formed on the MMT surface tend to be desorbed into the solution. These neutral complexes appear easily displaced from the exchange sites, presumably by the protons expelled from the porphyrin molecule during metallation.
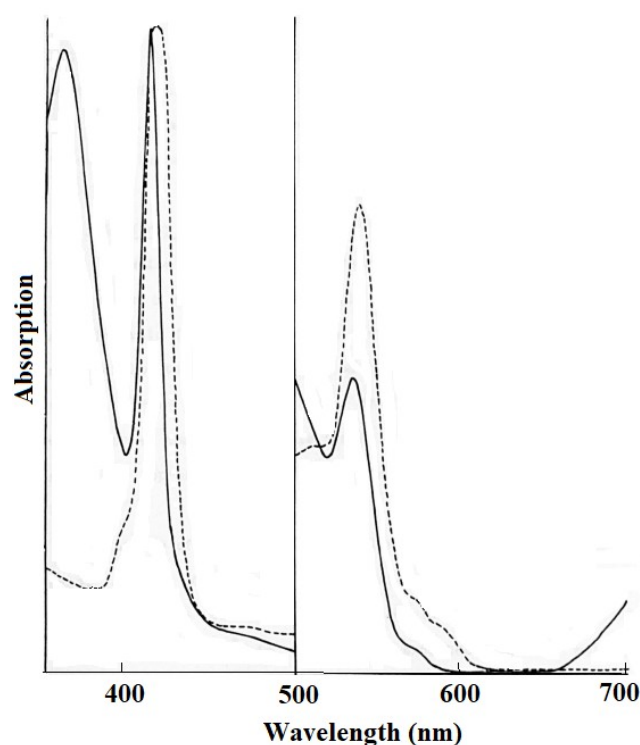
Figure 7: Visible absorption spectra of (———) TTPH$_2$ and (------) TNPH$_2$ on Cu(II) MMT. For clarity, the y-axis in the region from 500 nm to 700 nm has been magnified by 20 times.

3.3. X-ray Powder Diffraction

The MMT gives a basal spacing of 9.6 Å, when there are no molecules between the unit layers and 13 Å if there are water molecules (30). When Cu(II) MMT was reacted with TTPH$_2$ in a solvent miscible with water like acetone, the sample gave basal spacing of 14 Å, indicating a 4.4 Å interlayer separation, due to the intercalation of the porphyrin complex that formed. The 4.4 Å is lower than expected, as the molecule thickness is 4.7 Å (31) (Figure 8). Others (7) have also observed a basal spacing for MMT when it reacted with TPyPH$_2$, lower than expected from the molecular geometry. They attributed this to a twisting of the molecule in the MMT interlayer. This fact is supported herein by the higher shifts in the visible spectra found when the molecules are in the adsorbed state rather than in an acetic acid solution.

The TNPH$_2$ compound did not show a separation of the layers, probably because the naphthalene entity has difficulty lying in the same plane as the porphyrin plane (possibly due to steric constraints on ring rotation). Thus, TNPH$_2$ has a greater width than TTPH$_2$, and in this case it needs more space to enter the interlayer without special treatment. All other samples didn't show any interlayer separation.
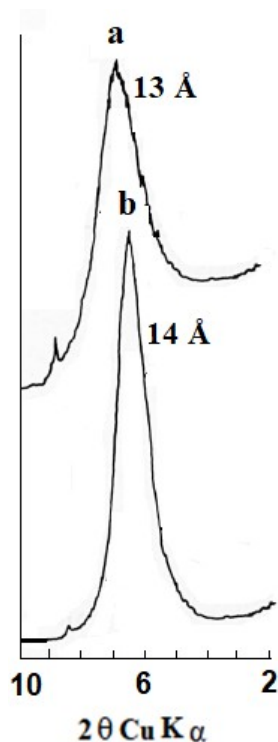
Figure 8: X-ray powder diffraction patterns of MMT (a) original sample, (b) Cu(II) MMT reacted with TTPH$_2$.

3.4. Electron Microscopy

The minerals of the MMT group are the most difficult clay minerals to be characterized by their morphology. To obtain adequate information about the samples, a high-resolution mode of operation was used. The MMT appeared as fibers under the electron microscope. The transmission electron micrograph of the Cu(II) MMT sample, which was reacted with TTPH$_2$ in acetone and had a basal spacing of 14 Å, is shown in Figure 9. The interlayer separation was 4.4 Å, which was attributable to porphyrin complex layering between the MMT interlayers. A group of striated black lines stacked between the MMT fabric may be seen in the micrograph. The porphyrin complex in the MMT interlayers is probably responsible for the dark lines.

Figure 9: Transmission electron micrographs of (left) MMT Sample, (right) Cu(II) MMT sample reacted with TTPH$_2$ in acetone.

4. CONCLUSION

When the two porphyrin compounds TTPH$_2$ and TNPH$_2$ react with MMT clay saturated with various cations, the former compound tends to be more planar in the MMT interlamellar and on the surface. If the metal ions on MMT, are of the suitable size to fit in the porphyrin ring such as Cu(II), a metal-porphyrin complex is formed (evidence presented herein). The later process takes place if the reaction is carried out in a solvent miscible with water like acetone, to penetrate the hydrated sphere of the metal ion. This type of complex has been formed in the reaction between Cu(II) MMT and both the porphyrins studied in this work. It has also been shown herein that larger porphyrins where the *meso* substituent is less free to rotate (here, TNPH$_2$) cannot penetrate the interlamellar spacings of the clays.

5. REFERENCES

1. Kosiur DR. Porphyrin Adsorption by Clay Minerals. Clays Clay Miner. 1977 Oct;25:365-71. Available from: <URL>.

2. Canesson P, Cruz MI, Van Damme H. X.P.S. study of the interaction of some porphyrins and metalloporphyrins with montmorillonite. Dev Sedimentol. 1979; 27; 217-25. Available from: <URL>.

3. Hassen JH. Spectroscopic analysis of adsorbed macrocyclic complexes on ceramic and related materials [PhD. Thesis]. [Colchester, England]: University of Essex; 1988.

4. Dias PM, de Faria DL, Constantino VR. Clay-porphyrin systems: Spectroscopic evidence of TMPyP protonation, non-planar distortion and *meso* substituent rotation. Clays Clay Miner. 2005 Aug; 53:361-71. Available from: <URL>.

5. Hassen J, Silver J. Stability of Fe(III) and Sn(IV) metalloporphyrins adsorbed on cation-exchanged montmorillonite. Trends Sci. 2022 Apr; 19(8):3426. Available from: <URL>.

6. Fujimura T, Shimada T, Hamatani S, Onodera S, Sasai R, Inoue H, et al. High density intercalation of porphyrin into transparent clay membrane without aggregation. Langmuir. 2013 Mar; 29(16):5060-65. Available from: <URL>.

7. Van Damme H, Crespin M, Obrecht F, Cruz MI, Fripiat JJ. Acid-base and complexation behavior of porphyrins on the intracrystal surface of swelling clays: *meso*-tetraphenylporphyrin and *meso*- tetra(4-pyridyl)porphyrin on montmorillonites. J Colloid Interface Sci. 1978 Aug;66(1):43-54. Available from: <URL>.

8. Nishina H, Hoshino S, Ohtani Y, Ishida T, Shimada T, Takagi S. Anisotropic energy transfer in a clay–porphyrin layered system with environment-responsiveness. Phys Chem Chem Phys. 2020 Jun;22(25):14261-67. Available from: <URL>.

9. Auwarter W, Ecija D, Klappenberger F, Barth JV. Porphyrins at interfaces. Nat Chem. 2015 Jan;7:105-20. Available from: <URL>.

10. Takagi S, Eguchi M, Tryk DA, Inoue H. Light-harvesting energy transfer and subsequent electron transfer of cationic porphyrin complexes on clay surfaces. Langmuir. 2006 Jan;22(4):1406-8. Available from: <URL>.

11. Ishida Y, Shimada T, Masui D, Tachibana H, Inoue H, Takagi S. Efficient excited energy transfer reaction in clay/porphyrin complex toward an artificial light-harvesting system. J Am Chem Soc. 2011 Aug;133(36):14280-86. Available from: <URL>.

12. Ishida Y, Masui D, Tachibana H, Inoue H, Shimada T, Takagi S. Controlling the microadsorption structure of porphyrin dye assembly on clay surfaces using the "size-matching rule" for constructing an efficient energy transfer system. ACS Appl Mater Interfaces. 2012 Jan; 4(2):811-16. Available from: <URL>.

13. Ishida Y, Shimada T, Tachibana H, Inoue H, Takagi S. Regulation of the collisional self-quenching of fluorescence in clay/porphyrin complex by strong host-guest interaction. J Phys Chem. A. 2012 Nov;116(49):12065-72. Available from: <URL>.

14. Egawa T, Watanabe H, Fujimura T, Ishida Y, Yamato M, Masui D, et al. Novel methodology to control the adsorption structure of cationic porphyrins on the clay surface using the "size-matching rule". Langmuir. 2011 Jul;27(17):10722-29. Available from: <URL>.

15. Takagi S, Eguchi M, Yui T, Inoue H. Photochemical Electron Transfer Reactions in Clay-porphyrin Complexes. Clay Sci. 2006; 12(2): 82-7. Available from: <URL>.

16. Takagi S, Konno S, Ishida Y, Ceklovsky A, Masui D, Shimada T, et al. A unique "Flattening effect" of clay on the photochemical properties of metalloporphyrins. Clay Sci. 2010; 14(6):235-39. Available from: <URL>.

17. Ishida Y, Fujimura, T, Masui D, Shimada T, Tachibana H, Inoue H, et al. What lowers the efficiency of an energy transfer reaction between porphyrin dyes on clay surface? Clay Sci. 2011; 15(4):169-74. Available from: <URL>.

18. Carrado KA, Wasserman SR. Stability of Cu(II)− and Fe(III)−porphyrins on montmorillonite clay: An x-ray absorption study. Chem. Mater. 1996 Jan;8(1):219-25. Available from: <URL>.

19. Bergaya F, Van Damme H. Stability of metalloporphyrins adsorbed on clays: A comparative study. Geochim Cosmochim Acta. 1982 Mar;46(3):349-60. Available from: <URL>.

20. Abdo S, Cruz MI, Fripiat JJ. Metallation-demetallation reaction of tin tetra(4-pyridyl) porphyrin in Na-hectorite. Clays Clay Miner. 1980 Apr; 28: 125-29. Available from: <URL>.

21. Crestini C, Pastorini A, Tagliatesta P, Metalloporphyrins immobilized on motmorillonite as biomimetic catalysts in the oxidation of lignin model compounds. J Mol Catal A Chem. 2004 Feb;208(1-2):195-202. Available from: <URL>.

22. Machado AM, Wypych F, Drechsel SM, Nakagaki S (2002) Study of the catalytic behavior of montmorillonite/iron (III) and Mn(III) cationic porphyrins. J Colloid Interface Sci. 2002 Oct; 254:158–64. Available from: <URL>.

23. Zyoud A, Jondi W, Mansour W, Majeed Khan MA, Hilal HS. Modes of tetra(4-pyridyl)porphyrinatomanganese(III) ion intercalation inside natural clays. Chem Cent J. 2016 Mar;10:12. Available from: <URL>.

24. Hassen JH, Silver J. Stability of Fe(III) and Sn(IV) Metalloporphyrins Adsorbed on Cation-Exchanged Montmorillonite. Trends Sci. 2022 Mar;19(8):3426-34. Available from: <URL>.

25. Adler AD, Lengo FR, Finarelli JD, Goldmacher J, Assour J, Korsakoff L. A simplified synthesis for meso-tetraphenylporphine. J Org Chem. 1967 Feb; 32(2):476. Available from: <URL>.

26. Noskov AV, Alekseeva OV, Shibaeva VD, Agafonov AV. (2020). Synthesis, structure and thermal properties of montmorillonite/ionic liquid ionogels. RSC Adv. 2020 Sep; 10(57):34885- 94. Available from: <URL>.

27. Rozenson I, Heller-Kallai L. Reduction and oxidation of Fe^{3+} in dioctahedral smectites-III. Oxidation of octahedral iron in montmorillonite. Clays Clay Miner. 1978 Apr;26:88-92. Available from: <URL>.

28. Holtzer M, Bobrowski A, Grabowska B. Montmorillonite: A comparison of methods for its determination in foundry bentonites. Metalurgija. 2011 Apr; 50(2):119-22.

29. Jeong D, Kang D-g, Joo T, Kim SK. Femtosecond-resolved excited state relaxation dynamics of copper (II) tetraphenylporphyrin (CuTPP) after soret band excitation. Sci Rep. 2017 Des;7:16865. Available from: <URL>.

30. Hassen J, Silver J. Montmorillonite surface as a catalyst for the formation of SAT metal tetra(p-sulphophenyl)porphyrins. J Teknol. 2020 Nov;82(6):1-9. Available from: <URL>.

31. Falk JE. Porphyrins and metalloporphyrins. Amsterdam; Elsevier; 1964. 266 p. Available from: <URL>.
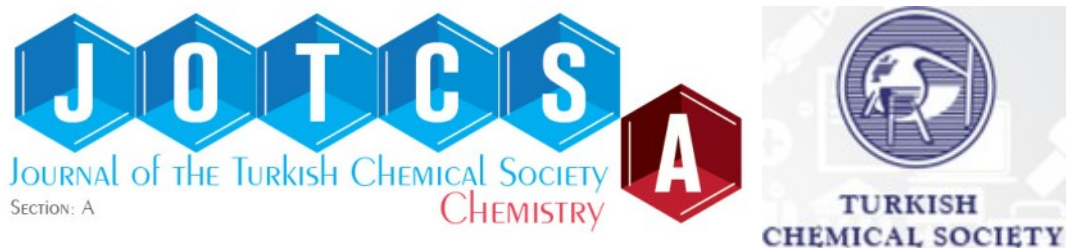
Design, Synthesis and Anti-Bacterial Activity Evaluation of Indole-Based Benzophenone and Their Derivatives

Fekadu Tumoro Erabe[1], Dagne Adisu Kure[1] iD , Salah Hamza Sherif[1]*

[1] Hawassa University, Department of Chemistry, Hawassa, Ethiopia

Abstract: Indole and benzophenone moiety are of significant interest to investigators because they are found in many natural products and pharmacologically active compounds. They represent versatile synthetic building blocks. The benzophenone and indole scaffolds are special structures in medicinal chemistry because these compounds are found in several biologically active natural products, compounds containing indole and benzophenone exhibit anticancer, antiinflammatory, antimicrobial, and antiviral activities. In this study, derivatives of 2-(diphenyl methylene) hydrazine, containing both indole and benzophenone moieties were successfully synthesized. The structural elucidation of the synthesized compounds were done using spectroscopic techniques like IR, ^{1}HNMR, and ^{13}CNMR. The synthesized target compounds were investigated for their in vitro antibacterial activity against two bacterial strains; *staphylococcus aureus (S. auras)*, and *Escherichia coli (E. coli)* using the disc diffusion method. All synthesized target compounds showed no significant activity against S*taphylococcus aureus (S. aureus)* but exhibited moderate activity against *Escherichia coli (E. coli)*. Among all the synthesized compounds, 2-*(diphenyl methylene)-1-((1-tosyl-1H-indol-3-yl) methylene) hydrazine* (BHT) (**7b**) showed a good inhibition at a concentration of 50 µg/mL with a zone of inhibition of 21.7 mm against *Escherichia coli (E.coli)* which was comparable with standard drug Ceftriaxone with the zone of inhibition of 26 mm. Thus, this compound could be considered as a lead molecule to design and develop novel antibacterial drugs.

1. INTRODUCTION

The steady increase in bacterial infections is becoming the major cause of high morbidity and mortality globally, especially in developing countries; this is due to the development of antibacterial and antifungal drug resistance (1). Because of the development of antibiotic resistance and the emergence of new microbial diseases, there is an urgent requirement to develop new antimicrobial agents for the treatment of microbial infections (2).

Heterocyclic compounds represent an important class of biological molecules (3). They are considered as a class of compounds having a great effect in the treatments of various diseases; compounds containing N and O are very active and important compounds in the preparation of drugs. Heterocyclic compounds containing nitrogen have been known to possess a very important role in the

field of medicinal chemistry (4). The indole ring system represents one of the most abundant and important heterocycle in the nature (5). Indole and other heterocyclic compounds containing indole moiety have proven to be versatile intermediates for the synthesis of a wide range of bioactive drugs. Amongst the various N-heterocycles, indole motifs have received significant attention due to their presence in proteins, amino acids, bioactive alkaloids, and drugs (6). Indole ring exists in several naturally occurring alkaloids (7). Its derivatives have exhibited a wide range of biological activities (8). In addition, it was reported that various 3-substituted indoles were used as starting materials for the synthesis of several alkaloids, pharmaceuticals, and perfumes (9,10). Compounds bearing an indole nucleus have considerable importance in the development of diverse bioactive compounds; such compounds have been reported to have various biological activities including antimicrobial (11-13),

anticancer (14,15), antiviral (16,17), anti-inflammatory (16-19), etc.

Natural and synthetic benzophenone derivatives have also known for their diverse biological activities. Several compounds belonging to this class of compounds have shown a wide range of biological activity, such as antimicrobial (20, 21), anticancer (22, 23), and anti-inflammatory (24, 25).

A combination of two or more different pharmacophores in a single molecular entity is a new strategy to develop new compounds having higher biological activity, therefore, the combination of indole and benzophenone moieties might provide new effective drugs against multidrug-resistant microbial infections (26).

Inspired by the above facts, we report herein the synthesis of new hybrid compounds combining indole and benzophenone; we hereby successfully report the synthesis and in vitro evaluation of their antibacterial activities against two bacterial strains, namely *Staphylococcus aureus* and *Escherichia coli.*

2. EXPERIMENTAL SECTION

2.1. Materials and Methods
Nuclear Magnetic Resonance (NMR) analysis was recorded on a Bruker Avance 400 MHz spectrometer with tetramethylsilane as internal standard, $CDCl_3$ and DMSO-d_6 as solvent. Infrared (KBr pellet) spectrum was recorded on a Perkin-Elmer BX infrared spectrometer in the range 400-4000 cm^{-1}, Thin Layer Chromatography (TLC) was done using silica gel 60 F254 (type 60) pre-coated

aluminum sheets, Electronic Melting Point apparatus were used (for determination of melting points of the synthesized compounds), the spots of the final compounds were visualized by irradiation with UV light at (254 nm and 365 nm) using an HP-UV/Visible lamp. Column chromatography was performed on silica gel (230-240 mesh). All the spectral analyses were carried out at the Department of Chemistry, Addis Ababa University, Ethiopia.

The chemicals used during the experiment were Benzophenone, indole, $POCl_3$, DMF, potassium carbonate (K_2CO_3), Acetone, Sodium hydroxide (NaOH), dichloromethane, glacial acetic acid, ethanol, ethyl acetate, n-hexane, and chloroform. All of them were analytical grade reagent and were used without further purification.

2.2. Chemistry
2.2.1. General procedures for the synthesis of target compounds
Indole (**1**) was used as starting material to synthesize the target compounds, which was reacted with phosphorus oxychloride ($POCl_3$) in the presence of DMF to form compound **2** by using a modified version of Vilsmeier Haack formylation reaction; on another root of reaction, benzophenone (**3**) reacted with hydrazine hydrate to form compound **4**. Then compound **2** and compound **4** were reacted together in ethanol using glacial acetic acid as a catalyst to form compound **5** as an intermediate compound, Finally, the target compounds (**7a** and **7b**) were obtained through substitution of the intermediate (**5**) with sulfonyl derivatives (**6a**) and (**6b**) using potassium carbonate as a mild base catalyst as shown in Scheme 1.
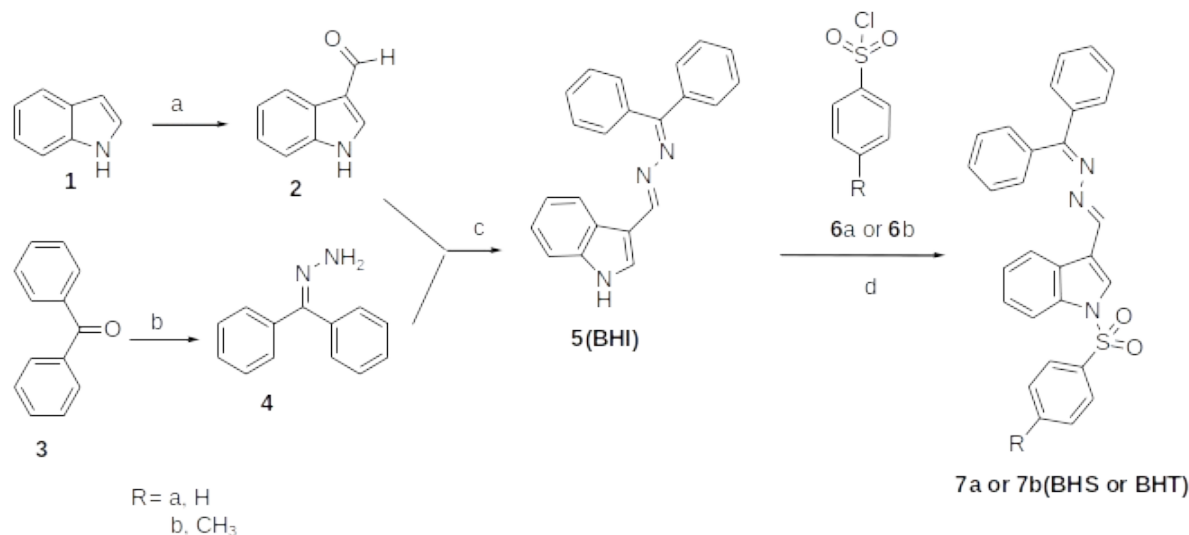
Scheme 1: Reagents and Conditions: a) $POCl_3$, NaOH (aq), DMF, reflux at 60 ᵒC, (b) ethanol, glacial acetic acid, reflux at 90 ᵒC for 6 h. (c) Ethanol, glacial acetic acid, reflux at 90ᵒC for 12 h (d), acetone, K_2CO_3, RT for 24 h.

2.3. Syntheses of the Intermediates and the Target Compounds
2.3.1. Synthesis of 1H-indole-3-carbaldehyde (2)
To dimethyl formamide (DMF) (5 mL, 4.45 mmol) cooled at 0 ᵒC, phosphorous oxychloride (1.75 mL;

10.3 mmol) was added dropwise and the mixture was stirred for 35 minutes then a solution of indole (1) (1 g, 8.5 mmol) in 5 mL of DMF was added dropwise to the reaction mixture and stirred for 2 h at room temperature, followed by the addition of

an aqueous solution of NaOH (15 mL); then the mixture was refluxed at 60 °C. For 2 h. The progress of the reaction was monitored by using TLC in the appropriate solvent 70:30 (n-hexane and ethyl acetate, v:v). When the reaction was completed, the reaction mixture was placed on an ice bath and the precipitate was extracted with ethyl acetate and washed with 30 mL of water. Then the collected organic layer was dried by using anhydrous sodium sulfate and concentrated under reduced pressure using a rotary evaporator. The crude product was further purified by column chromatography using a mixture of hexane ethyl acetate as eluent and concentrated using a rotary evaporator to give *1H*-indole -3-carboxaldehyde (**2**), yielding 90.49%.

2.3.2. Synthesis of 1-(diphenyl methylene) hydrazine (**4**)
To the solution of benzophenone (1 gram, 5.49 mmol) in 15 mL of ethanol, (3-5 drops) of glacial acetic acid was added and stirred at room temperature for 2-5 minutes. Then hydrazine hydrate (10 mL, 6.59 mmol) was added to the reaction mixture and refluxed at 90 °C. The progress of the reaction was monitored by using TLC in the appropriate solvent, 90:10 (n-hexane and ethyl acetate, v:v). When the reaction was complete, it was cooled to room temperature and extracted with ethyl acetate, and the extract was washed with 30 mL of water. Then the organic layer was collected and dried by anhydrous sodium sulfate and concentrated under reduced pressure using a rotary evaporator. The crude product was further purified by column chromatography using a mixture of hexane:ethyl acetate as eluent to give 1-(diphenyl methylene) hydrazine (**4**).

2.3.3 Synthesis of 1-((1H-indole-3-yl)-methylene)-2-(diphenyl methylene) hydrazine (BHI) (**5**)
1H-indole -3-carboxaldehyde (0.45 gram; 3.103 mmol) was dissolved in 15 mL of ethanol, and (3-5 drops) of glacial acetic acid was added and stirred at room temperature for 5-10 minutes, then 1-(diphenyl methylene) hydrazine (0.85 gram; 4.35 mmol) was added to the reaction mixture and refluxed at 90 °C. For 24 h; the completion of the reaction was checked using TLC in the appropriate solvent, 80:20 v:v ratios (n-hexane and ethyl acetate), when the reaction was completed, cooled to room temperature and extracted with ethyl acetate and washed with 30 mL of water. Then the organic layer was collected and dried with anhydrous sodium sulfate and concentrated under reduced pressure using a rotary evaporator. The obtained crude product was further purified by column chromatography using a mixture of hexane:ethyl acetate mixture as eluent and concentrated using a rotary evaporator to give 1-((1H-indole-3-yl)-methylene)-2-(diphenyl methylene) hydrazine (BHI) (**5**).

2.3.4 Synthesis of 2-(diphenyl methylene)-1-((1-tosyl-1H-indol-3-yl) methylene) hydrazine (BHT) (**7b**)
1-Tosyl-1H-indole-3-carbaldehyde (0.604 gram, 2.02 mmol) was dissolved in 15 mL of ethanol, and (3-5 drops) of glacial acetic acid was added and stirred at room temperature for 5-10 minutes. Then 1-(diphenyl methylene) hydrazine (0.33 gram; 1.68 mmol) was added to the reaction mixture and refluxed at 90 °C. The progress of the reaction was monitored by using TLC in the appropriate solvent, 90:10 ratios (n-hexane, and ethyl acetate, v:v). After completion of the reaction, the mixture was extracted with ethyl acetate and washed with 30 mL of water. Then the organic layer was collected and dried using anhydrous sodium sulfate and concentrated using a rotary evaporator. The crude product was further purified by column chromatography using a mixture of hexane ethyl acetate as eluent to give 2-(diphenyl methylene)-1-((1-tosyl-1H-indol-3-yl) methylene) hydrazine compound (**7b**)(BHT).

2.3.5 Synthesis of 2-(diphenyl methylene)-1-((benzenesulfonyl-1H-indol-3yl-) methylene) hydrazine (BHS)(**7a**)
1-Benzene sulfonyl-1H-indole-3-carbaldehyde (0.69 gram, 2.44 mmol) was dissolved in 15 mL of ethanol, and (3-5 drops) of glacial acetic acid was added and stirred at room temperature for 5-10 minutes. Then 1-(diphenyl methylene) hydrazine (0.4 gram, 2.04 mmol) was added to the reaction mixture and refluxed at 90 °C. For 24 h, the progress of the reaction was checked using TLC in the appropriate solvent 90:10 v:v ratio (n-hexane and ethyl acetate) of the solvent mixture. When the reaction was completed, cooled and extracted with ethyl acetate and washed with 30 mL of water. Then the organic layer was collected and dried by anhydrous sodium sulfate and concentrated under reduced pressure using a rotary evaporator. The crude product was further purified by column chromatography using a mixture of hexane and ethyl acetate as eluent to give the target compound (**7a**).

3. RESULTS AND DISCUSSION

3.1 Anti-Bacterial Activity Studies
The anti-bacterial activities of the synthesized target compounds were evaluated against two bacterial strains such as *Escherichia coli* (*E.coli*) and *Staphylococcus aureus* (*S. Aureus)*, and sensitivity testing was conducted by means of disc diffusion method using Ceftriaxone (30 μg/disc) as a standard drug.

3.1.1 Culture media and disk preparation
For quality control of the antibacterial activities, control strains of Escherichia coli (*E. coli*) and Staphylococcus aureus (*S. aureus*) from the American Type Culture Collection (ATCCs) were used. Antibiotic discs were punched out of Whatman filter paper and prepared at a diameter of 6 mm.

3.1.2 Preparation of chemical solution and media for the anti-bacterial activity
Solution for antibacterial activities was prepared as stated by Hoda et al. with minor modification to concentration. Briefly, 50 μg/mL and 25 μg/mL of each chemical was dissolved in 30 μg/mL dimethyl sulfoxide (DMSO) and mixed to form a homogenous solution. A fixed volume of 50 μg/L

and 25 µg/mL of solution were added to previously sterilized Whatman filter paper disks using a sterile micropipette.

For quality control purpose, strains were aseptically inoculated on a sterile nutrient agar plate and then incubated for 48 hours at 37 °C. 5 mL nutrient broth bacterial cultures were prepared by picking 3-5 colonies to form 0.5 McFarland standard. The culture suspension was then inoculated on sterile Muller Hinton agar plate using sterile cotton swab in three directions to get a uniform inoculum. Then a disk with a control Ceftriaxone and solution impregnated disks were placed on the culture plate and incubated for 48 hours at 37 °C. Each disk was labeled with its

unique ID number on the back of the Petri dish. The anti-bacterial activity was evaluated for the zone of inhibition around the disk.

3.1.3. Anti-bacterial activity
Antibacterial activity of all the synthesized compounds were evaluated against one gram-negative bacterial strain i.e. *Escherichia coli* and gram-positive *Staphylococcus aureus*. DMSO was used as a solvent control and Ceftriaxone as a positive control. Sensitivity testing was done by disc diffusion method and the diameter of zones of inhibition was measured in millimeters, documented (Table 1) and compared with the control.

Table 1: Zones of inhibition of synthesized compounds and the reference.

Compounds	Concentration (µg /mL)	Zone of inhibition (mm)	
		Gram +ve *S. aureus*	Gram –ve *E. Coli*
BHS (**7a**)	50	6.1	20.3
	25	6.1	14.5
BHT (**7b**)	50	13	21.7
	25	7.1	6.2
BHI (**5**)	25	6.1	12.1
	50	6.2	6.2
Ceftriaxone (+ve control)	30	30	26

Ceftriaxone is positive control prepared from 30 µg /mL in DMSO as solvent. The impregnated disc in samples, as well as positive control, is containing 6 mm in size. In this study, those with a zone of diameter greater than 6 mm (>6 mm) have anti-bacterial activity since the diameter of the disc is 6 mm.

3.2. Characterization

3.2.1. 1-((1H-indole-3-yl)-methylene)-2-(diphenyl methylene) hydrazine (BHI) (5)
White solid, yield 72.5%, melting point: 280-282 °C; IR (KBr, cm⁻¹): 3179.78 (N-H secondary amine) 3055.11 (aromatic C-H), 2921.26, 2853.19 (aliphatic C-H), 1600.04(C=N); ^{1}H-NMR (DMSO-d_6, 400 MHz) δ 11.74(1H,s N-H), 8.85(1H,s, H-8), 7.93(2H, d, J=2.9Hz, Ar-H), 7.69(1H,s, H-2), 7.59(2H,d, J =8.0Hz,Ar-H), 7.40 (2H, m, Ar-H), 7.13 (2H, m, Ar-H), 6.90(2H,t, J=7.5Hz, Ar-H); ^{13}C NMR (DMSO-d_6, 100 MHz): δ 164.4, 138.3, 137.5, 121.8, 112.2, 156.9, 133.3, 133.4, 129.7, 128.8, 128.7, 128.6, 128.3, 123.1, 122.6, 121.0, 112.4

3.2.2. 2-(diphenyl methylene)-1-((1-tosyl-1H-indol-3-yl) methylene) hydrazine (BHT) (7b)
Blue solid, yield 82.3%, melting point: 262-264 °C; IR (KBr, cm⁻¹): 3100 to 3000 (Aromatic C-H), 1561.16 (C=N- imine), 1656.38, 1561.16 (C=C stretch), 1313.57 (asymmetric stretch S (=O)), 1174.38 (symmetric stretch S(=O)), 684.92 (S-C stretch); ^{1}H-NMR (DMSO-d_6, 400MHz): δ 10.10 (2H, d, J=3.1Hz, Ar-H), 8.92 (2H,d, J=3.3 Hz, Ar-H), 8.15 (1H, s, N=CH), 8.13 (2H, d, *J*=3.7 Hz, Ar-H), 7.75 (2H, t, *J*=7.7Hz, Ar-H), 7.66 (2H, d, J=8.3 Hz, Ar-H), 7.98 (3H, m, Ar-H), 7.43 (4H, t, J=7.1Hz, Ar-H), 7.69

(1H, s, H-2), 2.50 (3H, s, CH₃); ^{13}C NMR (DMSO-d_6, 100 MHz): δ 159.5, 133.4, 135.5, 130.4, 126.6 133.1, 130.4, 130.0, 129.4,129.3, 129,0, 128.8, 128.5, 128.5, 40.6.

3.2.3. 2-(Diphenyl methylene)-1-((benzenesulfonyl-1H-indol-3yl-)methylene) hydrazine (BHS)(7a)
Blue solid, yield 79.9%, melting point: 244-246 °C; IR (KBr, cm⁻¹): 3024.46 (aromatic C-H stretch), 1659.85 (-C=N stretch), 1561.27 (aromatic C=C stretch), 1313.67 (Asymmetric S (=O) 2 stretch), 1174.03 (symmetric S (=O) 2 stretch), 684.89 (-S-C stretch); ^{1}H-NMR (DMSO-d_6, 400 MHz) δ: 7.76(2H,d, J=8.0Hz, Ar-H), 7.72 (4H, m, Ar-H), 7.68 (2H, m, Ar-H), 7.50 (2H,d, J=2.8Hz,Ar-H), 7.47(4H, dt, J=8.6Hz,Ar-H), 7.37(2H,d, J=7.2Hz, Ar-H), 7.29(1H,s, -N=CH), 7.41(1H,s, indole, H-2); ^{13}CNMR (DMSO-d_6, 100 MHz): δ 159.5, 135.5, 133.1, 130.4,129.4, 128.5, 133.2, 130.4, 130.1, 129.4, 129.3, 129.0, 128.8, 128.

4. CONCLUSION

In the present study, derivatives of 2-(diphenylmethylene) hydrazine, containing both indole and benzophenone moieties were successfully synthesized. The indole-based benzophenone and its derivatives were biologically active molecules with various activities. The chemical structures of all the synthesized compounds were elucidated by spectroscopic techniques such as IR, ^{1}HNMR and ^{13}CNMR. All the newly synthesized compounds were evaluated for in vitro antibacterial activity by the disc diffusion method and its zone of inhibition was determined

against two different bacterial strains. All the synthesized compounds were mostly active against E.coli and least active against *S. aureus* bacterial strains. Among the synthesized compounds; *2-(diphenyl methylene)-1-((1-tosyl-1H-indol-3-yl) methylene) hydrazine* (**7b**) (BHT) shows better activities with 21.7mm zone of inhibition at concentration of 50 µg/mL against *E.coli* which is comparable to the standard drug ceftriaxone with a zone of inhibition of 26 mm and BHI shows the least activity against *E. coli* at a concentration of 25 µg/mL. Generally, N-substituted derivatives show better activities.

5. CONFLICT OF INTEREST

There are no conflicts of interest.

6. ACKNOWLEDGMENTS

7. REFERENCES

1. Al-Wabli RI, Alsulami MA, Bukhari SI, Moubayed NM, Al-Mutairi MS, Attia MI. Design, synthesis, and antimicrobial activity of certain new Indole-1, 2, 4 Triazole conjugates. Molecules. 2021 Apr 15;26(8):2292. Available from: <URL>

2. Xue YJ, Li MY, Jin XJ, Zheng CJ, Piao HR. Design, synthesis and evaluation of carbazole derivatives as potential antimicrobial agents. Journal of Enzyme Inhibition and Medicinal Chemistry. 2021 Jan 1;36(1):296-307. Available from: <URL>

3. Carullo G, Mazzotta S, Giordano F, Aiello F. Green Synthesis of New Pyrrolo [1, 2-a] quinoxalines as Antiproliferative Agents in GPER-expressing Breast Cancer Cells. Journal of Chemistry. 2021 Oct 31;2021. Available from: <URL>

4. Kaur J, Utreja D, Jain N, Sharma S. Recent developments in the synthesis and antimicrobial activity of indole and its derivatives. Current Organic Synthesis. 2019 Jan 1;16(1):17-37. Available from: <URL>

5. Inman M, Moody CJ. Indole synthesis–something old, something new. Chemical Science. 2013; 4(1):29-41. Available from: <URL>

6. MahamadAlli Shaikh T, Debebe H. Synthesis and evaluation of antimicrobial activities of novel N-substituted indole derivatives. Journal of Chemistry. 2020 Apr 14; 2020 Available from: <URL>

7. Raju PA, Mallikarjunarao R, Gopal KV, Sreeramulu J, Reddy DM, Krishnamurthi KP, Reddy SR. Synthesis and biological activity of some new indole derivatives containing pyrazole moiety. J. Chem. Pharm. Res. 2013;5(10):21-7. Available from: <URL>

8. MahamadAlli Shaikh T, Debebe H. Synthesis and evaluation of antimicrobial activities of novel N-substituted indole derivatives. Journal of Chemistry. 2020 Apr 14;2020. Available from: <URL>

9. Gupta AK, Sharma M. Synthesis, Characterization and Anti-Microbial Activity of Indole Derivatives. Journal of Drug Delivery and Therapeutics. 2019 Aug 25;9(4-s):918-25. Available from: <URL>

10. Ibrahim M, Taha M, Almandil NB, Kawde AN, Nawaz M. Synthesis, characterization and electrochemical properties of some biologically important indole-based-sulfonamide derivatives. BMC chemistry. 2020 Dec;14(1):1-0. Available from: <URL>

11. Tiwari S, Kirar S, Banerjee UC, Neerupudi KB, Singh S, Wani AA, Bharatam PV, Singh IP. Synthesis of N-substituted indole derivatives as potential antimicrobial and antileishmanial agents. Bioorganic Chemistry. 2020 Jun 1;99:103787. Available from: <URL>

12. Shirinzadeh H, Süzen S, Altanlar N, Westwell AD. Antimicrobial activities of new indole derivatives containing 1, 2, 4-triazole, 1, 3, 4-thiadiazole and carbothioamide. Turkish Journal of Pharmaceutical Sciences. 2018 Dec;15(3):291. Available from: <URL>

13. Mane YD, Sarnikar YP, Surwase SM, Biradar DO, Gorepatil PB, Shinde VS, Khade BC. Design, synthesis, and antimicrobial activity of novel 5-substituted indole-2-carboxamide derivatives. Research on Chemical Intermediates. 2017 Feb;43(2):1253-75. Available from: <URL>

14. Pecnard S, Hamze A, Bignon J, Prost B, Deroussent A, Gallego-Yerga L, Peláez R, Paik JY, Diederich M, Alami M, Provot O. Anticancer properties of indole derivatives as IsoCombretastatin A-4 analogues. European Journal of Medicinal Chemistry. 2021 Nov 5;223:113656. Available from: <URL>

15. Ma J, Li J, Guo P, Liao X, Cheng H. Synthesis and antitumor activity of novel indole derivatives containing α-aminophosphonate moieties. Arabian Journal of Chemistry. 2021 Aug 1;14(8):103256. Available from: <URL>

16. Dorababu A. Indole–a promising pharmacophore in recent antiviral drug discovery. RSC Medicinal Chemistry. 2020; 11(12):1335-53. Available from: <URL>

17. Xue S, Ma L, Gao R, Li Y, Li Z. Synthesis and antiviral activity of some novel indole-2-carboxylate derivatives. Acta Pharmaceutica Sinica B. 2014 Aug 1;4(4):313-21. Available from: <URL>

18. Solanki D, Nakra VK, Tiwari A, Gupta AK, Gandhi S. Synthesis, characterization and anti-inflammatory activity of novel 1, 5-disubstituted indole derivatives. European Journal of Molecular &

Clinical Medicine. 2020;7(11):4622-35. Available from: <URL>

19. Abdellatif KR, Lamie PF, Omar HA. 3-Methyl-2-phenyl-1-substituted-indole derivatives as indomethacin analogs: design, synthesis and biological evaluation as potential anti-inflammatory and analgesic agents. Journal of Enzyme Inhibition and Medicinal Chemistry. 2016 Mar 3; 31(2):318-24. Available from: <URL>

20. Al-Ghorbani M, Lakshmi Ranganatha V, Prashanth T, Begum B, Khanum SA. *In vitro* antibacterial and antifungal evaluation of some benzophenone analogues. Der Pharma Chem. 2013;5:269-73. Available from: <URL>

21. Bushra Begum A, Khanum NF, Ranganatha VL, Prashanth T, Al-Ghorbani M, Khanum SA. Evaluation of Benzophenone-N-Ethyl morpholine ethers as antibacterial and antifungal activities. Journal of Chemistry. 2014 Jan 28;2014. Available from: <URL>

22. Zhang S, An B, Yan J, Huang L, Li X. The synthesis and evaluation of new benzophenone derivatives as tubulin polymerization inhibitors. RSC advances. 2016;6(91):88453-62. Available from: <URL>

23. Cortez-Maya S, Cortes Cortes E, Hernández-Ortega S, Apan TR, Martínez-García M. Synthesis of 2-aminobenzophenone derivatives and their anticancer activity. Synthetic Communications. 2012 Jan 1;42(1):46-54. Available from: <URL>

24. Gulnaz AR, Mohammed YH, Khanum SA. Design, synthesis and molecular docking of benzophenone conjugated with oxadiazole sulphur bridge pyrazole pharmacophores as anti inflammatory and analgesic agents. Bioorganic Chemistry. 2019 Nov 1; 92:103220. Available from: <URL>

25. Feng Z, Chen J, Feng L, Chen C, Ye Y, Lin L. Polyisoprenylated benzophenone derivatives from Garcinia cambogia and their anti-inflammatory activities. Food & Function. 2021;12(14):6432-41. Available from: <URL>

26. Shirinzadeh H, Altanlar N, Yucel N, Ozden S, Suzen S. Antimicrobial evaluation of indole-containing hydrazone derivatives. Zeitschrift für Naturforschung C. 2011 Aug 1;66(7-8):340-4. Available from: <URL>

27. Hoda S, Vijayaraghavan P. Evaluation of antimicrobial prospective of Parmotrema perlatum hexane extract. Int J Pharm Res Allied Sci. 2015 Jan 1;4(2):47-53. Available from: <URL>

Voltammetric Determination of Trace Amounts of Lead with Novel Graphite/Bleaching Earth Modified Electrode

Elif Tüzün[1]* iD

[1] Istanbul University-Cerrahpaşa, Department of Chemistry, Istanbul, 34320, Türkiye.

Abstract: Modified composite electrodes have gained considerable interest in the detection of heavy metal ions due to their excellent sensitivity, selectivity, stability, and rapid response. Generally, these sensors consist of binder, conductive substance, and modifier. This study examined into the performance of a novel modified electrode that used a graphite–bleaching earth (BE-MCPE) composite performed while detecting trace amounts of Pb(II) using a differential pulse voltammetric technique (DPASV). In order to investigate the properties of BE-MCPE, we employed several analytical techniques, including SEM, SEM-EDX, FTIR, and XRD. These techniques were used to characterize the physical, chemical, and elemental properties of BE-MCPE, as well as its Pb(II) adsorption capacity, providing a comprehensive understanding of its composition and structure. The electrochemical results showed that the modified electrode demonstrated superior sensitivity and selectivity, in detecting Pb(II) ions, with a linear response range of 2.10^{-7} mol/L to 10.10^{-7} mol/L , limit of detection (LOD) of 4.89×10^{-8} mol/L, and limit of quantification (LOQ) of 1.63×10^{-7} mol/L. This novel modified electrode can achieve the sensitive detection of trace amounts of Pb(II) in a wide range of wastewater applications.

1. INTRODUCTION

The development of modified composite electrodes has gained considerable attention, particularly in the field of sensing heavy metal ions (1). The market for modified composite electrodes is growing rapidly in the field of heavy metal ion detection due to their exceptional stability, sensitivity, flexibilty, selectivity, wearability, and rapid response time. These sensors are highly significant in detecting trace amounts of heavy metal ions in a variety of industrial and environmental applications thanks to their unique properties (2). Human activities have resulted in the discharge of a large number of contaminants into the environment, which has had a detrimental impact on the environment (3). These heavy metals can accumulate through food chains, plants, water, air, and soil, which can have a major adverse effect on environments and living organisms (4–6). This problematic issue involves several dangerous and harmful metals, including iron, mercury, arsenic, silver, copper, nickel, cobalt, and zinc. These metals

are known to be cumulative in nature, and their toxic effects can increase over time, making them particularly hazardous (7). Extremely dangerous environmental hazards including Pb(II) (5,8–10), Hg(II) (5,9), Cu(II) (9,11), and Cd(II) (5,9) can damage the liver, heart, bone, kidney, muscle, skin, teeth, and nervous system, among other organs in the body. Additionally, Pb(II) is a critical trace element for humans, but excessive amounts can accumulate in the body's tissues, leading to overdose and potentially fatal consequences such as renal damage. Therefore, it is crucial to monitor the concentration of these heavy metal ions carefully (12).

Nowadays, a number of methods have been suggested for the detection of heavy metal ions, including atomic emission spectroscopy (AES), inductively coupled plasma mass spectrometry (ICP-MS), atomic absorption spectroscopy (AAS) (13), etc. Currently, several methods such as ICP-MS (14), colorimetric method (15), AAS, near-infrared

spectroscopy (16), direct thermal release/electrothermal atomization atomic absorption spectrophotometric (ETA AAS) detection (17) and voltammetric method (18) have been proposed for detecting heavy metal ions.

The silver nanoparticles/silane grafted bentonite modified electrode investigated by Lalmalsawmi et al. demonstrated remarkable both sensitivity and selectivity for detecting a small quantity of Pb(II) in wastewater applications (19). Electrochemical sensing systems offer excellent advantages for detecting Pb(II) ions using modified glassy carbon electrode surface. For detecting contamination by heavy metals in both industrial and environmental situations, such a type of electrode may provide an efficient and economical solution. In another study, using linear scan anodic stripping voltammetry (LSASV) and cyclic voltammetry (CV), Jaber et al. investigated the selectivity of membrane filtration ceramic membranes fabricated from local clay against Pb(II) (20). The novelty of this study lies in the utilization of graphite-bleaching earth (BE-MCPE) composite as a novel modifier for the determination of trace amounts of Pb(II) using differential pulse anodic stripping voltammetry (DPASV). The graphite-bleaching earth composite working electrodes offer the advantages of simplicity, ease of preparation, and cost-effectiveness, while taking advantage of the reactivity and sensitivity of clay, making them suitable for routine analysis of Pb(II) in environmental medium. This study presents the high value of clay-modified electrodes in the perspective of ceramic membrane filtration for heavy metal ions, particularly Pb(II), in terms of efficiency. In order to investigate the properties of BE-MCPE, we employed several analytical techniques, including scanning electron microscopy (SEM), SEM combined with energy-dispersive X-ray spectroscopy (SEM-EDX), Fourier transform infrared spectroscopy (FTIR), and X-ray diffraction (XRD). These techniques were used to determine the physical, chemical, and elemental properties of BE-MCPE, as well as its Pb(II) adsorption capacity, providing a comprehensive understanding of its composition and structure. Using DPASV, our study examined the efficacy of a novel graphite-bleaching earth composite modified electrode for the selective detection of trace amounts of Pb(II). With a linear response range of 2.10^{-7} M to 10.10^{-7} M, LOD of 4.89×10^{-8} mol/L, and LOQ of 1.63×10^{-7} mol/L, the modified electrode demonstrated excellent sensitivity and selectivity, making it a promising solution for detecting Pb(II) in wastewater applications.

2. EXPERIMENTAL

2.1. Apparatus and Chemicals
The bleaching earth was collected from Edremit, Türkiye. The main component in bleaching earth, with a chemical formula of $Al_2O_3 4SiO_2 nH_2O$, is silicon dioxide. It is a very fine powder that can range from 57% to more, depending on the type (21). The clay material was manually ground with a mortar and pestle before being separated into various granular sizes with ASTM (American Society for Testing and Materials) specified sieves. The sieves were stacked on top of one another to collect around 4 sizes. The bleaching earth membrane supports were produced using fractions of a size in the 200–400 μm range. Lead(II) nitrate (≥ 99.0%), cadmium(II) nitrate (≥ 99.0%), mercury(II) nitrate (≥ 99.0%), and copper(II) nitrate (≥ 99.0%), were purchased from Sigma Aldrich Company. Graphite powder (particle size < 100μm) and spectroscopic-grade paraffin oil were procured from Fluka Company.

A Gamry (Inst.Ref.600 potentiostat/galvanostat) was used to regulate the current and voltage during electrochemical processes. A working electrode, a reference electrode, and a counter electrode makes up the 3-electrode configuration used. In this study, a BE-MCPE served as the working electrode. The counter electrode was Pt wire, and the reference electrode was a Ag/AgCl electrode in a 3 M KCl solution. The use of the reference and counter electrodes creates a stable baseline for comparison and result analysis, allowing for precise control and monitoring of the electrochemical reactions occurring on the BE-MCPE working electrode. The experiment was carried out with high-quality and precisely measured ingredients, increasing the likelihood of achieving exact and trustworthy results. The experiment used only analytical reagent grade chemicals. In addition, Millipore Direct-Q3 water, which has a high level of purity (18 Mega cm), was used to make all of the aqueous solutions for the experiment, reducing any sources of impurities or contaminants that might have an impact on the experiment's outcomes. It was necessary to use a buffer solution as a supporting electrolyte for the measurement of Pb(II) concentration. The buffer utilized was a 0.05 M NaOAc-HOAc solution with a pH of 4.75. The accuracy and precision of the data obtained depended heavily on selecting of this buffer solution. The buffer solution aids in preserving an electrochemical reaction's stable pH environment, ensuring that the reaction takes place under constant and dependable circumstances. In turn, this contributes to reducing experimental mistakes and improving the precision and clarity of the findings. A stock solution of Pb(II) (1×10^{-3} M) was prepared from the corresponding analytical grade metal nitrate. The BE-MCPE was prepared by mixing 0.5 g of graphite, 0.3 g of BE, and 100 μL of paraffin oil by hand-mixing in a mortar, and then the sample was homogenized. The MCPE was pressed into the cavity of the electrode body, and the electrical contact was established with a Pt. The surface and functional groups of the synthesized BE-MCPE were analyzed using various techniques such as SEM (Model: Hitachi SU3500 T2), EDX (Model: Oxford XACT), FTIR (Model: Jasco 6800), and XRD (Rigaku Miniflex 600). By scanning the surface with an electron beam at a 15 kV acceleration voltage in vacuum, we were able to obtain SEM images of solid powder samples. To identify the functional groups contained in the material, 32 scans were recorded across a range of 4000-400 cm^{-1} to create the FTIR spectra of the samples. Additionally, the crystal structure and average crystallite size of the BE-MCPE were determined using the XRD method with Cu K_α radiation (conditions: 40 kV and 15 mA).

2.2. Procedure

10 mL of pH 4.75 NaOAc-HOAc buffer solution in the voltammetric cell was filled with the BE-MCPE. The electrode was standardized for 5 minutes with an open circuit in the blank solution. After that, differential pulse voltammograms of blank solutions with the standardized electrode were recorded in the potential range of -0.8 V to -0.4 V until a stable voltammetric background was obtained. The electrode was removed, cleaned with water, and placed inside a different voltammetry cell that contains 10 mL of Pb(II) preconcentration solution. The accumulation step was carried out at -0.7 V for a selected time while stirring the solution at 650 and 500 rpm. After an appropriate preconcentration step, the electrode was rinsed with deionized water. Reduced lead was stripped from the electrode surface during the potential sweep from -0.8 V to -0.4 V, and well-defined stripping peaks were obtained between -0.54 V and -0.525 V, depending on the metal concentrations In Figure 1, the schematic experimental procedure is given.
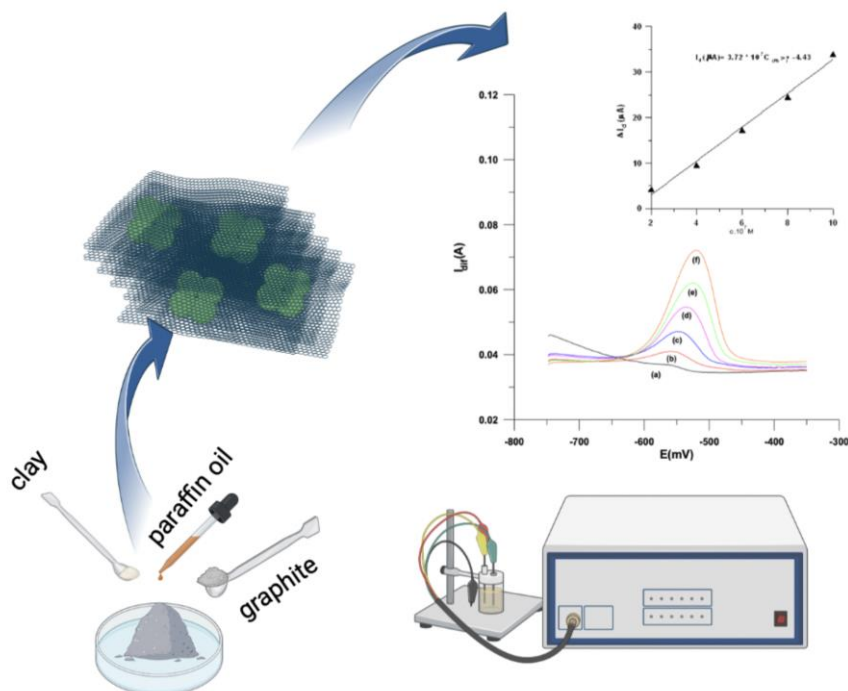
Figure 1: The schematic experimental procedure

3. RESULTS AND DISCUSSION

3.1. Characterization of Materials

FTIR analysis revealed characteristic peaks of functional groups for BE, BE-MCPE, and BE-MCPE /Pb. The technique was also utilized to illuminate the interactions between BE-MCPE and Pb(II) ions. In Figure 2 (a), the FTIR spectra of BE showed major characteristic peaks at about 3624, 3410, 1638, 1425, 1112,984, and 790 cm^{-1} which are attributed to the vibrations of O−H, stretching, O−H, stretching, −C=O, SiO, SiO, δAlAlOH, and silica, respectively. In Figure 2 (b), the FTIR spectra of BE-MCPE showed major characteristic peaks at about 3624, 2920, 2851, 1630, 1457, 1114, and 970 cm^{-1} which are attributed to the vibrations of O−H, stretching, −CH symmetric, −CH asymmetric, −C=O, SiO, SiO, and δAlAlOH, respectively. In Figure 2 (c), the FTIR spectra of BE-MCPE /Pb showed major characteristic peaks at about 2920, 2851, 1356, and 970 cm^{-1} which are attributed to the vibrations of −CH symmetric, −CH asymmetric, SiO, and δAlAlOH, respectively. The result is in good agreement with other literature reports (21−23). The absorption spectrum showed notable changes following the adsorption of Pb (Figure 2). Specifically, the peak corresponding to v (−OH) displayed a shift to 3619 cm^{-1}, while the peak associated with v (C=O) shifted to 1630 cm^{-1}. Additionally, the intensity of the peak related to v (C=O) significantly decreased, and the peak of 1638 cm^{-1} underwent a shift to 1457 cm^{-1} and decreased noticeably in intensity.
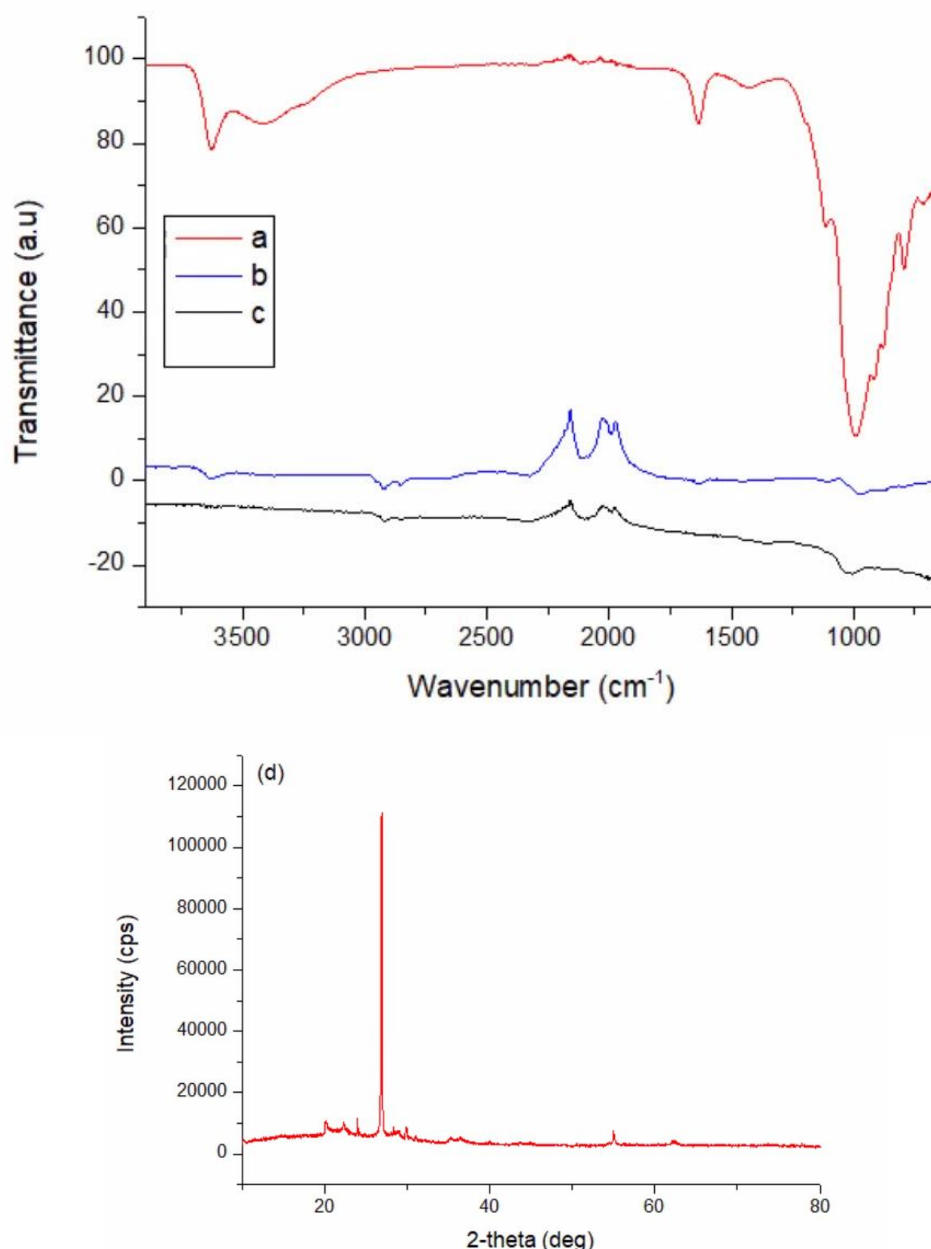
Figure 2: FTIR spectra of (a) BE, (b) BE-MCPE, (c) BE-MCPE/Pb, and (d) XRD graph of BE-MCPE.

In this study, SEM mapping and EDX data were utilized to analyze the BE-MCPE's composition and distribution, while also investigating its surficial properties. Figure 3 displays SEM images of samples (a) BE, (b) BE-MCPE's, and (c) BE-MCPE /Pb(II)'s. The SEM analysis of the BE showed that the sample contained particles with a plate-like morphology, indicating the presence of layered clay structures (24). These structures were thin and flat, similar to sheets or small plates stacked on top of each other. The SEM image of the BE-MCPE composite showed a morphology that resembled the distribution of several individual graphene layers gathering and folding into a layered clay structure during the formation of the composite. In this study, the elemental composition of the BE-MCPE/Pb(II) (Figure 3.d) was investigated using EDX analysis, and the obtained results are presented in Table 2. The results showed the presence of various elements, including silisium (27.72%), calcium (1.74%) lead (13.32%), iron (3.24%), potassium (1.00%), magnesium (1.12%), aluminum (8.83%), and oxygen (43.03%) in the sample. After adsorption, it was observed that the distance between the folded layers was partially closed and Pb(II) was dispersed on the structure. The SEM-EDX results confirmed this interaction. These images provide evidence of the successful formation of adsorption.
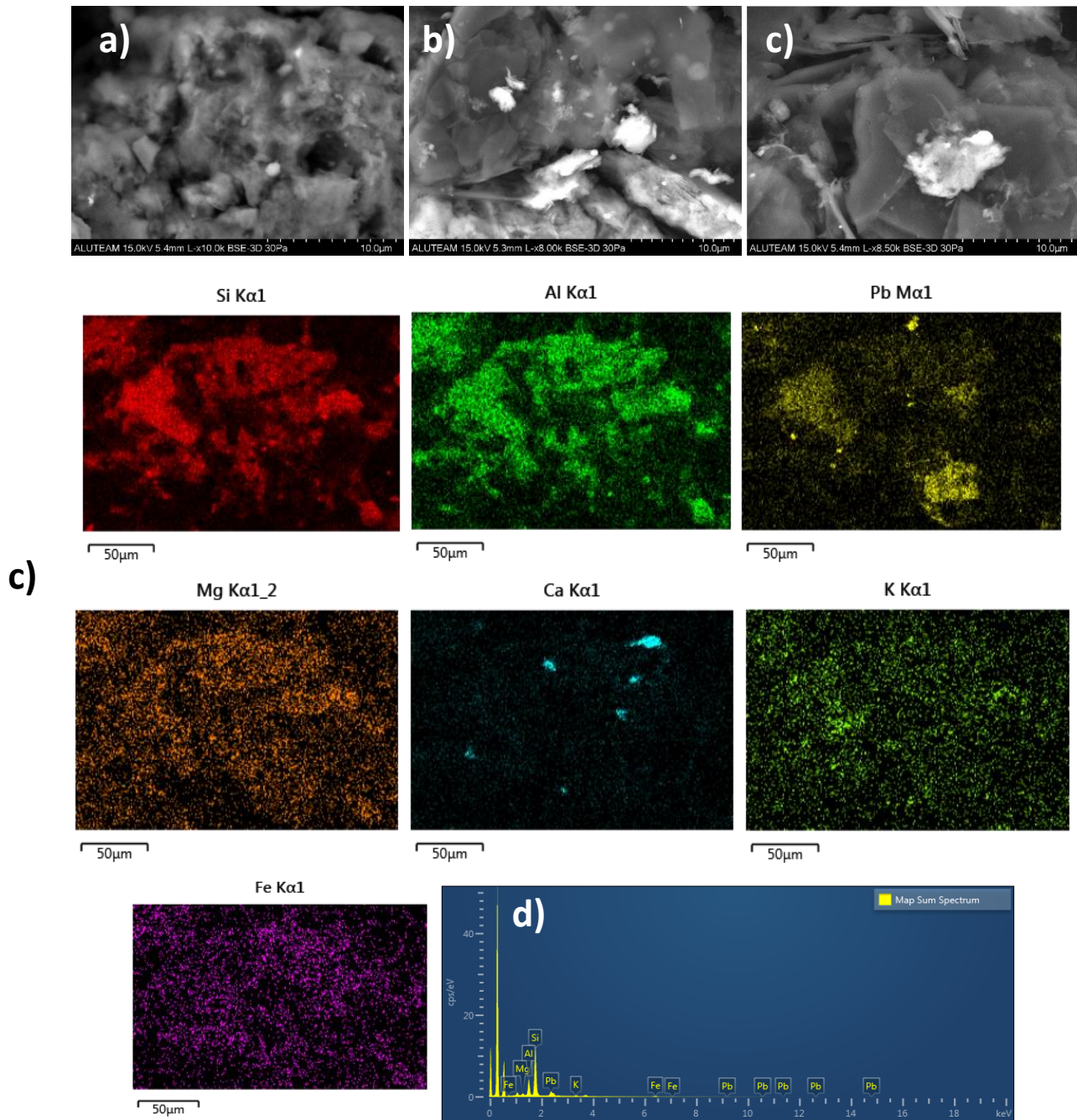
Figure 3: SEM images of (a) BE, (b) BE-MCPE, (c) BE-MCPE /Pb(II), (d) SEM mapping of BE-MCPE /Pb(II), and SEM-EDX graph of BE-MCPE /Pb(II).

The crystalline size of BE-MCPE was calculated using X-ray powder diffraction (XRD) analysis. The XRD pattern of the prepared BE-MCPE is presented in Figure 2 (d), which displays distinct peaks at $2\theta = 26.99^\circ$, 40.04° and 66.76° corresponding to JCPDS file 00-038-0449. Using the Scherrer Equation, the crystalline sizes of the BE-MCPE was found to be 17 nm, as depicted in Figure 3. These results were consistent with the SEM, and were in agreement with the findings of a related study (25). The formula for Debye-Scherrer equation (26) is:

$$n\lambda = 2d \sin \theta \qquad (3.1)$$

where the variable "n" represents the diffraction peak order, "λ" denotes the wavelength of X-rays applied, "d" stands for the interplanar spacing of the crystal lattice, and "θ" represents the angle of diffraction.

The calibration graphs of current of versus Pb(II) concentration in the range of $(2-10) \times 10^{-7}$ mol/L for an accumulation time of 5 minutes and a potential of -0.7 V and stirring rates of 500 rpm and 650 rpm at BE-MCPE are shown in Figures 4 and 5, respectively. Linear relationships were observed in the calibration graphs in the range of $(2-10) \times 10^{-7}$ mol/L for both mixing speeds. The detection limits and straight-line equations for all of the results are provided in Table 1.

The effect of mixing speed on BE-MCPE performance was investigated in the range of $(2-10) \times 10^{-7}$ mol/L. The signals for Pb(II) increased with increasing mixing speed of the enrichment solution up to 500 and/or 650 rpm and then slowed down. Higher mixing speeds resulted in lower signals due to surficial degeneration. Therefore, the stirring speed was optimized at 500 rpm and 650 rpm for all voltammetric experiments.

$I_d \ (\mu A) = 4,35 \times 10^{7} C_{Pb(II)} + -7.10$
r=0,996
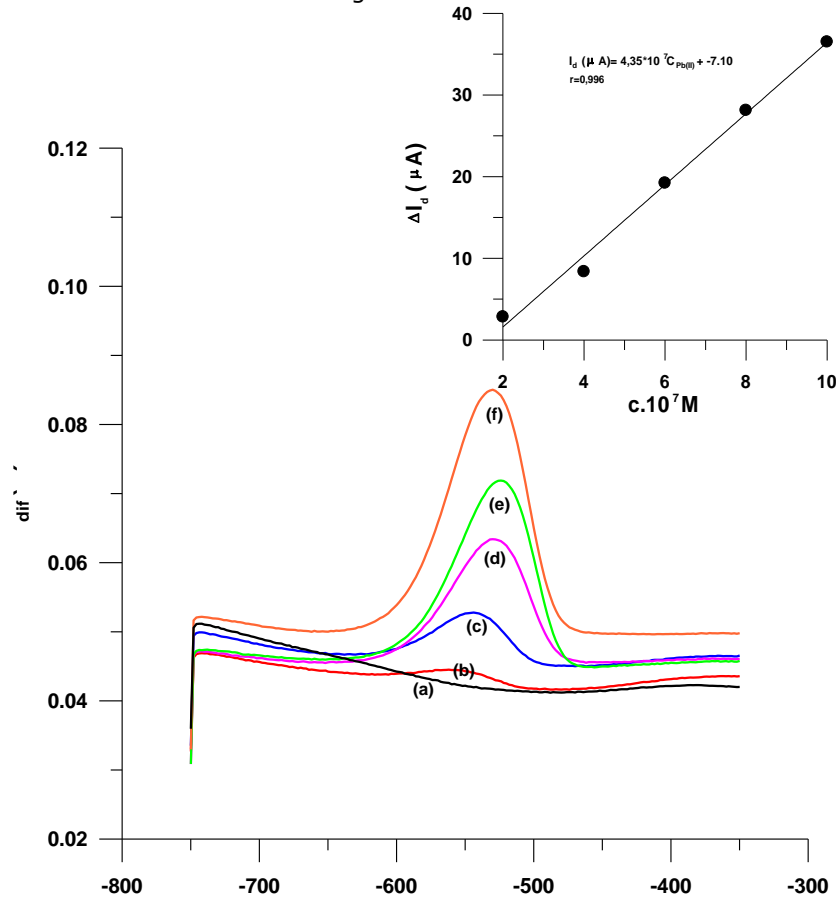
Figure 4: DPAS voltammograms and calibration graph of current vs Pb(II) concentrations (a) Blank, (b) 2.10^{-7} mol/L Pb(II), (c) 4.10^{-7} mol/L Pb(II), (d) 6.10^{-7} mol/L Pb(II), (e) 8.10^{-7} mol/L Pb(II), (f) 10.10^{-7} mol/L Pb(II) (-0.7 V, 5 min, 500 rpm)

Table 1: Comparison of analytical performance measurements of BE-MCPE with different modified electrodes in the literature for the determination of heavy metal ions.

Electrode	Technique	LOD	Ref.
N^1-hydroxy-N^1,N^2-diphenylbenzamidine- Carbon paste electrode(CPE)	SWASV	0.0094 nm (Pb)	(27)
Ion-imprinted polymers- CPE	DPASV	0.99 mg /L (Pb)	(28)
(Ag)/ (Au)-(NP)glassy carbon electrode(GCE)	DPASV	0.03×10^{-2} µg /L (Pb)	(29)
Bi oxycarbide /GCE	DPASV	3.97 µg /L (Pb) 4.24 µg /L (Cd)	(30)
Hg-Bi/ poly(1,2-diaminoanthraquinone)/GCE	ASV	0.069 µg /L (Pb) 0.195 µg /L (Cd) 0.169 µg /L (Zn)	(31)
Bi/carboxyphenyl-modified GCE	SWASV	10 µg /L (Pb) 25 µg /L (Cd)	(32)
Graphene quantum dots and Nafion modified GCE	SWASV	8.49 µg /L (Pb) 11.30 µg /L (Cd)	(33)
Ag nanoparticles-silane grafted bentonite material	DPASV	0.88 µg /L (Pb) 0.79 µg /L (Cd)	(19)
BE-MCPE	DPASV	4.89×10^{-8} mol /L (500 rpm)(Pb) 3.57×10^{-8} mol /L (650 rpm)(Pb)	This work

It is shown in Table 1 that the BE-MCPE sensor exhibits excellent sensitivity and selectivity for the detection of heavy metal ions, especially Pb(II), making it a promising tool for trace-level monitoring in various environmental applications. Table 1 also compares the analytical performance measurements of the BE-MCPE with other modified electrodes reported in the literature.
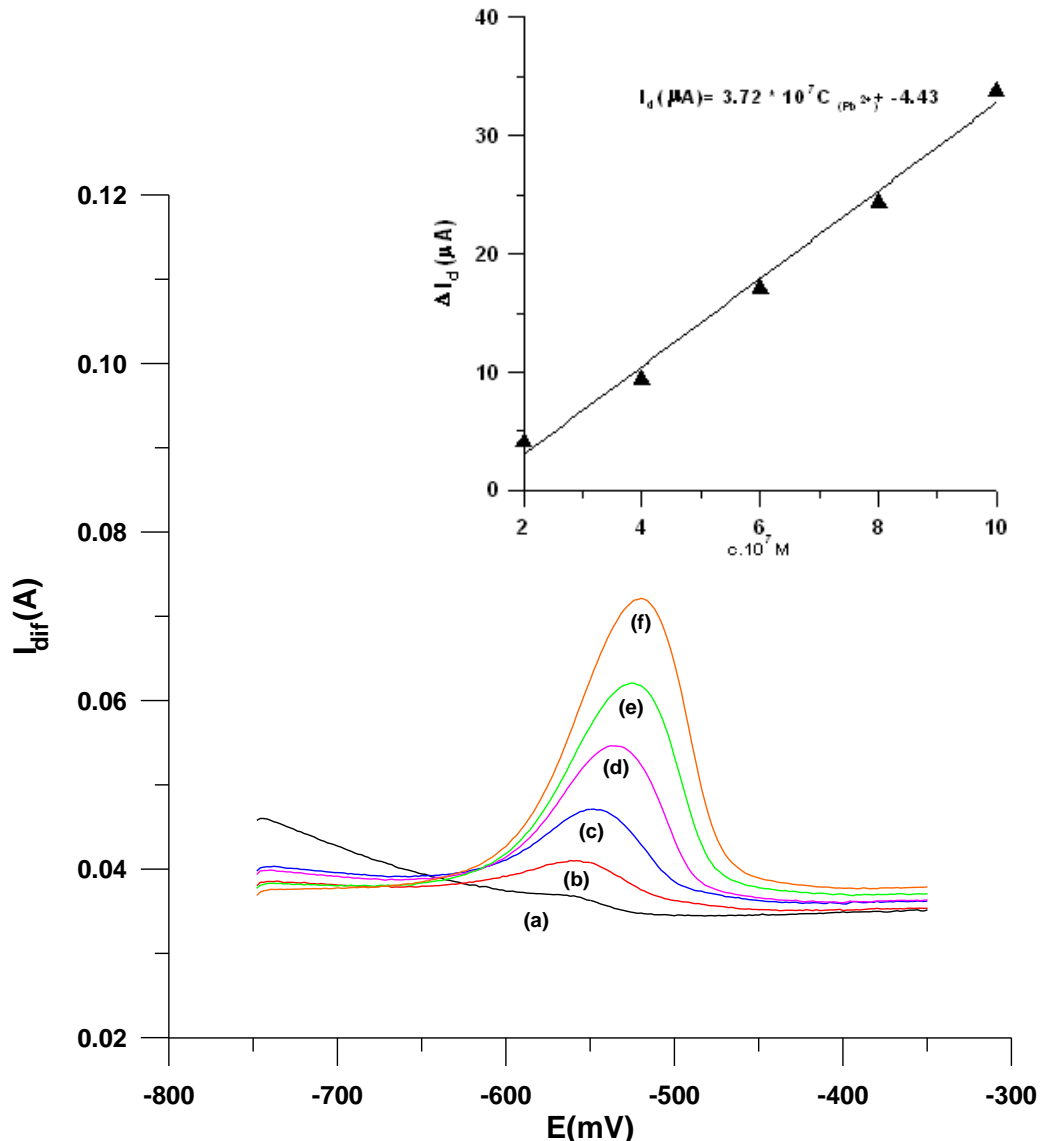
Figure 5: DPAS voltammograms and calibration graph of current vs Pb(II) concentrations (a) Blank (b) 2.10^{-7} mol/L Pb(II) (c) 4.10^{-7} mol/L Pb(II) (d) 6.10^{-7} mol/L Pb(II) (e) 8.10^{-7} mol/L Pb(II) (f) 10.10^{-7} mol/L Pb(II) (-0.7 V, 5 min, 650 rpm)

It is suggested that the reduction and oxidation of Pb(II) solution on the BE-MCPE surface occurs in a three-step reaction process, as described below (Equation 3.2-3.4), based on the results of this study and other relevant investigations (27).

$$(Pb^{2+}) \ (aq) + BE\text{-}MCPE \rightarrow (Pb^{2+} - BE\text{-}MCPE) \ complex \qquad (3.2)$$

$$(Pb^{2+} - BE\text{-}MCPE) \ complex + 2e^- \rightarrow (Pb - BE\text{-}MCPE) \ complex \qquad (3.3)$$

$$(Pb - BE\text{-}MCPE) \ complex - 2e^- \rightarrow (Pb^{2+}) \ (aq)/electrode + BE\text{-}MCPE \qquad (3.4)$$
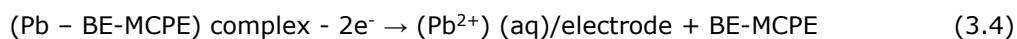
3.2. Optimization of the Solution pH

The effect of pH on the DPASV response was studied in 5.10^{-7} mol/L Pb(II) solution with a settling time of 5 minutes. Electrode current was measured at a potential of -0.7 V and stirring rate of 500 rpm at pH values ranging from 1.0 – 8.0 on BE-MCPE. The maximum peak current and peak potential were obtained at pH 5.20 (see Figure 6). The peak current and peak potential gradually increased with increasing pH of the pre-enrichment solution in the acidic range, reaching a maximum at pH 5.20, and then decreased sharply until reaching pH 8.01.
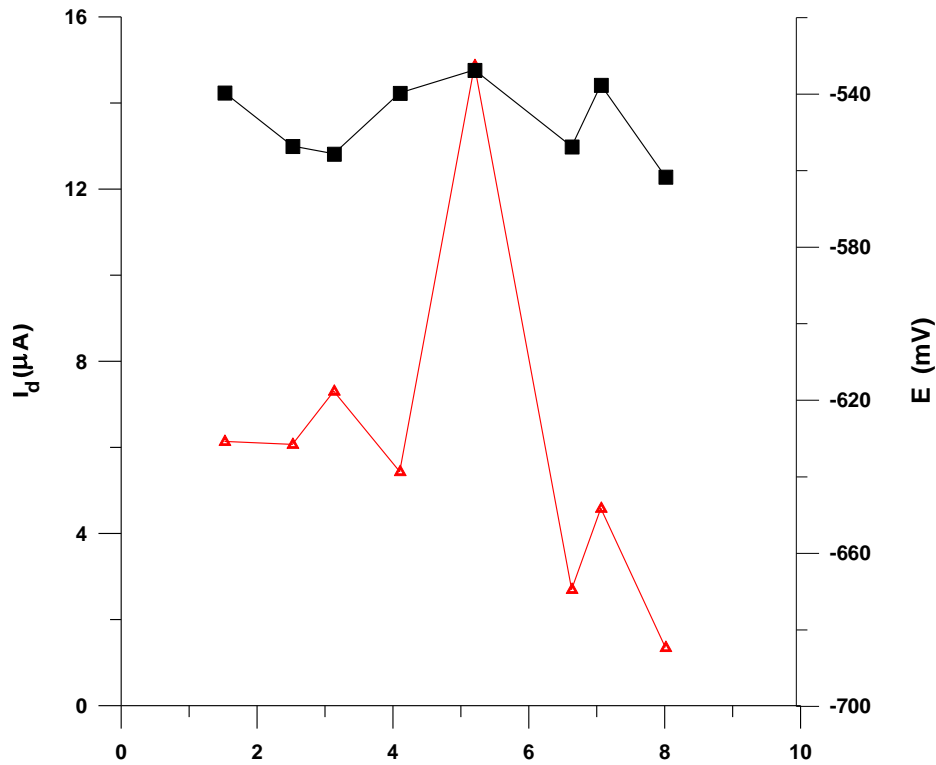
Figure 6: The influence of pH on diffusion currents and peak potentials of Pb(II) ion a) I_d vs pH b) E vs pH.

3.3. Simultaneous Determination of Heavy Metals in Binary Solutions

The effect of interference of some metal ions (Cd^{2+}, Hg^{2+} and Cu^{2+}) on the selectivity of BE-MCPE was also investigated. The tolerable concentrations of foreign species in the standard solution of Pb(II) concentration in the range of $(2-10) \times 10^{-7}$ mol/L were as high as a 10-fold excess. When determining Pb(II), the interferences from Cu(II) and Hg(II) exhibited different behaviors regarding selectivity for Pb(II) ions. The shape of peak signals of Pb(II) ion concentration in the range of $(2-10) \times 10^{-7}$ mol/L were not linear in the presence of 2×10^{-6} mol/L Cd(II) and Cu(II) ions (Figure 7) but were linear in presence of 2×10^{-6} mol/L Cd(II) and Hg(II) ions (Figure 8). The results showed that a 10 fold excess of Cu(II) ,Cd(II) and Hg(II) does not result in an interference in the determination of Pb(II). As a result, the carbon paste electrode modified with bleaching earth was proven to be a simple and selective sensor for the determination of Pb(II) in the trace concentration range.
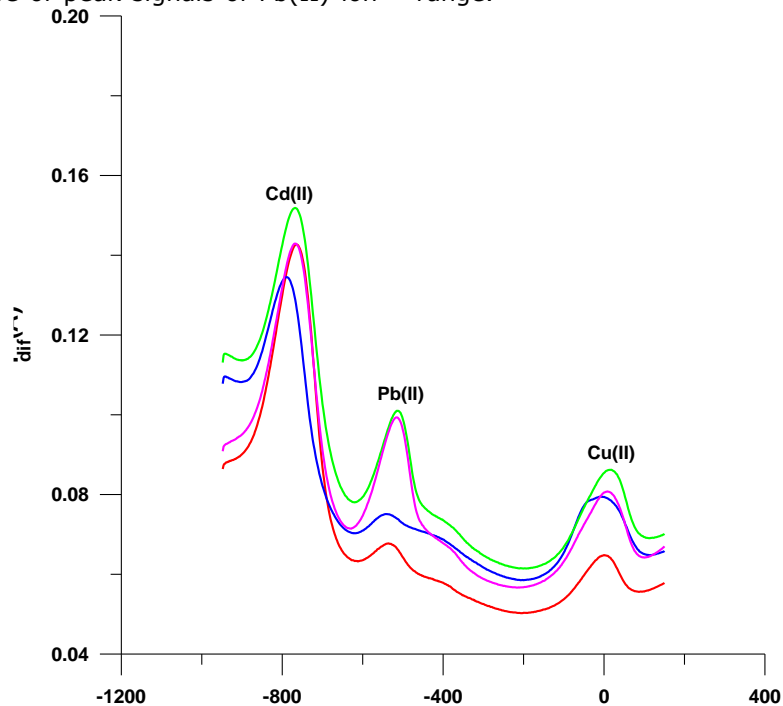
Figure 7: The effect of interference of some metal ions (Cd^{2+} and Cu^{2+}) on the Pb(II) ion selectivity of BE-MCPE.
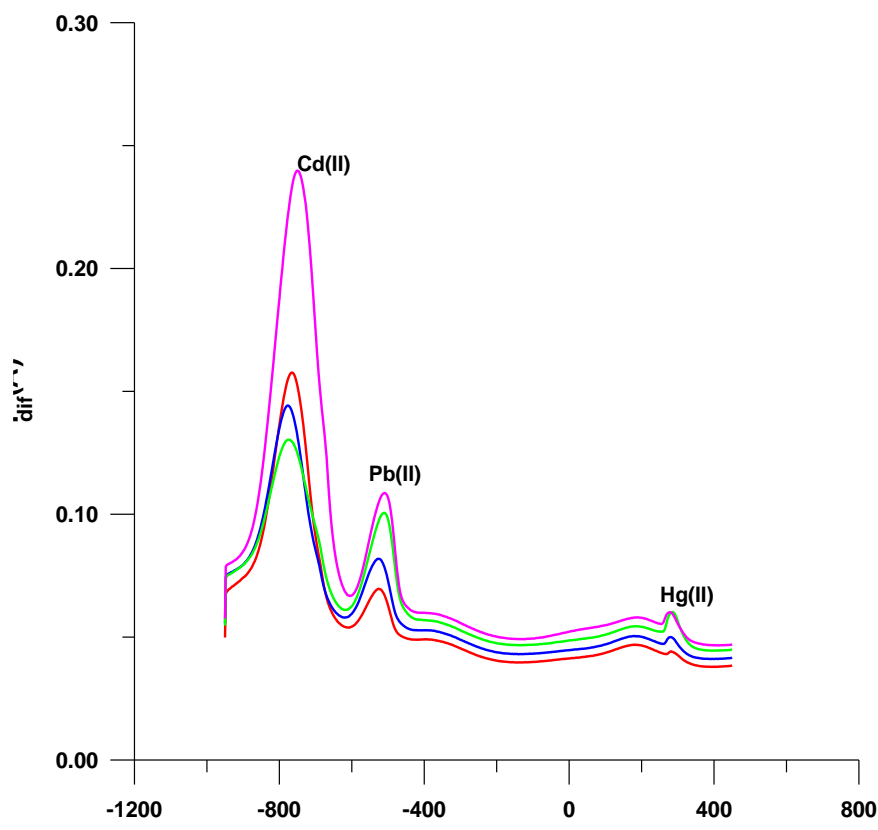
Figure 8: The effect of interference of some metal ions (Cd^{2+} and Hg^{2+}) on the Pb(II) ion selectivity of BE-MCPE.(34)

4. CONCLUSION

In conclusion, the use of modified composite electrodes has proven to be an effective approach for detecting heavy metal ions in wastewater applications. The novel (BE-MCPE) composite electrode, studied here, demonstrated excellent sensitivity, selectivity, stability, and rapid response in detecting trace amounts of Pb(II) using a differential pulse voltammetry technique. The utilization of SEM, SEM-EDX, FTIR, and XRD techniques allowed for a thorough investigation of the features of BE-MCPE. Through the use of these techniques, we were able to explore the physical, chemical, and elemental properties of BE-MCPE, as well as its Pb(II) adsorption capacity. According to the electrochemical results, the linear response range was between 2.10^{-7} mol/L and 10.10^{-7} mol/L, with a (LOD) of 4.89×10^{-8} mol/L and a (LOQ) of 1.63×10^{-7} mol/L. This modified electrode therefore has the potential to be employed as a reliable and successful tool for observing and identifying small amounts of Pb(II) in a variety of wastewater treatment applications.

5. CONFLICT OF INTEREST

I declare that there is no conflict of interest related to this work. Furthermore, the author confirms that the paper is not under consideration by any other journal and has not been published previously.

6. REFERENCES

1. Wu Q, Bi H-M, Han X-J. Research Progress of Electrochemical Detection of Heavy Metal Ions. Chinese J Anal Chem [Internet]. 2021 Mar 1;49(3):330–40. Available from: <URL>.

2. Falina S, Syamsul M, Rhaffor NA, Sal Hamid S, Mohamed Zain KA, Abd Manaf A, et al. Ten Years Progress of Electrical Detection of Heavy Metal Ions (HMIs) Using Various Field-Effect Transistor (FET) Nanosensors: A Review. Biosensors [Internet]. 2021 Nov 25;11(12):478. Available from: <URL>.

3. Kumar V, Agrawal S, Bhat SA, Américo-Pinheiro JHP, Shahi SK, Kumar S. Environmental impact, health hazards, and plant-microbes synergism in remediation of emerging contaminants. Clean Chem Eng [Internet]. 2022 Jun;2:100030. Available from: <URL>.

4. Mitra S, Chakraborty AJ, Tareq AM, Emran T Bin, Nainu F, Khusro A, et al. Impact of heavy metals on the environment and human health: Novel therapeutic insights to counter the toxicity. J King Saud Univ - Sci [Internet]. 2022 Apr 1;34(3):101865. Available from: <URL>.

5. Balali-Mood M, Naseri K, Tahergorabi Z, Khazdair MR, Sadeghi M. Toxic Mechanisms of Five Heavy Metals: Mercury, Lead, Chromium, Cadmium, and Arsenic. Front Pharmacol [Internet]. 2021 Apr 13;12:643972. Available from: <URL>.

6. İlhan Ceylan B. Oxovanadium(IV) and Nickel(II) complexes obtained from 2,2'-dihydroxybenzophenone-S-methyl-thiosemicarbazone: Synthesis, characterization, electrochemistry, and antioxidant capability. Inorganica Chim Acta [Internet]. 2021 Mar 1;517:120186. Available from: <URL>.

7. Ahmad W, Alharthy RD, Zubair M, Ahmed M, Hameed A, Rafique S. Toxic and heavy metals contamination assessment in soil and water to evaluate human health risk. Sci Rep [Internet]. 2021 Aug 20;11(1):17006. Available from: <URL>.

8. Collin MS, Venkatraman SK, Vijayakumar N, Kanimozhi V, Arbaaz SM, Stacey RGS, et al. Bioaccumulation of lead (Pb) and its effects on human: A review. J Hazard Mater Adv [Internet]. 2022 Aug 1;7:100094. Available from: <URL>.

9. Penticoff HB, Fortin JS. Toxic/metabolic diseases of the nervous system. In: Neurobiology of Brain Disorders (Second Edition): Biological Basis of Neurological and Psychiatric Disorders [Internet]. Elsevier; 2023. p. 379–401. Available from: <URL>.

10. Romero-Estévez D, Yánez-Jácome GS, Navarrete H. Non-essential metal contamination in Ecuadorian agricultural production: A critical review. J Food Compos Anal [Internet]. 2023 Jan 1;115:104932. Available from: <URL>.

11. Jomova K, Makova M, Alomar SY, Alwasel SH, Nepovimova E, Kuca K, et al. Essential metals in health and disease. Chem Biol Interact [Internet]. 2022 Nov 1;367:110173. Available from: <URL>.

12. Li G, Qi X, Zhang G, Wang S, Li K, Wu J, et al. Low-cost voltammetric sensors for robust determination of toxic Cd(II) and Pb(II) in environment and food based on shuttle-like α-Fe2O3 nanoparticles decorated β-Bi2O3 microspheres. Microchem J [Internet]. 2022 Aug 1;179:107515. Available from: <URL>.

13. Mohammed H, Sadeek S, Mahmoud AR, Zaky D. Comparison of AAS, EDXRF, ICP-MS and INAA performance for determination of selected heavy metals in HFO ashes. Microchem J [Internet]. 2016 Sep 1;128:1–6. Available from: <URL>.

14. Fei J, Wu X, Sun Y, Zhao L, Min H, Cui X, et al. Preparation of a novel amino functionalized ion-imprinted hybrid monolithic column for the selective extraction of trace copper followed by ICP-MS detection. Anal Chim Acta [Internet]. 2021 Jun 1;1162:338477. Available from: <URL>.

15. Geleta GS. A colorimetric aptasensor based on two dimensional (2D) nanomaterial and gold nanoparticles for detection of toxic heavy metal ions: A review. Food Chem Adv [Internet]. 2023 Oct 1;2:100184. Available from: <URL>.

16. Jiang H, Lin H, Lin J, Yao-Say Solomon Adade S, Chen Q, Xue Z, et al. Non-destructive detection of multi-component heavy metals in corn oil using nano-modified colorimetric sensor combined with near-infrared spectroscopy. Food Control [Internet]. 2022 Mar 1;133:108640. Available from: <URL>.

17. Volynkin SS, Demakov PA, Shuvaeva O V., Kovalenko KA. Metal-organic framework application for mercury speciation using solid phase extraction followed by direct thermal release–electrothermal atomization atomic absorption spectrophotometric detection (ETA AAS). Anal Chim Acta [Internet]. 2021 Sep 8;1177:338795. Available from: <URL>.

18. Phan TTT, Nguyen TD, Lee JS. Vacuum plasma treatment on carbon nanoparticles for highly sensitive square wave voltammetric sensor of heavy metal ions. Synth Met [Internet]. 2022 Dec 1;291:117203. Available from: <URL>.

19. Lalmalsawmi J, Sarikokba, Tiwari D, Kim D-J. Simultaneous detection of Cd^{2+} and Pb^{2+} by differential pulse anodic stripping voltammetry: Use of highly efficient novel Ag0(NPs) decorated silane grafted bentonite material. J Electroanal Chem [Internet]. 2022 Aug 1;918:116490. Available from: <URL>.

20. Jaber L, Elgamouz A, Kawde A-N. An insight to the filtration mechanism of Pb(II) at the surface of a clay ceramic membrane through its preconcentration at the surface of a graphite/clay composite working electrode. Arab J Chem [Internet]. 2022 Dec 1;15(12):104303. Available from: <URL>.

21. Alabarse FG, Conceição RV, Balzaretti NM, Schenato F, Xavier AM. In-situ FTIR analyses of bentonite under high-pressure. Appl Clay Sci [Internet]. 2011 Jan 1;51(1–2):202–8. Available from: <URL>.

22. Shi W, Wang Z, Li F, Xu Y, Chen X. Multilayer adsorption of lead (Pb) and fulvic acid by Chlorella pyrenoidosa: Mechanism and impact of environmental factors. Chemosphere [Internet]. 2023 Jul 1;329:138596. Available from: <URL>.

23. Jin G, Gu P, Qin L, Li K, Guan Y, Su H. Preparation of manganese-oxides-coated magnetic microcrystalline cellulose via KMnO4 modification: Improving the counts of the acid groups and adsorption efficiency for Pb(II). Int J Biol Macromol [Internet]. 2023 Jun 1;239:124277. Available from: <URL>.

24. Neelaveni M, Santhana Krishnan P, Ramya R, Sonia Theres G, Shanthi K. Montmorillonite/graphene oxide nanocomposite as superior adsorbent for the adsorption of Rhodamine B and Nickel ion in binary system. Adv Powder Technol [Internet]. 2019 Mar 1;30(3):596–609. Available from: <URL>.

25. Huang H, Yi D, Lu Y, Wu X, Bai Y, Meng X, et al. Study on the adsorption behavior and mechanism of dimethyl sulfide on silver modified bentonite by in situ FTIR and temperature-programmed desorption. Chem Eng J [Internet]. 2013 Jun;225:447–55. Available from: <URL>.

26. Debye P. Zerstreuung von Röntgenstrahlen. Ann

Phys [Internet]. 1915;351(6):809–23. Available from: <URL>.

27. Tesfaye E, Chandravanshi BS, Negash N, Tessema M. A new modified carbon paste electrode using N1-hydroxy-N1,N2-diphenylbenzamidine for the square wave anodic stripping voltammetric determination of Pb(II) in environmental samples. Sens Bio-Sensing Res [Internet]. 2022 Dec;38:100520. Available from: <URL>.

28. Rebolledo-Perales LE, Álvarez Romero GA, Ibarra I, Galán-Vidal CA, Flores-Aguilar JF, Pérez-Silva I. Quantitative Analysis of Pb(II) Based on Differential Pulse Anodic Stripping Voltammetry and IIP-Carbon Paste Electrodes. J Electrochem Soc [Internet]. 2022 May 1;169(5):057504. Available from: <URL>.

29. Yadav R, Berlina AN, Zherdev A V., Gaur MS, Dzantiev BB. Rapid and selective electrochemical detection of Pb^{2+} ions using aptamer-conjugated alloy nanoparticles. SN Appl Sci [Internet]. 2020 Dec 25;2(12):2077. Available from: <URL>.

30. Zhang Y, Li C, Su Y, Mu W, Han X. Simultaneous detection of trace Cd(II) and Pb(II) by differential pulse anodic stripping voltammetry using a bismuth oxycarbide/nafion electrode. Inorg Chem Commun [Internet]. 2020 Jan;111:107672. Available from: <URL>.

31. Hassan KM, Gaber SE, Altahan MF, Azzem MA. Single and simultaneous voltammetric sensing of lead(II), cadmium(II) and zinc(II) using a bimetallic Hg-Bi supported on poly(1,2-diaminoanthraquinone)/glassy carbon modified electrode. Sens Bio-Sensing Res [Internet]. 2020 Aug;29:100369. Available from: <URL>.

32. Phal S, Nguyễn H, Berisha A, Tesfalidet S. In situ Bi/carboxyphenyl-modified glassy carbon electrode as a sensor platform for detection of Cd^{2+} and Pb^{2+} using square wave anodic stripping voltammetry. Sens Bio-Sensing Res [Internet]. 2021 Dec;34:100455. Available from: <URL>.

33. Pizarro J, Segura R, Tapia D, Navarro F, Fuenzalida F, Jesús Aguirre M. Inexpensive and green electrochemical sensor for the determination of Cd(II) and Pb(II) by square wave anodic stripping voltammetry in bivalve mollusks. Food Chem [Internet]. 2020 Aug;321:126682. Available from: <URL>.

34. Munir A, Shah A, Nisar J, Ashiq MN, Akhter MS, Shah AH. Selective and simultaneous detection of Zn^{2+}, Cd^{2+}, Pb^{2+}, Cu^{2+}, Hg^{2+} and Sr^{2+} using surfactant modified electrochemical sensors. Electrochim Acta [Internet]. 2019 Nov 10;323:134592. Available from: <URL>.

RESEARCH ARTICLE

Design, Synthesis and Structural Characterization of Novel Thioanthraquinone Analogues from 1,5-Dichloroanthraquinone

Funda Özkök[1*] iD

[1] Organic Chemistry Division, Department of Chemistry, Faculty of Engineering, Istanbul University-Cerrahpaşa, Avcılar, 34320, Istanbul, Türkiye.

Abstract: Anthraquinone and its derivatives are considered intermediate agents with superior properties due to their activities in chemical and biological reaction. A new, economical, practical and one-step synthesis method was developed by our research team for the synthesis of amino and thioanthraquinones in previous studies (1). With this synthesis method, thioanthraquinone analogs **2(a-d)** were obtained from 1,5-Dichloroanthraquinone **(1)** and bioactive thiols. The synthesized organic molecules were purified by column chromatography and their structures were identified with spectroscopic methods. Fluorescence analyzes of synthesized thioanthraquinone analogues were performed. It was determined that all thioanthraquinone analogues synthesized and characterized in the study showed fluorescence activity. These new analogues with fluorescence are expected to find application in drug delivery systems and sensor studies.

1. INTRODUCTION

Cancer has still been at the top of the list of diseases that threaten human health and may result in death (2). Anthraquinones are one of the most active members of organic compounds. Anthraquinone and its analogs, which are biologically active, have antimicrobial, antifungal, antioxidant, anti-cancer, antitumor, anti-HIV, anti-Alzhiemer and anti-inflammatory properties (3-9). An amino anthraquinone derivative, mitoxantrone, which is one of the important anticancer drugs and accepted as an antineoplastic agent, is known to have effects against tumors in cancer types such as ovarian, breast, prostate, leukemia, and lymphoma (10-12) (Figure 1). Mitoxantrone, a topoisomerase II inhibitor found to be effective in the treatment of various tumors and multiple sclerosis disease, has been found to have potential neurotoxic effects (13).

In a study, Pan et al. (14) isolated anthraquinone derivatives as a secondary metabolite from the saprophytic sea fungus Alternaria tenuissima, which causes skin infections in some people (14-20). Wang et al. showed that water-soluble anthraquinone derivatives with antitumor properties killed tumor cells in the apoptotic pathway against gastric cancer cells (21-22). Anthraquinones have a redox system due to their acid-base properties (23) and they are reduced to hydroquinones under protic conditions (24-25). Hydroquinone is oxidized in the redox structure and becomes anthraquinone again (24-25). The capability of energy storage of quinones and especially the anthraquinones, allows them to be preferred as organic material in these redox flow systems (26-28). Although various derivatives of anthraquinones are found in the literature, studies on thio-anthraquinone analogs are limited. A new, practical and economical synthesis method for the synthesis of amino and thio-anthraquinone molecules has been developed in previous studies of our team (1). Various amino and thio-anthraquinone analogues were synthesized with this new synthesis method (29-31). It was determined that these amino and thioanthraquinone derivatives synthesized in previous studies show anticancer and antimicrobial activities (29-31). In a study by Şahin, Y.M. (32) an antimicrobial thioanthraquinone analogue was synthesized and a nanobiocomposite was obtained

from this thioanthraquinone analogue for use in tissue engineering applications. The aim of this study is to synthesize bioactive 1-substituted-5-chloro derivatives that can be used in health, medicine and materials fields and to characterize their structures.

Mitoxantrone

Doxorubicin

Pixantron
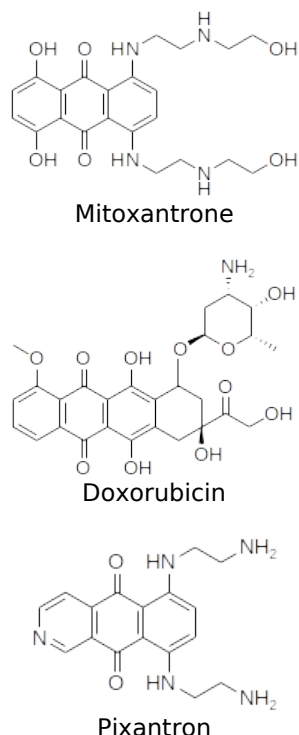
Figure 1. Anthraquinone analogues as anti-cancer drugs (4).

2. EXPERIMENTAL SECTION

2.1. Reagents and Instruments
All reagents used were obtained from Sigma-Aldrich. In the infrared (FT-IR) spectra, the Shimadzu FTIR-8101 spectrometer was used. Varian^{UNITY} INOVA 500 MHz device operating in NMR analysis was used. Mass spectrum analyzes were accordingly performed on a Thermo Advantage MAX LC/MS/MS instrument using APCI or ESI methods. Florescence spectra were recorded using Spectro-SpectroBlue fluorescence spectrophotometer. Buchi B-540 melting point device was used for melting point analysis. Silica gel (Fluka Silica gel 60, particle size 63-200 μm) was used for purification in column chromatography of the synthesized analogues. Silica 60F254 (Merck, Darmstadt) was used for TLC layers in the study.

2.2. General synthesis method (2a-d):
All novel anthraquinone analogues **2(a-d)** were obtained from the reaction of 1,5-Dichloroanthraquinone **(1)** and bioactive thiols according to the general synthesis method (1) for anthraquinone analogues. One equivalents molar of 1,5-Dichloro-9,10-anthrecenedione **(1)** and thiols were stirred in 110-120 °C a mixture of ethylene glycol (30 ml) and aqueous solution of KOH (1.2 g KOH and 8 ml water) for 48h with reflux system. Chloroform was added to the reaction mixture to separate the organic layer. Then, the organic layer

was washed with water (4x30 ml) and dried over Na_2SO_4. After filtering, the solvent was evaporated and the residues (**2a-d**) was purified by column choromatography on silicagel (Scheme 1).

2.2.1. 1-Chloro-5-(Dodecylthio)anthracene-9,10-dione (2a)
Yellow solid thioanthraquinone compound **2a** was obtained from the reaction of 1,5-Dichloroanthraquinone **(1)** and 1-Dodecanethiol according to the general synthesis method.

Dark yellow semi-solid. Yield: 0.37 g (23%). R_f (1 Petrolium ether / 1 Chloroform): 0.46. IR (KBr, cm^{-1}): υ = 2980, 2962, 2952 (C-H$_{arom}$), 2938, 2915, 2846 (C-H$_{alifatic}$), 1671 (C=O), 1573 (C=C). ^{1}H NMR (499.74 MHz, CDCl$_3$): δ = 7.26-8.27 (m, 6H, CH$_{arom}$) , 2.97-3 (t, 2H, J=2.98, -S-CH$_2$), 1.26-2.23 (m, 20H, CH$_2$), 0.86-0.88 (t, 3H, J= 0.87, CH$_3$). ^{13}C NMR (125.66 MHz, CDCl$_3$): δ = 183.1 (C=O), 159.4, 145.2, 136.9, 136, 135.3, 133, 129.3, 123.3, 121, 120.3 (C$_{arom}$ and CH$_{arom}$), 14.1 (CH$_3$). ESI(+): m/z= 461.1 [M+NH$_4$$^+$]$^+$, 274,85 [M-S(CH$_2$)$_{11}CH_3$]$^+$. (M= 443.04 g/mol). C$_{26}H_{31}ClO_2$S, (M, 443,04 g/mol).

2.2.2. Butyl-3-(1-Chloro-9,10-dihydro-9,10-dioxoanthracen-5-ylthio)propionate (2b)
Orange semi-solid thioanthraquinone compound **2b** was obtained from the reaction of 1,5-Dichloroanthraquinone (**1**) and Butyl-3-Mercaptopropionate according to the general synthesis method.

Orange semi-solid. Yield: 0.43 g (32%). R_f (Ethyl acetate): 0.45. IR (KBr, cm^{-1}): υ = 3464 (C=O$_{ester}$), 2954, 2915, 2870, 2850 (C-H$_{arom}$), 1658 (C=O), 1651 (C=C). ^{1}H NMR (499.74 MHz, CDCl$_3$): δ = 7.26-8.03 (m, 6H, CH$_{arom}$) , 4-4.3 (m, 2H, COO-CH$_2$), 2.97-2.99 (t, 2H, J=2.98, S-CH$_2$), 1.24-2 (m, 6H, CH$_2$), 0.92-0.94 (t, 3H, J= 0.93, CH$_3$). ^{13}C NMR (125.66 MHz, CDCl$_3$): 183, 183.1 (C=O), 159.4, 145.2, 136.9, 136, 135.3, 133, 129.2, 127.9, 123.3, 121.5, 120.9, 120.2 (C$_{arom}$ and CH$_{arom}$), 72 (COOCH$_2$), 32,31.4, 27.5, 22.3 (CH$_2$), 13.9 (CH$_3$). MS [-ESI]: m/z = 309.55 [M-C$_4$H$_9$-Cl]$^+$. C$_{21}$H$_{19}$ClO$_4$S, (M, 402.89 g/mol).

2.2.3. 1-Chloro-5-(pentylthio)anthracene-9,10-dione (2c)
Yellow solid thioanthraquinone compound **2c** was obtained from the reaction of 1,5-Dichloroanthraquinone **1** and Pentanethiol according to the general synthesis method.

Yellow solid. Mp: 187-188 °C. Yield: 0.22 g (17%). R_f (Ethyl acetate): 0.43. IR (KBr, cm^{-1}): υ = 3065 (C-H$_{arom}$), 2954, 2915, 2870, 2850 (CH$_{aliphatic}$), 1726 (C=O), 1651 (C=C). ^{1}H NMR (499.74 MHz, CDCl$_3$): δ = 7.26-8.05 (m, 6H, CH$_{arom}$) , 4.03-4.32 (m, 2H, S-CH$_2$), 1.37-3 (m, 6H, CH$_2$), 0.92-0.95 (t, 3H, J= 0.93, CH$_3$). ^{13}C NMR (125.66 MHz, CDCl$_3$): δ = 183.2 (C=O), 120.3, 121, 121.5, 123.3, 129.3, 133.1, 135.3, 136, 136.9, 145.2, 159.4 (C$_{arom}$ and CH$_{arom}$), 60.7 (S-CH$_2$), 22.3, 27.5, 31.4, 32 (CH$_2$), 13.9 (CH$_3$). MS [-ESI]: m/z = 368.90 [M+Na$^+$]$^+$. C$_{19}$H$_{17}$ClO$_2$S, (M, 344,86 g/mol).

*2.2.4. 1-(4-Fluorophenylthio)-5-chloroanthracene-9,10-dione **(2d)***
Yellow solid thioanthraquinone compound **2d** was obtained from the reaction of 1,5-Dichloroanthraquinone **1** and 4-Fluorothiophenol according to the general synthesis method.

Yellow solid. Mp: 191-192 °C. Yield: 0.28 g (21%). R_f (Ethyl acetate): 0.44. IR (KBr, cm^{-1}): υ = 3465, 3391, 3319, 3065, 2938, 2878 (C-H$_{arom}$), 1671 (C=O), 1578 (C=C). ^{1}H NMR (499.74 MHz, CDCl$_3$): δ = 7.27-8.25 (m, 10H, CH$_{arom}$). ^{13}C NMR (125.66 MHz, CDCl$_3$): δ = 183.1 (C=O), 120.8, 121, 122.5, 126.7, 127.3, 132.5, 133.5, 134.3, 134.8, 135.1, 135.4, 159.8 (C$_{arom}$ and CH$_{arom}$). MS [-ESI]: m/z = 393,05 [M+Na$^+$]$^+$. C$_{20}$H$_{10}$ClFO$_2$S, (M, 368,81g/mol).

2.3. Fluorescence Spectroscopy
All novel thioanthraquinone analogues synthesized in the study showed fluorescence properties. Delocalization of π-bond in the aromatic thioanthraquinone skeleton is effective in determining the fluorescence characteristic of molecules. Excitation and emission wavelengths in the fluorescence spectrum of the **2a** molecule were observed as 530 nm (λexc.) and 565 nm (λem.). Excitation and emission wavelengths in the fluorescence spectrum of the **2b** were observed as 518 nm (λexc.) and 567 nm (λem.). Excitation wavelengths in the fluorescence spectrum of the **2c** and **2d** were observed as 580 nm (λexc.) ve 505 nm (λem.), respectively. The fluorescence graphic of all synthesized novel thioanthraquinone analogues is demonstrated in Figure 2.
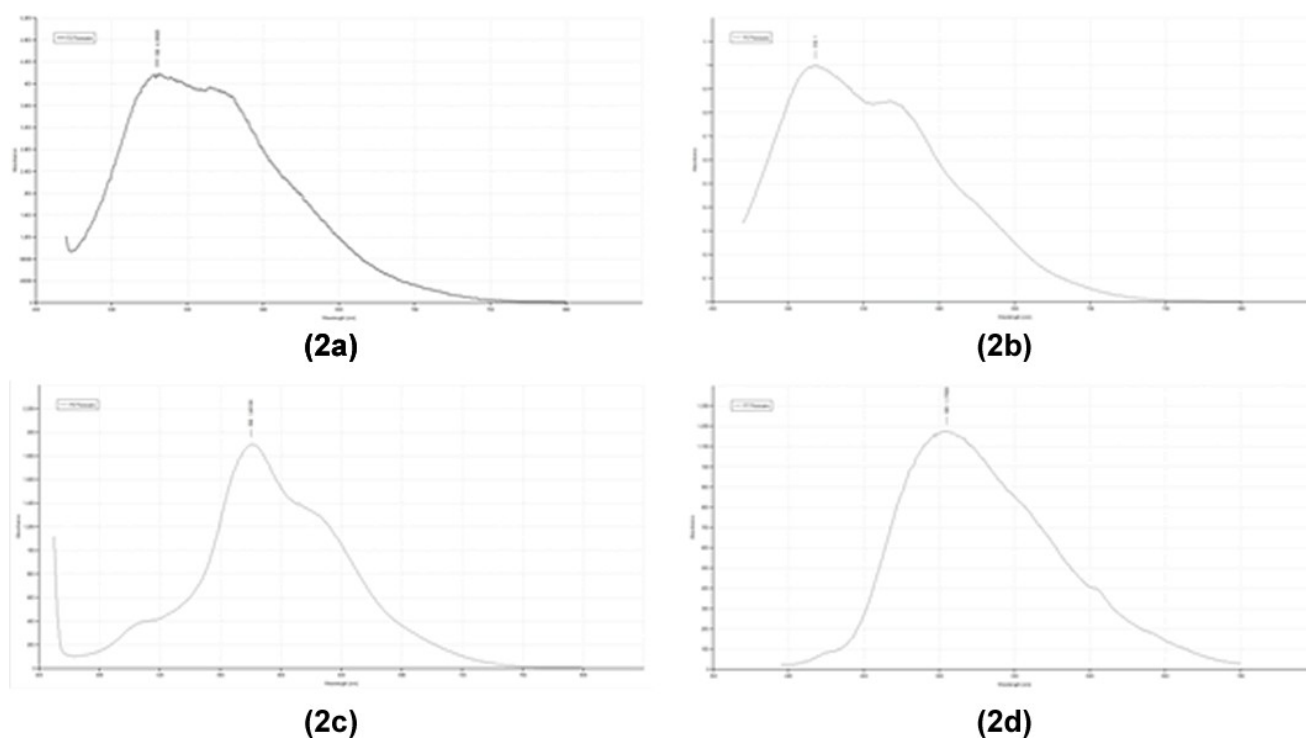
Figure 2. The fluorescence graphs of all synthesized novel thioanthraquinone analogues **(2a-d)**.

3. RESULTS AND DISCUSSION

In the first step of the study, 1-chloro-5-(dodecylthio)anthracene-9,10-dione **(2a)** was synthesized from the reaction of the starting material 1,5-Dichloro-9,10-anthracenedion **(1)** and Dodecanethiol according to the general procedure. In the second step, Butyl-3-(1-Chloro-9,10-dihydro-9,10-)dioxoanthracen-5-ylthio)propionate **(2b)** was obtained from the reaction of 1,5-Dichloro-9,10-anthracenedione **(1)** and butyl-3-mercaptopropionate according to the general procedure. In the third step, 1-chloro-5-(pentylthio)anthracene-9,10-dione **(2c)** was synthesized from the reaction of the starting material 1,5-dichloroanthraquinone **(1)** and 1-pentantiol according to the general procedure. In the last step of the study, 1-(4-fluorophenylthio)-5-chloroanthracene-9,10-dione **(2d)** was obtained from the reaction of the starting material 1,5-dichloroanthraquinone **(1)** and 4-fluorothiophenol according to the general procedure. All synthesized thioanthraquinone analogues are presented in Scheme 1.
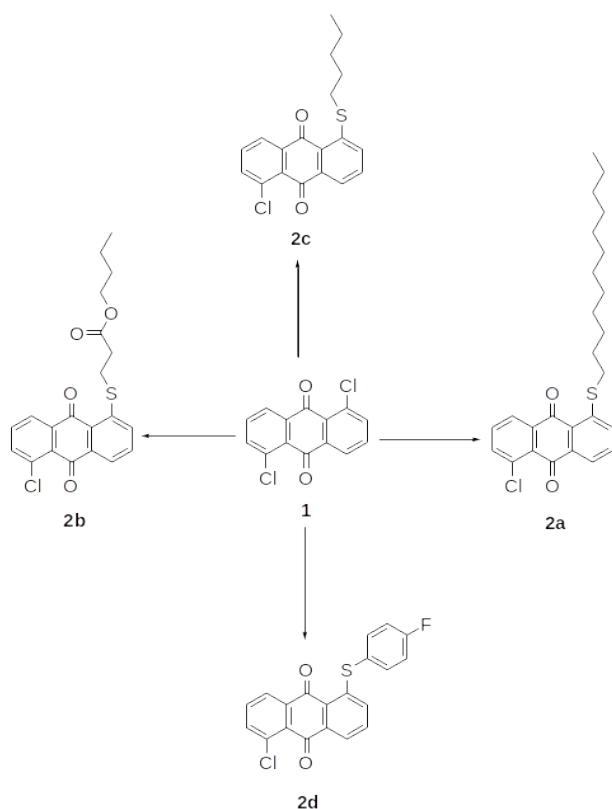
Scheme 1: Distribution of novel thioanthraquinone analogues.

In the FTIR spectra of synthesized thioanthraquinone derivatives **2(a-d),** characteristic absorptions belonging to the C=O group were seen at 1671, 1726 and 1671 cm^{-1}. In the ^{1}H-NMR spectrum, the CH$_3$ group peaks of the **(2a)** molecule were confirmed to be triplets between 0.86-0.88. Observation of the sulfur-bound CH$_2$ group in the molecule to be a triplet between 2.97-3 and the other aliphatic CH$_2$ groups to be multiplets between 1.26-2.23 confirms the structure of the thio-anthraquinone molecule **(2a).** The carbonyl group peaks in the ^{13}C-NMR spectrum of the synthesized analogues were confirmed at 183, 183.1, 183.2, respectively. While CH$_2$ bound to the ester group was observed at 72 by shifting to down domain in the ^{13}C-NMR spectrum of the **(2b)** molecule, other CH$_2$ groups in the chain were observed at 32, 31.4, 27.5 and 22.3, respectively.

4. CONCLUSION

Anthraquinone and its derivatives play an important role in chemical and biological reactions thanks to the redox system in their structure. At the same time, the electron exchange of anthraquinone and its derivatives in this redox system allows them to be active in energy storage systems. Although there are various studies on the synthesis and biological activities of amino anthraquinone analogs in the literature, studies on the synthesis, biological activity properties and material properties of new thioanthraquinone molecules are quite limited. The new molecules obtained via the new synthesis method developed and patented by our team for the synthesis of amino and thio-anthraquinones can be considered

as significant agents for reactions. The fluorescence aspects of the synthesized molecules render these molecules to be interesting in sensor studies. It is predicted for these novel thioanthraquinone molecules synthesized in this study that they may provide a new perspective to studies in the fields of chemistry, biology, medicine, pharmacy, material science and renewable energy.

5. CONFLICT OF INTEREST

The authors declare that there are no conflict of interests.

6. ACKNOWLEDGMENTS

7. REFERENCES

1. Ozkok F, Şahin YM. Biyoaktif antrakinon anologlarının sentezine yönelik özgün metot geliştirilmesi. TURKEY; TR 2016/19610; 2016.

2. Lytle NK, Barber AG, Reya T. Stem cell fate in cancer growth, progression and therapy resistance. Nat Rev Cancer [Internet]. 2018 Nov 18;18(11):669–80. Available from: <URL>.

3. Stasevich M V., Zvarich VI, Novikov VP, Zagorodnyaya SD, Povnitsa OY, Chaika MA, et al. 9,10-Anthraquinone Dithiocarbamates as Potential Pharmaceutical Substances with Pleiotropic Actions: Computerized Prediction of Biological Activity and Experimental Validation. Pharm Chem J [Internet]. 2020 Jan 16;53(10):905–13. Available from: <URL>.

4. Mohamadzadeh M, Zarei M, Vessal M. Synthesis, in vitro biological evaluation and in silico molecular docking studies of novel β-lactam-anthraquinone hybrids. Bioorg Chem [Internet]. 2020 Jan;95:103515. Available from: <URL>.

5. Zvarych V, Stasevych M, Novikov V, Rusanov E, Vovk M, Szweda P, et al. Anthra[1,2-d][1,2,3]triazine-4,7,12(3H)-triones as a New Class of Antistaphylococcal Agents: Synthesis and Biological Evaluation. Molecules [Internet]. 2019 Dec 13;24(24):4581. Available from: <URL>.

6. Comini LR, Núñez Montoya SC, Páez PL, Argüello GA, Albesa I, Cabrera JL. Antibacterial activity of anthraquinone derivatives from Heterophyllaea pustulata (Rubiaceae). J Photochem Photobiol B Biol [Internet]. 2011 Feb 7;102(2):108–14. Available from: <URL>.

7. Wang Q, Wang Y, Li Y, Wen B, Dai Z, Ma S, et al. Identification and characterization of the structure–activity relationships involved in UGT1A1 inhibition by anthraquinone and dianthrone constituents of Polygonum multiflorum. Sci Rep [Internet]. 2017 Dec 20;7(1):17952. Available from: <URL>.

8. Shadrack DM, K. Ndesendo VM. Molecular Docking and ADMET Study of Emodin Derivatives as Anticancer Inhibitors of NAT2, COX2 and TOP1 Enzymes. Comput Mol Biosci [Internet]. 2017 Mar 16;07(01):1–18. Available from: <URL>.

9. Ogbole OO, Akinleye TE, Faleye TOC, Adeniji AJ. Enterovirus inhibiting activities of two lupane triterpenoids and anthraquinones from senna siamea stem bark against three serotypes of echovirus. ACTA Pharm Sci [Internet]. 2019;57(3):105–15. Available from: <URL>.

10. Damiani RM, Moura DJ, Viau CM, Caceres RA, Henriques JAP, Saffi J. Pathways of cardiac toxicity: comparison between chemotherapeutic drugs doxorubicin and mitoxantrone. Arch Toxicol [Internet]. 2016 Sep 25;90(9):2063–76. Available from: <URL>.

11. Varadwaj P, Misra K, Sharma A, Kumar R. Mitoxantrone: an agent with promises for anticancer therapies. Electron J Biol [Internet]. 2010;6(2):36–42. Available from: <URL>.

12. Neuhaus O, Kieseier BC, Hartung H-P. Therapeutic role of mitoxantrone in multiple sclerosis. Pharmacol Ther [Internet]. 2006 Jan 1;109(1–2):198–209. Available from: <URL>.

13. Dias-Carvalho A, Ferreira M, Reis-Mendes A, Ferreira R, Bastos ML, Fernandes E, et al. Chemobrain: mitoxantrone-induced oxidative stress, apoptotic and autophagic neuronal death in adult CD-1 mice. Arch Toxicol [Internet]. 2022 Jun 19;96(6):1767–82. Available from: <URL>.

14. Pan D, Zhang X, Zheng H, Zheng Z, Nong X, Liang X, et al. Novel anthraquinone derivatives as inhibitors of protein tyrosine phosphatases and indoleamine 2,3-dioxygenase 1 from the deep-sea derived fungus *Alternaria tenuissima* DFFSCS013. Org Chem Front [Internet]. 2019 Sep 10;6(18):3252–8. Available from: <URL>.

15. Debbab A, Aly AH, Edrada-Ebel RA, Wray V, Müller WEG, Totzke F, et al. Bioactive metabolites from the endophytic fungus Stemphylium globuliferum isolated from Mentha pulegium. J Nat Prod [Internet]. 2009 Apr 24 [cited 2023 Jun 26];72(4):626–31. Available from: <URL>.

16. Lee HJ, Choi JS, Jung JH, Kang SS. Alaternin glucoside isomer from cassia tora. Phytochemistry [Internet]. 1998 Nov 5;49(5):1403–4. Available from: <URL>.

17. Zheng C-J, Shao C-L, Guo Z-Y, Chen J-F, Deng D-S, Yang K-L, et al. Bioactive Hydroanthraquinones and Anthraquinone Dimers from a Soft Coral-Derived *Alternaria* sp. Fungus. J Nat Prod [Internet]. 2012 Feb 24;75(2):189–97. Available from: <URL>.

18. Aly AH, Edrada-Ebel R, Wray V, Müller WEG, Kozytska S, Hentschel U, et al. Bioactive metabolites from the endophytic fungus Ampelomyces sp. isolated from the medicinal plant Urospermum picroides. Phytochemistry [Internet]. 2008 May 1;69(8):1716–25. Available from: <URL>.

19. Gill M, Giménez A, Jhingran AG, Qureshi A. Austrocortilutein stereoisomers from Australian fungi of the genus Dermocybe. Phytochemistry [Internet]. 1992 Mar 1;31(3):947–51. Available from: <URL>.

20. Yagi A, Okamura N, Haraguchi H, Abot T, Hashimoto K. Antimicrobial tetrahydroanthraquinones from a strain of Alternaria solani. Phytochemistry [Internet]. 1993 Apr 29;33(1):87–91. Available from: <URL>.

21. Wang S, Wang Q, Wang Y, Liu L, Weng X, Li G, et al. Novel anthraquinone derivatives: Synthesis via click chemistry approach and their induction of apoptosis in BGC gastric cancer cells via reactive oxygen species(ROS)-dependent mitochondrial pathway. Bioorg Med Chem Lett [Internet]. 2008 Dec 15;18(24):6505–8. Available from: <URL>.

22. Deep G, Oberlies NH, Kroll DJ, Agarwal R. Identifying the differential effects of silymarin constituents on cell growth and cell cycle regulatory molecules in human prostate cancer cells. Int J Cancer [Internet]. 2008 Jul 1;123(1):41–50. Available from: <URL>.

23. Gupta N, Linschitz H. Hydrogen-Bonding and Protonation Effects in Electrochemistry of Quinones in Aprotic Solvents. J Am Chem Soc [Internet]. 1997 Jul 1;119(27):6384–91. Available from: <URL>.

24. Quan M, Sanchez D, Wasylkiw MF, Smith DK. Voltammetry of Quinones in Unbuffered Aqueous Solution: Reassessing the Roles of Proton Transfer and Hydrogen Bonding in the Aqueous Electrochemistry of Quinones. J Am Chem Soc [Internet]. 2007 Oct 1;129(42):12847–56. Available from: <URL>.

25. Blankespoor RL, Hsung R, Schutt DL. Electroreductive cleavage of substituted 9,10-anthraquinones in 50% aqueous THF buffers: a pH-dependent process. J Org Chem. 1988 Jun 1;53(13):3032–5. Available from: <URL>.

26. Bachman JE, Curtiss LA, Assary RS. Investigation of the Redox Chemistry of Anthraquinone Derivatives Using Density Functional Theory. J Phys Chem A [Internet]. 2014 Sep 25;118(38):8852–60. Available from: <URL>.

27. Huskinson B, Nawar S, Gerhardt MR, Aziz MJ. Novel Quinone-Based Couples for Flow Batteries. ECS Trans [Internet]. 2013 May 3;53(7):101–5. Available from: <URL>.

28. Huskinson B, Marshak MP, Suh C, Er S, Gerhardt MR, Galvin CJ, et al. A metal-free organic–inorganic aqueous flow battery. Nature [Internet]. 2014 Jan 8;505(7482):195–8. Available from: <URL>.

29. Ozkok F, Boga M, Tuneg M, Enisoglu Atalay V, Onul N, Asgarova K, et al. Evaluation of Acetyl- and Butyrylcholinesterase Enzyme Inhibitory Activities and Cytotoxic Activities of Anthraquinone Derivatives. J Turkish Chem Soc Sect A Chem [Internet]. 2022 Aug 31;9(3):729–40. Available from: <URL>.

30. Celik S, Vagifli F, Akyuz S, Ozkok F, E. Ozel A, Dosler S, et al. Synthesis, vibrational spectroscopic investigation, molecular docking, antibacterial and antimicrobial studies of a new anthraquinone derivative compound. Spectrosc Lett [Internet]. 2022 Apr 21;55(4):259–77. Available from: <URL>.

31. Celik S, Ozkok F, Ozel AE, Müge Sahin Y, Akyuz S, Sigirci BD, et al. Synthesis, FT-IR and NMR characterization, antimicrobial activity, cytotoxicity and DNA docking analysis of a new anthraquinone

derivate compound. J Biomol Struct Dyn [Internet]. 2020 Feb 11;38(3):756–70. Available from: <URL>.

32. Sahin YM. Synthesis of an Antimicrobial Thioanthraquinone Compound to Produce Biodegradable Electrospun Mats for Tissue Engineering Purposes. J Turkish Chem Soc Sect A Chem [Internet]. 2018 Sep 1;5(3):1119–34. Available from: <URL>.

Development of Two Simple Spectrophotometric Methods to Assay Phenylephrine-HCl as Pure Form and in its Drug Forms

Hanan H. Ahmed[1*] iD, Salim A. Mohammed[1] iD

[1] University of Mosul, College of Science, Department of Chemistry, Mosul, 41001, Iraq.

Abstract: This work includes the development of two spectrophotometric methods which are sensitive, accurate, stable, and has good recovery for the determination of phenylephrine-HCl as free form and in the pharmaceutical preparations. In the method (A), phenylephrine is oxidized by potassium permanganate in a basic solution of sodium hydroxide and the bluish-green color of the resulting manganate (MnO_4^{2-}) is measured at wavelength 610 nm, which is linearly proportional to the amount of phenylephrine-HCl. Method (B), is involved the oxidation of phenylephrine-HCl by using an excess amount of N-bromosuccinimide in an acidic medium of hydrochloric acid solution, the remaining (unreacted) amount of N-bromosuccinimide is used to bleach indigo carmine dye and the absorbance of the blue color of the remaining dye is measured at the wavelength of 610 nm. which is directly proportional to the concentration of phenylephrine-HCl. The molar absorptivity coefficients of methods (A) and (B) are estimated and equal to 1.5722×10^4 and 5.5191×10^4 L/mol.cm, respectively. Beer's law of the both methods are linear in the concentration ranges 0.2–8.0 µg/mL (method A) and 0.2–3.5 µg/mL (method B). The relative standard deviation values of methods (A) and (B) are also found to be better than 0.0286 and 0.0114, respectively. The two proposed methods are applied to estimate phenylephrine-HCl in injection and drop.

1. INTRODUCTION

Phenylephrine-HCl (PPH) represents a type of sympathomimetics drugs that directly affects and stimulates alpha-1 adrenergic receptors found in blood vessels and smooth muscles (1). PPH is usually indicated to raise blood pressure in unstable patients with hypotension, especially causes from septic shock, and its nasal drops are used to treat symptoms such as itching of the nose and throat, sneezing and runny nose (2).

Chemically, PPH is (R)-1-(3-hydroxyPHEPHnyl)-2-methyl amino ethanol hydrochloride with chemical formula $C_9H_{13}NO_2 \cdot HCl$. It is a white crystalline powder having good solubility in alcohol and water with freely degrees. Scheme (1) explain the chemical structure of PPH (3).

$C_9H_{13}NO_2 \cdot HCl$
M.Wt. = 203.66 g/mol
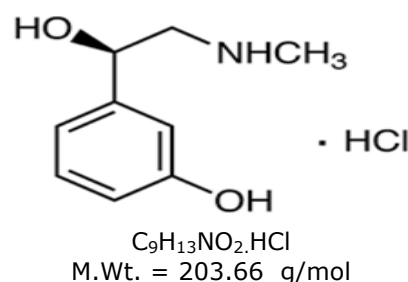
Sheme 1: The chemical structure of PPH.

PPH has been determined by using a wide variety of analytical techniques, these methods includes: RP-high performance liquid chromatography (4,5,6), high-performance thin layer chromatography (7,8) and RP-HPLC-PDA method (9), voltammetry (10,11), conductimetric titration (12), flow injection analysis (13,14), ultraviolet spectrophotometry (15,16), renewable electrode of carbon nanotubes ceramic electrode (17) and derivative spectrophotometric method (18) have also been reported for the determination of PPH.

The technique of UV and visible spectrophotometry is mostly used for the determination of PPH in aqueous medium because it offers advantages of simple and low cost instrument that are available at all laboratories. Most researches are described utilizing spectrophotometric methods for estimating PPH in the bulk and in its pharmaceutical formulations using different reactions and various reagents. Some of these methods involve diazotization and coupling reaction (19-24). Other methods base on the oxidative coupling reaction of PPH with 4-aminoantipyrine and potassium ferricyanide to yield dirty ping water soluble product (25), N,N-dimethyl-p-phenylenediamine in the presence of sodium persulfate in basic medium to give panic solution soluble product with maximum absorbance at 502 nm (26), and N,N-dimethyl-p-phenylenediamine dihydrochloride with ferric chloride in basic media to form green-blue soluble dye product (27,28). Other spectrophotometric methods based on the oxidation of PPH either with an excess amount of chloramine-T and the residual NBS is determined by bleaching the colour of indigo carmine dye (29) or by adding an excess amount of N-bromosuccinimide and then the residual NBS is estimated by bleaching the color of methyl orange dye (30). However, many of these methods suffer from various limitations, for instance, low sensitivity, low stability of the resulting product, and long operating time. Others required solvent extraction and expensive devices which may not be present in the laboratory. The aim of this current work describes two development spectrophotometric methods (direct and indirect) for assaying PPH in the bulk and in its pharmaceutical forms (injection and drop).

2. EXPERIMENTAL

2.1. Instrumentation
A Jasco V-630 digital double beam UV-Vis. spectrophotometer equipped with 1.0-cm matched fused quartz cells and Bp3001 professional bench top pH meter devices are used for all absorption spectra recording and pH measurements, respectively.

2.2. Chemical Reagents and Standard Solutions
All analytical reagents and chemicals used are of a high degree of purity, obtained from approved international and local origins. The standard material of PPH is procured from the state company for drug industries (SDI), Samarra- Iraq.

Standard Solution of PPH (100 µg/mL) ($4.910×10^{-4}$ M): It is prepared by weighing 0.0100 g of PPH and dissolving it in an appropriate volume of distilled water (Dw), and the solution is then transported to a volumetric flask of 100 mL and made it to the mark with Dw.

Working Solution of PPH (20 µg/mL) ($1.196×10^{-4}$ M): An appropriate volume of the standard solution of PPH is diluted with Dw to obtain the working solution.

Stock Solution of Potassium Permanganate (0.06 N): 0.3793 g of pure potassium permanganate ($KMnO_4$) (BHD) is weighed and dissolved in 50 mL of Dw. The solution is heated for 5 minutes to complete the dissolution and get rid of the remaining permanganate. The solution is cooled, filtered, and then diluted with the same solvent to 200 mL in a volumetric flask. The final solution obtained is titrated with a standard solution of sodium oxalate.

Working Standard $KMnO_4$ Solution (1000 µg/mL): Into a 100 mL volumetric flask, an appropriate volume of $KMnO_4$ stock solution is pipetted and then diluted to the mark with Dw. The prepared solution is kept in a dark bottle.

Sodium Hydroxide Solution (1 M): One ampoule of sodium hydroxide (at a concentration of 1 M/100 mL) (BHD) is diluted to a volume of one liter using Dw.

Solution of indigo carmine Dye ($5×10^{-4}$ M): 0.0232 g of indigo carmine dye is weighed and dissolved in a 100 mL Dw using a volumetric flask.

N-bromosuccinimide Solution ($2×10^{-3}$ M): 0.0356 g of N-bromosuccinimide (NBS) is dissolved in a portion volume of Dw and then completed to 100 mL with the same solvent in a volumetric flask.

Hydrochloric acid solution (1 M) is also prepared.

2.3. Analysis
2.3.1. Method A (direct method)
Under ideal conditions, aliquots of the standard solution of PPH (100 µg/mL) covering the concentration range of 0.2 - 200 µg/mL are placed in a series of 25 mL volumetric flasks. A 2.0 mL of 1 M NaOH solution and 1.0 mL of $KMnO_4$ (1000 µg/mL) solution are added. The sample solutions are placed in a water bath whose temperature is fixed at 40°C for ten minutes, the solutions are then cooled to the laboratory temperature. The volume of each flask will be brought to the mark with Dw and the absorbance of each is measured at the wavelength of 610 nm against the blank solution.

2.3.2. Method B (indirect method)
To a series of 10 mL volumetric flasks, an increasing amounts 0.2-3.5 µg/mL of the standard PPH solution (20 µg/mL), 0.5 mL of 1 M hydrochloric acid and 1.0 mL NBS ($2×10^{-3}$ M) oxidizing agents are added. The solutions are mixed thoroughly and heated for 10 minutes at 50 °C using thermostatic water bath to complete the oxidation process of the PPH. After cooling to room temperature a 1.6 mL of indigo carmine dye ($5×10^{-4}$ M) is added. The solutions are mixed thoroughly and kept constant for 3.0 minutes. Finally, the volume is adjusted up to the mark with Dw and mixed well. The absorbance of each solution is recorded at 610.0 nm against corresponding reagent blank.

2.3.3. Calibration graph
Under the optimum operating conditions, a linear calibration curve is obtained over the concentration ranges of 0.2 – 8.0 and 0.2 – 3.5 µg/mL of PPH with a molar absorption coefficients $1.5722×10^4$ and $5.5191×10^4$ L/mol.cm for methods A and B, respectively. The values of Sandell's sensitivity index are equal to 0.0129 µg.cm^{-2} for method A and 0.00369

$\mu g.cm^{-2}$ for method B. Fig.(1) explains the calibration curves of both suggested methods A and B.
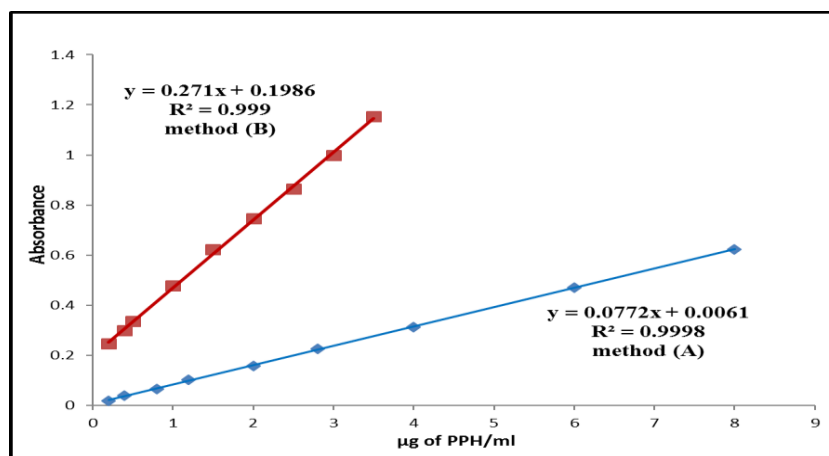
Figure 1: Calibration graphs of PPH estimation by using methods A and B.

2.4. Essential Procedure for Assaying PPH in Drugs

2.4.1. For nasofen (1%) drop solution
Three containers of nasofen drops (each one contains 1% PPH) are mixed well to get a homogeneous solution. An aliquot volume, equivalent to 0.01 g of PPH, is transported to a 100 mL volumetric flask and with Dw diluted to the mark. Each mL of this solution contains 100 μg of PPH. An aliquot of the diluted solution of the drop is then analyzed using the procedures designated in methods (A) and (B).

2.4.2. For injection PPH solution (500 μg/10 mL):
Three injections of PPH are mixed very well and transported to a washed dark bottle. Each mL of this solution contains 50 μg of PPH and an aliquot of the diluted drop is analyzed by using the procedures designated in (A) and (B) methods.

3. RESULTS AND DISCUSSION

3.1. Optimum Reaction Conditions
In method (A), phenylephrine is quantitatively oxidized with $KMnO_4$ in the presence of alkaline solution of sodium hydroxide to yield a bluish-green color of manganate (MnO_4^{2-}) which exhibits a peak with maximum absorption at the wavelength of 610 nm (Fig. 2).
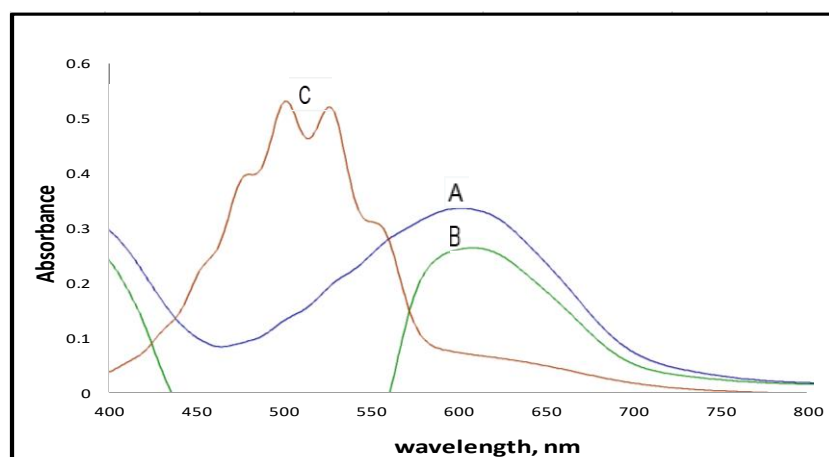
Figure 2: Absorption spectra of 100 μg/mL PPH Vs. (A) Dw, (B) blank solution, (C) blank solution Vs. Dw.

In method (B) the estimation of PPH includes two steps:
First step involves the oxidation of PPH by using an excess of oxidizing agent (NBS) in acidic medium.

PPH + NBS → oxidized PPH + NBS (residual)

Second step involves the residual and unreacted amount of NBS in bleaching the indigo carmine dye

and converting it to a colorless compound at the same media. The blue color of the residual indigo carmine dye is proportional to the PPH concentration that shows maximum absorption at 610 nm (Fig. 3).

NBS + Indigo carmine dye → Indigo carmine dye + Indigo carmine dye oxidized form residual
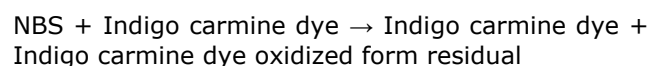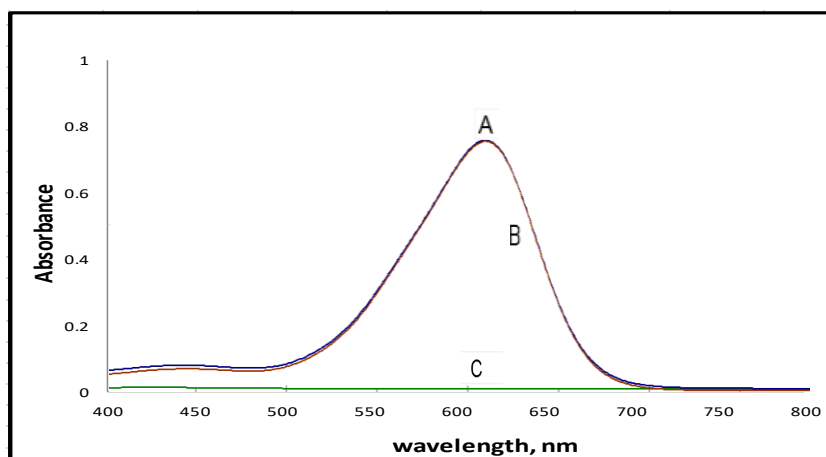
Figure 3: Absorption spectra of 20 μg/mL PPH Vs. (A) Dw, (B) blank solution, and (C) blank Vs. Dw.

The influence of diverse amounts (0.5-1.5 mL) of potassium permanganate on the absorbance of solutions containing increasing quantities of PPH (20–150 μg) in the presence of 1 M sodium hydroxide solution is studied. The experimental results in Figure 4 show that 1.0 mL of potassium permanganate is the appropriate amount for the oxidation of PPH in aqueous medium with a good determination coefficient value (R^2=0.9992). Therefore, 1 mL of potassium permanganate (1000 μg/mL) has been chosen as an optimum amount for the reaction.
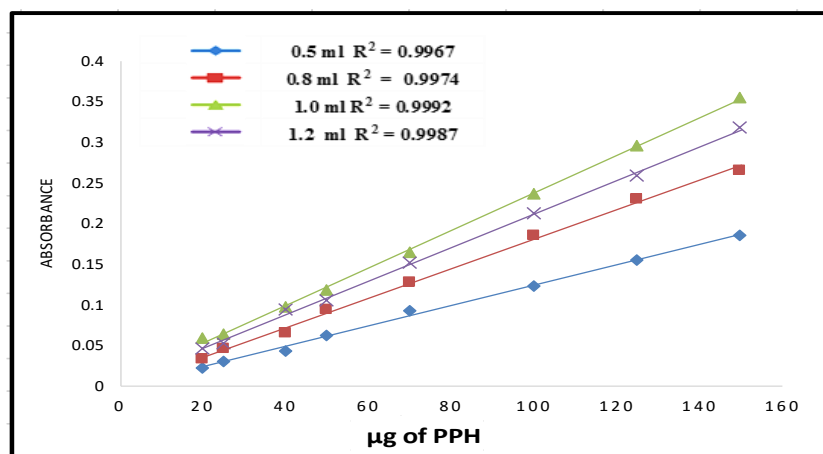
Figure 4: Effect of the amount of potassium permanganate (1000 μg/mL) on absorbance.

The influence of various strong and weak alkaline solutions (1 M) on the improving the absorbance value of the resulting product is investigated. The results in Figure 5 reveal that the maximum sensitivity is obtained on using 1.8-2.5 mL of NaOH solution. While Na_2CO_3 and $NaHCO_3$ display low sensitivity, which may due to pH variations. Therefore, 2.0 mL of 1 M NaOH solution has been relied upon for the subsequent experiments.
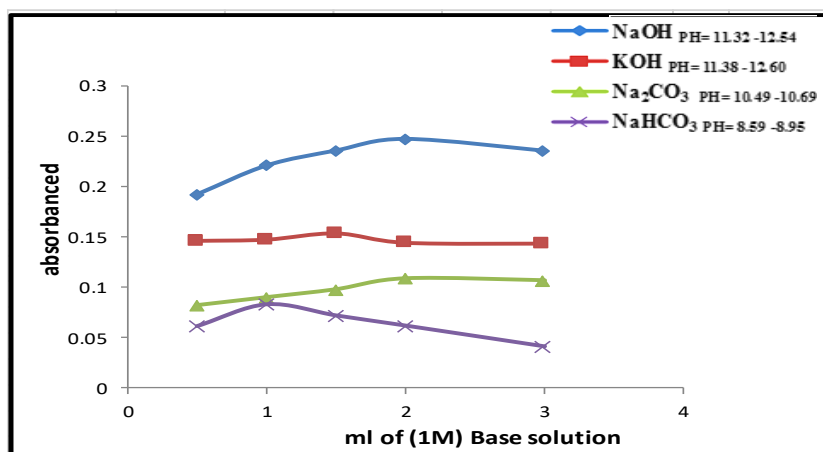
Figure 5: Influence of various alkaline solutions on absorbance.

The effect of addition sequence on the absorbance is also diagnosed. The experimental results indicated that the most favorable sequence of addition is PPH+NaOH+KMnO$_4$ due to its highest color intensity and development of maximum absorbance.

The effect of time that is required for the oxidation of PPH by KMnO$_4$ is investigated by following the color development of the product at different periods of time and temperatures up to 60 °C by using a water bath with thermostatic control. After completing the reaction at the fixed temperature and according to the approved method, the absorbance of the sample solution is measured at wavelength 610 nm against the reagent blank solution and the results are illustrated in Figure 6.
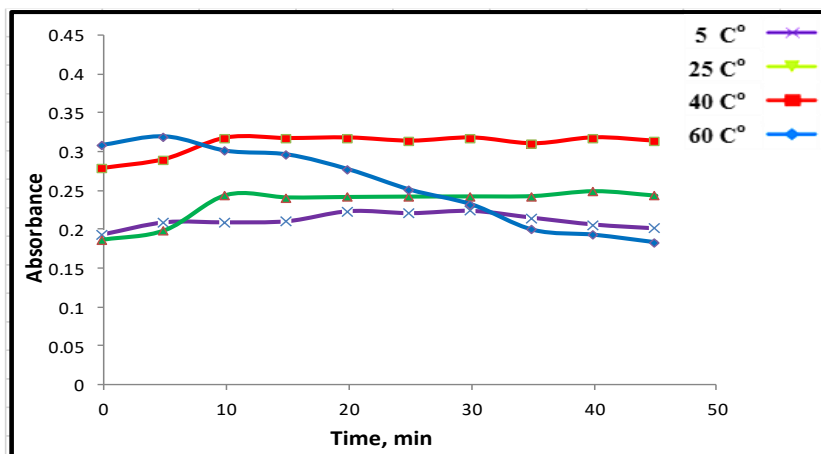
Figure 6: Effect of temperature and oxidation time on absorbance.

The results in Figure 6 indicate that the reaction of PPH with KMnO$_4$ in presence of NaOH solution is found to be complete in 10 min at temperature 40 °C. which gives a good sensitivity and stability. Therefore, these conditions are confirmed in the next experiments.

To find out the molar ratio of the oxidation reaction of PPH with KMnO$_4$ a molar ratio method is adopted (31), in which equal concentrations (4.910×10^{-4} M) of the drug compound and the oxidizing agent KMnO$_4$ are used. The results in Figure 7 reveal that the ratio is 1:2 of PPH: KMnO$_4$.
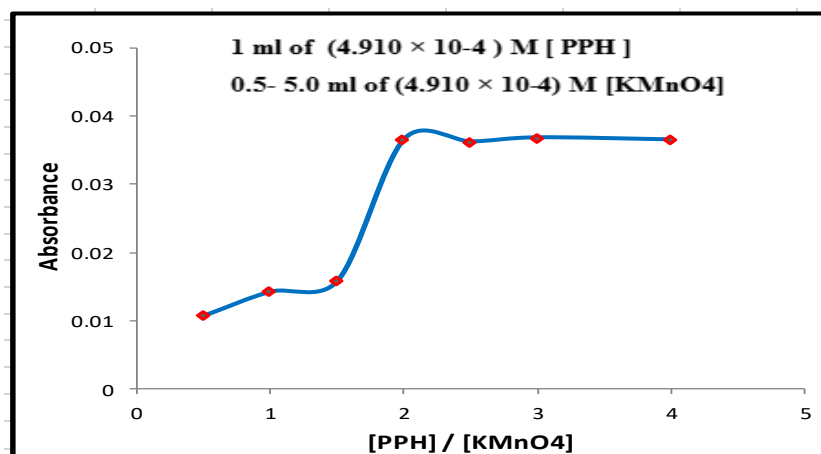
Figure 7: Molar ratio plot for reacting PPH with KMnO$_4$ under the optimum conditions.

Therefore, the chemical reaction equation of PPH with the oxidizing agent KMnO$_4$ in the basic medium can be written as:

PPH + MnO$_4^-$ → oxidation product of PPH + MnO$_4^{2-}$ (bluish-green color)
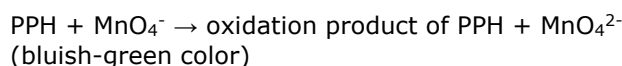
3.2. Optimum Reaction Conditions of method (B)
All experiments are conducted in 10 mL volumetric flasks with 20 µg/mL of PPH and the measuring absorption for colored product is carried out at 610 nm.

3.3. Effect of the Amount of Indigo Carmine dye
In order to find the appropriate amount of the indigo carmine dye used in the reaction, the influence of several quantities from 0.2 to 3.0 mL of indigo carmine dye in acidic medium on the absorbance is investigated. The absorbance is measured at the improved wavelength 610 nm against the blank solution and the results are shown in Figure 8.

$$(\bar{x} - \mu) \frac{\sqrt{N}}{S}$$
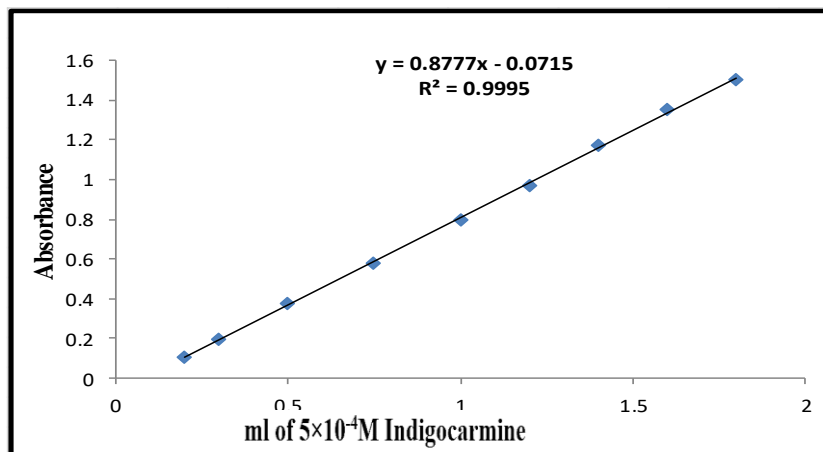
Figure 8: Standard curve of indigo carmine dye.

The results in Fig. 8 reveal that the linearity of the curve is continued to a volume of 1.8 mL of the dye, with determination coefficient of $R^2 = 0.9995$. Therefore, the amount 1.6 mL of the indigo carmine dye is chosen for the reaction.

3.4. Influence of the Amount of NBS
After the selecting the ideal amount of the indigo carmine dye, the effect of NBS amount required for the bleaching 5×10^{-4} M indigo carmine dye is being carried out. Accordingly, the effect of different quantities (0.3 -1.7 mL) of NBS (2×10^{-3}) M is studied in presence of 1 M HCl solution. The results in Figure 9 illustrate that a 1.0 mL of NBS is the optimal amount to reach almost complete dye color bleaching. Therefore, it has been proven and relied upon in subsequent experiments.
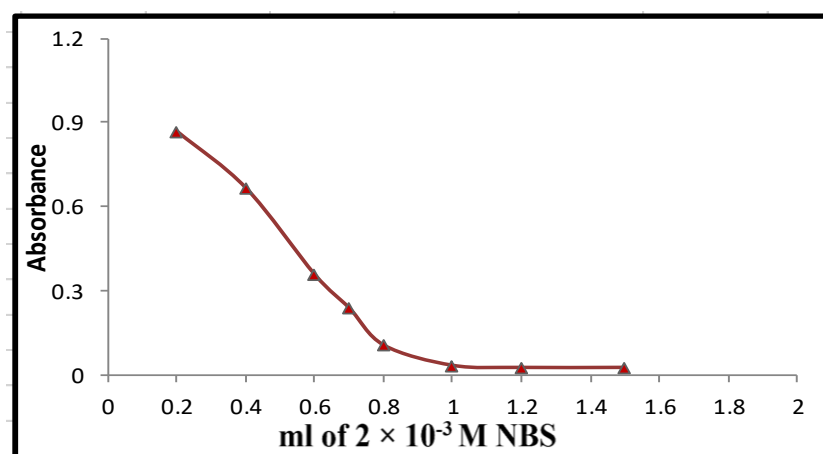
Figure 9: The effect of NBS amount on absorbance.

3.5. Effect of the Type of Acid and its Amount
The influence of various strong and weak acids on the absorbance is studied. The results are listed in Table 1.

The results in Table 1 show that the hydrochloric acid solution is the best, so the effect of different concentrations of HCl solution on the absorbance is diagnosed. The results are explained in Figure 10 indicate that 0.5 mL of HCl acid (1 M) is selected as the ideal concentration because, it gives the best value of determination coefficient ($R^2 = 0.9991$).

Table 1: Effect of the type of acid.

Type of acid (1 M)	HNO$_3$	H$_2$SO$_4$	HCl	H$_3$PO$_4$	CH$_3$COOH
Absorbance	0.0841	0.0623	**0.3225**	0.0694	0.1940
pH	1.98	2.04	**1.91**	2.34	2.82
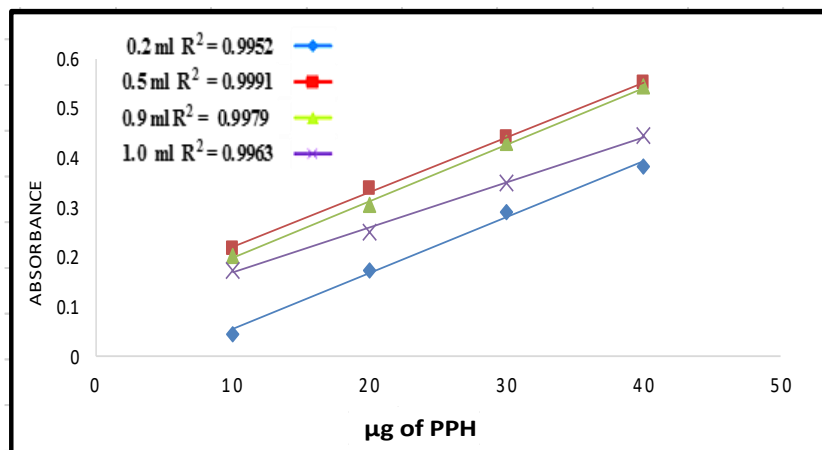
Figure 10: Effect of the amount of 1 M HCl solution on absorbance.

3.6. Effect of Oxidation Time and Temperature

It is necessary to investigate the ideal time and temperature that are required for the oxidation of PPH by NBS. The effect of different temperatures (5, 25, 40, 50 and 60 °C) on the absorbance using a water bath with thermostatic control is carried out (Figure 11).

The experimental results in Figure 11 show that the oxidation of PPH with NBS in the presence of HCl is optimum at temperature of 50 °C after waiting for 10 minutes.

The influence of bleaching time of the indigo carmine dye by the unreacted amount of NBS is also investigated. The data listed in Table 2 show that 3.0 to 7.0 minutes are the optimum time which give the highest absorption intensity at 610 nm. Therefore, the time of 3.0 minutes is relied upon in the next experiments.
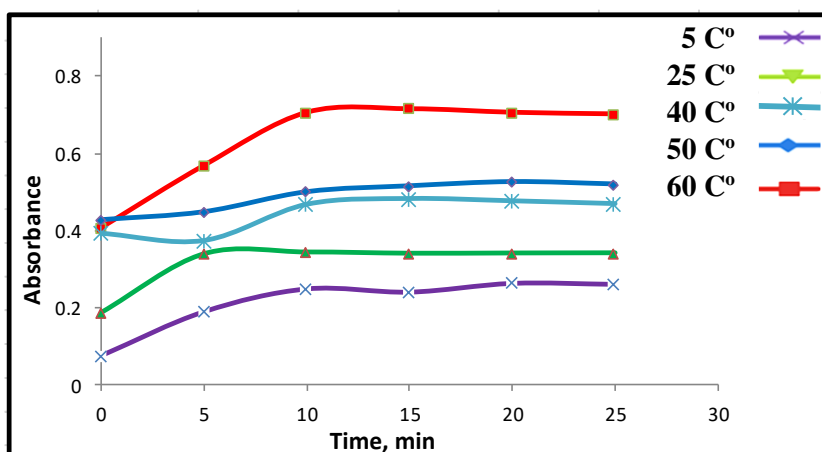
Figure 11: Effect of oxidation time and temperature on absorbance.

Table 2: Effect of bleaching time of indigo carmine dye on absorbance.

Time, min	2.0	3.0	5.0	7.0	10.0	15.0
Absorbance	0.7346	**0.7454**	0.7451	0.7450	0.7398	0.7386

The effect of different sequences on the intensity of absorption under the optimum experimental conditions is also tried. The experimental results indicated that the order of addition of (PPH + HCl + NBS + indigo carmine dye) is the best (A=0.7456).

3.7. Effect of Time on Color Development

In method (A), the absorption of the colored product of permanganate ion reaches the highest value after 10 minutes and remains stable for at least 40 minutes at room temperature. Whereas, in method (B) the blue color of the remaining indigo carmine dye after bleaching it with the excess of NBS stays stable for about an hour and there is no noticeable change in color and absorption during this period. The results for both methods are shown in Figure 12.
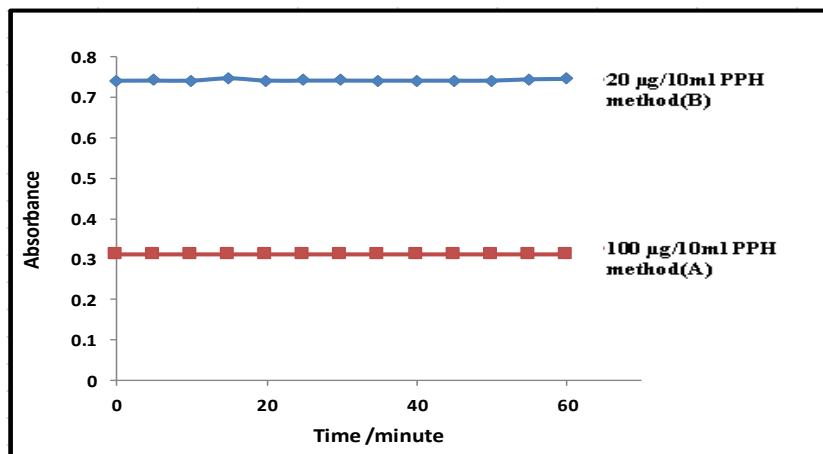
Figure 12: Effect of time on the development color for both methods (A) and (B).

3.8. Quantification
The limits of Beer's law, molar absorptivities, Sandell's sensitivities, accuracy (recovery %), and precisions (RSD) of the two methods (A) and (B) are evaluated. The linearity of both methods are also described by the equation of regression, as well as the corresponding determination coefficient (R^2) for PPH is calculated by the two recommended methods and represented excellent linearity. The limits of detection (LOD) and quantitation (LOQ) are found according to the ruling guidelines (32). The results are summarized in Table 3, which indicate that the proposed both methods are sensitive, precise, and accurate.

Table 3: Analytical data and optical characteristics of the proposed methods (A) and (B).

Parameters	Value	
	Method (A)	Method (B)
Beer's law range (µg/mL)	0.2 – 8.0	0.2 – 3.5
Molar absorptivity (L/mol.cm)	1.5722×10^4	5.5191×10^4
LOD (µg/mL)	0.00275	0.00077
LOQ(µg/mL)	0.00916	0.00258
Relative error range*	-0.1.066 to -0.32	-2.05 to -0.73
Recovery (%) range*	99.68 to 98.93	97.95 to 99.26
RSD*	0.0286 to 0.1783	0.0114 to 0.00846
Determination coefficient (R^2)	0.9998	0.9990
Slope (a)#	0.0772	0.271
Intercept (b)#	0.0061	0.1986
Sandell's sensitivity	0.0129	0.00369

*Average of five estimations, **#** Regression equation (X = b + ac), where c is (PPH) in µg/mL.

3.9. Application
Both methods (A) and (B) are applied to estimate PPH in its pharmaceutical preparations (injection and drop) for four different concentrations 20, 100, and 150 µg (method A) and 10, 20, and 30 µg of PPH (methods B). The results listed in Table 4 reveal that the proposed procedures (A) and (B) are in good agreement and with the declared content.

To evaluate the results of the proposed methods (A) and (B) a t-test has been carried out. The results of the t-test listed in Table 4 reveal that the values of t-exp. are less than the t-tabulated value at 95% confidence level and for four degrees of freedom (N = 4) (33). This means that the difference is statistically not significant, which confirms the success of the two proposed methods for assaying PPH in its drugs.

Table 4: Analysis of PPH in pharmaceuticals preparations for methods (A) and (B).

Drug Form	Certified Value	Method (A)			Method (B)		
		Found (µg)	Rec.(%) ± RSD (N=5)	Measured value	Found (µg)	Rec.(%) ± RSD (N=5)	Measured value
Phenylephrine injection (France)	500 µg PPH/10 mL	19.69	98.91± 0.410 **t=1.001**	494.55 µg	9.51	97.72 ± 0.624 **t=0.936**	488.6 µg
		99.84	98.397± 0.533 **t=1.010**	492 µg	18.68	98.77 ± 0.481 **t=2.450**	493.85 µg
		151.21	99.32 ± 0.941 **t=2.451**	496.6 µg	31.31	99.39 ± 0.441 **t=1.633**	499.65 µg
Nasofen drop (Pioneer-Iraq)	1.0%	19.82	98.94 ± 0.562 **t=1.633**	0.989%	9.37	98.34 ± 1.320 **t=1.512**	0.983%
		99.61	98.29 ±0.607 **t=1.643**	0.983%	17.73	98.29± 0.592 **t=1.001**	0.983%
		151.27	97.97 ± 0.273 **t=1.071**	0.979%	28.56	98.74± 0.377 **t=2.449**	0.987%

[a]t ± = $(\bar{x} - \mu)\frac{\sqrt{N}}{S}$, [a]Tabulated "t" value at 95% confidence level is equal to 2.776.

3.10. Evolution of the Proposed Methods
To prove the efficiency and credibility of the two proposed methods (A) and (B) in the estimation of PPH and to ensure that they are free from the interference of additives, a standard additions method is applied.

The results listed in Table 5 and shown in Figure 13 indicate that there is a high agreement between the standard additions method and the proposed methods (A and B) for the determination of PPH in its pharmaceutical preparations.
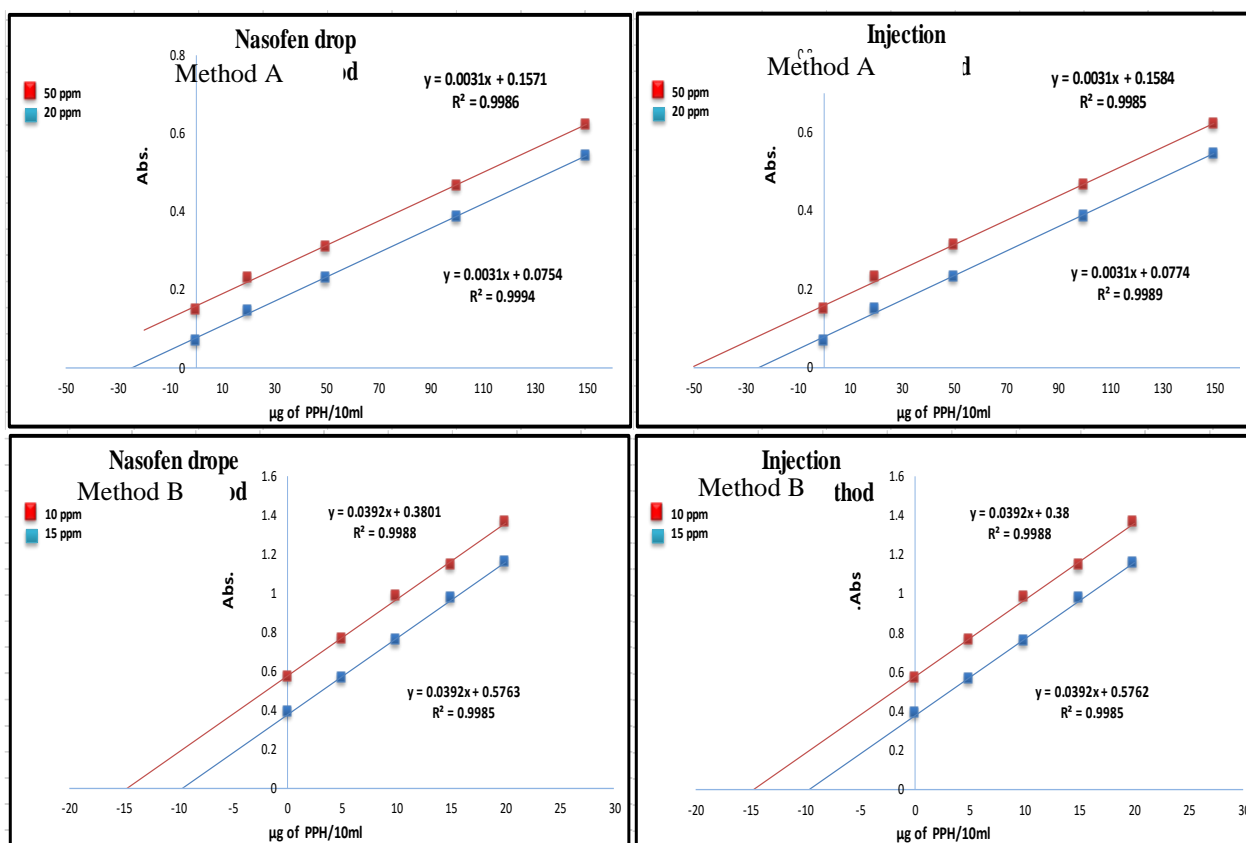
Figure 13: Standard addition curves for the estimation of PPH in pharmaceutical preparations by using methods (A) and (B).

Table 5: The results of standard addition methods for analysis of PPH in its drugs.

Drug	Certified Value	Method (A)		Average of recovery (%)	Average of measured value
		PPH Present (µg)	PPH Measured (µg)		
Phenylephrine injection (France)	500 µg PPH/mL	20 50	20.06 51.09	102.59	512.95 µg
Nasofen drop (Pioneer-Iraq)	1.0%	20 50	20.8 50.6	102.6	1.026 %
Method (B)					
Phenylephrine injection (France)	500 µg PPH/mL	10 15	9.69 14.69	97.42	487.08 µg
Nasofen drop (Pioneer-Iraq)	1.0%	10 15	9.69 14.70	97.45	0.975 %

4. CONCLUSION

Two simple spectrophotometric methods (direct and indirect) are developed for estimating PPH in the bulk and in the pharmaceutical formulations through the oxidation-reduction reactions. The two suggested methods have many advantages of being accurate, sensitive, and convenient for routine analysis in control laboratories. As well as the resulting colored products of both methods are characterized by high stability and did not exhibit a noticeable change in absorption for at least 60.0 minutes. Beer's law of the both methods are linear in the concentration ranges 0.2–8.0 and 0.2–3.5 µg/mL for method A and method B, respectively. The values of molar absorptivity of methods A and B are 1.5722×10^4 and 5.5191×10^4 L/mol.cm , respectively. Both methods A and B have been successfully applied for analysis of PPH in drop and injection drugs with an excellent recoveries from 97.97% to 99.32% for method A and 97.72% to 99.39% for method B. The future works will include an attempt to establish an analytical procedure for simultaneous estimation of PPH and tetracycline in the pharmaceutical formulations by using second derivative spectrophotometry.

5. CONFLICT OF INTEREST

The authors declare no potential conflict of interests.

6. ACKNOWLEDGMENTS

7. REFERENCES

1. K. Kareem N, Z. Thani M, F.Al-Rawi K. New approach for determination of Phenylephrine HCl in Pure and Pharmaceutical Formulation using a various Microextraction Methods. Res J Pharm Technol [Internet]. 2022 Apr 23;15(4):1648–52. Available from: <URL>.

2. Goth A. Medical Pharmacology: Principles and Concepts. Surv Anesthesiol [Internet]. 1961;5(6):642. Available from: <URL>.

3. Cartwright AC. The British pharmacopoeia, 1864 to 2014: medicines, international standards and the state. Routledge; 2016.

4. Barabde G, Pataskar P, Gaikar T, Bagul V, Patil T. Development and Validation of Fast, Simple RP-HPLC Method for Simultaneous Estimation of Brompheniramine, Dextromethorphan HBr and Phenylphrine HCl in Pharmaceutical Dosage Form. JAC. 2022;15(8):109–19.

5. Sonone R, Tandel L, Jain V. Novel Rapid Isocratic RP-HPLC Method for Simultaneous Estimation of Phenylephrine Hydrochloride, Paracetamol, Caffeine, Diphenhydramine Hydrochloride. Curr Pharm Anal [Internet]. 2021 Jul;17(6):792–800. Available from: <URL>.

6. Kommana R, Basappa P. Validated Stability Indicating RP-HPLC Method for Simultaneous Estimation of Codeine Phosphate and Chlorpheniramine Maleate from Their Combined Liquid Dosage Form. Chromatogr Res Int [Internet]. 2013 Mar 31;2013:1–7. Available from: <URL>.

7. El Yazbi FA, Hassan EM, Khamis EF, Ragab MAA, Hamdy MMA. Development and Validation of a High-Performance Thin-Layer Chromatographic Method for the Simultaneous Determination of Two Binary Mixtures Containing Ketorolac Tromethamine with Phenylephrine Hydrochloride and with Febuxostat. J Chromatogr Sci [Internet]. 2016 May;54(5):819–28. Available from: <URL>.

8. Ragab MAA, Abdel-Hay MH, Ahmed HM, Mohyeldin SM. Determination of Ibuprofen and Phenylephrine in Tablets by High-Performance Thin Layer

Chromatography and in Plasma by High-Performance Liquid Chromatography with Diode Array Detection. J Chromatogr Sci [Internet]. 2019 Aug 1;57(7):592–9. Available from: <URL>.

9. Nagarjuna P, Tharun Kumar B, Nalluri BN. Simultaneous Analysis of Phenylephrine HCl and Ketorolac Tromethamine in Bulk and Injectable Formulations by RP-HPLC-PDA Method. J Drug Deliv Ther [Internet]. 2020 Aug 15;10(4-s):39–45. Available from: <URL>.

10. Yagmur S, Ture M, Saglikoglu G, Sadikoglu M, Yilmaz S. The Quantitative Detection of Phenylephrine in Pharmaceutical Preparations and Spiked Human Urine by Voltammetry. Russ J Electrochem [Internet]. 2018 Oct 15;54(10):741–6. Available from: <URL>.

11. Amare M, Menkir G. Differential pulse voltammetric determination of salbutamol sulfate in syrup pharmaceutical formulation using poly(4-amino-3-hydroxynaphthalene sulfonic acid) modified glassy carbon electrode. Heliyon [Internet]. 2017 Oct 1;3(10):e00417. Available from: <URL>.

12. H. Hasan S, S. Othman N, M. Surchi K. Determination of Phenylephrine-HCl Using Conductometric Titration Method. Curr Anal Chem [Internet]. 2016 Jul 1;12(4):330–4. Available from: <URL>.

13. Rocha JRC, Galhardo CX, Natividade MAE, Masini JC. Spectrophotometric Determination of Phenylephrine Hydrochloride in Pharmaceuticals by Flow Injection Analysis Exploiting the Reaction with Potassium Ferricyanide and 4-Aminoantipyrine. J AOAC Int [Internet]. 2002 Jul 1 [cited 2023 Jul 12];85(4):875–8. Available from: <URL>.

14. Al-Abachi MQ, Subhi S. Flow injection-Spectrophotometric Determination of Phenylephrine Hydrochloride and Amoxicillin Trihydrate in Pharmaceutical Preparations. J Al-Nahrain Univ Sci [Internet]. 2013 Mar 1;16(1):42–52. Available from: <URL>.

15. Wadher SJ, Kalyankar TM, Panchal PP. Development and Validation of Simultaneous Estimation of Chlorpheniramine Maleate and Phenylephrine Hydrochloride in Bulk and Capsule Dosage Form by Ultra-Violet Spectrophotometry. Int J ChemTech Res CODEN(USA [Internet]. 2013;5(5):2410–9. Available from: <URL>.

16. Kazak Sarılmışer H, Özçelik NO, Özkırım Arslan B, Gökalp M, Ustaoğlu A, Dude UK, et al. Development and validation of a simple HPLC assay method for ibuprofen, pseudoephedrine hydrochloride and chlorpheniramine maleate in syrup form. J Chem Metrol [Internet]. 2017 Nov 2;11(2):61–7. Available from: <URL>.

17. Habibi B, Jahanbakhshi M. Simultaneous Determination of Ascorbic Acid, Paracetamol and Phenylephrine: Carbon Nanotubes Ceramic Electrode as a Renewable Electrode. Anal Bioanal Electrochem [Internet]. 2015;7(1):45–58. Available from: <URL>.

18. Aljeboree AM, Alshirifi AN. Determination of phenylephrine hydrochloride and Amoxicillin in binary mixture using Derivative Spectrophotometry methods. Int J Pharm Qual Assur [Internet]. 2019 Aug 30;10(03):168–77. Available from: <URL>.

19. Hasan S, Othman N, Surchi K. Using of Diazotized 2,4-Dinitroaniline in Spectrophotometric Estimation of Phenylephrine Hydrochloride. Rafidain J Sci [Internet]. 2020 Sep 2;29(3):37–46. Available from: <URL>.

20. Al-Sabha TN. Spectrophotometric Assay of Phenylephrine Hydrochloride Using 4-Aminoantipyrine and Copper (II). Pakistan J Anal Environ Chem [Internet]. 2010;11(1):1–7. Available from: <URL>.

21. Othman NS, Abdul Fatah NT. Spectrophotometric Determination of Phenylephrine Hydrochloride by Coupling with Diazotized 2-Aminobenzothiazole. Rafidain J Sci [Internet]. 2009;20(4):69–81. Available from: <URL>.

22. Mzban Q, Bahjat S, Hassan MJM. Dispersive liquid-liquid microextraction and spectrophotometric determination of cefazone and phenylephrine hydrochloride in their pure forms and pharmaceutical preparations. Plant Arch [Internet]. 2020;20(2):6771–7. Available from: <URL>.

23. Al-Uzri WA. Determination of phenylephrine hydrochloride in pharmaceutical preparations using spectro-photometric method. Asian J Pharm Clin Res [Internet]. 2019 Apr 9;12(5):339–43. Available from: <URL>.

24. Alteemi HS, Kadim KH. Colorimetric Determination of Phenylephrine hydrochloride Drug by Diazotization Reaction. J Phys Conf Ser [Internet]. 2020 Nov 1;1664(1):012097. Available from: <URL>.

25. Aljeboree AM, Alshirifi AN. Colorimetric Determination of phenylephrine hydrochloride drug Using 4-Aminoantipyrine: Stability and higher sensitivity. J Pharm Sci Res [Internet]. 2018;10(7):1774–9. Available from: <URL>.

26. Radia ND, Alshamusi QKM, Sahib IJ, Jasim LS, Aljeboree AM, Alkaim AF. Oxidative coupling of phenylephrine hydrochloride using N,N-dimethyl-p-phenylenediamine: Stability and higher sensitivity. In: AIP Conference Proceedings [Internet]. American Institute of Physics Inc.; 2022. p. 030026. Available from: <URL>.

27. Ahmed AMK, Anwar SM, Hattab AH. Spectrophotometric Determination of Phenylephrine Hydrochloride in Pharmaceutical Preparations by Oxidative Coupling Reaction. Int J Drug Deliv Technol [Internet]. 2020 Sep 25;10(03):323–7. Available from: <URL>.

28. Aljeboree AM, Alshirifi AN, Abdulrazzak FH, Abbas AS, Alkaim AF. Colorimetric Determination of pharmaceutical dyes Using 4-Aminoantipyrine : Oxidative coupling review. J Pharm Sci Res [Internet]. 2019;11(3):912–8. Available from:

<URL>.

29. Battu S, Gandu V, Nenavathu BP. Simple spectrophotometric method for estimation of drugs using chloraminet and indigo caramine dye couple. Asian J Biomed Pharm Sci [Internet]. 2020;10(69):19–24. Available from: <URL>.

30. Zakaria SA. Simple spectrophotometric method for determination of phenylephrine hydrochloride in pure and pharmaceutical forms. Iraqi Natl J Chem [Internet]. 2021;20(1):1–11. Available from: <URL>.

31. Code CS. SECOND YEAR (2017-2018 onwards) THIRD SEMESTER THEORY.

32. Booth PM. FDA implementation of standards developed by the international conference on harmonisation. Food Drug Law J [Internet]. 1997;52(2):203–23. Available from: <URL>.

33. Sinnema A. Structure Elucidation by NMR in Organic Chemistry E. [Internet]. Vol. 112, Recueil des Travaux Chimiques des Pays-Bas. 1993. 650 p. Available from: <URL>.

Synthesis and Chemical Characterization of Alkyd Resins Using Maleic and Phthalic Anhydrides and Seed Oil of *Luffa aegyptiaca*

Marili Funmilayo ZUBAIR [1*] (iD) **, Sulyman Olalekan IBRAHIM** [1] (iD) **,**

Kenneth STEPHEN [1] (iD) **, Abdulmumeen Amao HAMID** [2] (iD) **, Olamilekan Joseph IBUKUN** [3] (iD) **,**

Olubunmi ATOLANI [2] (iD)

[1] Department of Industrial Chemistry, Faculty of Physical Sciences, University of Ilorin, Ilorin, 240003, Nigeria

[2] Department of Chemistry, Faculty of Physical Sciences, University of Ilorin, Ilorin, 240003, Nigeria

[3] Indian Institute of Science Education and Research, Kolkata, West Bengal, 741246, India

Abstract: The study aimed to provide sustainable alternatives to reduce industries' over-reliance on edible vegetable oil for alkyd resin preparation as applicable in paint production. Alkyd resins were synthesized and characterized from sponge (Luffa aegyptiaca) seed oil. Condensation polymerization of monoglyceride with phthalic and maleic anhydride was carried out, and physico-chemical parameters such as drying time, total solids, viscosity, and chemical resistance were investigated following standard procedures. UV–visible, FT-IR, 1H, and 13C NMR spectroscopies were used to characterize the prepared alkyd resins. Sponge seed oil alkyd resins prepared with maleic anhydride (SPOMA) had a higher percentage yield (77.56%) than sponge seed oil prepared using phthalic anhydride (SPOPA) with 64.44%. The two alkyd resins showed a better drying time of 40 – 50 min than their commercial counterparts (70 min). This was attributed to the high degree of unsaturation of the seed oil due to the considerable proportion of linoleic acid in the seed oil. The alkyd resins were largely stable in 0.1 M HCl, 5% NaCl, and 0.1 M KOH, which caused the alkyd resins to whiten and shrink. The resins were generally soluble in xylene, kerosene, and petroleum ether. The nature of the alkyd resin can be described as nonpolar. This observation was consistent with the literature report. This study concluded that quality or industrial-grade alkyd resins could be prepared from sponge seed oil and thereby serve as a cheap and viable replacement for edible oils used in industries.

1. INTRODUCTION

Despite the abundance of renewable tropical plant seeds in Nigeria, a survey of the literature and personal interactions with vegetable oil-dependent companies revealed that the industries import oil as raw materials from Western countries. In Nigeria, there is a need for more of well-organized, accurate data and

information about the chemical composition and potential use of non-conventional seed oils. As a result, the raw-material supply chain for oil-based businesses could increase. In addition, the information gathered on seed oil will be added to the plant knowledge base.

The lack of interest in oil-based sectors to investigate indigenous raw materials may be

partly due to a lack of data on seed oil and a lack of synergy between industry and academia. Data obtained from this study would promote academic-industry ties while also assisting in the transferring research discoveries for everyone's benefit. More jobs could be created from the utilization of locally accessible plant seed oils as alternative and sustainable bio-stock for production of various end-user items, particularly in communities where these seeds are grown. The production of alkyd resins from plant seed oils in a sustainable manner would also assist in reducing global pollution. Examining the viability of the seed oils employed in this study, it was chosen for its environmental abundance and oil content.

Nigerian enterprises that rely on vegetable oil import oils as raw materials at excessive prices. Locally accessible oils can only cover a quarter of demand, exposing companies to unjustified competition for oil with food applications (1). In addition, many manufacturing businesses employ edible oil consumed in Nigeria, resulting in domestic-industry competition. With several tropical underutilized and undervalued seed-producing plants, such as *Luffa aegyptiaca,* the country can produce enough fixed oil for both local and industrial needs, and sufficient reserves for export at extremely affordable cost.

Luffa aegyptiaca, a fast-growing annual vine that matures in about four months are found in Asia, India, Brazil, and Nigeria (2). The plant often called luffa is a cucurbit that includes gourds, pumpkins, and cucumbers, all of which are members of the Cucurbitaceae family. Luffa is known by various names, including smooth loofah, loofah sponge, sponge gourd, vegetable sponge, dishrag gourd, and Chinese okra. *Luffa cylindrica* and *Luffa aegyptiaca* are the two species of luffa(3). From the literature, sponge seeds are high in unsaturated fatty acids with linoleic acid being the most abundant fatty acid in the seed (4,5).

The lack of information on the chemistry and application of accessible seeds with respect to their physicochemical features and prospective industrial applications is one of the reasons why some seeds/seed oils remain underutilized. As a result, research is essential to unravel the seed oil potentials and harness the data for profitable utilization (6,7). This research is thus aimed at exploring and characterizing the underutilized seeds of *Luffa aegyptiaca* seed as a renewable source of fixed oil and source of commercial raw materials for oil-based industries in tandem with the sustainable goal (SDG 11).

2. MATERIALS AND METHODS

Oil was extracted from dried and pulverized seeds of *Luffa aegyptiaca* according to standard procedure (8). The pulverized dried seed material (400 g) was extracted for 7 hours using n-hexane (2000 mL) at 55 °C using a soxhlet extractor. At 40°C, the oil was recovered from the solvent using a rotary evaporator (9).

2.1. Preparation of Alkyd Resin from the Seed Oil
The alkyd resin preparation was accomplished using the standard procedure (10). The oil was first alcoholized using stoichiometric quantities of oil and glycerol (Table 1) using sodium methoxide as a catalyst. Methanol was used to test the solubility of the produced monoglycerides. The reaction was cooled after the monoglycerides were formed, and then phthalic/maleic anhydride was added, followed by xylene to aid in the removing esterified water by producing an azeotrope. The reaction temperature was then raised to 235 °C for 5 hours. To check for a drop in acid value, aliquots were obtained from the reaction mixture at 1-hour intervals. By submerging the reaction vessel in cold water, the reaction was halted. The alkyd resin's formulation is presented in Table 1.

Table 1: Formulation of the alkyd resin.

Raw materials	Composition (%)
Seed oil	45
Glycerol	20
Phthalic anhydride/Maleic anhydride	25
Xylene	10

2.2. Physicochemical Analysis of the Alkyd Resin

To determine the acid value, viscosity, and total solids, the American Oil and Chemists Society's standard approach was used. In addition, standard procedures ASTMD1640-69 and ASTMD 1308-5-57 were used to determine the drying time and chemical resistance of alkyd samples in various solvents, as described in (11,12).

2.3. Chemical Stability of the Alkyd Resin

The chemical resistance of the prepared alkyd resins with their commercial counterparts was tested by dissolving little quantity of the alkyd in distilled water, 0.1 M KOH, 0.1 M HCl, 5% NaCl, petrol, methanol, and kerosene, respectively (13).

2.4. UV–Visible Spectroscopic Analysis of the Prepared Alkyd Resin

The synthesized alkyd resins were analyzed using UV–Vis spectroscopy operating in a range of 300 to 800 nm. A concentration of 1 µM was prepared in methanol or dichloromethane whilst using the solvents as blank for the analysis (14).

2.5. Fourier Transform Infrared (FT-IR) Spectroscopic Analysis of the Prepared Alkyd Resin

The infrared spectra were obtained on a Shimadzu 8400s using a KBr pellet, as described (15). In order to identify functional groups present in the seed oil, phthalic anhydride, maleic anhydride, and alkyd resins, the, infrared spectroscopic analysis was, performed on individual sample.

2.6. Nuclear Magnetic Resonance (NMR) Spectroscopic Analysis

^{1}H (Proton Nuclear Magnetic Resonance) and ^{13}C NMR (Carbon 13 Nuclear Magnetic Resonance) of SPOMA (Alkyd resin made from Sponge seed and Maleic anhydride) and SPOPA (Alkyd resin made from Sponge seed and Phthalic anhydride) dissolved in deuterated DMSO (Dimethyl sulfoxide) were recorded on a Bruker Avance III™ HD 500 MHz spectrometer equipped with a 5 mm wide helium-cooled probe and an automatic 24-sample converter. Avance III HD 500, three channels, BOSS III (36 magnetic field homogenity corrections), BSMS 2, amplifiers BLAX2H 300/100 and BLAX 300.

Table 2: Physicochemical Analysis of the Alkyd Resin.

Parameters	SPOPA	SPOMA	Control Resin
Yield, %	64.44	77.56	-
Acid Value	8.42	7.67	11.52
Viscosity (cst)	818.65	811.06	815.52
Total Solid (%)	89.42	94.37	51.56
Drying time (min)	40	50	70

SPOMA – Alkyd resin made from Sponge seed and Maleic anhydride
SPOPA – Alkyd resin made from Sponge seed and Phthalic anhydride
Control Resin – Commercial Alkyd resin

3. RESULTS AND DISCUSSION

3.1. Physicochemical Analysis of the Prepared Alkyd Resin

The two alkyd resins, SPOPA and SPOMA with distinct properties, were prepared by esterifying the resulting intermediate product of sponge seed oil with glycerol. According to the reviewed literatures, no precise standard exists because each alkyd is unique (16). However, two elements were discovered to influence the features of the alkylated resin produced. Table 2 shows the results obtained compared with commercial alkyd resin purchased from the market.

Alkyd resins prepared with maleic anhydride had a higher percentage yield than those made with phthalic anhydride. Sponge seed oil and maleic anhydride (SPOMA) afforded a maximum yield

3.2. Chemical Resistance of the Alkyd

of 77.56%, while SPOPA made from phthalic anhydride and the seed oil afforded a yield of 64.44%. The variation observed could be as a result of higher degree of unsaturation of phthalic anhydride. Low acid content, high viscosity, total solids, and short drying time are other properties that determine the quality of alkyd resin (11, 17).

SPOMA (40 min) has a shorter drying time than SPOPA (50 min), while both have comparable drying period of 70 mins for commercial alkyd resin. The prepared alkyd resins outperform the commercial alkyd resin in total solids, ranging from 89.42% for SPOMA to 94.37% for SPOPA, compared to 51.56% of the commercial alkyd resin. All prepared alkyd resins had a viscosity in the range of 811.06 cst to 818.65 cst, which is comparable to the commercial alkyd resin's viscosity of 815.52 cst.

Resins

The chemical stability of the alkyd resin was

determined by immersing different alkyd resins (prepared and commercial) alkyd in various solvents with different polarities. In distilled water, 0.1 M HCl, and 5% NaCl, all of the alkyds were largely stable. However, the KOH caused the alkyd resin to whiten and shrink, and it was generally unstable in xylene, kerosene, and petroleum ether (Table 3). The nature of the alkyd resin can be described as nonpolar. This conclusion is consistent with the findings of others (18,19).

3.3. Result of UV–Visible Spectroscopy Characterization of the Alkyd resin

UV–visible spectroscopy was also used to predict extent of the alkyd formed. The alkyd resins displayed a bathochromic (red) shift due to $\pi - \pi^*$ and $n - \pi^*$ transitions, as shown in the UV–visible spectrum in Figures 1 – 2 and Table 4. In the synthesis of SPOPA alkyd resin, a red shift to 426 nm was detected, compared to 314 and 278 nm for raw sponge seed oil and phthalic anhydride, respectively.

The appearance of a new absorption peak at 417 nm, consistent with literature report (20), lends credence to the claim about the alkyd resin formation (Table 4, Figure 1). This behavior was attributed to the elongation of conjugation coupled with the presence of several auxochromes in the new product (21). Similar observations were obtained in the synthesis of SPOMA alkyd resin, in which the alkyd resin exhibited a redshift in the absorption λ_{max} to 417 nm compared to 247 nm for maleic anhydride (Table 4, Figure 2).

3.4. FT-IR Characterization of the Alkyd Resin

Physical and chemical analyses of the resin, and FT-IR characterization, were used to determine the formation of the alkyd resin. As illustrated in Figures 3 and 4, the FT-IR spectrum revealed that the starting reagents (seed oil and polybasic acids) utilized all had distinct absorption bands. The FT-IR data of sponge seed oil, maleic/phthalic anhydride, and alkylated resins are given in Tables 5 and 6.

Table 3: Chemical Resistance of the Alkyd Resin.

Parameter	SPOPA	SPOMA	Control Resin
Distilled water Resistance	Stable	Stable	Stable
0.1M HCl Resistance	Stable	Stable	Stable
0.1M KOH	Decolorize/Shrinkage	Decolorize/Shrinkage	Shrinkage
5% NaCl	Stable	Stable	Stable
Xylene	Unstable	Unstable	Unstable
Petroleum ether	Unstable	Unstable	Unstable
Kerosene	Unstable	Unstable	Unstable

Table 4: UV–Visible Spectroscopic Characterization Data of the Alkyd Resin.

Samples	λ_{max} (nm)
Sponge seed oil	314
Maleic Anhydride	247
Phthalic anhydride	278
SPOPA	426
SPOMA	417
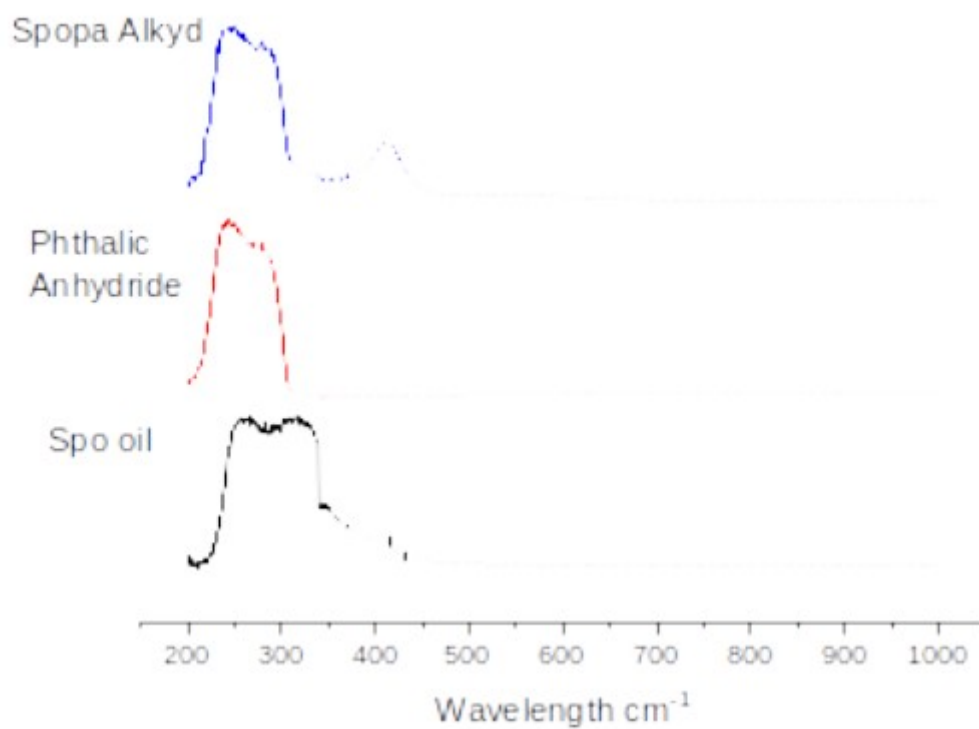
Figure 1: UV–Visible spectrum of SPOPA Alkyd Resin.
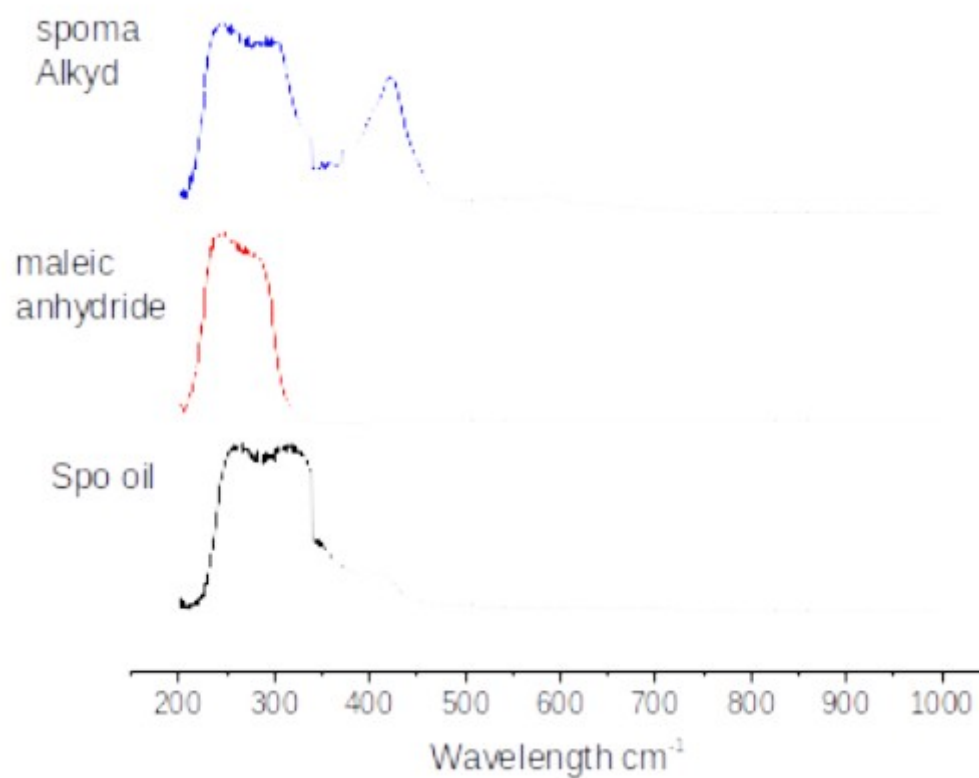
Figure 2: UV–Visible spectrum of SPOMA Alkyd Resin.

Table 5: FT-IR spectra analysis of sponge seed oil, phthalic anhydride and SPOPA Alkyd Resin.

Functional groups	Frequency of Absorption bands (cm^{-1})		
	Sponge seed oil	Phthalic anhydride	SPOPA
C-O	1262	1109 – 1257	1288
C=O	1712	1763	1716
C=C		1599	1599
C-H	2854 – 2926	3091	2926
O-H			3398

SPOPA – Alkyd resin made from Sponge seed and phthalic anhydride.

The stacked spectra of the seed oil, anhydrides, and corresponding alkyd resins produced are shown in Figures 3 and 4. The absence of a hydroxyl (OH) functional group in the seed oil, which is prominent in the alkyd resin at 3398 cm^{-1}, substantiated the success of the synthesized alkyd resin. Similarly, the absence of a hydroxyl (OH) functional group in the maleic and phthalic anhydrides in Tables 5 (SPOPA) and 6 (SPOMA), which were prominent in the alkyd resin at 3398 cm^{-1} and 3431 cm^{-1}, respectively, in Figures 3–4, confirmed the formation of the alkyd resin. For the C-O carboxylic functional group, corresponding peaks were detected in the range of 1109–1288 cm^{-1} for seed oil, maleic anhydride, and SPOPA, whereas the same peaks were observed in the range of 1273 cm^{-1} for SPOMA. For both SPOPA and SPOMA, the C=O carbonyl group was found in 1712–1763 cm^{-1} range. This is in line with (22) about FT-IR characterization of palm oil alkyd resin results.

Table 6: FT-IR spectra Analysis of Sponge seed oil, Maleic anhydride and SPOMA Alkyd Resin.

Functional groups	Frequency of Absorption bands (cm^{-1})		
	Sponge seed oil	Maleic anhydride	SPOMA
C-O	1262	1109 – 1257	1172 – 1273
C=O	1712	1763	1720
C-H	2854 – 2926	3091	2929
O-H			3431

SPOMA – Alkyd resin made from Sponge seed and Maleic anhydride
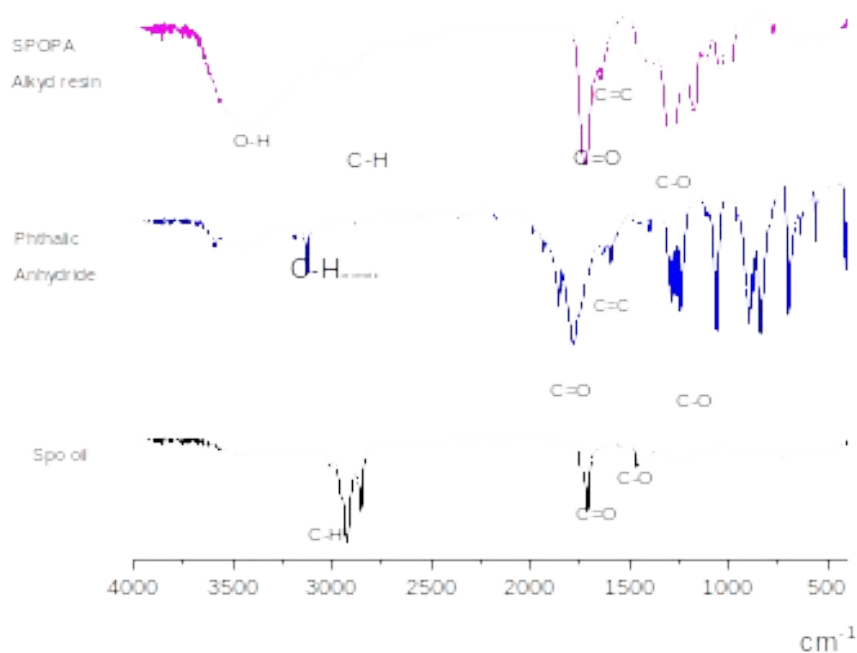
Figure 3: FT-IR Overlaid Spectral of Sponge seed oil, Phthalic anhydride and SPOPA.
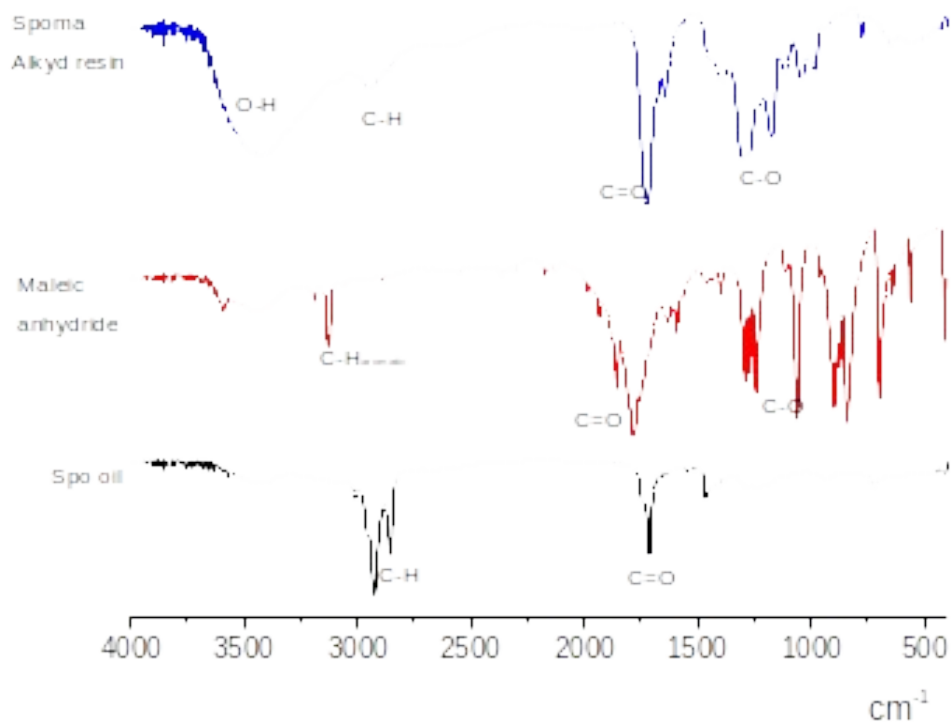
Figure 4: FT-IR Overlaid Spectra of Sponge seed oil, Maleic anhydride and SPOMA.

695

3.5. ¹H and ¹³C NMR Characterization of the Alkyd resins

Figure 5 depicts the structure of SPOPA alkyd resin, while Figure 6 depicts the SPOPA alkyd resin ¹H NMR spectrum with the assignment of the signal indicate in Table 7. The terminal alkyl group protons were confirmed at δ_H 0.85. Protons of all methylene (–CH$_2$) present in the long aliphatic chain are responsible for the strong signals between δ_H 1.24 and 1.38. The chemical shift observed between δ_H 3.38 and δ_H 3.75 is due to the protons connected to the carbon in which the hydroxyl group is attached, whereas the signal observed at δ_H 3.62 is due to

a methylene proton bonded to the carbon in which the hydroxyl group is attached.

The olefinic proton signal in the seed oil was verified in the alkyd resin at a slightly greater chemical shift of δ_H 5.32, attributed to the seed oil's unsaturation. In the same way, the aromatic proton signals in phthalic anhydride were found to exhibit a lower chemical shift signal in the δ_H 7.69–7.88 range. The peaks in the alkyd resins which were absent in the seed oil or anhydride used helps to confirm the SPOPA alkyd resin manufacture. Islam *et al.* (2014) (23), who used ¹H NMR to describe alkyd resin produced from palm oil, reported similar findings.

Where R = fattyl acyl
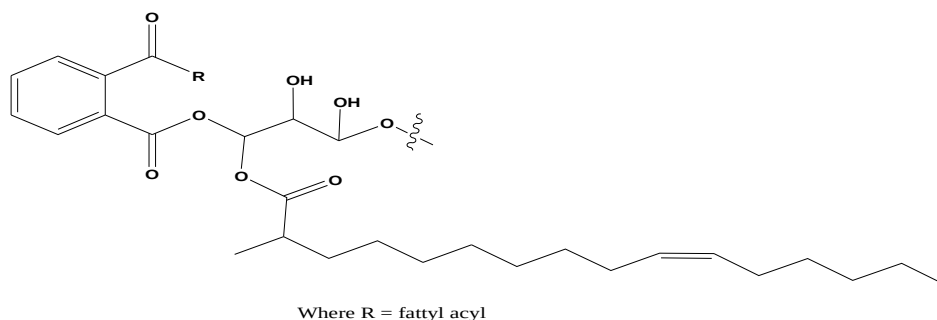
Figure 5: Structure (Proposed) for SPOPA alkyd resin.
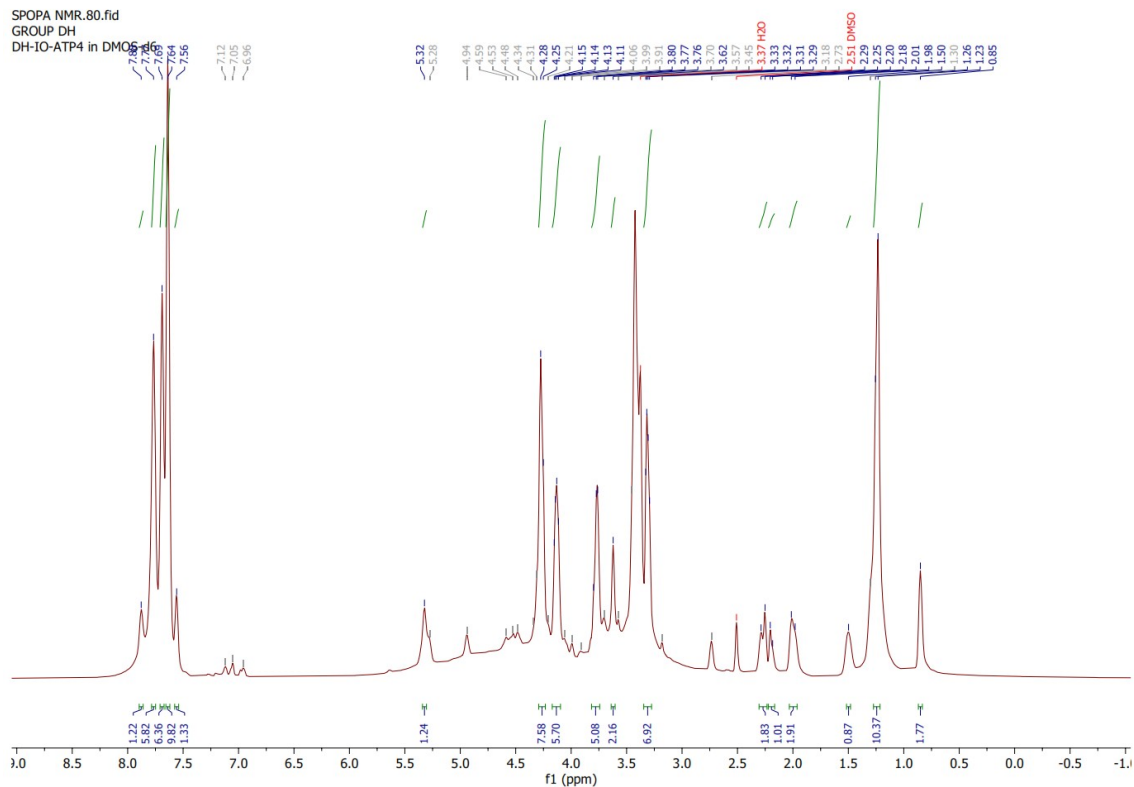
Figure 6: ¹H NMR Spectra of SPOPA Alkyd Resin.

Table 7: ^{1}H NMR Characterization of SPOPA Alkyd Resin.

[1]H Signal (ppm)	Chemical Shift	Assignment
0.85	CH_3	Terminal methyl (Saturated)
1.24 – 1.38	$(CH_2)n$ saturated aliphatic	All acyl chains
2.0	CH_2-OCOR	Bonded to the acyl chain
2.29	CH_2	α- methylene group
3.38	OH	Monotriglycerol
3.62	CH-(OH)	Monotriglycerol
3.75	OH	Monotriglycerol
4.33	CH_2-(OH)	Monotriglycerol
5.32	CH=CH (Olefinic group)	All unsaturated fatty acids
7.69	H-C*C-H	Aromatic ring
7.88	H-C*CH*C-H	Aromatic ring

The ^{13}C NMR spectra of SPOPA Alkyd resin is shown in Figure 7. In Table 8, the signal assignments are listed. At the chemical shift of δ_C 14.2, the signal for the terminal methyl group was confirmed. Due to overlaps of every methylene (–CH_2) present in the long aliphatic chain, strong signals between the area on δ_C 27.00–29.4 are caused. The chemical shift signal between δ_C 63 and δ_C 77.1 is due to the C–O carbon of esters or carboxylic groups, whereas the signal between δ_C 131.67 and 132.7 is due to the C=C on the benzene ring of the phthalic anhydride component of the alkyd resin. The presence of C=C in linoleic and vaccenic acids discovered in the fatty acid component of the alkyd resin can also be attributable to this finding. The presence of carbonyl (C=O) signals at δ_C 167.8, 168.6, and 168.9 indicates the formation of esters, thus confirming successful formation of the SPOPA alkyd resin. The absence of a signal at or above δ_C 180 indicated the absence of carboxylic acids, implying that all of the C=O in the fatty acids of the oil had been successfully converted to ester. Kanai *et al.* (2007) (24), who used ^{13}C NMR to describe alkyd resin produced from soybean oil, found similar results.

Figure 8 corresponds to the proposed structure of SPOMA alkyd resin, while Figure 9 corresponds to the SPOMA alkyd resin ^{1}H NMR spectrum with the signal assignment reported in Table 9. In the chemical shift of δ_H 0.84, was assigned to the terminal alkyl group. methylene (–CH_2) protons in the long aliphatic chain are responsible for the prominent signals at δ_H 1.24–1.48. The δ_H 3.34 and 3.64 signal was due to a proton on the monotriglycerol hydroxyl group, while the signal at δ_H 3.54, 4.19, and 4.42 are due to methine and methylene protons linked to the carbon in which the hydroxyl group is connected. Similarly, the vinyl protons in maleic anhydride were observed at δ_H 6.63–6.67. The peaks in the alkyd resins that were absent in the seed oil and anhydride help confirm the SPOMA alkyd resin formation and the data were consistent with literature (25) wherein ^{1}H NMR were adopted for the characterization of alkyd resin produced from sunflower seed oil.

The ^{13}C NMR spectra of SPOMA alkyd resin is shown in Figure 10 with the signal assignment in Table 10. The methylene carbon signal (–CH_2) found in the long aliphatic chain is responsible for the prominent signals at δ_C 31.35 ppm. The chemical shifts between δ_C 60.1–72.9 ppm are due to methylene carbon bound to the hydroxyl component on the glycerol chain, while the signal at δ_C 132.9–135.5 ppm are due to the methine carbons on the benzene ring of the maleic anhydride component of the alkyd resin. The carbonyl (C=O) signals at δ_C 164.6–166.2 indicate the formation of an ester and aid in the confirmation of SPOMA alkyd resin synthesis. The absence of a signal at δ_C 180 ppm for carbonyl carbon indicates the absence of carboxylic acids, which implies a successfully conversion of the fatty acids carboxylic in the oil to ester. This is consistent with the literature report (26).
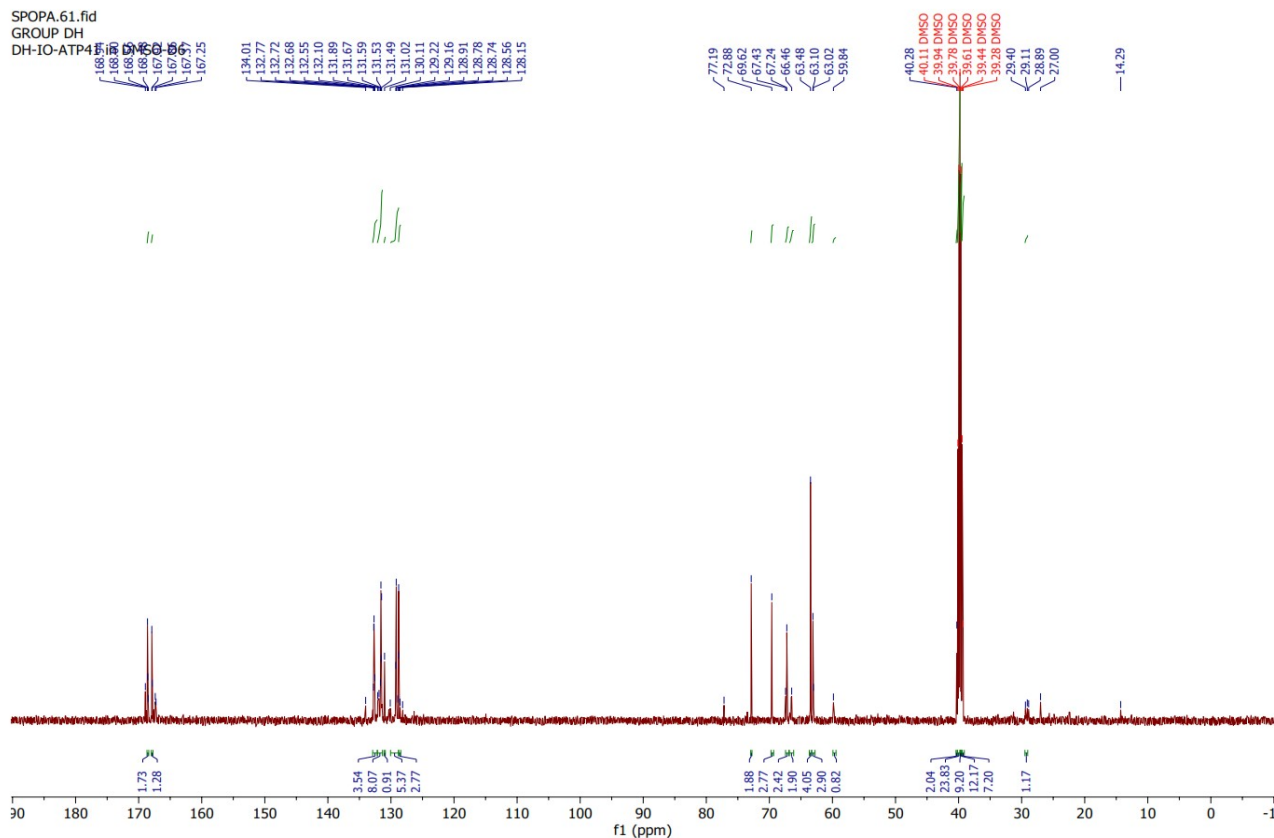
Figure 7: ^{13}C NMR Spectrum of SPOPA Alkyd Resin.

Table 8: ^{13}C NMR Characterization of SPOPA Alkyd Resin.

^{13}C Signal (ppm)	Chemical Shift	Type of Carbon	Assignment
14.2	$\underline{C}H_3$	Methyl	Terminal methyl
27.0 – 29.4	$\underline{C}H_2$	Methylene	
63.0 – 77.1	$\underline{C}H_2$-OH	Methylene	Monoglycerol chain
131.6 – 132.7	$\underline{C}H$	Methine	Benzene ring and Vinyl carbon
167.8	$\underline{C}$=O	Carbonyl	Ester
168.6	$\underline{C}$=O	Carbonyl	Ester
168.9	$\underline{C}$=O	Carbonyl	Ester

Where R = fattyl acyl
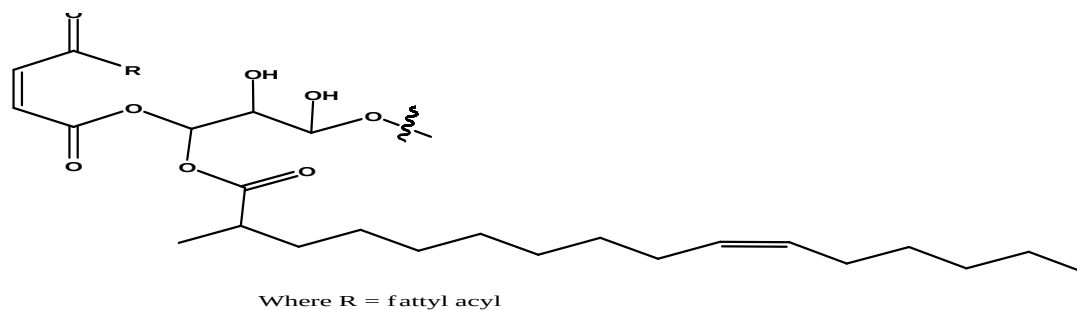
Figure 8: Structures (Proposed) for SPOMA alkyd Resin.

Figure 9: ^{1}H NMR Spectra of SPOMA Alkyd Resin.

Table 9: ^{1}H NMR Characterization of SPOMA Alkyd Resin.

[1]H Signal (ppm)	Chemical Shift	Assignment
0.84	CH_3	Terminal methyl (Saturated)
1.24 – 1.48	$(CH_2)n$ saturated aliphatic	Acyl chains
1.97	$CH_2CH=CH$	Unsaturated acyl chains
2.47	CH_2-OCOR	Bonded to the acyl chain
2.60 – 2.74	CH_2	α- methylene group
3.34	OH	Monotriglycerol
3.54	CH-(OH)	Monotriglycerol
3.64	OH	Monotriglycerol
4.19 - 4.42	CH_2-(OH)	Monotriglycerol
5.42	CH=CH (Olefinic group)	Unsaturated fatty acids
6.63 – 6.67	HC=C-H	Vinyl chain (Maleic anhydride)

Figure 10: ^{13}C NMR Spectrum of SPOMA Alkyd Resin.

Table 10: ^{13}C NMR Characterization of SPOMA Alkyd Resin.

^{13}C NMR Signal (ppm)	Chemical Shift	Type of Carbon	Assignment
31.3	$\underline{C}H_2$	Methylene	
60.1 – 72.9	$\underline{C}H_2$-OH	Methylene	Monoglycerol chain
132.9 – 135.5	$\underline{C}H=\underline{C}H$	Methine	Maleic chain
164.6 – 166.2	$\underline{C}=O$	Carbonyl	Ester

4. CONCLUSION

To minimize domestic and industrial rivalry for vegetable oils in Nigeria, alkyd resins were successfully synthesized using standard analytical techniques from underutilized seeds of *Luffa aegyptiaca*. The prepared alkyd outperformed the commercial alkyd used as a control sample for some parameter. Both prepared alkyds have higher total solids (89.42% for SPOPA and 94.37% for SPOMA), while the commercial alkyd employed as a control had a total solid content of 51.56 percent. The modified products were confirmed using fourier transform infrared spectroscopy (FT-IR), ultraviolet-visible spectroscopy (UV–visible), ^{1}H nuclear magnetic resonance (^{1}H NMR), and ^{13}C nuclear magnetic resonance (^{13}C NMR) spectroscopy. The study found that alkyd resin could be made cheaply from sponge seed oil thereby freeing up more conventional vegetable oil for human use and lowering domestic-industrial competition for vegetable oil, especially in developing countries where the seed are produced in abundance annually.

5. CONFLICT OF INTEREST

Authors declare no conflict of interest.

6. ACKNOWLEDGMENTS

7. REFERENCES

1.　　Akintayo E. Characteristics and composition of Parkia biglobbossa and Jatropha curcas oils and cakes. Biores technol. 2004;92(3):307-10. Available from: <u><DOI></u>.

2. Stephens J. Gourd Luffa-Luffa cylindrical, Luffaaegyptica and Luffaacutangula. J Hortic Sci Univ Florida. 2003;3:19-21. Available from: <URL>.

3. Udo GJ, Etesin UM, Awaka-Ama JJ, Nyong AE, Uwanta EJ. GCMS and FTIR Spectroscopy Characterization of Luffa Cylindrica Seed Oil and Biodiesel Produced from the oil. Commun Phys Sci. 2010;5(1,2,3): 378-90. Available from: <URL>.

4. Elemo GN, Elemo BO, Erukainure OL. Characterization of sponge gourd (Luffa aegyptiaca Mill.) seed oil. J Trop Agric. 2011;49:128-30. Available from: <URL>.

5. Oli C, Onuegbu T, Ezeudu E. Proximate composition, characterization and spectroscopic analysis of Luffa aegyptiaca Seed. Int J Life Sci Biotechnol Pharma Res. 2014;3(4):194. Available from: <URL>.

6. Khot SN, Lascala JJ, Can E, Morye SS, Williams GI, Palmese GR, et al. Development and application of triglyceride-based polymers and composites. J Appl Polym Sci. 2001;82(3):703-23. Available from: <DOI>.

7. Harry-O'Kuru R, Holser R, Abbott T, Weisleder D. Synthesis and characteristics of polyhydroxy triglycerides from milkweed oil. Ind Crop Prod. 2002;15(1):51-8. Available from: <DOI>.

8. Atolani O, Olabiyi ET, Issa AA, Azeez HT, Onoja EG, Ibrahim SO, et al. Green synthesis and characterisation of natural antiseptic soaps from the oils of underutilised tropical seed. Sust Chem Pharm. 2016;4:32-9. Available from: <DOI>.

9. Zubair MF, Atolani O, Ibrahim SO, Oguntoye OS, Abdulrahim HA, Oyegoke RA, et al. Chemical and biological evaluations of potent antiseptic cosmetic products obtained from Momordica charantia seed oil. Sust Chem Pharm. 2018;9:35-41. Available from: <DOI>.

10. Otabor G, Ifijen I, Mohammed F, Aigbodion A, Ikhuoria E. Alkyd resin from rubber seed oil/linseed oil blend: a comparative study of the physiochemical properties. Heliyon. 2019;5(5):e01621. Available from: <DOI>.

11. Kyenge B, Anhwange B, Ageh J, Igbum G. Comparative analysis of soybean seed oil modified alkyd resin and epoxidized soybean seed oil modified alkyd resin. Int J Modern Org Chem. 2012;1(2):66-71. Available from: <URL>.

12. Bora MM, Gogoi P, Deka DC, Kakati DK. Synthesis and characterization of yellow oleander (Thevetia peruviana) seed oil-based alkyd resin. Ind Crop Prod. 2014;52:721-8. Available from: <DOI>.

13. Nway N, Mya M. Manufacture of alkyd resin from castor oil. Proc Word Acad Sci Eng Technol. 2008;36:928-34. Available from: <URL>.

14. Dhole G, Gunasekaran G, Singh S, Vinjamur M. Smart corrosion sensing phenanthroline modified alkyd coatings. Prof Org Coat. 2015;89:8-16. Available from: <DOI>.

15. Jain RM, Mody K, Mishra A, Jha B. Physicochemical characterization of biosurfactant and its potential to remove oil from soil and cotton cloth. Carbohyd polym. 2012;89(4):1110-6. Available from: <DOI>.

16. Hlaing NN, Oo MM. Manufacture of alkyd resin from castor oil. World Acad Sci Eng Technol. 2008;48:155-61. Available from: <URL>.

17. Patil DM, Phalak GA, Mhaske ST. Design and synthesis of bio-based epoxidized alkyd resin for anti-corrosive coating application. Iran Polym J. 2018;27(10):709-19. Available from: <DOI>.

18. Ikhuoria EU, Aigbodion AI, Okieimen FE. Enhancing the quality of alkyd resins using methyl esters of rubber seed oil. Trop J Pharm Res. 2004;3(1):311-7. Available from: <URL>.

19. Spasojević P, Panić V, Džunuzović J, Marinković AD, Woortman A, Loos K, et al. High performance alkyd resins synthesized from postconsumer PET bottles. RSC Adv. 2015;5(76):62273-83. Available from: <DOI>.

20. Ramli MF, Gan SN, Lim WH, Phang SW. Application of a palm oil-based alkyd for the improvement of polyaniline properties. Polym Polym Compos. 2017;25(7):537-44. Available from: <DOI>.

21. Mahdavi R, Ashraf Talesh S. Experimental Investigation of Enhanced Self cleaning Properties of Alkyd Resin by Modified Zinc Oxide Nanoparticles. Nanoscale. 2018;5(1):73-81. Available from: <URL>.

22. Issam A, Cheun C. A study of the effect of palm oil on the properties of a new alkyd resin. Malay Polym J. 2009;4(1):42-9. Available from: <URL>.

23. Islam MR, Beg MDH, Jamari SS. Alkyd based resin from non-drying oil. Procedia Eng. 2014;90:78-88. Available from: <DOI>.

24. Kanai T, Mahato T, Kumar D. Synthesis and characterization of novel silicone acrylate–soya alkyd resin as binder for long life exterior coatings. Prog Org Coat. 2007;58(4):259-64. Available from: <DOI>.

25. Chiplunkar PP, Pratap AP. Utilization of sunflower acid oil for synthesis of alkyd resin. Prog Org Coat. 2016;93:61-7. Available from: <DOI>.

26. Uschanov P, Heiskanen N, Mononen P, Maunu SL, Koskimies S. Synthesis and characterization of tall oil fatty acids-based alkyd resins and alkyd–acrylate copolymers. Prog Org Coat. 2008;63(1):92-9. Available from: <DOI>.

Conductometric, Spectrophotometric, and Computational Investigation of Binary and Ternary Complexes of Co(II) and Cu(II) Bivalent Metal Ions with L-Valine Amino Acid and Paracetamol Drug

Aisha A. Al-Abbasi*[1] iD **, Mohamed Zidan[1], Nouria Shnin[1] and Bakr Aldoori[2]**

[1] Department of Chemistry, Faculty of Science/ Sebha University, Sebha, Libya
[2] Department of Chemistry, Faculty of Science/ Selcuk University, Konya, Turkey

Abstract: The conductivity and spectrophotometry techniques were employed to evaluate the binary and ternary complexes of the divalent metal ions Co(II) and Cu(II) with the physiologically relevant amino acid L-Valine (Val) and the analgesic paracetamol. The conductivity experiments were generated by direct conductivity equation from conductivity titration data, while the spectrophotometry experiments were performed using the continuous variations approach (Job's method). Both techniques were accomplished in an aqueous solution with a constant concentration of 0.004 M of divalent metal ions at (40.0 ± 0.1) °C. The binary complexes of Co(II) and Cu(II) have a 1:1 binding ratio of metal to paracetamol (M:para). However, the binary complexes of Co(II) and Cu(II) have metal: Val binding ratios of either 1:1 or 2:1. In addition, the Cu(II) binary complexes of both ligands have a higher stability constant than Co(II) binary complexes of paracetamol and Val ligands, which was in good agreement with the Rossotti-Willime order. The ternary complexes of Co(II) and Cu(II) have a 1:1:1 binding ratio of metal to paracetamol: L-valine, (M:para:Val). The stability constants were in order: The ternary metal complexes > The binary metal-L-Val complexes > The binary metal-para complexes. DFT (Density Functional Theory) simulations were used in order to gain a better understanding of the molecular interactions of Co(II) and Cu(II) divalent metal ions with L-Val and paracetamol. Calculations were made on the electronic structure, HOMOs and LUMOs, and molecular geometry of complexes and their corresponding ligands. The findings unequivocally demonstrate that the metal ion is bound to both the amide nitrogen in the paracetamol ligand and the oxygen atom of the carbonyl group. Moreover, the metal ion is bound to the nitrogen atom of the amine NH_2 group and the oxygen atom of the hydroxyl group for the L-Val ligand.

1. INTRODUCTION

Metal ions are required for the survival of all living organisms, including humans, animals, and plants. Their lack can contribute to diseases, tumorigenesis, or death. They further play a crucial role in the effective functioning of muscles and nerve cells, the central nervous system, the heart, and a variety of natural processes. Because of their unique electronic and stereochemical characteristics, as

well as their distinct molecular geometries (which organic molecules cannot easily access) and ligand transfer, oxidation/reduction, catalytic, and photochemical reactions, metal complexes are extensively utilized in the chemical and physical sciences. Such compounds can interact with biological macromolecules in different manners and therefore by different pathways of reactions (1). In addition, this field has important implications in many other sciences, ranging from medicine to the environment, where initial transition series play an important role in biological processes in many treatments related to humans, and the environment, for example, Ni(II), Cu(II) and Co(II) ions are important in the fields of drugs and clinical applications such as fungal (2), bacterial (3), and cancer inhibitors treatments (4). These transitional metals can form coordination compounds with ligands due to the presence of partially empty d orbital and ligands found either at the active sites or as structural components of several enzymes (5). Amino acids can be both free and bound, similar to a living creature. The bound amino acids are integrated into proteins or other molecular and cellular functional structures, and enzymes and polypeptide hormones direct and control metabolism in the body. The number and sequence of amino acids in a polypeptide chain or chains of a protein, starting with the free amino group and sustained by peptide bonds that link up each amino acid to the

next, governs how many amino acids are prevalent in the chain or chains (6). However, some free amino acids bind to metallic materials in the human body as bidentate, in which they can bind via (S, N), (N, O), or (S, O) donor atoms due to the body's acid-basic behavior (7-10). One such example is L-Val Figure 1, which demonstrates that the positively charged NH_3^+ group or the negatively charged COO^- group can behave externally as an acid or a base (11, 12), and L-Val is one of the 20 amino acids that go into making proteins. It is also an essential amino acid and a glycogen amino acid for mammals (13).

Numerous investigations are being made to determine how metal binding affects the activities of human biological processes (14, 15). For example, Paracetamol has two functional groups (NH amide / OH phenol) as in Figure 1, B, thus acting as a ligand with metal ions after entering the human body. In addition, It is used as a treatment for headaches and toothache, an antipyretic (non-narcotic) and fever for children after vaccination for children, and treatment for migraine attacks to moderate strength, cases of arthritis, and pains (16). However, unlike other combinations, paracetamol is not considered carcinogenic at the therapeutic dose. Also, it is not generally classified as a Non-steroidal Anti-inflammatory drug (NSAID) because it exhibits only weak anti-inflammatory activity (17).
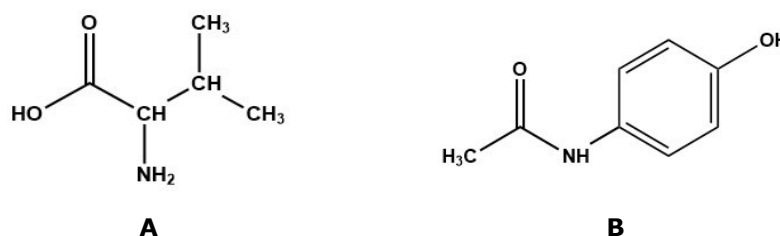
Figure 1: A. Structure of L-Val (chemically 2-amino-3-methyl butanoic acid). B. Structure of Para (chemically N-(4-Hydroxy phenyl) acetamide).

In a recently published paper by our group, the potentiometric method was used to determine the stability constant of Co(II) and Cu(II) binary and ternary complexes of L-Val ligands (18, 19). Thus, the present paper deals with the determination of the formation constants and the binding ratio of the binary and ternary complexes formed by Co(II) and Cu(II) with L-Val and Para using the conductometric and the spectrophotometric methods at (40 ± 0.1 °C) temperature. The method of conductometric (20, 21) as adopted by the direct conductivity method has been employed to determine K values, while the spectrophotometric using the continuous variation method has been employed to determine K values and binding ratio for the binary ligands-metal complexes (21-23).

2. EXPERIMENTAL SECTION

2.1. Materials and Methods
All the compounds used in this research were of the finest quality and analytical grade quality (AR). Valine (Fluka, >99%), paracetamol (CCM (Malaysia), 99.5%), metal salts including $CuCl_2.2H_2O$ (T-Baker lab chemicals, ≥99.99%), $CoCl_2.4H_2O$ (Surechem Products, 98%), sodium hydroxide (Shandong, 98.8%). The pH-conductivity meter (Thermo Electron/Orion4star /USA, with an accuracy of 0.002 and a cell constant equal to 0.55 cm^{-1}) was used to perform the conductometric procedure. before each titration, the conductivity meter was calibrated using a buffer solution

containing NaCl at concentrations of 1413 S/cm and 12.9 mS/cm. A Grant Instruments (Cambridge) Ltd/SUB28 Thermostat Water Bath Apparatus maintained the temperature constant (± 0.1). Spectrophotometric methods were recorded on UV/Visible spectrophotometer in the range of 200 to 800 nm.

2.2. Solutions and Procedure
The stock solution of L-Val (0.02 M) was freshly made by accurately diluting 0.9372 g of solution with a small portion of deionized water. The precise quantity (0.3023 g) of Para was dissolved in deionized water to formulate a stock solution (0.02 M), The required amount of each metal salt of 0.4754 g Co(II) and 0.3409 g Cu(II) were solubilized in distilled deionized water to prepare the stock solution. EDTA titrations were employed to calibrate the metal's salt final concentration. The experiment involves titrating 40 ml of each metal ion (4×10^{-3} M) with (2×10^{-2} M) of Para and (4×10^{-3} M) with (2×10^{-2} M) of L-Val solution in 1 mL intervals utilizing the conductometric technique at 313.15 K temperature. By multiplying the specific conductance values by a factor of (40+V)/40, where V is the volume of titrating added. According to the requirements of Job's approach, stock solutions of the ligand (4×10^{-3} M) and metal (4×10^{-3} M) were made for use in spectrophotometric methods. The total number of moles of metal plus the total number of moles of ligand were held constant in a series of flasks. First, the absorbance values were recorded after filling one of the cells with water as a reference and the other with an experimental solution. All measurements were performed using the same cells.

2.3. Molecular Reactivity
The structure of the studied binary complexes, the molecular geometry, HOMO and LUMO orbitals, and the active sites in ligands which will coordinate to the metal ion, the electronic structures and binding energies were calculated at the DFT level with DMol^3 using the Materials Studio suite of programs (version 5.5). Structure optimization calculations were performed using a generalized gradient approximation (GGA) function (24, 25) and a hybrid exchange–correlation function (Becke-Lee-Yang-Parr) BLYP (26, 27) with a double numeric plus polarization (DNP) basis set to map the orbital structure of the compound. Frontier molecular orbitals (HOMO and LUMO and the energy gap between them (ΔE) are used to predict the bonding atoms of the ligands molecules.

3. RESULTS AND DISCUSSION

3.1. Conductometric Method
3.1.1. Conductometric method of binary complexes
The formation constants for each metal in the stoichiometric binary Para-metal or L-Val-metal complexes were calculated using the experimental data of (Λm). The formation constants for each metal in the stoichiometric binary Para-metal or L-Val-metal complexes were calculated using the experimental data of (Λm). By graphing the correlation between the molar ratio of ligand to metal (L/M) concentrations and the molar conductance (Λm), seen in Figure 2, different lines are established, with sharp breaks reflecting the formation of a 1:1 or 1:2 (L:M) stoichiometric ratio.
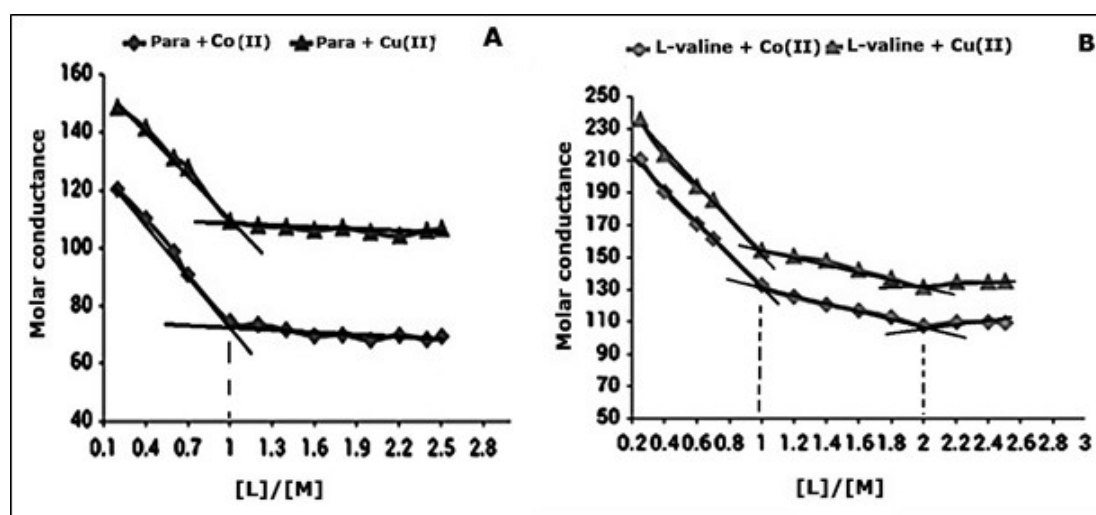
Figure 2. The relation between Λm and [L/M], A) Para-M(ll) and B) L-Val-M(ll) at 313.15 K.

The conductivity is decreased as concentration increased, and that, all solutions behave as Weak Electrolytes or natural. The formation constants (Kf) for binary Para + metal and L-Val + metal complexes were calculated for each metal of

complexes (1:1) or (2:1) (L: M) by using the Eq. 1-   3 (8, 20, 28):

For 1:1

$$K_f = \frac{[ML]}{[M][L]} = \frac{(\Lambda_M - \Lambda_{obs})}{(\Lambda_{obs} - \Lambda_{ML}) \times [L]} \tag{1}$$

For 2:1

$$K_f = \frac{[ML]}{[M][L]^2} = \frac{(\Lambda_M - \Lambda_{obs})}{(\Lambda_{obs} - \Lambda_{ML}) \times [L]^2} \tag{2}$$

In (1) and (2), the following equation will be used:

$$[L] = C_L - \left[C_M + \frac{(\Lambda_M - \Lambda_{obs})}{(\Lambda_M - \Lambda_{ML})} \right] \times [L] \tag{3}$$

Where Λ_m is the limiting molar conductance of the metal salt alone, Λ_{obs} is the molar conductance of solution during titration, and Λ_{mL} is the molar conductance of the complex. The obtained values

(K_f) for metal-ligand stoichiometric complexes are presented in (Table 1). The data show that binary Cu(ll) complexes are more stable (favoured) than binary Co(ll) complexes.

Table 1: Formation constants for 1:1 and 2:1 (L/M) (Para-Metal) and (L-Val-Metal) complexes in distilled water at 313.15 K.

Metal ion (M)	$K_{f\,(Para-M)(1:1)}$	$K_{f\,(L-Val-M)(1:1)}$	$K_{f\,(L-Val-M)(2:1)}$
Co(II)	3.717 ± 0.56	8.401 ± 0.49181	2.783 ± 0.6493
Cu(II)	4.09 ± 0.95	9.342± 0.49532	2.982 ± 0.4062

3.1.2. Conductometric method of ternary complexes
There were no derived lows to calculate the stability constant of the ternary complex by the conductivity method. Therefore, the electrolyte behavior of formed ternary metal complexes will be only disused here. The specific conductance values (K_s) of 0.004 M metal solution were measured experimentally in the presence of 0.004M ligand at 313.15 K. The molar conductance (Λ_m) values were calculated. The

limiting molar conductance (Λ_o) at infinite dilutions were estimated for all solutions of ternary metal complexes by extrapolating the relation between Λ_m (S.Cm^2.mol^{-1}) and $C_m^{1/2}$ to zero concentration Figure 3. The conductivity decreases with increased concentration. Moreover, the conductivity values for Cu(II)-L-Val-Para complexes are greater than that for Co(II)-L-Val-Para.
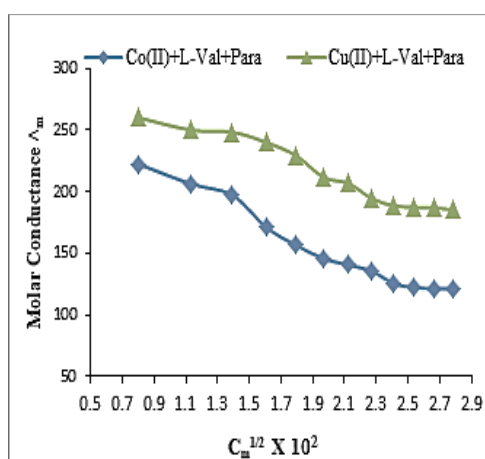
Figure 3: $C_m^{1/2}$ versus molar conductivity of metal- L-Val-Para complexes at 313.15 K.
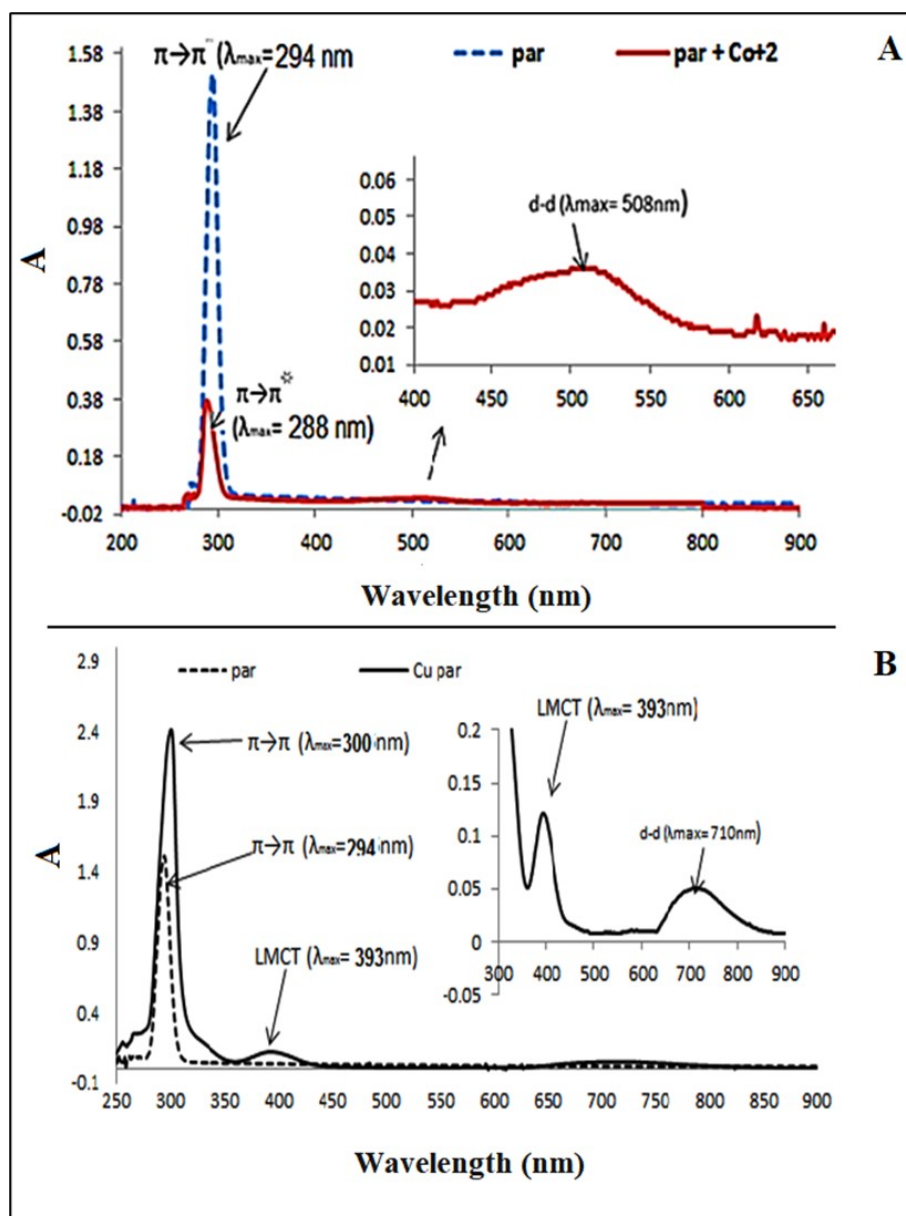
Figure 4: UV-Vis spectrum of A) Para+Co(ll) and B) Para+Cu(ll) complexes.

3.2. Spectrophotometric Measurements

This method is based on the absorption of visible and ultraviolet light by the molecules of the substance in the solution. The absorption of visible and ultraviolet radiation by chemical systems leads to the transition of one or more electrons in low-energy orbits (stability level) to high energy levels (the level of irritability). It should be noted that the nature of the electrons in the molecule is responsible for the extent to which the molecule can be absorbed in the visual and violet fields (29).

3.2.1. Para-Metal complexes

The UV spectra of Paracetamol demonstrated an absorption peak of the complex at the site (294 nm), which resulted from the electronic (π→π*) type excitation of it extended the π-conjugation system.

Upon light absorption, an π electron is excited from the ground state to the first excited state, and new absorption peaks of the formed complex (Para-M(II)) ions have been attributed to the d→d transition (17), as shown in (Table 2 and Figure 4).

The free ligand has an absorption maximum (λ_{max}) wavelength of around 294 nm depending on the solvent. Upon chelating with Co(II) ions, the absorption maxima (λ_{max}) were shifted to 288 nm and 510 nm, while chelating with Cu(II) ions, the absorption maxima (λ_{max}) were shifted to 300 nm, 393 nm, and 710 nm (20).

Job's method of continuous variation (20, 21), which is straightforward, quick, measurable, and

valid, was employed to ascertain the stoichiometry and formation constants of Para-metal(ll) complexes by spectrophotometry. Metals and Para were mixed in various ratios ranging from 0.188:1 to 1:0.188, and the absorbance of each mixture was measured at the complexes' maxima (17, 21).

The maximum absorbance was obtained at XL= 0.5-0.55, demonstrating that the stoichiometric ratio for the complexation of metals and Para is 1:1 as depicted in Figure 5. The graph of absorbance against molar ratios displays inflections correlating to different stoichiometries of the complexes.

Table 2: Electronic spectral data of Para ligand and its complexes formed at (0.004 M) and 313.15 K.

Assignment	(λ_{max})nm	Complex
$\pi \rightarrow \pi^*$	294	Para ligand
$\pi \rightarrow \pi^*$	288	(Para+Co(II))
$d \rightarrow d$	510	
$\pi \rightarrow \pi^*$	300	
$lmct$	393	(Para+Cu(II))
$d \rightarrow d$	710	
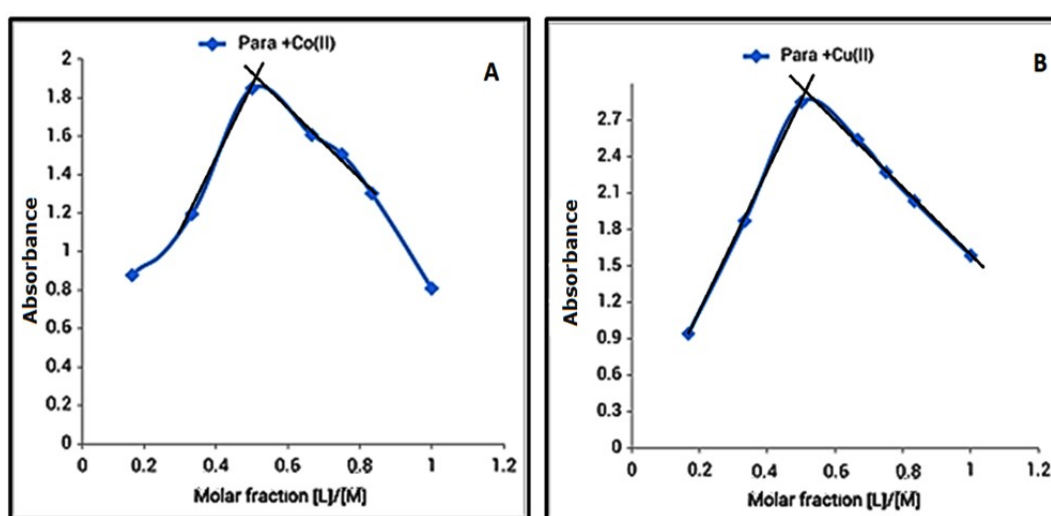
Figure 5. The Job's plot of absorbance at λ_{max} versus the molar fraction of metal ions with Para
A) Para+Co(ll), B) Para+Cu(ll).

$$M + nL \rightleftarrows ML_n \qquad (4)$$

$$K = frac(1-\alpha)C(\alpha C)(\alpha C) \rightarrow K = frac\ 1 - \alpha\ \alpha^2 C \qquad (5)$$

The formation constants are measured spectrophotometrically by measuring the absorbance of several sets of solutions of the metal salts Co(II) and Cu(II) and the ligands (Para and L-Val). The correlation seen in Eqs. 4 and 5 was employed to determine the amount of production of each complex, where K_f = formation constant. The

dissociation degree is given in α and C is the concentration, α = A_m - A_s/A_m, the absorbance of a solution containing an excess and a stoichiometric quantity of reagent is represented by A_m and A_s, respectively. Calculated K_f values for the prepared complexes are recorded below in (Table 3).

Table 3: Formation constants for 1:1 (L/M) Para-metal complexes in distilled water at 313.15 K.

Metal complexes	α	K_f
(Para+Co(II))	0.209	3.654
(Para+Cu(II))	0.145	4.007

3.2.2. L-Val-Metal complexes
The UV spectra of L-Val showed an absorption peak at the site (229 nm) which was due to (п→п*) transition, and an absorption peak at (250 nm) which was due to (n→п*) transition (11). The occurrence of displacement at the site of this summit was found in the composition of the complex consisting of (L-Val+M(ll)), which confirms the consistency between L-Val and M(ll). As well as the emergence of new absorption peaks of the formed complex (L-Val+M(ll)) due to the d → d transition as shown in (Table 4) and Figure 6.

Table 4: Electronic spectral data of L-Val ligand and its complexes formed at (0.004 M).

Assignment	(λ)nm	Complex
п→п*	229	L-Val ligand
n→п*	250	
п→п*	219	(L-Val+Co(II))
n→п*	228	
d→d	510	
п→п*	229	(L-Val+Cu(II))
n→п*	245	
d→d	700	

The determination of stoichiometry and formation constants of L-Val-Metal complexes by spectrophotometry was based on Job's method of continuous variation (21-23). The maximum absorbance was observed at XL=0.66–0.7, confirming that the stoichiometric ratio for the complexation of metals and Val is 1:2 as shown in Figure 7. The plot of absorbance against molar ratios reveals inflections corresponding to different stoichiometries of the complex.

By measuring the absorbance of two sets of solutions at λ_{max} (30), it could spectrophotometrically estimate the formation constants. The relationship seen in Equations 4 and 5 (21) was employed to determine the amount of formation of each complex (31). The prepared complexes' estimated K_f values are presented in Table 5 below.
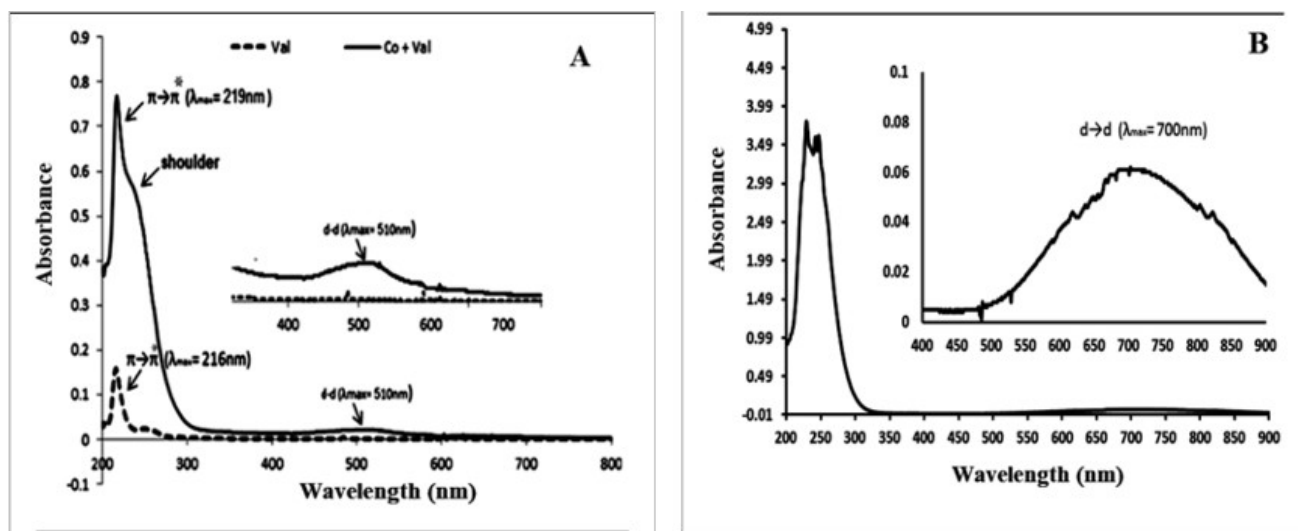
Figure 6: UV-Vis spectrum of A) Val+Co(ll) and B) Val+Cu(ll) complexes.
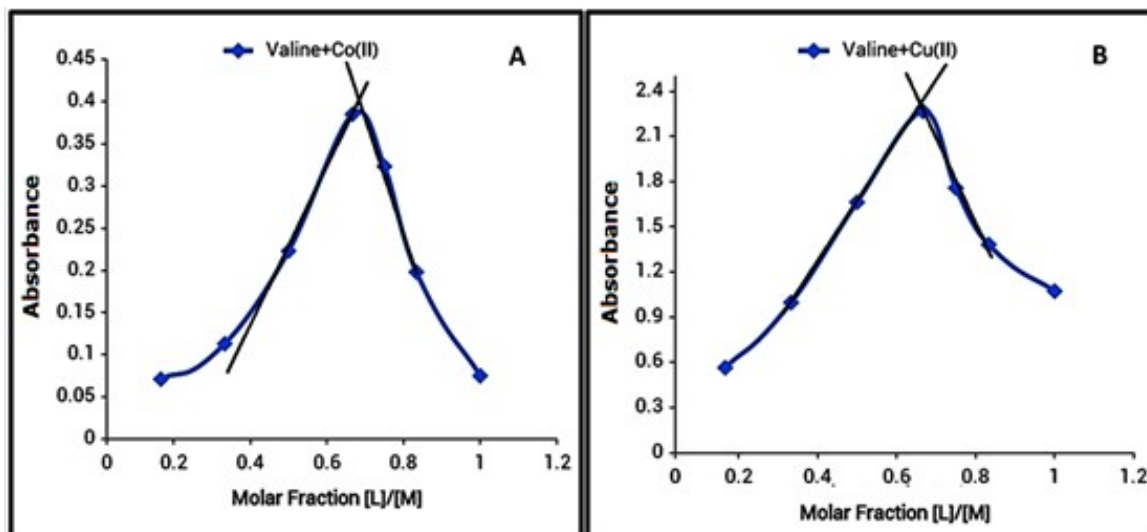
Figure 7: The Job's plot of absorbance at λ_{max} versus the molar fraction of metal ions with A) L-Val+Co(ll), B) L-Val+Cu(ll).

The data show that binary Cu(ll) complexes are more stable than binary Co(ll) complexes, these results were noted great with data of the conductometric method.

Table 5: Formation constants for 1:2 (M/L) L-Val complexes in distilled water at 313.15 K.

Metal complexes	α	K_f
(L-Val+Co(II))	0.476	2.763
(L-Val+Cu(II))	0.392	2.996

3.2.3. Spectrophotometric measurements of M-L-Val-Para complexes

There were no derived lows to calculate the stability constant of the ternary complex by the spectropho-tometry method. Therefore, the electronic spectra of formed ternary metal complexes will be only discussed here. The UV–Vis absorption spectra of [Co(L-Val)(Para)] and [Cu(L-Val)(Para)] show a $d{\to}d$ maximum at 678 and 747 nm, respectively, in the visible range of the spectrum (see Figure 8). However, The maximum absorption in the UV range was 308, 308, 316 for [Co(Para)(L-Val)], [Ni(Para)(L-Val)] and [Cu(Para)(L-Val)], respectively. These transitions were assigned to a $\pi{\to}\pi$ mixed with $n{\to}\pi$ transitions from the coordinate ligands, which red-shifted upon coordination as shown in Table 6.
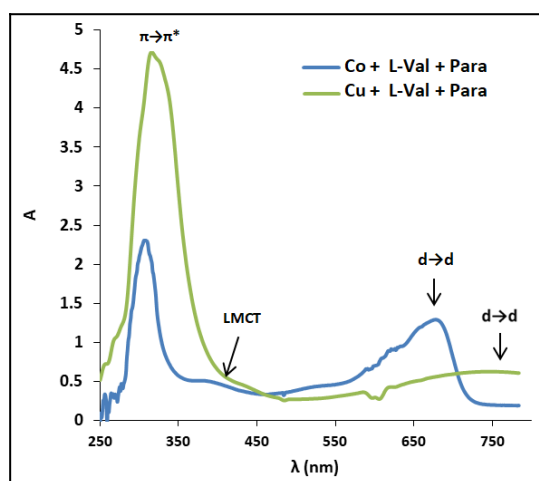
Figure 8: The spectrum of the maximum wavelength of M-L-Val-Para complexes.

710

Table 6: Results of measurements of the electronic spectra of ligands and M-L-Val-Para complexes formed at (0.004 M) and 313.15 K.

Ternary Complexes 1:1:1	λ_{max}	Assignment
Co + L-Val + Para	308	п→п*
	377	LMCT
	678	d→d
Cu + L-Val +Para	316	*п→п
	747	d→d

3.3. The Role of the Structure of the Binary and Ternary Complexes

Coordination substances have certain bond types and structures. A large number of compounds found in nature are categorised as coordination substances due to their structure, characteristics, and biological action. As a lot of distinct ligands are anticipated to compete for metal ions in vivo, binary and ternary complexes (Mixed ligand complexes) play a significant role in biological chemistry. This is because mixed chelation is common in biological fluids. Coordination compounds with biological activity include haemoglobin, myoglobin, and vitamin B_{12} as well as enzymes that contain metals. It is common practise to dissolve renal and the gallbladder stones in the bladder utilising a particular class of chemicals that have the capacity to form complexes with several cations. Because they bind the metal ions that catalyse oxidation reactions, they are utilised as stabilisers in blood conservation. They operate as stabilisers in the maintenance of blood because they bind the metal ions that catalyse oxidation reactions. Additionally, they are utilised to cleanse the body of radioactive isotopes and harmful metal ions. The largest stability constant, which is the strongest and most stable, is typically what determines whether a binary or ternary complex forms. And they depend on the geometry and configuration of the metal and the ligand. The distinctive properties of metal ions, such as their tiny size, positive charge, and electron spin configuration, enable them to carry out a wide range of biofunctions (32, 33). However, the ligand's nature, the chelating activity, and the macrocyclic effect The stability of binary and ternary complexes is also impacted by steric or steric hindrance effects.

Amino acids, Paracetamol, and its derivatives are some of these ligands. Leach and Angelici (34) described a Cu(II) combination with a wide range of L-amino acid affinities. According to a set of stability constants calculated by potentiometry, Cu(II) forms stronger complexes with L-leucine, L-phenylalanine, alanine, L-serine, and valine than with the respective antipodes. Complexes of Mn(II), Fe(II),

Co(II), Ni(II), Cu(II), and Cd(II) ions with L-valine as a main ligand and 1,10-phenanthroline as a secondary ligand had been created by Noori et al. (35). According to the research, Co(II) has an octahedral geometry. Six unique mixed ligand complexes of metals(II) were synthesised by Fayad et al. (36) employing saccharin and l-valine as primary and secondary ligands, respectively. In the other hand, paracetamol complexes with Mn(II), Co(II), Fe(III), Zn(II), and Cu(II) were created by Refat et al. (37, 38). In these complexes, paracetamol behaves as a monobasic bidentate ligand, and elemental analysis, FT-IR spectroscopy, and thermal analysis have all been used to confirm the structures of those complexes. Complexes of Co(II), Ni(II), and Fe(III) with paracetamol were produced and studied by Obaleye et al. (39, 40). The oxygen of the hydroxyl and amide groups are coordinated by the paracetamol ligand, which, according to studies, functions as a bidentate chelating agent (Fig. 11). Aspirin and ascorbic acid mixed metal complexes with the ions Fe(II), Co(II), Ni(II), Cu(II), and Zn(II) were created by Babamale et al. (41).

3.4. Computational Study

According to the literature review and the conductivity and spectrophotometry results of this study, it is possible to give the general formula of prepared metal complexes of Para and L-Val ligands depending on I) the most commonly the coordination bonding of amino acids with metal ions by N, O atoms of the amine and carboxylate groups respectively, in which forms a five chelated ring (42-45). Thus, simple mixing of Co(ll) and Cu(ll) metal salts with solutions of L-Val amino acids often provides neutral binary complexes that favor octahedral coordination. II) paracetamol ligand tends to behave like a mono-negative ion (-1) by deprotonation of the NH amidic group. Thus paracetamol is attached to Co(ll) and Cu(ll) metal ions by N, O atoms of the amidic group, which forms a four-chelated ring (18, 23, 40, 41, 46). III) The conductivity of all formed complexes indicates that all complexes are neutral complexes which support 1:2 metal to L-Val complex by replacement

of both chloride ions in the starting metal complex salts of $CuCl_2$ and $CoCl_2$, and 1:1 metal to paracetamol by replacement of one chloride ion in the starting metal salts to form a neutral metal complex. By taking all of these notes, the general structure of metal complexes is shown in Figure 9 (A to D).

A	B	C	D
$[Co(Para)(H_2O)_3(Cl)]$	$[Cu(Para)(H_2O)_3(Cl)]$	$[Co(L-Val)_2(H_2O)_2]$	$[Cu(L-Val)_2(H_2O)]$
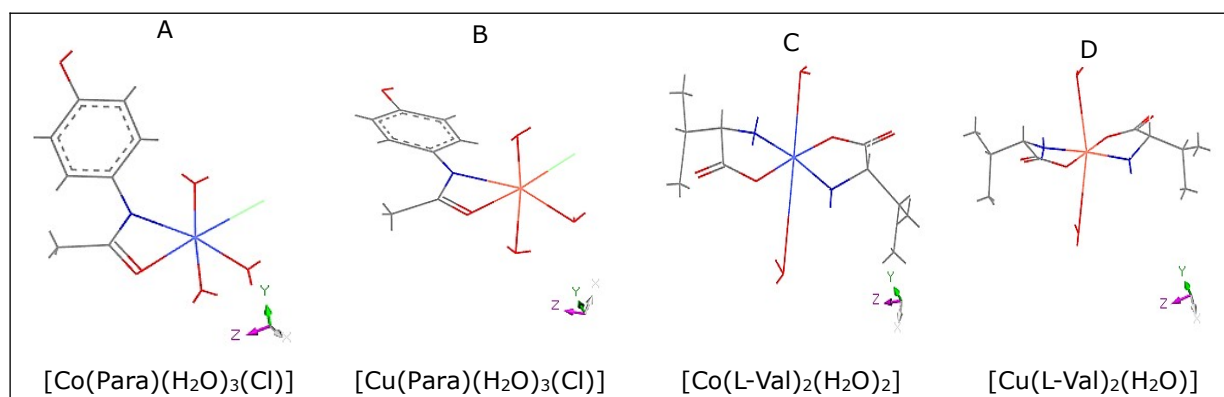
Figure 9: Different geometric shapes of complexes according to DFT.

It can be ascertained where the metal ion is bonded to paracetamol and L-Val using the DFT. Geometric factors and the energy difference between HOMO-LUMO confirmed the donor atom sites in Figures 10 and 11.
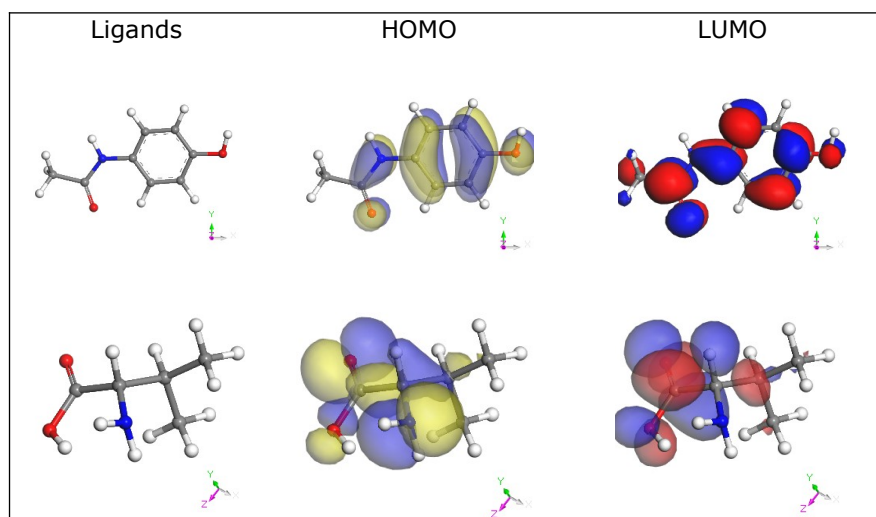
Figure 10: The obtained optimized structures, HOMO and LUMO of the neutral para and L-Val ligands molecules.

The molecular reactivity of the studied drug was investigated via analysis of frontier molecular orbitals of HOMO and LUMO. The energy of HOMO is associated with the electron-donating ability of a ligand to donate electrons to the metal atom with an empty molecular orbital. On the other hand, the energy of LUMO is associated with the electron-accepting ability of ligands (47-49). The presence of nitrogen and oxygen atoms together with several p-electrons on the entire paracetamol and L-Val molecules enhances the ability of ligands to react with metal ions.

The optimized structures and frontier molecule orbital density distributions of HOMO & LUMOs of the investigated ligands and their metal complexes were presented in Figures 10 and 11. As seen from the Figure, the HOMO and LUMO are distributed around the whole ligands molecules. This indicates the high reactivity of these ligands to bond to metal ions. The DFT results of the calculations of binary metal complexes are proposed in Figure 10 and Table 7, which clearly show the metal ions of Co(ll) and Cu(ll) to bond to the oxygen atom of the carbonyl group and the amide nitrogen in paracetamol ligand. In addition, the oxygen atom of

the hydroxyl group and the nitrogen atom of the amine NH_2 group for the L-Val ligand. From Figure 11, it's clear that the HOMOs and LUMOs of binary meta L-Val complexes are metal based, however, the HOMOs and LUMOs of binary metal-paracetamol complexes are ligand-based. As a consequence, the binding energies for metal-L-Val complexes are higher than the metal-paracetamol complexes (see Table 7). In addition, the DFT results of the calculations of ternary metal complexes are proposed in Figure 11 and Table 7, which clearly show the HOMOs and LUMOs are metal-based.

Table 7: Comparison between binary M-(Para) and (L-Val) complexes and ternary M-L-Val-Para complexes.

Type	Complexes	HOMO (eV)	LUMO (eV)	$\Delta E_{LUMO-HOMO}$ (eV)	Binding Energy (kcal/mol)
Binary Para complexes	[Cu(Para)(H2O)3(Cl)]	-4.458	-4.025	0.433	-3024.44
	[Co(Para)(H2O)3(Cl)]	-4.448	-3.607	0.841	-3187.95
Binary L-Val complexes	[Cu(L-Val)2(H2O)2]	-4.465	-3.59	0.875	-4181.39
	[Co(L-Val)2(H2O)2]	-4.354	-3.482	0.872	-4212.6
Ternary (Mixed) complexes	[Cu(L-Val)(Para)(H2O)2]	-3.998	-1.598	2.4	-4545.66
	[Co(L-Val)(Para)(H2O)2]	-4.938	-3.003	1.935	-4764.733

The sites of the donor atoms were confirmed by the geometric variables and the energy difference between HOMO-LUMO extracted from the calculations. Consequently, the value of the ΔE gap provides a measure of the strength of the crystal field of formed complexes, where the higher value of ΔE; the higher the crystal field is. The decrease in band gap is due to the decrease in strength of the crystal field, which is inversely proportional to the metal–ligands bond length. The strong-field ligands produced large electrostatic repulsion between the HOMO and the LUMO orbitals, which lead to a large band gap. Table 7 and Figure 12 depicted that the band gap order is: The ternary metal complexes > The binary metal-L-Val complexes > The binary metal-Para complexes. This consequence is in good agreement with the stability constant those calculated from the conductivity and spectrophotometry methods, in which, ternary M-L-Val-Para complexes are more stable than the binary complexes of M-para or complexes of M-L-Val. Moreover, the binary M-L-Val complexes are more stable than binary M-Para complexes.

Complexes	Configurations	HOMOs	LUMOs
$[Cu(L-Val)_2(H_2O)]$			
$[Co(L-Val)_2(H_2O)_2]$			
$[Cu(Para)(H_2O)_3(Cl)]$			
$[Co(Para)(H_2O)_3(Cl)]$			
$[Cu(L-Val)_2(H_2O)]$			
$[Co(L-Val)_2(H_2O)_2]$			
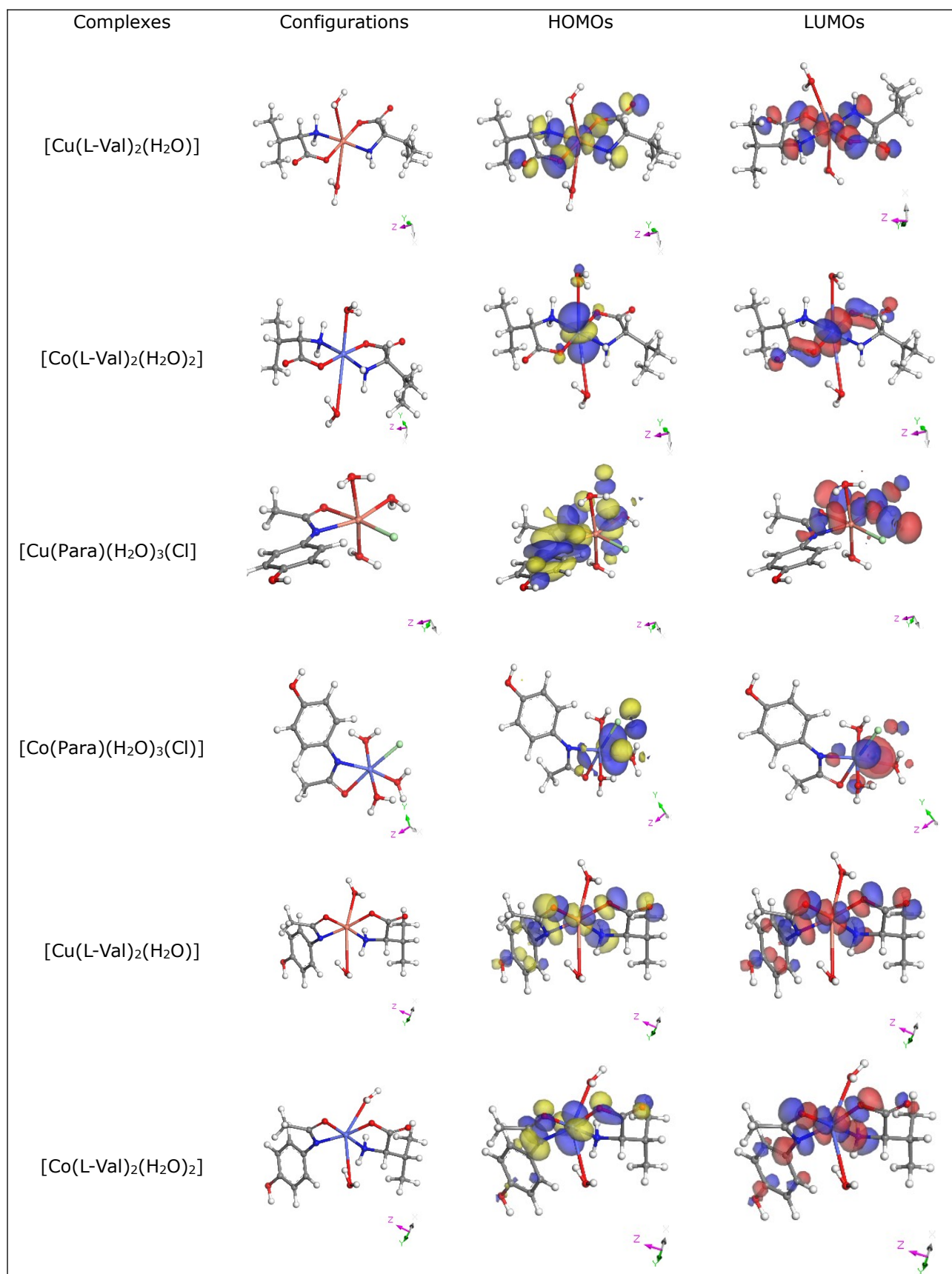
Figure 11: The obtained optimized structures, HOMO and LUMO of the binary and ternary metal complexes of para and L-Val ligands.
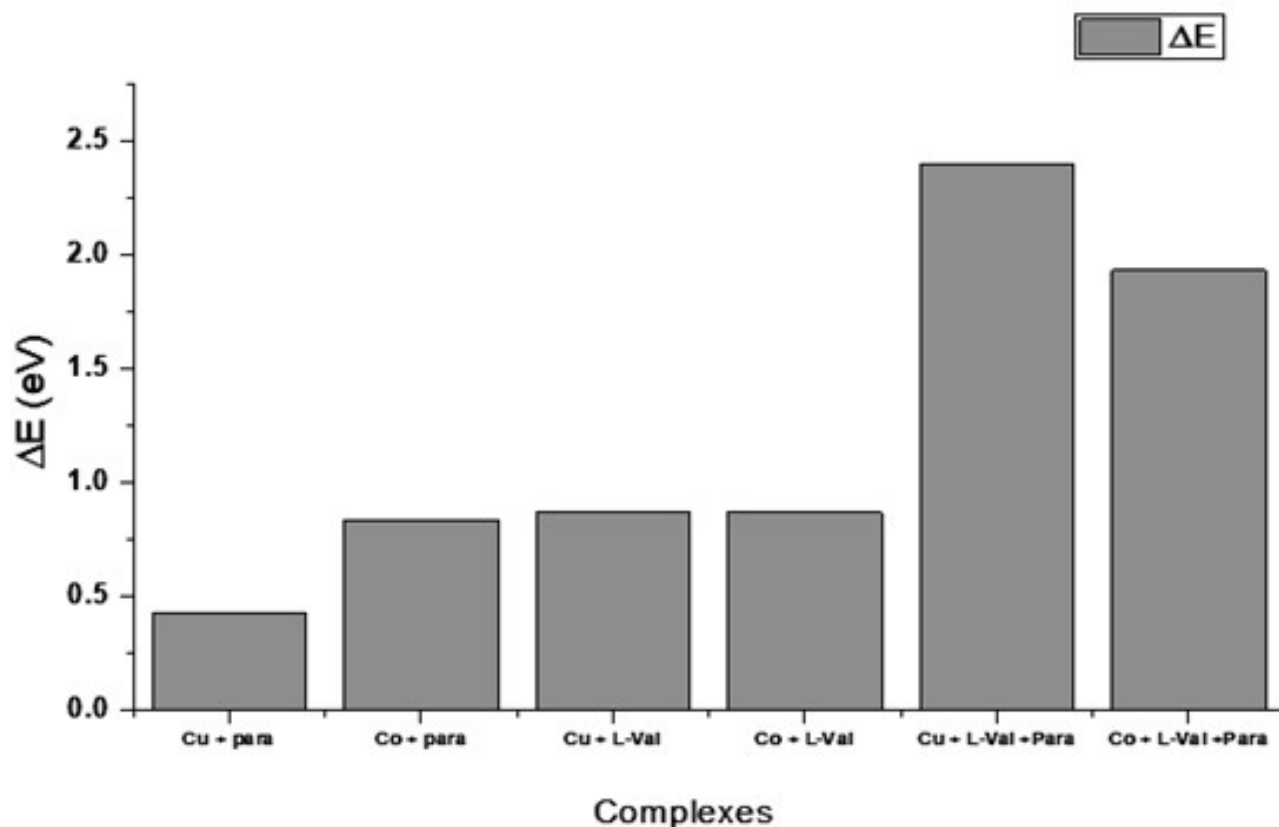
Figure 12: The band gap of binary M-(Para) and (L-Val) complexes and ternary M-L-Val-Para complexes.

4. CONCLUSION

The binary complexes of L-Val and Para with Co(II) and Cu(II) were investigated by conductometric and spectrophotometric methods based on formation constants (K_f) and stoichiometric (L:M): The formation constants for the binary-metal complexes were computed from conductivity titrations in the constant concentrations of (0.004 M) of metal ions, which Para-M(II) and L-Val-M(II) complexes were kept in a range 3.7 to 4.08 for Para-M(II) (1:1) complexes and a range 11.18 to 12.32 for L-Val-M(II) complexes (2:1), where these complexes were formed from the L-Val as primary ligand and the Para as a secondary ligand with metal ions. The values of formation constants of binary Cu(II)

complexes bigger than the values of stability constants of binary Co(II) complexes, where these values great with the order is following Irving-Williams order of stability, indicating that the order of stability is Cu(II) > Co(II). While Stoichiometry and formation constants of binary-Metal complexes by spectrophotometry were based on Job's method of continuous variation, where the result was a maximum absorbance at XL= 0.66-0.7, confirming that the stoichiometric ratio for the complexation of metals and L-Val is 1:2, while the result was a maximum absorbance at XL= 0.5-0.55, confirming that the stoichiometric ratio for the complexation of metals and para is 1:1. The formation constants are obtained spectrophotometrically by measuring the absorbance of two sets of solutions at λ_{max}.

5. LIST OF ABBREVIATIONS

λ_{max}	Absorption maximum
A_m	Absorbance of a solution containing an excess of reagent
A_s	Absorbance of a solution containing a stoichiometric quantity
BLYP	Becke-Lee-Yang-Parr
α	Degree of dissociation
DFT	Density Functional Theory
Cu(II)	Divalent copper

Co(II)	Divalent cobalt
DNP	Double numeric plus polarization
ΔE	Energy gap
K_f	Formation constants
GGA	Generalized gradient approximation
HOMOs	High occupied molecular orbital
LUMOs	Lower unoccupied molecular orbital
L-Val	L-Valine amino acid
Λ_o	Limiting molar conductance at infinite dilutions
Λ_m	Molar conductance
Λ_{mL}	Molar conductance of the complex
Λ_{obs}	Molar conductance of solution
NSAID	Non-steroidal anti-inflammatory drug
Para	Paracetamol
K_s	Specific conductance values

5. CONFLICT OF INTEREST

The authors declare no conflict of interest.

7. ACKNOWLEDGMENTS

8. REFERENCES

1. Karges J, Stokes R, Cohen S. Metal complexes for therapeutic applications. Trends Chem. 2021;3(7):523-34. Available from: <URL>.

2. Yin X, Ma K, Wang Y, Sun Y, Shang X, Zhao Z, et al. Design, synthesis, and antifungal evaluation of 8-hydroxyquinoline metal complexes against phytopathogenic fungi. J Agric. Food Chem. 2020;68(40):11096-104. Available from: <URL>.

3. Shi J, Shu R, Shi X, Li Y, Li J, Deng Y, et al. Multi-activity cobalt ferrite/MXene nanoenzymes for drug-free phototherapy in bacterial infection treatment. RSC Adv. 2022;12(18):11090-9. Available from: <URL>.

4. Li Y, Liu B, Shi H, Wang Y, Sun Q, Zhang Q. Metal complexes against breast cancer stem cells. Dalton Trans. 2021;50(41):14498-512.

5. Nelson J, Schelter E. Sustainable inorganic chemistry: metal separations for recycling. Inorg. Chem. 2019;58(2):979-90. Available from: <URL>.

6. Bhattacharya P, Samnani P. Metal ions in biochemistry: CRC Press; 2020. ISBN: 9781000292640.

7. Ahmed N, Al-Omar M, A. A, Obaidullah A, Bhat M, Kalmouch A, et al. Synthesis, characterization, and anti-diabetic activity of some novel vanadium-folate-amino acid materials. Biomolecules. 2020;10(5):781. Available from: <URL>.

8. Suhud K, Heng L, Rezayi M, Al-abbasi A, Hasbullah S, Ahmad M, et al. Conductometric Studies of the Thermodynamics for Complexation of 1,1-Diethyl-3-(4-methoxybenzoyl)thiourea and Cobalt(II) Cation in Aqueous Binary Mixtures of Polar Organic Solvents. Journal of Solution Chemistry. 2015;44(2):181-92. Available from: <URL>.

9. Al-abbasi A, Mohamed T., Kassim M. N-(Pyrrolidin-1-ylcarbothioyl)benzamide. Acta Crystallographica Section E. 2012;68(1):o201. Available from: <URL>.

10. Al-abbasi A, Mohamed Tahir M, Kassim M. 1,1-Diethyl-3-(4-methoxybenzoyl)thiourea. Acta Crystallographica Section E. 2011;67(12):o3414. Available from: <URL>.

11. Su J, Suo B, Cassam-Chenaï P. Theoretical Study of the Anisotropy Spectra of the Valine Zwitterion and Glyceraldehyde. J Phys. Chem. A. 2020;124(34):6824-33. Available from: <URL>.

12. Kamatchi K, Umarani P, Radhakrishnan T, Raja C. Investigation on organic-inorganic hybrid NLO crystal L-Valine Potassium Penta Borate octa hydrate (LVPPB) for NLO applications. Optik. 2018;172:674-9. Available from: <URL>.

13. Afzal Siddiqui H, Nadeem M, Azeem M, Arshad M, Haider A, Malik M. Topological properties of supramolecular chain of different complexes of N-Salicylidene-L-Valine. Polycycl. Aromat. Compd. 2022;42(9):6185-98. Available from: <URL>.

14. Martín J, Alés M, Asuero A. An overview on ligands of therapeutically interest. Pharm. Pharmacol. Int. J. 2018;6(3):198-214.

15. Chen A, Adamek R, Dick B, Credille C, Morrison C, Cohen S. Correction to Targeting Metalloenzymes for Therapeutic Intervention. Chem. Rev.. 2019;119(12):7719-.

16. Hejaz H, Kanan A, Al Mohtaseb M, Ja'bari A. Development and characterization of paracetamol medicated lollipops. Pharm. Technol. Hosp. Pharm. 2020;5(1). Available from: <URL>.

17. Alsamarrai K, Ameen S. Simultaneous Ratio Derivative Spectrophotometric Determination of Paracetamol, Caffeine and Ibuprofen in Their Ternary Form. Baghd. Sci J. 2022:1276-. Available from: <URL>.

18.   Belkher N, Al-abbas A, Zidan M. Potentiometric Studies on Stability Constant of the Complexes of Some Essential Transition Metal Ions with L-Valine. Journal of Pure & Applied Sciences. 2019;18(3):59-63.

19.   Al-abbası A. BN, Ahmida K., Zidan M. . Potentiometric Studies on Binary and Ternary Complexes of Ni(II) and Cu(II) Ions with L-Valine and Paracetamol. Journal of the Turkish Chemical Society Section A: Chemistry. 2023;10(2):325-38. Available from: <URL>.

20.   Yang L, He X, Dincă M. Triphenylene-bridged trinuclear complexes of Cu: Models for spin interactions in two-dimensional electrically conductive metal–organic frameworks. J Am. Chem. Soc. 2019;141(26):10475-80. Available from: <URL>.

21.   Upadhyay S, Hari O. Spectrophotometric and conductometric study of the interaction of saponin with chromium (VI) and lead (II). International Journal of Environmental Science and Technology. 2019;16(12):7997-8004. Available from: <URL>.

22.   Helmy E, Gomaa E, Elleef EA, Negm A. Conductometric, Spectrophotometric and In vivo Investigation of the Interaction of Ca (II) Ion with Oxytetracycline Hydrochloride. International Journal of Pharma Medicine and Biological Sciences. 2015;4(3):197. Available from: <URL>.

23.   Chandrathilaka A, Ileperuma, O. Hettiarachchi, C. Spectrophotometric and pH-metric studies on Pb(II), Cd(II), Al(III) and Cu(II) complexes of paracetamol and ascorbic acid. Journal of the National Science Foundation of Sri Lanka. 2013;41(4):337–44. Available from: <URL>.

24.   Perdew J, Burke K, Wang Y. Generalized gradient approximation for the exchange-correlation hole of a many-electron system. Physical Review B. 1996;54(23):16533. Available from: <URL>.

25.   Baker J, Kessi A, Delley B. The generation and use of delocalized internal coordinates in geometry optimization: The Journal of Chemical Physics. 1996; 192-212 p. Available from: <URL>.

26.   Becke A. Density-functional exchange-energy approximation with correct asymptotic behavior. Physical Review A. 1988;38(6):3098. Available from: <URL>.

27.   Lee C, Yang W, Parr R. Development of the Colle-Salvetti correlation-energy formula into a functional of the electron density. Physical Review B. 1988;37(2):785. Available from: <URL>.

28.   Fouad R, Shaaban I, Ali T, Assiri M, Shenouda S. Co (ii), Ni (ii), Cu (ii) and Cd (ii)-thiocarbonohydrazone complexes: spectroscopic, DFT, thermal, and electrical conductivity studies. RSC. Adv. 2021;11(60):37726-43. Available from: <URL>.

29.   Al-Abachi M, Abed S. Spectrophotometric determination of phenylephrine hydrochloride and salbutamol sulphate drugs in pharmaceutical preparations using diazotized metoclopramide hydrochloride. Baghd. Sci. J. 2015;12(1):167-77. Available from: <URL>.

30.   Abdel-Rahman L, Ismail N, Ismael M, Abu-Dief A, Ahmed E, Abdel-Hameed. Synthesis, characterization, DFT calculations and biological studies of Mn (II), Fe (II), Co (II) and Cd (II) complexes based on a tetradentate ONNO donor Schiff base ligand. J Mol. Struct. 2017;1134:851-62. Available from: <URL>.

31.   Stauffer M, Weller W, Kubas K, Casoni K. Limiting reactants in chemical analysis: influences of metals and ligands on calibration curves and formation constants for selected iron-ligand chelates. Stoichiometry and Research–The Impotance of Quantity in Biomedicine. 2012. p. 311-34. ISBN: 9789535101987.

32.   Mandal S, Das G, Askari H. Physicochemical investigations of the metal complexes of l-valine with doubly charged ions of nickel, copper and zinc: a combined experimental and computational approach. RSC Adv. 2014;4(47):24796-809. Available from: <URL>.

33.   Dudev T, Lim C. Metal Binding Affinity and Selectivity in Metalloproteins: Insights from Computational Studies. Annual Review of Biophysics. 2008;37(1):97-116. Available from: <URL>.

34.   Leach B, Angelici R. Stereoselective interaction of optically active amino acids and esters with (L; valine-N-monoacetato) copper (II). Journal of the American Chemical Society. 1969;91(23):6296-300. Available from: <URL>.

35.   Fayad N, Al-Noor T, Mahmood A, Malih I. Synthesis, Characterization, and Antibacterial Studies of Mn (II), Fe (II), Co (II), Ni (II), Cu (II) and Cd (II) Mixed-Ligand Complexes Containing Amino Acid (L-Valine) And (1, 10-phenanthroline). Synthesis. 2013;3(5).

36.   Fayad N, Al-Noor T, Ghanim F. Synthesis, characterization, and antibacterial activities of manganese (II), cobalt (II), iron (II), nickel (II), zinc (II) and cadmium (II) mixed-ligand complexes containing amino acid (L-Valine) and saccharin. Advances in Physics Theories and Applications. 2013;9:1-13.

37.   Refat M, El-Korashy S, Hussien M. Ligational, Spectroscopic (Infrared and Electronic) and Thermal Studies on the Mn (II), Co (II), Fe (II) and Cu (II) Complexes with Analgesic Drugs. Canadian Chemical Transactions. 2014;2(1):24-35. Available from: <URL>.

38.   Refat M, Mohamed G, El-Sayed M, Killa H, Fetooh H. Spectroscopic and thermal degradation behavior of Mg (II), Ca (II), Ba (II) and Sr (II) complexes with paracetamol drug. Arabian Journal of Chemistry. 2017;10:S2376-S87. Available from: <URL>.

39.   Amolegbe S, Adewuyi S, Akinremi C, Adediji J, Lawal A, Atayese A, et al. Iron(III) and copper(II) complexes bearing 8-quinolinol with amino-acids mixed ligands: Synthesis, characterization and antibacterial investigation. Arabian Journal of Chemistry. 2014;24. Available from: <URL>.

40.   Lawal A, Obaleye J. Synthesis, characterization and antibacterial activity of aspirin and paracetamolmetal complexes. Biokemistri. 2007;19(1). Available from: <URL>.

41. Babamale H, Lawal A, Rajee O, Oloyede E. Synthesis, characterization and biological activity studies of mixed paracetamol-ascorbic acid metal complexes. Journal of Applied Sciences and Environmental Management. 2016;20(4):1157-61. Available from: <URL>.

42. Neeraja R, Hima Bindu G. Speciation study involving mononuclear binary transition metal (CoII, NiII and CuII) complexes of L-methionine in non-ionic micellar medium. Heliyon. 2021;7(4):e06729. Available from: <URL>.

43. Zheng C, Shi R, Jin X, Qiu Q, Li H. Three complexes with helical frameworks based on l-glutamine and l-asparagine: Crystal structures and circular dichroism properties. Inorganic Chemistry Communications. 2016;65:16-20. Available from: <URL>.

44. Doğan A, Kiliç E. Potentiometric studies on the stability constants of some α-amino acid-copper(II) and nickel(II) systems in ethanol-water mixture. Indian Journal of Chemistry - Section A Inorganic, Physical, Theoretical and Analytical Chemistry. 2003;42:1632-5. Available from: <URL>.

45. Wu Y, Koch W, Berezansky P, Holland L. The dissociation constant of amino acids by the conductimetric method: I. pK1 of MOPSO-HCl at 25°C. Journal of Solution Chemistry. 1992;21(6):597-605. Available from: <URL>.

46. Sandhu RS, Kalia RK. Complexation reaction of metal ions with peptide systems. VII. Equilibrium studies of N-benzoyl-L-valine, N-benzoyl-glycyl-L-valine and isovaleric acid with metal(II) ion systems. Thermochimica Acta. 1980;40(2):305-9. Available from: <URL>.

47. Madkour L, Elshamy I. Experimental and computational studies on the inhibition performances of benzimidazole and its derivatives for the corrosion of copper in nitric acid. International Journal of Industrial Chemistry. 2016;7(2):195-221. Available from: <URL>.

48. Al-abbasi A, Kassim M. 1-Ethyl-1-methyl-3-(2-nitrobenzoyl)thiourea. Acta Crystallographica Section E. 2011;67(7):o1840.

49. Al-abbasi A, Tan S, Kassim M. 1-Benzoyl-3-(4-hydroxyphenyl)thiourea. Acta Crystallographica Section E. 2010;66(12):o3181. Available from: <URL>.

RESEARCH ARTICLE

Removal of Sumifix Yellow EXF Reactive Azo Dye By Electro-Fenton Method

Elif ÖZKUL[1]* ID **, Belgin KARABACAKOĞLU[2]** ID

[1] Pamukkale University, Department of Chemical Engineering, Denizli, 20160, Türkiye
[2] Osmangazi University, Department of Chemical Engineering, Eskişehir, 26040, Türkiye

Abstract: Reactive dyes can be found in large quantities in textile industry wastewater due to their widespread use for dyeing cotton fabrics and their durable nature. In the treatment of wastewater containing dyestuffs in this class, advanced treatment methods have become necessary due to the inadequacy of conventional treatment methods and their disadvantages. For this reason, electro-Fenton, an electrochemical advanced oxidation method, is a strong alternative as a treatment technology that provides complete disintegration of dye molecules. In this study, the electro-Fenton method was used to treat model wastewater containing the reactive azo dye Sumifix Yellow EXF. The electro-Fenton process is based on the in situ generation of hydroxyl radicals ($\cdot OH$), a strong oxidant, using Fe^{2+} and H_2O_2 released at the electrodes or added from outside. In the electrochemical cell used, carbon fiber was used as the cathode and iron was used as the anode. While Fe^{2+} ion was produced at the anode, H_2O_2 was added to the cell externally. In the experiments carried out at room temperature, a 250 mL glass beaker was used as a reactor. In the study, the optimization of the parameters was achieved by using the classical experimental design method. According to this method, one parameter is changed and other parameters are kept constant. In order to achieve the highest dyestuff removal, experiments were conducted by varying the voltage (5–10 V), H_2O_2 concentration (9–74 mM), Na_2SO_4 concentration (6–25 mM), and pH (3-5), and the impact of these factors on dye removal and energy consumption was evaluated. It was found that for the best dye removal, voltage is 7.5 V, the H_2O_2 concentration is 74 mM, the Na_2SO_4 concentration is 25 mM and the optimum pH value is 4. At these values, 98.14% removal at 30 minutes was achieved with an energy consumption of 7.98 Wh/L. The electro-Fenton method was found to be a highly effective approach for wastewater treatment and environmental remediation, showing remarkable dye removal efficiency with reasonable energy consumption under optimized conditions.

1. INTRODUCTION

Dyes are recognized as a wide variety of organic pollutants transmitted from different industries such as textile, leather, paper, food, beverage, pharmaceutical, and cosmetics to wastewater treatment systems or natural water sources. There are an estimated 10.000 different textile dyes. During the dyeing process, 10-25% of these dyes and 2-20% are mixed with water as aqueous wastes with different components, and large volumes of wastewater containing high amounts of dyes are discharged from industries to water bodies without being treated or sufficiently treated. As a result, one of the sectors that causes serious water pollution is the textile sector. The discharge of many dyes and degradation products from this industry into the aquatic environment can be toxic, carcinogenic, and/or mutagenic for life (1,2). Therefore, the treatment of dye compounds and degradation by-products that negatively affect life has become more important.

Reactive dyes are a type of dye that is widely used in the textile industry because they contain reactive groups that allow textile fibers to be bonded to each other through the formation of covalent bonds. Thanks to this feature, which improves the interaction of dye with textile fibers, low energy consumption is possible (3,4). Many reactive dyes are available in the azo dye category. Reactive azo dyes are anionic dyes with one or more azo (-N =N-) functional groups (5,6). These dyes are not biodegradable due to their aromatic nature and high stability (7). These paints, which have toxic, mutagenic and carcinogenic effects and are very difficult to remove from water, require good treatment.

Many different methods, including physical, chemical, and biological are used in the treatment of textile wastewater (8). Chemical coagulation, biological oxidation, and adsorption are the traditional methods for treating dyed wastewater. Biological methods are low-cost and easy to implement. However, dyed wastewater cannot be removed to a large extent with the activated sludge method, which is a classical biological treatment method. Therefore, in the presence of toxic and persistent organics in wastewater, biological treatment is not sufficient. In chemical coagulation and adsorption methods, there is only the transfer of pollutants from one phase to another; large amounts of sludge and waste are formed and further treatment becomes necessary to remove them. Therefore, the focus has been on the development of new purification technologies that provide complete degradation of dye molecules. Among these treatment technologies, electro-Fenton is an electrochemical advanced oxidation method. This method uses a highly oxidative hydroxyl radical (•OH) produced by the reaction of Fe^{2+} and H_2O_2 reagents produced in situ or added externally under an electrical field for the removal of persistent organics. •OH radicals are very effective oxidants and can easily decompose organic materials. Electro-Fenton reactions generally take place by means of the chain reactions given below (9,10).

$$Fe^{2+} + H_2O_2 \rightarrow Fe^{3+} + OH^- + \bullet OH \quad (1)$$
$$H_2O_2 + \bullet OH \rightarrow H_2O + HO_2\bullet \quad (2)$$
$$Fe^{3+} + HO_2\bullet \rightarrow Fe^{2+} + H^+ + O_2 \quad (3)$$
$$Fe^{2+} + HO_2\bullet \rightarrow Fe^{3+} + HO_2\bullet \quad (4)$$
$$\bullet OH + RH \rightarrow R\bullet + H_2O \quad (5)$$
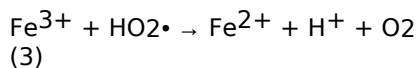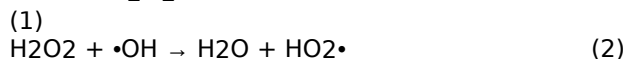
H_2O_2 added to the electrochemical cell reacts with the Fe^{2+} ion, which acts as a catalyst, to form •OH radicals (Equation 1). The Fe^{2+} ion is produced at the anode in the electrochemical cell. In addition, the reduction of the Fe^{3+} ion provides regeneration of the Fe^{2+} ion (Equations 2 and 3). Finally, pollutants (RH) are converted into non-toxic

compounds such as CO_2 and H_2O with •OH radicals (Equation 5). In addition, H_2O_2 can be produced at the cathode in an acidic and oxygen-containing environment inside the cell (Equation 6) (11).

$$O_2 + 2H^+ + 2e^- \rightarrow H_2O_2 \quad (6)$$

The electro-Fenton method is effective for the treatment of synthetic and real wastewater contaminated with different organic substances such as pharmaceuticals, personal care products, endocrine disrupting compounds, pesticides, textile wastes, polycyclic aromatic hydrocarbons, surfactants, and landfill leachate (12).

In this study, the electro-Fenton method, which is an advanced oxidation method, was used to remove Sumifix Yellow EXF Reactive Azo dye from an aqueous solution. The effects of some important parameters (voltage, H_2O_2 concentration, Na_2SO_4 concentration, pH) on dye removal and energy consumption were investigated, and optimum working conditions were determined. 98.14% color removal and 7.98 Wh/L energy consumption were achieved under optimum operating conditions. The aim of this study is to investigate the usability of the electro-Fenton method for the reactive azo dyestuff used in this study, to determine the optimum working conditions for each parameter examined, and to be a source for further studies.

2. EXPERIMENTAL SECTION

2.1. Chemicals
Hydrogen peroxide (H_2O_2 (35%), Merck) and sulfuric acid (H_2SO_4, Merck) were used in the studies. All chemicals used were of analytical grade and were used without further purification. Stock standard solutions were diluted to form working solutions. All experiments were performed at room temperature. A pH meter (OHAUS pH meter) and a spectrophotometer (Thermo Electron Corparation) were used in the study. Sumifix Yellow EXF was used as a reactive azo dyestuff. This dyestuff was purchased from a local company (Türkiye). Dye solutions were prepared by diluting the stock solution prepared by dissolving 1 g of dye in 1 L of distilled water. The solution with a dye concentration of 100 mg/L was used in all experiments.

Some physical and chemical properties and chemical structure of the commercial textile dye Sumifix Yellow EXF are given in Table 1.

Table 1: Some properties and chemical structure of Sumifix Yellow EXF

Chemical Structure	Commercial name:	Sumifix Yellow EXF
	Mol wt (g/mol):	1026,25
	Molecular formula:	C28H20ClN9Na4O16S5
	Color Index name:	Reactive yellow 145 (RY145)
	Class:	Single azo
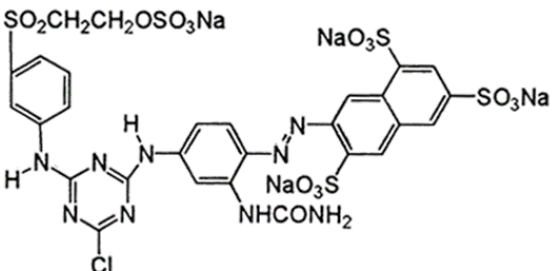
2.2. Electrochemical System

The apparatus used in the study consists of three main units: a DC power supply, a magnetic stirrer, and an electrochemical cell (Figure 1). The electrochemical cell is also called the electro-Fenton reactor. Experiments were carried out at room temperature in an undivided and cylindrical 250-mL glass beaker. The usable volume of the reactor was 200 mL. Electro-Fenton times of 0–30 minutes were used for all studies. An iron (anode) and a carbon fiber (cathode) with dimensions of 50 mm by 60 mm were used as electrodes. In the electro-Fenton reactor, electrodes parallel to each other and separated by 2 cm were connected to the direct current power supply (Stone). Current and voltage control were carried out with this power supply. As long as the active surface area did not change with the dissolution effect, the use of the anode continued. For each experiment, the EF reactor was filled with 200 mL of wastewater and stirred continuously at 500 rpm with a cylindrical magnetic rod. The anode was washed with concentrated HCl (37%), then with distilled water. Thus, the iron oxide compounds that had accumulated on the surface were removed. Since Fenton reactions occur in an acidic environment, the initial pH of the dye solution was adjusted to the desired level before the Fenton reagent H_2O_2 was added to all experiments. To create a 100 mg/L stock solution, a dye solution at a concentration of 1 g/L was prepared. 0.1 M H_2SO_4 was used for pH adjustment in all experiments. The pH-adjusted solution was placed in the experimental setup. Na_2SO_4 was used to provide conductivity in the solution. Before each experiment, the amount of iron dissolved in the anode was measured by weighing the Fe electrode. Electrolysis was carried out by giving the desired voltage to the system. Then, the time was started, and 35% H_2O_2 was added after 1 minute. The production of •OH radicals was achieved by adding H_2O_2.
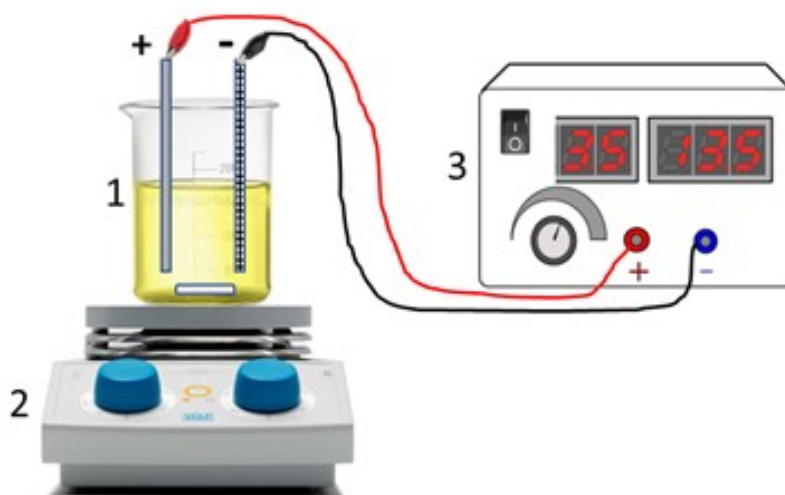
Figure 1: Experimental Setup (1:EF reactor; 2:Magnetic stirrer; 3:DC power supply).

2.3. Analytical System

The dyestuff concentration (ppm) of the samples was determined by a UV-VIS spectrophotometer (Thermo Electron Corporation) at a wavelength of 423 nm. The color removal efficiency of the removal process was analyzed by evaluating the difference in absorbance values of the dye solution before and after removal. The Sumifix Yellow EXF removal efficiency was calculated according to the following equation:

$$\text{Removal efficiency} \,(\%) = \left(\frac{C_0 - C}{C_0} \right) \times 100 \tag{7}$$

Where C_0 and C are the dye concentration in mg/L at t=0 and t, respectively.

The energy consumption in the Electro-Fenton process is calculated using the following equation:

$$\text{Energy consumption} \,(Wh/L) = \frac{V \times I \times t}{L} \tag{8}$$

Where V applied voltage(V) ; I current strength(A) ; t is time (h) and volume of dye solution treated (L).

In this study, the effects of voltage, pH, H_2O_2 concentration and Na_2SO_4 amount on the removal percentage and energy consumption were examined according to the single factor method each time. For this, while the effect of one variable was examined, the other three variables were kept constant. The duration of the experiments is 30 minutes. The experiment conditions are given in Table 2.

Table 2: Operating range of the parameters analyzed in the experiments.

Examined Variables	Operating Range	Constant Variables and Values
Voltage (V)	5; 7.5, and 10	pH: 3; H_2O_2: 37 mM; Na_2SO_4: 25 mM
Na_2SO_4 (mM)	6; 12, and 25	pH: 3; H_2O_2: 37 mM; E: 7.5 V
pH	3, 4, and 5	E: 7.5 V; H_2O_2: 37 mM; Na_2SO_4: 25 mM
H_2O_2 (mM)	9; 18; 37, and 74	pH: 4; Na_2SO_4: 25 mM; E: 7.5 V

3. RESULTS AND DISCUSSION

3.1. The Effect of Voltage

Increasing the voltage and hence the current density to the optimum value in electro-Fenton processes will increase the transition of Fe^{2+} from the anode electrode to the solution. In addition, ·OH radicals will be produced by causing more H_2O_2 formation at the cathode (Equation 1). As a result, as the voltage value increases to an optimum value, the amount of ·OH radical, the removal efficiency will also increase. In addition, higher voltage values provide faster Fe^{2+} regeneration at the cathode electrode (Equation 9) (13).
Cathode Reaction:
$$Fe^{3+} + e^- \rightarrow Fe^{2+} \tag{9}$$

Along with these, since the rate of parasitic reactions increases, the efficiency decreases when the voltage value is increased above the optimum value, resulting in the removal of the same or less pollutants compared to low voltage values (14). The optimum voltage value was selected as 7.5 V in view of high removal and low energy consumption (Figure 2).

3.2. The Effect of Electrolyte (Na_2SO_4) Concentration

Supporting electrolytes should be used in electro-Fenton processes to treat wastewater with low conductivity. Electrolytes help increase the conductivity of solutions and accelerate electron transfer. The commonly used supporting electrolyte type in electro-Fenton processes is Na_2SO_4 (15). In addition to Na_2SO_4, NaCl, KCl, NaClO4, NaNO3, and NaHCO3, there are other types of supporting electrolytes. The structure of the supporting electrolyte affects the degradation kinetics, as it may lead to the presence of some ions in the solution (14). When Na_2SO_4 is used in solution, ·OH radicals in the presence of sulfate ions and H_2O_2 in the presence of $SO_4^{·-}$ can be consumed (Equations 10, 11, and 12) (16–18).

$$SO_4^{2-} + ·OH \rightarrow SO_4^{·-} + OH^- \tag{10}$$
$$SO_4^{·-} + H_2O_2 \rightarrow SO_4^{2-} + H^+ + HO_2· \tag{11}$$
$$SO_4^{·-} + HO_2· \rightarrow SO_4^{2-} + H^+ + O_2 \tag{12}$$
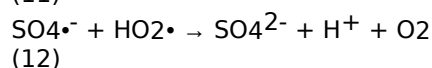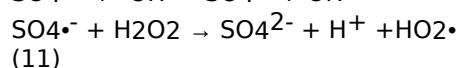
Generally, 50 mM Na_2SO_4 is used in electro-Fenton processes because it provides a large current flow. Increasing the concentration to a value above this value may cause side reactions to occur (19).

In this study, 0.177, 0.355 and 0.71 g of Na_2SO_4 were used for a 200 mL solution volume. Their concentrations are 6 mM, 12 mM, and 25 mM, respectively. The highest removal and energy consumption occurred in the presence of 25 mM Na_2SO_4 in solution, as shown in Figure 3.
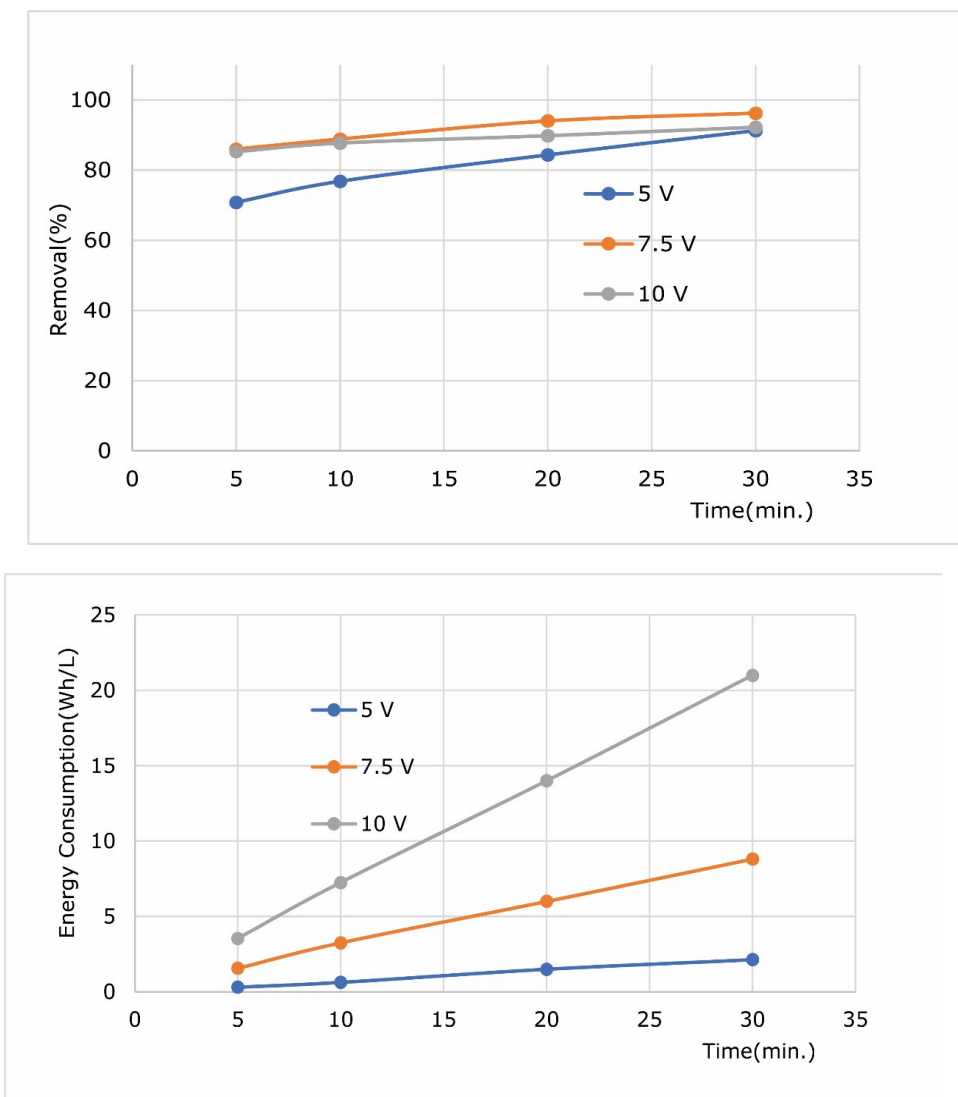
Figure 2: The effect of applied voltage on the percentage of dye removal and energy consumption (Na2SO4: 25 mM; H2O2: 37 mM; pH: 3)
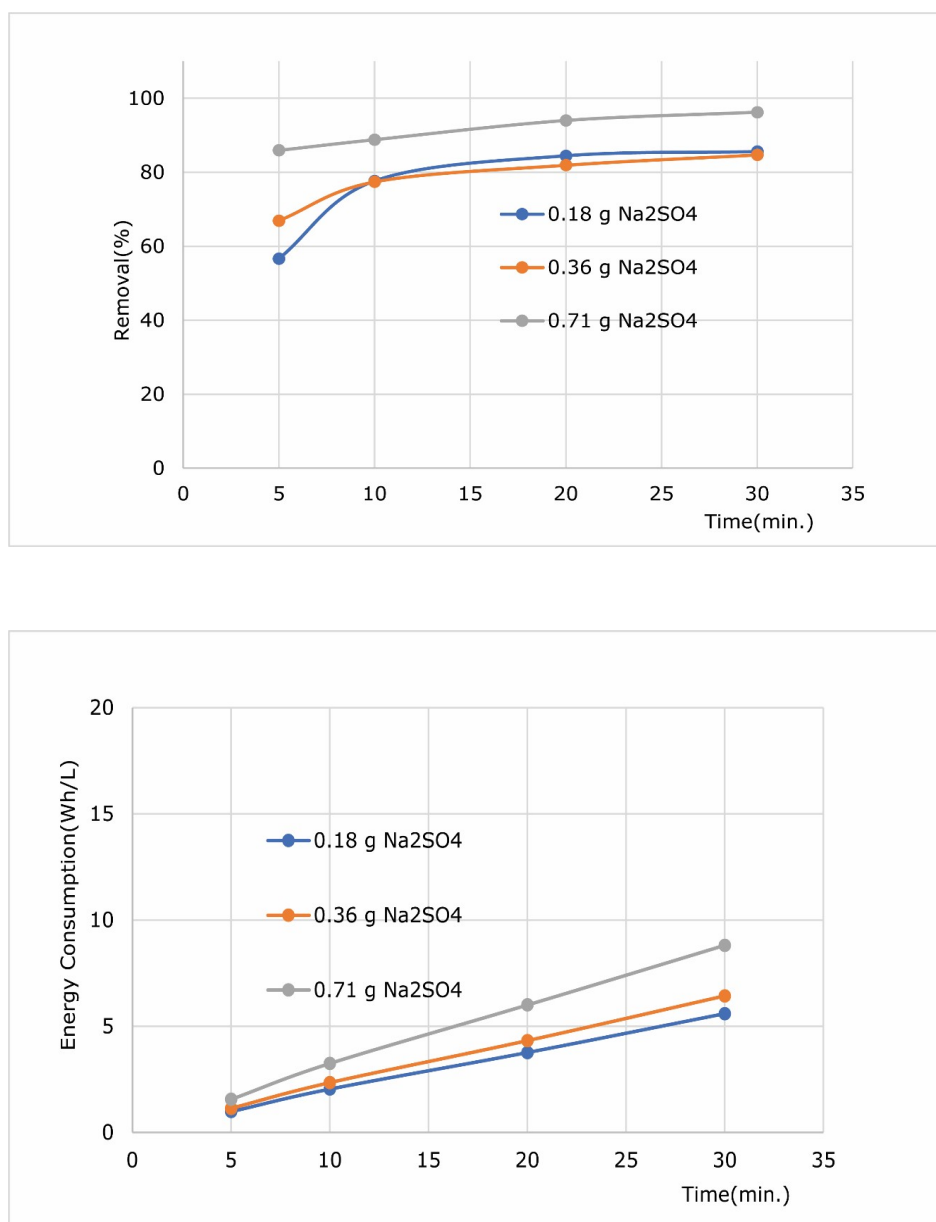
Figure 3: The effect of the amount of supporting electrolyte on the percentage of dye removal and energy consumption (pH: 3; H2O2 : 37 mM; E: 7.5 V).

3.3. The Effect of pH

The pH of the solution has a significant influence on the electro-Fenton process as it regulates the Fe^{2+} concentration and the formation of •OH radicals (20). In general, Fenton reactions take place in an acidic environment. In the color removal studies performed with the electro-Fenton process, it has been confirmed that the best color removal efficiencies are obtained when the pH range of the environment is 2-5 (21,22).

Many studies have reported pH 3 as the pH at which Fenton reactions occur well (11,21,23,24). At higher pH levels, iron species begin to precipitate as their hydroxides. Iron species form stable complexes with H2O2 even at low pH levels. As a result, the removal efficiency decreases in both cases. An acidic environment is necessary for the production of H2O2 (Equation 6). However, an acidic environment limits the production of H2O2 (Equations 13 and 14) (25).

$$H2O2 + 2H^+ + 2e^- \rightarrow 2H2O \qquad (13)$$
$$2H^+ + 2e^- \rightarrow H2 \qquad (14)$$
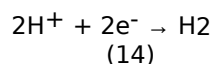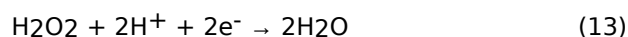
In addition, oxonium ions are formed at pH< 3 (Equation 15) (11).
$$H2O2 + H^+ \rightarrow H3O2^+ \qquad (15)$$

The efficiency of the electro-Fenton process decreases due to the instability of H2O2, especially at pH> 5. H2O2 rapidly decomposes into water and oxygen (Equation 16) (26,27).

$$2H2O2 \rightarrow 2H2O + O2 \qquad (16)$$

In this study, pH values of 3, 4 and 5 were studied to find the best removal efficiency. The best removal efficiency is at 97.31% at the end of 30 minutes at pH 4. The lowest energy consumption occurred at pH 5, as seen in Figure 4.
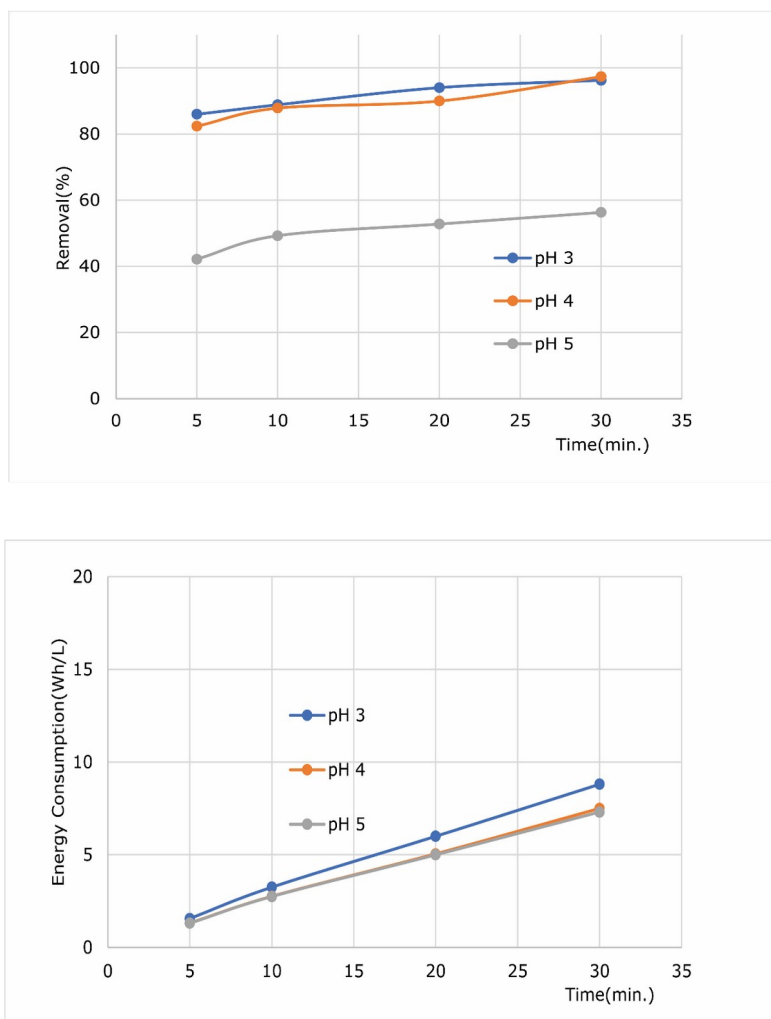
Figure 4: The effect of solution pH on the percentage of dye removal and energy consumption (Na2SO4 : 25 mM; H2O2 : 37 mM; E: 7.5 V).

3.4. The Effect of Initial H$_2$O$_2$ Concentration

In this study, 0.125 mL, 0.25 mL, 0.5 mL, and 1 mL H$_2$O$_2$ amounts were added to a 200 mL solution, and the removal efficiency resulted in 88.25%, 97.36%, 97.31%, and 98.14%, respectively, after 30 minutes. The concentrations of H2O2 in solution are 9 mM, 19 mM, 37 mM,and 74 mM, respectively. The highest removal efficiency is 98.14% at a 74 mM H$_2$O$_2$ concentration (Figure 5).
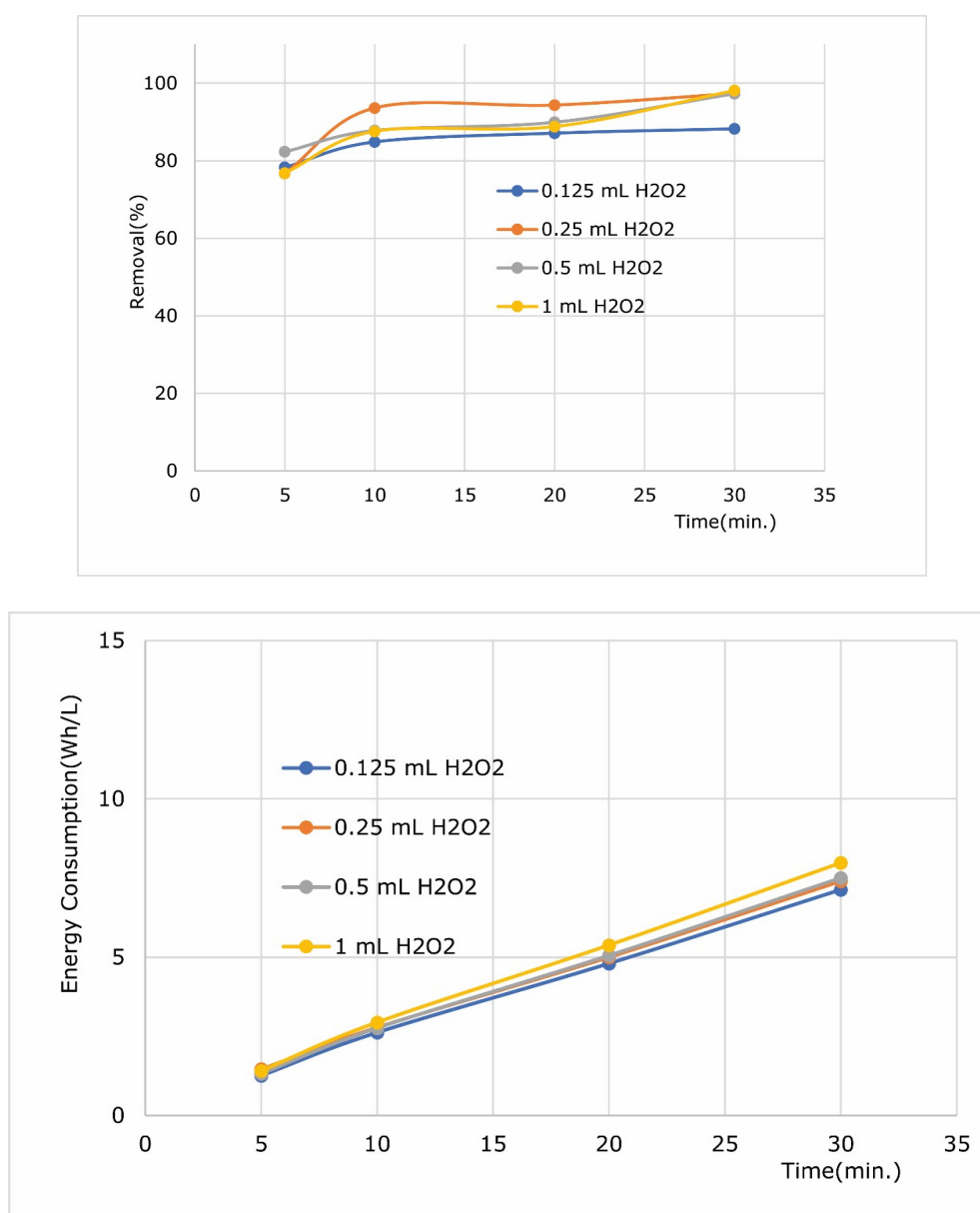
Figure 5: The effect of the amount of H2O2 on the percentage of dye removal and energy consumption (Na2SO4 :25 mM; pH: 4; E: 7.5 V).

The initial concentration of H2O2 is an important parameter in electro-Fenton processes. Because it is the main source of H2O2 •OH radicals. Removal of pollutants increases with increasing H2O2 concentration. As the H2O2 concentration increases to an optimum value, the concentration of the •OH radical also increases (Equation 1) (28,29). However, at concentrations higher than the optimum value of H2O2, the decrease in removal efficiency is due to the scavenging effect of H2O2 on •OH radicals (Equations 17 and 18) and recombination of the OH radical (Equation 19) (20).

$$•OH + H_2O_2 \rightarrow HO_2• + H_2O \qquad (17)$$
$$HO_2•+ •OH \rightarrow H_2O + O_2 \qquad (18)$$
$$2•OH \rightarrow H_2O_2 \qquad (19)$$
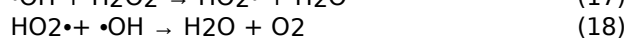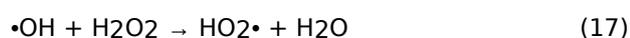
4. CONCLUSION

In this study, color removal and energy consumption studies were carried out by the electro-Fenton method on aqueous solutions of Sumifix Yellow Reactive Azo dyes. In this method, the effects of voltage (5, 7.5, and 10 V), electrolyte (Na2SO4) concentration (6, 12, and 25 mM), pH (3, 4, and 5), and initial H2O2 concentration (9, 18, 37, and 74 mM) were investigated. As a result of studies of optimization, at 7.5 volts, 25 mM Na2SO4, pH 4, and 74 mM H2O2 for 30 minutes, the highest color removal efficiency value of 98.14% was obtained. The energy consumption at these parameter values is 7.98 Wh/L. According to Faraday's law, as the voltage applied to the cell increases, the amount of iron dissolved at the anode increases, and accordingly, the rate of disintegration of the dyestuff increases with the increase in Fe^{2+} concentration. However, the degradation rate decreased above a certain concentration (Figure 2). As a result, determining the optimum voltage value becomes necessary both for the removal of pollutants and for reducing energy consumption. As the concentration of

Na$_2$SO$_4$ used as the supporting electrolyte increases, the solution conductivity increases, and the current intensity increases according to Ohm's law. All other variables being constant, energy consumption increased with the increase in current intensity (Figure 3). Since the removal is higher at pH 4 and the energy consumption is less than pH 3, subsequent experiments were carried out at pH 4. The best removal occurred at 74 mM H$_2$O$_2$ when the H$_2$O$_2$ concentration was changed while keeping all other parameters constant. In the study, dye removal was investigated between 5-30 minutes and it was observed that the dye removal efficiency increased with the effective realisation of the reactions due to increased Fe^{2+} formation and hydroxyl radical production as the time progressed for all parameters examined. In addition, energy consumption increased significantly with increasing time of treatment. This study successfully shows that Sumifix Yellow EXF azo dyestuff from an aqueous solution can be removed at a value close to 100% with low energy consumption in as little as 30 minutes.

5. CONFLICT OF INTEREST

The authors state that there is no conflict of interest.

6. ACKNOWLEDGMENTS

7. REFERENCES

1.   Babuponnusami A, Muthukumar K. A review on Fenton and improvements to the Fenton process for wastewater treatment. Vol. 2, Journal of Environmental Chemical Engineering. Elsevier Ltd; 2014. p. 557–72. Available from: <URL>

2.   Carmen Z, Daniela S. Textile Organic Dyes-Characteristics, Polluting Effects and Separation/Elimination Procedures from Industrial Effluents-A Critical Overview [Internet]. Available from: <URL>

3.   Zhang S, Tappe H, Helmling W, Mischke P, Rebsamen K, Reiher U, et al. Reactive Dyes. In: Ullmann's Encyclopedia of Industrial Chemistry [Internet]. Weinheim, Germany: Wiley-VCH Verlag GmbH & Co. KGaA; p. 1–20. Available from: <URL>

4.   Şahinkaya S. COD and color removal from synthetic textile wastewater by ultrasound assisted electro-Fenton oxidation process. Journal of Industrial and Engineering Chemistry. 2013 Mar 25;19(2):601–5. Available from: <URL>

5.   Hunger K, Mischke P, Rieper W. Azo Dyes, 1. General. In: Ullmann's Encyclopedia of Industrial Chemistry. Wiley-VCH Verlag GmbH & Co. KGaA; 2011. Available from: <URL>

6.   Jager D, Kupka D, Vaclavikova M, Ivanicova L, Gallios G. Degradation of Reactive Black 5 by electrochemical oxidation. Chemosphere. 2018;190:405–16. Available from: <URL>

7.   Liu X, Yin H, Lin A, Guo Z. Effective removal of phenol by using activated carbon supported iron prepared under microwave irradiation as a reusable heterogeneous Fenton-like catalyst. J Environ Chem Eng. 2017 Feb 1;5(1):870–6. Available from: <URL>

8.   Wang X, Jiang J, Gao W. Reviewing textile wastewater produced by industries: characteristics, environmental impacts, and treatment strategies. Vol. 85, Water Science and Technology. IWA Publishing; 2022. p. 2076–96. Available from: <URL>

9.   Do TM, Byun JY, Kim SH. An electro-Fenton system using magnetite coated metallic foams as cathode for dye degradation. Catal Today. 2017 Oct 15;295:48–55. Available from: <URL>

10.   Kremer ML. Mechanism of the Fenton reaction. Evidence for a new intermediate. Physical Chemistry Chemical Physics. 1999 Aug 1;1(15):3595–605. Available from: <URL>

11.   Zhou M, Yu Q, Lei L, Barton G. Electro-Fenton method for the removal of methyl red in an efficient electrochemical system. Sep Purif Technol. 2007 Oct 15;57(2):380–7. Available from: <URL>

12.   Ganiyu SO, Zhou M, Martínez-Huitle CA. Heterogeneous electro-Fenton and photoelectro-Fenton processes: A critical review of fundamental principles and application for water/wastewater treatment. Vol. 235, Applied Catalysis B: Environmental. Elsevier B.V.; 2018. p. 103–29. Available from: <URL>

13.   Zhang H, Fei C, Zhang D, Tang F. Degradation of 4-nitrophenol in aqueous medium by electro-Fenton method Degradation of 4-nitrophenol in aqueous medium by electro-Fenton method. J Hazard Mater. 2007 Jun 25;145(1–2):227–32. Available from: <URL>

14.   Moreira FC, Boaventura RAR, Brillas E, Vilar VJP. Electrochemical advanced oxidation processes: A review on their application to synthetic and real wastewaters. Vol. 202, Applied Catalysis B: Environmental. Elsevier B.V.; 2017. p. 217–61. Available from: <URL>

15.   Nidheesh P v., Gandhimathi R. Trends in electro-Fenton process for water and wastewater treatment: An overview. Vol. 299, Desalination. 2012. p. 1–15. Available from: <URL>

16.   Smith, R. M., Martell, A. E. Critical Stability Constants, 4, Inorganic Complexes; 1976. 270 p. ISBN: 0608093653, 9780608093659. Available from: <URL>

17.   Neta P, Huie RE, Ross AB. Rate·Constants for Reactions of Inorganic Radicals in Aqueous Solution [Internet]. Available from: <URL>

18.   de Laat J, Truong Le G, Legube B. A comparative study of the effects of chloride, sulfate and nitrate ions on the rates of decomposition of H$_2$O$_2$ and organic compounds by Fe(II)/H$_2$O$_2$ and Fe(III)/H$_2$O 2. Chemosphere. 2004;55(5):715–23. Available from: <URL>

19.   Gökkuş Ö, Yıldız YŞ. Application of electro-Fenton process for medical waste sterilization plant wastewater. Desalination Water Treat. 2016 Nov 7;57(52):24934–45. Available from: <URL>

20.   Muruganandham M, Swaminathan M. Decolourisation of Reactive Orange 4 by Fenton and

photo-Fenton oxidation technology. Dyes and Pigments. 2004 Dec;63(3):315–21. Available from: <URL>

21.   Ghoneim MM, El-Desoky HS, Zidan NM. Electro-Fenton oxidation of Sunset Yellow FCF azo-dye in aqueous solutions. Desalination. 2011 Jul 1;274(1–3):22–30. Available from: <URL>

22.   Lei H, Li H, Li Z, Li Z, Chen K, Zhang X, et al. Electro-Fenton degradation of cationic red X-GRL using an activated carbon fiber cathode. Process Safety and Environmental Protection. 2010 Nov;88(6):431–8. Available from: <URL>

23.   Wang CT, Hu JL, Chou WL, Kuo YM. Removal of color from real dyeing wastewater by Electro-Fenton technology using a three-dimensional graphite cathode. J Hazard Mater. 2008 Apr 1;152(2):601–6. Available from: <URL>

24.   Ai Z, Mei T, Liu J, Li J, Jia F, Zhang L, et al. Fe@Fe$_2$O$_3$ core-shell nanowires as an iron reagent. 3. Their combination with CNTs as an effective oxygen-fed gas diffusion electrode in a neutral electro-fenton system. Journal of Physical Chemistry C. 2007 Oct 11;111(40):14799–803. Available from: <URL>

25.   Wang CT, Chou WL, Chung MH, Kuo YM. COD removal from real dyeing wastewater by electro-Fenton technology using an activated carbon fiber cathode. Desalination. 2010 Apr;253(1–3):129–34. Available from: <URL>

26.   Shemer H, Linden KG. Degradation and by-product formation of diazinon in water during UV and UV/H2O2 treatment. J Hazard Mater. 2006 Aug 25;136(3):553–9. Available from: <URL>

27.   Wang Q, Lemley AT. Kinetic model and optimization of 2,4-D degradation by Anodic Fenton treatment. Environ Sci Technol. 2001 Nov 15;35(22):4509–14. Available from: <URL>

28.   Ting WP, Lu MC, Huang YH. Kinetics of 2,6-dimethylaniline degradation by electro-Fenton process. J Hazard Mater. 2009 Jan 30;161(2–3):1484–90. Available from: <URL>

29.   Akyol A, Can OT, Demirbas E, Kobya M. A comparative study of electrocoagulation and electro-Fenton for treatment of wastewater from liquid organic fertilizer plant. Sep Purif Technol. 2013 July 10;112: 11–9. Available from: <URL>

Assessment of Total Phenolic Compounds, Antioxidant Capacity, β-Carotene Bioaccessibility, HMF Formation, and Color Degradation Kinetics in Pumpkin Pestils

Azime Özkan Karabacak (iD)

[1]Bursa Uludag University, Gemlik Asim Kocabiyik Vocational School, Food Technology Program, 16600 Gemlik, Bursa–Türkiye
[2]Bursa Uludag University, Science and Technology Application and Research Center, 16059, Gorukle, Bursa–Türkiye

Abstract: Pestil, often known as fruit leather, is one of the most significant traditional foods manufactured and consumed throughout Türkiye. Due to its practical consumption, the availability of numerous nutrients, and the ability to meet energy requirements, pestil is recognized as a snack food. The aim of this study was to evaluate the bioaccessibility of total phenolic compounds (TPC), antioxidant capacity (AOC), and β-carotene in pumpkin pestils dried by hot air drying (HAD), vacuum drying (VCD), and microwave drying (MD) methods using an *in vitro* digestion model. Additionally, 5-hydroxymethylfurfural (HMF) formation and color degradation of pestils were evaluated. Changes in TPC and AOC were determined using spectrophotometric methods, whereas the detections of β-carotene and HMF were carried out with high performance liquid chromatography–photodiode array detector (HPLC–PDA). Significantly higher TPC (10.99–105.70%) and AOC (15.30–118.58%, 21.88–401.04% and 89.28–482.14%, in CUPRAC, FRAP, and DPPH assays, respectively) values were observed after drying ($p < 0.05$). Moreover, it was observed that there were statistically significant increases in TPC and AOC values after digestion for all pumpkin pestils compared to undigested samples ($p < 0.05$). Drying process resulted in lower β-carotene content (between 32.15–61.11%) in pumpkin pestils; however, it increased the percentage of bioaccessible β-carotene (max 62.16%) in the pestil samples. Compared to HD and VCD techniques, pumpkin pestils dried with MD exhibited significantly higher TPC, AOC and β-carotene content ($p < 0.05$). All of the pumpkin pestils except those dried by MD at 180 W contain HMF below the Turkish Standards Institute legal limit of 50 mg/kg. *L** value of pestils were described adequately to the zero- and first-order kinetic models while *a** and *b** values were only fitted to zero-order model. In conclusion, the findings obtained in this study pointed out that drying processes (especially by MD method) increased the bioaccessibility of TPC, AOC, and β-carotene.

1. INTRODUCTION

One of the most significant fruits produced worldwide is the pumpkin (*Cucurbita moschata*), which is valued for both its meaty shell and the seeds' ability to protect health (1). The latest recent official statistics show that Türkiye is the World's sixth pumpkins, squash, and gourds (771651 tonnes in 2021) producer with 100,853 ha of harvested area (2). To promote their increased consumption and usage for nutritional and technological purposes, it is important to be aware of the nutritional worth of food, especially fruits and vegetables. Carotenoids (especially β-carotene), water-soluble vitamins, and amino acids are all abundant in pumpkin. Due to its chemical structure, which is high in phenolics, vitamins, and antioxidants, pumpkin has a significant health-protective effect (3). On the other hand, it is known that the human health promoting activities of bioactive components depend on their bioaccessibility in the gastrointestinal system. The amount of a bioactive component that is made accessible for small intestinal absorption by the removal from the food matrix is referred to as bioaccessibility (4). The use of *in* vitro digestion methods, which are practical, reliable, and unrestricted due to ethical concerns, is quite common for the simulation of gastrointestinal conditions (5). There are many food processing factors affecting the bioacessibility of bioactive components, one of which is drying.

Cooked or pureed, pumpkin is highly regarded and has a wide range of culinary applications as a fruit or as a component in pies, soups, stews, breads, and several other meals (3). Since pumpkin contains a high percentage of water (96%), the product is susceptible to spoilage (1). Given that drying decreases the activity of water and significantly lengthens shelf life compared to fresh fruits and vegetables, it is possible to preserve food in a stable and safe ways (6).

One of the best dried products that appeals to individuals of all ages is pestil (7). Fruit pestils are made by applying various drying processes to fruit juice concentrate or puree. The pestils are directly marketed for human consumption without refrigeration and serve as economically and practically preserved versions of fruits in a variety of forms and sizes (8). Drying technique and drying temperature of the production process play a crucial role in determining the product's color, texture, minerals, vitamins, carotenoids, antioxidant capacity (AOC), total phenolic compound (TPC), and 5-hydroxymethylfurfural (HMF) formation (9). The quality of the final product may be improved by carefully choosing the raw material's drying procedure.

A common preservation technique for agricultural products is hot air drying due to its ease of usage and low cost. However, it results in the deterioration of sensitive compounds, causing the dried product' sensory and other crucial features to be lost (1).

In chemical and engineering processes, vacuum drying is a unit operation in which fresh material is dehydrated under sub-atmospheric pressures. Compared to the conventional hot air procedure at atmospheric pressure, lower pressure allows drying temperatures to be decreased and higher quality to be attained. Most frequently used materials for vacuum drying include those sensitive to temperature, low sensitivity to oxidation, and biotechnology products (10).

As a quick and efficient substitute drying method for convectional drying, microwave drying, a relatively new technology, has been suggested (11). When microwaves interact with the polar water molecules in fruits and vegetables, heat is produced, and a considerably higher drying rate than with air drying was attained (1). However this technique has adverse effects including the potential for textural damage, non-uniform heating caused by the geometry of the materials, reduced conversion of microwave energy to heat at decreased moisture content, and limited microwave penetration into the sample (6).

In the current study, pumpkin fruit was converted into pestil as a substitute product. This study is a continuation of our previous one (12). In our previous study, drying characteristics, mineral content, texture and sensory properties of pumpkin pestil produced by using microwave, hot air, and vacuum methods were investigated. The literature contains many studies on the bioaccessibility of fresh, cooked, and dried pumpkins' polyphenols and carotenoids (13-18). However, there is a very limited research on pumpkin pestil in the literature (19, 20). To the best of our knowledge, the bioaccessibility of TPC, AOC and β-carotene in pumpkin pestil has not been studied in previous researches. In this study, the TPC, AOC, β-carotene biaccessibility, color degradation kinetics, and HMF formation of the pumpkin pestil were firstly revealed. To the best of our knowledge, this is a first-ever attempt to explore the nutritional and quality factors of pumpkin pestils dried by hot air, vacuum, and microwave methods.

2. MATERIALS AND METHODS

2.1. Materials
Pumpkins (*Cucurbita moschata*) were purchased from a greengrocer in Bursa, Turkey, and kept in the refrigerator at 4±0.5°C until needed. Wheat starch, sucrose, and cinnamon, which were all from Turkey: Selva, Torku, and Bagdat brands, respectively were obtained from market.

2.2. The Procedure for Producing Pumpkin Pestil and Drying

The production procedure of pumpkin pestils were given in our previous research (12). By using a mold with a length of 8 cm, a width of 8 cm and a thickness of 4 mm, all pestil samples were dried uniformly to a moisture content of 0.12 g water/g dm.

Drying treatments were performed by using hot air drying (HD) at 50 °C, 60 °C, 70 °C, vacuum drying (VCD) at 50 °C, 60 °C and 70 °C with the absolute pressures of 300 mbar and microwave drying (MD) at 90 W and 180 W power settings. All drying methods were described previously (12).

2.3. *In vitro* Digestion Procedure

The INFOGEST *in vitro* digestion model simulating gastric and intestinal digestion was applied for the determination of TPC, AOC and β-carotene bioaccessibility in pumpkin pestils with small modifications (21). As previously mentioned, simulated saliva fluid (SSF), simulated gastric fluid (SGF), and simulated small intestinal fluid (SIF) were prepared (21). Oral, gastric, and intestinal electrolyte solutions contain potassium chloride (0.5 mol/L), potassium dihydrogen phosphate (0.5 mol/L), sodium bicarbonate (1 mol/L), sodium chloride (2 mol/L), magnesium chloride hexahydrate (0.15 mol/L), ammonium carbonate (0.5 mol/L) and hydrochloric acid (6 mol/L) were prepared as specified in the protocol. To simulate the digestion in the mouth, 4 mL of SSF, 0.025 mL of 0.3 M calcium chloride, and 0.975 mL of distilled water were added to 5 g of the sample and shaken in a water bath (JB50-D, Memmert, Germany) at 37 °C for 2 minutes. Since analysis was not planned after the oral phase, the sample was not collected after this phase. For the simulation of gastric digestion, 7.5 mL of SGF, 1.6 mL of pepsin (Sigma-Aldrich, Germany) with 25000 U/mL activity, 0.005 mL of 0.3 M calcium chloride were added and the pH was adjusted to 3 with 1 M hydrochloric acid. After completing the total volume to 10 mL with distilled water, it was shaken in a water bath at 37°C for 2 hours. After collecting 10 mL of post-digestion extracts, 5.5 mL of SIF to simulate small intestinal digestion, 2.5 mL of pancreatin enzyme (Sigma-Aldrich, Germany) with 800 U/mL activity, 1.25 mL of 160 mM bile, 0.02 mL of 0.3 M calcium chloride and the pH was adjusted to 7 with 1 M sodium hydroxide (Merck, Germany). After completing the total volume to 20 mL with distilled water, it was shaken in a water bath at 37 °C for 2 hours, and then samples were collected after small intestinal digestion. After the gastric and intestinal digestion simulation, the collected liquids were centrifuged (Sigma 3K 30, Germany) at 4 °C, 3500 rpm for 10 minutes, and the supernatants were stored at -20 °C until analysis.

2.4. Extraction for Total Phenolic Compound (TPC) and Antioxidant Capacity (AOC)

Pestil samples were extracted using the method specified by Kamiloglu and Capanoglu (22). 5 mL of extraction solution (75% methanol, 0.1% formic acid-containing aqueous solution) was added to 2 g of the sample and kept in a cooled ultrasonic water bath (Bandelin Sonorex RK 510 H, Germany) for 15 minutes. Then, the samples were centrifuged at 2700 rpm at 4 °C for 10 minutes (Sigma 3K 30, Germany) and the supernatant was collected at the end of extraction. Again, 5 mL of extraction solution was added to the residue and this process was repeated 3 more times. All collected supernatants were finally combined in a tube and stored at -20 °C until analysis.

2.5. TPC Determination

TPC analysis was performed according to the spectrophotometric Folin-Ciocalteu method. For this analysis, a calibration curve (R^2=0.9992) was obtained with different concentrations in the range of 5 – 50 ppm of standard gallic acid (Sigma-Aldrich, Germany) solution. The results were calculated using the regression equation of the obtained curve and expressed as mg gallic acid equivalent (GAE)/100 g dry matter (dm). In this method, 0.5 mL of extract is mixed with 0.5 mL of Folin-Ciocalteu (diluted 3 times with distilled water) reagent. After 5 minutes, 1 mL of saturated sodium carbonate solution (35%) is added to this mixture and vortexed and diluted to 3 mL with 1 mL of distilled water. After the incubation for 30 minutes, the absorbance was read in a spectrophotometer (UV-1800, Shimadzu) at 700 nm (23).

2.6. AOC Determination with DPPH, CUPRAC, and FRAP Assays

For DPPH (1,1-diphenyl-2- picrylhydrazyl) assay, 2 mL 6×10^{-3} M DPPH reagent was added to 100 μL of sample extract. After mixing by vortex and incubation at room temperature for 30 minutes, absorbances were read at 515 nm with a UV-Vis spectrophotometer (UV-1800, Shimadzu) (24). The Trolox® standard calibration curve showed linearity in the range of 5-150 ppm (R^2= 0.9897) and the results were expressed as μmol Trolox® equivalent (TE)/ g.

Determination of AOC with the CUPRAC (Copper ion reducing antioxidant capacity) assay was performed as previously stated in the literature (25). In 100 μL of extract, 1 mL of each reagents (10 mM copper(II) chloride, 7.5 mM neocuproin, 1 M ammonium acetate, and distilled water) were added. After the mixtures were kept at room temperature for 30 minutes, absorbance was measured at 450 nm with a UV-Vis spectrophotometer (UV-1800, Shimadzu). The Trolox® standard calibration curve showed linearity in the range of 5-800 ppm (R^2=0.972) and the results were expressed as μmol TE/g.

AOC determination by FRAP assay was performed as previously stated in the literature (26). Extracted 100 μL samples were mixed with 300 μL of distilled water and 3 mL of FRAP reagent and incubated at 37 °C for 30 minutes. Their absorbance was measured at 595 nm immediately at the end of the incubation period. The Trolox® standard calibration curve showed linearity in the range of 5-200 ppm (R^2=0.9971) and the results were expressed as μmol TE/g.

2.7. β-carotene Extraction

β-carotene extraction was carried out according to Barba et al. method (27). After adding 10 mL of the 50: 25: 25 (v/v/v) mixture of n-hexane, acetone, and ethanol, respectively to the 5.00±0.01 g sample, it was vortexed for 5 minutes. After 10 minutes of centrifugation at 10,000 g and 4 °C, the supernatant was transferred to a clean tube and evaporated with nitrogen gas. Following evaporation, the residue was diluted in 1 mL of 50/50 tetrahydrofuran (THF) and methanol.

2.8. Determination of β-Carotene with High Performance Liquid Chromatography - Photodiode Array Detector (HPLC-PDA)

After passing through 0.45 m membrane filters, all collected samples were injected to HPLC-PDA (Shimadzu LC-2030, Kyoto, Japan) with 10 μL volume. C18 column (250 mm × 4 mm, 5 μm, Nucleosil® 100-5) at 30 °C was used as stationary phase and methanol : acetonitrile (90:10 v/v) was used as mobile phase. Isocratic elution with a flow rate of 1 mL/ min was applied. In the identification of β-carotene, retention time in the column and characteristic UV spectra were taken into account, and spectral measurements were performed at 475 nm. The calibration curve of the β-carotene standard (Sigma-Aldrich, Germany) showed linearity in the range of 0.5-50 ppm (R^2≥0.9997), and the results were expressed as mg/100 g dm.

2.9. 5-Hydroxymethylfurfural (HMF) Determination

A modified version of Rufian-Henares and Delgado-Andrade's method (28) was used to perform the HMF analysis. 1.00±0.01 g of the sample was combined with 7 mL of distilled water and vortexed. The supernatant was then transferred to another tube after it had been centrifuged at 4500 g for 10 minutes at 4 °C. The residue was subjected to two more centrifugations after being mixed with 2 mL of distilled water. 0.250 mL of Carrez I (potassium ferrocyanide, 15% w/v) and 0.250 mL of Carrez II (zinc acetate 30% w/v) solutions were added on the collected supernatants. The volume was made up to 10 mL with distilled water following a final centrifugation. Samples taken into vials by passing through membrane filters (0.45 μm) were injected into the HPLC-PDA in a volume of 20 μL. C18 column (250 mm × 4 mm, 5 μm, Nucleosil® 100-5) at 32 °C was used as stationary phase and

acetonitrile:distilled water (5 : 95 v/v) was used as mobile phase. Isocratic elution with a flow rate of 1 mL/min was applied. In the identification of HMF, retention time in the column and characteristic UV spectra were taken into account, and spectral measurements were performed at 280 nm. The calibration curve of the HMF standard (Sigma-Aldrich, Germany) showed linearity in the range of 0.5-50 ppm (R^2≥0.9999), and the results were expressed as mg/100 g dm.

2.10. Color Analyses and Calculation of Kinetic Parameters

Color measurements of the pestil samples were carried out with a chroma meter (CR-5, Konica Minolta, Osaka-Japan). Obtained *L*, a*, b** values represented lightness or darkness, redness, or greenness, yellowness or blueness, respectively. Colors of the samples were measured before and throughout drying at specified time intervals in triplicate, and the average was used for further calculations.

Degradation kinetics of color in pestil samples were investigated with the following zero-order (Equation 1) and first-order (Equation 2) kinetic models (29-31).

$$C = C_0 \pm k_0 t \tag{1}$$

$$C = C_0 \exp(\pm k_1 t) \tag{2}$$

In which; *C* and C_0 are measured color values (*L*, a*, b**) at time *t* and time *0*, respectively; *t* is drying time; k_0 and k_1 are zero-order and first-order reaction rate constants, respectively; (+) and (-) represents formation and degradation of color values, respectively.

2.11. Statistical Analysis

For the evaluation of statistical analyses, SPSS 15.0 (SPSS Inc., USA) was employed. The Duncan's multiple range test was applied when there were significant variations between means (p<0.05).

3. RESULTS AND DISCUSSION

3.1. *In vitro* Bioaccessibility of Total Phenolic Content (TPC) and Antioxidant Capacity (AOC)

The effects of *in vitro* digestion on TPC of fresh and dried pumpkin pestils are given in Table 1. For undigested samples, dried fruit pestils were found to contain higher amounts of TPC (10.99–105.70%) compared to the ND mix. This could be due to the increment in the level of free flavonols by heat treatment and the concentration of phenolics as a result of drying procedures (32, 33). Additionally, heating methods may also weaken the fruit's cell walls, which encourages the release of phenolic compounds into the extraction solution and, as a result, increases the phenolic and AOC of the

extracts (33, 34). The highest TPC was recorded in pestils dried by MD at 180 W whereas the lowest content was found in the case of pestils dried by HD at 50 °C. Pumpkin pestils dried by MD had significantly higher TPC compared to HD and VCD methods (p<0.05). Similarly, Arslan and Ozcan (35) found that drying onion slices in both conventional and microwave ovens increased the total phenolic content of the samples, with the MD method obtaining the highest values. Furthermore, Ghanem et al. (36) found that compared to fresh peels, MD increases the TPC of dried Thompson navel orange peels. Additionally, according to Hamrouni-Sellami et al. (37), TPC increased 4.2-fold when drying sage plants by MD at 800 W as compared to fresh plants. It can be observed in Table 1 that an increase in drying temperature (especially VCD) has an important effect on TPC (p<0.05). The availability of precursors of phenolic molecules through non-enzymatic interactions between phenolic molecules may be the source of TPC increment at high temperatures (38).

ND mix showed an increase of 1.67 and 2.88 fold after gastric and small intestine digestion, respectively, compared to undigested one. After gastric digestion simulation, the *in vitro* bioaccessibility of pumpkin pestils increased between 1.92 and 4.05 fold. This finding is consistent with the data obtained in previous studies with vegetable juices (39), dried fruits, and nuts (40). These increases observed in TPC indicate that the extraction of phenolic compounds continues during gastric digestion and the released phenolic compounds remain stable in the acidic environment of the stomach (41). Statistically significant increases were observed in the TPC of pumpkin pestils after intestinal digestion compared to the data obtained after gastric digestion (2.84–97.14%) (p<0.05). In some previous studies, increases in the TPC were observed after intestinal digestion, and this was explained by the increase in the contact time of foods with intestinal fluids and the facilitation of the release of phenolic compounds by intestinal enzymes (41-43). Moreover, the increase in TPC bioaccessibility can be explained by the increased release of phenolics due to heat treatment during the drying process. Heat treatment can cause degradation of the food matrix and increase phenolic release (44, 45). In a study investigating the effect of drying on melon polyphenols, it was observed that the drying process caused an increase in the amount of bioaccessible TPC (46). In agreement with our findings, Kamiloglu et al. (47) also reported that cakes improved with black carrot pomace led to a rise in TPC following intestinal digestion.

Table 1: Changes in TPC of pumpkin pestils during *in vitro* digestion.

	Undigested	Simulated gastric digestion	Simulated small intestinal digestion
TPC (mg GAE /100 g dm)			
Non-dried mixture (ND mix)	40.65±0.00 [cC]	67.98±11.79 [eB]	117.24±15.17 [fA]
HD 50 °C	45.12±4.06 [cB]	172.32±2.47 [cA]	177.22±3.67 [eA]
HD 60 °C	74.30±12.51 [abC]	142.42±7.70 [dB]	225.33±12.34 [cdA]
HD 70 °C	67.95±2.31 [bC]	145.35±4.43 [dB]	286.55±3.66 [bA]
VCD 50 °C & 300 mbar	52.95±2.91 [cC]	181.69±4.99 [bcB]	199.78±5.08 [deA]
VCD 60 °C & 300 mbar	53.89±12.27 [cB]	187.65±15.64 [bcA]	207.53±10.79 [deA]
VCD 70 °C & 300 mbar	69.17±0.40 [bC]	176.05±11.08 [cB]	290.48±12.00 [bA]
MD 90 W	69.10±9.09 [bC]	197.87±8.80 [bB]	259.84±45.90 [bcA]
MD 180 W	83.62±7.76 [aB]	338.65±19.24 [aA]	377.61±54.21 [aA]

Values followed by different lowercase letters within the same column are significantly different (p < 0.05)
Values followed by different capital letters within the same row are significantly different (p < 0.05)

Changes in AOC as a result of *in vitro* digestion of pumpkin pestils and ND mix were determined and the results are given in Table 2. The highest AOC values were obtained with the CUPRAC method, followed by the FRAP and DPPH methods, respectively: CUPRAC > FRAP > DPPH. This may be due to the fact that DPPH assay only measures hydrophobic antioxidants, whereas FRAP assay only measures hydrophilic antioxidants and CUPRAC assay measures both of them (48). In addition, the formation of biologically unrelated nitrogen radicals in the DPPH method causes the antioxidant capacity to be underestimated from its true value (49). As for the TPC of the undigested samples, there were increases in the range of 15.30–118.58%, 21.88–401.04% and 89.28–482.14%, respectively, in the CUPRAC, FRAP and DPPH assays after drying. This increment was explained by Nicoli et al. (50) as the result of the formation of Maillard reaction products with high AOC. According to some studies, dried

fruits have superior antioxidant qualities because of their high polyphenol content and because their monomer derivatives are produced as a result of the complex polymeric molecules' hydrolysis or breakdown during dehydration (51, 52). Consistent to this findings, Karabacak (53) reported that drying cause an increment in CUPRAC values of blackthorn pestils compared to paste mixture. In contrast, dried fruits like pepino (54) and chokeberry (55) showed a decrease in AOC after dehydration. The fruit variety, drying techniques, drying applications and extraction and analysis methodologies of AOC could be the cause of the differences between these researches (33). Additionally, thermal treatments have the ability to significantly increase the overall antioxidant capacity of processed fruits and vegetables, even while drying destroys heat-, light-, and oxygen-sensitivephytochemicals (50, 56). Due to diversity of fruits and dehydration treatments, various results have been reported.

Compared to HD and VCD techniques, pumpkin pestils dried with MD exhibited significantly higher AOC (p<0.05). Similar to this, Benlloch-Tinocoet al. (57) found that microwave heating increased the AOC of kiwi fruit more than traditional heating provided.

After gastric digestion, a statistical increase was observed in the AOC values, as well as in the TPC results (p<0.05). However, varying results were obtained after small intestinal digestion. It was observed that there were statistically significant increases in AOC values after digestion for all pumpkin pestils compared to undigested samples (p<0.05). This finding is consistent with a previous studies for plant-based milks and blackthorn leathers in the literature, and the increase in AOC was explained by the release of phenolic compounds by enzyme activities after digestion or the formation of new compounds with antioxidant properties (58). Additionally, the variations in pH values caused by the deprotonation of the hydroxyl moiety located on the aromatic ring of phenolic compounds could be

the cause of the increases in AOC observed after small intestinal digestion. Based on these findings, it may be assumed that intestinal cells may be sufficiently protected from oxidative stress by superior polyphenol scavenging activity because the intestine has a lower pH than the stomach (59).

3.2. *In vitro* Bioaccessibility of β-Carotene

β-carotene is a carotenoid found in pumpkins that has been reported to exhibit beneficial health effects (13). For this reason, the concentration of β-carotene was determined in the pumpkin pestils and their ND mix before and after digestion by HPLC analysis. Chromatograms of β-carotene standard and pumpkin pestil were given in Figure 1a and Figure 1b, respectively. β-carotene content of ND mix was 59.53 mg/100 g dm. It is clear from the findings in Table 3 that drying caused a large loss of β-carotene (p<0.05) (32.15–61.11%). While the lowest loss was observed in MD at 180 W (32.15%), HD at 70 °C (61.11%) showed the highest degradation of β-carotene. Similar to this research, Hernández-Ortega et al. (60) found that carrot pomace powders dried by microwave method had higher β-carotene than samples dried with hot air. Since β-carotene is a component that is sensitive to oxidative thermal degradation, the short drying time of MD may decrease its degradation. Carotenoids' sensitivity to heat, oxygen, light, and enzymes may be the cause of the decrease in β-carotene after drying. Similarly, previous studies have reported that significant reductions in carotenoid content of coriander seeds (61), carrots, sweet potatoes, yellow bell peppers, broccoli (62), and pumpkin (63) were observed after drying. β-carotene was more degraded in HD method (between 56.89 – 61.11%) when compared with VCD method (between 35.14 – 52.48%). The VCD method could remove the oxygen in the oven and thus limit the carotenoid loss (17). Due to the high internal temperature and the high exposure to ambient oxygen in the HD method, the relative β-carotene losses in pumpkin pestils are significantly higher than those of the samples dried by VCD.

Table 2: Changes in AOC of pumpkin pestils during *in vitro* digestion.

	Undigested	Simulated gastric digestion	Simulated small intestinal digestion
DPPH (µmol TE/g dm)			
ND mix	0.28±0.06 [eC]	1.37±0.07 [eA]	0.80±0.13 [dB]
HD 50 °C	0.64±0.13 [dB]	1.47±0.04 [deA]	1.27±0.16 [cA]
HD 60 °C	0.60±0.07 [dB]	1.58±0.19 [cdA]	0.89±0.34 [dB]
HD 70 °C	0.53±0.02 [dC]	1.65±0.10 [bcA]	1.30±0.11 [bcB]
VCD 50 °C & 300 mbar	1.22±0.11 [cC]	1.67±0.11 [bcA]	1.48±0.02 [bcB]
VCD 60 °C & 300 mbar	1.22±0.06 [cA]	1.52±0.01 [cdeA]	1.32±0.30 [bcA]
VCD 70 °C & 300 mbar	1.21±0.09 [cB]	1.65±0.03 [bcA]	1.61±0.04 [bcA]
MD 90 W	1.44±0.05 [bB]	1.79±0.06 [bA]	1.65±0.20 [abAB]
MD 180 W	1.63±0.07 [aB]	2.01±0.04 [aA]	1.95±0.02 [aA]
FRAP (µmol TE/g dm)			
ND mix	0.96±0.06 [eA]	1.02±0.04 [eA]	0.17±0.08 [dB]
HD 50 °C	1.18±0.07 [deB]	1.46±0.09 [dAB]	1.96±0.42 [bA]
HD 60 °C	1.27±0.08 [cdA]	1.67±0.42 [cdA]	1.37±0.18 [bcA]
HD 70 °C	1.17±0.06 [deB]	2.05±0.34 [cA]	1.82±0.13 [bcA]
VCD 50 °C & 300 mbar	1.23±0.34 [cdeA]	2.01±0.18 [cA]	1.77±0.57 [bcA]
VCD 60 °C & 300 mbar	1.23±0.19 [cdeB]	1.90±0.27 [cA]	1.22±0.43 [cB]
VCD 70 °C & 300 mbar	1.47±0.03 [cA]	1.76±0.04 [cdA]	1.44±0.37 [bcA]
MD 90 W	2.94±0.09 [bA]	3.10±0.13 [bA]	1.44±0.13 [bcB]
MD 180 W	4.81±0.14 [aB]	6.02±0.17 [aA]	2.74±0.28 [aC]
CUPRAC (µmol TE/g dm)			
ND mix	1.83±0.08 [eB]	6.82±0.68 [fA]	0.13±0.08 [eC]
HD 50 °C	2.25±0.05 [dB]	10.27±0.29 [dA]	2.80±0.52 [dB]
HD 60 °C	2.25±0.03 [dB]	8.68±0.54 [eA]	8.36±0.23 [cA]
HD 70 °C	2.11±0.05 [dC]	13.05±0.26 [cA]	12.15±0.39 [bB]
VCD 50 °C & 300 mbar	2.14±0.06 [dC]	13.06±0.44 [cA]	10.75±0.58 [bB]
VCD 60 °C & 300 mbar	2.18±0.10 [dC]	14.94±1.32 [bA]	12.65±1.07 [bB]
VCD 70 °C & 300 mbar	2.46±0.09 [cC]	15.15±0.40 [bA]	12.21±1.93 [bB]
MD 90 W	3.27±0.14 [bB]	15.39±1.19 [bA]	14.58±0.91 [aA]
MD 180 W	4.00±0.14 [aC]	17.08±0.97 [aA]	14.65±1.70 [aB]

Values followed by different lowercase letters within the same column are significantly different (p < 0.05)
Values followed by different capital letters within the same row are significantly different (p < 0.05)
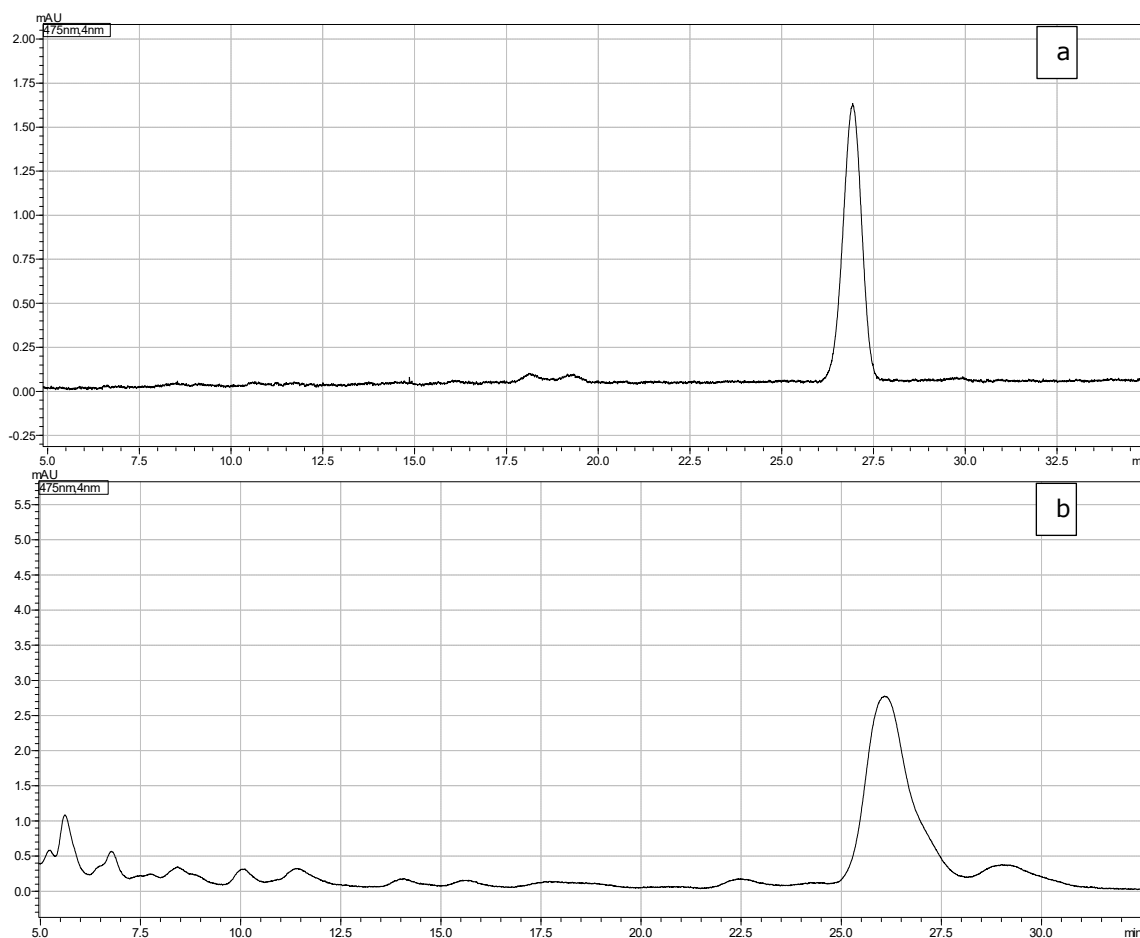
Figure 1: HPLC chromatogram of β-carotene standard (a) and pumpkin pestil sample (b).

Pumpkin pestils and their ND mix's bioaccessibility were decreased after gastric digestion with the ratio of 74.87–83.52% and 67.81%, respectively. The gastric phase's agitation and incubation were found to significantly decrease particle size and disrupt the food's structure, which facilitated the easier release of carotenoids from the cells and hence the β-carotene in the pumpkin pestils was found to be decreased (64).

There were statistically significant increases in β-carotene values after digestion for all pumpkin pestils compared to undigested samples ($p<0.05$). β-carotene in pumpkin pestils increased gradually with the pH value rising in the small intestine phase (pH = 7). It's probable that a high pH value will make carotenoids more stable (65). Bioaccessibility of β-carotene in pumpkin pestils dried by MD at 180 W (62.16%) was significantly higher than their ND mix (53.84%). By loosening the food matrix, heat processing is thought to increase the bioaccessibility of β-carotene and so facilitate its absorption. The kind and intensity of food processing affect the food matrix and, consequently, the bioaccessibility of carotenoids (66). The higher bioaccessibility of carotenoids by heat treatment was also reported from the other studies (13, 66, 67).

3.3. HMF Content

HMF is used as an indicator of non-enzymatic browning reactions. Since HMF is not found in fresh and unprocessed foods, its formation is directly related to the heat intensity applied to the food (28). Under the influence of heat, Maillard reactions involving reducing sugars and amino acids can take place during food preparation and preservation. The nutritional content of food is reduced, unfavourable taste and color changes occur, and product quality degrades as a result of the HMF formation, a significant Maillard reaction intermediate product, whose amount is restricted in many products due to its potential carcinogenic effect (68). The Maillard reaction is influenced by a lot of variables, including pH, temperature, metal ions, sugar type, and other factors (9). According to the Turkish Standards Institute (Grape pestil, TS12680), the legal limit for the HMF concentration of pestil is 50 mg/kg (69). In the current study, the HMF content of the pumpkin pestil was found to be between 29.73 to 115.86 mg/kg dm (Figure 2). The pumpkin pestil dried by MD at 180 W had the highest HMF concentration while the lowest HMF was obtained by VCD at 50 °C & 300 mbar method. All of the pumpkin pestils except dried by MD at 180 W contain HMF below the

Turkish Standards Institute legal limit (Grape pestil, TS12680) of 50 mg/kg. Due to the rapid increase of temperature in sample during microwave heating, it may be thought that the pestil samples were subjected to a high temperature and had higher HMF content as a result of this (70). Additionally, it was seen that the HMF content increased along with the magnetron power in MD method. Therefore, the HMF concentration in the product is affected by factors such as drying temperature, processing time, presence or absence of oxygen and magnetic waves (71). In both HD and VCD methods, pumpkin pestils dried at a medium temperature of 60 °C contained lower HMF than those dried at other temperatures (50 °C and 70 °C). This can be explained by the fact that drying at 60 °C takes a shorter time than at 50 °C and is less exposed to

Maillard reactions than that at 70 °C. Similarly, Wang et al. (72) reported that HMF formation in bee pollen increased with the increase in pulsed vacuum drying temperature. Additionally, Kanar and Mazi (70) investigated the change of HMF in pollen samples dried by freeze drying, hot air, vacuum, microwave, and microwave-assisted vacuum drying methods. They reported that hot air and vacuum drying methods did not cause a significant increase in the HMF content of the pollen. On the other hand, researchers, similar to this study, reported that the amount of HMF during microwave drying changed significantly depending on the applied microwave power. They reported that the highest amount of HMF was obtained from the samples dried with microwave and microwave assisted vacuum drying at 450 and 600 W power levels.

Table 3: Changes in β-Carotene of pumpkin pestils during *in vitro* digestion.

	Undigested	Simulated gastric digestion	Simulated small intestinal digestion
β-carotene (mg/100 g dm)			
ND mix	59.53±0.52 [aB]	19.16±0.66 [aC]	91.58±5.31 [aA]
HD 50 °C	24.15±0.26 [hB]	4.31±0.20 [dC]	25.21±0.18 [gA]
HD 60 °C	25.66±0.21 [gB]	4.23±0.15 [dC]	29.19±1.60 [fA]
HD 70 °C	23.15±0.23 [iB]	3.94±0.09 [dC]	24.97±1.56 [gA]
VCD 50 °C & 300 mbar	31.95±0.03 [dA]	7.73±0.15 [cB]	31.50±0.30 [efA]
VCD 60 °C & 300 mbar	38.61±0.16 [cB]	8.75±1.68 [cC]	48.06±0.81 [cA]
VCD 70 °C & 300 mbar	28.29±0.32 [fB]	4.45±0.06 [dC]	33.52±0.79 [deA]
MD 90 W	31.00±0.17 [eB]	4.64±0.09 [dC]	36.19±0.70 [dA]
MD 180 W	40.39±0.43 [bB]	10.15±0.26 [bC]	65.50±2.14 [bA]

Values followed by different lowercase letters within the same column are significantly different (p < 0.05)
Values followed by different capital letters within the same row are significantly different (p < 0.05)
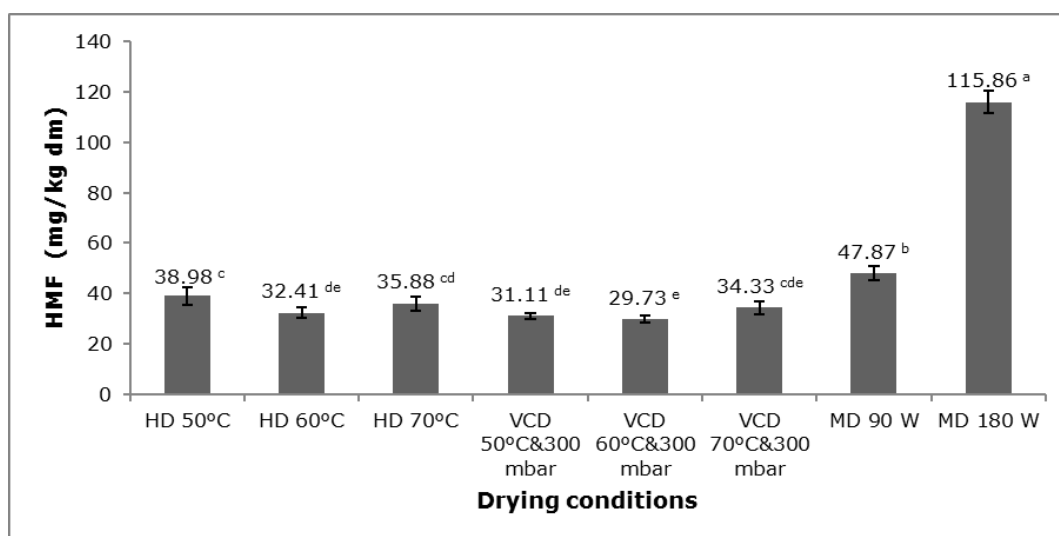
Figure 2: HMF content in pumpkin pestils.
Different lowercase letters in bars displays significant differences (p<0.05)

737

3.4. Kinetics of Color Change During Drying

The results of color values obtained from HAD, VD, and MWD of pumpkin pestils were presented in Figures 3, 4, and 5. As it can be observed from Figure 3a and 3b, *L** decreased through drying time. The reduction in *L** values changed from 32.81 (paste mixture) to 27.65 and 31.09 between the drying treatments representing the most, and the least damage occurred by MWD at 180 W and VD at 50 °C & 300 mbar, respectively. Besides, the decrement in *L** values indicated that pumpkin pestils became darker. A similar behaviour was reported by Maskan (29), Dadali et al. (30), Swain et al. (31) and Hou et al. (73). It has been defined that, falling values in brightness of the pestils might be resulted from the non-enzymatic Maillard reaction. The results for *a** values were given in Figure 4a and 4b. During different drying conditions an increment in *a** values were found, explaining that the pestils lost their color and became more red. This increment might be explained by decomposition of the pigments and the formation of the browning pigments (29, 74, 75). Similar results were expressed by other researchers in yellow sweet pepper (31), spinach (30), and purple carrot (76). A decrement in *b** value (Figure 5a and 5b) was also observed from the drying conditions. It was reduced from 40.50 to 15.04 during HAD at 60°C. This might be attributed to the decomposition

of carotenoid pigments due to longer drying times and higher drying temperatures leading to the detriment of yellowness (77).

Zero-order and first-order kinetic models were utilized for the determination of color changes in pumpkin pestils and kinetic parameters achieved from these models are represented in Table 4. The results revealed that *L** values were fitted to both of the zero- and first-order kinetic models whereas the zero-order kinetic model was found to be appropriate for *a** and *b** values of pumpkin pestils.

*L** values of pumpkin pestils were described adequately both to the zero- and first-order kinetic models as a result of very close R^2 values. On the other hand, zero order kinetic model had higher R^2 for *a** and *b** color values when compared to the first order reaction model. As a result of this situation, zero order kinetic model was better fitted than the first order model in terms of *a** and *b** values.

Current findings were in agreement with the literature in which several researchers reported that zero and first order models were fitted to the *L** values of kiwifruit (29), and zero order kinetic model was better fitted to *a** and *b** values of cabbage (78).
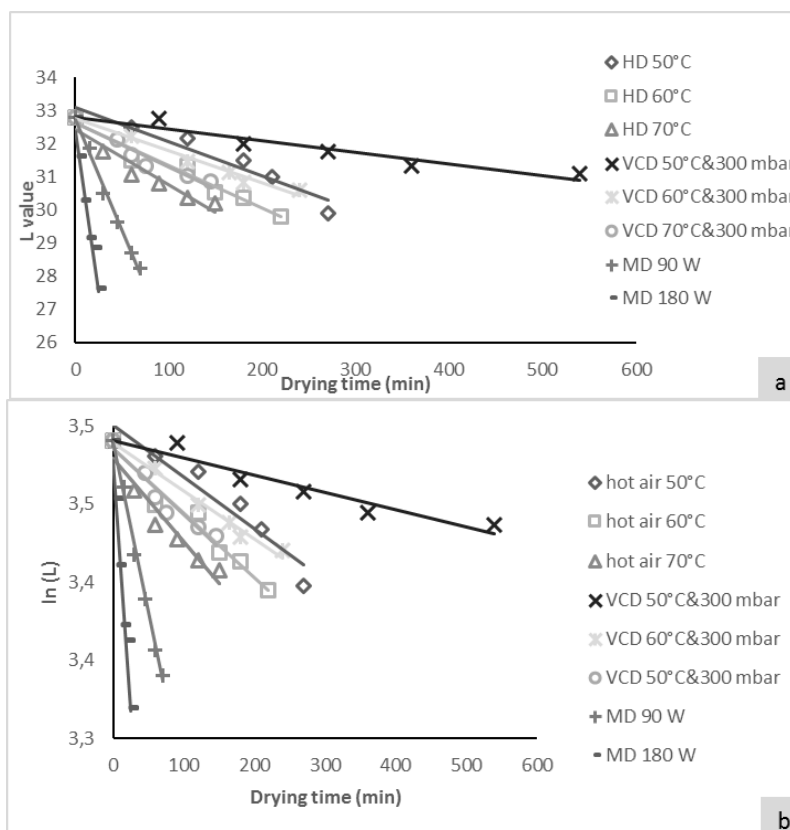
Figure 3: Kinetics of *L** color value changes in pestil samples as a function of drying time for different methods: zero-order model (a) and first-order model (b)

738
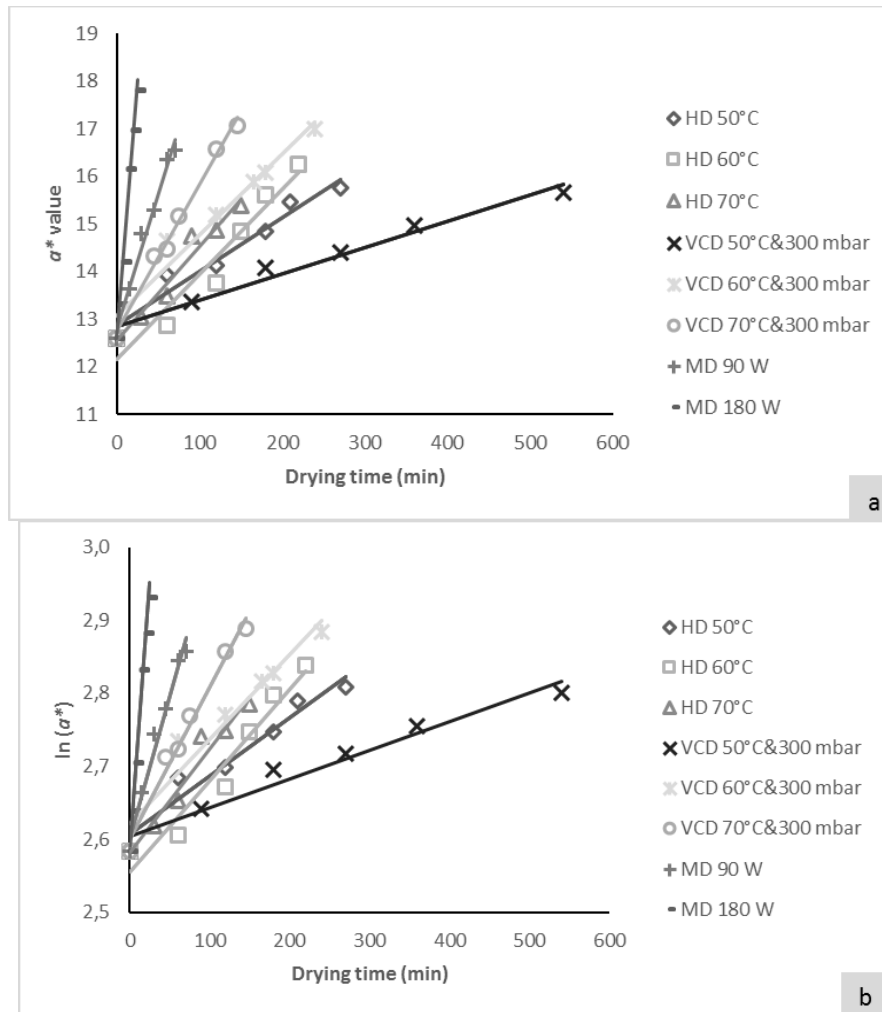
Figure 4: Kinetics of *a** color value changes in pestil samples as a function of drying time for different methods: zero-order model (a) and first-order model (b).

Table 4: The kinetic parameters of zero-order and first-order models for color values of pumpkin pestil.

Color parameter	Drying conditions	Zero-order model			First-order model		
		k_0(min^{-1})	C_0	R^2	k_1(min^{-1})	C_0	R^2
L*	HD 50 °C	0.0104	33.1030	0.9289	0.0003	3.5004	0.9221
	HD 60 °C	0.0129	32.6250	0.9542	0.0004	3.4855	0.9562
	HD 70 °C	0.0167	32.4280	0.9204	0.0005	3.4791	0.9265
	VCD 50 °C & 300 mbar	0.0035	32.8040	0.9286	0.0001	3.4907	0.9313
	VCD 60 °C & 300 mbar	0.0097	32.7550	0.9805	0.0003	3.4893	0.9819
	VCD 70 °C & 300 mbar	0.0135	32.6380	0.9305	0.0004	3.4856	0.9337
	MD 90 W	0.0666	32.7330	0.9932	0.0022	3.4897	0.9954
	MD 180 W	0.1933	32.3560	0.9520	0.0064	3.4778	0.9587
a*	HD 50 °C	-0.0114	12.8640	0.9542	-0.0008	2.5565	0.9452
	HD 60 °C	-0.0178	12.1500	0.9441	-0.0013	2.5047	0.9357
	HD 70 °C	-0.0197	12.5460	0.9599	-0.0014	2.5321	0.9592
	VCD 50°C&300 mbar	-0.0056	12.8400	0.9716	-0.0004	2.5546	0.9599
	VCD 60 °C & 300 mbar	-0.0171	13.0590	0.9510	-0.0012	2.5716	0.9317
	VCD 70 °C & 300 mbar	-0.0310	12.7350	0.9912	-0.0021	2.5507	0.9831
	MD 90 W	-0.0571	12.7800	0.9828	-0.0039	2.5517	0.9747
	MD 180 W	-0.2176	12.6030	0.9846	-0.0144	2.5413	0.9783
b*	HD 50 °C	0.1121	45.3540	0.9255	0.0040	3.8746	0.9115
	HD 60 °C	0.1271	42.0560	0.9835	0.0048	3.7962	0.9728
	HD 70 °C	0.1850	44.6770	0.9444	0.0065	3.8555	0.9241
	VCD 50 °C & 300 mbar	0.0391	40.0990	0.9346	0.0056	3.8136	0.8744
	VCD 60 °C & 300 mbar	0.0861	41.5610	0.9565	0.0028	3.7489	0.9412
	VCD 70 °C & 300 mbar	0.1694	44.6200	0.9544	0.0056	3.8486	0.9452
	MD 90 W	0.3214	45.8580	0.9036	0.0101	3.8670	0.8758
	MD 180 W	0.5726	42.6430	0.9337	0.0161	3.7596	0.9216

4. CONCLUSION

To the best of our knowledge, this is the first study to evaluate the effects of drying processes on the *in vitro* bioaccessibility of TPC, AOC, and β-carotene of pumpkin pestils. Additionally, HMF formation and color degradation kinetics after drying processes were also assessed.

The results of this study showed that the bioaccessible phenolic compounds, antioxidant capacity, and β-carotene increased as a result of drying the pumpkin pestils by HD, VCD, and MD methods. The highest TPC, AOC, and β-carotene values were observed by MD method in all drying treatments. However, pumpkin pestils dried by MD at 180 W showed HMF content above the Turkish Standards Institute's legal limit of 50 mg/kg for grape pestil. After drying *L** and *b** values decreased while *a** value increased significantly (p<0.05). The degradation of *L** value during drying was described well by both of the kinetic models (zero- and first- order) while *a** and *b** values were only fitted to zero-order kinetic model.

In this study, it has been seen that a functional product with high bioaccessibility of phenolic compounds and carotenoids can be developed by using pumpkin in fruit pestil production.

The MD method at 90 W can be recommended for both of the highest bioaccessible phenolic, antioxidant, and carotenoid content and reasonable HMF formation. In future studies, *in vivo* studies are also needed to fully understand the effect of drying processes on the bioaccessibility of pumpkin pestil's phenolics and carotenoids. Additionally, to reduce HMF formation, pre-cooking can be applied under vacuum at low temperatures, the amount of sugar added to the product formulations can be optimized, and new drying methods can be applied that allow the product to dry faster while preserving its nutritional value at lower temperatures.

5. REFERENCES

1. Seremet L, Botez E, Nistor OV, Andronoiu DG, Mocanu GD. Effect of different drying methods on moisture ratio and rehydration of pumpkin slices. Food Chemistry. 2016;195:104-9. Available from: <URL>.

2. FAO. FAO Stat Crops and livestock product 2023 [Available from: <URL>.

3. Guine RPP, Pinho S, Barroca MJ. Study of the convective drying of pumpkin (Cucurbita maxima). Food and Bioproducts Processing. 2011;89(C4):422-8. Available from: <URL>.

4. Yang ZH, Amrit BK, Zhao WR, Shi LH, Wu HJ, Barrow C, et al. Bioaccessibility and bioavailability changes of phenolic compounds in pumpkins (Cucurbita moschata): A review. Food Bioscience. 2022;47. Available from: <URL>.

5. Özdemirli N, Kamiloğlu S. Dondurma işleminin mandalina polifenollerinin biyoerişilebilirliği üzerine etkisi. Gıda ve Yem Bilimi Teknolojisi Dergisi. 2023(30):10-21. Available from: <URL>.

6. Zhang M, Tang J, Mujumdar AS, Wang S. Trends in microwave-related drying of fruits and vegetables. Trends in Food Science & Technology. 2006;17(10):524-34. Avaliable from: <URL>.

7. Bandaru H, Bakshi M. Fruit Leather: Preparation, packaging and its effect on sensorial and physico-chemical properties: A review. Journal of Pharmacognosy and Phytochemistry. 2020;9(6):1699-709. Available from: <URL>.

8. Nizamlioglu NM, Yasar S, Bulut Y. Chemical versus infrared spectroscopic measurements of quality attributes of sun or oven dried fruit leathers from apple, plum and apple-plum mixture. Lwt-Food Science and Technology. 2022;153. Available from: <URL>.

9. Tontul I, Topuz A. Effects of different drying methods on the physicochemical properties of pomegranate leather (pestil). Lwt-Food Science and Technology. 2017;80:294-303. Available from: <URL>.

10. Arevalo-Pinedo A, Murr FEX. Kinetics of vacuum drying of pumpkin (Cucurbita maxima): Modeling with shrinkage. Journal of Food Engineering. 2006;76(4):562-7. Available from: <URL>.

11. Horuz E, Bozkurt H, Karatas H, Maskan M. Effects of hybrid (microwave-convectional) and convectional drying on drying kinetics, total phenolics, antioxidant capacity, vitamin C, color and rehydration capacity of sour cherries. Food Chemistry. 2017;230:295-305. Available from: <URL>.

12. Karabacak AO, Suna S, Dorak S, Copur OU. Drying characteristics, mineral content, texture and sensorial properties of pumpkin fruit leather. Latin American Applied Research. 2021;51(3):193-201. Available from: <URL>.

13. Koh S, Loh S. In vitro bioaccessibility of β-carotene in pumpkin and butternut squash subjected to different cooking methods. International Food Research Journal. 2018;25(1):188-95. Available from: <URL>.

14. Lencina MS, dos Santos Ferreira C, Archaina D, Gómez MB, Mazzobre MF. Stability and bioaccessibility of iron in pumpkin discs vacuum impregnated with ferrous gluconate, β-cyclodextrin and ascorbic acid. LWT. 2022;161:113342. Available from: <URL>.

15. Bergantin C, Maietti A, Tedeschi P, Font G, Manyes L, Marchetti N. HPLC-UV/Vis-APCI-MS/MS determination of major carotenoids and their bioaccessibility from "Delica"(Cucurbita maxima) and "Violina"(Cucurbita moschata) pumpkins as food traceability markers. Molecules. 2018;23(11):2791. Available from: <URL>.

16. Aydin E. Evaluation of phenolic acid, total phenolic content, antioxidant capacity and in-vitro simulated bioaccessibility of healthy snack: Aromatized pumpkin chips. Emirates Journal of Food and Agriculture. 2022. Available from: <URL>.

17. Zhang Z, Wang X, Li Y, Wei Q, Liu C, Nie M, et al. Evaluation of the impact of food matrix change on the in vitro bioaccessibility of carotenoids in pumpkin (Cucurbita moschata) slices during two drying processes. Food & function. 2017;8(12):4693-702. Available from: <URL>.

18. Nagao A, Kotake-Nara E, Hase M. Effects of fats and oils on the bioaccessibility of carotenoids and vitamin E in vegetables. Bioscience, biotechnology, and biochemistry. 2013;77(5):1055-60. Available from: <URL>.

19. Seymen S, Özcan Sinir G, Çopur Ö. Physicochemical and quality properties of pumpkin (Cucurbita Moschata Duch.) jam, marmalade and fruit leather. Philippine Agricultural Scientist. 2020;103(3).

20. Thaosatien B. Development of fruit leather using Japanese pumpkin (Cucurbita maxima) and black plum (Prunus salicina) from the Royal Project. 2008. Available from: <URL>.

21. Minekus M, Alminger M, Alvito P, Ballance S, Bohn T, Bourlieu C, et al. A standardised static in vitro digestion method suitable for food - an international consensus. Food & Function. 2014;5(6):1113-24. Available from: <URL>.

22. Kamiloglu S, Capanoglu E. In vitro gastrointestinal digestion of polyphenols from different molasses (pekmez) and leather (pestil) varieties. International Journal of Food Science and Technology. 2014;49(4):1027-39. Available from: <URL>.

23. Obanda M, Owuor PO, Taylor SJ. Flavanol composition and caffeine content of green leaf as quality potential indicators of Kenyan black teas. Journal of the Science of Food and Agriculture. 1997;74(2):209-15. Available from: <URL>.

24. Katalinic V, Milos M, Kulisic T, Jukic M. Screening of 70 medicinal plant extracts for antioxidant capacity and total phenols. Food Chemistry. 2006;94(4):550-7. Available from: <URL>.

25.   Apak R, Guclu K, Ozyurek M, Celik SE. Mechanism of antioxidant capacity assays and the CUPRAC (cupric ion reducing antioxidant capacity) assay. Microchimica Acta. 2008;160(4):413-9.

26.   Benzie IFF, Strain JJ. The ferric reducing ability of plasma (FRAP) as a measure of ''antioxidant power'': The FRAP assay. Analytical Biochemistry. 1996;239(1):70-6. Available from: <URL>.

27.   Barba AIO, Hurtado MC, Mata MCS, Ruiz VF, de Tejada MLS. Application of a UV-vis detection-HPLC method for a rapid determination of lycopene and beta-carotene in vegetables. Food Chemistry. 2006;95(2):328-36. Available from: <URL>.

28.   Rufian-Henares JA, Delgado-Andrade C. Effect of digestive process on Maillard reaction indexes and antioxidant properties of breakfast cereals. Food Research International. 2009;42(3):394-400. Available from: <URL>.

29.   Maskan M. Drying, shrinkage and rehydration characteristics of kiwifruits during hot air and microwave drying. Journal of Food Engineering. 2001;48(2):177-82. Available from: <URL>.

30.   Dadali G, Demirhan E, Ozbek B. Color change kinetics of spinach undergoing microwave drying. Drying Technology. 2007;25(10):1713-23. Available from: <URL>.

31.   Swain S, Samuel DVK, Bal LM, Kar A. Thermal kinetics of colour degradation of yellow sweet pepper (Capsicum annum L.) undergoing microwave assisted convective drying. International Journal of Food Properties. 2014;17(9):1946-64. Available from: <URL>.

32.   Stewart AJ, Bozonnet S, Mullen W, Jenkins GI, Lean MEJ, Crozier A. Occurrence of flavonols in tomatoes and tomato-based products. Journal of Agricultural and Food Chemistry. 2000;48(7):2663-9. Available from: <URL>.

33.   Ozcan MM, Al Juhaimi F, Ahmed IAM, Uslu N, Babiker EE, Ghafoor K. Effect of microwave and oven drying processes on antioxidant activity, total phenol and phenolic compounds of kiwi and pepino fruits. Journal of Food Science and Technology-Mysore. 2020;57(1):233-42. Available from: <URL>.

34.   Szychowski PJ, Lech K, Sendra-Nadal E, Hernandez F, Figiel A, Wojdylo A, et al. Kinetics, biocompounds, antioxidant activity, and sensory attributes of quinces as affected by drying method. Food Chemistry. 2018;255:157-64. Available from: <URL>.

35.   Arslan D, Ozcan MM. Study the effect of sun, oven and microwave drying on quality of onion slices. Lwt-Food Science and Technology. 2010;43(7):1121-7. Available from: <URL>.

36.   Ghanem N, Mihoubi D, Kechaou N, Mihoubi NB. Microwave dehydration of three citrus peel cultivars: Effect on water and oil retention capacities, color, shrinkage and total phenols content. Industrial Crops and Products. 2012;40:167-77. Available from: <URL>.

37.   Hamrouni-Sellami I, Rahali FZ, Rebey IB, Bourgou S, Limam F, Marzouk B. Total Phenolics, Flavonoids, and Antioxidant Activity of Sage (Salvia officinalis L.) Plants as Affected by Different Drying Methods. Food and Bioprocess Technology. 2013;6(3):806-17. Available from: <URL>.

38.   Que F, Mao LC, Fang XH, Wu T. Comparison of hot air-drying and freeze-drying on the physicochemical properties and antioxidant activities of pumpkin (Cucurbita moschata Duch.) flours. International Journal of Food Science and Technology. 2008;43(7):1195-201. Available from: <URL>.

39.   Wootton-Beard PC, Moran A, Ryan L. Stability of the total antioxidant capacity and total polyphenol content of 23 commercially available vegetable juices before and after in vitro digestion measured by FRAP, DPPH, ABTS and Folin-Ciocalteu methods. Food Research International. 2011;44(1):217-24. Available from: <URL>.

40.   Kamiloglu S, Pasli AA, Ozcelik B, Capanoglu E. Evaluating the in vitro bioaccessibility of phenolics and antioxidant activity during consumption of dried fruits with nuts. Lwt-Food Science and Technology. 2014;56(2):284-9. Available from: <URL>.

41.   Özdemirli N, Beştepe SK. Kavun çekirdeği şerbetinde (sübye) fenolik bileşiklerin biyoerişilebilirliğinin değerlendirilmesi. Gıda. 2022;47(6):1130-9. Available from: <URL>.

42.   Bouayed J, Hoffmann L, Bohn T. Total phenolics, flavonoids, anthocyanins and antioxidant activity following simulated gastro-intestinal digestion and dialysis of apple varieties: Bioaccessibility and potential uptake. Food Chemistry. 2011;128(1):14-21. Available from: <URL>.

43.   Kamiloglu S. Taze ve dondurulmuş elmalarda ve elma posasinda polifenol biyoerişilebilirliğinin değerlendirilmesi. Gıda. 2019;44(3):409-18. Available from: <URL>.

44.   Dewanto V, Wu XZ, Liu RH. Processed sweet corn has higher antioxidant activity. Journal of Agricultural and Food Chemistry. 2002;50(17):4959-64. Available from: <URL>.

45.   Kayacan S, Karasu S, Akman PK, Goktas H, Doymaz I, Sagdic O. Effect of different drying methods on total bioactive compounds, phenolic profile, in vitro bioaccessibility of phenolic and HMF formation of persimmon. Lwt-Food Science and Technology. 2020;118. Available from: <URL>.

46.   Karabacak AO, Tunckal C, Tamer CE, Copur OU, Omeroglu PY. Bioacesibility of total phenolics and antioxidant activity of melon slices dried in a heat pump drying system. Journal of Food Measurement and Characterization. 2022;16(3):2154-71. Available from: <URL>.

47.   Kamiloglu S, Ozkan G, Isik H, Horoz O, Van Camp J, Capanoglu E. Black carrot pomace as a source of polyphenols for enhancing the nutritional value of cake: An in vitro digestion study with a standardized static model. LWT. 2017;77:475-81. Available from: <URL>.

48.   Capanoglu E, Kamiloglu S, Ozkan G, Apak R. Evaluation of antioxidant activity/capacity measurement

methods for food products. Measurement of Antioxidant Activity & Capacity: Recent Trends and Applications. 2018:273-86. Available from: <URL>.

49. Capanoglu E, Kamiloglu S, Demirci Cekic S, Sozgen Baskan K, Avan AN, Uzunboy S, et al. Antioxidant activity and capacity measurement. Plant Antioxidants and Health. 2020:1-66. Available from: <URL>.

50. Nicoli MC, Anese M, Parpinel M. Influence of processing on the antioxidant properties of fruit and vegetables. Trends in Food Science & Technology. 1999;10(3):94-100. Available from: <URL>.

51. Al-Farsi M, Alasalvar C, Morris A, Baron M, Shahidi F. Comparison of antioxidant activity, anthocyanins, carotenoids, and phenolics of three native fresh and sun-dried date (Phoenix dactylifera L.) varieties grown in Oman. Journal of Agricultural and Food Chemistry. 2005;53(19):7592-9. Available from: <URL>.

52. Chang CH, Lin HY, Chang CY, Liu YC. Comparisons on the antioxidant properties of fresh, freeze-dried and hot-air-dried tomatoes. Journal of Food Engineering. 2006;77(3):478-85. Available from: <URL>.

53. Karabacak AO. Effects of different drying methods on drying characteristics, colour and in-vitro bioaccessibility of phenolics and antioxidant capacity of blackthorn pestil (leather). Heat and Mass Transfer. 2019;55(10):2739-50. Available from: <URL>.

54. Di Scala K, Vega-Galvez A, Uribe E, Oyanadel R, Miranda M, Vergara J, et al. Changes of quality characteristics of pepino fruit (Solanum muricatum Ait) during convective drying. International Journal of Food Science and Technology. 2011;46(4):746-53. Available from: <URL>.

55. Samoticha J, Wojdylo A, Lech K. The influence of different the drying methods on chemical composition and antioxidant activity in chokeberries. Lwt-Food Science and Technology. 2016;66:484-9. Available from: <URL>.

56. Devahastin S, Niamnuy C. Modelling quality changes of fruits and vegetables during drying: A review. International Journal of Food Science and Technology. 2010;45(9):1755-67. Available from: <URL>.

57. Benlloch-Tinoco M, Igual M, Rodrigo D, Martinez-Navarrete N. Comparison of microwaves and conventional thermal treatment on enzymes activity and antioxidant capacity of kiwifruit puree. Innovative Food Science & Emerging Technologies. 2013;19:166-72. Available from: <URL>.

58. Aly E, Sanchez-Moya T, Darwish AA, Ros-Berruezo G, Lopez-Nicolas R. In vitro digestion effect on CCK and GLP-1 release and antioxidant capacity of some plant-based milk substitutes. Journal of Food Science. 2022;87(5):1999-2008. Available from: <URL>.

59. Tagliazucchi D, Verzelloni E, Bertolini D, Conte A. In vitro bio-accessibility and antioxidant activity of grape polyphenols. Food Chemistry. 2010;120(2):599-606. Available from: <URL>.

60. Hernández-Ortega M, Kissangou G, Necoechea-Mondragón H, Sánchez-Pardo ME, Ortiz-Moreno A.

Microwave dried carrot pomace as a source of fiber and carotenoids. 2013. Available from: <URL>.

61. Divya P, Puthusseri B, Neelwarne B. Carotenoid content, its stability during drying and the antioxidant activity of commercial coriander (Coriandrum sativum L.) varieties. Food Research International. 2012;45(1):342-50. Available from: <URL>.

62. Zhang ZY, Wei QY, Nie MM, Jiang N, Liu CJ, Liu CQ, et al. Microstructure and bioaccessibility of different carotenoid species as affected by hot air drying: Study on carrot, sweet potato, yellow bell pepper and broccoli. Lwt-Food Science and Technology. 2018;96:357-63. Available from: <URL>.

63. Rojas ML, Silveira I, Augusto PED. Ultrasound and ethanol pre-treatments to improve convective drying: Drying, rehydration and carotenoid content of pumpkin. Food and Bioproducts Processing. 2020;119:20-30. Available from: <URL>.

64. Lyu Y, Bi JF, Chen QQ, Wu XY, Qiao YN, Hou HN, et al. Bioaccessibility of carotenoids and antioxidant capacity of seed-used pumpkin byproducts powders as affected by particle size and corn oil during in vitro digestion process. Food Chemistry. 2021;343. Available from: <URL>.

65. Zhao Y, Yang QS, Zhou Q, Lu ZM, Fan RY, editors. Stability of Carotenoids in Russula alutacea Fr. Extraction. Advanced Materials Research; 2014: Trans Tech Publ. Available from: <URL>.

66. Veda S, Platel K, Srinivasan K. Enhanced bioaccessibility of beta-carotene from yellow-orange vegetables and green leafy vegetables by domestic heat processing. International Journal of Food Science and Technology. 2010;45(10):2201-7. Available from: <URL>.

67. Ribeiro EMG, Chitchumroonchokchai C, de Carvalho LMJ, de Moura FF, de Carvalho JLV, Failla ML. Effect of style of home cooking on retention and bioaccessibility of pro-vitamin A carotenoids in biofortified pumpkin (Cucurbita moschata Duch.). Food Research International. 2015;77:620-6. Available from: <URL>.

68. Elif K, Ömeroğlu PY. Geleneksel anjelika (melek otu) reçelinin fizikokimyasal ve duyusal özellikleri. Akademik Gıda. 2019;17(4):485-96. Available from: <URL>.

69. TSE. Turkish Standards Institute, Grape pestil, TS12680. Ankara, Turkey 2000. Available from: <URL>.

70. Kanar Y, Mazi BG. HMF formation, diastase activity and proline content changes in bee pollen dried by different drying methods. Lwt-Food Science and Technology. 2019;113. Available from: <URL>.

71. Turkiewicz IP, Wojdyło A, Lech K, Tkacz K, Nowicka P. Influence of different drying methods on the quality of Japanese quince fruit. LWT. 2019;114:108416. Available from: <URL>.

72. Wang SY, Bi YX, Zhou ZD, Peng WJ, Tian WL, Wang H, et al. Effects of pulsed vacuum drying temperature on drying kinetics, physicochemical properties

and microstructure of bee pollen. Lwt-Food Science and Technology. 2022;169. Available from: <URL>.

73. Hou LX, Ling B, Wang SJ. Kinetics of color degradation of chestnut kernel during thermal treatment and storage. International Journal of Agricultural and Biological Engineering. 2015;8(4):106-15. Available from: <URL>.

74. Weemaes CA, Ooms V, Van Loey AM, Hendrickx ME. Kinetics of chlorophyll degradation and color loss in heated broccoli juice. Journal of Agricultural and Food Chemistry. 1999;47(6):2404-9. Available from: <URL>.

75. Lopez A, Pique MT, Boatella J, Romero A, Ferran A, Garcia J. Influence of drying conditions on the hazelnut quality .3. Browning. Drying Technology. 1997;15(3-4):989-1002. Available from: <URL>.

76. Uyan SE, Baysal T, Yurdagel O, El SN. Effects of drying process on antioxidant activity of purple carrots. Nahrung-Food. 2004;48(1):57-60. Available from: <URL>.

77. Chen BH, Peng HY, Chen HE. Changes of carotenoids, color, and vitamin-a contents during processing of carrot juice. Journal of Agricultural and Food Chemistry. 1995;43(7):1912-8. Available from: <URL>.

78. Jaiswal AK, Abu-Ghannam N. Degradation kinetic modelling of color, texture, polyphenols and antioxidant capacity of York cabbage after microwave processing. Food Research International. 2013;53(1):125-33. Available from: <URL>.

Structural Properties, Photoluminescence, and Judd-Ofelt Parameters of Eu^{3+}- Doped CoNb$_2$O$_6$ Phosphor

Mustafa İlhan[*a] iD **, Lütfiye Feray Güleryüz**[b]**,** iD **Mete Kaan Ekmekçi**[c] iD

[a*]Department of Environmental Engineering, Faculty of Engineering, Marmara University, Maltepe, 34854, İstanbul, Türkiye
[b]Department of Mechanical Engineering, Faculty of Engineering, Ege University, Bornova, 35040, İzmir, Türkiye
[c]Marmara University, Department of Chemistry, Faculty of Science, Marmara University, Kadıköy, 34722, Istanbul, Türkiye

Abstract: Trivalent Eu-activated CoNb$_2$O$_6$ phosphors were fabricated using the molten salt method, which provides enhanced homogeneity and low sintering temperature. The ceramic samples were examined by spectral and structural analyses. In X-ray diffractions, the single phase of orthorhombic columbite type CoNb$_2$O$_6$ structure was obtained for 0.5-10 mol% Eu^{3+} doping concentrations, while a two theta peak shift towards the smaller angles occurred. SEM examinations show an irregular morphology and sub-micron grain sizes. In photoluminescence (PL) spectra, the phosphors showed typical Eu^{3+} emissions with the $^5F_0 \rightarrow {}^7F_J$ (J=0, 1, 2, 3, 4) transitions, and high emission peaks were observed at the $^5D_0 \rightarrow {}^7F_2$ transition. The photoluminescence of CoNb$_2$O$_6$:Eu^{3+} decreased over 5 mol% because of the concentration quenching. The energy transfer mechanism and critical distance of the phosphor are the dipole-dipole (d–d) interaction, and 15.70 Å, respectively. The spectral features of the phosphors were assessed by calculating the Judd-Ofelt intensity parameters (Ω_2, Ω_4) from the PL emission spectrum. The low Ω_2 parameter values or/and the $\Omega_4 > \Omega_2$ trend for CoNb$_2$O$_6$:Eu^{3+} phosphors were related to the less covalent or more ionic character of the Eu^{3+}−O^{2-} bond and the high local symmetry of the Eu^{3+} sites, while the high Ω_4 parameter values may be ascribed to the decrease in the electron density in the ligands.

Keywords: CoNb$_2$O$_6$; XRD; Eu^{3+} doping; photoluminescence; Judd-Ofelt analysis.

1. INTRODUCTION

Rare earth (RE) ions with 4f–4f inner shell transitions have undoubtedly contributed in a great manner to the development of luminescent applications and the increase in their use. Therefore, the RE ion-activated phosphors lead to numerous innovations in the development of new generation devices in various fields such as screen-display technology, lighting technology, and optical data communication due to some positive features such as long life, energy saving, improved physical durability, fast switching, small size, environmental friendliness, and high efficiency (1-16). The trivalent europium ion (Eu^{3+}) is known for its strong luminescence in the red spectral region, which exhibits interesting spectral properties, as well as having non-degenerate (J=0) first levels of transitions in both the absorption and luminescence spectrum and has a great advantage over other RE ions (10-14). The trivalent europium ion has $^5D_0 \rightarrow {}^7F_J$ (J=0, 1, 2, 3, 4, 5, 6) transitions. Among the transitions, $^5D_0 \rightarrow {}^7F_2$ is electric dipole (hypersensitive transition) and its intensity very strongly dependent

on environment, while the $^5D_0 \rightarrow {}^7F_1$ transition is magnetic dipole and intensity largely independent of environment (12-14).

The columbite-type structured divalent metal-niobium oxide compounds with orthorhombic symmetry can be formulated as MNb_2O_6 (M= Co, Mg, Sr, Mn, Ni, Cd, etc). The MNb_2O_6 structure has a significant benefit in that it can host guest ions that have ionic sizes comparable to those of the Nb and divalent M^{2+} ions present in the structure. As MNb_2O_6 structure, cobalt niobate ($CoNb_2O_6$) compound consisting of the CoO_6-NbO_6 octahedral (15-18) has been studied due to its magnetic (19-22), neutron scattering (23), dielectric (24), optical (25-27), gas sensing (28,29) magnetic-thermodynamic (29,30) properties. MNb_2O_6 (M= Ni, Zn, Co) sensing electrodes (SEs) were produced and studied for NO_2 detection at high temperature where $CoNb_2O_6$ electrode has the highest sensibility at 750 °C among the oxide SEs (29). The transitions of magnetic phase for $CoNb_2O_6$ were studied by measuring the specific heat, magnetic phase diagram, and magnetic susceptibility at 2.9 and 1.9 K (30). The low-temperature heat capacity and spin entropy properties of $CoNb_2O_6$ have been investigated (31). The molten salt method is one of the favorite synthetic methods used in the synthesis of niobates due to its advantageous properties such as short reaction time, low sintering temperature, improved homogeneity, and crystallinity (15, 18, 25-27). The superiority of the molten salt method may be assessed by comparison of the conventional solid-state method. The fabrication of $CoNb_2O_6$ by solid state reaction has been reported by different researchers as 900 (32), 900-1300 (24), and 1400 °C (33) as sintering temperatures and sintering times as 72, 6, and 22 h, respectively. Besides, $CoNb_2O_6$ has produced by the molten salt method at 800 °C for 4 h period (25-27).

In the study, the structural, photoluminescence properties and Judd-Ofelt intensity parameters of $Co_{1-x}Nb_2O_6$:xEu^{3+} (x=0.5, 1.5, 3, 5, 7, and 10 mol%) phosphors were studied. The spectroscopic and structural analyses of the samples were performed by XRD, SEM-EDS and PL.

2. EXPERIMENTAL

The $Co_{1-x}Nb_2O_6$:xEu^{3+} (x=0.005, 0.015, 0.03, 0.05, 0.07, 0.1 or x=0.5, 1.5, 3, 5, 7, 10 mol%) powders were fabricated by the molten salt route. In the synthesis, cobalt nitrate hexahydrate ($Co(NO_3)_2$.$6H_2O$) (Sigma-Aldrich, 98.5%), niobium oxide (Nb_2O_5) (Alpha Aesar, 99.9%), and europium oxide (Eu_2O_3) (Alpha Aesar, 99.9%) were used. For the synthesis, Li_2SO_4/Na_2SO_4 (salt/salt), and Li_2SO_4+Na_2SO_4/CoO+Nb_2O_5+Eu_2O_3 (salt/oxide) molar ratio were taken as 0.635/0.365 and 2/1 weight

ratio, respectively. The oxide mixtures and salt mixtures were prepared according to their stoichiometric ratios and mixed well in an agate mortar to provide homogeneity. The resulting mixtures were subsquently placed in an alumina crucible and sintered for 15 h at 800 °C in air atmosphere using an electric furnace. After the sintering, the phosphor powders were washed down several times with bi-distilled water to get rid of the ionic salts and filtered using a vacuum pump several times. The remnants of Cl$^-$ ions in the solution were controlled by qualitative analysis.

The phase structure of the ceramics was investigated by X-ray diffraction (XRD), (D2 PHASER, Bruker Corp., Germany) using Cu-K$_v$ radiation, Ni filter, scan rate = 2 °/min, 2θ=20-65°. The grain morphology and elemental identification were examined by scanning electron microscopy (SEM) (JSM-5910LV, JEOL Ltd., Japan) equipped with energy dispersive spectroscopy (EDS) (INCAx-Sight 7274, Oxford Industries, UK) after Au coating. PL (photoluminescence) results were obtained using fluorescence spectrometer (FLS920, Edinburgh Inst., UK) with a 450 W xenon lamp.

3. RESULTS AND DISCUSSION

3.1. XRD and SEM-EDS Results
Figure 1 presents the X-ray diffraction patterns of Eu^{3+}-doped $CoNb_2O_6$ samples. XRD results of the ceramic samples was defined by orthorhombic columbite symmetry (JCPDS no: 32-0304) with space group *Pbcn*60. As seen in Figure 1, there is no secondary or a minor phase in the XRD patterns of Eu^{3+}-doped $CoNb_2O_6$ samples, which may be attributed to the successful incorporation of Eu^{3+} ions into the columbite structure. The cell parameters of orthorhombic $CoNb_2O_6$ are a=14.167 Å, b=5.714 Å, c=5.046 Å, and V=408.47 Å^3 (30). The schematic representation of the $CoNb_2O_6$ crystalline structure consisting of corner-shared and edge-shared NbO_6 and CoO_6 octahedra is shown in Figure 2. Based on the ionic radius and coordination number (CN), the formation of the single-phase may be attributed to the substitution of Eu^{3+} ions with ionic radius 0.947 Å (for 6 C.N) by Co^{2+} ions (r=0.745 Å, for C.N. 6). The XRD peaks of the (131) reflection are shown in Figure 3. There are shifts towards smaller two-theta angles of the (131) XRD peak with the increase of Eu^{3+} concentration. Accordingly, the expansion of the lattice due to the large ionic radius of the Eu^{3+} ion, where the Eu^{3+} substitution instead of Co^{2+} is also likely to affect the charge balance and form some stress in the structure. However, despite some expansion in the lattice volume, the existence of the single-phase structure was preserved up to 10 mol% concentration, indicating that the dopant ion has located into the structure successfully.
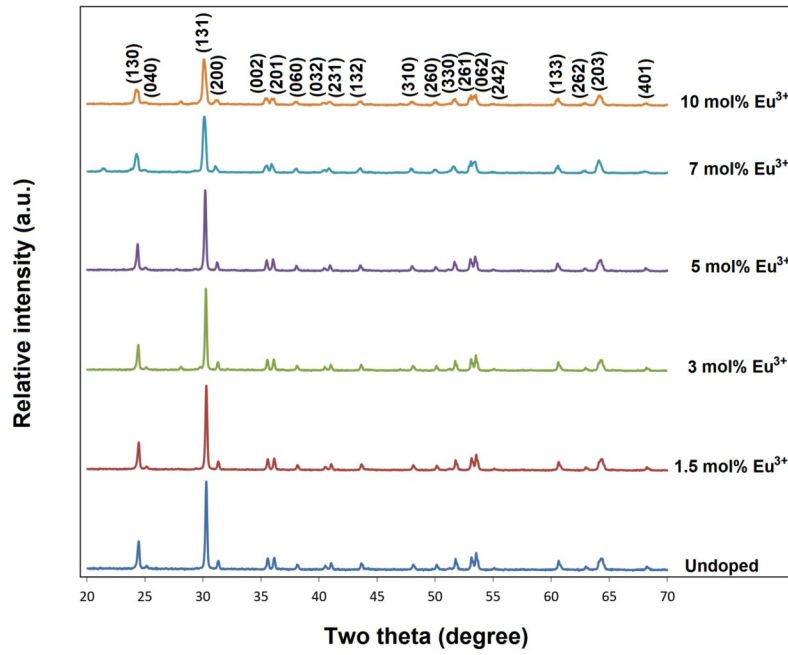
Figure 1: X-ray diffraction results of undoped and 0.5, 1.5, 3, 5, 7, and 10 mol% Eu^{3+} doped samples.
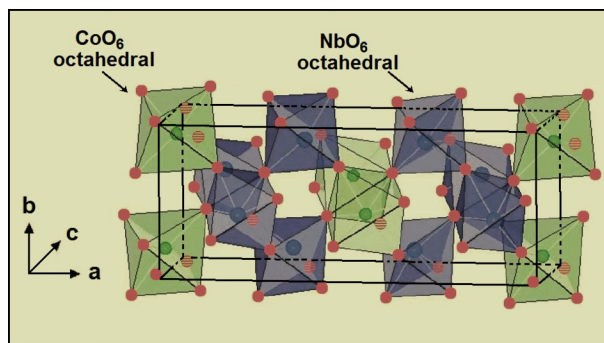
Figure 2: Schematic illustration of the CoNb$_2$O$_6$ crystal structure.
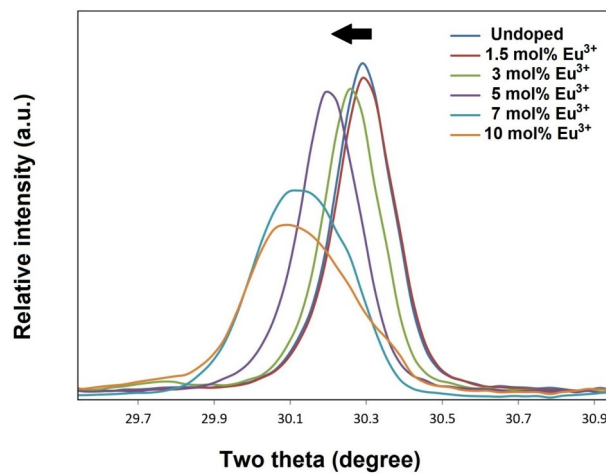
Figure 3: XRD two theta angles (131) shifted to lower angles with Eu^{3+} concentration.
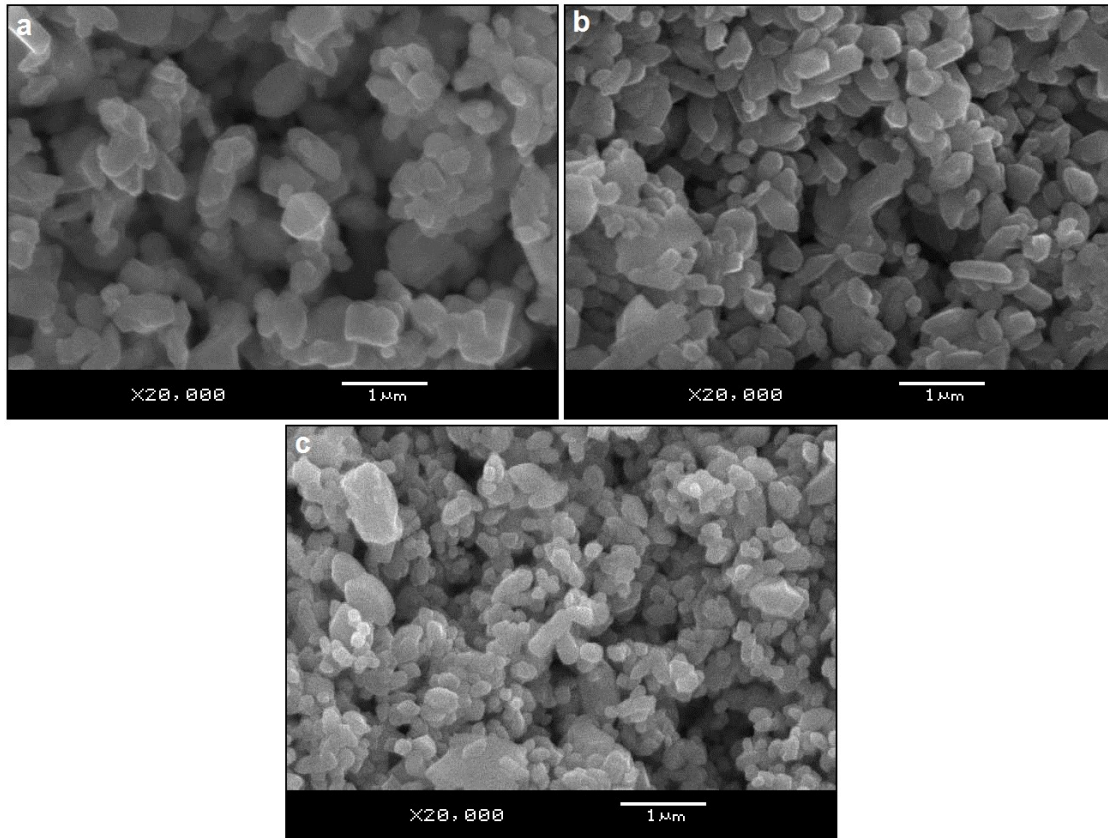
Figure 4: SEM micrographs of (a) undoped, (b) 5, (c) 10 mol% Eu^{3+} doped samples at 20000× magnifications and 20 kV acceleration voltage.
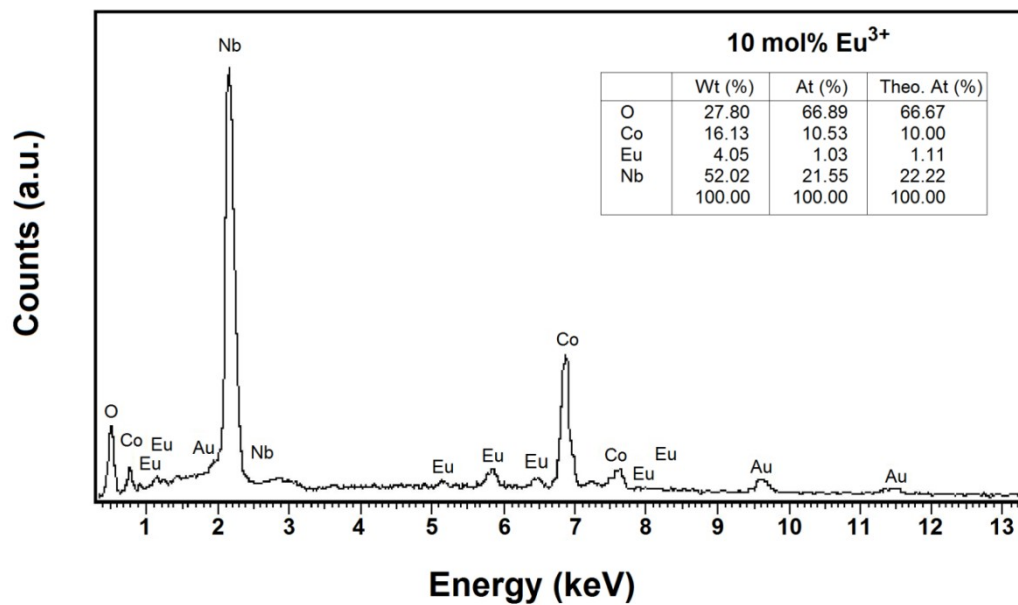
Figure 5: EDS spectrum and wt%, at% elemental compositions, and theoretical at% values for 10 mol% Eu^{3+}-doped sample.

Figure 4(a-c) shows the SEM micrographs at 20000x magnification for undoped $CoNb_2O_6$, 5, and 10 mol% Eu^{3+} doped samples, respectively. As seen in the SEM micrographs, the morphology of the grains was affected by the Eu^{3+} concentration. The grain shapes of the Eu^{3+} doped samples had a roundish, angular and irregular morphology, while the grain sizes, mostly in submicron scale, ranged from 0.05 to 2 µm. As seen from the SEM micrographs, the grain size reduced slightly as the concentration increases. The reason for the decrease in grain size with an increase in Eu^{3+} concentration could be attributed to the suppression of grain growth due to lattice restriction (15,34). Figure 5 shows the elemental compositions for the sample of $CoNb_2O_6$ doped with 10 mol% Eu^{3+} obtained using EDS, as weight (%) and atomic (%), by applying SEM acceleration voltage of 20 kV. According to the EDS results, the atomic compositions (%) and theoretical atomic compositions (%) of O, Co, Eu, Nb elements are 66.89, 10.53, 1.03, 21.55 and 66.67, 10.00, 1.11, 22.22, respectively, where the elemental compositions of Eu^{3+} doped $CoNb_2O_6$ agree with the theoretical compositions.

3.2. Photoluminescence of $CoNb_2O_6$:Eu^{3+}
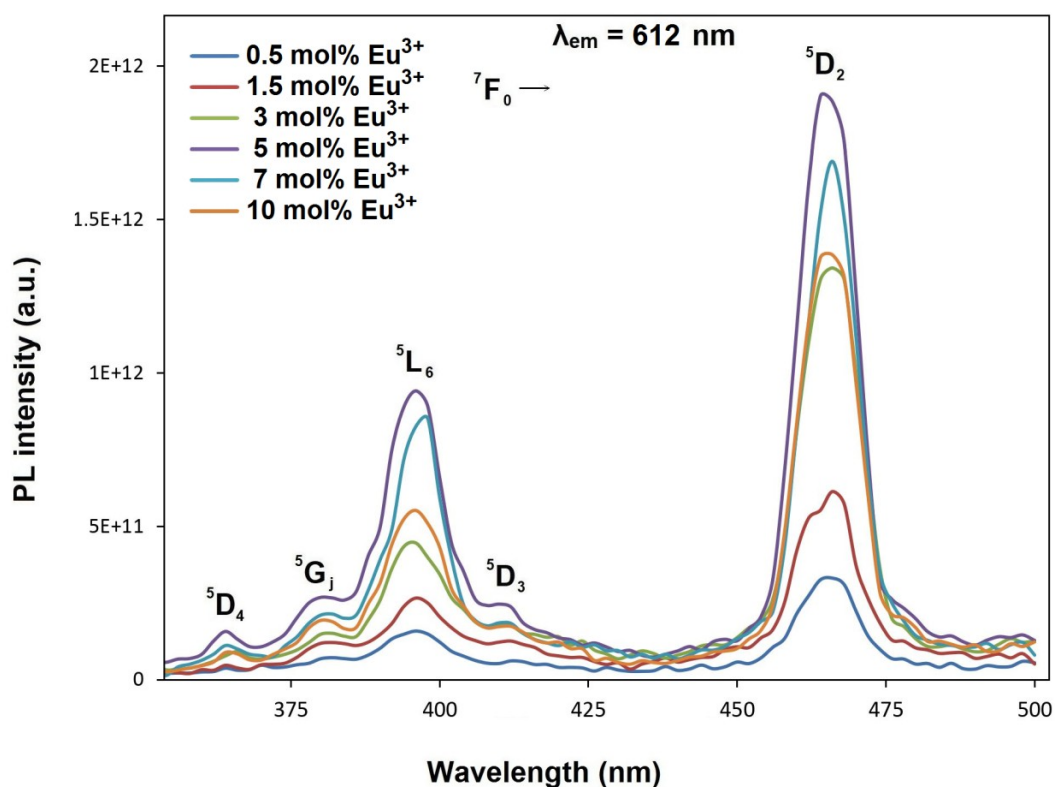
Figure 6: PL excitation spectra of the 0.5-10 mol% range of Eu^{3+} doped $CoNb_2O_6$ phosphors under 612 nm emission.
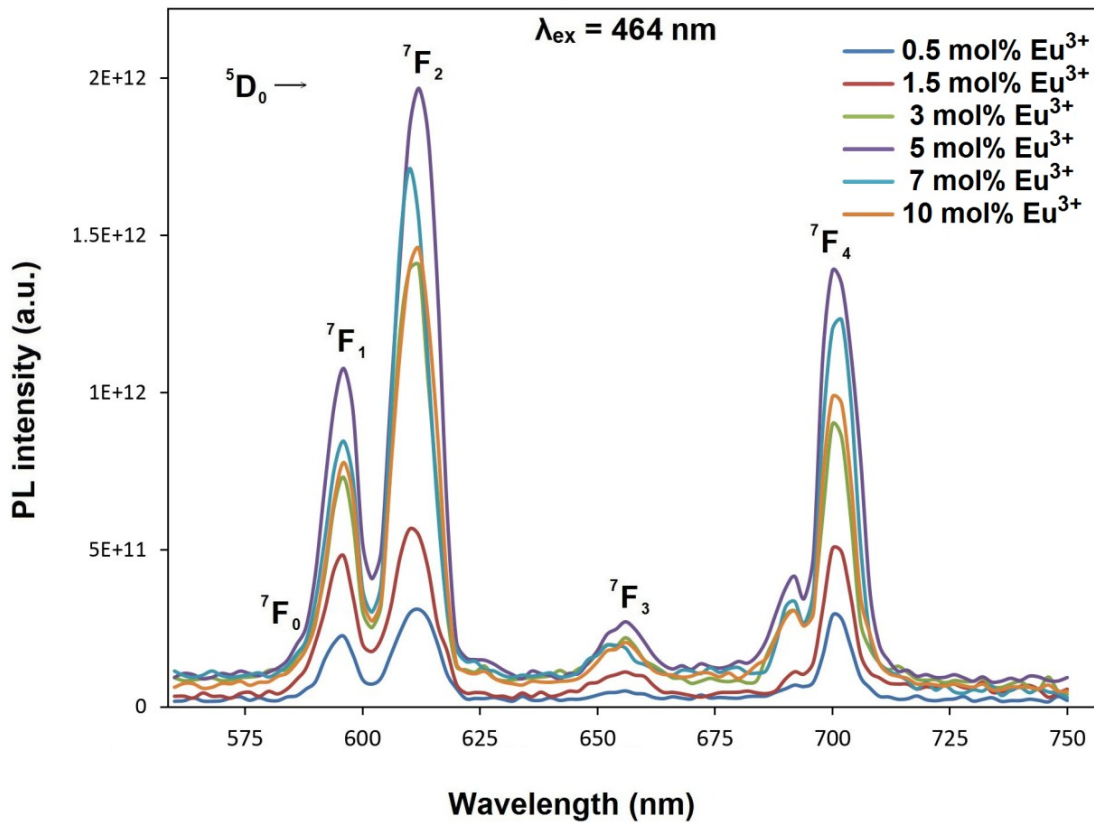
Figure 7: PL emission spectra of the 0.5-10 mol% range of Eu^{3+}-doped $CoNb_2O_6$ phosphors with the excitation of 464 nm.

Figure 6 shows the PL excitations of $CoNb_2O_6$:Eu^{3+} phosphors were recorded at emission wavelength of 612.0 nm, where the PL excitations were assigned with transitions of $^7F_0{\rightarrow}^5D_4$, $^7F_0{\rightarrow}^5G_J$, $^7F_0{\rightarrow}^5L_6$, $^7F_0{\rightarrow}^5D_3$, and $^7F_0{\rightarrow}^5D_2$. The PL emissions of $CoNb_2O_6$:Eu^{3+} phosphors were monitored at the $^5D_0{\rightarrow}^7F_0$, $^5D_0{\rightarrow}^7F_1$, $^5D_0{\rightarrow}^7F_2$, $^5D_0{\rightarrow}^7F_3$, $^5D_0{\rightarrow}^7F_4$ transitions with the excitation of 464 nm are shown in Figure 7. In all samples, the emission intensities of the $^5D_0{\rightarrow}^7F_2$ (electric dipole) transition are higher than the $^5D_0{\rightarrow}^7F_1$ (magnetic dipole) transition, which indicates Eu^{3+} ions occupying crystallographic sites without an inversion center (34,35). As given in Figure 7, the phosphor's PL emission increased by increasing concentration to 5 mol%, but decreased at 7 and 10 mol% due to concentration quenching. As the concentration of Eu^{3+} increases, the distance between Eu^{3+} ions decreases and non-radiative energy transfer becomes more significant. Accordingly, when the concentration of dopant ion reached the critical level, the critical distance (R_c) will be important for concentration quenching which promotes non-radiative energy transfer. The critical distance (R_c) for the energy transfer between Eu^{3+}-Eu^{3+} ions can be found by Eq. (1) (36):

$$R_C \approx 2\left(\frac{3V}{4\pi X c N}\right)^{1/3} \tag{1}$$

where V represents the volume of a unit cell, N (or Z) denotes the quantity of sites where a dopant ion can be placed, and X_c is the minimum concentration required for the dopant ion to be effective. For $CoNb_2O_6$:Eu^{3+} phosphor, it is X_c =0.05 mol ion in the unit cell, V=408.47 Å³ (30), and N=4. The critical distance (R_c) between Eu^{3+}–Eu^{3+} ions for energy transfer was calculated as 15.70 Å. According to Blasse's theory (37), if the distance between Eu^{3+}– Eu^{3+} ions is greater than 5 Å, the effective mechanism for energy transfer will be multipolar interaction, while the mechanism of exchange interaction will not be effective. The interaction type of energy transfer mechanism can be estimated by Van Uitert's theory (38). The theory suggests that if energy transfer occurs between dopants of the same type, Eq. (2) can be used to determine the

type of multipolar interaction mechanism, based on changes in emission intensity and ion concentration:

$$\frac{I}{x} = K\left[1+\beta(x)^{\Theta/3}\right]^{-1} \tag{2}$$

where the character of the multipolar interaction is represented by θ, while the RE concentration is represented by x. The ratio of emission intensity (I) to phosphor concentration (x) is represented by I/x. The constants K and β belong to the phosphor and are measured at the same excitation wavelength.

The values of $\theta=6$, $\theta=8$, and $\theta=10$ represent dipole–dipole (d–d), dipole–quadrupole (d–q), and quadrupole–quadrupole (q–q) interactions, respectively. If $\beta(x)^{\theta/3} \gg 1$ is accepted, Eq. (2) can be modified into Eq. (3):

$$\log(I/x) = K' - \Theta/3 \log x \, (K' = \log K - \log \beta) \tag{3}$$
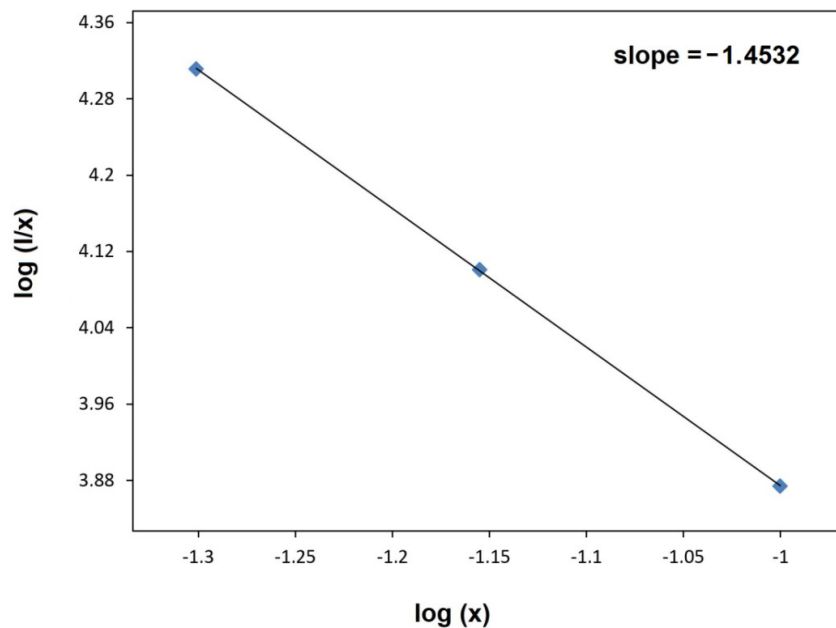
Figure 8: Relation between the $\log_{10}(I/x)$ and $\log_{10}(x)$ of $CoNb_2O_6:Eu^{3+}$ phosphors.

The θ parameter can be estimated from the slope of equation (3) which is plotted between the log (I/x) and log (x). The graph of log (I/x) as a function of log (x) for $CoNb_2O_6:Eu^{3+}$ phosphors is given in Figure 8. The critical concentration of Eu^{3+} was taken as $x \geq 0.05$. This plot shows the dependence of log (I/x) on log (x) of Eu^{3+} where the estimated value of the slope is about -1.4532. The θ value was determined as 4.36, which is close to 6. Correspondingly, the energy transfer mechanism of the phosphor can be ascribed to the dipole-dipole (d–d) interaction.
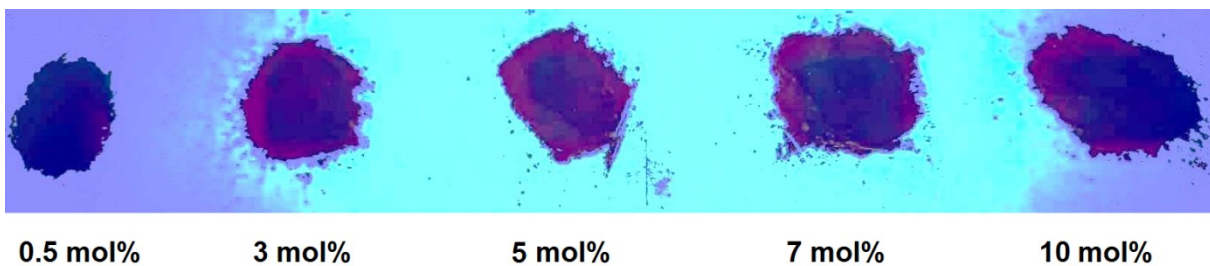
Figure 9: UV lamp photos of $CoNb_2O_6:xEu^{3+}$ ($x=0.5, 3, 5, 7, 10$) phosphors at 365 nm.

The UV lamp photographs of the phosphors under 365 nm are given in Figure 9. As seen from the pictures, the Eu^{3+}-doped phosphors have pale purple color, while the brightness slightly increased depending on the Eu^{3+} concentration.

Judd-Ofelt analysis and radiative properties
JO (Judd-Ofelt) intensity parameters are important in assessing the effectiveness of luminescent materials (39,40). The Eu^{3+} has distinctive properties among the RE^{3+} ions in determining JO intensity parameters because of its magnetic dipole transition ($^5D_0 \rightarrow {}^7F_1$), which is not affected by the surrounding environment and can serve as a standard for transitions originating from the $^5D_0$ level. By utilizing the emission spectra of materials containing Eu^{3+}, JO intensity parameters Ω_J (J=2,4,6) can be calculated using Eq. (4) (41,42):

$$\Omega_J = \frac{S_{MD}(V_1{}^3)}{e^2 V_J{}^3} \frac{9n^3}{n(n^2+2)^2} \frac{\int I_1(V_1)}{|\langle J \| U^J \| J' \rangle|^2 \int I_J(V_J)}$$

(4)

where the transition frequencies V_1, V_J and the integrated intensities I_1, I_J correspond to the $^5D_0 \rightarrow {}^7F_1$ and $^5D_0 \rightarrow {}^7F_J$ transitions, respectively. The magnetic dipole line strength is $S_{MD}=9.6 \cdot 10^{-42}$ (esu^2cm^2), and the refractive index is denoted by n. The elementary charge e is equal to $4.803 \cdot 10^{-10}$ (esu). The total angular momenta of the initial and final states are represented by J and J', respectively. The double reduced matrix elements for unit tensor operators are expressed as $|\langle J \| U^J \| J' \rangle|^2$. Only the $^5D_0 \rightarrow {}^7F_2$ ($U^2=0.0032$), $^5D_0 \rightarrow {}^7F_4$ ($U^4=0.0023$), and $^5D_0 \rightarrow {}^7F_6$ ($U^6=0.0002$) transitions have non-zero reduced matrix elements for all electric dipole (ED) transitions originating from the $^5D_0$ level (35).

The radiative transition probabilities are determined using the $^5D_0 \rightarrow {}^7F_J$ (J=1, 2, 4, 6) transitions, while the $^5D_0 \rightarrow {}^7F_J$ (J=0, 3, 5) transitions are not allowed and are therefore excluded from the JO calculation. Although the Ω_6 parameter is related to the $^5D_0 \rightarrow {}^7F_6$ transition, it was not incorporated in the calculation due to its inability to be detected by PL in the infrared region. Nonetheless, this transition's impact on the calculation is insignificant, as some studies have reported (18,41). The dipole strength determines the spontaneous transition probability (A), which can be expressed using Eq. (5):

$$A(J, J') = \frac{64\pi^4 V^3}{3h(2J+1)}[X_{ED} S_{ED} + X_{MD} S_{MD}]$$

(5)

where S_{ED} and S_{MD} are line strengths of electric and magnetic dipole moments respectively, and are expressed as esu^2cm^2 units. Planck's constant is denoted by "h". The formula for calculating the electric dipole line strengths (S_{ED}) based on the JO parameters is given by Eq. (6):

$$S_{ED}(J, J') = e^2 \sum_{J=2,4,6} \Omega_J \times |\langle J \| U^J \| J' \rangle|^2$$

(6)

The local field corrections for the ED and MD transitions are represented by the X_{ED} and X_{MD}, which can be obtained using Eq. (7) and Eq. (8) correspondingly:

$$X_{ED} = \frac{n(n^2+2)^2}{9}$$

(7)

$$X_{MD} = n^3$$

(8)

$$\frac{n^2-1}{n^2+2} \times \frac{1}{\rho} = \frac{\sum l_i r_i}{M}$$

(9)

where n is the refractive index. The n value for $CoNb_2O_6$ can be estimated from the Lorenz-Lorentz formula Eq. (9) (42-45):

where the compound's molar mass (*M*), density (□), and specific refraction (*r*$_i$) were used to determine its refraction index (*n*) value, while *l*$_i$ represents the atomic number of the element in the compound's nominal chemical formula. For $CoNb_2O_6$, the refraction index was found to be 1.974. Table 1 shows the Judd-Ofelt intensity parameters (Ω_2, Ω_4). The Ω_2 parameter is related to the hypersensitive $^5D_0 \rightarrow {}^7F_2$ electric dipole transition, which indicates the covalency of the Eu-O bond and the changes in the Eu^{3+} ion's environment. The Ω_4 parameter is associated with the electron density of the neighboring ligands, and the higher values of Ω_4

parameter indicate lower electron density. The Ω_2 parameter reflects short-range effects, whereas the Ω_4 parameter reflects long-range effects (46, 47). In Table 1, the Ω_2 and Ω_4 parameters are in the range of 2.547-4.242 and 4.504-6.297, respectively. The low Ω_2 parameter values or/and the $\Omega_4 > \Omega_2$ trend are considered as a decrease in the Eu^{3+}-O^{2-} covalent bond and the high local symmetry of the Eu^{3+} sites, where the nature of the Eu^{3+}–O^{2-} bond is less covalent or more ionic. Additionally, the high values of Ω_4 parameter may be attributed to a decrease in electron density in the ligands.

Table 1 J-O parameters (Ω_2, Ω_4), radiative transition and total transition probabilities ($A(J,J')$, (A_r)), branching ratios ((β_{cal}), (β_{exp})), and branching ratio differences (%) of $CoNb_2O_6$:Eu^{3+} phosphor.

Eu^{3+} conc. (mol%)	Eu^{3+} transitions	Ω_2 (10^{-20} cm^2)	Ω_4 (10^{-20} cm^2)	$A(J,J')$ (s^{-1})	A_r (s^{-1})	β_{cal} (%)	β_{exp} (%)	Difference (%)
0.5	$^5D_0 \rightarrow {}^7F_1$	2.878	5.118	92.081	424.436	21.70	23.23	6.61
	$^5D_0 \rightarrow {}^7F_2$			179.116		42.20	43.91	3.89
	$^5D_0 \rightarrow {}^7F_4$			153.239		36.10	32.86	8.98
1.5	$^5D_0 \rightarrow {}^7F_1$	2.547	4.504	91.845	385.917	23.80	25.40	6.29
	$^5D_0 \rightarrow {}^7F_2$			159.150		41.24	42.86	3.77
	$^5D_0 \rightarrow {}^7F_4$			134.923		34.96	31.74	9.20
3	$^5D_0 \rightarrow {}^7F_1$	4.015	4.909	91.660	488.782	18.75	19.98	6.13
	$^5D_0 \rightarrow {}^7F_2$			250.146		51.18	52.86	3.19
	$^5D_0 \rightarrow {}^7F_4$			146.976		30.07	27.16	9.67
5	$^5D_0 \rightarrow {}^7F_1$	3.522	5.219	91.905	468.080	19.63	20.94	6.24
	$^5D_0 \rightarrow {}^7F_2$			219.757		46.95	48.73	3.66
	$^5D_0 \rightarrow {}^7F_4$			156.418		33.42	30.33	9.25
7	$^5D_0 \rightarrow {}^7F_1$	4.242	6.297	91.886	544.752	16.87	18.03	6.47
	$^5D_0 \rightarrow {}^7F_2$			265.035		48.65	50.65	3.94
	$^5D_0 \rightarrow {}^7F_4$			187.831		34.48	31.32	9.17
10	$^5D_0 \rightarrow {}^7F_1$	3.816	5.395	91.840	491.815	18.67	19.91	6.20
	$^5D_0 \rightarrow {}^7F_2$			238.079		48.41	50.23	3.63
	$^5D_0 \rightarrow {}^7F_4$			161.896		32.92	29.86	9.29

Table 1 presents the radiative transition probabilities ($A(J,J')$), total radiative transition probabilities ($\Sigma A(J,J')$ or A_r), and branching ratios (β_{cal}) for the JO intensity parameters. The branching ratio (β or β_{cal}) of the Judd-Ofelt theory can be obtained using Eq. (10) (41,47) from the radiative transition probability ($A(J,J')$) and total radiative transition probability ($\Sigma A(J,J')$):

$$\beta(\%) = \frac{A(J,J')}{\sum A(J,J')} \cdot 100\% \tag{10}$$

The values of branching ratio ($\beta > 50\%$) are associated with the potential of laser emission (41,47). However, the branching ratios (β_{cal}) of $^5D_0 \rightarrow {}^7F_2$ transition for $CoNb_2O_6$:Eu^{3+} were found to be between 41.24-51.18% and slightly below 50%. The experimental branching ratios (β_{exp}) obtained

from the emission spectrum can be used to evaluate the branching ratios (β_{cal}) of Judd-Ofelt theory. On the other hand, this theory typically has an inherent error of approximately 15%, on describing spectral intensities (41,48). The variations between the experimental (β_{exp}) and calculated values (β_{cal}) of all

phosphors were determined to be between 3.19-9.67%, as shown in Table 1, which are less than 15%. In addition, the radiative lifetime found based on the JO parameterization is comparable to the

theoretical lifetime value, which is obtained from the Eu^{3+} emission spectrum, and can be determined via Eq. (11) (48):

$$\tau th = \frac{n_1^3}{14.65} \frac{I_1}{I_{tot}} \tag{11}$$

where the $^5D_0 \rightarrow {}^7F_1$ transition's integrated intensity is represented by I_1, the refractive index is represented by n, and I_{tot} represents the total integrated intensity. Table 2 displays the tabulated values for both the radiative lifetime (τ) and the theoretical radiative lifetime (τ_{th}). The τ and τ_{th}

values of $CoNb_2O_6:Eu^{3+}$ phosphors from 0.5 to 10 mol% Eu^{3+} varied between 2356-2033 µs and 2217-1925 µs, respectively, and the compatibility of radiative lifetimes was found in the range of 91.37-97.24%.

Table 2: Comparison of radiative lifetimes calculated according to JO parameters and Eq. (11).

Eu^{3+} conc. (mol%)	τ_{exp} (µs)	τ_{th} (µs)	Compatibility (%)
0.5	2356	2217	94.12
1.5	2591	2368	91.37
3	2046	1953	95.44
5	2136	2034	95.21
7	1836	1785	97.24
10	2033	1925	94.66

4. CONCLUSION

The structural, spectral properties and Judd-Ofelt parameterization of Eu^{3+} doped $CoNb_2O_6$ phosphors fabricated by the molten salt synthesis route were investigated in the study. In XRD results, the single-phase orthorhombic columbite structure of Eu^{3+} doped $CoNb_2O_6$ was determined between 0.5 and 10 mol% concentrations. SEM micrographs of the grains showed irregular morphology and the grain sizes varied from 0.05 to 2 ᴗm. EDS results indicated that the elemental compositions of Eu^{3+}-doped $CoNb_2O_6$ agree with the theoretical compositions. The phosphors displayed Eu^{3+} emissions with $^5F_0 \rightarrow {}^7F_J$ (J=0, 1, 2, 3, 4) transitions, and showed dominant peaks at the $^5D_0 \rightarrow {}^7F_2$ transition in PL spectra. Concentration quenching caused a decrease in the PL emissions of $CoNb_2O_6:Eu^{3+}$ over 5 mol%. The critical distance and energy transfer mechanism of the phosphor were determined to be 15.70 Å and dipole-dipole (d–d) interaction, respectively. The Judd-Ofelt intensity parameters (Ω_2, Ω_4) were calculated from the PL emission spectrum to evaluate the spectral properties of the phosphors. The high Ω_4 parameter values or/and the $\Omega_4 > \Omega_2$ trend for the phosphors

were explained by the high local symmetry of the Eu^{3+} ion, in which the Eu^{3+}–O^{2-} bond has the less covalent or more ionic character. The high values of the Ω_4 parameter was associated with the decrease in electron density in the ligands. The differences of the experimental and calculated branching ratios of all phosphors were estimated between 3.19-9.67%, which is below 15%.

5. CONFLICT OF INTEREST

There is no conflict of interest.

6. REFERENCES

1. Lohan R, Kumar A, Sahu MK, Mor A, Kumar V, Deopa N, Rao AS. Structural, thermal, and luminescence kinetics of $Sr_4Nb_2O_9$ phosphor doped with Dy^{3+} ions for cool w-LED applications. J. Mater. Sci: Mater. Electron 2023;34:694. Available from: <URL>.

2. Kanmani GV, Ponnusamy V, Rajkumar G, Kennedy SMM. A new Eu^{3+}-activated milarite-type potassium magnesium zinc silicate red-emitting phosphor for forensic applications. J. Mater Sci:

Mater Electron 2023;34:765. Available from: <DOI>.

3. Swathi BN, Krushna BRR, Manjunatha K, Wu SY, Subramanian B, Prasad BD, Nagabhushana H. Single phased vivid red-emitting $CaLa_2ZnO_5:Eu^{3+}$ nanophosphor: WLEDs, visualization of latent fingerprints and anti-counterfeiting applications, Mater. Res. Bull. 2023;165:112279. Available from: <DOI>.

4. Ekmekçi MK, İlhan M, Başak AS, Deniz S. Structural and luminescence properties of Sm^{3+} doped TTB-type $BaTa_2O_6$ ceramic phosphors. J. Fluoresc. 2015;25:1757–1762. Available from: <DOI>.

5. Güleryüz LF. Effect of Nd^{3+} doping on structural, near-Infrared, and cathodoluminescent properties for cadmium tantalate phosphors. JOTCSA. 2023;10:77–88. Available from: <DOI>.

6. Hajlaoui T, Pinsard M, Kalhori H, Légaré F, Pignolet A. Second harmonic generation in ferroelectric $Ba_2EuFeNb_4O_{15}$-based epitaxial thin films. Opt. Mater. Express 2020;10: 1323–1334. Available from: <DOI>.

7. İlhan M, Keskin İÇ. Evaluation of the Structural, near-infrared luminescence, and radioluminescence properties of Nd^{3+} activated TTB-lead metatantalate phosphors. JOTCSA. 2023;10:453–66. Available from: <DOI>.

8. Sheikh S, Hussain F. Structural, Dielectric, and Magnetic Properties of $Ba_2Bi_{9-xFe5}+xTi_8O_{39}$ tetragonal tungsten bronze ceramics. Mater. Res. Express 2023;10:036103. Available from: <DOI>.

9. İlhan M, Güleryüz LF. Cathodoluminescence and photoluminescence of $BaTa_2O_6:Sm^{3+}$ phosphor depending on the sintering temperature. Chem. Pap. 2022;76:6963-6974. Available from: <DOI>.

10. Shrivastava R, Khaparde S. Luminescence studies of diopside doped with various concentrations of Dysprosium (III). Res. Chem. Intermed. 2022;48:969-982. Available from: <DOI>.

11. Li J, Wang X, Cui R, Deng C. Synthesis and photoluminescence studies of novel double-perovskite phosphors, Ba_2GdTaO_6: Eu^{3+} for WLEDs. Optik 2020;201:163536. Available from: <DOI>.

12. İlhan M, Güleryüz LF. Boron doping effect on the structural, spectral properties and charge transfer mechanism of orthorhombic tungsten bronze β-$SrTa_2O_6:Eu^{3+}$ phosphor. RSC. Adv. 2023;13:12375. Available from: <DOI>.

13. Binnemans K. Interpretation of europium(III) spectra, Coord. Chem. Rev. 2015;295: 1–45. Available from: <DOI>.

14. Walrand CG, Binnemans K. *Handbook on the physics and chemistry of rare earths*, Elsevier, Belgium, 1998, pp.101–264.

15. Ekmekçi MK, İlhan M, Ege A, Ayvacıklı M. Microstructural and radioluminescence characteristics of Nd^{3+} doped columbite-type $SrNb_2O_6$ phosphor. J. Fluoresc. 2017;27:973–979. Available from: <DOI>.

16. Pullar RC. The Synthesis, Properties, and Applications of Columbite Niobates ($M^{2+}Nb_2O_6$): A Critical Review. J. Am. Ceram. Soc., 92;2009:563–577. Available from: <DOI>.

17. İlhan M, Ekmekçi MK, Oraltay RG, Başak AS. Structural and near-infrared properties of Nd^{3+} activated Lu_3NbO_7 Phosphor. J. Fluoresc. 2017;27:199–203. Available from: <DOI>.

18. İlhan M, Ekmekçi MK, Keskin İÇ. Judd–Ofelt parameters and X-ray irradiation results of $MNb_2O_6:Eu^{3+}$ (M = Sr, Cd, Ni) phosphors synthesized via a molten salt method. RSC Adv. 2021;11:10451. Available from: <DOI>.

19. Scharf W, Weitzel H, Yaeger I, Maartense I, Wanklyn BM. Magnetic structures of $CoNb_2O_6$. J. Magn. Magn. Mater. 1979;13:121-124. Available from: <DOI>.

20. Sarvezuk PWC, Kinast EJ, Colin CV, Gusmao MA, Cunha JBM da, Isnard O. New investigation of the magnetic structure of $CoNb_2O_6$ columbite. J. Appl. Phys. 2011;109: 07E160. Available from: <DOI>.

21. Xu Y, Wang LS, Huang YY, Ni JM, Zhao CC, Dai YF, Pan BY, Hong XC, Chauhan P, Koohpayeh SM, Armitage NP, and Li SY. Quantum critical magnetic excitations in spin-1/2 and Spin-1 chain systems. Physical Review X 2022;12:021020. Available from: <DOI>.

22. Lei S, Wang C, Guo D, Gao X, Cheng D, Zhou J, Cheng B, Xiao Y. Synthesis and magnetic properties of MNb_2O_6 (M = Fe, Co, Ni) nanoparticles. RSC Adv. 2014;4:52740. Available from: <DOI>.

23. Ringler JA, Kolesnikov AI, Ross KA. Single-ion properties of the transverse-field Ising model material $CoNb_2O_6$. Phys. Rev. B 2022;105:224421. Available from: <DOI>.

24. Zhang Y, Liu S, Zhang Y, Xiang M. Microwave dielectric properties of low-fired $CoNb_2O_6$ ceramics

with B_2O_3 addition. J Mater Sci: Mater Electron 2016;27:11293–11298. Available from: <DOI>.

25. Erdem R, İlhan M, Ekmekçi MK, Erdem Ö. Electrospinning, preparation and photoluminescence properties of $CoNb_2O_6$:Dy^{3+} incorporated polyamide 6 composite fibers. Appl. Surf. Sci. 2017;421:240-246. Available from: <DOI>.

26. Ekmekçi MK, İlhan M, Güleryüz LF, Mergen A. Study on molten salt synthesis, microstructural determination and white light emitting properties of $CoNb_2O_6$:Dy^{3+} phosphor. Optik. 2017;128:26–33. Available from: <DOI>.

27. Ekmekçi MK, Erdem M, Başak AS, Mergen A. Molten salt synthesis, visible and near-IR region spectral properties of europium or neodymium doped $CoNb_2O_6$ columbite niobate. Dalton Trans. 2015;44:5379. Available from: <DOI>.

28. Balamurugan C, Maheswari AH, Lee DW. Structural, optical and selective ethanol sensing properties of p-type semiconducting $CoNb_2O_6$ nano powder. Sens. Actuators B Chem. 2014;205:289-297. Available from: <DOI>.

29. Liu F, Wang B, Yang X, Guan Y, Sun R, Wang Q, Liang X, Sun P, Lu G. High-temperature stabilized zirconia-based sensors utilizing MNb_2O_6 (M: Co, Ni and Zn) sensing electrodes for detection of NO_2. Sens. Actuators B Chem. 2016;232:523–530. Available from: <DOI>.

30. Hanawa T, Shinkawa K, Ishikawa M, Miyatani K, Saito K, Kohn K. Anisotropic spesific heat of $CoNb_2O_6$ in magnetic fields. J. Phys. Soc. Japan 1994;63:2706-2715. Available from: <DOI>.

31. Liang T, Koohpayeh SM, Krizan JW, McQueen TM, Cava RJ, Ong NP. Heat capacity peak at the quantum critical point of the transverse Ising magnet $CoNb_2O_6$. Nat. Commun. 2015;6:7611. Available from: <DOI>.

32. Mulla IS, Natarajan N, Gaikwad AB, Samuel V, Guptha UN, Ravi V. A coprecipitation technique to prepare $CoTa_2O_6$ and $CoNb_2O_6$. Mater. Lett. 2007;61:2127–2129. Available from: <DOI>.

33. Felten EJ, Sprang PG, Rosen S. Phase Relations in the System $CoNb_2O_6$-$CoTa_2O_6$. J. Am. Ceram. 1966;49:273-276. Available from: <DOI>.

34. İlhan M, Keskin İÇ, Gültekin S. Assessing of photoluminescence and thermoluminescence properties of Dy^{3+} doped white light emitter TTB-lead metatantalate phosphor. J. Electron. Mater. 2020;49:2436-2449. Available from: <DOI>.

35. Saraf R, Shivakumara C, Behera S, Nagabhushana H, Dhananjaya N. Photoluminescence, photocatalysis and Judd-Ofelt analysis of Eu^{3+}-activated layered BiOCl phosphors. RSC Adv. 2015;5:4109–4120. Available from: <DOI>.

36. Blasse G. Energy transfer between inequivalent Eu^{2+} ions. Solid State Chem. 1986;62:207–211. Available from: <DOI>.

37. Blasse G. Energy transfer in oxidic phosphors. Philips Res. Rep. 1969;24:131-144.

38. Van Uitert LG. Characterization of energy transfer interactions between rare earth ions. J. Electrochem. Soc. 1967;114:1048–1053. Available from: <DOI>.

39. Judd BR. Optical Absorption Intensities of Rare-Earth Ions. Phys Rev. 1962;127:750. Available from: <DOI>.

40. Ofelt GS. Intensities of crystal spectra of rare-earth ions. J. Chem. Phys. 1962;37: 511. Available from: <DOI>.

41. İlhan M, Keskin İÇ. Analysis of Judd–Ofelt parameters and radioluminescence results of $SrNb_2O_6$:Dy^{3+} phosphors synthesized via molten salt method. Phys. Chem. Chem. Phys. 2020;22:19769. Available from: <DOI>.

42. Batsanov SS. *Structurnaya refractometria*, Moscow "Visshaya Shkola", 1976.

43. Shannon RD, Fischer RX. Empirical electronic polarizabilities in oxides, hydroxides, oxyfluorides, and oxychlorides. Phys. Rev. B. 2006;73:235111. Available from: <DOI>.

44. Bokii GB, Koshits MAP. *X-ray Structure Analysis*, MSU, Moscow, 1964.

45. Korotkov AS, Atuchin VV. Prediction of refractive index of inorganic compound by chemical formula. Opt. Commun. 2008;281:2132–2138. Available from: <DOI>.

46. İlhan M, Keskin İÇ. Evaluation of structural behaviour, radioluminescence, Judd-Ofelt analysis and thermoluminescence kinetic parameters of Eu^{3+} doped TTB–type lead metaniobate phosphor. Phys. B: Condens. Matter 2020;585:412106. Available from: <DOI>.

47. İlhan M, Güleryüz LF, Keskin İÇ, Katı Mİ. A comparison of spectroscopic properties of Dy^{3+}-doped tetragonal tungsten bronze MTa_2O_6 (M = Sr, Ba, Pb) phosphors based on Judd–Ofelt parameters.

RESEARCH ARTICLE

Mater. Sci: Mater. Electron 2022;33:16606–16620. Available from: <DOI>.

48. Werts MHV, Jukes RTF, Verhoeven JW. The emission spectrum and the radiative lifetime of Eu^{3+} in luminescent lanthanide complexes. Phys. Chem. Chem. Phys., 2002;4:1542–1548. Available from: <DOI>.

Synthesis, Characteristics and Applications of Graphene Composites: A Survey

Biswajit Patra[1], Niharika Das[1], Ruturaj Sahoo[1], Dipak Kumar Sahoo[1], Biswajit Dalai[2]* iD
Chhatrapati Parida[3] and Sarat Kumar Dash[4]**

[1] Department of Physics, School of Sciences, GIET University, Gunupur, 765022, India.
[2] Department of Physics, School of Sciences, GIET University, Gunupur, 765022, India.
[3] Department of Physics, Odisha University of Agriculture and Technology, Bhubaneswar, 751003, India.
[4] Department of Physics, Regional Institute of Education (NCERT), Bhubaneswar, 751022, India.

Abstract: Graphene is the name for a monolayer sheet of carbon atoms that are bonded together in a repeating pattern of hexagons. This sheet is only one atom thick. Monolayers of graphene stacked on top of each other. In this article, we have compared the characterization results of graphene and graphene oxide along with synthesis via different methods. A sigma bond connects each atom in a graphene sheet to its three closest neighbours and each atom also contributes one electron to a conduction band that covers the entire graphene sheet. Graphene when oxidized is called graphene oxide (GO) and is mostly used in photoelectric, materialistic, catalyst and energy fields due to its thermal, electrical and mechanical characteristics. It is also used in the field of medical science, drug delivery and biomedical applications. Graphene have been improved due to import of 3D printing technology. In last few years, graphene has taken the attention of most material science researchers due to its various applications. Graphene based polymers and nanocomposites are widely used in sensors, optoelectronics, magneto transport, automotive, biosensors, electronics and aerospace fields.

1. INTRODUCTION

In continuation to our earlier review on perovskite materials (1) and extraction of thorium (2), we have reported here the various synthesis routes of graphene and graphene oxide with their characteristics and applications. Graphene is a hexagonal planner carbon ring which is derived from 3D massive covalent structured graphite. Graphene based materials exist in both 2D and 3D structures (3-6). A single layer of graphene (SLG) was obtained by Novoselov et. al. (3, 4). Graphene is a sp^2 bonded carbon structure where atoms densely packed in a honeycomb crystal lattice and a two-dimensional crystal. Graphite oxide is mostly used for producing expandable amount of graphene oxide (GO) and reduced graphene oxide. GO produces stable dispersion because of its negative charge and interacts with the functional groups of textiles. Wearable e-textiles are flexible, washable, and long-lasting. To coat textiles with graphene, vacuum filtering, brush coating, direct electrochemical technique and screen-printing methods are employed. Single layer graphene shows high mobility of electrons, high optical transparency, high mechanical strength, high thermal conductivity and high surface area (3-6). A mono layer graphene sheet and graphene membranes are shown in Fig. 1.
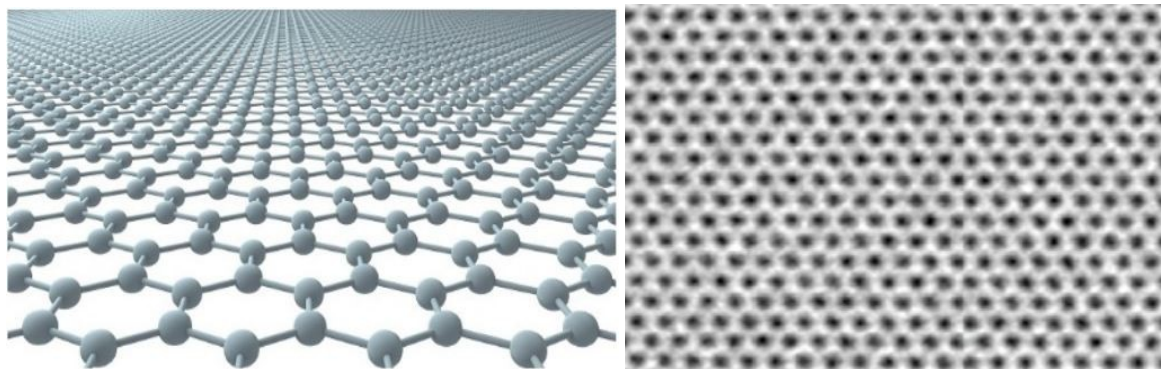
Figure 1: a. Mono layer graphene sheet **b.** Single layer graphene membranes.

Apart from these, graphene shows a countless advantage and it is a favourable for the evolution of recently invented applied science. Therefore, graphene is regarded as product material for high value applications such as sensor, water treatment, biomedical application, structural application (6-14). Graphene exhibits a whole range of electronic application due to its mechanical and other properties (14–17). Graphene based materials like GO & rGO are manufactured into wearable E-textiles which is safer for nature (16-22). Raman spectroscopy is used to find graphene optical phonons G-peak and 2D band (23-25). It is also used to count the number of atomic planes in few layers graphene (FLG) (25-27).

GO is formed by oxidizing graphene and it contains various oxygen-containing reactive groups such as carbonyl groups, epoxy groups, hydroxyl groups, and carboxylic groups (27, 28). The oxidation of bulk graphite powders using a chemical oxidation technique produces graphene oxide nanosheets (28-30). In 1859, Brodie had reported the developing work on production of GO (by adding a portion of potassium chloride to a slurry of graphite in fuming nitric acid) (30). The exact structure of GO is a difficult task to establish. GO and its products have been recently used in bio devices, biotechnology, bio sensors, energy storage and antifungal activity (28-31). GO is the forerunner of reduced graphene oxide (rGO).

2. EXPERIMENTAL SECTION

2.1. Synthesis of Graphene
2.1.1. Synthesis of graphene in top-down method
The top-down synthesis of graphene (Figure 2) includes the reduction of powered graphite. The commonly used synthesis processes are (i) mechanical exfoliation (ME), (ii) chemical exfoliation-reduction (CER), (iii) atomic force microscope (AFM) method, (iv) liquid phase exfoliation (LPE) method and (v) electrochemical exfoliation (ECE) method. Mechanical exfoliation method was developed by Novaselov et al. (3) SLG (single-layer graphite) with a lateral size of micrometer of highly oriented pyrolytic graphite, was physically peeled using household scotch tape in this procedure. As this process only produced small area of SLG, it was not suitable for large scale production (31–35). AFM method also produces FLG (1 to 6 layers) to MLG (multi-layer graphite: layers may vary up to 30 layers). Liquid phase exfoliation method includes two main steps: (i) a reduction

reaction reduces Vander Waal stresses and increases graphite interlayer separation (33-35) and then (ii) Graphite exfoliated by rapid heating and sonication (or high shear forces) to yield graphene with single to several sheets (35, 36-39). An electric voltage is used in electrochemical exfoliation to force ionic species to interact and form graphite rods, where they create a gaseous molecule capable of exfoliating different graphene layers.
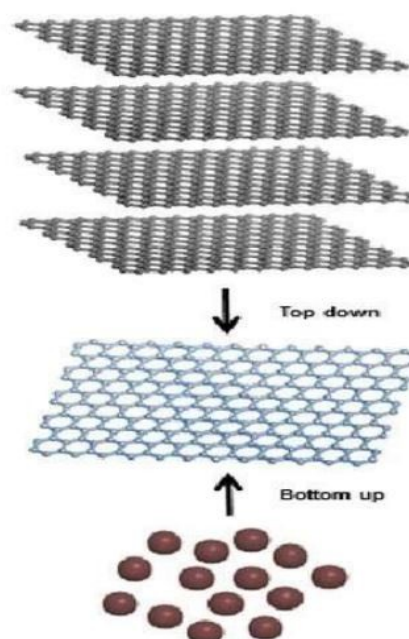
Figure 2: Synthesis of graphene by top down and bottom-up approach

Chemical oxidation reduction of graphite is the most standard method for synthesizing graphene (38-40). Graphite is first transformed to graphite oxide, which is then reduced to graphene by chemical, thermal, or electrochemical techniques. There are varieties of oxidation techniques: Staudenmaier's, Hummer's and Tour's methods (39-42). They oxidize graphite by adding concentrated acids and strong oxidants.

2.1.2. Synthesis of graphene by bottom-up method
This synthesis method (Figure 2) involves the use of hydrocarbon compounds as precursors (23, 24). Most commonly used bottom-up synthesis approaches are chemical vapour deposition (CVD), thermal pyrolysis, epitaxial growth, laser assisted synthesis and organic synthesis. CVD is a very

popular method of synthesizing carbon nanomaterial. Graphene is synthesized by the use of solid transition catalyst (41-43). It was produced in planer FLG films from camphor hydrolyzation, a Ni substrate using thermal CVD. Now we use this technique for production of a high-quality graphene. Further CVD modified including atmospheric CVD (APCVD) (23, 42–50). In this approach various carbon precursor from liquid and solid to gaseous molecules have been introduced to produce SLG to FLG. Precursors are: (i) gaseous: C_2H_2, C_2H_4, C_2H_6, C_3H_8 and (ii) liquid: C_6H_6, C_6H_{14}, C_2H_5OH, C_3H_7OH and (iii) solid: camphor source C_6Cl_6 multiwalled carbon nanotubes, fluorine, coronene (poly methyl methacrylate polystyrene and polycyclic aromatic hydrocarbon and waste plastic for preparation of graphene). There are numerous types of substrates including metals (copper, nickel, ferrum, gallium, silicon), alloys (CuNi and AuNi) oxides (Fe_2O_3, Al_2O_3, SiO_2 and MgO) stainless steel, mica germanium hexagonal boron nitrite and various glasses have been used for production of SLG to MLG using CVD. Mechanically exfoliated graphene produces similar graphene. The growth parameter influences the properties of CVD graphene, such as gas mass transfer, partial pressure, substrate selection, and carbon. Researchers are attempting to manage the amount of graphene layers, as well as the size, density, and flaws of grain boundaries and flaws.

2.1.3. Graphene synthesis in cleavage and exfoliation method

Many graphene sheets are piled together to form graphite, which is held together by a weak Vander wall force. Exfoliation and cleavage, which use mechanical or chemical energy to break these weak bonds and separate apart individual graphene sheets, can be used to generate graphene from a high purity graphite sheet. Exfoliation is the process of repeatedly peeling. Dry etching in oxygen plasma was used to create several 5 m deep mesas on a sheet of commercially available highly oriented pyrolytic graphite (HOPG) material. This was then applied to a photoresist, baked to adhere the mesas to the photoresist, released in acetone, and transferred to a Si substrate, where the graphene sheets were produced from a single to few layers thick. The scotch tape method of making graphene from HOPG is shown in Fig. 3.
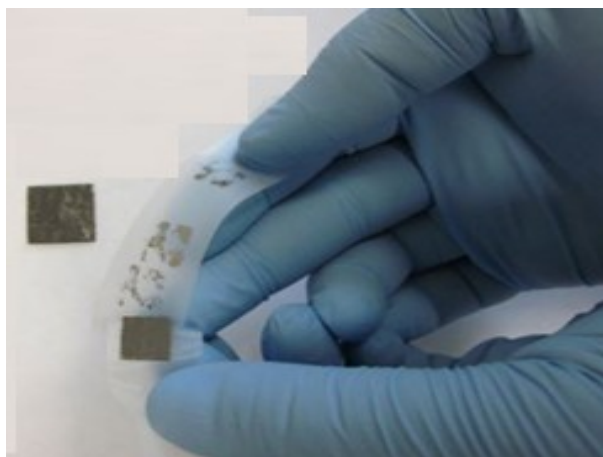
Figure 3: Graphene in scotch tape method.

2.1.4. Synthesis of graphene nanoribbons and nanographene flakes

The substrate used for on-surface synthesis normally involved a clean single-crystalometalic surface of Au, Ag, Cu, Ni, Pt etc. Metal surface act as both catalytic support and template to facilitates the absorption, chemical transformation and re-organization of molecular precursors into the required product. Various chemical reactions including aryl-aryl coupling, glaser coupling, radial polymerization, and oxidative cyclo-dehydrogenation, are used in the strategies to prepare the surface assisted transformation. Such an approach is frequently used for the synthesis of graphene nanoribbons (GNRs) and nanographene flakes (49).

2.2. Synthesis Process of Graphene Oxide
2.2.1. Improved Hummer's method
There are two main problems arose in Hummer's method (51-53). First one is intercalating agents and high consumption of oxidants was inevitable. Secondly it is a time-consuming process. Both these problems result in poor scalability and high cost in practical applications. Hence an economical and efficient method was demanded, which is popularly known as improved Hummer's method. In 2016, Huitao Yu et al. (52) had used improved Hummer's method for the synthesis of GO where they took boric acid (H_3BO_3) in place of $NaNO_3$, partly replaced $KMnO_4$ with K_2FeO_4 and reduced the amount of sulphuric acid. They first took 10 g of graphite flake, 6 g of $KMnO_4$, 4g of Potassium Ferrate (K_2FeO_4), 0.01 g of boric acid (H_3BO_3) and then dispersed the mixture in 100 mL of conc. H_2SO_4 in a vessel and stirred for 1.5 hours at less than 5 °C. Further they added $KMnO_4$ and put the vessel into a water bath at about 35°C and stirred for 3 hours more to complete the oxidation process. Then they added 250 mL of deionized water slowly adjusting the temperature to about 95°C and kept for 15 minutes, when the brownish suspension was yielded indicating the hydrolysis and absolute exfoliation of intercalated graphite oxide. This brown suspension was then treated with 12 mL of H_2O_2 (30%) to reduce the residual oxidants and intermediates to soluble sulphate. After it was centrifuged at 10,000 rpm for 20 minutes to remove the residual graphite and then washed with 1 mL/L HCl and deionized water repeatedly, and finally GO was obtained. It is the improved Hummer's method where sodium nitrate is replaced by H_3PO_4 (phosphoric acid) with an extra amount of $KMnO_4$. There is no evolution of toxic gases in this method and provides easy temperature control and GO powders with a high degree of oxidation are then resulted (53–61).

2.2.2. Modified Hummer's method
This method is the modified synthesis route proposed by Hummer. This was employed by Jianguo Song et al. (51) to synthesize GO. They combined 108 mL of H_2SO_4 and 12 mL of H_3PO_4 with 5 g of graphite and 2.5 g of $NaNO_3$ and then swirled the mixture for 10 min in an ice bath. The liquid was then progressively heated to below 5°C while 15 g of $KMnO_4$ was added. The suspension was then chilled for 2 hours, swirled for 60 minutes, and then stirred once more for 60 minutes in a water bath of 40°C. They continued adding water with a temperature of about 98 °C for 60 minutes. To make the suspensions volume 400 mL, more deionized water was added with it. An amount 15

mL of H_2O_2 was then added after 5 minutes. The final product was centrifuged and repeatedly rinsed with deionized water and a 5 % HCl solution. The product was then dried at 60 °C to synthesize GO (58-63).

2.2.3. Electrochemical method
Being ecofriendly, highly efficient, and low cost, electrochemical (EC) methods have been widely used now for the purpose of GO synthesis. Songfeng Pei *et al.* (57) were used electrochemical method in which they used flexible graphite paper (FGP) as a raw material. The FGP has similar structure as graphite, high tensile strength, and electrical conductivity. They dipped FGP slice having dimension 10 x 4 cm^2 into 200 mL concentration H_2SO_4 for EC intercalation. During EC intercalation FGP slice and Pt wire were used as anode and cathode respectively with a DC power supply of 1.6 V and found graphite intercalation compound paper (GICP). Then the GICP was subjected EC oxidation in diluted H_2SO_4 (50wt.%) where GICP and Pt wire were used as anode and cathode, respectively, with a DC power supply of 5 V. Then the blue-coloured GICP was turned to yellow coloured graphite oxide within a few seconds along with exfoliation indicating a quick oxidation and exfoliation. The exfoliated graphite oxide was collected by vacuum filtration. Then they washed the obtained filter cake with distilled water several times to clean the absorbed acid and finally GO was obtained.

2.2.4. Modified Marcano's method
The presence of Mn residues, emission of toxic gases (such as NO_2 and N_2O_4) and the explosive nature of reactions was prevailing while synthesizing GO. Keeping this in mind, Marcano et al. (37) modified Hummer's method, i.e., Marcano's method, where they claimed total elimination of Mn residues as well as toxic gas generation. Ranjan et al. (56) also used Marcano's methods with some modifications to prepare GO.

3. RESULTS AND DISCUSSION

The real image of graphene is displayed in Fig. 4. For the structure analysis of the grapheme-based materials, X-Ray Diffraction & Raman Spectroscopy were taken.
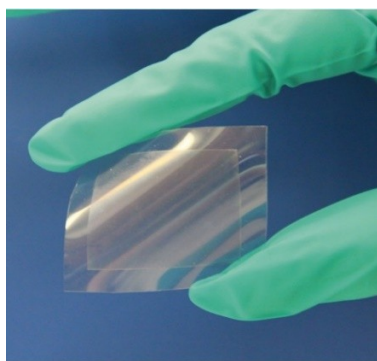
Figure 4: Real image of graphene.

3.1. Characterization Using XRD
3.1.1. Graphene Nano sheets (62-65)
Materials used - Spectral graphite (50 µm), distilled water, aqueous solution of resistivity 18.2 MΩ, ammonia, hydrazine hydrate, K_2HPO_4/KH_2PO_4. Synthesis method: Graphene was synthesized using Modified Hummers' method. Instrument model: XRD patterns were taken using SRD-6000 X-Ray diffractometer (Shimadzu, Japan) by Cu – Kα radiation. Results: XRD pattern of graphene was observed having a high peak at Bragg angle of 2θ=26.6° having inter planner spacing value (*d*)= 0.335 nm of plane (002).

3.1.2. Reduced GO (rGO) using different treatments of GO (63-66)
Materials used- Graphite (purity of 99%), H_2SO_4 (98% purity) and H_2O_2 (30% purity), $KMnO_4$, L-ascorbic acid (purity 99%) and ethylene glycol. Synthesis method: Graphene oxide (GO) was prepared in sonication method and rGO was formed then. Instruments used: XRD (D/Max 2200V/PC, Rigaku, Japan) where Cu – Kα has the wavelength (λ= 0.15 nm) using 2θ ranging (5°-80°) at a scanning rate of 2°/ min where voltage and current values were 40 kV and 40 mA, respectively. Results: XRD was done to find if any changes occur to the structure crystal after the conversion of graphene-to-graphene oxide and after the reduction of GO to rGO. It can be seen that the graphene shows a high intensity and sharp peak at 2θ value 24° to 28° which shows large crystallite size and crystallinity morphology of graphite.

3.1.3. GO Nanosheets via modified Hummers' method (62, 67)
Materials used- purified graphite powder, 35% hydrogen peroxide (H_2O_2), sodium nitrate ($NaNO_3$), 37% HCl, $KMnO_4$, and 95%–97% concentrated H_2SO_4. Each chemical was at analytical quality. Synthesis method: The GO was synthesized by oxidation via modified Hummer's method. Instruments used: High Resolution XRD (Bruker D8 Advance) where Cu-Kα (λ= 0.154 nm) radiation in 2θ ranging between 10° to 40°. Structural analysis: The interlayer changes and crystalline properties of GO were observed by XRD. Here a high diffraction peak was observed near 12° which has base plane (002) and appx. 0.737 nm d-spacing. The presence of oxygenated functional group on GO during oxidation of graphite powder made large interlayer spacing of GO. This result was proved the formation of GO.

3.1.4. Thermal reduction of GO: Chemicals used (68)
Powdered graphite (98%), H_2SO_4 (98%), fuming nitric acid (68%), pure $KMnO_4$, hydrogen peroxide (30%), ortho phosphoric acid (88%), HCl (35%) and ethanol. All materials were analytical grade. Synthesis method: GO was synthesized in Tour's method and exfoliation of GO produces rGO. Analysis: XRD pattern was observed from GO and rGO by using powder XRD under Cu-Kα (λ = 0.154 nm) of radiation in 2θ in range 10° to 90° where the step size is 0.05° and a time per step of 0.4 sec. Structural analysis: Here also in the conversion from GO to rGO, the first peak was observed in between 20° to 30° (in 2θ). With the change in d-spacing, a shift in first major peak was observed. The second major peak gets flattened with increase of reduction temperature. In all rGO specimens, the presence of (002) and (100) planes were found.

Patra B et al. JOTCSA. 2023; 10(3): 757-772

REVIEW ARTICLE

3.1.5. Thermal and morphological study of graphene based polyurethane composites (68-70)

Materials used- graphene, Pearl bond DIPP 119 Polyurethane, and n-Dimethyl formamide (DMF). Preparation method: with varying weight percentages of graphene of 2.5, 5 and 10 wt percent, polyurethane nanocomposites (PU025, PU050, and PU100) were created by melt mixing in the presence of a solvent, and films were created using the solvent casting method. Instrument model: XRD - D8 advance, Bruker, Germany. The analysis was conducted in the range of $2\theta = 10°$ to $60°$ at 0.03 s per step in one scan. Results: the presence of graphene in the nanocomposite was studied using XRD patterns where the highest peak was found at around 20° value of 2θ of (110) crystalline plane. For pure graphene, the highest peak was observed at $2\theta \sim 27°$.

3.1.6. Graphene films by modified hummer's method (71-76)

Materials used- graphene flakes (99.8% pure), $KMnO_4$ (98.5% pure), H_2SO_4 (98% pure), hydrofluoric acid (40% pure), hydrogen peroxide (30% pure), hydrochloric acid (35-37% pure), $NaNO_3$ (98% purity), acetone, distilled water and deionized water. Synthesis method: Graphite flakes were purified and then synthesized to GO by modified hummer's method. Results: at $2\theta \sim 10°$, a diffraction peak of GO was observed with interlayer spacing, d = 0.8 nm with miller indices (001). But with interlayer spacing, d = 0.34 nm of indices (002), the diffraction peak was observed at $2\theta \sim 26°$. In case of dried GO, the main peak of graphite vanishes totally and this peak was broader and lower in intensity than the natural graphite.

3.1.7. Reduced graphene oxide by modified Hoffman method (71-74)

Materials used- graphite powder, $KClO_3$, $NaBN_4$, H_2SO_4, H_2O_2, HCl, diethyl ether, distilled water, HNO_3. Synthesis method: Modified Hoffman method was used for the preparation of rGO and was compared with conventional Hoffman method. XRD model: the diffraction pattern of the powder rGO was observed by using Philips X'pert pro PMD (operated at 40 kV and 30 mA) with Cu-Kα radiation at 2θ range from 20° to 80° in continuous mode. Results: when GO and rGO were processed through modified Hoffman method and conventional Hoffman method then the XRD pattern showed its peak at Bragg's angle 2θ value of 26° with inter planner spacing, d at 0.33 nm and the miller indices (002). After chemical oxidation an additional peak was formed having Bragg's angle value $2\theta = 12.30°$ (approx.) and d = 0.73 nm.

3.1.8. Comparative study of different scalable routes to synthesize graphene oxide and reduced graphene oxide (71-73)

Materials used-graphite powder (<20μm), HCl (37%), $KMnO_4$ (99%), H_2SO_4 (96%), H_2O_2(33%), ethanol (99.5%), K_2FeO_4 (92%). Preparation method: Graphite Oxide was first synthesized using improved Hummer's method and also using ferrate method

XRD model: The X-Ray diffraction pattern was observed using a PHILLIPS, PW-1171 with Cu-Kα radiation λ = 1.5404 Å. Results; the XRD pattern observed for the GO synthesized using Modified Hummer's method has a sharp peak at Bragg's angle value $2\theta = 26.5°$ where the plane has indices (002) and the inter planner spacing d = 0.34 nm. Whereas for the GO synthesized using ferrate method, the graph observed using XRD pattern has a high peak at Bragg's angle value at $2\theta = 26.6°$.

3.1.9. Graphene nanostructures via arc discharge method (74, 75)

Materials used- composition of graphite electrodes (99.99% purity), buffer gasses (He and N_2). Preparation: Arc discharge method was used to synthesize pure carbon nanostructures in a stainless-steel reactor. There was a stainless-steel reactor connected to a DC power supply and buffer of mixture of gases of nitrogen and helium. On managing the distance between anode and cathode, a constant discharge current of 150 A was set. By continuing the process for 10-12 minutes, the anode graphite rod was consumed completely. After each stage of complete discharge pulse, the black carbon shoot was collected from the anode. Instruments used: The X-Ray diffraction was conducted using a Bruker™ D8 Advance series diffractometer with Cu-Kα radiation at a range of 2θ value from 10° to 90° (λ = 1.5406 Å) at 35 kV, 40 mA operating at a speed of 2° per minute. Results: The X-Ray diffraction showed a highest peak of Braggs angle value $2\theta= 12.85°$ for inter planner spacing value 9.141 nm with indices of the plane (002).

3.1.10. Synthesis and characterization of graphene oxide nanosheets (76, 77)

Materials used- H_2SO_4, $KMnO_4$, deionized water. Synthesis method: GO was synthesized using Modified Hummer's Method. XRD model: XPERT-PRO diffractometer was used, operating at 40 kV and 30 mA, the XRD pattern was observed in the Bragg's angle 2θ at range of 5°-50°. Result: after the chemical oxidation of GO the XRD pattern showed the highest peak at Bragg's angle value $2\theta =10.40°$ and d = 0.846 nm for (001).

3.1.11. Highly controllable and green reduction of graphene oxide to flexible graphene film with high strength (77-79)

Materials used- sodium citrate, carboxyl group, sodium borohydride. Synthesis method: Modified Hummer's method was used to synthesize the graphite oxide and its exfoliation was done by ultra-sonication method for 30 minutes and GO was formed. XRD model; the morphology of the powder was formed by Rigaku D/Max-2400X where Cu-Kα radiation was at 40 kV and 100 mA. Results: in the reduction of GO to CCG a continuous reaction occurred and at first when GO was examined by XRD analysis and patterns were observed, it showed a high sharp at Bragg's angle value of $2\theta = 11°$ where the inter planner spacing (d) was 0.758 nm and the indices of the plane was (001). After 1 h, a broad peak appeared at $2\theta = 24°$ with (002).

Table 1: Variation in Bragg's angle (2ϴ) and inter planner spacing (d) in different synthesis methods observed through XRD.

Sl. No	Materials used	Instruments	Synthesis Method	Results	Reference
01	Spectral graphite, distilled water, aq. Solution (18.2 MΩ), NH_3, K_2HPO_4 / KH_2PO_4	SRD-6000 X-RAY Diffractometer	MHM	2ϴ = 26.6° d=0.335 nm (002)	(62)
02	Graphite, H_2SO_4, H_2O_2, $KMnO_4$ Ascorbic acid, ethylene glycol	D-MAX 2200 V/PC 40 kV-30 mA	Sonication Method	2ϴ = 9° d=7.37 nm (002) 2ϴ = 26.7° d=3.35 nm	(63)
03	Graphite powder, H_2O_2, $NaNO_3$, HCl, $KMnO_4$, H_2SO_4	Bruker D8 Advance	MHM	2ϴ =12° d =7.37 nm (002)	(55)
04	Graphite, H_2SO_4, HNO_3, $NaNO_3$, $KMnO_4$, H_2O_2 Orthophospheric acid, HCl	PANALYTICAL XPERT^3 Powder diffractometer	Tour's Method	2ϴ = 25° (002)	(64)
05	Pearl bond DIPP 199, polyurithene, n-Dimethyl formide	D8 advance Bruker, Germany	Polyurithene nanocomposites fabricated using melt mixing & flims were fabricated in solvent casting method	2ϴ = 20° (110) 2ϴ = 27° (001)	(68)
06	Graphite powder, $KClO_3$, $NaBN_4$, H_2SO_4, H_2O_2, HCl, HNO_3	PHILLIPS XPERT PRO PMD 40 kV-30 mA	MHM Conventional HOFFMANN Method	2ϴ = 26° d = 0.33 nm (002)	(73)
07	Graphite powder, HCl, $KMnO_4$, H_2SO_4, H_2O_2, ethanol, K_2FO_4	PHILLIPS PW-1171	Improved HM Ferrate Method	2ϴ =26.5° d = 0.34 nm (002)	(74)
08	Graphite, Nitrogen (N_2) Helium (He)	Bruker™D8 Advance series 35 kV – 40 mA	Arc discharge Method	2ϴ = 12.85° d = 0.914 nm (002)	(75)
09	H_2SO_4, $KMnO_4$, Deionised water	GO XPERT-PRO 40 kV-30 mA	MHM	2ϴ =10.40° d = 0.846 nm (001)	(76)
10	Sodium nitrate, carbonyl group, Sodium Borohydrate	D/MAX-2400X 40 kV – 100 mA	MHM	2ϴ = 24° (002) 2ϴ =11° (001)	(77)
11	$Ni(NO_3)_2.6H_2O$, $Co(NO_3)_2.6H_2O$, $C_2H_6O_7$, $LiNO_3$	XRD-600, 40 kV – 30 mA	CVD	2ϴ = 26.6° d = 0.335 nm (001)	(78)

3.1.12. Improvement of Li-ion batteries energy storage by graphene additive (78, 79)
Materials used- $Ni(NO_3)_2 \cdot 6H_2O$, $Co(NO_3)_2 \cdot 6H_2O$, $C_6H_6O_7$ and $LiNO_3$ (everything were of 99.99% purity) and were received from m Harris Chemicals Corporation in England, deionized water. XRD model: The X-Ray diffraction was performed by XRD-6000 of 2ϴ operating at 40 kV and 30 mA were using Cu-Kα (λ = 0.154 nm). Results: the XRD

pattern of pure graphene doped with LCNOG at 850°C has a high peak at 2ϴ = 26.6° with d = 0.335 nm for (003).

The above said results of interplanar spacings (d) and their corresponding Bragg's angles (2ϴ) are displayed in Figure 5, and the summary of XRD characterization results were presented in Table 1.
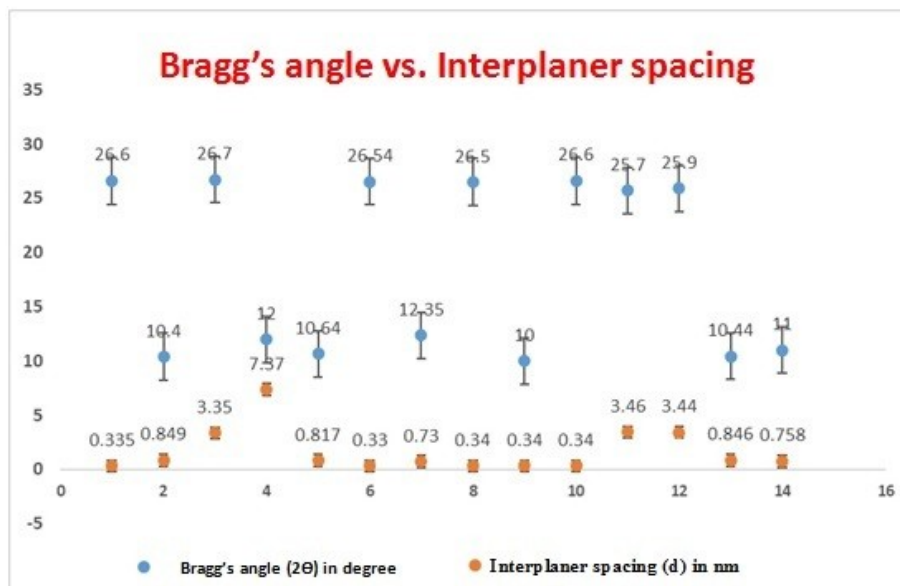
Figure 5: Variation of interplanar spacing with respect to Bragg's angle.

3.2. Characterization Using Raman Spectroscopy

Raman spectroscopy is typically preferred to evaluate the changes that take place during oxidation and exfoliation. Graphene was produced from GO using the modified Hummers method by Fatima Tuz Johra et al. (79). One D band was found at 1353 cm^{-1}, whereas the G band found at 1605 cm^{-1} of GO, which corresponds to the E_{2g} phonon of the sp^2 C atoms. However, the G band in the instance of graphene was around 1600 cm^{-1}, indicating a minor displacement from the GO's position. The D band is a sign of disorder and can be caused by a number of flaws, including vacancies, grain boundaries (79-82) and amorphous carbon species (83, 84). The product's quality is indicated by the intensity ratio of these two bands. Relative intensity (I_D / I_G) dropped from 1.00 to 0.96. The I_D / I_G ratio of reduced graphene oxide treated with hydroiodic acid and acetic acid was increased (85, 86), showing that the reduction process changed the structure of GO and caused a significant number of structural flaws (86- 88)

GO was obtained from Graphene as a 0.4 weight percent water solution with a reported monolayer content > 95 percent by V. Scardaci and G. Compagnini (84, 85). After a 30-minute ultrasonic bath, the solution was applied. Raman spectroscopy was used to assess the acquired rGO's quality by contrasting it with GO and various scanning speeds. The G and D bands visible in these spectra are typical carbon nanostructures. The degree of disorder has been calculated inside the material using relative intensity (I_D / I_G) (85-88). Raman spectroscopy was used to assess the quality of the obtained material after a thorough investigation of the laser reduction of GO under a variety of experimental conditions. The scan speed is an important parameter because a slow speed would have a negative impact on the material's quality, while material density was found to have less of an impact. For greater density samples, a second laser pass over a surface that has already received treatment improves the final rGO quality. Modified Tour's method for the synthesis of GO was used by Iman Sengupta et al. (64) and then followed thermal reduction method to form graphene from GO. They captured these peaks for three samples since the D and G peaks are the specific characteristics of carbon compounds, presented in Table 2.

Table 2: Raman spectroscopy data for different samples (64).

Sample Name	D-peak (in cm^{-1})	G-peak (in cm^{-1})
Graphite	1352	1580
GO	1370	1608
Laser modified GO	1370	1608

The above table makes it clear that due to graphite oxidation and exfoliation, there is a notable reduction in the size of sp^2 planes. After the lowering of GO, the intensities of the D and G peaks both raised, and the peaks are sharpened, indicating a structural shift.

Modified Hummer's approach for the synthesis of GO was used by MF Hanihah et al. (87). Raman analysis of GO was performed in order to evaluate its structural and electronic properties because it is a non-destructive method, and the results are shown in the Table 3.

Table 3: Raman spectroscopy data for GO (87)

Sample Name	D-peak in cm^{-1}	G-peak in cm^{-1}	I_D / I_G
GO	1353	1600	0.90

Elvin Aliyev et al (88) produced base washed GO using Hummer's method for its synthesis by dispersing GO in 1.0 M sodium hydroxide, shaking for 3 hours, refluxing for an hour at 80 °C, and vacuum-filtering to remove 30 weight percent of oxidative debris from the CGO dispersion. Following the creation of reduced GO and reduced base washed GO separately, they dispersed 2.0 g of each in 1.0 L of ultrapure water in two separate flasks, sonicated the mixture, and then reacted with 10 mL of hydrazine monohydrate at 100°C for an entire day. They had produced base washed GO by dispersing GO in 1.0 M sodium hydroxide and shaking for 3 hours. They followed Hummer's method for the synthesis of GO (87, 89).

For the pure graphite, they discovered D-peak and G-peak at 1360 and 1580 cm^{-1}, respectively. When graphite is converted to GO, it is found that the degree of order in the structure has changed; the intensity of the D-band is higher than it is for graphite, and the intensity of the G-band is lower for reduced forms. Between 1342 cm^{-1} and 1356 cm^{-1}, D peak appears in oxidized forms. Thus, they demonstrated that GO samples have a massive number of flaws and are in a distorted version of the

sp^2 crystal structure. The activation of the D peak typically takes place in crystal areas of 3–4 nm size that are near flaws or an edge (90-92). The activation of 2D and 2D' bands doesn't require any faults (93). As a result, figuring out the number and orientation of graphene layers can be helped by the 2D peak's (2700 cm^{-1}) structure. Single-layer graphene is thought to exist if there is a single sharp peak at the 2D-band peak. Graphene oxide samples in bulk form were employed in the studies, and the findings indicate that there are numerous single layers in the GO samples. This result indicated that exfoliation was necessary in order to obtain single-layer GO layers from the graphene oxide samples which they had synthesized.

Bilayer graphene film was made on commercial Cu (0.5% Ni) foil (92, 93). Cu (0.5% Ni) foils were put into an AP-CVD quartz tube set up for monolayer and bilayer graphene synthesis before cleaning and removing any residue with the electro polishing procedure. The graphene films were subsequently applied to SiO$_2$/Si substrates that were 300 nm thick. Raman spectroscopy was used to analyse graphene / SiO$_2$ /Si samples (graphene films). The result of Raman spectra is summarized in Table 4.

Table 4: Raman spectroscopy data for graphene.

Sample Name	D-peak in cm^{-1}	G-peak in cm^{-1}	2D-peak in cm^{-1}
Graphene	1350	1590	2690

For the creation of graphene on 4H-SiC (001) semi-insulating on-axis, K. Grodecki et al. (94) utilized a commercial horizontal CVD hot-wall reactor (Aixtron VP508). Lorentz fitting had employed for the area and FWHM of the 2D band to calculate the

thicknesses of graphene structures. Wire 3.4 software was used to measure both metrics. The values of FWHM for 2D bands different layers of graphene structures are presented in Table 5.

Table 5: Raman spectroscopy data for different samples.

Number of layers in Graphene	Range of FWHM in cm^{-1}	Number of Lorentzian peaks fitted
Monolayer (ML)	30-45	1
Bilayer (BL)	45-60	4
Trilayer (TL)	60-75	3

The regions marked as ML have a smaller 2D area than regions marked as bilayered, trilayered, and tetralayered graphene.

By following the improved Hummers method for the synthesis of GO, B. Dehghanzada et al. (95) employed hydrazine hydrate to reduce GO. They dispersed GO and dodecyl amine in 200 mL of DMF for the Synthesis of functionalized GO (FGO).

To create reduced functionalized graphene oxide (rFGO), they used hydrazine hydrate as a reducing agent. Rapid thermal processing of GO produced exfoliated graphene sheets, which were then used to create thermally reduced GO (TRG). The corresponding data of Raman spectra of pure graphite, GO, FGO, rFGO and TRG samples are presented in the Table 6.

Table 6: Raman spectroscopy data for different samples.

Sample	D-peak in cm^{-1}	G-peak in cm^{-1}	I$_D$/I$_G$	L(Å) =44/(I$_D$/I$_G$)
Graphite	1360	1580	0	--
GO	1284	1597	1.54	28.57
FGO	1289	1586	1.57	28.02
RFGO	1330	1582	1.6	27.5
TRG	1290	1580	1.75	25.14

The important parameter in Raman spectroscopy is the determination of the intensities of D-peak to

that of G-peak (I$_D$/I$_G$) in order to examine the level of modification of pure graphite following oxidation as

Patra B et al. JOTCSA. 2023; 10(3): 757-772

REVIEW ARTICLE

well as reduction. I_D/I_G is zero for pure graphite, indicating that there are no flaws in the material.

The following equation, provided by Tuinstra et al. (80) was used to calculate the average distance (L) between two neighbour defects, L (Å) = 44/ (I_D/I_G). An increase in the I_D/I_G ratio indicates that there are more faults and that the distance between each defect is getting closer.

For the synthesis of GO, A. Malas et al. (53) used a modified version of the Hummers method and used a variety of techniques for reduced GO. First approach: It involved the reduction by sodium borohydride ($NaBH_4$) to obtain the end product i.e., $NaBH_4$ reduced GO (NarGO). Second approach: The reducing agent in the second process was hydrazine monohydrate ($N_2H_4.H_2O$) to obtain $N_2H_4.H_2O$ reduced GO (HyrGO). Third approach: NarGO was transferred into a new round-bottom flask containing 300 mL of water, and the second reduction method's steps were then carried out with the aid of 3 mL of $N_2H_4.H_2O$. NaHyrGO is the abbreviation for the final product following two treatments with two reducing agents. Fourth approach: They performed thermal treatment to generate thermally reduced graphene oxide (TrGO).

In order to study the relative contributions of ordered and disordered regions in carbonaceous structures, Raman spectroscopy is frequently regarded as a significant instrument. Summarizing the results of Raman spectra of graphite, GO and the reduced GO generated by different ways (63, 71, 96), presented in Table 7.

Table 7: Raman spectroscopy data for different samples.

Sample	D-peak in cm^{-1}	G-peak in cm^{-1}	I_D/I_G
Graphite	1328	1573	0.19
GO	1335	1602	1.10
NarGO	1327	1598	1.24
HyrGO	1327	1596	1.27
NaHyrGO	1328	1586	1.35
TrGO	1344	1597	1.02

The size of the sp^2 hybridized carbon atoms is inversely proportional to the ratio of the intensities of the D-peak and G-peak, or relative intensity (I_D/I_G). Since it is clear from the above table that all chemically reduced GO have relative intensities that are higher than GO. It is important to note that, with the exception of thermally reduced GO, the size of sp^2 hybridized carbon atoms decreases throughout reduction. The authors speculate that the relative intensity of thermally reduced GO is lower than that of GO. The removal of oxygen groups may result in dangling bonds that introduce sp^3 carbons. It has been established that a reduced GO Raman spectra with a lower relative intensity compared to GO denotes defect correction and a greater distance between them (87, 95).

In order to manufacture the three different forms of graphene oxides—GO1, GO2, and GO3, M. Wojtoniszakand and E. Mijowska (96) had employed three distinct techniques. The following steps were used to prepare GO1: 1 g of graphite was dissolved in 350 mL of a 4:3 volume ratio mixture of perchloric and nitric acids, and then 6 g of K_2CrO_4 was added. After that, the mixture was heated to 50°C, and the reaction was run for 24 hours. The resulting mixture was then passed through a polycarbonate (PC) membrane and washed three times with ethanol and 10 percent hydrochloric acid to remove any remaining metal ions. Finally, distilled water was added to the mixture until the pH level reached 7. The material was then dried in the air for 24 hours at 100°C. rGO1, rGO2, and rGO3 are the equivalent reduced graphene oxides.

To prepare GO2, graphite, perchloric acid, nitric acid, and K_2CrO_4 were mixed and then heated. This procedure took place at room temperature for 6 hours. Following the oxidation process, the same methods of purification, filtration, and drying as in the previous procedure were used to produce GO2.

To prepare GO3, the same steps as for second type synthesis were used, with the exception that the oxidation process' time and temperature were increased to 48 hours and 100°C. Here, glucose was employed as a reducing agent in the preparation of rGO1, rGO2 and rGO3.

Characterization of Raman: One 2D band of two and more layered graphene is composed of two halves, 2D1 and 2D2. As the number of layers rises, both the blue shift of the 2D peak and the relative power of the 2D2 peak both noticeably increase. However, graphene with a single sheet only shows a single 2D peak. Graphite has a single 2D peak. Additionally, rGO3 only has one 2D peak, and their individual values. rGO3 is single layered whereas other two types reduced graphene oxides (rGO1 and rGO2) are composed of multi-layers.

4. APPLICATIONS

Graphene is flexible and transparent (Fig. 6) and has various applications due to its unique structures and properties.

Patra B et al. JOTCSA. 2023; 10(3): 757-772

REVIEW ARTICLE
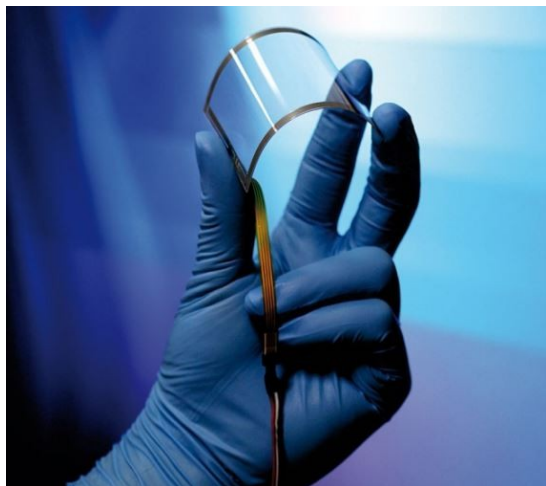
Figure 6: Graphene used as smartphone screen.

4.1. Graphene Transistors: Development of GFETs (graphene field effect transistors)

There are two familiar transistors, i.e., analog transistors and logic transistors. In order to get low energy consumption and to maintain a high interpretation, earlier it is characterized by a high I_{on}/I_{off} ratio and later it is used as an amplifier in high frequency application. Electrical property of graphene is used in both logic and analog transistor (49-54, 59).

4.1.1. Logic transistor

With the fabrication of MOSFET, CMROs technology has dominated the logic industry for around 40 years. By reducing the length of transistors gate we can get higher transistor density and high electrical fields in channel region but when the size is reduced, problems arise like hot electron effect, velocity saturation effect and punch through effect. Due to its monoatomic thickness, graphene reduces all these effects providing a high mobility channel. For modifying a graphene bandgap several techniques are used.

4.1.1.1. Bilayer graphene

By using the application of transverse electric field these structures allow opening of band gap as the symmetry of bilayer stack breaks. SiC is the substrate used by bilayer graphene where light doping is provided to the bottom graphene layer by the substrate and by the adsorption of potassium atoms upper graphene layer is doped. This material is used by several groups for the design of FET devices.

4.1.1.2. Graphene nanoribbons

Graphene nanoribbons are also used to modify graphene. Here the graphene plane is engineered and an extra charge carrier sheet is added. It remains one dimensional and the confinement opens a transport gap.

4.1.1.3. Nano-mesh graphene

Pattern hole in a graphene sheet is another way of including a bandgap in graphene. The required I_{on}/I_{off} ratio for this technique is of the order of 100 at room temperature for size of patterned holes approximate 7 nm. When the on-off ratio increases, at the same time neck width of the hole decreases. Scalability is the main advantage of this technique.

4.1.1.4. Graphene nano bubbles

Several studies show engineering from graphene nano bubbles introduces bandgap by taking psudo magnetic fields which results Landau quantization. By patterning a substrate of holes or steps, nanobubbles can be formed, with substantial energy gaps exceeding 0.1 eV margin.

4.1.2. Analog transistor

Other type of transistor is the analog transistor. The logic transistor is not used in this device and bandgap also not required. They are used in radio frequency applications. Graphene is the most important material for making analog transistor due to its high cutoff frequency.

4.2. Optoelectronics

Optical properties; Graphene used in optoelectronic devices. Graphene has high transparency low reflection, high carrier mobility and near ballistic transparent at room temperature. Due to these properties, graphene used as transparent electrodes. High absorption is another property of graphene which can be described by its structure constant α (constant, shows interaction of matter and electromagnetic field). Absorption of FLG is proportional to number of layers of graphene used in many optoelectronic and photonic devices, also used in photodetectors, structurable absorbers and optical limiters.

Transparent conducting electrodes; These are mostly used in academic and industrial settings to commercial devices. Initially they worked by inserting charge according to the device. In some part of electromagnetic spectrum, they are highly translucent. ITO (Indium Tin Oxide) is the mostly used material for TCEs. It is very costly because of the low supply of Indium. Benefits of organic TCEs are low cost, flexibility and stability but they are unable to acquire the amount of charge mobility as inorganic material. Graphene as TCE; high optical transmittance and low sheet resistance are most essential parameters of TCE materials. By using a four-terminal sensing measurement technique, the sheet resistance can be obtained. In most cases graphene either matches or exceeds the transmittance of other materials.

4.3. Graphene Sensor

Graphene used in sensor application because of its highly reactivity to adsorbed materials.

Electrochemical sensor; As compared to Graphite, glassy carbon electrodes and CNTs, graphene shows better electrochemical response. Researchers proved that at 7.0 pH value of phosphate buffered saline solution graphene showed electrochemical potential window of ca. 2.5 V in 0.2 m. When CNTs decorated with nanoparticles it can detect gasses. Researcher demonstrates that rGO can detect poisonous gas with ppb sensitivity. rGO based sensor and CNT based sensor have same performance. The only difference is rGO based sensor release very less noise.

4.3.1. Graphite as a biosensor

The electrode reaction of hydrogen peroxide on rGO is highly efficient as compared to glassy carbon,

graphite and CNTs. It is same as the reaction of NADH on graphene-based electrodes. As compared to the bare edge plane pyrolytic graphite electrode (EPPGE), oxidation of NADH on graphene is strongly observed. As compared with ascorbic acid, dopamine and serotonin, graphene shows superior sensing ability.

5. CONCLUSIONS

Graphene is being exhibited a huge number of amazing electrical and physical properties. Graphene and graphene oxide (GO) shows less similarly with most number of the artificial compound. A variety of synthesis methods for graphene and graphene oxide were discussed, i.e. top-down synthesis, bottom-up, mechanical delamination, π magnetism, exfoliation and cleavage method. It is found that CVD technique is the most suitable for the synthesis of high quality graphene. CVD method is commercially usable and trustable for the application of GNRs. Researchers developed different methods of production which was suitable for cost, scalability and environment friendly. GO based graphene synthesis method produced low quality graphene leading to low conductivity. Good quality graphene can be obtained from electrochemical exfoliation process, which also mostly used in industrialization. In this review we have discussed the importance of graphene in different fields due to its application in biomedical science, weather proofing and packaging, transistor, semiconductor, super capacitor, rust free future, sensor and optoelectronics. The results of different samples, characterized by XRD and Raman Spectroscopy were discussed in this review article.

6. CONFLICT OF INTEREST

No conflict of interest.

7. ACKNOWLEDGEMENTS

8. REFERENCES

1. Kuanar B, Mohanty HS, Behera D, Nayak P, Dalai B. An elementary survey on structural, electrical, and optical properties of perovskite materials. Eng Appl Sci Res [Internet]. 2022;49(2):288–99. Available from: <URL>.

2. Dash S, Hial PK, Senapati S, Dalai B. A Survey on Various Methods of Extraction and Recovery of Thorium. J Turkish Chem Soc Sect A Chem [Internet]. 2021 Nov 30;8(4):1197–210. Available from: <URL>.

3. Novoselov KS, Geim AK, Morozov S V., Jiang D, Zhang Y, Dubonos S V., et al. Electric Field Effect in Atomically Thin Carbon Films. Science [Internet]. 2004 Oct 22;306(5696):666–9. Available from: <URL>.

4. Novoselov KS, Fal'ko VI, Colombo L, Gellert PR, Schwab MG, Kim K. A roadmap for graphene. Nature [Internet]. 2012 Oct 10;490(7419):192–200. Available from: <URL>.

5. Peigney A, Laurent C, Flahaut E, Bacsa RR, Rousset A. Specific surface area of carbon nanotubes and bundles of carbon nanotubes. Carbon [Internet]. 2001 Apr 1;39(4):507–14. Available from: <URL>.

6. Gadipelli S, Guo ZX. Graphene-based materials: Synthesis and gas sorption, storage and separation. Prog Mater Sci [Internet]. 2015 Apr 1;69:1–60. Available from: <URL>.

7. Bae S, Kim H, Lee Y, Xu X, Park J-S, Zheng Y, et al. Roll-to-roll production of 30-inch graphene films for transparent electrodes. Nat Nanotechnol [Internet]. 2010 Aug 20;5(8):574–8. Available from: <URL>.

8. Yang W, Ni M, Ren X, Tian Y, Li N, Su Y, et al. Graphene in Supercapacitor Applications. Curr Opin Colloid Interface Sci [Internet]. 2015 Oct;20(5–6):416–28. Available from: <URL>.

9. Tsai I-L, Cao J, Le Fevre L, Wang B, Todd R, Dryfe RAW, et al. Graphene-enhanced electrodes for scalable supercapacitors. Electrochim Acta [Internet]. 2017 Dec;257:372–9. Available from: <URL>.

10. Nag A, Mitra A, Mukhopadhyay SC. Graphene and its sensor-based applications: A review. Sensors Actuators A Phys [Internet]. 2018 Feb;270:177–94. Available from: <URL>.

11. Gusain R, Kumar N, Ray SS. Recent advances in carbon nanomaterial-based adsorbents for water purification. Coord Chem Rev [Internet]. 2020 Feb 15;405:213111. Available from: <URL>.

12. Shao C, Zhao Y, Qu L. Tunable Graphene Systems for Water Desalination. ChemNanoMat [Internet]. 2020 Jul 21;6(7):1028–48. Available from: <URL>.

13. Shen H, Zhang L, Liu M, Zhang Z. Biomedical Applications of Graphene. Theranostics [Internet]. 2012;2(3):283–94. Available from: <URL>.

14. Phiri J, Gane P, Maloney TC. General overview of graphene: Production, properties and application in polymer composites. Mater Sci Eng B [Internet]. 2017 Jan 1;215:9–28. Available from: <URL>.

15. Hu K, Kulkarni DD, Choi I, Tsukruk V V. Graphene-polymer nanocomposites for structural and functional applications. Prog Polym Sci [Internet]. 2014 Nov 1;39(11):1934–72. Available from: <URL>.

16. Geim AK. Graphene: Status and Prospects. Science [Internet]. 2009 Jun 19;324(5934):1530–4. Available from: <URL>.

17. Yu G, Hu L, Vosgueritchian M, Wang H, Xie X, McDonough JR, et al. Solution-Processed Graphene/MnO_2 Nanostructured Textiles for High-Performance Electrochemical Capacitors. Nano Lett [Internet]. 2011 Jul 13;11(7):2905–11. Available from: <URL>.

18. Liu L, Yu Y, Yan C, Li K, Zheng Z. Wearable energy-dense and power-dense supercapacitor yarns enabled by scalable graphene–metallic textile composite electrodes. Nat Commun [Internet]. 2015 Jun 11;6(1):7260. Available from: <URL>.

19. Shateri-Khalilabad M, Yazdanshenas ME. Preparation of superhydrophobic electroconductive graphene-coated cotton cellulose. Cellulose [Internet]. 2013 Apr 5;20(2):963–72. Available from: <URL>.

20. Ren J, Wang C, Zhang X, Carey T, Chen K, Yin Y, et al. Environmentally-friendly conductive cotton fabric as flexible strain sensor based on hot press reduced graphene oxide. Carbon [Internet]. 2017 Jan 1;111:622–30. Available from: <URL>.

21. Abdelkader AM, Karim N, Vallés C, Afroj S, Novoselov KS, Yeates SG. Ultraflexible and robust graphene supercapacitors printed on textiles for wearable electronics applications. 2D Mater [Internet]. 2017 Jul 24;4(3):035016. Available from: <URL>.

22. Karim N, Afroj S, Malandraki A, Butterworth S, Beach C, Rigout M, et al. All inkjet-printed graphene-based conductive patterns for wearable e-textile applications. J Mater Chem C [Internet]. 2017 Nov 16;5(44):11640–8. Available from: <URL>.

23. Lim JY, Mubarak NM, Abdullah EC, Nizamuddin S, Khalid M, Inamuddin. Recent trends in the synthesis of graphene and graphene oxide based nanomaterials for removal of heavy metals — A review. J Ind Eng Chem [Internet]. 2018 Oct 25;66:29–44. Available from: <URL>.

24. Balandin AA. Phononics of Graphene and Related Materials. ACS Nano [Internet]. 2020 May 26;14(5):5170–8. Available from: <URL>.

25. Ferrari AC, Meyer JC, Scardaci V, Casiraghi C, Lazzeri M, Mauri F, et al. Raman Spectrum of Graphene and Graphene Layers. Phys Rev Lett [Internet]. 2006 Oct 30;97(18):187401. Available from: <URL>.

26. Ferrari AC. Raman spectroscopy of graphene and graphite: Disorder, electron–phonon coupling, doping and nonadiabatic effects. Solid State Commun [Internet]. 2007 Jul 1;143(1–2):47–57. Available from: <URL>.

27. Ferrari AC, Basko DM. Raman spectroscopy as a versatile tool for studying the properties of graphene. Nat Nanotechnol [Internet]. 2013 Apr 4;8(4):235–46. Available from: <URL>.

28. He Y, Yi C, Zhang X, Zhao W, Yu D. Magnetic graphene oxide: Synthesis approaches, physicochemical characteristics, and biomedical applications. TrAC Trends Anal Chem [Internet]. 2021 Mar 1;136:116191. Available from: <URL>.

29. Chen J, Yao B, Li C, Shi G. An improved Hummers method for eco-friendly synthesis of graphene oxide. Carbon [Internet]. 2013 Nov 1;64:225–9. Available from: <URL>.

30. Brodie BC. XIII. On the atomic weight of graphite. Philos Trans R Soc London [Internet]. 1859 Dec 31;149:249–59. Available from: <URL>.

31. Singh DP, Herrera CE, Singh B, Singh S, Singh RK, Kumar R. Graphene oxide: An efficient material and recent approach for biotechnological and biomedical applications. Mater Sci Eng C [Internet]. 2018 May 1;86:173–97. Available from: <URL>.

32. Bhuyan MSA, Uddin MN, Islam MM, Bipasha FA, Hossain SS. Synthesis of graphene. Int Nano Lett [Internet]. 2016 Jun 9;6(2):65–83. Available from: <URL>.

33. Liu W-W, Chai S-P, Mohamed AR, Hashim U. Synthesis and characterization of graphene and carbon nanotubes: A review on the past and recent developments. J Ind Eng Chem [Internet]. 2014 Jul 25;20(4):1171–85. Available from: <URL>.

34. Lee HC, Liu W-W, Chai S-P, Mohamed AR, Aziz A, Khe C-S, et al. Review of the synthesis, transfer, characterization and growth mechanisms of single and multilayer graphene. RSC Adv [Internet]. 2017 Mar 9;7(26):15644–93. Available from: <URL>.

35. Shmavonyan GS, Sevoyan GG, Aroutiounian VM. Enlarging the surface area of monolayer graphene synthesized by mechanical exfoliation. Armen J Phys [Internet]. 2013;6(1):1–6. Available from: <URL>.

36. Wu YH, Yu T, Shen ZX. Two-dimensional carbon nanostructures: Fundamental properties, synthesis, characterization, and potential applications. J Appl Phys [Internet]. 2010 Oct 1;108(7):071301. Available from: <URL>.

37. Marcano DC, Kosynkin D V., Berlin JM, Sinitskii A, Sun Z, Slesarev A, et al. Improved Synthesis of Graphene Oxide. ACS Nano [Internet]. 2010 Aug 24;4(8):4806–14. Available from: <URL>.

38. Park S, An J, Jung I, Piner RD, An SJ, Li X, et al. Colloidal Suspensions of Highly Reduced Graphene Oxide in a Wide Variety of Organic Solvents. Nano Lett [Internet]. 2009 Apr 8;9(4):1593–7. Available from: <URL>.

39. Hummers WS, Offeman RE. Preparation of Graphitic Oxide. J Am Chem Soc [Internet]. 1958 Mar 1;80(6):1339. Available from: <URL>.

40. Razaq A, Bibi F, Zheng X, Papadakis R, Jafri SHM, Li H. Review on Graphene-, Graphene Oxide-, Reduced Graphene Oxide-Based Flexible Composites: From Fabrication to Applications. Materials (Basel) [Internet]. 2022 Jan 28;15(3):1012. Available from: <URL>.

41. Cockerell TDA. An Alien *Clematis* in New Mexico. Science [Internet]. 1899 Dec 15;10(259):898–9. Available from: <URL>.

42. Du W, Jiang X, Zhu L. From graphite to graphene: direct liquid-phase exfoliation of graphite to produce single- and few-layered pristine graphene. J Mater Chem A [Internet]. 2013 Aug 20;1(36):10592–606. Available from: <URL>.

43. Schniepp HC, Li J-L, McAllister MJ, Sai H, Herrera-Alonso M, Adamson DH, et al. Functionalized Single Graphene Sheets Derived from Splitting Graphite

Patra B et al. JOTCSA. 2023; 10(3): 757-772

REVIEW ARTICLE

Oxide. J Phys Chem B [Internet]. 2006 May 1;110(17):8535–9. Available from: <URL>.

44. Hlekelele L, Franklyn PJ, Tripathi PK, Durbach SH. Morphological and crystallinity differences in nitrogen-doped carbon nanotubes grown by chemical vapour deposition decomposition of melamine over coal fly ash. RSC Adv [Internet]. 2016 Aug 10;6(80):76773–9. Available from: <URL>.

45. Ye R, James DK, Tour JM. Laser-Induced Graphene. Acc Chem Res [Internet]. 2018 Jul 17;51(7):1609–20. Available from: <URL>.

46. Antonatos N, Ghodrati H, Sofer Z. Elements beyond graphene: Current state and perspectives of elemental monolayer deposition by bottom-up approach. Appl Mater Today [Internet]. 2020 Mar 1;18:100502. Available from: <URL>.

47. Hlekelele L, Franklyn PJ, Dziike F, Durbach SH. TiO$_2$ composited with carbon nanofibers or nitrogen-doped carbon nanotubes synthesized using coal fly ash as a catalyst: bisphenol-A photodegradation efficiency evaluation. New J Chem [Internet]. 2018 Mar 12;42(6):4531–42. Available from: <URL>.

48. Knieke C, Berger A, Voigt M, Taylor RNK, Röhrl J, Peukert W. Scalable production of graphene sheets by mechanical delamination. Carbon N Y [Internet]. 2010 Sep 1;48(11):3196–204. Available from: <URL>.

49. Song S, Su J, Telychko M, Li J, Li G, Li Y, et al. On-surface synthesis of graphene nanostructures with π-magnetism. Chem Soc Rev [Internet]. 2021 Mar 15;50(5):3238–62. Available from: <URL>.

50. Cooper DR, D'Anjou B, Ghattamaneni N, Harack B, Hilke M, Horth A, et al. Experimental Review of Graphene. Int Sch Res Not [Internet]. 2012 Apr 26;2012:501686. Available from: <URL>.

51. Song J, Wang X, Chang C-T. Preparation and Characterization of Graphene Oxide. J Nanomater [Internet]. 2014;2014:276143. Available from: <URL>.

52. Yu H, Zhang B, Bulin C, Li R, Xing R. High-efficient Synthesis of Graphene Oxide Based on Improved Hummers Method. Sci Rep [Internet]. 2016 Nov 3;6(1):36143. Available from: <URL>.

53. Malas A, Bharati A, Verkinderen O, Goderis B, Moldenaers P, Cardinaels R. Effect of the GO Reduction Method on the Dielectric Properties, Electrical Conductivity and Crystalline Behavior of PEO/rGO Nanocomposites. Polymers (Basel) [Internet]. 2017 Nov 14;9(11):613. Available from: <URL>.

54. Bhargava R, Khan S. Effect of reduced graphene oxide (rGO) on structural, optical, and dielectric properties of Mg(OH)2 /rGO nanocomposites. Adv Powder Technol [Internet]. 2017 Nov 1;28(11):2812–9. Available from: <URL>.

55. Zaaba NI, Foo KL, Hashim U, Tan SJ, Liu W-W, Voon CH. Synthesis of Graphene Oxide using

Modified Hummers Method: Solvent Influence. Procedia Eng [Internet]. 2017 Jan 1;184:469–77. Available from: <URL>.

56. Ranjan P, Agrawal S, Sinha A, Rao TR, Balakrishnan J, Thakur AD. A Low-Cost Non-explosive Synthesis of Graphene Oxide for Scalable Applications. Sci Rep [Internet]. 2018 Aug 13;8(1):12007. Available from: <URL>.

57. Pei S, Wei Q, Huang K, Cheng H-M, Ren W. Green synthesis of graphene oxide by seconds timescale water electrolytic oxidation. Nat Commun [Internet]. 2018 Jan 10;9(1):145. Available from: <URL>.

58. Kavinkumar T, Manivannan S. Improved dielectric behaviour of graphene oxide-multiwalled carbon nanotube nanocomposite. Vacuum [Internet]. 2018 Feb 1;148:149–57. Available from: <URL>.

59. Jo J, Lee S, Gim J, Song J, Kim S, Mathew V, et al. Facile synthesis of reduced graphene oxide by modified Hummer's method as anode material for Li-, Na- and K-ion secondary batteries. R Soc Open Sci [Internet]. 2019 Apr 24;6(4):181978. Available from: <URL>.

60. Smith AT, LaChance AM, Zeng S, Liu B, Sun L. Synthesis, properties, and applications of graphene oxide/reduced graphene oxide and their nanocomposites. Nano Mater Sci [Internet]. 2019 Mar;1(1):31–47. Available from: <URL>.

61. Eissa S, N'diaye J, Brisebois P, Izquierdo R, Tavares AC, Siaj M. Probing the influence of graphene oxide sheets size on the performance of label-free electrochemical biosensors. Sci Rep [Internet]. 2020 Aug 12;10(1):13612. Available from: <URL>.

62. Guo H-L, Wang X-F, Qian Q-Y, Wang F-B, Xia X-H. A Green Approach to the Synthesis of Graphene Nanosheets. ACS Nano [Internet]. 2009 Sep 22;3(9):2653–9. Available from: <URL>.

63. Zainuddin MF, Nik Raikhan NH, Othman NH, Abdullah WFH. Synthesis of reduced Graphene Oxide (rGO) using different treatments of Graphene Oxide (GO). IOP Conf Ser Mater Sci Eng [Internet]. 2018 May 1;358(1):012046. Available from: <URL>.

64. Sengupta I, Chakraborty S, Talukdar M, Pal SK, Chakraborty S. Thermal reduction of graphene oxide: How temperature influences purity. J Mater Res [Internet]. 2018 Dec 14;33(23):4113–22. Available from: <URL>.

65. Dideikin AT, Vul' AY. Graphene oxide and derivatives: The place in graphene family. Front Phys. 2019 Jan 28;6:149. Available from: <URL>.

66. Thiyagu C, Manjubala I, Narendrakumar U. Thermal and morphological study of graphene based polyurethane composites. Mater Today Proc [Internet]. 2021;45:3982–5. Available from: <URL>.

67. Verma M, Chauhan SS, Dhawan SK, Choudhary V. Graphene nanoplatelets / carbon nano-tubes/polyurethane composites as efficient

shield against electromagnetic polluting radiations. Compos Part B Eng [Internet]. 2017 Jul 1;120:118–27. Available from: <URL>.

68. Gedam SS, Chaudhary AK, Vijayakumar RP, Goswami AK, Bajad GS, Pal D. Thermal, mechanical and morphological study of carbon nanotubes-graphene oxide and silver nanoparticles based polyurethane composites. Mater Res Express [Internet]. 2019 May 10;6(8):085308. Available from: <URL>.

69. Surekha G, Krishnaiah KV, Ravi N, Padma Suvarna R. FTIR, Raman and XRD analysis of graphene oxide films prepared by modified Hummers method. J Phys Conf Ser [Internet]. 2020 Mar 1 [cited 2023 Jun 22];1495(1):012012. Available from: <URL>.

70. Rao S, Upadhyay J, Polychronopoulou K, Umer R, Das R. Reduced Graphene Oxide: Effect of Reduction on Electrical Conductivity. J Compos Sci [Internet]. 2018 Apr 9;2(2):25. Available from: <URL>.

71. Khan QA, Shaur A, Khan TA, Joya YF, Awan MS. Characterization of reduced graphene oxide produced through a modified Hoffman method. Suvarapu LN, editor. Cogent Chem [Internet]. 2017 Jan 1;3(1):1298980. Available from: <URL>.

72. Romero A, Lavin-Lopez MP, Sanchez-Silva L, Valverde JL, Paton-Carrero A. Comparative study of different scalable routes to synthesize graphene oxide and reduced graphene oxide. Mater Chem Phys [Internet]. 2018 Jan 1;203:284–92. Available from: <URL>.

73. He J, Fang L. Controllable synthesis of reduced graphene oxide. Curr Appl Phys [Internet]. 2016 Sep 1;16(9):1152–8. Available from: <URL>.

74. Borand G, Akçamlı N, Uzunsoy D. Structural characterization of graphene nanostructures produced via arc discharge method. Ceram Int [Internet]. 2021 Mar 15;47(6):8044–52. Available from: <URL>.

75. Wang C, Song M, Chen X, Li D, Xia W, Xia W. Effects of Buffer Gases on Graphene Flakes Synthesis in Thermal Plasma Process at Atmospheric Pressure. Nanomaterials [Internet]. 2020 Feb 11;10(2):309. Available from: <URL>.

76. Muniyalakshmi M, Sethuraman K, Silambarasan D. Synthesis and characterization of graphene oxide nanosheets. Mater Today Proc [Internet]. 2020 Jan 1;21:408–10. Available from: <URL>.

77. Wan W, Zhao Z, Hu H, Gogotsi Y, Qiu J. Highly controllable and green reduction of graphene oxide to flexible graphene film with high strength. Mater Res Bull [Internet]. 2013 Nov 1;48(11):4797–803. Available from: <URL>.

78. AL-Saedi SI, Haider AJ, Naje AN, Bassil N. Improvement of Li-ion batteries energy storage by graphene additive. Energy Reports [Internet]. 2020 Feb 1;6:64–71. Available from: <URL>.

79. Johra FT, Lee J-W, Jung W-G. Facile and safe graphene preparation on solution based platform. J Ind Eng Chem [Internet]. 2014 Sep 25;20(5):2883–7. Available from: <URL>.

80. Tuinstra F, Koenig JL. Raman Spectrum of Graphite. J Chem Phys [Internet]. 1970 Aug 1;53(3):1126–30. Available from: <URL>.

81. Schönfelder R, Rümmeli MH, Gruner W, Löffler M, Acker J, Hoffmann V, et al. Purification-induced sidewall functionalization of magnetically pure single-walled carbon nanotubes. Nanotechnology [Internet]. 2007 Sep 19;18(37):375601. Available from: <URL>.

82. Herranz D, Muñoz-Martin M, Cañamero M, Mulero F, Martinez-Pastor B, Fernandez-Capetillo O, et al. Sirt1 improves healthy ageing and protects from metabolic syndrome-associated cancer. Nat Commun [Internet]. 2010 Apr 12;1(1):3. Available from: <URL>.

83. Wang H, Robinson JT, Li X, Dai H. Solvothermal Reduction of Chemically Exfoliated Graphene Sheets. J Am Chem Soc [Internet]. 2009 Jul 29;131(29):9910–1. Available from: <URL>.

84. Scardaci V, Compagnini G. Raman spectroscopy data related to the laser induced reduction of graphene oxide. Data Br [Internet]. 2021 Oct 1;38:107306. Available from: <URL>.

85. Scardaci V, Compagnini G. Raman Spectroscopy Investigation of Graphene Oxide Reduction by Laser Scribing. J Carbon Res [Internet]. 2021 Jun 17;7(2):48. Available from: <URL>.

86. Ferrari AC, Robertson J. Interpretation of Raman spectra of disordered and amorphous carbon. Phys Rev B [Internet]. 2000 May 15;61(20):14095. Available from: <URL>.

87. Hanifah MFR, Jaafar J, Aziz M, Ismail AF, A. Rahman M, Othman MHD. Synthesis of Graphene Oxide Nanosheets via Modified Hummers' Method and Its Physicochemical Properties. J Teknol [Internet]. 2015 Apr 15;74(1):189–92. Available from: <URL>.

88. Aliyev E, Filiz V, Khan MM, Lee YJ, Abetz C, Abetz V. Structural Characterization of Graphene Oxide: Surface Functional Groups and Fractionated Oxidative Debris. Nanomaterials [Internet]. 2019 Aug 18;9(8):1180. Available from: <URL>.

89. Stankovich S, Dikin DA, Piner RD, Kohlhaas KA, Kleinhammes A, Jia Y, et al. Synthesis of graphene-based nanosheets via chemical reduction of exfoliated graphite oxide. Carbon N Y [Internet]. 2007 Jun 1;45(7):1558–65. Available from: <URL>.

90. Zenkel C, Albuerne J, Emmler T, Boschetti-de-Fierro A, Helbig J, Abetz V. New strategies for the chemical characterization of multi-walled carbon nanotubes and their derivatives. Microchim Acta [Internet]. 2012 Oct 12;179(1–2):41–8. Available from: <URL>.

91. Cançado LG, Jorio A, Ferreira EHM, Stavale F, Achete CA, Capaz RB, et al. Quantifying Defects in Graphene via Raman Spectroscopy at Different

Excitation Energies. Nano Lett [Internet]. 2011 Aug 10;11(8):3190–6. Available from: <URL>.

92. Zhang Y, Tang T-T, Girit C, Hao Z, Martin MC, Zettl A, et al. Direct observation of a widely tunable bandgap in bilayer graphene. Nature [Internet]. 2009 Jun 11;459(7248):820–3. Available from: <URL>.

93. Fang W, Hsu AL, Caudillo R, Song Y, Birdwell AG, Zakar E, et al. Rapid Identification of Stacking Orientation in Isotopically Labeled Chemical-Vapor Grown Bilayer Graphene by Raman Spectroscopy. Nano Lett [Internet]. 2013 Apr 10;13(4):1541–8. Available from: <URL>.

94. Grodecki K, Jozwik I, Baranowski JM, Teklinska D, Strupinski W. SEM and Raman analysis of graphene on SiC(0001). Micron [Internet]. 2016 Jan 1;80:20–3. Available from: <URL>.

95. Dehghanzad B, Razavi Aghjeh MK, Rafeie O, Tavakoli A, Jameie Oskooie A. Synthesis and characterization of graphene and functionalized graphene via chemical and thermal treatment methods. RSC Adv [Internet]. 2016;6(5):3578–85. Available from: <URL>.

96. Wojtoniszak M, Mijowska E. Controlled oxidation of graphite to graphene oxide with novel oxidants in a bulk scale. J Nanoparticle Res [Internet]. 2012 Nov 30;14(11):1248. Available from: <URL>.

A simple, stable, and highly sensitive spectrophotometric method for the determination of arsenic(III) from different biological media in presence of nanosilica-cysteine composite

Omar Alnasra[1]* (iD) **and Fawwaz Khalili** [1] (iD)

[1]The University of Jordan, Faculty of Science, Department of Chemistry, Amman, 11942, Jordan

Abstract: This paper describes a selective and fairly stable colorimetric approach to determine trace amounts of arsenic conjugated with nanosilica-cysteine composite in various aqueous and biological samples in milligram per liter (mg/L) using Leucocrystal Violet (LCV) as a chromogenic reagent. Attenuated total reflectance-Fourier-transform infrared (ATR-FTIR) spectroscopy analysis was applied to characterize the composite. Novelty of this method is dealing with the presence of nanosilica which is reflected in the difficulty of obtaining a clear solution. The maximum absorbance is measured and Beer's law shows linearity over the concentration range of (0.75 to 5.00 mg/L) of As(III) at 590 nm. The molar absorptivity, Sandell's sensitivity, and detection limit of the method were found to be 6.00×10^5 L/mol.cm, 8.55×10^{-2} µg/cm^2, and 0.043 mg/L, respectively. The optimum reaction conditions and other analytical parameters were evaluated. Arsenic was successfully detected in a variety of aqueous and biological samples using the proposed method.

1. INTRODUCTION

Arsenic is a chemical element that has the symbol As, atomic number 33, and standard atomic weight of 74.922 g/mol. Arsenic is a metalloid, its compounds are found all over the natural world, and have both metallic and nonmetallic properties. The two most prevalent oxidation states are trivalent (arsenite) and pentavalent (arsenate) (1-3). Arsenic is primarily absorbed by humans through drinking water, which is regarded as the most important source globally. According to the NRC's Washington 2001 report, drinking water containing inorganic arsenic species has detrimental effects on one's health when exposed for an extended period of time, including damage to the gastrointestinal tract, skin and internal cancers, cardiac damage, and vascular disorders. According to WHO recommendations (4), the maximum permissible level of arsenic in drinking water is 10 µg/L. According to Kohlmeyer and his co-workers (5), certain regions in India, Bangladesh, China, and Mongolia, groundwater arsenic levels exceed 1000 ng/mL. Arsenic's toxicity, availability, and environmental mobility are completely unrelated to its chemical form. Arsenic can be found in many environmental matrices, including natural water and soil, in various oxidation states, and organic and inorganic forms. An accurate assessment of the environmental and biological effects of arsenic necessitates precise knowledge of the system's arsenic compounds, which has increased the demand for analytical methods for their determination at trace levels (6). In literature, various approaches to the analysis of arsenic have been described, including spectrophotometry (7), cathodic and anodic stripping voltammetry (8,9), hydride generation atomic absorption spectrometry (10), ion chromatography and coupled plasma mass spectrometry (11), neutron activation analysis (12), potentiometry (13), hydride generation atomic fluorescence spectroscopy (14), and electrothermal atomic absorption spectrometry (15). The spectrophotometric methods are the most popular

among these because of their low cost performance, but in general, the other methods are expensive and require trained staff. Spectrophotometry is a simple and sensitive method for the determination of arsenic. An extensive range of reagents is appropriate for the spectrophotometric determination of arsenic, according to the literature review, such as ammonium-hexamethylenedithiocarbamate (16), 2,4-dihydroxy benzophenone-2-amino thiophenol (17), azure B (6), ammonium pyrrolidine dithiocarbamate (18), Toluidine blue or Safranine O (19), Leuco malachite green (20), Rhodamine B (21), and Leucocrystal Violet (22). The majority of these methods are constrained by the following: interference from a lot of ions, low sensitivity, and the need for heating or extraction into organic solvents (23). As for these spectrophotometric methods, The LCV method is easily carried out without the use of solvent extraction (22,24,25). The process relies on the release of iodine from the reaction of As(III) with potassium iodate in an acidic medium. Iodine that has been released oxidizes the dye, which results in colour development.

Modified silica nanoparticles find wide use as supports of catalytic systems, fillers in the production of nanocomposites, optical electronic devices, electrochemical sensors, photonics (26), and also in drug delivery (27). Silica particles with a hydrophilic surface layer are biologically inert, which determines their promising use in medicine and biotechnology (27). The structures of functional silica nanoparticles can be very diverse (26). However, nanotechnology in the biomedical and environmental domains has vastly increased the chances of integrating various inorganic metals (i.e. arsenic) due to the help of adsorption and binding forces (27). But the problem is dealing with this irritated nano-system while the determination of the focused ion/s. The presences of nano particles as suspended particles interfere with the spectrophotometric determination. For this reason, a brand-new method must be developed to address the deficiencies in arsenic determination in the presence of nano silica currently in use. The goal of the current work is to address the shortcomings that currently exist and offer a spectrophotometric determination of arsenic at ppm level (mg/L) that is simple, sensitive, and inexpensive.

2. EXPERIMENTAL SECTION

2.1. Instruments
Utilizing RADWAG® AS 220.R2, Electronic Balance, weight was measured. The pH of solutions was measured using BANTE pH–meter (PHS-25CW). Centrifugation was achieved using (DJB Lab Care-AIC PK 130) at 4000 RPM speed. Samples were shaken using GFL-85 thermostatic shaker. DHP-9052 heating incubator was used to heat the samples. GRIFFIN (1-150) vacuum oven was used to dry samples at 25.0ºC, and 630 mm Hg. The attenuated total reflectance-Fourier transform infrared spectrum was recorded on a Bruker Vertex 70-FT-IR spectrometer at room temperature coupled with a

vertex Pt-ATR-FTIR accessory. A method was used to calculate the As(III) concentration utilizing Vis-spectrophotometer from METASH model V-5100, and a 1.0 cm quartz cell. Sharp (SJ-K145-SL3) Refrigerator, China used to cool (5.0ºC) and freeze investigated samples (-3.0ºC).

2.2. Reagents and solutions
Silicon dioxide (SiO_2) nano powder, 10-20 nm particle size (BET), 99.5% trace metals basis, L-Cysteine ($C_3H_7NO_2S$) ($\geq$ 98%) from non-animal source and Leucocrystal Violet (4,4′,4″-Methylidynetris(N,N-dimethylaniline) from Sigma Aldrich, Ninhydrin ($C_9H_6O_4$) from Bio Basic Inc. Potassium iodate (KIO_3) and hydrochloric acid (HCl) (37%) from VWR Chemicals, cadmium(II) chloride ($CdCl_2$) and sodium nitrate ($NaNO_3$) (99%) from Riedel-de Haën, arsenic trioxide (As_2O_3) (99.5%) from BDH Chemicals Ltd Poole England. Ortho-phosphoric acid (H_3PO_4) (85%) from Labchem Laboratory Chemicals. Nitric acid (HNO_3) (69.5%) from Scharlau and glacial acetic acid (CH_3COOH) from Tedia. Sodium hydroxide pellets (NaOH) from Merck and absolute ethanol (C_2H_5OH) (99.9%) from BBC Chemicals for Lab. Normal saline solution (0.9% w/v NaCl) and dextrose 5% solution from DEMO Pharmaceutical Industry, Greece. Ringer lactate solution from Pharmaceutical Solutions Industry, in Saudi Arabia. Qualitative filter paper (Whatman 2) from Whatman International Ltd., England. Quantitative filter paper (grade 94) and Glass microfiber (grade 161) from Ahlstrom, USA, hydrophobic PTFE and hydrophilic Nylon (0.22 µm syringe filters) were obtained from Hawach Scientific, China.

2.3. Spectrophotometric procedure for As(III)
2.3.1. Preparation of Leucocrystal Violet indicator solution
Leucocrystal violet solution was prepared by adding 250 ± 0.1 mg of Leucocrystal Violet i.e. 4,4',4"-methylidynetris-(N,N'-dimethylaniline) into 200.0 ± 0.1 mL of distilled water with 3.0 ± 0.1 mL of 85% phosphoric acid in a 1 L volumetric flask and shaken gently until the dye dissolved. The content of the flask was diluted to 1 L with distilled water. This indicator was stable for several months and was used as a spectrophotometric reagent in the determination of As(III) concentration.

2.3.2. Preparation of standard curve of As(III)
The stock solution of arsenic (1000 ± 1 mg/L) was prepared by dissolving 500 ± 0.1 mg of arsenic trioxide in 20 ± 0.1 mL of 2 g ± 0.1 mg NaOH, which was neutralized by adding dilute HCl to make acid. The solution was then made up to the mark in a 500 mL volumetric flask by adding distilled water. From stock solution, a working solution of 100 ± 1 mg/L has been prepared. These two solutions were used to build up an analytical calibration curve with different concentrations (0.75, 1.25, 1.50, 2.50, 3.00, 4.00, and 5.00 mg/L).

2.3.3. Optimizing experimental conditions

The experimental conditions were optimized by studying the influence of the following parameters (reagents concentration, temperature and duration of heating, and pH) with 6.5 mL of 5.00 mg/L As(III) solution.

2.3.4. Amount of potassium iodate
Through various volumes (0.10 - 1.00 mL) and different concentrations (0.5 – 2.0 %), the impact of potassium iodate concentration on the reaction system was investigated. This amount was added to As(III) aliquot in acidic media in which As(III) reacts with potassium iodate to release iodine quantitatively.

2.3.5. Amount of acid
Four acids (sulfuric, phosphoric, hydrochloric, and acetic acid) were tested for their effect on the liberation of iodine in the procedure. Different volumes (0.10 - 0.50 mL) of acid concentration ranges from 0.1 – 0.5 M were evaluated to see how well iodine was released from iodate by the reaction with As(III).

2.3.6. Volume of LCV
A volume range (0.10 – 1.00 mL) of 0.025 % LCV was investigated to achieve the optimum conditions in order to obtain the desired violet colour, which is produced when LCV is selectively oxidized by the freed iodine when As(III) reacts with potassium iodate.

2.3.7. Volume of NaOH
LCV is oxidized to crystal violet (CV) in a mild acidic medium (i.e. pH~4.5). A range of (1 - 10 drops) of 2.0 M NaOH solution was investigated to find the right number of drops that required reaching pH~4.5.

2.3.8. Effect of temperature and duration of heating
For complete colour development, the reagent system requires heating. A heating incubator was used to investigate the effect of temperature and the duration of heating on an aliquot of 7.5 ± 0.1 mL of reaction mixture containing 5.00 mg/L As(III) to achieve the required colour. A temperature range of $(25, 30, 35, 40, 45, 50) \pm 0.5$ºC for 10, 15, 20, 25, and 30 min duration time were instigated.

2.3.9. Effect of pH
Before making a spectrophotometric determination, the pH of the medium affects the formation and stability of the CV indicator. The effect of pH was studied by varying the pH from 2.00 ± 0.01 to 9.00 ± 0.01 using drops of 0.1 M HCl or 0.1 M NaOH for an aliquot of 7.5 ± 0.1 mL of reaction mixture containing 5.00 mg/L As(III).

2.4. Modification of nanosilica with cysteine
A 36 g ± 0.1 mg (0.6 mole) of the nanosilica was dissolved in 600.0 ± 0.1 mL of distilled water then adjust the pH to 5.60 ± 0.01. A 36 g ± 0.1 mg (0.3 mole) of cysteine was added to nanosilica solution and shaken using a magnetic stirrer for 48 hrs. Then the mixture was filtered by centrifugation for 30 min

at 4000 rpm and in a vacuum oven, the solid was dried at 25 ± 0.5ºC for 5 days (yield 90%). The product is labeled as (SiO_2-Cys).

2.5. Loading modified form of nanosilica with arsenic trioxide
A 50 ± 0.1 mg of (SiO_2-Cys) was dissolved in 25.0 ± 0.1 mL of 50 ± 1 mg/L As(III) at pH 6.00 ± 0.01 and 25.0 ± 0.5ºC, shook for 96 hour, then centrifuged and dried in vacuum oven at 25.0 ± 0.5ºC for another 5 days. The product (SiO_2-Cys/ATO) is called modified nanosilica with ATO.

2.6 Characterization using Attenuated total reflectance-Fourier Transform Infrared (ATR-FTIR) Spectroscopy Analysis
SiO_2-Cys and SiO_2-Cys with As(III) (SiO_2-Cys/ATO) spectra of ATR-FTIR were recorded using a Vertex 70-FT-IR spectrometer (Bruker, Germany) at room temperature coupled with a vertex Pt-ATR-FTIR accessory.

2.7. Obtaining a method for the determination of As(III) in presence of nanosilica-cysteine composite from aqueous media
A 10 ± 0.1 mg of prepared (SiO_2-Cys/ATO) was added to vessels containing 50.0 ± 0.1 mL of distilled water and shook for 48 hr at 250 rpm. A blank sample was prepared in the same manner using (SiO_2-Cys). In order to deal with colloidal nanoparticles solution, different filtration techniques are investigated before applying determination procedure; including centrifugation, gravity filtration using qualitative and quantitative filter papers, and vacuum filtration (suction) using previous types of filter papers in addition to microfiber filter paper. Micro-filters (0.22 μm hydrophilic and hydrophobic) were also tried. Moreover, cooling at 5.0 ± 0.5ºC for 24 hr, freezing at $(-3.0 \pm 0.5$ºC) for 12 hr, and settling for 24, 48 or 72 hr have been investigated. Each technique/ method was followed by 60 min centrifugation at 4000 rpm to insure separation. After that an aliquot of 6.5 ± 0.1 mL was taken out for subsequent steps of the determination process, and readings were compared with a blank water sample.

2.8. Determination of As(III) in presence of nanosilica-cysteine composite from different media
Adding 10 ± 0.1 mg of (SiO_2-Cys/ATO) to vessels containing 50.0 ± 0.1 mL media solution (normal saline, dextrose, ringer lactate, water (all at pH=7.40 ± 0.01), and 0.1 M HCl were shook at 250 rpm for 48 hr and 37.5 ± 0.5ºC. After that the samples were settled for 48 hr and an aliquot was taken out for the determination procedure of As(III) ions. The concentration of As(III) in each sample was determined by comparison with a calibration curve based on the absorption maximum at 590 nm according to the proposed procedure.

3. RESULTS AND DISCUSSION

3.1 Characterization using ATR-FTIR Spectroscopy Analysis

The ATR-FTIR analysis was performed in order to establish the changes in the functional groups of SiO_2-Cys to insure loading of As(III). The spectrum of SiO_2-Cys (Figure 1b) shows distinctive peaks at three main wavenumbers: 1077, 800 and 453 cm^{-1} which corresponds to the asymmetric, symmetric modes of Si–O–Si, bending O-Si-O, respectively and a characteristic peak at 962 cm^{-1} for the silanol group stretching vibration (28). The red shift in asymmetric Si–O–Si band from original 1060 cm^{-1} on nanosilica to 1077 cm^{-1} on SiO_2-Cys indicated the interaction of amino acid with surface silanols of nanosilica (29). Another peaks: 1583 cm^{-1} (COO^- asymmetric stretching), 1486 cm^{-1} (N-H bending) and 1406 cm^{-1} (COO^- symmetric stretching) were also observed. The existence of COO^- and N-H peaks showed that cysteine is present as a zwitterion molecule (30).

ATR-FTIR spectra of the bare As_2O_3 (Figure 1c) shows the prominent peak of As–O stretching vibration at 802 cm^{-1} and another peak at 474 cm^{-1} which is related to As–O bending (31).

3.2. Reaction mechanism

In acidic medium of low pH (pH~1), As(III) reacts with potassium iodate to release iodine quantitatively. Crystal violet (CV) dye is produced (Scheme 1) when LCV is selectively oxidized by the freed iodine to give a violet colour in the presence of sodium hydroxide (pH~4.5)(22). The reaction steps are as follows:

Step 1
$$5H_3AsO_3 + 2KIO_3 + 2HCl \rightarrow 5H_3AsO_4 + I_2 + H_2O$$
Step 2
$$I_2 + 2LCV \rightarrow 2I^- + 2CV^+$$

Scheme 1: LCV oxidation to CV
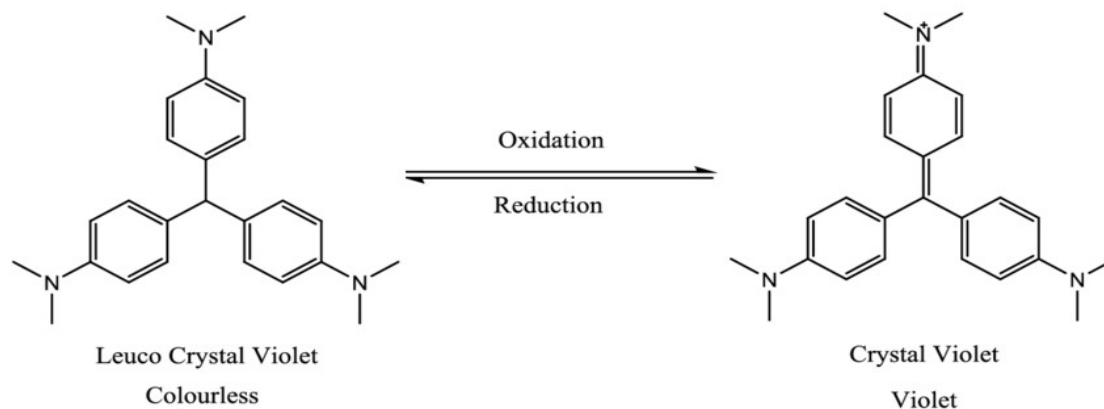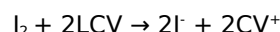
From Figure 1, the highest absorption for CV dye was at 590 nm while the blank had a negligible absorbance at this wavelength.
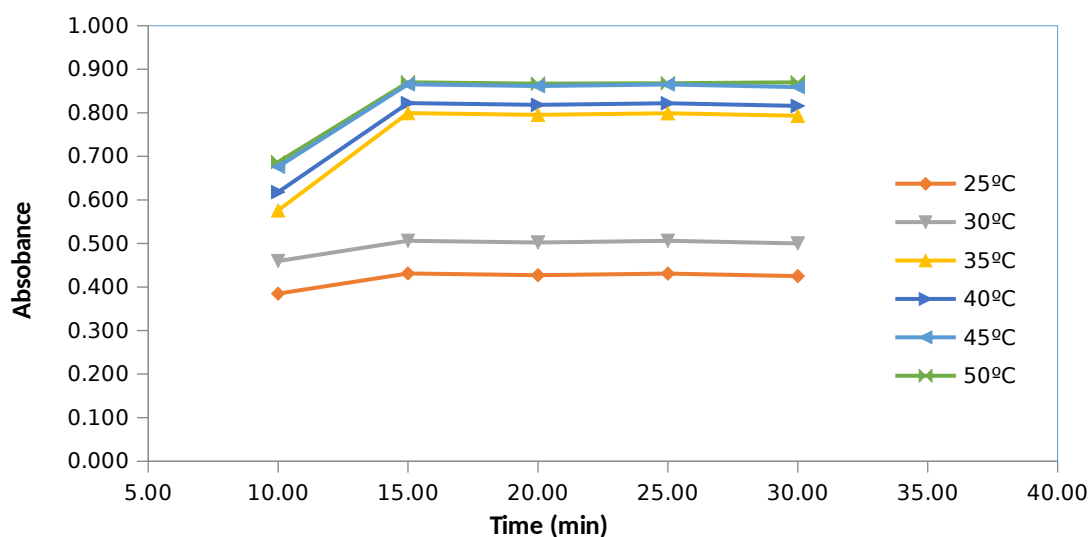
Figure 2: Absorption spectra of a) CV dye [3 mg/L As] versus reagent blank, b) reagent blank versus

distilled water.
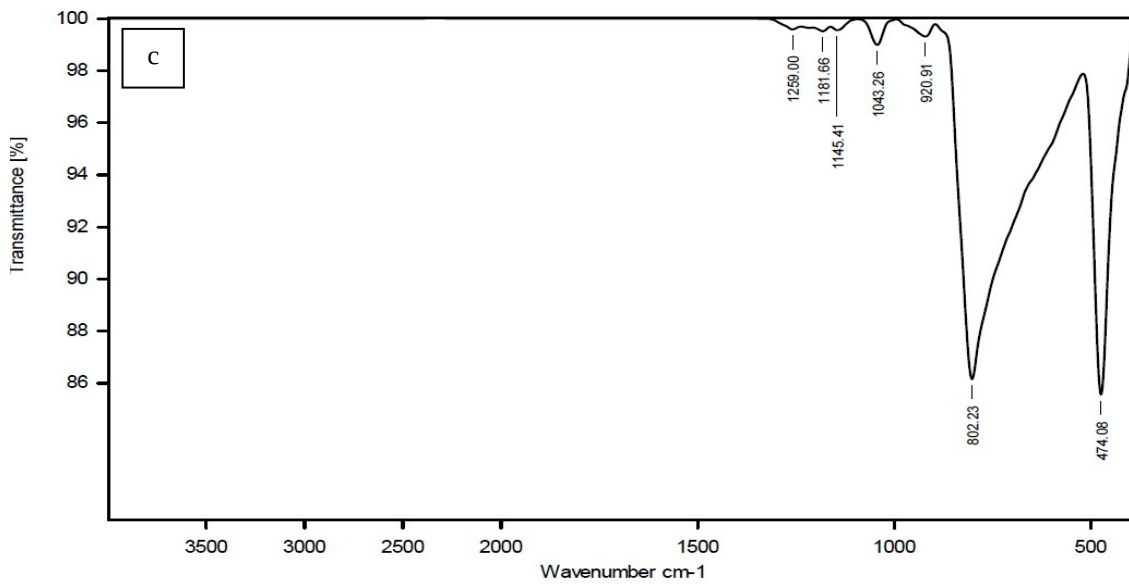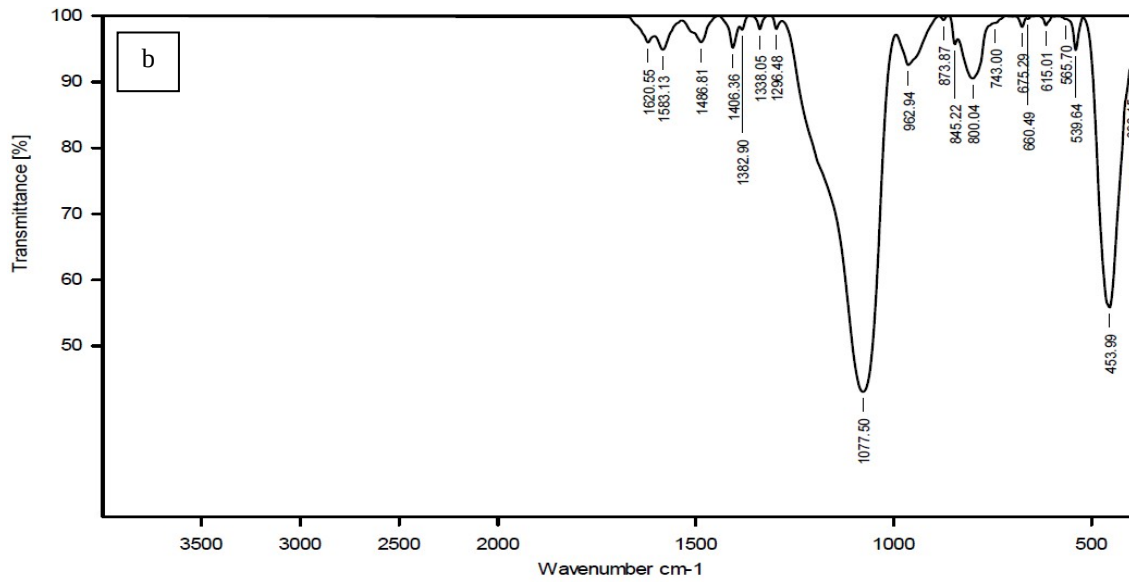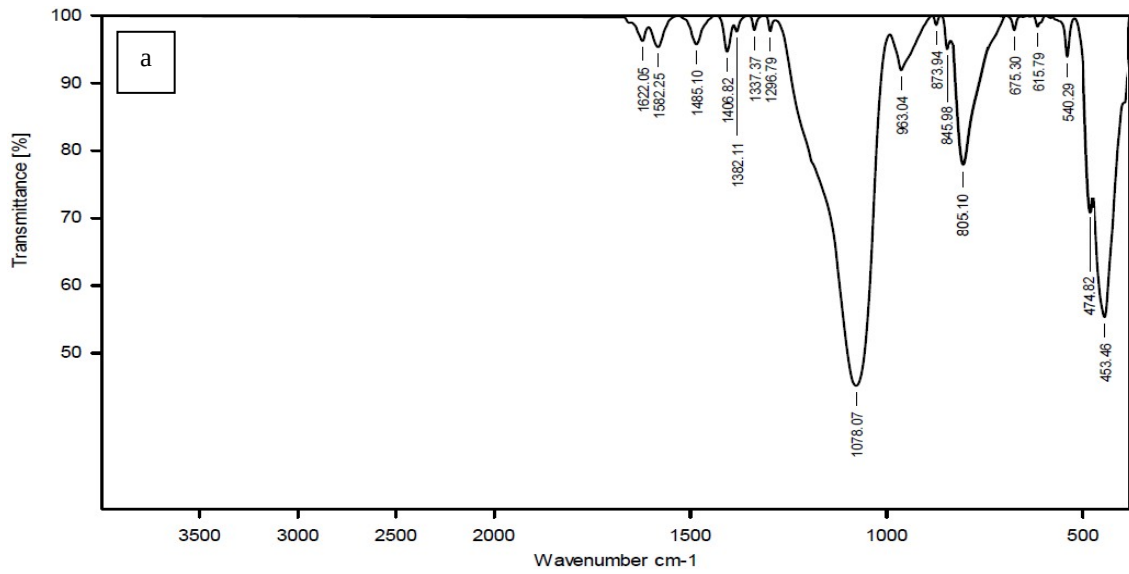
Figure 1: ATR-FTIR spectra for a) SiO_2-Cys/ATO, b) SiO_2-Cys, and c) ATO

The experimental setup was perfected by looking at the impact of the following parameters with 5.00 mg/L As(III) in an approximately final volume of 7.50 ± 0.1 mL in order to make the colour system as sensitive as possible.

3.3. Amount of reagents

The reaction system's response to the concentration of potassium iodate was studied with (0.10 - 1.00 mL) of different concentrations (0.5 – 2.0 %). According to Table 1, it was found that 0.50 mL of 1 % KIO_3 or 1.00 mL of 0.5 % KIO_3 solution was sufficient for quantitative liberation of iodine.

Table 1: Effect of potassium iodate amount on the reaction system

KIO_3 Concentration (w/v)	KIO_3 Volume (mL)	Absorbance of 5.00 mg/L As(III)		
	0.10 ± 0.01	N/A	N/A	N/A
	0.25 ± 0.01	0.167	0.164	0.168
0.5 %	0.50 ± 0.01	0.332	0.328	0.329
	0.75 ± 0.01	0.504	0.511	0.508
	1.00 ± 0.01	0.669	0.660	0.665
	0.10 ± 0.01	0.133	0.133	0.130
	0.25 ± 0.01	0.339	0.337	0.331
1.0 %	0.50 ± 0.01	0.666	0.669	0.670
	0.75 ± 0.01	0.660	0.668	0.663
	1.00 ± 0.01	0.658	0.665	0.665
	0.10 ± 0.01	0.208	0.199	0.200
	0.25 ± 0.01	0.490	0.498	0.500
1.5 %	0.50 ± 0.01	0.567	0.560	0.556
	0.75 ± 0.01	0.656	0.666	0.658
	1.00 ± 0.01	0.664	0.660	0.657
	0.10 ± 0.01	0.256	0.261	0.265
	0.25 ± 0.01	0.643	0.637	0.638
2.0 %	0.50 ± 0.01	0.649	0.656	0.651
	0.75 ± 0.01	0.661	0.653	0.655
	1.00 ± 0.01	0.651	0.661	0.658

It was noticed that hydrochloric acid is more suitable and efficient than other acids (sulfuric, phosphoric, and acetic acid) liberation of iodine from iodate by the reaction with As(III). A concentration of 0.5 M hydrochloric acid through different volumes (0.25 - 0.50 mL) in an overall volume of 7.5 mL of reaction mixture was effective for the liberation of iodine from iodate by the reaction with As(III); precisely 0.25 ± 0.01 mL of 0.5 M hydrochloric acid (Table 2). So adding this amount of HCl to the reaction mixture prior to the subsequent steps is the most appropriate for the reaction process.

Table 2: Effect of acid amount on the reaction system

Acid	Acid Concentration (M)	Acid pH	Acid Volume (mL)	Absorbance of 5.00 mg/L As(III)		
Sulfuric acid	0.1	0.70	0.10 ± 0.01	0.220	0.214	0.218
			0.25 ± 0.01	0.305	0.299	0.303
			0.50 ± 0.01	0.320	0.314	0.318
	0.3	0.22	0.10 ± 0.01	0.433	0.426	0.431
			0.25 ± 0.01	0.541	0.534	0.539
			0.50 ± 0.01	0.558	0.552	0.556
	0.5	0.00	0.10 ± 0.01	0.663	0.656	0.661
			0.25 ± 0.01	0.785	0.779	0.784
			0.50 ± 0.01	0.799	0.792	0.797
Phosphoric acid	0.1	1.55	0.10 ± 0.01	N/A	N/A	N/A
			0.25 ± 0.01	N/A	N/A	N/A
			0.50 ± 0.01	0.118	0.111	0.116
	0.3	1.32	0.10 ± 0.01	0.226	0.219	0.224
			0.25 ± 0.01	0.256	0.249	0.254
			0.50 ± 0.01	0.308	0.301	0.306
	0.5	1.21	0.10 ± 0.01	0.378	0.372	0.376
			0.25 ± 0.01	0.416	0.408	0.413
			0.50 ± 0.01	0.518	0.511	0.516
Hydrochloric acid	0.1	1.00	0.10 ± 0.01	0.238	0.231	0.236
			0.25 ± 0.01	0.317	0.308	0.313
			0.50 ± 0.01	0.328	0.321	0.327
	0.3	0.52	0.10 ± 0.01	0.456	0.449	0.454
			0.25 ± 0.01	0.567	0.559	0.564
			0.50 ± 0.01	0.578	0.571	0.576
	0.5	0.30	0.10 ± 0.01	0.678	0.671	0.676
			0.25 ± 0.01	0.815	0.809	0.813
			0.50 ± 0.01	0.818	0.810	0.816

			0.10 ± 0.01	N/A	N/A	N/A
	0.1	2.88	0.25 ± 0.01	N/A	N/A	N/A
			0.50 ± 0.01	N/A	N/A	N/A
			0.10 ± 0.01	N/A	N/A	N/A
Acetic acid	0.3	2.64	0.25 ± 0.01	0.111	0.105	0.109
			0.50 ± 0.01	0.118	0.111	0.116
			0.10 ± 0.01	N/A	N/A	N/A
	0.5	2.53	0.25 ± 0.01	0.113	0.109	0.116
			0.50 ± 0.01	0.132	0.125	0.130

A 0.025 % LCV was considered to be the most appropriate concentration to use in the determination of As(III) as obtained by Agrawal and his team (22). It was noticed that the values of absorbance were constant in the volume range 0.25 – 0.50 mL of 0.025 % LCV under the optimum conditions (Table 3). Lower concentrations of the indicator caused a drop in absorbance, and higher concentrations caused turbidity to form. As a result, an optimum volume of 0.25 ± 0.01 mL of 0.025 % LCV was used in the method to obtain the desired dye colour. Nevertheless, in order to oxidize LCV to CV, a mild acidic medium (i.e. pH~4.5) is achieved using 1-2 drops of 2 M NaOH solution to the final reaction mixture and was adequate to reach the desired results.

Table 3: Effect of LCV amount on the reaction system

LCV Concentration	LCV Volume (mL)	Absorbance of 5.00 mg/L As(III)		
	0.10 ± 0.01	0.635	0.629	0.633
	0.25 ± 0.01	0.866	0.867	0.863
0.025 %	0.50 ± 0.01	0.863	0.869	0.857
	0.75 ± 0.01	> 1.3	> 1.3	> 1.3
	1.00 ± 0.01	> 1.3	> 1.3	> 1.3

3.4. Effect of temperature and duration of heating
Under optimum conditions, the reagents system required heating at 45.0 ± 0.5ºC in a thermostat oven for complete colour development (Figure 2), since absorbance was markedly affected below this temperature. However, duration time of 15 min is efficient to achieve the required colour. The development of the colour was unaffected by an increase in temperature (> 45ºC) or by duration of heating (> 15 min).

3.5. Effect of pH
The formed CV dye was pale violet in colour below pH 5.00 (after addition of 2.0 M NaOH). The colour of CV dye (Figure 3) developed to the full violet colour with decreasing acidity to 5.50 – 6.50 with an optimum pH of 6.00 ± 0.01. An increase of pH above 6.50 severely affected the stability and sensitivity of the dye. Colour development did not take place below pH 3.50. It was also found that a 15 min time period is needed for a complete colour development after adjusting the pH prior to the colorimetric measurement. The formed dye was stable for several weeks.

3.6. Optimum procedure for the determination of As(III) in aqueous solutions
Under the proposed reaction conditions, 0.50 ± 0.01 mL of 1 % potassium iodate and 0.25 ± 0.01 mL of 0.5 M HCl were added to a 6.50 ± 0.01 mL aliquot of As(III) solution and the mixture was shaken gently at 150 rpm for 5 min, followed by addition of 0.25± 0.01 mL of LCV and 2 drops of 2.0 M NaOH solution. The solution was kept in an incubator at 45.0 ±

0.5ºC for 15 min. The pH was adjusted to 6.00 ± 0.01 and stand for 15 min before the colorimetric measurement. The absorbance was measured at 590 nm against a reagent blank that was prepared in the same manner as mentioned above.

A linear correlation was found between absorbance and concentration of As(III). The calibration graph (Figure 4) shows linear relationship with a coefficient of determination (R^2= 0.995) in the concentration range (0.75 – 5.0 mg/L) of As(III). This calibration graph was used to obtain As(III) concentration in solutions.

3.7. Analytical data
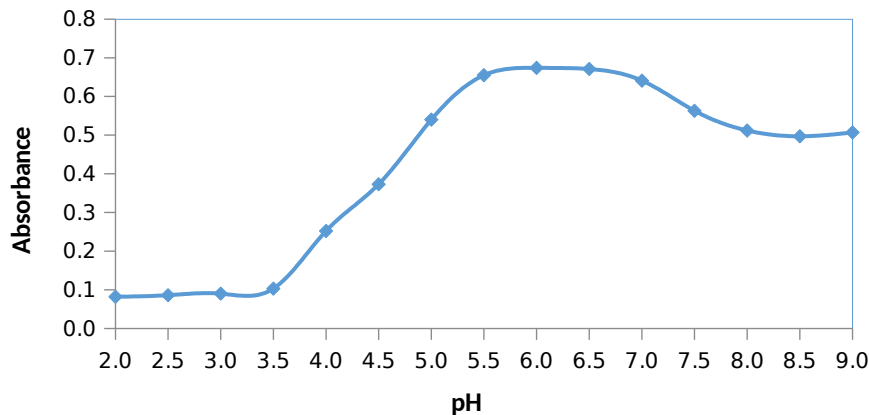
Figure 3: Effect of temperature and duration of heating on the reaction system through average absorbance of three determinations

$f(x) = 0.177750933997509\ x + 0.062783312577833$
$R^2 = 0.994991680128753$
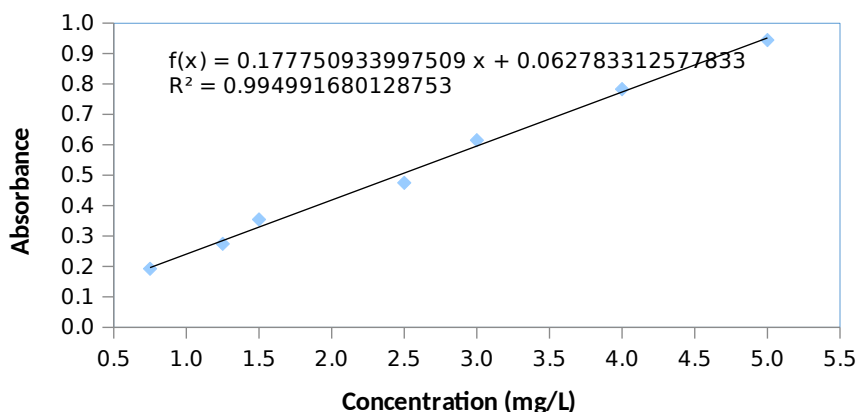
Figure 4: Effect of pH on the absorbance on CV dye [5 mg/L As(III)]

781
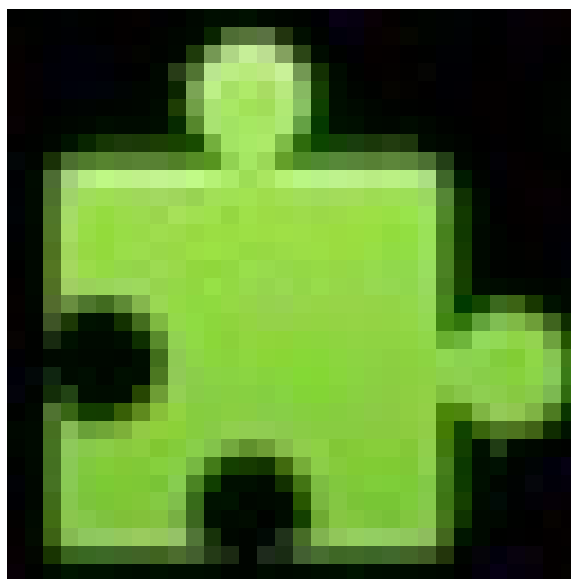
Figure 5: Calibration graph for As(III) determination

Measurement of the magnitude of analytical background response is performed by analyzing an appropriate number of blank samples and calculating the standard deviation of these responses (32). Herein, the absorbance values of six blank water samples were: 0.156, 0.150, 0.153, 0.153, 0.155, and 0.157 in which the standard deviation ($\sigma = 0.0025$).

Limit of detection (LOD) and limit of quantification were calculated according to ICH guidelines as LOD $= 3.3 \times \sigma/S$ and LOQ $= 10 \times \sigma/S$, where σ is standard deviation of response and S is slope of calibration curve (32). LOD and LOQ values were found to be 0.043 and 0.141 mg/L, respectively.

The molar absorption coefficient (ε) could be calculated from Beer–Lambert law ($A = \varepsilon bc$), where A is absorbance, c is concentration of the absorbing species in mol/L and b is path length in cm. So for ε, the equation becomes $\varepsilon = A/bc$. However, in a graph of A versus c, the slope will be εb. Since the path length in our experiment is 1 cm, and converting the slope from 0.117 mg/L to 5.9×10^{-7} mol/L, the molar absorption coefficient is 1.69×10^6 L/mol.cm.

Sensitivity of proposed method is determined by calculating Sandell's sensitivity (33), which can be defined as the concentration of the analyte in ppm (mg/L) which will give an absorbance of 0.001 in a cell of 1 cm path length. Sandell's sensitivity is expressed as: (0.001 * 1cm)/slope, and was found to be 0.0855 µg/cm^2.

The accuracy of the method was established by analyzing As(III) at three concentration levels covering the specified range and the precision was ascertained by calculating the relative standard deviation of ten replicate determinations on the same solutions at three concentration levels are presented in Table 4. The relative error and relative standard deviation indicates the high accuracy and precision for this method.

Table 4: Evaluation of accuracy and precision

Amount added (mg/L)	Amount found (mg/L)*	RE (%)	SD (mg/L)	RSD (%)
	1.22 ± 0.04	0.020		
1.25	1.23 ± 0.03	0.016	0.015	1.26 %
	1.20 ± 0.05	0.008		
	2.94 ± 0.11	0.020		
3.00	2.89 ± 0.07	0.017	0.025	0.86 %
	2.91 ± 0.13	0.010		

	4.90 ± 0.22	0.018		
5.00	4.94 ± 0.16	0.012	0.020	0.41 %
	4.92 ± 0.19	0.014		

*Mean value of five determinations

RE - Relative Error; SD - Standard Deviation; RSD - Relative Standard Deviation

3.8. Obtaining a method for the determination of As(III) in presence of nanosilica-cysteine composite from aqueous media

Much attention is given in the recent time to functionalized derivatives of silica nanoparticles. The structures of functional silica nanoparticles can be very diverse (26). However, the solutions of silica nanoparticles form stable colloids, these suspensions considered to be a disadvantage while dealing with colorimetric detection. Colorimetric methods for the determination of arsenic in environmental and biological samples using LCV were conducted, but none has proven effective when dealing with colloidal solutions in presence of silica nanoparticles (22-24), or in environmental and biological samples (7,17,20-21,34).

Therefore, development of a method in order to deal with the nanoparticles solution is applied by using different filtration techniques and methods. Table 5 illustrates the absorbance achieved for blank and spiked samples.

According to results shown in Table 5, using centrifugation as a single filtration technique at different times did not resolve the interference caused by the presence of nanosilica which is clear from the SiO_2-Cys absorbance results. So for the gravity and suction filtration techniques, neither SiO_2-Cys nor SiO_2-Cys/ATO absorbance results seems real, even with applying different types of filter papers. However, solutions obtained from previous techniques still having colloid properties. Using a 0.22 µm hydrophilic (Nylon) and hydrophobic polytetrafluoroethylene (PTFE) filters shows an improvement in results but still not reaching the desired ones. Having the samples cooled in the refrigerator at 5.0 ± 0.5ºC for 24 hr prior to the determination process shows a similar behaviour to the filters technique. Freezing the samples at -3.0 ± 0.5ºC and thawing after 12 hr lead up to settling the particles in the solution including the As(III) ions which result in a failure in the determination process of SiO_2-Cys/ATO.

From Table 5, it's noticed that leaving the sample (suspension) to settle for 48 hr prior to the determination process has the best absorbance relative to blank water sample, in which it could be explained that this period of time is necessary for the settling of the colloid nanoparticles and achieve a much better clear solution. Increasing settling time did not improve the results. Regarding to other filtration techniques, it was found that a turbid solution is always achieved which gives false measurement values. As a result, we developed a suitable procedure commensurate with the constraints that accompany the detection process in order to achieve actual results for the determination of arsenic in such systems.

3.9. Determination of As(III) in presence of nanosilica-cysteine composite in different media

When dealing with drug delivery and stability, various biological solutions are options that could be used. The most popular ones were chosen as shown in Table 6. After the solutions have been shaken as in the proposed procedure, they were left to settle for 48 hr prior to the determination process. It can be noticed that the highest stability is in Ringer lactate and the lowest is in 0.1 M HCl.

Table 5: Absorbance of blank and nanosilica-cysteine composite solutions using different filtration techniques and methods.

Filtration technique/ Method		Centrifugation Time (min)	Absorbance of blank water	Absorbance of SiO_2-Cys*	Absorbance of SiO_2-Cys/ATO*
Centrifuge		30		> 1.5	> 1.5
		60	0.064	1.301	> 1.5
		120		1.292	> 1.5
Gravity filtration	Qualitative filter paper	60	0.064	> 1.5	1.497
	Quantitative filter paper			1.292	1.355
Vacuum filtration (suction)	Qualitative filter paper	60	0.064	1.355	> 1.5
	Quantitative filter paper			1.286	> 1.5
	Glass microfiber			1.065	> 1.5
0.22 µm filters	Hydrophilic Nylon	60	0.064	0.581	1.136
	Hydrophobic PTFE			0.579	1.089
Settling	24 hr	60	0.064	0.242	0.799
	48 hr			0.153	0.301
	72 hr			0.150	0.299
Cooling (5.0ºC)	24 hr	60	0.064	0.568	1.286
Freezing (-3.0ºC)	12 hr	60	0.064	0.260	N/A

*Mean value of three determinations

Table 6: Determination of 5.00 mg/L As(III) in presence of nanosilica-cysteine composite from different media at 25ºC

Media	pH	Absorbance of SiO$_2$-Cys*	Absorbance of SiO$_2$-Cys/ATO*	Amount of As(III) detected (mg/L)
Normal saline	7.40 ± 0.01	0.131	0.361	0.949
Dextrose	7.40 ± 0.01	0.102	0.236	0.407
Ringer lactate	7.40 ± 0.01	0.102	0.219	0.311
Water	7.40 ± 0.01	0.125	0.271	0.475
0.1 M HCl	1.00 ± 0.01	0.122	0.376	1.085

*Mean value of three determinations

4. CONCLUSION

The use of Leucocrystal Violet as a reagent for the spectrophotometric measurement of arsenic is described in this paper. It provides sensitivity, selectivity, simplicity, and cost-effectiveness. Since there is no extraction steps involved into an organic solvent, it is considered a green method. The method's usefulness is demonstrated by the method's satisfactory applicability to the determination of arsenic in environmental and biological samples in presence of nanosilica-cysteine composite. Spectrophotometry is still a common and necessary method for determining arsenic at trace levels despite the availability of many sophisticated alternatives, particularly in laboratories in developing nations with limited budgets due to factors like instrument's low cost, simplicity, minimal maintenance requirements, and no consumables required. However determination of arsenic in urine and serum samples in presence of nanosilica-cysteine composite has not been investigated yet, in which could be a scope of future work.

5. CONFLICT OF INTEREST

There is no conflict of interest to report.

6. ACKNOWLEDGMENTS

There is no acknowledgment to report.

7. REFERENCES

1. Tatken RL, Lewis RJ. Registry of Toxic Effect of Chemical Substance. 1981–82 ed. US Dept of Health and Human Services, Cincinnati; 1983.

2. Cullen WR, Reimer KJ. Arsenic Speciation in the Environment. Chem. Rev. 1989;89:713-764. Available from: <URL>.

3. Ghazy SE. Removal of Cadmium, Lead, Mercury, Tin, Antimony, and Arsenic from Drinking and Seawaters by Colloid Precipitate Flotation. Sep. Sci. Technol. 1995;30:933. Available from: <URL>.

4. AWWA. Water quality and treatment. American water works association, Washington, DC; 1992.

5. Kohlmeyer U, Jantzen E, Kuballa J, Jakubik S. Benefits of high resolution IC-ICP-MS for the routine analysis of inorganic and organic arsenic species in food products of marine and terrestrial origin. Anal Bioanal Chem. 2003;377:6–13. Available from: <URL>.

6. Cherian T, Narayana B. A New Spectrophotometric Method for the Determination of Arsenic in Environmental and Biological Samples. Anal Lett. 2005; 38: 2207–2216. Available from: <URL>.

7. Dasgupta PK, Huiliang HL, Zhang GF, Cobb GP. Photometric measurement of trace As(III) and As(V) in drinking water. Talanta. 2002;58:153-164. Available from: <URL>.

8. Ferrerira MA, Barros AA. Determination of As(III) and Arsenic(V) in natural waters by cathodic stripping voltammetry at a hanging mercury drop electrode. Anal Chim Acta. 2002;459:151-159. Available from: <URL>.

9. Kopanicia M, Novotny L, Determination of traces of arsenic(III) by anoidic stripping voltammetry in solutions, natural waters and biological materials. Anal Chim Acta. 1998;368:211-218. Available from: <URL>.

10. Bundelaska JM, Stafilov T, Appadjian S. Direct analysis of natural waters for arsenic species by hydride generation atomic absorption spectrometry. Int J Environ Anal Chem. 2005;85:199-207. Available from: <URL>.

11. Heitkemper DT, Vela NP, Stewart KR, Westphal CS. Determination of total and speciated arsenic in rice by ion chromatography and inductively coupled plasma mass spectrometry. J Anal At Spectrom. 2001;16:299-306. Available from: <URL>.

12. Boadu M, Osae EK, Golow AA, Serfor-Armah Y, Nyarko BJ. Determination of arsenic in some water bodies, untreated ore and tailing samples at Konnongo in Ashanti region of Ghana and its surrounding town and villages by instrumental neutron activation analysis. J Radioanal Nucl Chem. 2001;249:581-585. Available from: <URL>.

13. Gupta VK, Agarwal S. PVC based 5,10,15,20-tetrakis (4-methoxyphenyl) porphyrinatocobalt(II) membrane potentiometric sensor for arsenite. Talanta. 2005;65:730-734. Available from: <URL>.

14. Gomez MM, Kovecs M, Palacios MA, Pizarro I, Camara C. Effect of the mineralization method on arsenic determination in marine organisms by hydride generation

atomic fluorescence spectroscopy. Microchim Acta. 2005;150:9-14. Available from: <URL>.

15. Abdolmohammad-Zahen H, Jouyban A, Amini R. Ultratrace determination of arsenic in water samples by electrothermal atomic absorption spectrometry after pre-concentration with Mg-Al-Fe ternary layered double hydroxide nano-sorbent. Talanta. 2013;116:604-610. Available from: <URL>.

16. Karayunlu S, Ay U. Spectrophotometric determination of total inorganic arsenic with hexamethylene ammonium-hexamethylenedithiocarbamate in nonionic triton X-100 micellar media. J Anal Chem. 2010;65:244-248. Available from: <URL>.

17. Deepa K, Lingappa Y. A simple spectrophotometric method for the determination of arsenic in industrial and environmental samples using 2,4-dihydroxy benzophenone-2-amino thiophenol. Spectrochim Acta, Part A. 2014;124:102-107. Available from: <URL>.

18. Yuji S, Kato T, Nukatsuka I, Ohzeki K. Spectrophotometric determination of arsenic(III) based on solid phase extraction of the arsenic-APDC complex and the conversion to the copper complex. Bunseki Kagaku. 2003;52:1153-1158. Available from: <URL>.

19. Pasha C, Narayana B. Determination of arsenic in environmental and biological samples using toluidine blue or safranine O by simple spectrophotometric method. Bull Environ Contam Toxico. 2008;81:47-51. Available from: <URL>.

20. Revanasiddappa HD, Dayananda BP, Kumar TN. A sensitive spectrophotometric method for the determination of arsenic in environmental samples. Environ Chem Lett. 2007;5:151-155. Available from: <URL>.

21. Pillai A, Sunita G, Gupta VK. A new system for the spectrophotometric determination of arsenic in environmental and biological samples. Anal Chim Acta. 2000;408:111-115. Available from: <URL>.

22. Agrawal O, Sunita G, Gupta K. A Sensitive Colorimetric Method for the Determination of Arsenic in Environmental and Biological Samples. J. Chin. Chem. Soc. 1999;46:4. Available from: <URL>.

23. Stancheva K., Pasha C. Spectrophotometric Determination of Trace Amounts of As(III) and As(V) Using Safranine O and Fuchsine as New Reagents. Oxid. Commun. 2016;39(2):1538–1546. Available from: <URL>.

24. Kamaya M, Ito Y, Otomura Y, Ginatullina E. Comparative Study of Leuco Dyes as Reagents for Spectrophotometric Determination of Arsenic (III). Asian J. Appl. Sci. 2015;3(1).

25. Moore R, Holt K, Zhao H, Salas F, Hasan A, Lucero D. Sorption of Arsenic from Drinking Water to Mg(OH)2 Sorrel's Cements, and Zirconium Doped Materials. Environmental Decisions and Program Development Sandia National Laboratories, United States; 2002.

26. Gorbatsevich OB, Kholodkov DN, Kurkin TS, Malakhova YN, Strel DR, Buzin AI, et al. Synthesis and properties of water soluble silica nanoparticles. Russ. Chem. Bull. 2017;66(3):409-417. Available from: <URL>.

27. Bajpai S, Tiwary S, Sonker M, Joshi A, Gupta V, Kumar Y, et al. Recent Advances in Nanoparticle-Based Cancer Treatment: A Review. ACS Appl. Nano Mater. 2021;4:6441−6470. Available from: <URL>.

28. Fan T, Liu Y, Feng B, Zeng G, Yang C, Zhou M, Zhou H, Wang X. Biosorption of cadmium(II), zinc(II) and lead(II) by Penicillium simplicissimum: Isotherms, kinetics and thermodynamics. J. Hazard. Mater. 2008;160(2):655–661. Available from: <URL>.

29. Du M, Zheng Y. Modification of silica nanoparticles and their application in UDMA dental polymeric composites. Polym. Compos. 2007;28:198–207. Available from: <URL>.

30. Khataee A, Movafeghi A, Nazari F, Vafaei F, Dadpour M, Y. Hanifehpour Y, Joo S. The toxic effects of L-Cysteine-capped cadmium sulfide nanoparticles on the aquatic plant Spirodela polyrrhiza. J. Nanopart. Res. 2014;16:2774-2784. Available from: <URL>.

31. Jadhav V, Sachar S, Chandra S, Bahadur D, Bhatt P. Synthesis and Characterization of Arsenic Trioxide Nanoparticles and Their In Vitro Cytotoxicity Studies on Mouse Fibroblast and Prostate Cancer Cell Lines. J. Nanosci. Nanotechnol. 2016;16:7599–7605. Available from: <URL>.

32. Miller JN, Miller JC. Statistics and Chemometrics for Analytical Chemistry, Prentice Hall, UK, 2005.

33. Shetty D, Narayana B, Samshuddin S. Sensitive methods for the spectrophotometric determinations of some anti-malarial drugs. J. Chem. Pharm. Res. 2012;4(3):1647-1653.

34. Echioda S, Adepeju O, Salisu S, Abdulrasheed A, Chindo I, Kolo A. UV-Vis Spectrophotometric Determination of Selected Heavy Metals (Pb, Cr, Cd and As) in Environmental, Water and Biological Samples with Synthesized Glutaraldehyde Phenyl Hydrazone as the Chromogenic Reagent. EJ-CHEM. 2021;2(3). Available from: <URL>.

Comparison on Total Phenolics and Flavonoids and Antioxidant Activities of Methanol Extract of Horseshoe Crab (*Tachypleus gigas*) Eggs

Elvira Ratna Aisa[1] (iD) **, Tukiran Tukiran**[1*] (iD)

[1]Universitas Negeri Surabaya, Department of Chemistry, Surabaya, 60231, Indonesia

Abstract: The marine environment can be a source of abundant bioactive compounds. One of the horseshoe crab species scattered in Indonesian sea waters is *Tachypleus gigas*. It was reported that the eggs of *T. gigas* contained flavonoids, saponins, alkaloids, and steroids. Flavonoids are polyphenol compounds that have the ability as natural antioxidants. In this study, total phenolics, flavonoids, and antioxidant activity tests were carried out on the methanol extract of *T. gigas* eggs. The total phenolics content used the Folin Ciocalteu method, the total flavonoids used the aluminum chloride colorimetric method, and the antioxidant activity test used the FRAP and DPPH methods. The test results showed that the total phenolics and flavonoids were 0.53506 ± 0.001335 mg GAE/g extract and 0.52067 ± 0.000731 mg QE/g extract, respectively. Meanwhile, the results of the antioxidant activity test with the FRAP method obtained a total antioxidant capacity of 29.85 µmol Fe^{2+}¿$^{/gDW}$¿ in the medium category and antioxidant activity with the DPPH method obtained an IC$_{50}$ value of 597.0397 µg/mL in the very weak category.

1. INTRODUCTION

In the body, oxidation reactions can be the initial cause of most diseases. These reactions can cause continuous and cumulative oxidative damage to essential macromolecules, especially DNA (1). Oxidative damage occurs as a consequence of the excessive production of free radicals, which cannot be processed caused of the insufficient availability of antioxidants, so they accumulate (2). Free radicals are produced during normal metabolic activity in the body and trigger the emergence of various diseases, such as neurodegenerative diseases, cataracts, rheumatoid arthritis, asthma, and others (3). Related to that, an antioxidant is a necessary agent that can reduce the occurrence of oxidative processes and the harmful effects caused by free radicals (4).

Antioxidants are substances that can protect body cells from damage because of free radicals as unstable molecules (5). Antioxidants can slack down the lipid oxidation process by capturing or deactivating free radicals; initiation and propagation reactions can be inhibited (6). The antioxidant activity of a compound works through a series of reaction mechanisms, including the ability to transfer single electrons, release hydrogen electrons, or chelate transition metals (7).

Antioxidants based on the sources are distinguishable into two types endogenous and exogenous (8). Endogenous antioxidants are a type of antioxidant as a natural defense produced by the human body (9). The body also needs exogenous antioxidants to overcome the excess free radicals generated by oxidative stress (10). Exogenous antioxidants are obtained from food or supplements consumed, which consist of natural antioxidants like vitamins A, C, E, phenolic acids, flavonoids, and carotenoids, for synthetic antioxidants are like butylhydroxytoluene, octyl gallate, propyl gallate, and tertiary-butylhydroquinone (11). However, synthetic antioxidants have side effects that are bad for health. Therefore, natural antioxidants can be an alternative to antioxidant agents that are safer to consume than synthetic antioxidants (12).

The horseshoe crab is an aquatic animal known as a living fossil from the Limulidae family (13). Here are four types of horseshoe crab animals scattered worldwide, three of which are found in Indonesia: *Carcinoscorpius rotundicauda, T. tridentatus,* and *T. gigas* (14). It has been discovered that coastal communities consume lots of this part of the horseshoe crab egg (15).

T. gigas eggs contain flavonoids, steroids, saponins, and alkaloids (16). Flavonoids are phenolic compounds with essential biological abilities, their activity both as free radical scavengers, namely antioxidants (17).

This study tested the antioxidant activity of the methanol extract of *T. gigas* eggs using the 2,2-diphenyl-1-picrylhydrazyl (DPPH) and Ferric Reducing Antioxidant Power (FRAP) methods. In the DPPH method, antioxidant compounds act as proton donor compounds to DPPH free radicals, reducing DPPH free radicals to form stable compound molecules (DPPH-H). The DPPH free radical becomes a stable molecule characterized by a color change from purple to yellow as a non-radical compound (reduced diphenylpicrylhydrazine, DPPH-H) (18). Meanwhile, the mechanism in the FRAP method is electron donation, where the antioxidant compounds in the sample act as reducing agents (19). In the FRAP method, antioxidant compounds will reduce the yellow Fe^{3+}-TPTZ complex to blue Fe^{2+} (20). Based on the description above, it is necessary to know about the potential and efficacy as an antioxidant from the methanol extract of *T. gigas* eggs using the DPPH and FRAP methods, which begins with testing the total phenolic and total flavonoid levels.

2. MATERIAL AND METHODS

2.1. Materials
Horseshoe crab (*T. gigas*) eggs were taken from south coast of Madura Island, aquades, methanol p.a. (Merck, Germany), Folin-Ciocalteu (Merck, Germany), Na_2CO_3 (Merck, Germany), gallic acid (42649, Merck), quercetin (Sigma Aldrich, USA), L(+)-ascorbic acid (Merck, Germany), $AlCl_3$ (Merck, Germany), CH_3COOK (Merck, Germany), $CH_3COONa.3H_2O$ (Merck, Germany), glacial acetic acid (Sigma Aldrich, USA), HCl p.a. (Merck, Germany), TPTZ (Sigma Aldrich, USA), $FeCl_3.6H_2O$ (Merck, Germany), $FeSO_4.7H_2O$ (Merck, Germany), and DPPH (Himedia, India).

2.2. Extract Preparation
As much as 200 g of *T. gigas* egg simplicia which had been dried and mashed, was then macerated with 400 mL methanol p.a. Maceration was carried out in a closed container for 24 hours with three repetitions. The maceration results were then filtered, the sample filtrate was obtained, then concentrated using a vacuum rotary evaporator, and a thick methanol extract of *T. gigas* eggs was obtained. Then calculated the amount of extract yield using the calculation as Equation (1) (21):

$$\text{Extract yield (\%)} = \frac{Wa}{Wb} \times 100 \text{ (1); with Wa being}$$

the mass of the extract obtained (g), and Wb being the mass of the simplicia powder (g).

2.3. Total Phenolic Content Test
Total phenolic levels were defined with the Folin Ciocalteu (FC) method (22). As much as 100 mg extract was dissolved in 10 mL of methanol p.a., and a concentration of 10,000 µg/mL was obtained. Next, 0.4 mL of the extract was added with 2 mL of 10% Folin-Ciocalteu and 1.6 mL of 7.5% Na_2CO_3 and vortexed for 1 minute, then the sample was incubated at room temperature for half an hour. The absorbance of the sample was read using UV-Vis spectrophotometry against a blank (sample extract was replaced with only methanol p.a.) at the maximum wavelength, namely 754.5 nm. The calibration curve uses gallic acid with a concentration of (2.5-40) µg/mL. The absorbance of the methanol extract sample obtained was interpolated in the standard curve linear regression equation. The total phenolic content will be represented in mg of gallic acid equivalent per g of extract (mg GAE/g extract).

2.4. Total Flavonoid Content Test
The total flavonoid content of the methanol extract of *T. gigas* eggs was measured utilizing the aluminum chloride colorimetric method with quercetin as a standard (23). 100 mg of extract dissolved in methanol p.a. 10 mL to obtain a concentration of 10,000 µg/mL. Quercetin was used as a standard calibration curve with a concentration range of 5-80 µg/mL. 0.5 mL (sample, standard, and methanol as blank) was added with 1.5 mL methanol p.a., 0.1 mL $AlCl_3$ 10%, 0.1 mL CH_3COOK 1 M, and 2.8 mL distilled water. Then, the mixture was vortexed for 1 minute and incubated at room temperature for 30 minutes. The absorbance was read by UV-Vis spectrophotometry on a blank at a maximum wavelength of 429.5 nm. Total flavonoid content is represented in mg quercetin equivalent per g of extract (mg QE/g extract).

2.5. Antioxidant Activity Test
The antioxidant activity test of the methanol extract of *T. gigas* eggs was carried out using FRAP and DPPH.

2.5.1. FRAP Method Antioxidant Activity Test
An antioxidant activity test by the FRAP method on a sample is performed as a procedure (24,25). FRAP method is used to calculate the total antioxidant capacity (26). The FRAP reagent was prepared to consist of 300 mmol acetate buffer solution (pH 3.6), 10 mmol/L TPTZ solution in 40 mmol/L HCl, and 20 mmol/L $FeCl_3.6H_2O$ with a ratio of 10:1:1 respectively. The FRAP reagent was heated in a water bath at 37°C for 10 minutes. Samples of egg methanol extract of *T. gigas* were prepared by dissolving 100 mg of the extract in 10 mL of methanol p.a. The standard for the calibration curve uses $FeSO_4.7H_2O$ (200-700) µmol/L. A total of 100 µL (sample, standard, and methanol as blank) was mixed with 300 µL of distilled water and 3 mL of FRAP reagent. Then, the

mixture was vortexed for 1 minute and incubated in the dark at 37 °C for 4 minutes. The absorbance is read at the maximum wavelength of 595 nm. The antioxidant activity of a sample using the FRAP method will be expressed as µmol Fe^{2+}/g DW.

2.5.2. DPPH Method Antioxidant Activity Test
Antioxidant activity test of the methanol extract of *T. gigas* eggs was carried out using the DPPH method based on references from (27,28). The DPPH method measures free radical inhibition or inhibition (29). DPPH free radicals were prepared at a concentration of 0.1 mM in methanol. Samples of egg methanol extract of *T. gigas* were carried out by designing solutions with various concentrations of 400-2000 ppm. Vitamin C, gallic acid, and quercetin were used as comparisons or positive controls. Vitamin C is dissolved at a concentration of (1 - 3) µg/mL, quercetin (0.5 – 1.7) µg/mL, and gallic acid (0.2 - 1.4) µg/mL. A total of 4.5 mL (sample, standard, and methanol as a blank) was mixed with 0.5 mL of 0.1 mM DPPH and vortexed for 1 minute, then incubated in the dark room at 37 °C for half an hour. The absorbance is read at the maximum wavelength of 515 nm. The percentage of inhibitory activity is calculated as Equation (2):

$$\frac{(|blank|-|sample|)}{|blank|} \times 100 \qquad (2)$$

Information:
Abs blank: Absorbance of DPPH in the absence of sample
Abs sample: Absorbance of DPPH + sample

The IC_{50} value (50% inhibitory concentration) is a concentration of the test sample to inhibit free radicals (DPPH) up to 50%. The IC_{50} value is calculated based on the % inhibition obtained from each test sample concentration. Furthermore, it is substituted in the regression equation where concentration is on the x-axis and % inhibition is on the y-axis. In the regression equation y = ax + b, if the y value is substituted by number 50, the x value will be obtained as the IC_{50} value.

3. RESULTS AND DISCUSSION

3.1. Preparation of *T. gigas* egg methanol extract
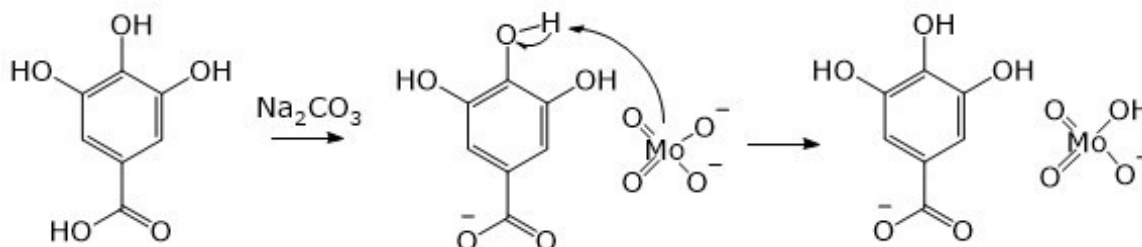
Extraction is separating materials or withdrawing a dissolved component by an appropriate solvent (30). Extraction by maceration method is carried out because this method is a simple, straightforward method and does not require heating, so there is less possibility of damage to natural materials. The maceration method, which requires a long time, allows many compounds to be extracted perfectly (31). The maceration method is a safe extraction method and is often used to determine polyphenolic compounds (32).

The solvent used in the above extraction is methanol, a polar solvent. Flavonoids are polyphenolic compounds with many hydroxyl groups, which make them polar. Thus, methanol can be very suitable as a good solvent in extracting flavonoid compounds (33). After being macerated using methanol solvent, the macerate is filtered using a buchner funnel and concentrated with a vacuum rotary evaporator to produce a thick extract. The yield percentage of the resulting viscous extract is 11.74%. The yield value is the weight of the secondary metabolite compounds obtained from the sample (34).

3.2. Total Phenolic Content
The ability of a phenolic compound to form phenoxy radicals which are stable in the oxidation process makes this compound widely used as an antioxidant agent (35). The total phenolic content test is done to determine the number of phenolic compounds contained in the egg extract of *T. gigas*. Measurement of total phenolic levels using the Folin-Ciocalteu (FC) method. The FC method is based on reducing FC reagents by phenolic compounds in an alkaline state (36). The hydroxyl group of the phenolic compound will react with the FC reagent containing phosphomolybdate-phosphotungstate, which will then form a blue tungsten-molybdenum complex (37). Na_2CO_3 7.5% is added to make the atmosphere alkaline so that the protons in phenolic compounds dissociate into phenolic ions (38). The formation of phenolic ions serves to reduce FC reagents so that the molybdenum ion center will receive one electron from a phenolic antioxidant which causes a reduction of the ion Mo^{+6} to Mo^{+5} followed by a color change from yellow to blue (39−40), the reaction as shown in Figure 1.

Figure 1. Reaction mechanism between FC reagent and gallic acid.

Measurement of total phenolic levels uses gallic acid as a standard because gallic acid is a pure and stable compound (41). Gallic acid (3,4,5-trihydroxy benzoic acid) is a phenolic compound with vigorous antioxidant activity. The total phenolic content contained in an extract is expressed as GAE, which

is the amount equivalent to mg of gallic acid in 1 g of the sample (42). The results of the standard calibration curve for gallic acid with a concentration of (2.5-40) µg/mL obtained a linear regression equation, $y = 0.0173x + 0.0184$, with $R^2 = 0.9982$. Based on the calculation results, the total phenolic content contained in the methanol extract of *T. gigas* eggs is 0.53506 ± 0.001335 mg GAE/g extract.

3.3. Total Flavonoid Content
Flavonoids have biological activity as antioxidants, where their potency is highly dependent on the number and position of the free-OH group (43). Hydroxyl radicals from flavonoid compounds can inhibit the action of free radicals and mediate the

effects of antioxidant activity related to health benefits (44). The total flavonoid content test was carried out to determine the number of flavonoids contained in *T. gigas* egg extract. Measurement of the total flavonoid content is done using the colorimetric method with the addition of an $AlCl_3$ reagent.

Aluminum chloride can react with flavonoid group compounds to produce a stable acid complex with C_4 as a ketone group and C_3 or C_5 as hydroxyl groups of flavones or flavonol compounds, forming yellow compounds (37). The reaction that occurs between flavonoids and $AlCl_3$ is described as follows in Figure 2 (45).
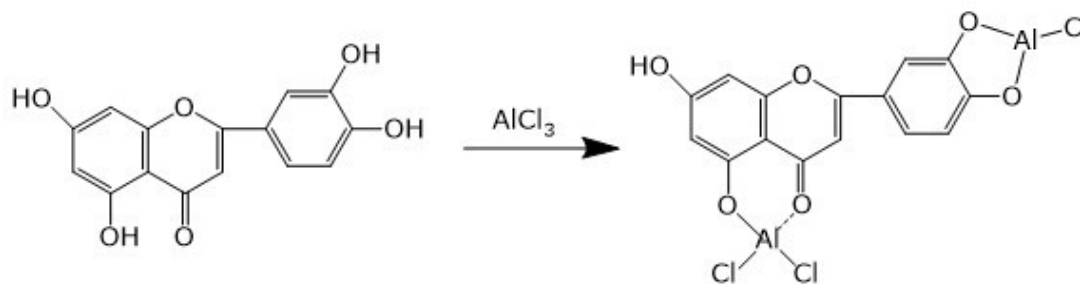
Figure 2. Reaction between flavonoids-$AlCl_3$.

The standard used in measuring total flavonoid levels is quercetin because quercetin is one of the flavonoid compounds of the flavonol group, which has a ketone group at C_4 and a hydroxyl group at C_3 and C_5 (37). Quercetin is the most effective flavonoid compound for capturing free radicals such as superoxide, hydroxyl, and peroxyl radicals. Quercetin can also inhibit various oxidation reactions due to phenolic radicals, which are stabilized by the resonance effect of aromatic rings (46).

The total level of flavonoids in the sample extract is expressed as quercetin equivalents (QE), namely the equivalent amount of mg quercetin in 1 g of the sample using the linear equation of the standard calibration curve. Quercetin standard calibration curve with a concentration of (5-80) µg/mL has obtained a linear equation, $y = 0.0079x - 0.0075$, with $R^2 = 0.9998$. Based on sample absorbance calculations, the total level of flavonoids contained in the methanol extract of *T. gigas* eggs was 0.52067 ± 0.000731 mg QE/g extract.

3.4. Antioxidant Activity with FRAP Method
Antioxidant activity using the FRAP method aims to define the total antioxidant capacity contained in

the sample. FRAP method can measure the total antioxidant content of a sample based on the principle of the ability of an antioxidant compound to reduce Fe^{3+}-TPTZ (2,4,6-tri(2-pyridyl)-1,3,5-triazine) to Fe^{2+}-TPTZ which is blue in acid condition (47). The Fe^{3+}-TPTZ complex compound is an oxidizing agent that may exist in the body and can damage the body's cells (48) Samples that have the ability as antioxidants are thought to reduce Fe^{3+}-TPTZ so that the Fe^{3+}-TPTZ compound cannot react anymore, which causes damage to body cells (49). This Fe^{3+}-TPTZ complex compound is an iron salt from a mixture of TPTZ with $FeCl_3$ in an acidic medium, known as the FRAP reagent (39). The replenishment of $FeCl_3$ aims to form complex compounds Fe^{3+}. The low pH condition 3.6 aims to simplify the reduction process (50).

Qualitatively, the total amount of antioxidants can be seen from the intensity of the blue color Fe^{2+}-TPTZ complex compound formed. The darker the color, the greater of antioxidant capacity of the material being tested (51). The reaction that occurs between antioxidant compounds and the Fe^{3+}-TPTZ complex is as follows in Figure 3 (39).
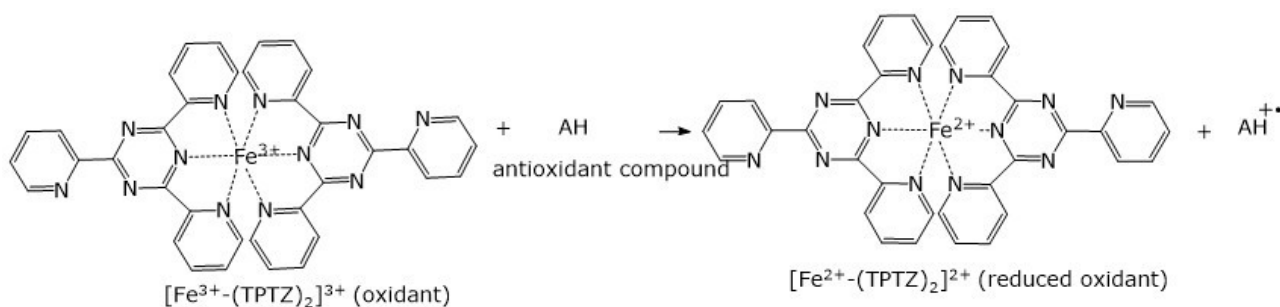
Figure 3. The reaction between FRAP reagents and antioxidant compounds.

In this study, the data measured to determine the total antioxidant capacity was in the form of absorbance measurements. The capacity of the total antioxidant content in the sample extract will be expressed in μmol Fe^{2+}/g DW. Absorbance measurements are done at the maximum wavelength derived from a standard solution of 1000 μmol/L $FeSO_4.7H_2O$ added with FRAP reagent. The absorbance of the sample obtained was then substituted in the standard $FeSO_4.7H_2O$ calibration curve equation at a concentration range of 200-700 μmol/L. A linear equation obtains the standard calibration curve, y = 0.0015x - 0.0953, with R^2 = 0.9976, where y is the absorbance and x is the concentration.

The positive control comparators used were vitamin C, gallic acid, and quercetin. Vitamin C acts as a secondary antioxidant that can catch free radicals and prevent chain reactions from occurring. Vitamin C has free hydroxyl groups capable of being free radical scavengers (52). As a non-enzymatic antioxidant, vitamin C breaks free radicals chain reaction by trapping peroxyl and other reactive radicals (53). Based on the results of sample absorbance calculations, the amount of total antioxidant capacity contained in the positive control compound and the methanol extract of *T. gigas* eggs) is in Table 1.

Table 1: FRAP value results.

Sample	FRAP Value (μmol Fe^{2+}/g DW)
Methanol extract of *T. gigas* eggs	29.85
Gallic Acid	20899.47
Quercetin	11559.11
Vitamin C	8098.35

There is a difference in the change in the intensity of the color formed in each sample, indicating a difference in the composition of the antioxidants. The FRAP value of a sample is categorized based on its antioxidant activity as follows: very high (>500 μmol Fe(II)/g), high (100-500 μmol Fe(II)/g), moderate (10-100 μmol Fe(II)/ g), and low (<10 μmol Fe(II)/g) (54). The antioxidant activity of the methanol extract of *T. gigas* eggs has been reported with a FRAP value was 29.85 μmol Fe^{2+}/g DW, so this extract has moderate antioxidant activity. Meanwhile, the positive control comparators of gallic acid, quercetin, and vitamin C had very high antioxidant activity.

3.5. Antioxidant Activity with DPPH Method
The DPPH method is a method of testing Antioxidant activity utilizing 2,2-diphenyl-1-picrylhydrazyl as a free radical source (55). Measurement of antioxidant activity was carried out when purple DPPH free radicals were mixed with reducing compounds or antioxidants, the absorbance decreased and the formation of reduced DPPH-H color turned pale yellow (39).

There is a color change in DPPH (purple) because antioxidant compounds can donate their hydrogen to these free radicals (56). DPPH compounds by antioxidant compounds are converted into DPPH-H (57). The reaction between DPPH and antioxidant compounds can be shown in Figure 4 below.

The antioxidant activity measured by the DPPH method is expressed as an IC_{50} value. IC_{50} is the concentration of antioxidant compound required to reduce DPPH free radicals by up to 50% (58). Lower IC_{50} values indicate a higher ability of antioxidant activity (59). By plotting the concentration (μg/mL) of the test solution on the horizontal axis and the rate of percent reduction value on the vertical axis, the IC_{50} value was determined based on the linear regression equation.

The percentage of inhibition activity (IC_{50}) in the methanol extract of *T. gigas* eggs and the positive controls for gallic acid, quercetin, and vitamin C based on absorbance readings at a maximum wavelength of 515 nm are shown in Table 2.
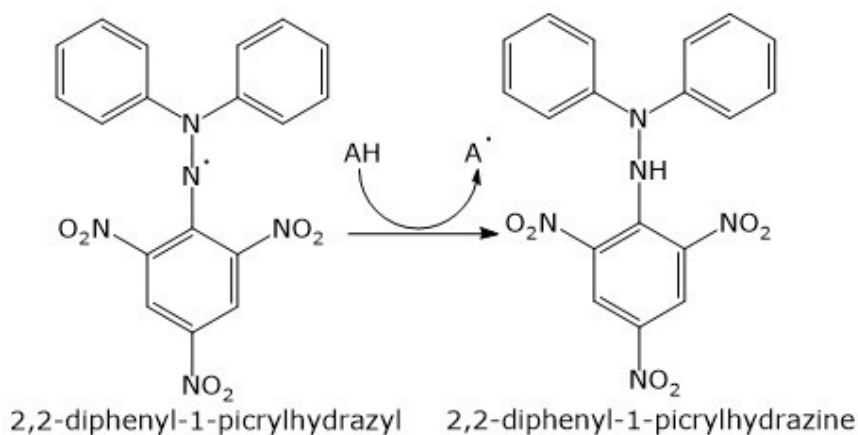
Figure 4: The reaction between DPPH and antioxidant compounds.

Table 2: IC_{50} value of the samples test.

Sample	R^2	IC_{50} (µg/mL)
Methanol extract of *T. gigas* eggs	0.9933	597.0397
Gallic acid	0.9939	0.8329
Quercetin	0.9934	1.5169
Vitamin C	0.9815	2.2095

The strength of the antioxidant activity utilizing the DPPH method can be categorized as follows: very strong (<50 ppm), strong (51-100 ppm), moderate (101-150 ppm), weak (151-200 ppm), and very weak (> 200 ppm) (60). Based on this category, the antioxidant activity of *T. gigas* eggs methanol extract of 597.0397 µg/mL was in the very weak category. In contrast, for the positive control comparison, gallic acid, quercetin, and vitamin C had very strong antioxidant activity.

All results of the determination of total phenolic content (TPC), total flavonoid content (TFC), and antioxidant activity using the FRAP and DPPH methods in the methanol extract of *T.gigas* eggs are shown in the following Table 3.

Table 3: The total phenolic, flavonoid content, and antioxidant activity of *T.gigas* eggs methanol extract.

Sample	TPC (mg GAE/g extract)	TFC (mg QE/g extract)	FRAP Value (µmol Fe^{2+}/g DW)	IC_{50} DPPH (µg/mL)
Methanol extract of *T. gigas* eggs	0.53506 ± 0.001335	0.52067 ± 0.000731	29.85	597.0397

4. CONCLUSION

The methanol extract of *T. gigas* eggs contained total phenolics and total flavonoids content of 0.53506 ± 0.0013 mg GAE/g extract and 0.52067 ± 0.000731 mg QE/g extract, respectively. Antioxidant activity using the FRAP method obtained a total antioxidant capacity of 29.85 µmol Fe^{2+}/g DW which is included in the moderate category, while antioxidant activity using the DPPH method obtained an IC_{50} value of 597.0397 ppm which indicates its activity as a very weak antioxidant. The results of research conducted by Suwandi et al. (2019) regarding the antioxidant activity of the ethanol extract of *T.gigas* in the very weak category with an IC_{50} of 330.47 ppm. It can be concluded that *T.gigas* eggs have very weak antioxidant activity.

5. CONFLICT OF INTEREST

The authors declare there is nothing conflict of interest

7. REFERENCES

1.   Barbouti A, Lagopati N, Veroutis D, Goulas V, Evangelou K, Kanavaros P, et al. Implication of dietary iron-chelating bioactive compounds in molecular mechanisms of oxidative stress-induced cell ageing. Antioxidants. 2021 Mar 1;10(3):1–21. Available from: <DOI>.

2.   Warraich U e. A, Hussain F, Kayani HUR. Aging - Oxidative stress, antioxidants and computational

Aisa ER et al. JOTCSA. 2023; 10(3):787-796.

RESEARCH ARTICLE

modeling. Heliyon. 2020 May 1;6(5):e04107. Available from: <DOI>.

3. Phaniendra A, Jestadi DB, Periyasamy L. Free Radicals: Properties, Sources, Targets, and Their Implication in Various Diseases. Indian Journal of Clinical Biochemistry. 2015 Jan;30(1):11–26. Available from: <DOI>.

4. Gulcin İ. Antioxidants and antioxidant methods: an updated overview. Arch Toxicol. 2020 Mar;94(3):651–715. Available from: <DOI>.

5. Khadim RM, Al-Fartusie FS. Antioxidant vitamins and their effect on immune system. In: Journal of Physics: Conference Series. 2021 Dec 17;1853:1-12. Available from: <DOI>.

6. Kebede M, Admassu S. Application of Antioxidants in Food Processing Industry: Options to Improve the Extraction Yields and Market Value of Natural Products. Advances in Food Technology and Nutritional Sciences. 2019 Jul 18;5(2):38–49. Available from: <DOI>.

7. Ofoedu CE, You L, Osuji CM, Iwouno JO, Kabuo NO, Ojukwu M, et al. Hydrogen Peroxide Effects on Natural-Sourced Polysacchrides: Free Radical Formation/Production, Degradation Process, and Reaction Mechanism—A Critical Synopsis. Foods. 2021 Mar 25;10(4):699. Available from: <DOI>.

8. Marino A, Battaglini M, Moles N, Ciofani G. Natural Antioxidant Compounds as Potential Pharmaceutical Tools against Neurodegenerative Diseases. ACS Omega. 2022 Jul 19;7(30):25974–90. Available from: <DOI>.

9. Liakopoulos V, Roumeliotis S, Bozikas A, Eleftheriadis T, Dounousi E. Antioxidant Supplementation in Renal Replacement Therapy Patients: Is There Evidence? Oxid Med Cell Longev. 2019 Jan 15;2019:9109473. Available from: <DOI>.

10. Simioni C, Zauli G, Martelli AM, Vitale M, Sacchetti G, Gonelli A, et al. Oxidative stress: role of physical exercise and antioxidant nutraceuticals in adulthood and aging. Oncotarget. 2018 Mar 30;9(24):17181–98. Available from: <DOI>.

11. Teleanu RI, Chircov C, Grumezescu AM, Volceanov A, Teleanu DM. Antioxidant therapies for neuroprotection-a review. J Clin Med. 2019 Oct 11;8(10):1659. Available from: <DOI>.

12. Sharma S, Cheng SF, Bhattacharya B, Chakkaravarthi S. Efficacy of free and encapsulated natural antioxidants in oxidative stability of edible oil: Special emphasis on nanoemulsion-based encapsulation. Trends Food Sci Technol. 2019 Sep 1;91:305–18. Available from: <DOI>

13. Meilana L, Wardiatno Y, Butet NA, Krisanti M. Morphological Character and Molecular Identification With CO1 Gene Marker of Horseshoe Crabs (*Tachypleus gigas*). Jurnal Ilmu dan Teknologi Kelautan Tropis. 2016;8(1):145–58. Available from: <DOI>.

14. Nuraisah R, Aini NK, Mashar A, Zairion Z, Hastuti YP, Funch P, et al. Food habit of horseshoe crabs, *Tahcypleus gigas* (Müller, 1785) and *Carcinoscorpius rotundicauda* (Latreille, 1802) di Balikpapan coastal waters, East Kalimantan. Journal of Natural Resources and Environmental Management. 2020 May 14;10(2):153–62. Available from: <DOI>.

15. Xu P, Bai H, Xie X, Wang C-C, Huang X, Wang X, et al. Tri-Spine Horseshoe Crab Aquaculture, Ranching and Stock Enhancement: Perspectives and Challenges. Front Mar Sci. 2021 Feb 9;8(608155):1-15. Available from: <DOI>.

16. Suwandi R, Nurjanah, Ula MZ, Pertiwi RM. Characteristics of chemical compounds of horseshoe crabs *Tachypleus gigas* in different body proportions. In: IOP Conference Series: Earth and Environmental Science. 2019; 404(2020):1-7. Available from: <DOI>.

17. Ciucure CT, Geană E-I. Phenolic compounds profile and biochemical properties of honeys in relationship to the honey floral sources. Phytochemical Analysis. 2019 Jul 1;30(4):481–92. Available from: <DOI>.

18. Ozcan T, Sahin S, Akpinar-Bayizit A, Yilmaz-Ersan L. Assessment of antioxidant capacity by method comparison and amino acid characterisation in buffalo milk kefir. Int J Dairy Technol. 2019 Feb 1;72(1):65–73. Available from: <DOI>

19. Ab Rahim N, Zakaria N, Habib Dzulkarnain SM, Mohd Azahar NMZ, Mahmood Ameen Abdulla. Antioxidant Assay of *Alstonia Angustifolia* Ethanolic Leaf Extract. Journal of Advanced Research in Fluid Mechanics and Thermal Sciences. 2020 Dec 1;42(1):80–6. Available from: <DOI>.

20. Soural I, Švestková P, Híc P, Balík J. Different values obtained by the FRAP method for the determination of slowly and rapidly reacting phenols. Acta Aliment. 2022 Feb 28;51(1):84–92. <DOI>.

21. Ngamkhae N, Monthakantirat O, Chulikhit Y, Boonyarat C, Maneenet J, Khamphukdee C, et al. Optimization of extraction method for Kleeb Bua Daeng formula and comparison between ultrasound-assisted and microwave-assisted extraction. J Appl Res Med Aromat Plants. 2022 Apr;28:100369. Available from: <DOI>.

22. Reza MS, Jashimuddin M, Ahmed J, Abeer M, Naznin NE, Jafrin S, et al. Pharmacological investigation of analgesic and antipyretic activities of methanol extract of the whole part of *Aeginetia indica*. J Ethnopharmacol. 2021 May 10;271:113915. Available from: <DOI>.

23. Islam S, Fahad FI, Sultana A, Sayem SAJ, Roy SB, Islam MN, et al. Evaluation of Antioxidant, Cytotoxic, Anti-Inflammatory, Antiarthritic, Thrombolytic, and Anthelmintic Activity of Methanol Extract of *Lepidagathis hyalina* Nees Root. Evidence-Based Complementary and Alternative Medicine. 2022 Feb 15;2022:2515260. Available from: <DOI>.

24. Rummun N, Somanah J, Ramsaha S, Bahorun T, Neergheen-Bhujun VS. Bioactivity of nonedible parts of *Punica granatum L.*: A potential source of functional ingredients. Int J Food Sci. 2013 Jul 8;2013:602312. Available from: <DOI>.

25. Xiao F, Xu T, Lu B, Liu R. Guidelines for antioxidant assays for food components. Food Front. 2020 Apr 9;1(1):60–9. <DOI>.

26. Koczka N, Stefanovits-Bányai É, Ombódi A. Total Polyphenol Content and Antioxidant Capacity of Rosehips of Some Rosa Species. Medicines. 2018 Aug 4;5(3):84. Available from: <DOI>.

27. Uju, Dewi NPSUK, Santoso J, Setyaningsih I, Hardingtyas SD, Yopi. Extraction of phycoerythrin from *Kappaphycus alvarezii* seaweed using ultrasonication. IOP Conf Ser Earth Environ Sci. 2020;414(1):012028. Available from: <DOI>.

28. Afshar Mehrabi F, Sharifi A, Ahvazi M. Effect of chitosan coating containing *Nepeta pogonosperma*

extract on shelf life of chicken fillets during chilled storage. Food Sci Nutr. 2021 Aug 1;9(8):4517–28. Available from: <DOI>.

29. Zhang S, Zhang L, Wang L, Zhao Y. Total phenols, flavonoids, and procyanidins levels and total antioxidant activity of different Korean pine (*Pinus koraiensis*) varieties. J For Res (Harbin). 2019 Oct 1;30(5):1743–54. Available from: <DOI>.

30. Cikita I, Hasibuan IH, Hasibuan R. Pemanfaatan Flavonoid Ekstrak Daun Katuk (*Sauropus androgynus (L) Merr*) sebagai Antioksidan pada Minyak Kelapa. Jurnal Teknik Kimia USU. 2016 Mar;5(1):45-51. Available from: <DOI>.

31. Rahimah S, Maryam FB, Ayu Limbong. The Toxicity Test of Ethanol Extract of Leaves *Averrhoa bilimbi L*. Using Brine Shrimp Lethality Test (BSLT). Journal of Pharmaceutical and Medicinal Sciences. 2019 Jul 10; 4(1):10-14. Available from:<DOI>.

32. Sridhar A, Ponnuchamy M, Kumar PS, Kapoor A, Vo D-VN, Prabhakar S. Techniques and modeling of polyphenol extraction from food: a review. Environ Chem Lett. 2021 Mar 17;19(4):3409–43. <DOI>.

33. Ahmed D, Khan MM, Saeed R. Comparative analysis of phenolics, flavonoids, and antioxidant and antibacterial potential of methanolic, hexanic and aqueous extracts from *Adiantum caudatum* leaves. Antioxidants. 2015 Jun 1;4(2):394–409. Available from: <DOI>.

34. Triyasmono L, Rahmanto B, Halwany W, Lestari F, Rizki MI, Anwar K. Daya Reduksi Ekstrak Etanol Biji *Aquilaria microcarpa, Aquilaria malaccensis, dan Aquilaria beccariana* terhadap Ion Ferri (Fe^{3+}) dengan Metode FRAP (Ferric Reducing Antioxidant Power). Jurnal Pharmascience. 2017 Feb;04(01):116–21. Available from: <DOI>.

35. Manongko PS, Sangi MS, Momuat LI. Uji Senyawa Fitokimia dan Aktivitas Antioksidan Tanaman Patah Tulang (*Euphorbia tirucalli L*.). Jurnal Mipa. 2020 Aug 1;9(2):64–9. <DOI>.

36. Munteanu IG, Apetrei C. Analytical Methods Used in Determining Antioxidant Activity: A Review. Int J Mol Sci. 2021 Mar 25;22(7):3380. Available from: <DOI>.

37. Hasim H, Arifin YY, Andrianto D, Faridah DN. Ekstrak Etanol Daun Belimbing Wuluh (*Averrhoa bilimbi*) sebagai Antioksidan dan Antiinflamasi. Jurnal Aplikasi Teknologi Pangan. 2019 Aug 12;8(3):86-93. Available from: <DOI>.

38. Prakoso AW, Abdillah S. Antioxidant and anti-AGEs (Advanced glycation end-product) activities of ethanolic extract of *Ficus carica* Linn from Indonesia. Journal of Pharmacognosy and Phytochemistry. 2018 Aug 18;7(5):598-601.

39. Echegaray N, Pateiro M, Munekata PES, Lorenzo JM, Chabani Z, Farag MA, et al. Measurement of antioxidant capacity of meat and meat products: Methods and applications. Molecules. 2021 Jul;26(13):3880. Available from: <DOI>.

40. Christodoulou MC, Orellana Palacios JC, Hesami G, Jafarzadeh S, Lorenzo JM, Domínguez R, et al. Spectrophotometric Methods for Measurement of Antioxidant Activity in Food and Pharmaceuticals. Antioxidants. 2022 Nov 8;11(11):2213. Available from: <DOI>.

41. Senet MRM, Raharja I, Darma IKT, Prastakarini KT, Dewi NMA, Parwata I. Penentuan kandungan total flavonoid dan total fenol dari akar kersen (*Mutingia calabura*) serta aktivitasnya sebagai antioksidan. Jurnal Kimia. 2018 Jan 15;12(1):13–8. Available from: <DOI>

42. Marjoni MR. Phenolics compounds, flavonoids, and antioxidant activity methanol extract of arum manis leaves (*Mangifera indica* L. Var. Arumanis). International Journal of Green Pharmacy (IJGP). 2018;12(03):51-6. Available from: <DOI>.

43. Panche AN, Diwan AD, Chandra SR. Flavonoids: an overview. J Nutr Sci. 2016 Dec 29;5:e47. Available from: <DOI>.

44. Khan J, Deb PK, Priya S, Medina KD, Devi R, Walode SG, et al. Dietary flavonoids: Cardioprotective potential with antioxidant effects and their pharmacokinetic, toxicological and therapeutic concerns. Molecules.2021 Jun 30;26(4021):1-24. Available from: <DOI>.

45. Guntarti A, Annisa J, Mughniy M, Rizqi F. Effect of Regional Variation on the Total Flavonoid Level of Ethanol Extract of Mangosteen (*Garcinia mangostana*) Peels. Jurnal Kedokteran dan Kesehatan Indonesia. 2017 Jun 17;8(2):136–43. Available from: <DOI>.

46. A. Makuasa DA, Ningsih P. The Analysis of Total Flavonoid Levels In Young Leaves and Old Soursop Leaves (*Annona muricata* L.) Using UV-Vis Sepctrofotometry Methods. Journal of Applied Science, Engineering, Technology, and Education. 2020 May 13;2(1):11–7. Available from: <DOI>

47. Wang J, Mao S, Liang M, Zhang W, Chen F, Huang K, et al. Preharvest Methyl Jasmonate Treatment Increased Glucosinolate Biosynthesis, Sulforaphane Accumulation, and Antioxidant Activity of Broccoli. Antioxidants. 2022 Jun 29;11(7):1298. <DOI>.

48. Wahyuningsih SPA, Winarni D, Pramudya M, Setianingsih N, Mwendolwa AA, Nindyasari F. Antioxidant Potential of Red Okra Pods (*Abelmoschus esculentus Moench*). Proceedings of KOBI 2nd International Confer. 2021;1:158–63. Available from: <URL>.

49. Yefrida, Ashikin N, Refilda. Validasi Metoda FRAP Modifikasi pada Penentuan Kandungan Antioksidan Total dalam Sampel Mangga dan Rambutan. Jurnal Riset Kimia. 2015 Mar 15;8(2):170–5. Available from: <DOI>.

50. Sukweenadhi J, Yunita O, Setiawan F, Kartini, Siagian MT, Danduru AP, et al. Antioxidant activity screening of seven Indonesian herbal extract. Biodiversitas. 2020 May 1;21(5):2062–7. Available from: <DOI>.

51. Hajiabdolah N, Parsa A, Anaraki-Ardakani H, Jalali-Jahromi H. Iron (III) reduction as a measure of "antioxidant power" using homo and copolymer of pyrrole and aniline electrosynthesized. Revue Roumaine de Chimie. 2020 Mar 1;65(3):247–54. Available from: <DOI>.

52. Kurniawati P, Maulida IR, Muhaimin. The determination of antioxidant activity of Brazil-cherry (*Eugenia uniflora* L.) leaves extract using FRAP method. In: AIP Conference Proceedings. American Institute of Physics Inc.; 2017. Available from: <DOI>

53. Samsul NR, Johannes E, Syahribulan S. Analysis of Antioxidant Content in Pollen and Honey Produced by Bees *Trigona spp* At Several Locations In South Sulawesi. International Journal of Applied Biology. 2022;6(1):26–37. Available from: <DOI>.

54.   Wong CC, Li H bin, Cheng KW, Chen F. A systematic survey of antioxidant activity of 30 Chinese medicinal plants using the ferric reducing antioxidant power assay. Food Chem. 2006 Aug 1;97(4):705–11. Available from: <DOI>.

55.   Anitha S, Krishnan S, Senthilkumar K, Sasirekha V. A comparative investigation on the scavenging of 2,2-diphenyl-1-picrylhydrazyl radical by the natural antioxidants (+) catechin and (-) epicatechin. J Mol Struct. 2021 Oct 15;1242:130805. Available from: <DOI>.

56.   Marjoni MR. Extraction of antioxidants from fruit peel of *Artocarpus altilis*. International Journal of Green Pharmacy (IJGP). 2018 Feb 22;12(1):284-9. Available from: <DOI>.

57.   Sriwatcharakul S. Evaluation of bioactivities of *Delonix regia* extracts from different regions of Thailand. Energy Procedia. 2018 Oct 1;153:258–62. Available from: <DOI>.

58.   Gupta M, Karmakar N, Sasmal S. In Vitro Antioxidant Activity of Aqueous and Alcoholic Extracts of Polyherbal Formulation Consisting of *Ficus glomerata Roxb*. and *Symplocos racemosa Roxb*. Stem Bark Assessed in Free Radical Scavenging Assays. International Journal of Pharmacognosy and Phytochemical Research. 2017 Feb 15;9(2):181-9. Available from: <DOI>.

59.   Belinda NS, Swaleh S, Mwonjoria KJ, Wilson MN. Antioxidant activity, total phenolic and flavonoid content of selected Kenyan medicinal plants, sea algae and medicinal wild mushrooms. African Journal of Pure and Applied Chemistry. 2019 Mar 31;13(3):43–8. Available from: <DOI>.

60.   Pratama MA, Pambudi MAS, Bachtiar E, Ismail MR, Mulyani Y, Arsad S, et al. Study of Phytochemistry and Potential of Endophyte Fungi Extract in *Avicennia marina* Roots as Antioxidants Inhibiting Early Aging. Journal of Aquaculture and Fish Health. 2022 Feb 1;11(1):37–46. Available from: <DOI>.

3- and 4-Arm Star Polymers (PEG$_3$ and PEG$_4$) via Metal-Free Azide-Alkyne Click Reaction

Ufuk Saim Gunay^{1*} iD

^{1}Istanbul Technical University, Department of Chemistry, İstanbul, 34469, Türkiye

Abstract: Star polymers are known for their different structural and functional properties. Depending on their structure, they may display a wide range of characteristics. Star polymers can be synthesized using either a core-first or arm-first strategy. Numerous synthetic approaches can be used in both cases. In this work, 3- and 4-arm star polymers were prepared via the metal-free azide-alkyne click reaction. Trifunctional and tetrafunctional propiolate (acetylenecarboxylate) ester-containing cores were prepared and then subjected to a metal-free azide-alkyne reaction with azide end-functionalized PEG (PEG-N$_3$) to yield A$_3$ and A$_4$-type star polymers, respectively. All the structures were characterized using ^{1}H and ^{13}C NMR spectroscopy and GPC.

1. INTRODUCTION

A particular category of macromolecules known as star polymers displays distinct structural and functional characteristics. Star polymers are within the category of branched polymers with a single branching point. When compared to linear chains, the branching of a polymer chain produces a considerably more compact structure, altering the polymer's crystallographic, mechanical, and viscoelastic behavior as well as its physical properties and processability. Star polymers are distinguished from their linear or branched polymer analogs by their unique architecture, which gives them outstanding versatility and performance in a variety of applications, including drug delivery, polymeric coatings, electronics, and material science (1).

Either a core-first or an arm-first approach can be used to make star polymers. The multifunctional cores, also known as core molecules or core initiators, are used in the core-first approach to start the formation of the polymer arms. This technique allows for the synthesis of targeted star polymers with controlled molecular weights, tunable arms,

and dispersites. The arm-first strategy, on the other hand, binds a multifunctional core to linear polymeric arms with reactive end groups. Both of the approaches used for the synthesis of star polymers can be carried out using a variety of techniques, such as anionic and cationic polymerization as well as controlled-living polymerization techniques like ATRP, NMP, and RAFT (1, 2).

The click chemistry term was introduced by Sharpless, which indicates key features for a reaction such as high yields, functional group tolerance, and stereoselectivity (3). Among these, the Cu(I)-catalyzed 1,3-cycloaddition reaction (or the Cu(I)-catalyzed azide-alkyne cycloaddition (CuAAC) reaction) gained tremendous attention among polymer chemists (4-6). CuAAC has been used to synthesize various polymer topologies for a wide range of applications and maintains its interest in the development of new materials (7).

Yet, the use of Cu salt has also raised toxicity concerns and pushed polymer chemists to develop new metal-free methods in order to synthesize functional well-defined materials for tailored

applications. One of the metal-free methods to overcome this toxicity issue is using activated alkynes, alkynes that contain electron-withdrawing groups (EWGs), in the azide-alkyne cycloaddition reaction (8). With this knowledge, we envisioned a strategy to synthesize 3- and 4-arm star polymers via the metal-free azide-alkyne click reaction. In this study, two core compounds with activated alkyne units, called propiolate esters, were designed to undergo the metal-free azide-alkyne click reaction with PEG-N_3 to yield A_3 and A_4-type star polymers (PEG$_3$ and PEG$_4$).

2. EXPERIMENTAL SECTION

2.1. Materials
1,1,1-Tris(hydroxymethyl)ethane (98%, Sigma-Aldrich), pentaerythritol (99%, Sigma-Aldrich), propiolic acid (prop-2-ynoic acid or acetylenecar-boxylic acid) (95%, Sigma-Aldrich), *p*-toluenesulfonic acid monohydrate (pTsOH, 98.5%, Aldrich), anhydrous sodium sulfate (Na_2SO_4, ≥99.0%, Aldrich) were used as received. *N,N*-dime-thylformamide (DMF, 99.8%, Sigma-Aldrich) and dichloromethane (DCM, 99.8%, Aldrich) were anhydrous, and used without further purification. Other reagents were all purchased from Sigma Aldrich and used as received. Mono azide end-functionalized poly(ethylene glycol) (PEG-N_3) was synthesized by using poly(ethylene glycol) methyl ether (average M_n ~2,000, Sigma-Aldrich) according to a published procedure (9).

2.2. Instrumentation
^{1}H NMR (500 MHz) and ^{13}C NMR (125 MHz) spectra were recorded using an Agilent VNMRS 500 instrument in CDCl$_3$. Gel permeation chromato-graphy (GPC) measurements were carried out with an Agilent Instrument (series 1100), using a refractive index detector, loaded with Waters Styragel columns (HR 5E, HR 4E, HR 3, HR 2, 4.6 mm internal diameter, 300 mm length, packed with 5 µm particles). The effective molecular weight ranges of the columns are 2,000−4,000,000; 50−100,000; 500−30,000; and 500−20,000 g/mol, respectively. THF was used as an eluent at a flow rate of 0.3 mL/min at 30 ºC, and 2,6-di-*tert*-butyl-4-methylphenol (BHT) was used as an internal standard. The number-average molecular weight (M_n), weight-average molecular weight (M_w), and polydispersity ($Đ$) of the polymers were calculated based on narrow linear polystyrene (PS) standards (Polymer Laboratories) ranging between 2300−3,050,000 g/mol.

2.3. Synthesis of 2-methyl-2-((propioloyloxy) methyl)propane-1,3-diyldipropiolate (1)
1,1,1-Tris(hydroxymethyl)ethane (1 g, 8.32 mmol), propiolic acid (3.5 mL, 49.93 mmol) and pTsOH (0.158 g, 0.83 mmol) were added to a round-bottomed flask and dissolved in 40 mL of benzene. The flask was attached to a Dean-Stark trap utilized with a condenser and placed in an oil bath at 105 °C for 24 h. After 24 h, benzene was removed by using a rotary evaporator, and the remaining yellow liquid was dissolved in DCM. The organic phase was

washed three times with 50 mL of distilled water. The washed solution was dried with Na_2SO_4 and evaporated to obtain the pure product. ^{1}H NMR (500 MHz, CDCl$_3$, δ, ppm): 4.17 (s, 6H, CCH_2), 2.95 (s, 3H, CCH), 1.11 (s, 4H, CCH_3).

2.4. Synthesis of 2,2-bis((propioloyloxy) meth-yl)propane-1,3-diyldipropiolate (2)
Pentaerythritol (1 g, 7.34 mmol), propiolic acid (4.11 mL, 58.76 mmol) and pTsOH (0.138 g, 0.73 mmol) were added to a round-bottomed flask and dissolved in 40 mL of benzene. The flask was attached to a Dean-Stark trap utilized with a condenser and placed in an oil bath at 105 °C for 24 h. After 24 h, benzene was removed by using a rotary evaporator, and the remaining yellow liquid was dissolved in DCM. The organic phase was washed three times with 50 mL of distilled water. The washed solution was dried with Na_2SO_4 and evaporated to obtain the pure product. ^{1}H NMR (500 MHz, CDCl$_3$, δ, ppm): 4.31 (s, 8H, CCH_2), 2.99 (s, 4H, CCH).

2.5. Synthesis of 3-Arm Star Polymer (PEG$_3$)
To a 25 mL Schlenk flask, compound **1** (100 mg, 0.36 mmol) and PEG-N_3 (2.39 g, 1.19 mmol) were added and dissolved in 5 mL of DMF. After 3 freeze-pump-thaw cycles, the flask was placed in an oil bath at 80 °C for 48 h. At the end of 48 h, the solution was precipitated into diethyl ether. The dissolution-precipitation cycle was repeated twice. The purified product was dried in a vacuum oven for 24 h. ^{1}H NMR (500 MHz, CDCl$_3$, δ, ppm): 8.43-8.11 (m, 3H, NCH), 4.61 (t, 6H, NCH_2), 3.91 (d, 6H, CCH_2), 4.47 (m, 6H, NCH$_2$CH_2), 3.91 (COOCH_2), 3.64 (m, 570H, OCH_2CH_2), 3.38 (s, 9H, OCH_3), 1.25 (s, 3H, CCH_3).

2.6. Synthesis of 4-Arm Star Polymer (PEG$_4$)
To a 25 mL Schlenk flask, compound **2** (100 mg, 0.29 mmol) and PEG-N_3 (2.55 g, 1.28 mmol) were added and dissolved in 5 mL of DMF. After 3 freeze-pump-thaw cycles, the flask was placed in an oil bath at 80 °C for 48 h. At the end of 48 h, the solution was precipitated into diethyl ether. The dissolution-precipitation cycle was repeated twice. The purified product was dried in a vacuum oven for 24 h. ^{1}H NMR (500 MHz, CDCl$_3$, δ, ppm): 8.47-8.12 (m, 4H, NCH), 4.67 (s, 8H, NCH_2), 4.61 (t, 8H, NCH$_2$CH_2), 3.92 (t, 8H, CCH_2), 3.64(m, 744H, OCH_2CH_2), 3.38 (s, 12H, OCH_3).

3. RESULTS AND DISCUSSION

3-Arm and 4-arm star polymers, PEG$_3$ and PEG$_4$, respectively, were successfully synthesized using multifunctional propiolate ester containing cores along with PEG-N_3 via the metal-free azide-alkyne click reaction.

Firstly, Scheme 1 depicts the preparation of multifunctional cores by an esterification reaction of 1,1,1-tris(hydroxymethyl)ethane and pentaerythritol in the presence of propiolic acid using a catalytic amount of pTsOH to yield core compounds 1 and 2, respectively.
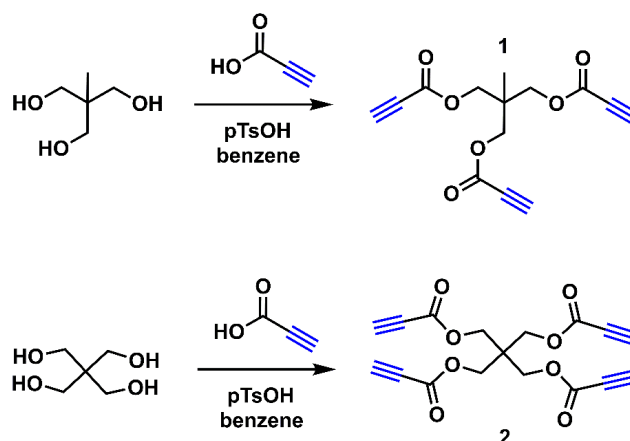
Scheme 1: Synthesis of the core compounds, **1** and **2**.
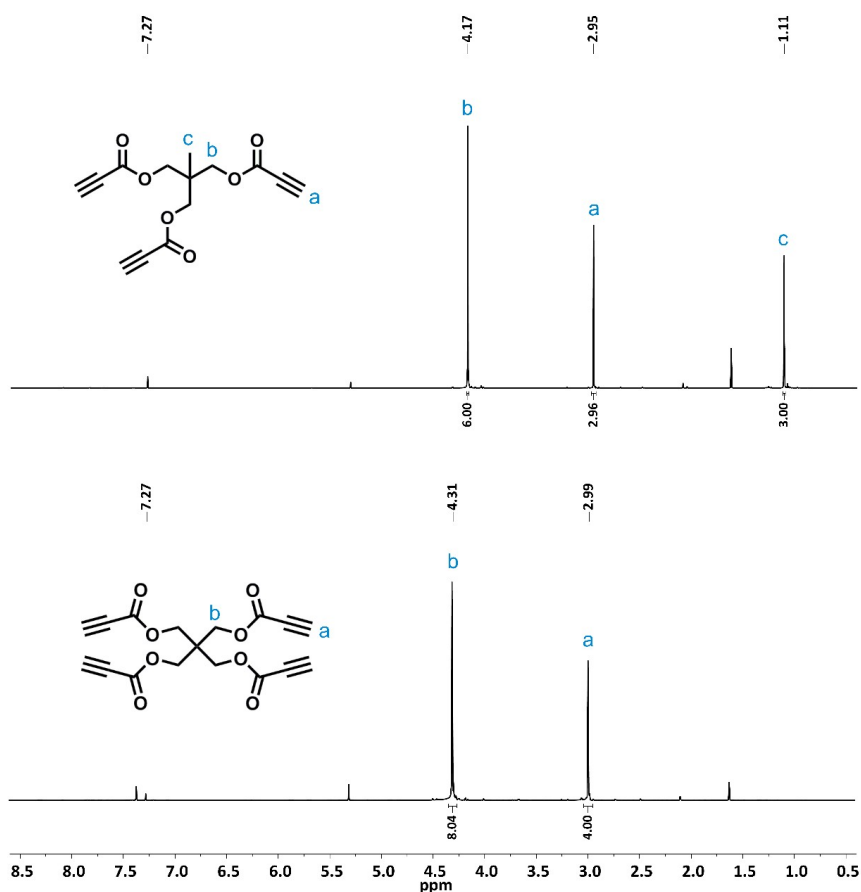
Figure 1: ^{1}H NMR spectra of **1** (top) and **2** (bottom) in CDCl$_3$ (500 MHz).

The structures of **1** and **2** were confirmed by using both ^{1}H and ^{13}C NMR. From the ^{1}H NMR spectra of **1** and **2** (Figure 1), methylene protons regarding the propiolate ester resonated at δ 4.17 ppm for **1** (top) and δ 4.35 ppm for **2** (bottom). In addition, the methine proton of the propiolate groups in **1** and **2** resonated at 2.95 and 2.99 ppm, respectively, showing that the alkyne group was still intact after the esterification. It should also be noted here that the integral values of the resulting structures were found to be consistent with the resulting structures. Also, from the ^{13}C NMR spectra (Figure 2), the peaks regarding propiolate units resonated at δ 75.80 ppm for **1** (top) and 76.41 ppm for **2** (bottom), further validating the structures.

3- and 4-arm star polymers were prepared by the metal-free azide-alkyne click reaction, as depicted in

799

Scheme 2. To this end, **1** and **2** were used as the core structures, and PEG-N$_3$ was used as the arms in the reactions to yield PEG$_3$ and PEG$_4$, respect-ively. Briefly, to perform the reactions, PEG-N$_3$ was intentionally used in excess with respect to **1** and **2** and carried out in DMF at 80 °C for 48 h. The resulting PEG$_3$ and PEG$_4$ star polymers were then characterized by ^{1}H and ^{13}C NMR spectroscopy and GPC.
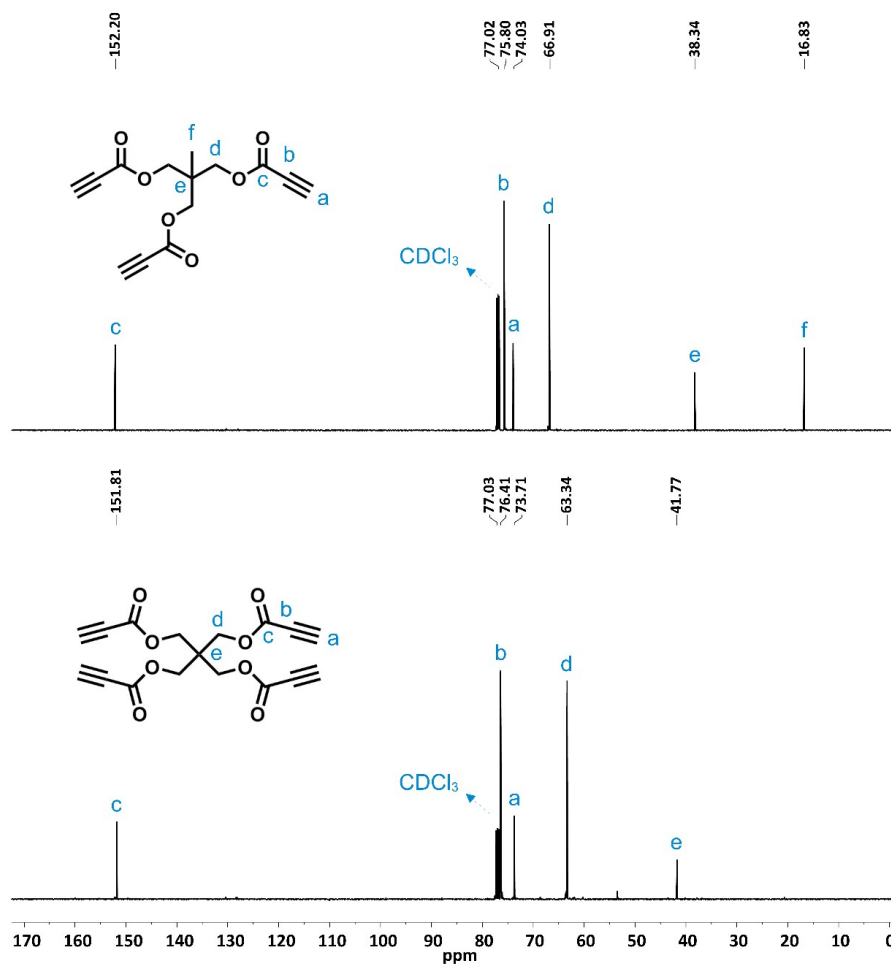
Figure 2: ^{13}C NMR spectra of **1** (top) and **2** (bottom) in CDCl$_3$ (125 MHz).
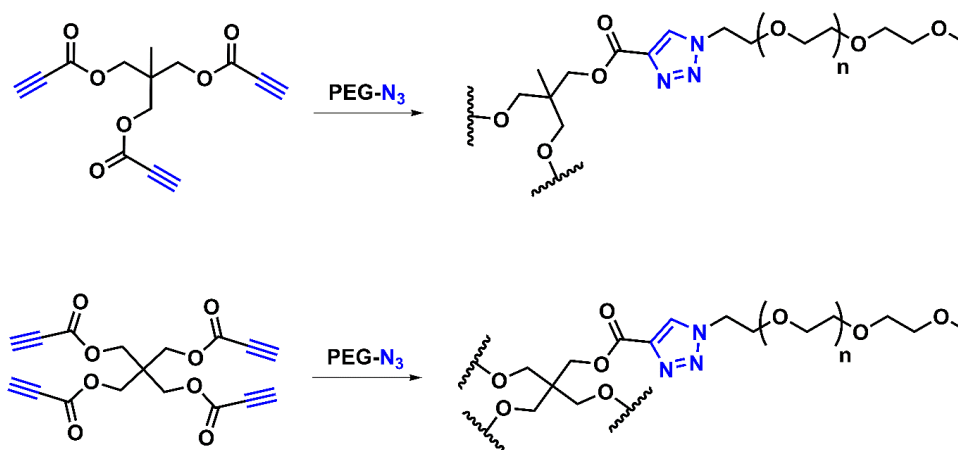
Scheme 2: Synthesis of the PEG$_3$ and PEG$_4$ star polymers (only one arm was shown for clarity).
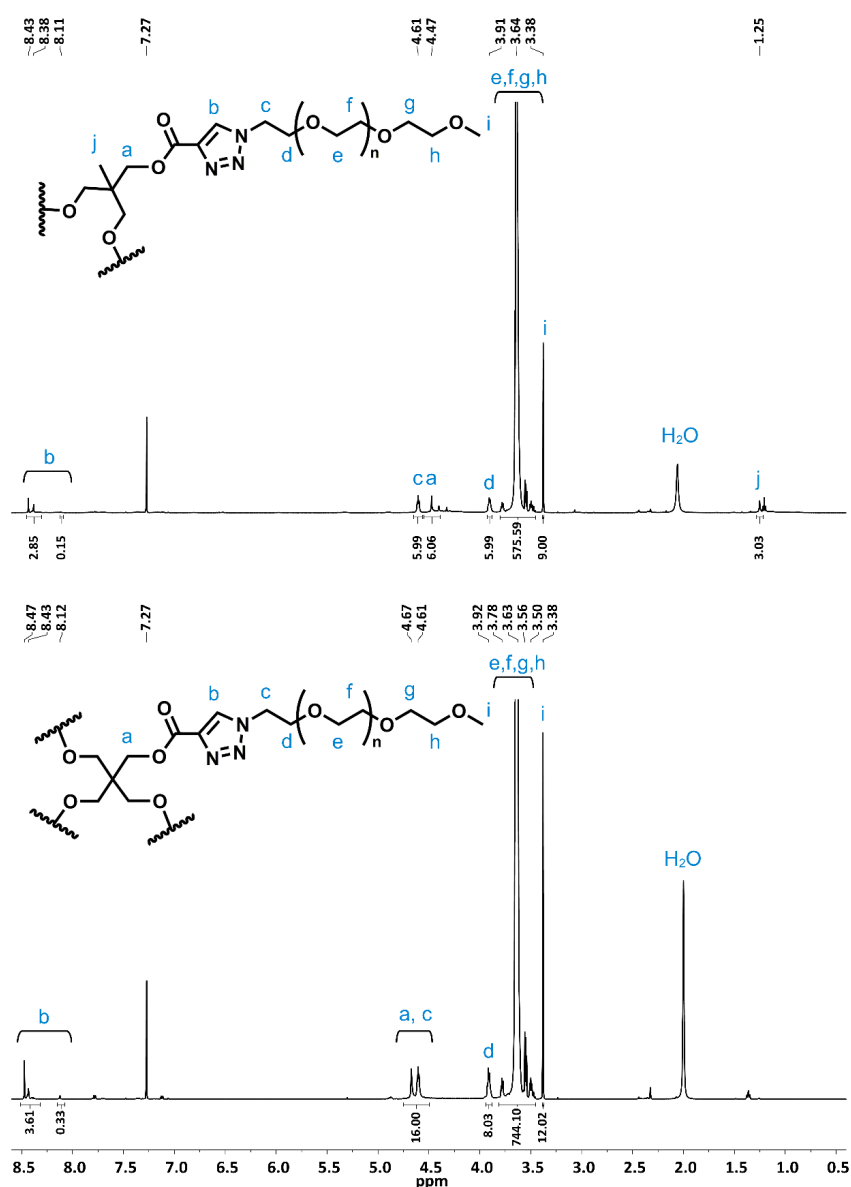
Figure 3: ^{1}H NMR spectra of PEG$_3$ (top) and PEG$_4$ (bottom) in CDCl$_3$ (500 MHz).

From the ^{1}H NMR spectra of the resulting structures (Figure 3), the ester methylene protons were found to shift to δ 4.47 for PEG3 (top) and 4.67 ppm for PEG4 (bottom) after the click reaction. Also, for both star polymers, the aromatic proton of the triazole unit resonated between δ 8.40 and 8.10 ppm, and the methylene group next to the triazole unit was found around δ 4.61 ppm, which clearly indicated a smooth reaction. In addition, it is important to notice that the integral values of the protons align with the star polymers that were obtained.

^{13}C NMR spectra of the star polymers (Figure 4) showed the successful synthesis of PEG$_3$ and PEG$_4$ star polymers as well. The disappearance of the alkyne carbons and the appearance of the aromatic carbons regarding the triazole unit resonated between δ 140 and 130 ppm, which was indicative of the star polymers.
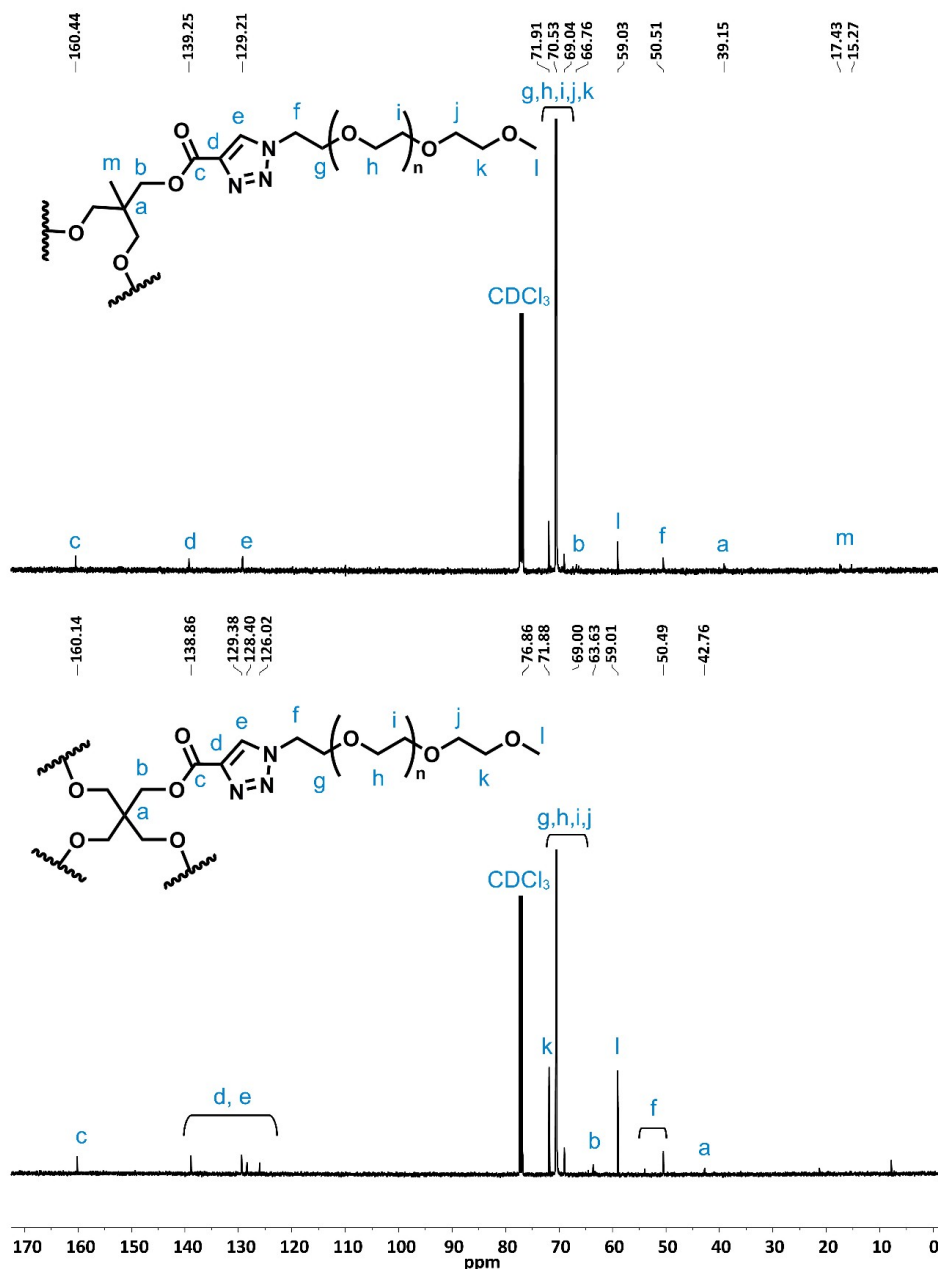
Figure 4: ^{13}C NMR spectra of PEG$_3$ (top) and PEG$_4$ (bottom) in CDCl$_3$ (125 MHz).

Finally, GPC traces of the star polymers showed a monomodal distribution with relatively narrow polydispersities. Also, as expected, PEG$_4$ was found to be in a relatively higher molecular weight region when compared to PEG$_3$, and both showed a shift to the higher molecular weight region when compared with PEG-N$_3$.

M_n = 11.45kDa
$Đ$ = 1.06

M_n = 8.88kDa
$Đ$ = 1.10

M_n = 2.58kDa
$Đ$ = 1.04

— A4
— A3
— PEG-N3

Retention Time (min)
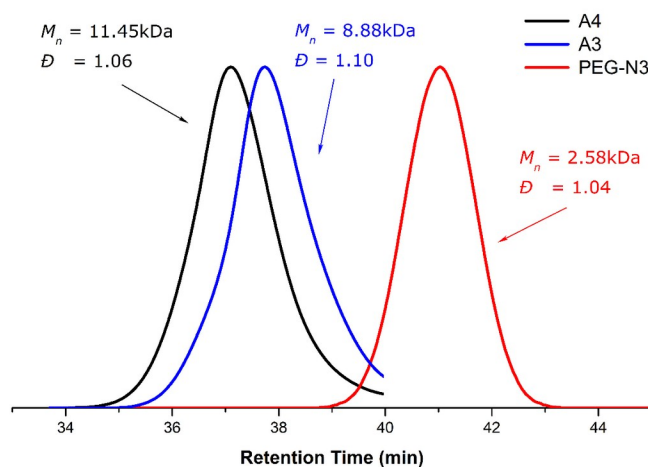
Figure 5: GPC curves (in THF) of PEG-N$_3$ (red), PEG$_3$ (blue) and PEG$_4$ (black).

4. CONCLUSION

The metal-free azide-alkyne click reaction was utilized in the synthesis of 3- and 4-arm star polymers using propiolate esters. Multifunctional cores were specifically designed to carry out a metal-free azide-alkyne cycloaddition reaction using PEG-N$_3$ as the arms. The reaction was conducted at 80 °C for 48 h to yield PEG$_3$ and PEG$_4$ star polymers. Both the cores and the star polymers were characterized by ^{1}H and ^{13}C NMR spectroscopy, indicating the success of the strategy. In addition, the resulting polymers were also analyzed by GPC, resulting in a monomodal distribution with relatively narrow dispersities, further showing the smooth transition. It is believed that the metal-free approach for the synthesis of well-defined star polymers with this proposed method can be a very efficient tool for synthesizing functional polymers for polymer chemists and can be extended to a wide range of applications.

5. CONFLICT OF INTEREST

No potential conflict of interest was reported by the author.

6. ACKNOWLEDGMENTS

7. REFERENCES

1. Ren JM, McKenzie TG, Fu Q, Wong EHH, Xu J, An Z, Shanmugam S, Davis TP, Boyer C, Qiao GG. Star Polymers. Chem Rev. 2016;116(12):6743–6836. Available from: <DOI>.

2. Dag A, Durmaz H, Hizal G, Tunca U. Preparation of 3-arm star polymers (A3) via Diels–Alder click reaction. J Polym Sci Part A: Polym Chem. 2008;46(1):302-313. Available from: <DOI>.

3. Kolb HC, Finn MG, Sharpless KB. Click Chemistry: Diverse Chemical Function from a Few Good Reactions. Angew Chem Int Ed. 2001;40(11):2004–2021. Available from: <DOI>.

4. Tornoe CW, Christensen C, Meldal M. Peptidotriazoles on Solid Phase: [1,2,3]-Triazoles by Regiospecific Copper(I)-Catalyzed 1,3-Dipolar Cycloadditions of Terminal Alkynes to Azides. J Org Chem. 2002;67(9):3057-3064. Available from: <DOI>.

5. Demko ZP, Sharpless KB. A Click Chemistry Approach to Tetrazoles by Huisgen 1,3-Dipolar Cycloaddition: Synthesis of 5-Sulfonyl Tetrazoles from Azides and Sulfonyl Cyanides. Angew Chem Int Ed. 2002;41(12):2110–2113. Available from: <DOI>.

6. Rostovtsev VV, Green G, Fokin VV, Sharpless KB. A Stepwise Huisgen Cycloaddition Process: Copper(I)-Catalyzed Regioselective "Ligation" of Azides and Terminal Alkynes. Angew Chem Int Ed. 2002;41(14):2596–2599. Available from: <DOI>.

7. Neumann S, Biewend M, Rana S, Binder WH. The CuAAC: Principles, Homogeneous and Heterogeneous Catalysts, and Novel Developments and Applications. Macromol Rapid Commun. 2020;41(1):1900359. Available from: <DOI>.

8. Cetin M, Esen C, Daglar O, Luleburgaz S, Hizal G, Durmaz H, Tunca U. 1, 3-Dipolar and Diels–Alder cycloaddition reactions on polyester backbones possessing internal electron-deficient alkyne moieties. Polym Chem. 2016;7(46):7094-7100. Available from: <DOI>.

9. Jia H, Li Q, Bayaguud A, She S, Huang Y, Chen K, Wei Y. Tosylation of alcohols: an effective strategy for the functional group transformation of organic derivatives of polyoxometalates. Scientific Reports. 2017;7:12523. Available from: <DOI>.

REVIEW ARTICLE

Ethnomedicinal Uses, Phytochemistry and Pharmacology of Few Species of Genus *Atalantia* (Rutaceae): A Review

Pournima A. Shelar [1,2*] 🆔, **Santosh Kumar Singh**[1]

[1] Suresh Gyan Vihar, School of Pharmacy, Jaipur, Rajasthan, 302017, India
[2] Arvind Gavali College of Pharmacy, Jaitapur, Satara, 415004, India

Abstract: Synthetic drugs show major side effects, as well as the fact that they have been discovered to be extremely harmful to human assistance, many synthetic medications claimed to be used for treatment are of the least interest today. Therefore, herbal medicines have acquired prominence in recent decades. This review's primary objective is to give a complete overview of three distinct species of the Genus *Atalantia* mainly *Atalantia monophylla* (Roxb) DC, *Atalantia racemaosa* Wight, *Atalantia wightii* Tanaka. The Genus *Atalantia* belongs to Rutaceae family and there are 22 accepted species of which three species are selected because these are available in Western Ghat region of Maharashtra, these species have ethnopharmacological significance and many of their facets are still unexplored. The *Atalantia* genus is utilized in conventional medicine to treat a diverse array of ailments like fever, rheumatic pains, cough, allergy, swelling, and as a blood purifier, etc. The current work is a comprehensive analysis of the published literature on phytochemical and pharmacological reports of the above species of *Atalantia* genus in an effort to deliver comprehensive information and suggest future research avenues. Out of these three species, *Atalantia monophylla* has received the most research attention but the remaining two species are not much explored. The aim of this review is to discuss the potential application of these three species as herbal medicine. The plant characteristics, ethnobotanical uses, phytochemistry, and pharmacological activities are summarized as a guide for phytochemical and pharmacological investigations.

1. INTRODUCTION

Phytochemicals are the bioactive compounds isolated from medicinal plants, also called plant-derived chemicals, reduce the risk of various chronic diseases. As most of the phytoconstituents have been identified until now but still numerous constituents need to be characterized. However, most of the affirmation suggests that the phytochemicals are more beneficial as compared to current therapy as phytoconstituents are potent in their action, and also, they are safe for use (1).

There are 22 accepted species in the *Atalantia* genus (Rutaceae), which are distributed in the Indian mainland, Andaman and Nicobar Island, Srilanka, Myanmar, Thailand, Peninsular Malaya, North and South Vietnam, Laos, Cambodia, south China, Sumatra, and Java (2). Three of these species are found in southern India such as

Atalantia monophylla (Roxb.) DC, *Atalantia racemosa* Wight, *Atalantia wightii* Tanaka. Atalantia genus species are generally found in the areas like forest edges, roadsides, around the sides of streams, and at the periphery of water bodies having sufficient sunlight (3).

The plants of this genus have large spins and are tiny to medium-sized trees or shrubs resembling citrus fruits in general aspects. The plants bear white fragrant flowers and small globose fruits having the appearance of tiny greenish-yellow limes or oranges. Citrus pulp vesicles are stalked, whereas sessile pulp vesicles are distinct. Leaves are unifoliate similar to citrus but shows differences like more prominent, numerous lateral veins and veinlets which form reticulations between lateral veins (3, 4).

Due to the increasing importance of this species, its utilization as traditional herbal medicine to treat a variety of illnesses has increased (5). *Atalantia monophylla* (Roxb.) DC is mostly found in evergreen South Indian forests that means at an altitude of 600m. Its common name is "wild lemon." *Atalantia racemosa* Wight is known as Bombay Atalantia. It is usually encountered at elevations between 150 and 1000 meters in peninsular Sri Lanka and India's evergreen regions. Nilgiri atalantia is a common name of *Atalantia wightii* and is indigenous to Western Ghats Shola forests with an altitude of 100 and 1700 meters (4).

2. METHODOLOGY

A systematic review of published research and peer-reviewed journals was conducted for this study. The electronic versions of the reviewed literature were obtained from PubMed, Science Direct, Scopus, Google Scholar, Springer Link, Taylor, and Francis, and Web of Science Core Collection. Using a search engine such as Google, an additional search was conducted to locate further reports, documents, and botanical databases up to January 2023. The literature reported in the last 10 years was taken into account for information. The keywords used while searching were Genus *Atalantia*, Phytochemistry, Pharmacology, and Traditional uses. The reports were scrutinized for relevance and included in the review.

3. RESULT AND DISCUSSION

These species are rich in phytochemicals which include several classes like alkaloids, steroids, flavonoids, tannins, terpenoids, saponins, coumarins, and phenolic compounds. These species contain triterpenes like friedelin, flavonoids like pyranoflavone, atalantaflavone, racemoflavone, and coumarins such as xanthyletin, xanthotoxin, luvangetin, racemosin, etc. These species mainly contain acridone alkaloids like cycloatalantaphylline-A, N-Methyl cyclo-atalantaphylline-A, N-Methylbuxifoliadine-E. It also contains caryophyllene, β- caryophyllene, caryophyllene oxide, D-limonene, decanal, β-phellandrene, eugenol, umbelliferone, rutarin, rutaretin, and furanocoumarins. The alkaloids possess several biological activities like inhibition of Epstein-Barr Virus, induction of human promyelocytic leukemia cell differentiation, and antiproliferative.

3.1. *Atalantia monophylla* Linn

Atalania monophylla contains essential oils in which methyl eugenol, elemicine, and sabinene are the major constituents. The root bark contains atalantin, stigmasterol, xanthyletin, sitosterol, tetratriterprnoid, and acridone alkaloids. The leaves contain friedelin and epifreidlanol.

The parts like leaves, roots, and fruits of this species are used medicinally. Traditional medicinal practitioners use leaves of *Atalantia monophylla* for treatment of glandular swelling, and rheumatoid arthritis. Decoction of leaves is used in skin problems and dysentery. Leaves and roots are used as blood purifiers. Oil from berries is used as a stimulant, anti-inflammatory, and in chronic rheumatism. The root is antiseptic, antispasmodic, and used in the treatment of snake bites. The leaf decoction is used in the treatment of cough, asthma, and bronchitis.

3.1.1. Ethnopharmacological activities of *Atalantia monophylla* Linn.
3.1.2. Chemical composition of *Atalantia monophylla* Linn

Atalantia monophylla root bark has been found to contain alkaloids and limonoids. Additionally, a terpenoid called atalatin was derived from acetone and is beneficial in treating rheumatism. Also other components like N-methylatalaphylline (IIb), N-methylbicycloatalaphylline IV, xanthyletin **(2)** were isolated. Atalaphylline **(1)** was recovered using pet. ether root extract (IIa) (22). Acridone alkaloids, cycloatalaphylline-A, N-methylcycloatalaphylline-A, and N-methyl buxifoliadine-E **(3)** were recovered from dichloromethane extract. It contains 8 types of known acridone alkaloids such as buxifoliadine-E, N-methylataphylline, atalaphylline, citrusinine–I **(4)**, N-methylatalaphyllin, yukocitrine, junosine, and two recognized coumarins as *Atalantia monophylla* auraptene and 7-O-geranyl scopoletin were isolated from acetone extract of roots, among them buxifoliadine –E shows potent anti-allergic property. 5-hydroxydictamnine and ß-sitosterol were extracted from *Atalantia monophylla* hardwood petroleum ether extract (23). Methanolic fruit extract contains hexadecanoic acid (**5**), brassicaterol (**6**), 3-bromocholest-5-ene, sinapinaldehyde, etc (52).

The bark from the roots of the *Atalantia monophylla* has been proven to include three different forms of limonoids, such as atalantolide, atalantin (24) and dehydroatalantin (25) (24). There seem to be further findings of two tetranotriterpenoids with biogenetically unique properties in root bark (25).

Table 1: Ethnopharmacological activities of *Atalantia monophylla* Linn.

Part Used	Treatment	Method of preparation	Treatment with dosage	References
Leaves, fruits	Rheumatic pain, Joint pain	Aqueous extract, Fruits juice	twice per day Externally applied	5
Leaves, fruits	Skin infection	Leaf extracts	Externally applied twice per day	13
Root	Cough with phlegm	Root decoction	One glass decoction per day for 2-3 days	14
Leaves	Rheumatic pains	Leaves decoction	One cup orally once a day	15
Leaves, Fruits	Chronic Rheumatic pain, Paralysis	Leaf oil	Apply twice per day for 8–10 days	16
Fruits	Stimulant	Mature fresh fruit juice	1 glass once a day for a week	17
Leaves	Fever in adult	Leaf powder	About 10 g daily in the morning for a week	18
Leaves	Swelling and Joint pain	Aqueous extract of leaves	Used externally for applying 2 times a day for 5–8 days	19
Leaves	Fever, cough	Aqueous extract of leaves	Daily early morning 2 times for 2–3 days	20
Leaves, Fruits, bark	Coetaneous complaints, itch, Antispasmodic, Stimulant	A decoction of the leaves	Applied externally in apply 2 times 5–8 days	21
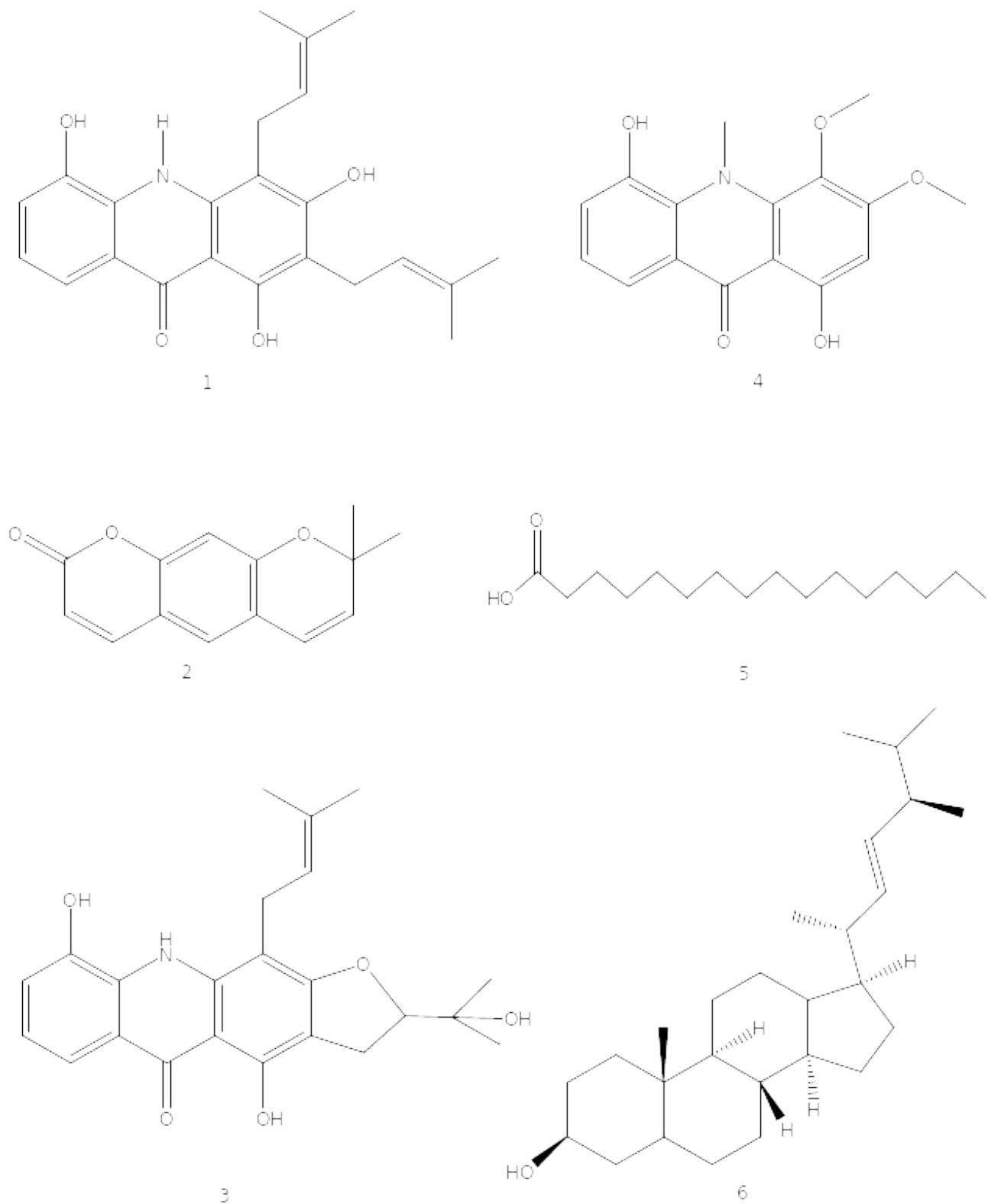
Figure 1: Structure of chemical moieties from *Atalantia monophylla* Linn.

3.1.3. Pharmacological activities of *Atalantia monophylla* Linn

Table 2: Pharmacological activities are summarized in the following table.

Activity	Part Used	Treatment	Method of preparation	References
Larvicidal and antifeedant activity against *Earias vittella* fab	Hexane, chloroform, as well as ethylacetate extracts from leaves	Bhendi fruit borer method	Hexane extract exhibited great larvicidal and antifeedant activity.	26
Synthesis of new alkaloid-5-Hydroxydictamnine	Petroleum ether from the heartwood	The extracts were then chromatographed by eluting them with increasing amounts of polar solvents	The eluents collected from Benzene: chloroform shows β-sitosterol while chloroform: ethyl-acetate shows 5-Hydroxy-dictamine	27
Ability to combat diabetes in alloxan-induced mice.	Methanolic bark extract	Levels of lipids, and sugar in serum were measured, including total cholesterol, triglycerides, HDL, LDL, and VLDL.	Methanolic bark extract showed potent antidiabetic activity	12
Investigation of ovicidal capacity	Leaves were extracted by using hexane, ethyl acetate, and chloroform.	Eggs of *Spodoptera litura* Fab treated with the extract.	The ovicidal property was shown by fractions of hexane extracts.	28
The pharmacognostic study, physicochemical evaluation, and phytochemical analysis	Leaves	Morphology, microscopy, leaf constants, total/acid insoluble/ water soluble ash, extractive values, preliminary screening, etc.	The standardization of the plant is aided by using this data.	29
Testing bioefficacy against *S. litura* Fab	Leaves were extracted by using chloroform, Hexane, and ethyl-acetate.	Anti-feedant, larvicidal, pupicidal activity	Potent action was shown by hexane extract. Out of 12 fractions of hexane extracts, 9th fraction showed maximum activity	30
Immuno-modulatory activity	Pet. ether, chloroform, and methanolic fractions of root ethanolic extracts	*E. coli*- induced abdominal sepsis, carbon clearance test, cell-mediated immune response, sheep erythrocyte agglutination test.	The methanolic fraction of ethanolic extract showed significant immunomodulatory activity.	31
Antioxidant, and antibacterial effect of oil	Essential oil from leaves	Hydro distillation and analysis of essential oil for its chemical composition, five different antioxidant methods, and antibacterial potential by using the broth dilution method	Oil had shown potent bioactive compounds and shows potent antibacterial and antioxidant activity.	32
In vitro antioxidant potential of ethanolic extracts from leaves	Ethanolic extract of leaves	DPPH-photometric assay, Iron-chelating Superoxide/, Hydroxyl/ Nitrous oxide radical scavenging, Ferric-ability power, and Total phenol/flavonoids/antioxidant content was used to assess antioxidant activity	Phenolic and flavonoids may act as the main antioxidants, and might serve as free radical inhibitors and thus possess antioxidant activity.	33

Anti-genotoxic and apoptotic activities	Oil from leaves	Prevention of DNA damage from H_2O_2 through anti-genotoxic characteristics (100 M) in 3T3-L1 cells and inhibition of growth of cervical cancer cells (HeLa)	The oil contains a promising natural compound that can be used to obstruct the growth of cancer cells and other dreadful ailments.	34
Toxic effects on *Sitophilus oryzae* and *Callosobruchus maculatus*	Oil from leaves	Toxicity was tested by methods like repellent activity, ovicidal activity, fecundity, and fumigation activity.	Oil showed good insecticidal, repellent, and ovicidal activity, also reduced Adult fecundity and emergence in test insects.	35
Free radical scavenging effect of stem and leaves	Pet ether, $CHcl_3$, CH_3H_6O, and CH_3OH extracts of stems and leaves.	DPPH, superoxide radical scavenging activity, phosphomolybdenum analysis, metal chelating, FRAP assay.	Methanolic extract of leaves and stems possess high antioxidant activity.	36
Phytochemical evaluation and anti-microbial activity	Ethanol, chloroform, and ethyl-acetate extract from leaves	3 Gram-positive and 6 Gram-negative bacteria were tested by the diffusion method	The potent activity was shown by the ethanolic extract.	37
A unique flavonoid in *A. monophylla* (Linn) DC leaves	Leaves are extracted by using hexane, ethyl acetate, and methanol.	*In vitro* cholinesterase and antioxidant activity.	Isolated atlantraflavon and eight known compounds show anticholinesterase and antioxidant activity.	38
Characterization and antibacterial evaluation of nanoparticles made from *A. monophylla* leaf extract.	Zinc oxide nanoparticles from methanolic leaf extract	Agar well diffusion method	Nanoparticles effectively destroyed bacteria and fungi more than plant extracts and conventional medications	39
Novel limonophyllines A–C that are poisonous to HepG2 and cholangiocarcinoma cell lines.	Hexane, ethyl acetate, and methanolic extracts of stem	All isolates were tested against KKU-M-156, Hep-G2, and cholangiocarcinoma cell lines.	All isolated compound structures were identified by spectroscopic analysis such as 1D and 2D NMR, IR, and mass spectrometry, and possess anticancer activity.	40
Anti-bacterial properties were studied on portions isolated from *C. guianensis* and *A. monophyla*	Ethanolic extract of leaves	Agar disc diffusion assay	Among the three fractions, fractions II and III showed the highest zone of inhibition	41
Extraction of Styrene from *Atalantia monophylla* seeds	Hexanes, ethyl acetate, and methanolic extracts from seeds	^1H NMR spectroscopy, ^{13}C NMR spectroscopy	Atalantrenes A-D (1-4), four novel dimeric styrenes, was extracted from ethyl acetate, and structures were identified from spectroscopic analysis.	42

3.2. *Atalantia racemosa* Wight & Arn

The leaves of *Atalantia racemosa* contains terpene, friedelin and four coumarins like xanthyletin, luvangetin, racemosin and xanthotoxin. It also contains umbelliferone, rutaretin, rutarin, pyranoflavones like atalantoflavone, racemoflavone.

Atalantia racemosa has been used traditionally in skin itching, snake bite, paralysis, and chronic

rheumatism. The leaves decoction is used treatment of bronchitis, asthma, and cough. The poultice of leaves is applied to wounds and the extract of leaves is used to treat eczema. The roots are used to combat dropsy.

3.2.1. Ethnopharmacological activities of *Atalantia racemosa* Wt

Table 3: Ethnopharmacological activities of *Atalantia racemosa* Wt

Part Used	Treatment	Method of preparation	References
Leaves	Asthma, cough, bronchitis	Decoction	7
Leaves	Bronchitis	Chewed	7
Leaves, roots	Blood purifier	Decoction	7
Root	Allergy	Root paste	44
Leaves	Repeating fever	Leaves in boiled water for bath	44
Leaves	Acidity	Leaf juice	45
Fruit oil	Paralysis and Chronic Rheumatism	Oil from fruit	46

3.2.2. Chemical composition of *Atalantia racemosa* Wt

Atalantia racemosa was found to contain pyranocoumarins, atalantin **(24),** xanthyletin **(2)**, atalaphyllinine **(26)**, friedelin **(27)**, recemosin **(15)**, umbelliferone **(16)**, rutaretin, triterpene friedelin, xanthotoxin, etc. It also contains pyranoflavones like atalantoflavone **(17)**, racemoflavone. Other compounds present are stigmasterol **(7)**, campesterol **(8)**, β-sitosterol (**9**), n-Hexadecanoic acid **(5)**, eicosanoic acid (**10**) (2). Methanolic extract of the fruit contains heptafluorobutyrate (**11**), N-octadecanoic acid methyl ester (**12**), tetradecanoic acid (**13**), campesterol (**8**), stigmast-4-en-3-one **(14),** etc (52).

7

8

9

10

11

12

13

14
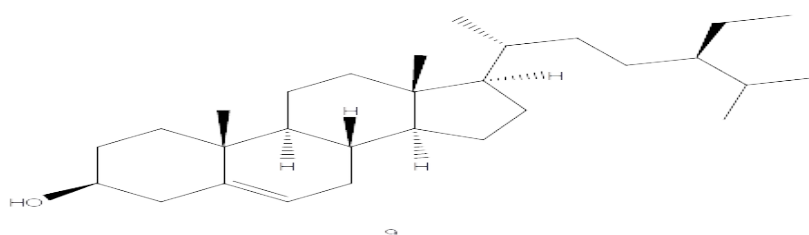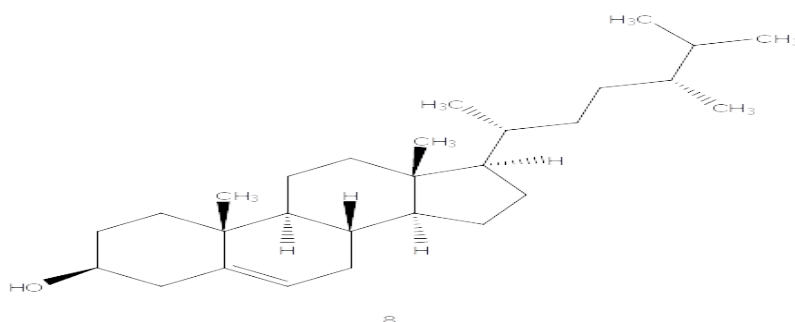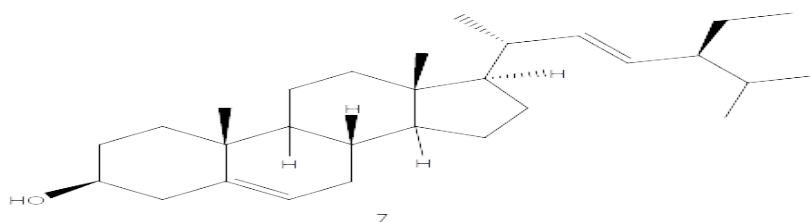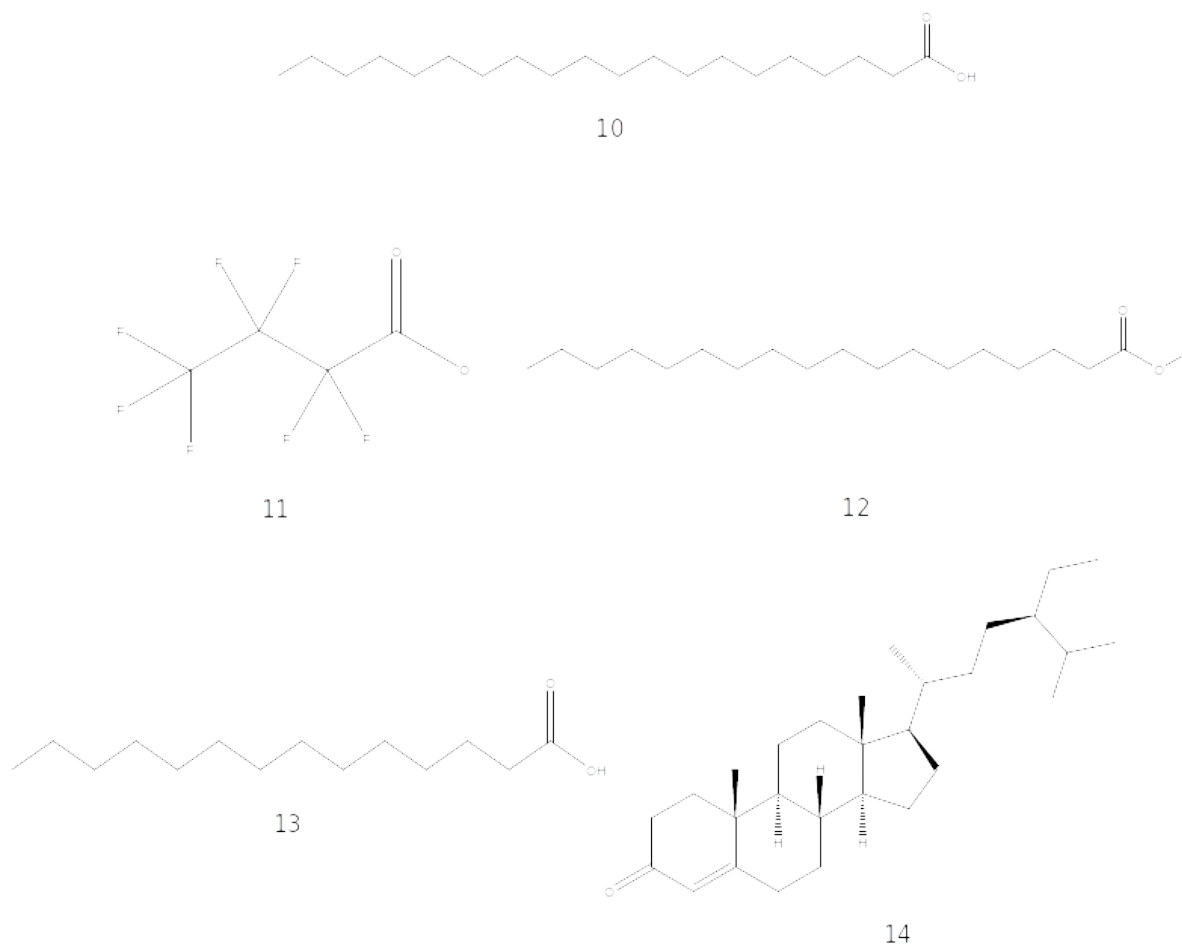
Figure 2: Structure of chemical moieties from *Atalantia racemosa* Wight & Arn

3.2.3. Pharmacological activities of *Atalantia racemosa* Wt

Table 4: Pharmacological activities are summarized in the following table.

Activity	Part Used	Treatment	Method of preparation	References
Comparison of three *Atalantia* species for volatile oil composition	Leaves	GC-MS analysis	*A monophylla* mostly contains ether compounds while Sesquiterpenes are the significant component in both *A racemosa* and *A wightii*.	47
Examination of three different species of *Atalantia* genus for their larvicidal efficacy and essential oil content.	Oil obtained from leaves by distillation	The larvicidal activity was tested on mosquito vectors like *A. aegypti*, *A. stephensi*, and *C. quinquefasciatus* and GC-MS analysis.	The larvicidal activity was shown by all species and GC-MS analysis shows that *A monophylla*, *A racemosa*, and *A wightii* contain 27, 65, and 64 compounds respectively.	48
Ability to combat diabetes in alloxan-induced mice.	Methanolic bark extract	Levels of lipid, sugar in serum were measured, including total cholesterol, triglycerides, HDL, LDL,	Methanolic bark extract showed potent antidiabetic activity	12

		and VLDL.		
Antioxidant potential and isolation of bio-active compounds by GCMS	Methanolic fruit extracts	DPPH and Phospho-molybdenum method	In DPPH method *Atalantia monophylla* and in the phospho-molybdenum method all extracts showed significant activity.	2
In vitro antioxidant and antimicrobial potential	Leaf extracts	*In vtrio* assays such as DPPH, hydroxy radical scavenging, ABTS radical cation, phosphomolybdenum, and ferric reducing power assay and well diffusion	Possess a powerful source of antioxidants that can combat a variety of free radicals.	49
Evaluated several medicinal plants for anti-microbial properties	Methanol, ethyl acetate, and acetone extracts from leaves	Agar well diffusion method	All extracts were found to be significant against bacteria and fungi.	50
Qualitative analysis of compounds of selected medicinal plants	Acetone, ethyl-acetate, methanol, and water extracts	Phytochemical screening	Quinoline derivatives, coumarins, phenolic compounds, flavonoids, tannins, catechins, alkaloids, terpenoids, and saponins are prevalent in these plants	51
Antioxidant, a-glucosidase, and Alpha-amylase inhibitory properties	Different crude solvent extracts of leaves.	Antioxidant activity by radical activities of scavenging of DPPH and ABTS methods. Antidiabetic by using the alpha-amylase and alpha-glucosidase inhibition assay.	Potent antioxidant, α-amylase, and α-glucosidase inhibitory activities were shown by *A. racemosa* extracts.	52
Investigation of the morpho-anatomical characteristics	Roots, stems, and leaves	Morphological and microscopical analysis	Characteristics clearly distinguish it from other adulterant taxa in terms of anatomy	43
Phytochemical analysis and anti-bacterial effect	Chloroform, acetone, methanol, and aqueous extracts	Agar plate well diffusion method against four different bacterial strains namely *Bacillus subtillis, Staphylococcus, Escherichia,* and *Klebsiella.*	Methanolic extract gave more positive results than the other extracts.	53
Anatomy of the leaf.	Leaf	Sectioning and Photomicrographs	Anatomical findings show the presence of different structures in the midrib and lamina portions, which help in the authentication of plant.	54

3.3. *Atalantia wightii* Tanaka

Atalantia wightii is used to shock the fish during fishing activity (57). Coumarins like umbelliferone and geranyl umbelliferon were revealed to exist in *Atalantia wightii.* Also, a few triterpenes like lupeol, lupenone, and epi-friedelinol were proven to occur in *Atalantia wightii* (58)*.*

3.3.1. Ethnopharmacological activities of *Atalantia wightii* Tanaka

Table 5: Ethnopharmacological activities of *Atalantia wightii* Tanaka

Part Used	Treatment	Method of preparation	References
Fruits	Rheumatism	Oil from fruit	2
Fruits	Edible purpose	Pickle	2

3.3.2. Chemical composition of *Atalantia wightii* Tanaka

Atalantia wightii was found to contain umbelliferone **(16),** atalantin **(24)**, dehydroatalantin **(25)**, hexadecenoic acid methyl ester **(5)**, heptadecoinoic acid methyl ester **(23)**, racemosin (**15**), umbelliferone (**16**), atlantoflavone (**17**), undecanoic acid methyl ester (**18**), etc (2). Methanolic extract of the fruit contains 1,1 dichloro-2-dodecanol (**19**), Methyl 10-undecenoate (**20**), heptadecanoic acid (**21**), Phthalic acid **(22)**, ditridecyl ester, stigmasterol (**7**), β-sitosterol **(9)**, etc (52).

24

26

25

27
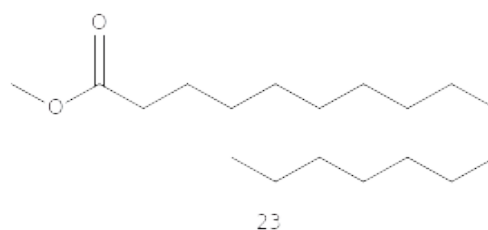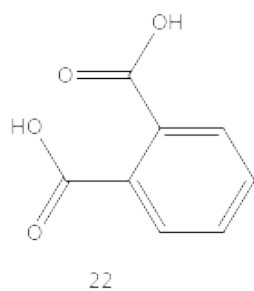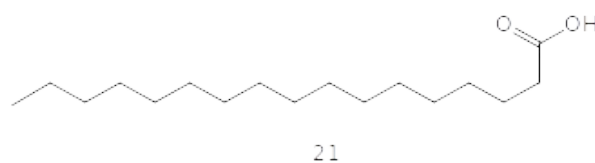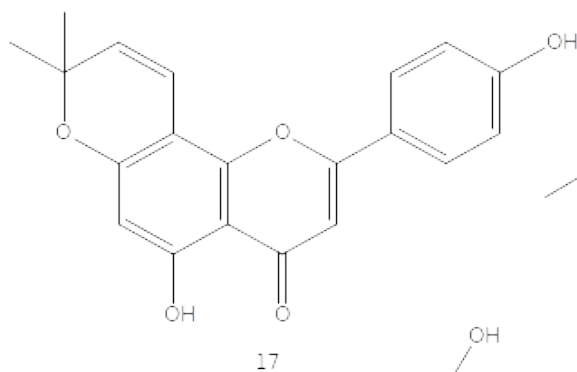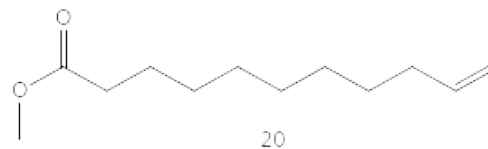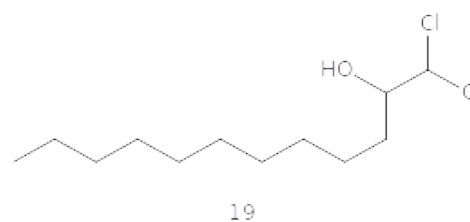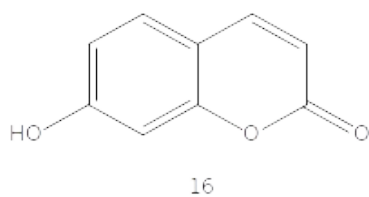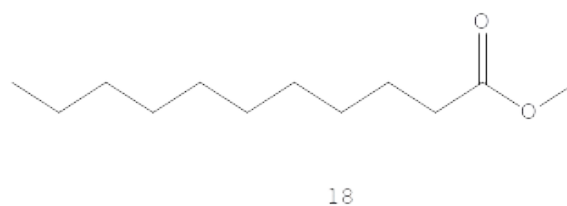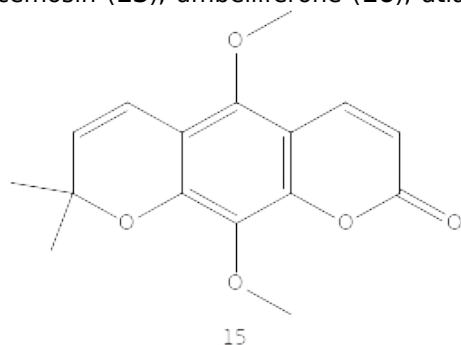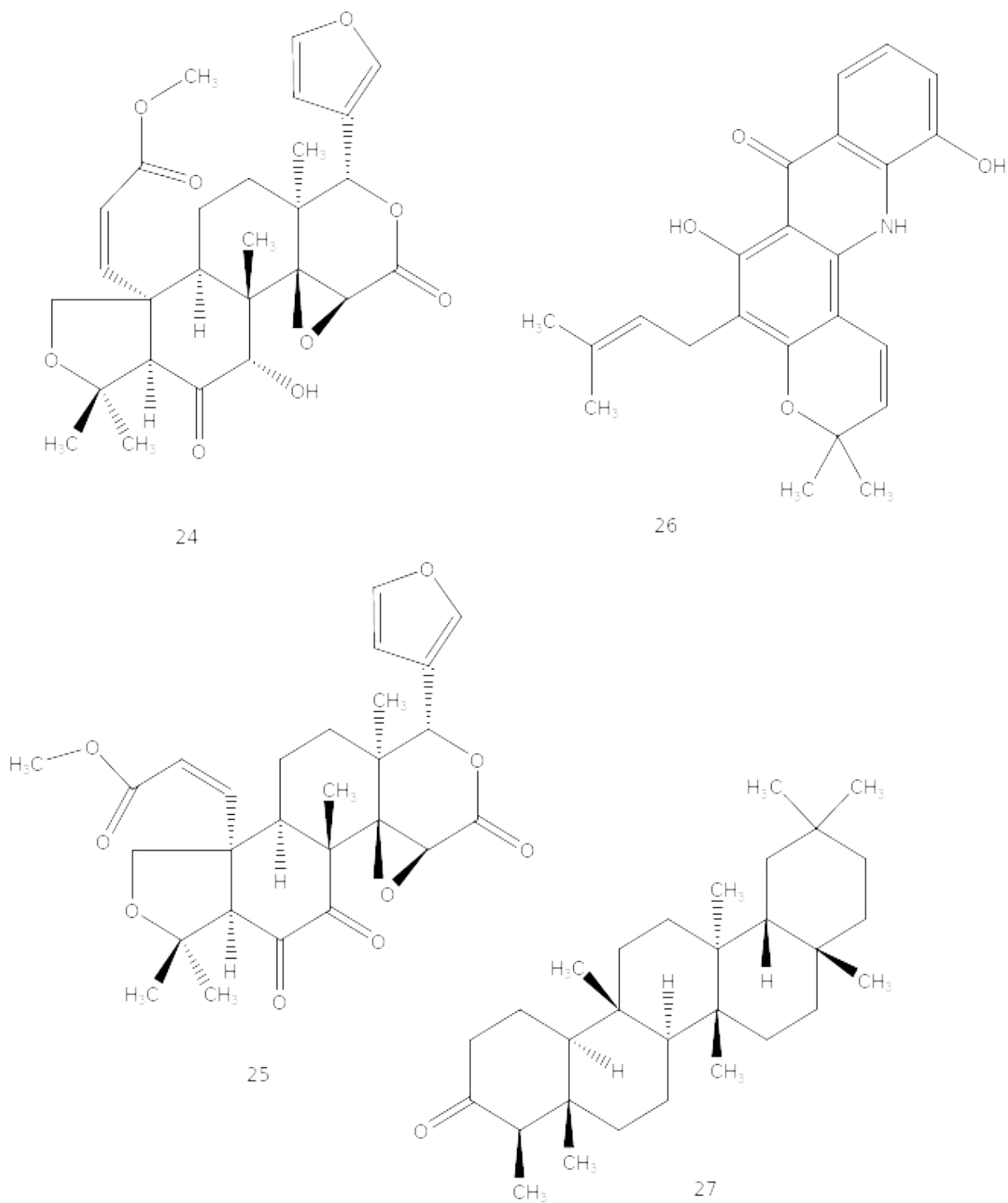
Figure 3: Structure of chemical moieties from *Atalantia wightii* Tanaka

3.3.3. Pharmacological activities of *Atalantia wightii* Tanaka

Table 6: Pharmacological activities are summarized in the following table.

Activity	Part Used	Treatment	Method of preparation	References
Investigation and comparison of the chemical nature of oils from three Atalantia species	Fresh leaves	GC-MS analysis	The percentage of oil was found to be 0.2% in *A. monophylla*, 0.17% in *A. racemosa*, and 0.31% in *A. wightii*	47
Phytochemical investigation.	Leaves extracted using water, chloroform, and ethanol	Phytochemical screening	Alkaloids, glycosides, amino acids, phenolic compounds, proteins, and tannins were present	59
Antioxidant potential of 3 different species of the Atalantia genus	Fruits methanolic extract	Phospho-molybdenum method	Free radical scavenging was shown by all extracts	2

4 CONCLUSION

Based on ethnopharmacological claims of the genus *Atalantia*, the current review discusses conventional uses, phytochemical moieties, and pharmacological activities. A detailed literature survey indicated that most of the varieties are utilized traditionally in various countries including India. Only a couple of varieties have undergone scientific evaluation to determine which phytochemical components may be responsible for a certain pharmacological activity. This review is an in-depth explanation of the traditional use, chemical composition, and therapeutic aspects of the genus *Atalantia* using *Atalantia monoplylla, Atalantia racemosa, and Atalantia wightii*. The species *Atalantia monophylla* has received the most research attention and is crucial to the manufacture of biodiesel. Although these two species have ethnomedical claims to be useful for the human ailment, there hasn't been much of an evaluation. Therefore, additional meticulously planned and in-depth clinical research that concentrates on mechanism-based *in vitro* and *in vivo* studies is needed to comprehend the underlying mechanisms connected to ethnopharmacological applications.

5 CONFLICT OF INTEREST

The authors declare no conflict of interest in this article.

7. REFERENCES

1. Nigussie G. A review on traditionally used medicinal plants for scabies therapy in Ethiopia. ADV TRADIT MED (ADTM). 2021 Jun; 21(2):199–208. Available from: <URL>

2. Swingle WT. "The Botany of Citrus and its Wild Relatives in the Citrus Industry," University of California Press, Berkely. 1967; 190-430.

3. Das AK, Swamy PS. Antioxidant activity and determination of bioactive compounds by GC-MS in methanolic fruit extract -a comparative analysis of three Atalantia species from south India. Journal of Applied Pharmaceutical Science. 2016; 6 (02): 130-134. Available from: <URL>

4. Khare CP. Indian Medicinal Plants; An Illustrated Dictionary. New York. Springer. 2007.

5. Ezekiel Amri, Daniel PK. Ethnomedicinal study of plants used in villages around Kimboza forest reserve in Morogoro, Tanzania. Journal of Ethnobiology and Ethnomedicine. 2012; 8 (1): 1-9. Available from: <URL>

6. Carl WC. Indian Atalantia, An ornamental tree for landscaping in southern florida. Process Florida State Horticulture Society. 1979; 92:215.

7. Pullaiah T. Encyclopaedia of World Medicinal Plants. Volume 1. Daya books publisher. New Delhi: Regency. 2006.

8. Parthasarathy N, Karthikeyan R. Plant biodiversity inventory and conservation of two

Shelar PA et al. JOTCSA. 2023; 10(3):805-820.

REVIEW ARTICLE

tropical dry evergreen forests on the Coromandel coast, south India. Biodiversity and conservation. 1997;6: 1063-1083. Available from: <URL>

9. Parthasarathy N, Selwyn M, Udaykumar M. 2008. Tropical dry evergreen forests of peninsular India; ecology and conservation significance. Tropical Conservation Science. 1(2): 89-110. Available from: <URL>

10. Venkateswaran R, Parthasarathy N. Tree population changes in a tropical dry evergreen forest of south India over a decade (1992–2002). Biodiversity and conservation. 2005;14: 1335-1344. Available from: <URL>

11. Panda H. Handbook on Medicinal Herbs with uses. India; Asia Pacific Business Press Inc. 2004.

12. Radhakrishnan M, Jindal A, Baldev G, Bhatt S, Pandey D. Evaluation of anti-diabetic activity of methanolic extract from the bark of *Atalantia monophylla* (Linn.) in alloxan-induced diabetic mice. International Journal of Green Pharmacy. 2012; 6(2):133-137. Available from: <URL>

13. Shrikant G, Rajeshwari N, Vasudeva R, Ganeshaiah KN. Floristic composition of the kaan forests of Sagar Taluk: sacred landscape in the central Western Ghats, Karnataka, India. Journal of Biodiversity Data. 2015; 11(3): 1626. Available from: <URL>

14. Bharath Kumar R, Suryanarayana B. Ethnomedicinal recipes for respiratory and bronchial diseases from Tribals of Sriharikota Island, Andhra Pradesh. Journal of Ethnobotanical Leaflet. 2008;12: 896–911. Available from: <URL>

15. Kottaimuthu P, Vasudevan N. Traditional Medicine among the Palliyars of Palani Hills, Western Ghats, India. International Journal of Arts, Science and Humanities. 2021; 8 (1): 10-14. Available from: <URL>

16. Lalbiakngheti T, Lucy L. Commonly used medicinal plants in N. Mualcheng, Mizoram, India. Science Vision. 2020; 20(4): 156–161. Available from: <URL>

17. Rekka R, Nirubama K, Suganya B, Rubavathigokila M. Sacred groves–an ancient tradition of nature conservation of sthalavrikshas in coimbatore, Tamil nadu, India. Kongunadu Research Journal. 2021; 8(2):1-7. Available from: <URL>

18. David RS, Alina AM, Jesse TJ, Beena R, Agnes H. Herbs as Antidote for Snake Bite Treatment-Traditional Practices and Its Future Prospects- A Review. Journal of Natural Remedies. 2022; 22(3): 269-290. Available from: <URL>

19. Rajkumar P, Natranjan S, Bhasha M, Ismailkhan A. Floristic and medicinal plant survey at Karaivetti bird sanctuary, Tamil Nadu, India, Spatula DD. 2015; 5 (1):27–34. Available from: <URL>

20. Prabakaran RT, Senthil T, Rao M. Role of non-timber forest products in the livelihood of Malayali tribe of Chitteri hills of southern eastern Ghats, Tamil Nadu India. Journal of Applied Pharmaceutical Science. 2013; 3 (5): 56–60. Available from: <URL>

21. Senthil Kumar R, Moorthy K, Raja V, Punitha T. Antimicrobial efficacy and phytochemical analysis of *Indigofera Trita* Linn. African Journal of Traditional, Complementary and Alternative Medicine. 2013; 10 (3): 518–525. Available from: <URL>

22. Rastogi R, Mehrotra B. Compendium of Indian Medicinal Plants, Central Drug Research Institute; Publications & Information Directorate, New Delhi. 1990; (2): 1970–1979.

23. Maurya DK, Nandkumar N, Paul T. Anticancer property of gallic acid in A-549, a human lung adenocarcinoma cell line, and possible mechanisms. Journal of Clinical Biochemistry and

Nutrition. 2011; 48 (1): 85–90. Available from: <URL>

24. Dreyer DL, Bennett RD, Basa SC. Limonoids from *Atalantia monophylla* isolation and structure. Tetrahedron. 1976; 32: 2367–2373. Available from: <URL>

25. Yogeshwari C, Kumudha P. Ethnobotany of Sholaga tribes of Kathri hills, Chennampatti Range, Western Ghats, India. Research Journal of Pharmacognosy and Phytochemistry. 2018: 10 (2): 179-182. Available from: <URL>

26. Chellaiah M, Kathirvelu B, Selvadurai K, Savarimuthu I. Bioefficacy of *Atalantia monophylla* (l.) correa. against *Earias vittella* fab. Journal of Central European Agriculture. 2010; 11: 27-30. Available from: <URL>

27. Sanath Kumar, Krupadanam D, Akshay Kumar K. A new alkaloid 5-Hydroxydictamnine from *Atalantia monophylla*. Natural Product Research. 2010; 24(16), 1514–1517. Available from: <URL>

28. Kathirvelu B, Chellaih M, Gnanaprakasam A, Selvadurai K, Savarimuthu I. Ovicidal activity of *Atalantia monophylla* (L) Correa against *Spodoptera litura* Fab. (Lepidoptera: Noctuidae). Asian pacific journal of tropical biomedicine. 2012; 2(12): 987-991. Available from: <URL>

29. Pandian P. Pharmacognostic, physicochemical and phytochemical investigation of *Atalantia monophylla* (l.) Correa leaves. Rapports De Pharmacie. 2015; 1 (3): 152-160.

30. Kathirvelu B, Chellaih M, Savarimuthu I. Bio Efficacy of *Atalantia monophylla* (L) Correa (Rutaceae) against *Spodoptera litura Fabricius* (Lepidoptera: Noctuidae). Entomology, Ornithology & Herpetology: Current research. 2015; 4(2): 1-5. Available from: <URL>

31. Patil VR, Thakare V, Joshi V. Immunomodulatory Activity of *Atalantia monophylla* DC. Roots. Pharmacognosy Journal. 2015; 7(1): 37-41. Available from: <URL>

32. Thirugnanasampandan R, Gunasekar R, Gogulramnath M. Antioxidant and antibacterial activity evaluation, Chemical composition analysis of essential oil of *Atalantia monophylla* Correa. Pharmacognosy Research. 2015; 7(1): S52-S56. Available from: <URL>

33. Pandian P, Selvamuthukumar S. Evaluation of in vitro antioxidant activity of ethanolic extracts from *Atalantia monophylla* leaves. Journal of Pharmaceutical Sciences & Research. 2016; 8(12): 1378-1383.

34. Thirugnanasampandan R, Gunasekar R, Gogulramnath M. Antigenotoxic and apoptotic activities of essential oil of *Atalantia monophylla* Correa. Indian Journal of Pharmacology. 2016; 48(6): 720-724. Available from: <URL>

35. Nattudurai G, Kathirvelu B, Pulraj M, Islam V. Toxic effect of *Atalantia monophylla* essential oil on *Callosobruchus maculatus* and *Sitophilus oryzae*. Environmental Science and Pollution Research. 2016; 24(2):1619-1629. Available from: <URL>

36. Sujatha S, Seker T, Pavithra S. Free-radical scavenging activity of stem and leaf of *Atalantia monophylla* (L.) Corr. Serr. International Journal of Herbal Medicine. 2017; 5(4): 47-53. Available from: <URL>

37. Premalatha S, Karthi A. Phytochemical screening and antimicrobial activity of leaf of *Atalantia monophylla* (l.) Corr (Rutaceae). International Journal of Pharmacy and Biological Sciences. 2017; 7(4):179-184. Available from: <URL>

38. Posri P, Suthiwong J, Takomthong P, Wongsa C. A new flavonoid from the leaves of *Atalantia monophylla* (L.) DC. Natural Product Research. 2018; 33(8): 1115-1121. Available from: <URL>

39. Subramaniyan V. Mahadevan S, Arulmozhi P, Subramanian S. Green synthesis of zinc oxide nanoparticles using *Atalantia monophylla* leaf extracts: Characterization and antimicrobial analysis. Materials Science in Semiconductor Processing. 2018; 82; 39-45. Available from: <URL>

40 Aonnicha Sombatsri. 2018. New limonophyllines A-C from the stem of *Atalantia monophylla* and cytotoxicity against cholangiocarcinoma and HepG2 cell lines. Archives of Pharmacal Research. 41(4):431-437. Available from: <URL>

41. Premalatha S, Ramar G. Anti-bacterial properties of fractions isolated from Couroupita guianensis and Atalantia monophylla. The Pharma Innovation Journal. 2019; 8(1): 542-547. Available from: <URL>

42. Thurdpong S, Yutthapong T, Suphantip P, Veerapol K, Sarawut T. Isolated styrenes from the Seeds of *Atalantia monophylla*. Journal of Natural Product. 2019; 82(8): 2246–2251. Available from: <URL>

43. Naga Padmavathi V, Chetty KM. Morpho-Anatomical studies of *Atalantia racemosa* Wight ex Hook., an important medicinal plant of Chittoor Dt. of Andhra Pradesh, India. International Journal of Bio-Pharma Research. 2019; 8(2): 2491-2499. Available from: <URL>

44. Harsha VH, Hebbar SS, Shripathi V. Ethnomedicobotany of Uttara Kannada District in Karnataka, India—plants in treatment of skin diseases. Journal of Ethnopharmacology. 2003; 84(1): 37-40. Available from: <URL>

45. Devi Prasad AG, Shyma TB, Raghavendra MP. Plants used by the tribes for the treatment of digestive system disorders in Wayanad district, Kerala. Journal of Applied Pharmaceutical Science. 2013; 3(8):171-175. Available from: <URL>

46. Sathiyaraj R, Sarvalingam A, Arulbalachandran, Rama KR. Diversity of Ethnomedicinal Plants in Bodamalai Hills Eastern Ghats, Namakkal District, Tamil Nadu. Journal of Plant Sciences. 2015; 3(2): 77-84. Available from: <URL>

47. Das AK, Swamy PS. Comparison of the volatile oil composition of three *Atalantia* species. Journal of Environmental Biology. 2013; 34: 569-571. Available from: <URL>

48. Das AK, Suresh Kumar J, Swamy PS. Larvicidal activity and leaf essential oil composition of three species of genus Atalantia from south India. International Journal of Mosquito Research. 2015; 2(3): 25-29. Available from: <URL>

49. Arumugam P, Saraswathi K. Mahakashmi B, Rajesh V. 2017. Invitro evaluation of the antioxidant and antimicrobial potential of leaves of *Atalantia racemosa* Wight ex Hook. International Journal of Pharma Research and Health Sciences. 5 (6): 2031-37. Available from: <URL>

50. Kokkaiah I, Sethupandian G, Palanichamy M. Antimicrobial activity of selected indian folk medicinal plants: *Myristica fatua*, *Alstonia boonei*, *Helictere sisora*, *Vitex altissima*, and *Atalantia racemosa*. Asian Journal of Pharmaceutical and Clinical Research. 2017; 10 (2): 277-280. Available from: <URL>

51. Kokkaiah I, Vadivel S. Qualitative phytochemical constituents assay of diverse solvent extracts of chosen medicinal plants. International Journal of Green and Herbal Chemistry. 2018; 7(4): 741-748. Available from: <URL>

52. Adhav Rahul, Deokule S. Evaluation of antioxidant, α-glucosidase and α-amylase inhibitory activities of *Atalantia racemosa* and *Senna uniflora* leaves. Asian Journal of Pharmaceutical and Clinical Research. 2018; 11(5): 254-258. Available from: <URL>

53. Parthipan G, Shanthi K. Phytochemical studies and antibacterial activities on *Atlantia racemosa* Wight & Arn. International Journal of Green and Herbal Chemistry. 2019; 8(4): 446-451. Available from: <URL>

54. Parthipan G, Shanthi K. Leaf anatomical studies of *Atalantia racemosa* wight Ex Hook, an important medicinal plant of Tiruvannamalai, Tamilnadu, India. International journal of current research. 2020; 12 (2): 10303-10308. Available from: <URL>

55. Ganer R, Kamble MA. Evaluation of Analgesic and In-vitro Anti-Inflammatory Potential of Fruit Flesh Extract of *Terminalia catappa* Linn. Research Journal of Pharmacognosy and Phytochemistry. 2017; 9(4): 228-230. Available from: <URL>

56. Matthew KM. The Flora of Palni Hills, The Rapinat herbarium, St. Joseph's College, Tiruchirappalli, 1999; 178-191.

57. Ayyanar M. Traditional Herbal Medicines for Primary Healthcare among Indigenous People in Tamil Nadu, India. Journal of Homeopathy & Ayurvedic Medicine. 2013; 2(5): 1-7. Available from: <URL>

58. Govindchari TR. Chemical and Biological Investigations on Indian Medicinal Plants. Indian New Natural Products and Plant Drugs with Pharmacological, Biological or Therapeutical Activity. 1976; 212-226. Available from: <URL>

59. Sethuraman MG, Ramesh V, Gopan R, Anil J, George V. Chemical Composition of the Leaf, Stem and Root Oils of *Pleiospermium alatum*. Journal of Essential Oil Research. 2011; 23(6):1-4. Available from: <URL>

Önal A et al. JOTCSA. 2023; 10(3): 821–828.

RESEARCH ARTICLE

Eco–friendly dyeing of fabric and wool yarn samples with *Morus nigra* leaf extracts

Adem ÖNAL [1*] (iD) **, Oğuz ÖZBEK** [2] (iD) **,**
Pakize DÜZGÜN [1] (iD) **, Sama NACHED** [1] (iD)

[1] Tokat Gaziosmanpaşa University, Faculty of Science and Letters, Department of Chemistry, Tokat, 60100, Turkiye

[2] Science and Technology, Application and Research Center, Zonguldak Bülent Ecevit University, 67600, Zonguldak, Turkey

Abstract: *Morus nigra* L. is a biologically important plant. In addition to the biological importance of the extracts obtained from its various parts, it is used as a material in various fields. In this work, dyeing properties of the cotton fabrics and the wool yarns with *Morus nigra* L. leaf extracts were investigated. In dyeing studies using *Morus nigra* L. leaf extracts, yellow tones were obtained in dyeing cotton fabrics, and green and yellow tones were obtained in dyeing wool yarns. Washing, rubbing and light fastness of dyed textile products were examined. According to the results, cotton fabrics showed better dyeing potential than wool yarns. As a result, *Morus nigra* L. leaf can be used as a natural dyeing agent in the dyeing of textile products.

1. INTRODUCTION

The use of synthetic dyes in the textile industry is increasing day by day and poses a great concern for the environment. Since most of the synthetic dyes are produced from toxic chemicals, they have negative effects on human health and the eco-system. Harmful effects such as mutagenicity or toxicity arising from the production and application of synthetic dyes direct the studies in the field of textiles to eco-friendly natural dyes (1). It is thought that natural dyes are safer for the environment than synthetic dyes and produce less harmful waste during the dyeing process. However, the lower affinity of natural dyes for textile products is considered a disadvantage (2). The simple extraction processes used for the production of natural dyes make it more advantageous and greener than synthetic dyes, which are produced in multiple steps and where many synthetic processes are involved (3).

Extracts obtained from various parts of plants have an important place in material chemistry in addition to their strong biological properties. The natural dyes used especially in the dyeing of textile products are obtained from plant extracts, and are a very important alternatives to synthetic dyes due to their properties such as being biodegradable, non-allergenic and non-toxic (4, 5). In addition, natural

dyes prepared by using parts of plants such as leaves and fruits can be considered environmentally friendly and economical.

Mulberry trees can live in different climatic conditions, such as tropical, subtropical and moderate, throughout the world and show a wide distribution from sea level to heights exceeding 4000 meters (6). Various morphological parts of mulberry such as leaves, fruits, roots and stems have been used for different purposes (7). *Morus nigra* L. (Moraceae), known as ''black mulberry'' or "wild mulberry" belongs to the genus Morus and used as an expectorant, antiseptic, sedative, diuretic, laxative antioxidant, and anthelmintic (8, 9). It has important effects due to the presence of flavonoids, tannins, coumarins, triterpenoids and steroids in its composition (10). The studies in the literature have shown that *Morus nigra* L. has anti-oxidant, anti-bacterial, cytotoxic, anti-inflammatory and anti-cancer properties (11–15). It has also been reported that it can be used for dyeing textile products (16).

The aim of this study is to investigate the usability of *Morus nigra* L. leaves for dyeing textile products. The findings obtained in the study showed that black *Morus nigra* L. leaves can be used successfully in the dyeing of textile products (wool yarn and cotton fabric). The studies show that there is plenty of isoquercitrin in *Morus nigra* L. leaves (9, 17). The complex between the mordants used and isoquercitrin (Figure 1) shows the property of dyestuff.

2. EXPERIMENTAL

2.1. Materials
Morus nigra L. leaves were collected in July from Tokat, Turkey. Iron(II) sulfate heptahydrate ($FeSO_4.7H_2O$), copper(II) sulfate pentahydrate ($CuSO_4.5H_2O$) and aluminum potassium sulfate dodecahydrate ($AlK(SO_4)_2.12H_2O$) were used as mordant and were obtained from Merck. The color properties of the dyed textile products were evaluated by Spectrophotometer (Premier Colorscan SS 6200A). Light, washing and rubbing fastnesses of dyed textile products were determined using Atlas weather–ometer, Launder–ometer and 255 model crock–meter, respectively. Spectral reflectance measurements were determined with a Konica Minolta 3600d spectrophotometer.
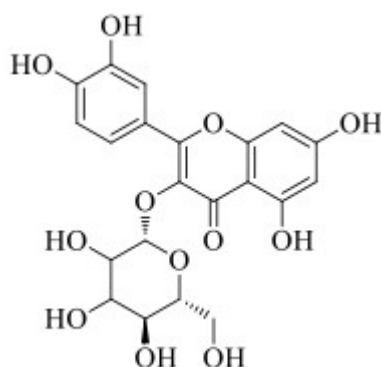
Figure 1: The structure of isoquercitrin.

2.2. Method
Dried *Morus nigra* L. leaves (100 g) were refluxed on soxhlet tool using distilled water. This process was continued until the mixture became colorless. We applied pre–, meta– and post– mordanting methods as in our other studies (18–20).

2.2.1. Pre–mordanting method
The textile products (5 g) were heated in 0.1 M mordant solution (100 mL) for 1 h at 90 °C. The textile products (5 g) was heated in 0.1 M mordant solution (100 mL) for 1 h at 90 °C. After cooling the samples, it was rinsed with distilled water and put into dye–bath solution (100 mL). It was heated at 90 °C for 1 h. The dyed samples were rinsed with distilled water and dried.

2.2.2. Meta–mordanting method
0.1 M mordant solution, dyestuff solution and textiles were placed in the flask and heated at 90 °C for 1 h. After cooling, it was rinsed and dried.

2.2.3. Post–mordanting method
The textile products (5 g) were first treated with the dyestuff solution at 90°C for 1h. After cooling, it was rinsed with distilled water and put into 0.1 M mordant solution (100 mL) and heated for 1h at 90°C. The dyed samples were rinsed with distilled water and dried.
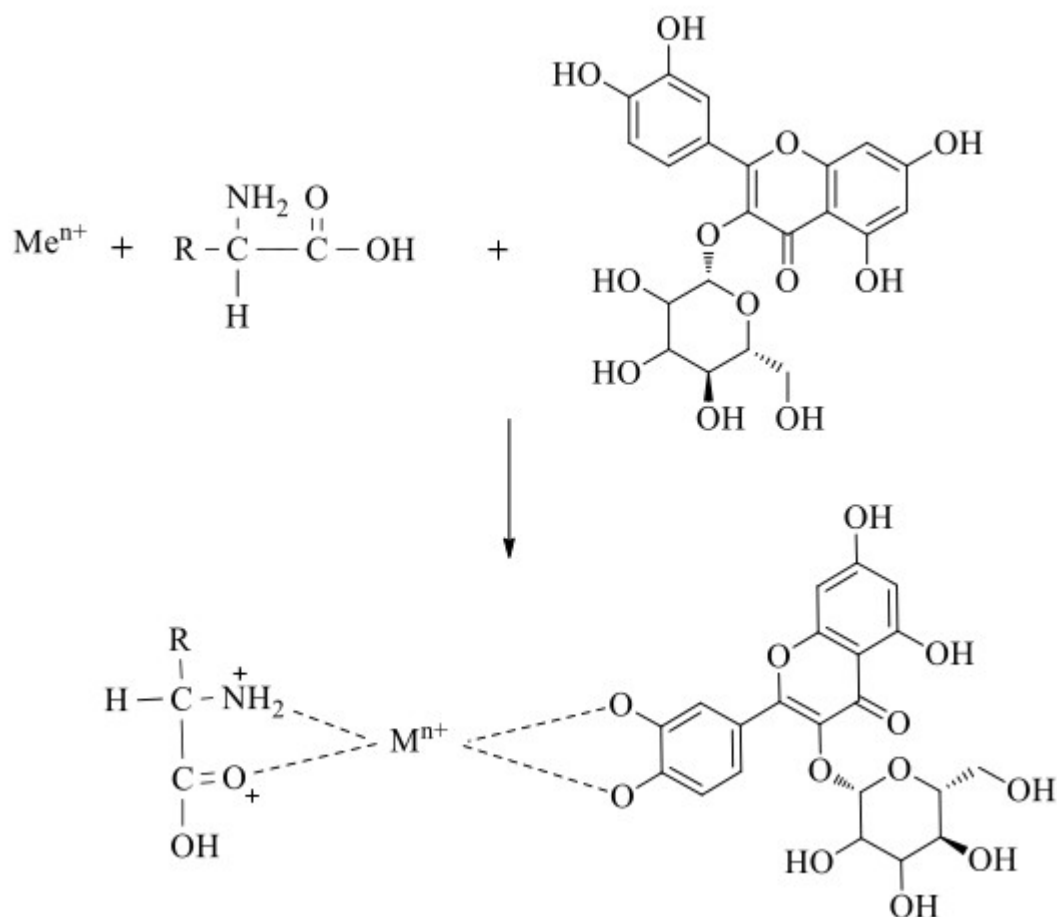
Figure 2: The proposed mechanism of dyestuff with mordants for wool yarn.

3. RESULTS AND DISCUSSION

The studies have shown that *Morus nigra* L. leave extracts contain abundant isoquercitrin (4, 14). Therefore, we suggested the mechanisms in Figures 3 and 4, considering that the dyestuff in *Morus nigra* L. leaves is isoquercitrin. Mordants are the most important agents used in natural dyes to exhibit dye properties. It provides better adhesion of the dyestuff to the fiber or fabric and increases the fastness of dyed fibers. In this study, we used $CuSO_4$, $FeSO_4$ and $AlK(SO_4)_2$ metal salts as mordants.

Free amino ($–NH_2$) and carboxyl groups ($–COOH$) of wool yarn are suitable for complexing with metals. At the same time, the oxochrome groups of the dyestuff can form stable complexes with metals (Figure 2). The metal complex formed between the $–CH_2O$ groups in the cellulose molecules in the cotton fabric and the $–OH$ groups in the dyestuff isoquercitrin shows dyestuff properties (Figure 3).

Fastness values and color codes for dyed textile products are given in Table 1. Color codes were determined using the Pantone Color Guide (Table 1). From green to beige for $CuSO_4$, gray tones for $FeSO_4$, and yellow tones for $AlK(SO_4)_2$ were obtained. Fastness values are listed as $CuSO_4$, $FeSO_4$ and $AlK(SO_4)_2$. When Table 1 is examined, the fastness values for all three mordants are higher in the post mordanting method. Green tones were obtained for $CuSO_4$, brown tones for $FeSO_4$, and yellow tones for $AlK(SO_4)_2$. If we are to rank, the fastness results can be listed as $CuSO_4$, $AlK(SO_4)_2$ and $FeSO_4$. As a dyeing method, we can list it as post–, meta– and pre–mordanting method.
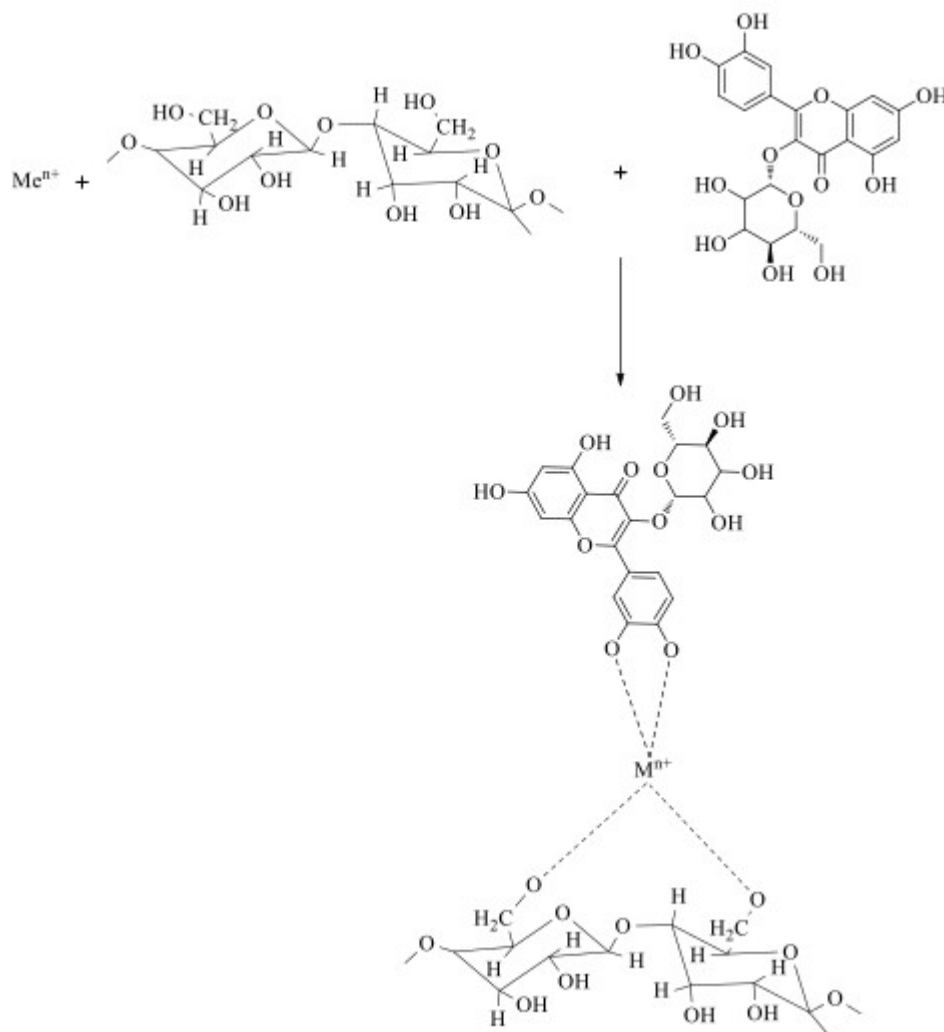
Figure 3: The proposed mechanism of dyestuff with mordants for cotton fabric.

CIE-Lab is a three-dimensional color space with $L*$, $a*$, $b*$ parameters. The $L*$ axis takes values between 0 and 100, and 0 represents black and 100 represents white. $a*$ is the red/green axis and negative values of $a*$ represent green and positive values represent redness. $b*$ is the yellow/blue axis and negative values of $b*$ indicate blueness and positive values indicate yellowness (21, 22). The K/S values of the dyed samples were determined using the Kubelka-Munk equation (23). K/S and $L*$, $a*$, $b*$ values of textile products are given in Table 2. In this study, while yellow and pale yellow color tones are obtained in cotton fabrics, green, dark green and yellow color tones are obtained in woolen yarns. All dyed textile samples with *Morus nigra* L. leaves extracts are as in Figure 4.

Table 1: Wash, rubbing and light fastness values of dyed samples.

	Method	Mordant	Wash fastness[a]	Rubbing fastness[b] (wet–dry)	Light fastness[c]	Color code (Pantone)
Cotton	Pre–	FeSO$_4$	3	4/5–4/5	3/4	481 CS
	Meta–		4	4/5–5	4	7530 CS
	Post–		5	5–5	4/5	482 CS
	Pre–	CuSO$_4$	3/4	5–5	4/5	4545 CS
	Meta–		4	4/5–5	4/5	4535 CS
	Post–		5	5–5	4/5	7535 CS
	Pre–	AlK(SO$_4$)$_2$	3	4/5–4/5	4/5	7492CS
	Meta–		3/4	5–5	4/5	586 CS
	Post–		5	5–5	5	587 CS
	unmordant		3	5–5	3/4	580 CS
Wool yarn	Pre–	FeSO$_4$	3	4/5-4/5	2/3	4495 CS
	Meta–		3/4	5–5	4	403 CS
	Post–		4	4/5–5	4	7536 CS
	Pre–	CuSO$_4$	3	4/5–4/5	3/4	620 CS
	Meta–		3/4	5–5	4/5	5763 CS
	Post–		4/5	5–5	4/5	557 CS
	Pre–	AlK(SO$_4$)$_2$	3	4–4/5	4	7404 CS
	Meta–		3/4	4/5–5	4/5	7402 CS
	Post–		4	5–5	4/5	557 CS
	unmordant		4	5-5	3/4	617 CS

[a]Wash and [b]rub fastness 1 = poor, 5 = very good, [c]Light fastness 1 = very poor, 8 = outstanding

Table 2: K/S and *L* *a* *b* values of textile products.

Fabric	Mordant	*L*	*a*	*b*	K/S
Cotton	FeSO$_4$	60.55	–4.55	29.38	5.86
		59.25	–4.50	27.32	5.70
		56.99	–3.00	26.40	5.62
	CuSO$_4$	51.66	5.44	28.45	11.26
		55.45	5.0	22.28	9.35
		57.95	5.46	21.09	10.20
	AlK(SO$_4$)$_2$	66.25	–0.99	43.35	5.90
		6829	–0.90	40.30	5.95
		69.75	–0.35	44.33	6.12
Wool	FeSO$_4$	62.01	–3.03	30.01	6.87
		61.90	–2.46	29.05	5.11
		63.01	0.98	32.66	6.88
	CuSO$_4$	52.88	5.89	20.52	11.01
		50.05	5.65	21.67	7.05
		53.06	7.99	24.45	5.99
	AlK(SO$_4$)$_2$	70.72	–0.20	40.36	5.63
		69.36	0.54	38.99	5.60
		72.75	–0.64	42.44	5.75
unmordant–cotton	–	64.36	–0.98	26.19	4.70
unmordant–wool	–	66.45	–1.5	27.21	5.89

Figure 4. Samples dyed with *Morus nigra* L. leaf extract.

4. CONCLUSION

Natural dyes are an important alternative to synthetic dyes because they are environmentally friendly and economical. In this present work, the *Morus nigra* L. leaves aqueous solution was used for dyeing of cotton fabric and wool yarn. Yellow color tones were obtained in the dyeing of cotton fabrics. Green, dark green and yellow color tones were obtained in the dyeing of wool yarns. As a result, considering that *Morus nigra* L. is a natural product, it can be concluded that it can be an easy-to-access and environmentally friendly textile dye. It also offers an economical dyeing opportunity.

5. REFERENCES

1   Adeel S, Rehman FU, Khosa MK, Rajab S, Zia KM, Zuber M, Batool, F. Eco-friendly isolation of colorant from arjun bark for dyeing of bio-mordanted cotton fabric: short title: dyeing of bio-mordanted cotton with arjun bark colorant. J. Nat. Fibers 2022, 19(12); 4684-4695. Available from: <DOI>.

2   Haji A, Naebe M. Cleaner dyeing of textiles using

plasma treatment and natural dyes: A review. J. Clean. Prod. 2020, 265; 121866. Available from: <DOI>.

3   Hossain S, Jalil MA, Kader A, Kamal SAB. Excellent dyeing properties of a natural dye extracted from the leaves of *Phoenix dactylifera* Linn on cotton and silk fabrics. J. Nat. Fibers 2022, 19(15); 9803-9812. Available from: <DOI>.

4   Önal A, Özbek O, Tombul KC, Nached S. Investigation of the dyeing properties of cotton fabrics and wool yarns using *Prunus persica* leaf extract. J. Indian Chem. Soc. 2021, 98;100092. Available from: <DOI>.

5   Önal A, Özbek O, Vanlıoğlu F, Teker AT, Boyraz D. Investigation of the dyeing properties of the colorant extracted from *Juglans regia* L. leaves on cellulosic and protein fabrics. J. Turk. Chem. Soc., Sect. A: Chem. 2021, 8;453–460. Available from: <DOI>.

6   Akmeşe O, Acet T, Özcan K. Determination of antioxidant and antimicrobial activities and synergistic effect with antibiotics of *Morus nigra* L. extracts grown in Elazig province. Gümüşhane Univ J Sci Technol. 2020, 10;983995. Available from: <DOI>.

Önal A et al. JOTCSA. 2023; 10(3): 821–828.

RESEARCH ARTICLE

7   Polumackanycz M, Wesolowski M, Viapiana A. *Morus alba* L. and *Morus nigra* L. leaves as a promising food source of phenolic compounds with antioxidant activity. Plant Foods Hum. Nutr. 2021, 76;458–465. Available from: <DOI>.

8   Melo RSS, Reis SAGB, Guimarães AL, Silva NDDS, Rocha JM, El Aouad N, Almeida JRGDS. Phytocosmetic Emulsion Containing Extract of *Morus nigra* L. (Moraceae): Development, Stability Study, Antioxidant and Antibacterial Activities, Cosmetics 2022, 9; 39. Available from: <DOI>.

9   de Freitas MM, Fontes PR, Souza PM, William Fagg C, Neves Silva Guerra E, de Medeiros Nóbrega YK, Silveira D, Fonseca-Bazzo Y, Simeoni LA, Homem-de-Mello M, Magalhães PO. Extracts of *Morus nigra* L. leaves standardized in chlorogenic acid, rutin and isoquercitrin: tyrosinase inhibition and cytotoxicity. PloS One, 2016, 11;e0163130. Available from: <DOI>.

10   Queiroz GT, Santos, TR, Macedo R, Peters VM, Leite, MN, Sá RCS, Guerra MO. Efficacy of Morus nigra L. on reproduction in female Wistar rats. Food Chem. Toxicol. 2012, 50;816–822. Available from: <DOI>.

11   Abay M, Eruygur N. Investigation of Antioxidant Activities of Fruit, Leaf, and Branche Extracts of White (*Morus alba* L.) and Black (*Morus nigra* L.) Mulberry Species from Diyarbakır. Turk J Agric Res. 2021, 8;177–183. Available from: <DOI>.

12   Souza GR, Oliveira-Junior RGD, Diniz TC, Branco A, Lima-Saraiva SRG, Guimarães AL, Oliveira AP, Pacheco AGM, Silva MG, Moraes-Filho MO, Costa MP, Pessoa CÓ. Almeida JRGS. Assessment of the antibacterial, cytotoxic and antioxidant activities of *Morus nigra* L. (Moraceae). Brazilian Journal of Biology. 2018, 78;248–254. Available from: <DOI>.

13   Qadir MI, Ali M, Ibrahim Z. Anti-cancer activity of Morus nigra leaves extract, Bang J Pharmacol. 2014 9;496–497. Available from: <DOI>.

14   Thabti I, Elfalleh W, Tlili N, Ziadi M, Campos MG, Ferchichi A. Phenols, flavonoids, and antioxidant and antibacterial activity of leaves and stem bark of *Morus* species, Int J. Food Prop. 2014, 17;842–854. Available from: <DOI>.

15   Lim SH, Choi CI. Pharmacological Properties of *Morus nigra* L. (Black Mulberry) as apromising Nutraceutical resource. Nutrient 2019, 11;437. Available from: <DOI>.

16   Yilmaz F. The importance of using natural dyestuffs in children's clothing and in this context the use of black mulberry leaves in wool dyeing. J Art Iconograph. 2021, 1;1–6. Available from: <URL>.

17   Carneiro ADA, Sinoti SBP, de Freitas MM, Simeoni LA, Fagg CW, Magalhães PDO, Silveira D, Fonseca-Bazzo YM. Hydroethanolic Extract of *Morus*

nigra L. Leaves: A dual PPAR-α/γ agonist with anti-ınflammatory properties in lipopolysaccharide-stimulated RAW 264.7. Plants 2022, 11; 3147. Available from: <DOI>.

18   Önal A, Tombul KC, Nached S. Investigation of dyeing properties of different fabric species with *curcuma longa* extracts. Rev. Roum. Chim. 2020, 65;983–988. Available from: <DOI>.

19   Önal A, Özbek O, Nached S. The production of antiviral–breathing mask against SARS-CoV-2 using some herbal essential oils. J. Turk. Chem. Soc., Sect. A: Chem. 2020, 7;821–826. Available from: <DOI>.

20   Onal A. Extraction of dyestuff from onion (*Allium cepa* L.) and its application in the dyeing of wool, feathered-leather and cotton. Turk. J. Chem. 1996, 20;194–203. Available from: <URL>.

21   Leon K, Mery D, Pedreschi F, Leon J. Color measurement in L^* a^* b^* units from RGB digital images. Food Res. Int. 2006, 39;1084–1091. Available from: <DOI>.

22   Ly BCK, Dyer, EB, Feig JL, Chien AL, Del Bino S. Research techniques made simple: cutaneous colorimetry: a reliable technique for objective skin color measurement. J. Invest. Dermatol. 2020, 140; 3-12. Available from: <DOI>.

23   Džimbeg-Malčić, Z. Barbarić-Mikočević, K. Itrić, Kubelka-munk theory in describing optical properties of paper (I). Teh. Vjesn. 2011, 18;117–124. Available from: <URL>.

Production of SBS Reinforced Polyester Composite: Characterization of Physical and Chemical Properties

Hakan Şahal[1] iD **, Ercan Aydoğmuş[2]*** iD

[1] Munzur University, Vocational School of Tunceli, Department of Food Processing, Tunceli, Türkiye.
[2] Fırat University, Faculty of Engineering, Department of Chemical Engineering, Elazığ, Türkiye.

Abstract: In this study, dissolved styrene butadiene styrene (SBS) copolymer is homogeneously reinforced into orthophthalic unsaturated polyester (UP) resin. Polyester composite production is carried out with the help of methyl ethyl ketone peroxide (MEKP) and cobalt octoate (Co Oc) catalysts. The density, Shore D hardness, thermal conductivity coefficient, thermal stability, morphological surface structure, and chemical bond structure of the obtained composite have been examined. According to the results, SBS reinforcement decreases the density of the composite and increases the thermal conductivity coefficient. The addition of SBS at different weight ratios (1%, 3%, 5%, 7%, and 10% w/w) reduces both the hardness and thermal stability of the polyester composite. According to the test and analysis results, 5 wt.% SBS reinforced polyester composite production is determined as the optimum ratio. 7 wt.% and above SBS reinforcement negatively affect the physical and chemical properties of the obtained composite. For example, when 10 wt. % SBS reinforced composite is examined by scanning electron microscope (SEM), and irregular pores are observed in the surface morphology. Also, it is understood by Fourier transform infrared spectroscopy (FTIR) that there is a physical interaction between SBS and polyester and that no chemical bond is formed. The thermal decomposition behavior of the composite has been determined according to the decrease in the activation energy. As SBS ratio increases, it is understood that the thermal stability of the product obtained with the decrease in the activation energy of the polyester composite weakens.

1. INTRODUCTION

Today, composites have become widespread as an alternative to traditional products. Particularly, the properties of doped polymer composites such as insulation, thermal stability, density, hardness, and porosity have led to an increase in studies in this field. Polymer composites are widely used in many industrial applications such as automotive, aerospace, sports, household appliances, medicine, electrical-electronics, and defense (1,2). The desire to produce lighter and more efficient materials has led researchers to investigate various composite materials and their applications (3). The high density and electrical conductivity, in addition to the low corrosion and contamination resistance of conventional metals or metal-doped components, have prompted researchers to explore alternative materials for thermal applications (4).

Thermoplastic elastomers (TPEs) are an important class of materials that combine elastomeric behavior with thermoplastic properties. Usually, these are ABA-type triblock copolymers such as polystyrene-polybutadiene-polystyrene (SBS) or polystyrene-polyisoprene-polystyrene (SIS) combining a soft central block with glassy end blocks (5,6). Although these materials find widespread commercial applications, unsaturated double bonds in the middle segments make the structure susceptible to oxidation, shortening its useful life (7). These TPEs have some drawbacks such as poor chemical, heat, and UV resistance due to the unsaturated soft blocks as well as low service temperature limited by the glass transition temperature of the polystyrene block (8).

SBS, which is in the thermoplastic elastomer group, consists of hard styrene blocks and softer butadiene blocks, which are widely used in commercial applications due to their mechanical strength. Polybutadiene (PB) is the main component in the SBS block copolymer and forms the continuous matrix, while polystyrene (PS) forms the discontinuous phase (domains). Due to the rubbery character of SBS, high-performance self-supported hollow fibers are difficult to prepare by phase inversion. Therefore, membrane configurations can be obtained only by coating SBS on existing hollow fiber supports or by blending SBS with a glassy polymer in appropriate concentrations (9,10).

For this reason, there are studies developed by adding many physical and chemical additives according to the purpose of the use of polymers in the literature. Many organic or inorganic reinforcing materials are used in composite construction with unsaturated polyesters. In a study, it has been reported that improvements are observed in both the mechanical and thermal properties of the composite obtained with waste crumb rubber added to unsaturated polyester (11). Thermal decomposition kinetics of thermoplastic polyesters and optimized polypropylene/poly(lactic acid) mixture and thermal degradation kinetics of fumed silica reinforced polyester composites were conducted (12,13).

In studies using synthetic materials, the response of a polyester matrix composite with the addition of marble waste as filler under vacuum and vibro-compression was investigated (14). In another research, the thermal, mechanical, and morphological properties of synthetic graphite and carbon fiber-filled polybutylene terephthalate polyester composites were investigated (15).

In this study, the production and some physical and chemical properties of SBS reinforced polyester composites have been investigated. It is aimed to use SBS, which has thermoplastic properties, as a reinforcement material in the production of polyester composites. The use of certain proportions of SBS in polyester reduces the density and hardness of the obtained composite, facilitates its workability, and increases its elastic properties. Another unique aspect of this study is that since SBS is mixed with unsaturated polyester as a dissolved gel, not as a powder, a more homogeneous composite matrix is obtained. SBS reinforcement is made to improve the thermoplastic properties of polyester composites. In this way, it

can be processed easily and becomes more flexible than brittle structure. Also, this study will be an example for the development of composite materials with low density and low stiffness.

2. MATERIALS AND METHODS

2.1. Methods Used in the Experimental Study
Methyl ethyl ketone peroxide (MEKP), cobalt octoate (Co Oc), and orthophthalic unsaturated polyester resin (UP) used in experimental studies were supplied from Turkuaz Polyester Company (Türkiye). Also, chemicals used for the synthesis and analysis were purchased from the following: Toluene (Sigma-Aldrich), and SBS-Kumho KTR 101 (Kumho Petrochemical).

2.2. Methods Used in the Experimental Study
The matrix density of the samples obtained is calculated by proportioning the weight of the composites to the volume since they have a uniform geometry in standard molds. Shore D hardness is measured with the LX-D-2 double-needle durometer. Thermal conductivity coefficient measurement was made with TLS-100 Thermtest device. Chemical bond structures of polyester polymer are examined with Fourier transform infrared spectrometer (FTIR). A Shimadzu IRSpirit (QATR-S) branded device is used for FTIR spectral measurements. Thermal decomposition experiments are performed in an isolated PID-controlled reactor system. The thermal degradation behavior of the samples was studied at a heating rate of 10 °C/min from about room temperature to 600 °C in an inert environment. Besides, the surface morphology of the produced polyester composite was examined with Zeiss Evo/MA10 SEM device (16-18). SBS block copolymer used as a supplement in our study was dissolved by using 20 mL of toluene for each 10 g to gel it. The resulting solution was allowed to remove from the toluene in a vacuum oven for 4 hours. Afterward, a homogeneous mixture was obtained by mixing orthophthalic unsaturated polyester (UP) resin with SBS at room temperature. Experimental studies were carried out at approximately 25 °C and atmospheric pressure. At the last stage, MEKP and Co Oc were added to the mixture and the gelling mixture was poured into standard molds. After waiting for 24 hours for curing, the necessary physical tests and chemical analyses were carried out (22-25). In Figure 1, a brief schematic of polyester composite production is given.
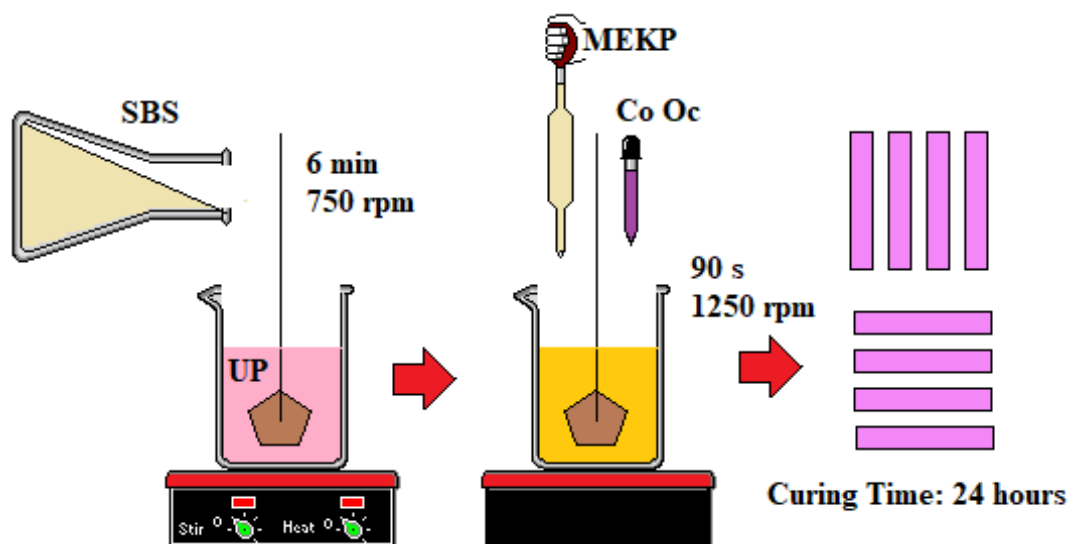
Figure 1: Production scheme of SBS reinforced polyester composite.

The experimental study plan and chemical composition ratios are given in Table 1. In this table, it is seen that polyester composites are produced by keeping Co Oc and MEKP ratios constant and SBS reinforcement at different weight ratios.

Table 1: Components and quantities used to obtain composites.

Experiment No	SBS (wt.%)	UP (wt.%)	Co Oc (wt.%)	MEKP (wt.%)
1	0	98	0.6	1.4
2	1	97	0.6	1.4
3	3	95	0.6	1.4
4	5	93	0.6	1.4
5	7	91	0.6	1.4
6	10	88	0.6	1.4

3. RESULTS AND DISCUSSIONS

3.1. The Density of SBS Reinforced Polyester Composite

In this research, some physical and chemical properties of SBS reinforced polyester composite have been evaluated. It is seen in Figure 2 that the density of the produced composite decreases with SBS reinforcement. While the density of pure polyester polymer is approximately 1206 kg/m^3, the density of 10 wt.% SBS reinforced polyester composites decrease to 1174 kg/m^3.
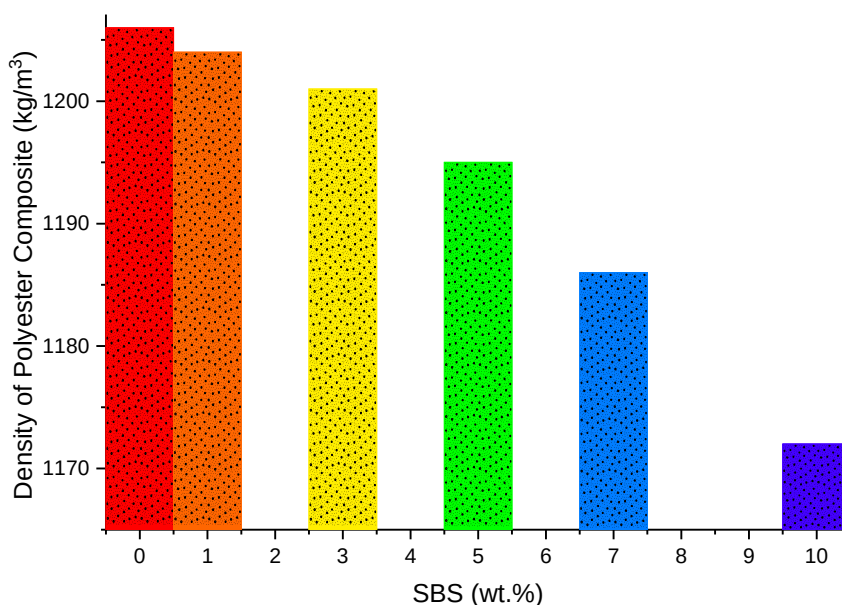
Figure 2: Effect of SBS reinforcement on the density of polyester composite.

3.2. The Hardness of SBS Reinforced the Composite

In Figure 3, it is stated that SBS reinforcement reduces the density of the polyester composite. While inorganic fillers generally increase the surface hardness of polyester composites, thermoplastic polymers and wastes can reduce it (28-31). Shore D hardness of pure polyester polymer is around 78 and this value decreases to about 71 with 10 wt.% SBS reinforcement.
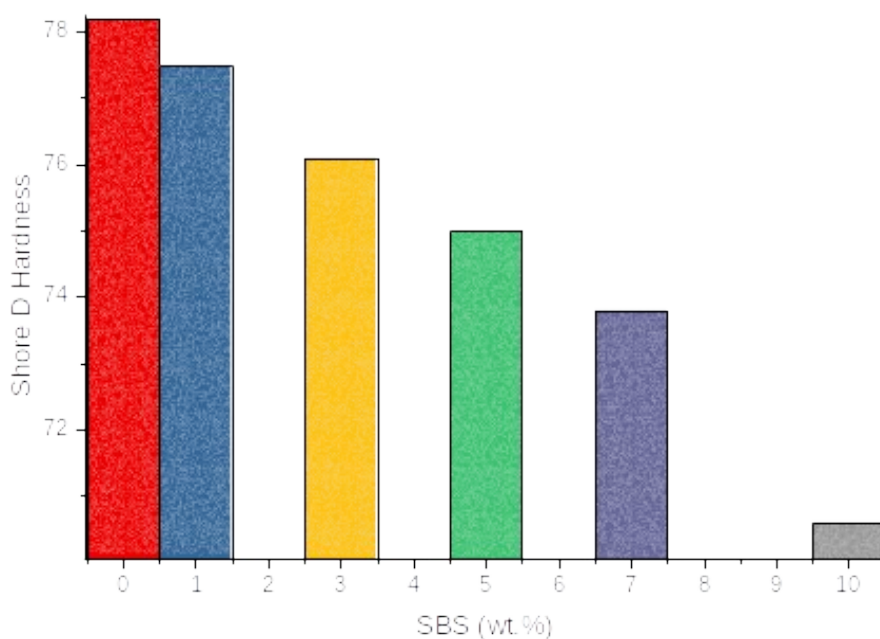
Figure 3: Effect of SBS reinforcement on Shore D hardness of the composite.

3.3. The Thermal Conductivity of SBS Reinforced the Polyester Composite

It is seen in Figure 4 that the addition of SBS slightly increases the thermal conductivity coefficient of the polyester composite. While the thermal conductivity coefficient of pure polyester polymer is around 0.056 W/m·K, this coefficient increases up to approximately 0.062 W/m·K with 10 wt.% SBS supplementation.
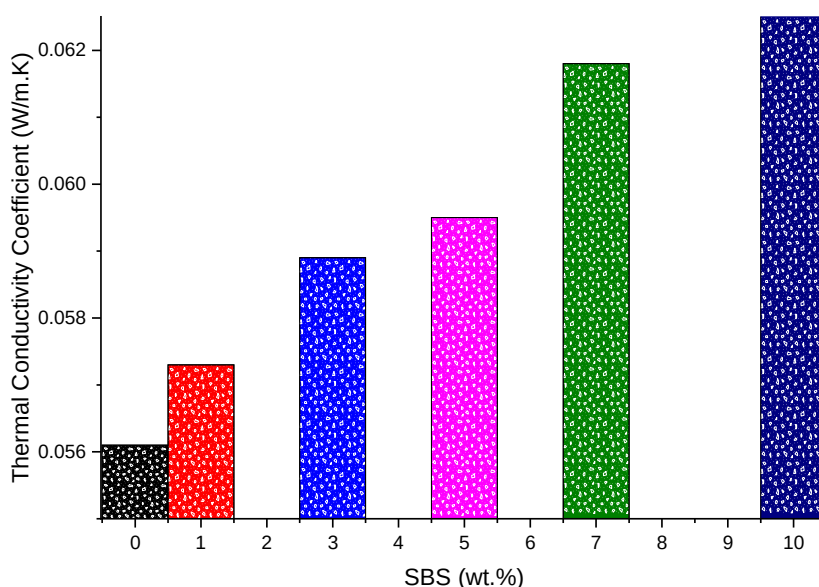
Figure 4: Effect of SBS reinforcement on thermal conductivity of composite.

3.4. The Activation Energy of SBS Reinforced the Composite

The thermal decomposition behavior of the composites was carried out in an inert environment (nitrogen gas) with a temperature increase rate of 10 °C/min from 25 °C to 600 °C. Activation energies of composites were calculated by Coats-Redfern using data from thermal degradation experiments (26,27). In this method, calculations were made by choosing the function (three-dimensional diffusion) with the highest correlation ($R^2 \geq 0.9830$) coefficient. In Figure 5, it is determined that the addition of SBS

reduces the activation energy of the polyester composite.
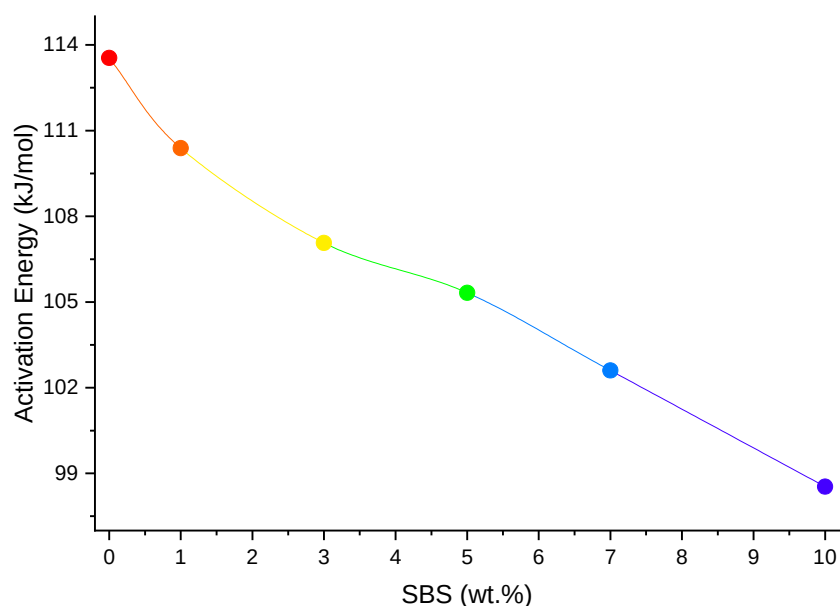
Figure 5: Effect of SBS reinforcement on the activation energy of the composite.

3.5. FTIR Spectra of the Polyester Composite

Figure 6 shows the FTIR spectrum of the pure polyester polymer. The band seen at a wavelength of about 3450-3500 cm^{-1} expresses the stretching vibrations of the hydroxyl groups. The bands in the wavelength range of 2800–2950 cm^{-1} show the stretching vibrations of the CH groups. The vibrations of the carbonyl group in the polyester composite are evident at a wavelength of 1718 cm^{-1}. When the peaks of SBS are examined, C=C stretching vibrations at a wavelength of approximately 1640 cm^{-1} are striking. Besides, cis HC=, vinyl $H_2C=$, and trans HC= deformation peaks are observed at approximately 700, 910, and 960 cm^{-1} wavelengths. In the wavelength range of 1400 and 1460 cm^{-1}, it expresses the vibrations of the aromatic ring. Besides, the band seen at a wavelength of 1255 cm^{-1} represents the torsional vibration of CH_2 groups (19-21). There is no chemical bond between SBS and polyester polymer and only a physical interaction can be said by looking at Figure 7.
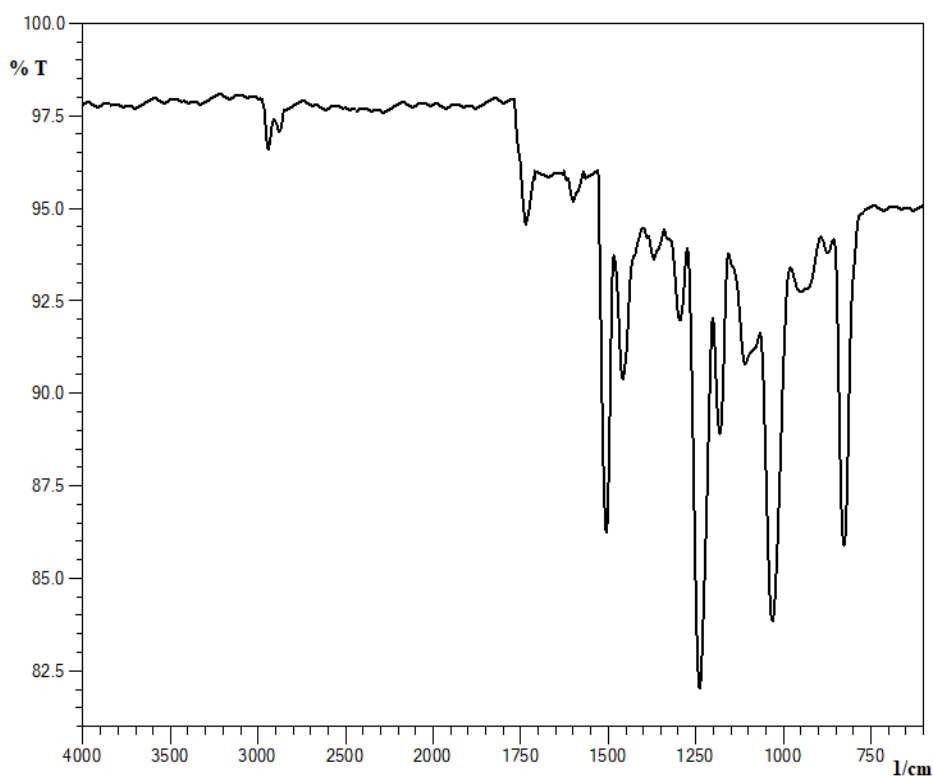
Figure 6: FTIR spectrum of pure polyester polymer.
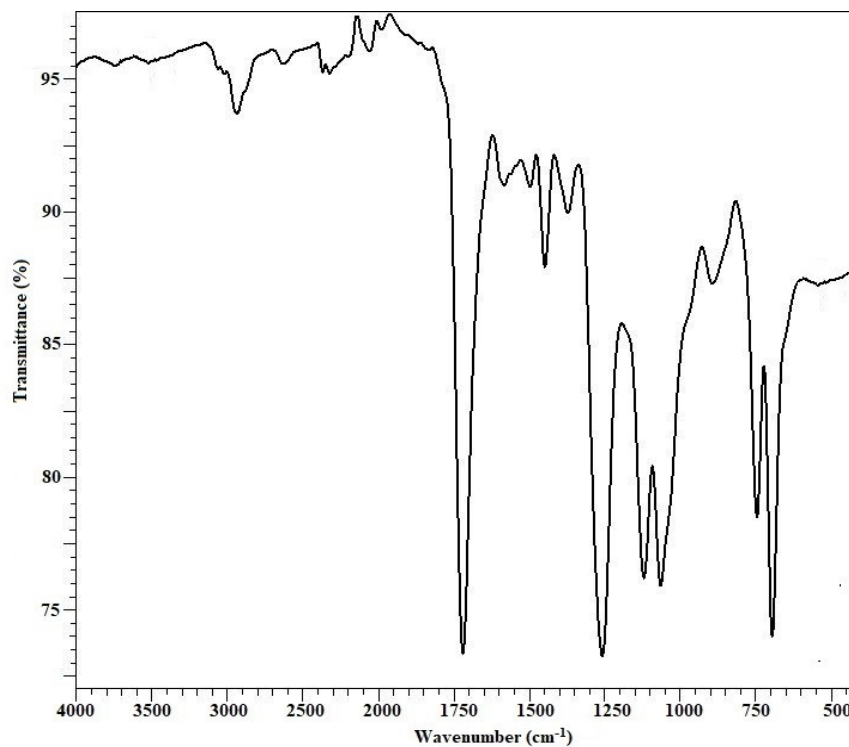
Figure 7: FTIR spectrum of 5 wt.% SBS reinforced polyester composite.

3.6. SEM Image of the Polyester Composite

Figure 8 shows the surface image of the pure polyester polymer. As can be understood from the surface morphology, there is no complex formation in the pore structure and distribution. In Figure 9, the surface structure of 10 wt.% SBS reinforced polyester composite is negatively affected due to excessive use of filler. According to the results, the use of filler below 7 wt.% is important for both a homogeneous and smoother surface morphology.
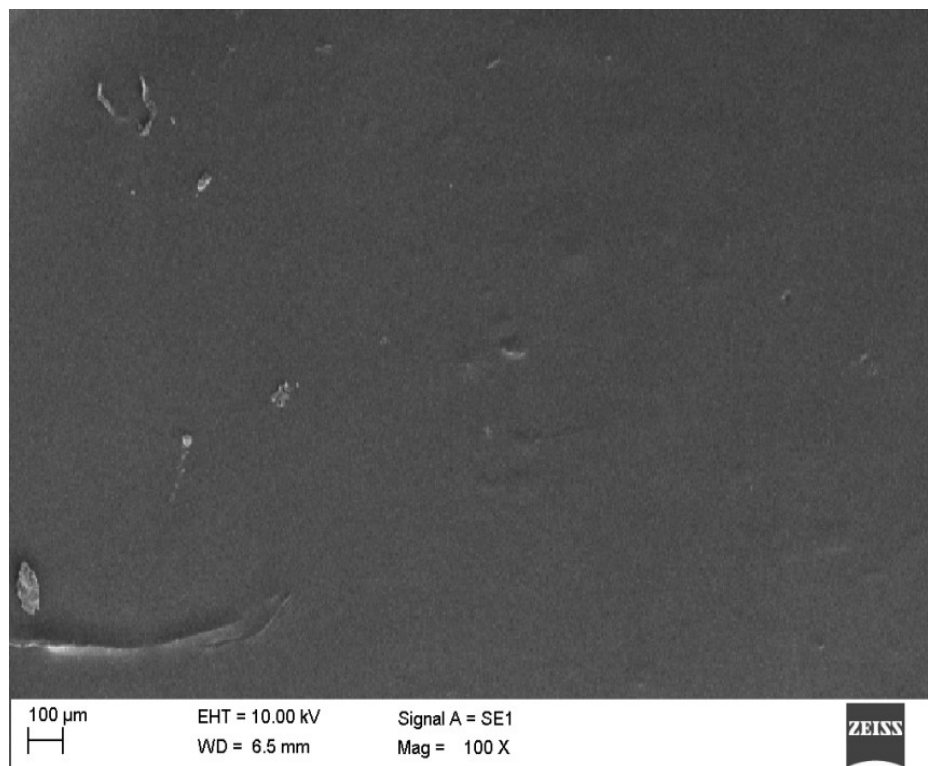
Figure 8: SEM image of pure polyester polymer.
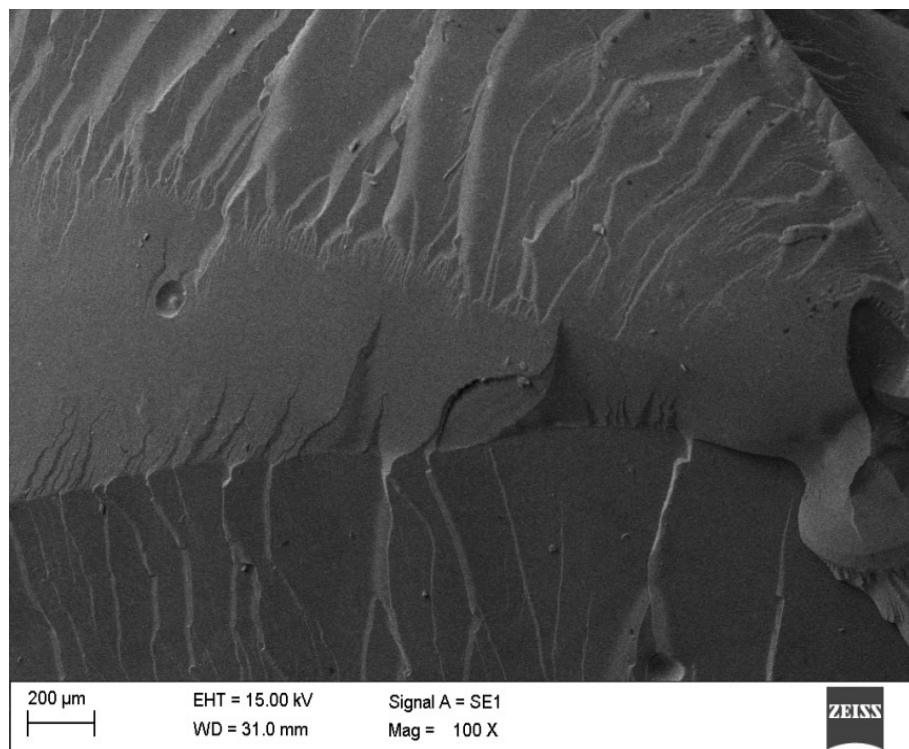
Figure 9: SEM image of 10 wt.% SBS reinforced polyester composite.

4. CONCLUSIONS

In this research, easy-to-process, flexible, low hardness and density SBS reinforced polyester composites have been produced. To provide a homogeneous mixture, SBS is mixed into UP in gel form. According to the results obtained, SBS reinforcement reduces both the density and hardness of the polyester composite. Besides, SBS slightly increases the thermal conductivity coefficient of the composite, while decreasing its thermal stability slightly. As SBS reinforcement ratio increases, the calculated activation energy decreases, indicating that the thermal stability of the composite also decreases. When the chemical bond structure of SBS reinforced composite is examined in FTIR spectrums, polyester polymer formation can be seen. Here, it is understood that the addition of SBS does not make a chemical bond with which it interacts physically in the composite. Also, when the surface morphology of the obtained polyester structures is examined, SBS reinforcement of 7 wt.% and above is not recommended for composite production.

As a result, it has been determined as the optimum ratio in the production of 5 wt.% SBS reinforced polyester composite. At this ratio, the homogeneity, surface structure, flexibility, workability, physical properties, and thermoplastic behaviors of the composite have been improved. Therefore, both the type and amount of filler are effective to produce polyester composites at the desired standards according to the intended use (32-35).

5. REFERENCES

1. Chirtoc M, Horny N, Tavman I, Turgut A, Kökey I, Omastová M. Preparation and photothermal characterization of nanocomposites based on high density polyethylene filled with expanded and unexpanded graphite: Particle size and shape effects. Int J Therm Sci [Internet]. 2012 Dec 1;62:50–5. Available from: <URL>.

2. Mohan VB, Lau K, Hui D, Bhattacharyya D. Graphene-based materials and their composites: A review on production, applications and product limitations. Compos Part B Eng [Internet]. 2018 Jun 1;142:200–20. Available from: <URL>.

3. Neto J, Banea M, Cavalcanti D, Queiroz H, Aguiar R. Analysis of mechanical and thermal properties of epoxy multiwalled carbon nanocomposites. J Compos Mater [Internet]. 2020 Dec 1;54(30):4831–40. Available from: <URL>.

4. Marchetto DB, Moreira DC, Ribatski G. A review on polymer heat sinks for electronic cooling applications. In: Proceedings of the 17th Brazilian Congress of Thermal Sciences and Engineering, ABCM, Águas de Lindóia, SP, Brazil. 2018. p. 25–8.

5. Holden G, Bishop ET, Legge NR. Thermoplastic elastomers. J Polym Sci Part C Polym Symp [Internet]. 2007 Mar 8;26(1):37–57. Available from: <URL>.

6. Holden G, Legge NR, Quirk R, Schroeder HE. Thermoplastic Elastomers. 2nd edition. Munich, Germany; 1996.

7. Legge NR, Holden G, Schroeder HE. Thermoplastic Elastomers, A Comprehensive Review. Munich, Germany; 1987.

8. Jerome R, Fayt R, Teyssie P, Legge NR, Holden G, Schroeder HE. Thermoplastic elastomers. Munich, Germany; 1987.

9. Sengoz B, Isikyakar G. Evaluation of the properties and microstructure of SBS and EVA polymer modified bitumen. Constr Build Mater [Internet]. 2008 Sep;22(9):1897–905. Available from: <URL>.

10. Galooyak SS, Dabir B, Nazarbeygi AE, Moeini A. Rheological properties and storage stability of

bitumen/SBS/montmorillonite composites. Constr Build Mater [Internet]. 2010 Mar 1;24(3):300–7. Available from: <URL>.

11. Aydoğmuş E, Demirel MH. Waste Tire Rubber Reinforced Polyester Composite Production and Characterization. In: 8th International Conference on Materials Science and Nanotechnology for Next Generation, Elazığ. 2021.

12. Levchik S V., Weil ED. A review on thermal decomposition and combustion of thermoplastic polyesters. Polym Adv Technol [Internet]. 2004 Dec;15(12):691–700. Available from: <URL>.

13. Aydoğmuş E, Arslanoğlu H. Kinetics of thermal decomposition of the polyester nanocomposites. Pet Sci Technol [Internet]. 2021 Jul 18;39(13–14):484–500. Available from: <URL>.

14. Ribeiro CEG, Rodriguez RJS, Vieira CMF, de Carvalho EA, Candido VS, Monteiro SN. Production of Synthetic Ornamental Marble as a Marble Waste Added Polyester Composite. Mater Sci Forum [Internet]. 2014 Jan;775–776:341–5. Available from: <URL>.

15. Yenier Z, Aker S, Seki Y, Altay L, Bigun O, Sarikanat M. Improving thermal conductivity of polybutylene terephthalate composites with hybrid synthetic graphite and carbon fiber. J Thermoplast Compos Mater [Internet]. 2023 Feb 19;36(2):595–614. Available from: <URL>.

16. Aydoğmuş E, Arslanoğlu H, Dağ M. Production of waste polyethylene terephthalate reinforced biocomposite with RSM design and evaluation of thermophysical properties by ANN. J Build Eng [Internet]. 2021 Dec 1;44:103337. Available from: <URL>.

17. Orhan R, Aydoğmuş E, Topuz S, Arslanoğlu H. Investigation of thermo-mechanical characteristics of borax reinforced polyester composites. J Build Eng [Internet]. 2021 Oct 1;42:103051. Available from: <URL>.

18. Yanen C, Aydoğmuş E. Characterization of Thermo-Physical Properties of Nanoparticle Reinforced the Polyester Nanocomposite. Dicle Univ J Inst Nat Appl Sci [Internet]. 2021;10(2):121–32. Available from: <URL>.

19. Aydoğmuş E. Biohybrid nanocomposite production and characterization by RSM investigation of thermal decomposition kinetics with ANN. Biomass Convers Biorefinery [Internet]. 2022 Oct 11;12(10):4799–816. Available from: <URL>.

20. Şahal H, Aydoğmuş E, Arslanoğlu H. Investigation of thermophysical properties of synthesized SA and nano-alumina reinforced polyester composites. Pet Sci Technol [Internet]. 2022 Aug 8;Article in Press:1–17. Available from: <URL>.

21. Aydoğmuş E, Dağ M, Yalçın ZG, Arslanoğlu H. Synthesis and characterization of waste polyethylene reinforced modified castor oil-based polyester biocomposite. J Appl Polym Sci [Internet]. 2022 Jul 15;139(27):e52526. Available from: <URL>.

22. Şahal H, Aydoğmuş E. Investigation of Thermophysical Properties of Polyester Composites Produced with Synthesized MSG and Nano-Alumina. Eur J Sci Technol [Internet]. 2022 Feb 15;34:95–9. Available from: <URL>.

23. Demirel MH, Aydoğmuş E. Production and Characterization of waste Mask Reinforced Polyester Composite. J Inonu Univ Heal Serv Vocat Sch [Internet]. 2022 Mar 10;10(1):41–9. Available from: <URL>.

24. Demirel MH, Aydoğmuş E. Waste Polyurethane Reinforced Polyester Composite, Production, and Characterization. J Turkish Chem Soc Sect A Chem [Internet]. 2022 May 31;9(2):443–52. Available from: <URL>.

25. Yanen C, Dağ M, Aydoğmuş E. Investigation of Thermophysical Properties of Colemanite, Ulexite, and Tincal Reinforced Polyester Composites. Eur J Sci Technol [Internet]. 2022 May 3;36:155–9. Available from: <URL>.

26. Orhan R, Aydoğmuş E. Production and Characterization of Waste Corncob Reinforced Polyester Composite. Eur J Sci Technol [Internet]. 2022 Oct 26;42:176–9. Available from: <URL>.

27. Orhan R, Aydoğmuş E. Investigation of some thermophysical properties of Asphodelus aestivus reinforced polyester composite. Firat Univ J Exp Comput Eng [Internet]. 2022;1(3):103–9. Available from: <URL>.

28. Yılmaz E, Aydoğmuş E, Demir A. Life Cycle Assessment and Characterization of Tincal Ore Reinforced Polyester and Vinylester Composites. J Turkish Chem Soc Sect B Chem Eng [Internet]. 2022;5(2):183–94. Available from: <URL>.

29. Pekdemir E, Aydoğmuş E, Arslanoğlu H. Thermal decomposition kinetics of synthesized poly(N-isopropylacrylamide) and Fe 3 O 4 coated nanocomposite: Evaluation of calculated activation energy by RSM. Pet Sci Technol [Internet]. 2023 Feb 7;Article in:1–18. Available from: <URL>.

30. Karataş M, Aydoğmuş E. Obtaining Pectin Reinforced Polyester Composite and Investigation of Thermophysical Properties. Eur J Sci Technol [Internet]. 2023 Mar 25;48:64–6. Available from: <URL>.

31. Dağ M, Aydoğmuş E, Yalçin ZG, Arslanoğlu H. Diatomite reinforced modified safflower oil-based epoxy biocomposite production: Optimization with RSM and assessment of outcomes by ANN. Mater Today Commun [Internet]. 2023 Jun 1;35:106327. Available from: <URL>.

32. Buran A, Durğun ME, Aydoğmuş E, Arslanoğlu H. Determination of thermophysical properties of Ficus elastica leaves reinforced epoxy composite. Firat Univ J Exp Comput Eng [Internet]. 2023;2(1):12–22. Available from: <URL>.

33. Karataş M, Aydoğmuş E. Use of Inorganic Wastes as Fillers in Production of Polyester Composites and Evaluation of Properties of Obtained Composite. Int J Adv Nat Sci Eng Res [Internet]. 2023 Apr 22;7(4):20–4. Available from: <URL>.

34. Şahal H, Aydoğmuş E. Use of Sunflower Seed Shells as Filler in Polyester Resin and Characterization of Obtained Composite. In: 2nd International Conference on Engineering, Natural and Social Sciences [Internet]. 2023. p. 233–6. Available from: <URL>.

35. Karataş M, Aydoğmuş E. Physical and Chemical Properties of Organic Waste Reinforced Polyester Composites. Int J Adv Nat Sci Eng Res [Internet]. 2023 Apr 22;7(4):16–9. Available from: <URL>.

Synthesis and Determination of Acid Dissociation Constants of Bis-Acyl Thiourea Derivatives

Cagla Efeoglu[1] iD **, Sit Tiken[1]** iD **, Hayati Sari[2]** iD **, Yahya Nural[1]*** iD

[1]Mersin University, Faculty of Pharmacy, Department of Analytical Chemistry, 33169, Mersin, Turkey
[2]Department of Chemistry, Faculty of Science and Arts, Tokat Gaziosmanpasa University, Tokat 60250, Turkey

Abstract: N,N'-((dodecane-1,12-diylbis(azanediyl))bis(carbonothioyl))bis(4-nitrobenzamide) 5 and N,N'-((dodecane-1,12-diylbis(azanediyl))bis(carbonothioyl))bis(3-nitrobenzamide) 6 as bis acyl thiourea derivatives were synthesized and their molecular structures were characterized using 1 H NMR, 13 C NMR, COSY, DEPT, HMQC, FT-IR, and HRMS techniques. The acid dissociation constants (p K a) of the bis-acyl thiourea derivatives 5, 6 were determined potentiometrically and spectrophotometrically. The pKa values of products 5, 6 were determined in 50% (v/v) dimethyl sulfoxide–water hydro-organic solvent in the presence of 0.1 mol⸱L ⸱1 ionic strength of NaCl and in the acidic medium at 25±0.1 °C, and two p K a values were calculated for each compound with the HYPERQUAD computer program using the data obtained from the potentiometric titrations performed. In addition, three pK a values for each compound were determined in the calculations using the HypSpec program from the data obtained from the spectrophotometric titrations performed under the conditions where the potentiometric titrations were performed. For compounds 5 and 6, spectrophotometrically, pK a1 was 3.56±0.08 and 3.87±0.01, respectively, pK a2 was 7.11±0.08 and 7.05±0.01, respectively, and pK a3 was 12.30±0.08 and 11.82±0.02, respectively. It can be said that pK a1 , pK a2 , and pK a3 values may belong to enol, enthiol, and NH, respectively. Moreover, for compounds 5 and 6, potentiometrically, pK a2 was 7.06±0.13 and 6.94±0.11, respectively, and pK a3 was 12.11±0.06 and 11.17±0.06, respectively, and it can be said that pK a2 and pK a3 values may belong to enthiol and NH, respectively. It is seen that the pK a values determined spectrophotometrically and potentiometrically are compatible with each other.

1. INTRODUCTION

Acyl thiourea derivatives are widely studied in analytical chemistry because they show chemosensory properties in the determination of various anions, cations, and neutral compounds (1–5) and can be used in heavy metal removal due to their very good chelating properties with metal ions (6,7). In addition, acyl thiourea derivatives have an important place in pharmaceutical chemistry (8,9) because they can be used as an intermediate product in the synthesis of many bioactive molecules (10,11) and show a wide range of bioactivity such as anti(mico)bacterial (12–14), antifungal (15,16), antioxidant (17), and anticancer (18) as well as enzyme inhibitory (19–23) properties. Since acyl thiourea compounds can easily form chelate complexes on carbonyl and thiocarbonyl

groups, their Pt(II), Ni(II), Zn(II), Co(II), and other many metal complexes have been synthesized (24–30).

It is also known that various bis-acyl thiourea derivatives have been synthesized (31,32) to examine their bioactivity and that these compounds show antimicrobial (33) and antifungal (34,35), anticancer (36–38), antioxidant (39) as well as anti-diabetic (40) and tissue-nonspecific alkaline phosphatase inhibitor properties (41). It has also been stated that some bis-acyl thiourea derivatives may be potential drug candidates for Alzheimer's disease by showing acetylcholinesterase enzyme inhibition activity (42). Pt(II), Ni(II), Cu(II), and Zn(II) complexes of various bis-acyl thiourea derivatives are also synthesized (43–45). It has been stated that the Ni(II) and Cu(II) complexes of bis-acyl thiourea derivatives show anticancer properties as well as DNA and protein binding properties (46). The chemosensory properties of bis-acyl thiourea derivatives were also investigated and it was determined that some compounds showed chemosensory properties against Cu(II) ions (47,48). Moreover, hexamethylene-1,6-bis[(*N*'-benzoyl)thiourea], a bis-acyl thiourea derivative, showed high palladium extraction properties in hydrochloric acid solutions (49).

The pK_a value, which provides information about the acidity/basicity of the compounds, their solubility in the solvent and pH environments they are in, and their ability to interact with the receptors in the environments where they will exert pharmacological effects, is a very useful parameter. Since drug molecules generally show activity in ionized form, it is important to determine the relevant pK_a values, which give information about the ionization state of each functional group in the molecule. The pK_a values are also an important parameter in knowing which ionized forms of the molecule will be effective in various pH environments. Since pK_a values provide critical information about molecules, they are also very important parameters in the development of molecular docking programs, which have a very important place in drug design (50–55). pK_a values carry critical information about the complexes that ligands to be used in heavy metal removal will form with metal ions and their adsorption properties (56). While potentiometric (57) and spectrophotometric (58,59) titrations are widely used in determining pK_a values of compounds, voltammetric (60), chromatographic (61,62), and nuclear magnetic resonance (NMR) spectroscopy (63) methods are also known to be used.

Herein, we report the synthesis of *N*,*N*'-((dodecane-1,12-diylbis(azanediyl))bis(carbonothioyl)) bis(4-nitrobenzamide) and *N*,*N*'-((dodecane-1,12-diylbis(azanediyl))bis(carbonothioyl))bis(3-nitrobenzamide) as bis acyl thiourea derivatives and the determination of their pK_a values potentiometrically and spectrophotometrically in 50:50 v/v DMSO: water hydro-organic medium.

2. MATERIAL AND METHODS

2.1. Materials and Instrumentation
All used chemicals were of reagent grade. They were purchased from Merck or Aldrich and used without further purification. Fourier transform infrared (FTIR) and NMR spectra were recorded using the Varian Scimitar Series 1000 FTIR spectrophotometer and a Bruker Ultrashield Plus Biospin GmbHt at 400 MHz, respectively. Melting points were determined on a Mettler Toledo MP90 apparatus and were uncorrected. High-resolution mass spectra were recorded by electrospray ionization technique in Waters SYNAPT G1 MS (ESI-TOF-MS). Potentiometric titrations were performed using a Titroline 7000 automated titrator with SI-Analytics combined with a glass pH electrode and having an automatic micro-burette that could be controlled by a computer. Spectrophotometric titrations were performed using a Shimadzu 1800 240V model UV-Vis spectrophotometer.

2.2. Synthesis
Potassium thiocyanate (10.3 mmol) was added to a stirred solution of 4-nitrobenzoyl chloride or 3-nitrobenzoyl chloride in acetone (75 mL) and then the mixture was stirred and heated to reflux for 4 h. After the reaction was complete, the mixture was filtered through filter paper. The filtrate was added dropwise to the stirred flask containing 1,12-diaminododecane (1g, 5 mmol) dissolved by heating in chloroform (100 mL) and heated to reflux temperature for 36 h (Scheme 1). After completion of the reaction monitored using TLC, the solvent was removed using a rotary evaporator and the crude product was purified using column chromatography (ethyl acetate:hexane, 1:4 v/v). The molecular structures of the desired pure products were characterized using NMR, FT-IR, and HRMS techniques.

2.2.1. N,N'-((dodecane-1,12-diylbis(azanediyl))bis (carbonothioyl))bis(4-nitrobenzamide) (**5**). Brown powder. Yield, 0,52 g, 84%. m.p.: 107-109 °C. FT-IR (cm⁻¹): υ_{max} 3399, 3237, 3111, 3081, 2919, 2850, 1668, 1604, 1552, 1515, 1489, 1435, 1345, 1303, 1250, 1202, 1158, 1042. ¹H NMR (400 MHz, DMSO-d_6): δ 11.67 (s, 2H, 2 x C(O)NH), 10.74 (t, 2H, J = 5.1

Hz, 2 x NH), 8.31 (d, 4H, J = 8.7 Hz, Ar-H), 8.11 (d, 4H, J = 8.7 Hz, Ar-H), 3.62-3.58 (m, 4H, C1H$_2$, C12H$_2$), 1.66-1.59 (m, 4H, C2H$_2$, C11H$_2$), 1.34-1.26 (m, 16H, C3H$_2$, C4H$_2$, C5H$_2$, C6H$_2$, C7H$_2$, C8H$_2$, C9H$_2$, C10H$_2$). ^{13}C NMR (100 MHz, DMSO-d_6): ☐ 179.6 (2 x C=S), 166.5 (2 x C=O), 149.7 (2 x C4'), 138.1 (2 x C1'), 130.1 (2 x C2', 2 x C6'), 123.2 (2 x C3', 2 x C5'), 44.8 (C1, C12), 28.92 (C2, C11), 28.89 (C5, C8), 28.6 (C6, C7), 27.5 (C4, C9), 26.4 (C3, C10). HRMS (ESI-TOF-MS): calcd. for C$_{28}$H$_{37}$N$_6$O$_6$S$_2$ [MH]$^+$ 617.2211; found 617.2216.

2.2.2.   N,N'-((dodecane-1,12-diylbis(azanediyl)) bis(carbonothioyl))bis(3-nitrobenzamide) (**6**). White powder. Yield, 0,48 g, 78%. m.p.: 142-144 °C. FT-IR (cm^{-1}): υ_{max} 3376, 3236, 3158, 3049, 2924, 2849, 1668, 1615, 1557, 1519, 1470, 1346, 1307, 1260, 1189, 1149, 1073. ^{1}H NMR (400 MHz, DMSO-d_6): δ 11.73 (s, 2H, 2 x C(O)NH), 10.74 (t, 2H, J = 5.2 Hz, 2 x NH), 8.73-8.72 (m, 2H, Ar-H), 8.46-8.44 (m, 2H, Ar-H), 8.33-8.30 (d, 2H, J = 8.7 Hz, Ar-H), 7.82-7.78 (m, 2H, Ar-H), 3.63-5.57 (m, 4H, C1H$_2$, C12H$_2$), 1.65-1.59 (m, 4H, C2H$_2$, C11H$_2$), 1.33-1.23 (m, 16H, C3H$_2$, C4H$_2$, C5H$_2$, C6H$_2$, C7H$_2$, C8H$_2$, C9H$_2$, C10H$_2$). ^{13}C NMR (100 MHz, DMSO-d_6): δ 179.7 (2 x C=S), 166.1 (2 x C=O), 147.4 (2 x C3'), 134.9 (2 x C1'), 134.0 (2 x C6'), 130.1 (2 x C5'), 127.1 (2 x C4'), 123.5 (2 x C2'), 44.8 (C1, C12), 28.91 (C2, C11), 28.88 (C5, C8), 28.6 (C6, C7), 27.5 (C4, C9), 26.3 (C3, C10). HRMS (ESI-TOF-MS): calcd. for C$_{28}$H$_{37}$N$_6$O$_6$S$_2$ [MH]$^+$ 617.2211; found 617.2216.

2.3. Determination of Acid Dissociation Constants
Potentiometric determination: Potentiometric determination of the pK_a values of the products was performed using an automatic titrator which is controlled with a computer, with an ultra-combination pH electrode in 50% (v/v) DMSO–water hydro-organic solvent in the presence of 0.1 mol·L^{-1} ionic strength of NaCl and in the acidic medium at 25±0.1 °C. Stock solutions of the bis-acyl thiourea derivatives **5**, **6** were prepared with a concentration of 1×10^{-3} mol·L^{-1} in DMSO. NaOH, HCl, and NaCl stock solutions were prepared with concentrations of 0.025, 0.1, and 1.0 mol·L^{-1} in deionized water, respectively. Potentiometric titrations were performed in a double-walled glass titration cell, the temperature was kept constant at 25.0±0.1 °C using a thermostat. The titration cell was washed and dried before and after each titration, and the syringe was washed several times with deionized water and then the base solution. 5 mL of the stock solution of **5** or **6**, 20 mL of DMSO solution, 1 mL of the stock HCl solution, 5 mL of the NaCl solution, and 19 mL of deionized water were added to the titration cell. The titration cell was kept closed during titration, the solution in the titration cell was stirred at a constant

rate throughout the titration using a magnetic stirrer, and nitrogen gas (99.9%) was continuously passed through the titration cell throughout the titration process. After nitrogen has passed through the titration cell for 5 minutes titration process was started, and the titration process with the additions of 0.04 mL of the stock NaOH solution was carried out using an automatic titrator and computer program. Using the data obtained from potentiometric titration, pK_a values were calculated with HYPERQUAD, one of the most widely used computer programs in this field (64).

Spectrophotometric determination: Determination studies of pK_a values were carried out under conditions (50% (v/v) DMSO–water hydro-organic solvent in the presence of 0.1 mol·L^{-1} ionic strength of NaCl and in the acidic medium at 25±0.1 °C) where the pK_a values of bis-acyl thioureas **5**, **6** were determined potentiometrically, and were calculated using the HypSpec program using the data obtained as a result of titrations performed spectrophotometrically. 0.5 mL of the stock solution of **5** or **6**, 24.5 mL of DMSO solution, 1 mL of the stock HCl solution, 5 mL of the NaCl solution, and 19 mL of deionized water were added to the titration cell. The titration cell was kept closed during titration, the temperature was kept constant at 25.0±0.1 °C using a thermostat, the solution in the titration cell was stirred at a constant rate throughout the titration using a magnetic stirrer, and nitrogen gas (99.9%) was continuously passed through the titration cell throughout the titration process. After nitrogen has been passed through the titration cell for 5 minutes titration process was started. Blank measurement was made using only DMSO in the UV-Vis spectrophotometer. In the first measurement, the pH of the titration cell and then the absorbance of the solution was measured without the use of a titrant. For other measurements, 0.025 M NaOH titrant was added to the titration cell so that at least six absorbances were measured in each pH range between pH 3 and pH 12. At each addition of titrant, first, the pH and then immediately the absorbance were measured. Using the data obtained from spectrophotometric titration, pK_a values were calculated with the HypSpec computer program.

3. RESULTS AND DISCUSSION

3.1. Synthesis
Bis-acyl thiourea derivatives **5**, **6** were synthesized by the reaction of 4-nitrobenzoyl isothiocyanate or 3-nitrobenzoyl isothiocyanate, which were prepared with the reaction of potassium thiocyanate and the corresponding acyl chloride, and 1,12-

diaminododecane in 84% and 78% yields, respectively (**Scheme 1**). Molecular structures of the bis-acyl thioureas **5**, **6** were characterized using ^{1}H NMR, ^{13}C NMR, COSY, DEPT, HMQC, FT-IR, and HRMS techniques (Figure S1-S12).

In the FT-IR spectra, NH stretching vibrations of **5** were observed at 3399 cm^{-1} and 3237 cm^{-1}, while NH stretching vibrations of **6** were observed at 3376 cm^{-1} and 3236 cm^{-1}. Aromatic C-H vibration band of **5** and **6** was observed at 3081 cm^{-1} and 3049 cm^{-1}, respectively, while vibration bands of the aliphatic C-H of **5** and **6** were assigned in the range of 2919–2850 cm^{-1} and 2924–2849 cm^{-1}, respectively. For **5** and **6**, the amide C=O vibration band was observed at 1668 cm^{-1}, while the C–O vibration band was observed at 1250 and 1260 cm^{-1}, respectively. In addition, vibration band of the C=S of compounds **5** and **6** was assigned at 1345 and 1346 cm^{-1}, respectively.

The bis-acyl thioureas **5**, **6** were characterized using ^{1}H and ^{13}C NMR, COSY, DEPT, and HMQC spectra (Figure S1-S12). The C(O)N*H*C(S) protons signal of **5** and **6** were observed as a singlet at 11.67 ppm and 11.73 ppm, respectively. Moreover, the other NH proton signal was observed as a triplet at 10.74 ppm for both **5** and **6**. Aromatic protons of **5** were observed in the range of 8.31–8.11 ppm, while aromatic protons of **6** were observed in the range of 8.73–7.78 ppm. In the ^{13}C NMR spectra of **5**, the thiocarbonyl and carbonyl carbon atoms peaks were observed at 179.6 ppm and 166.5 ppm, respectively, while the thiocarbonyl and carbonyl carbon atoms peaks of **6** were observed at 179.7 ppm and 166.1 ppm, respectively. All of the proton and carbon atoms peaks on the ^{1}H and ^{13}C NMR spectra, respectively, were assigned by using COSY, DEPT, and HMQC spectra.
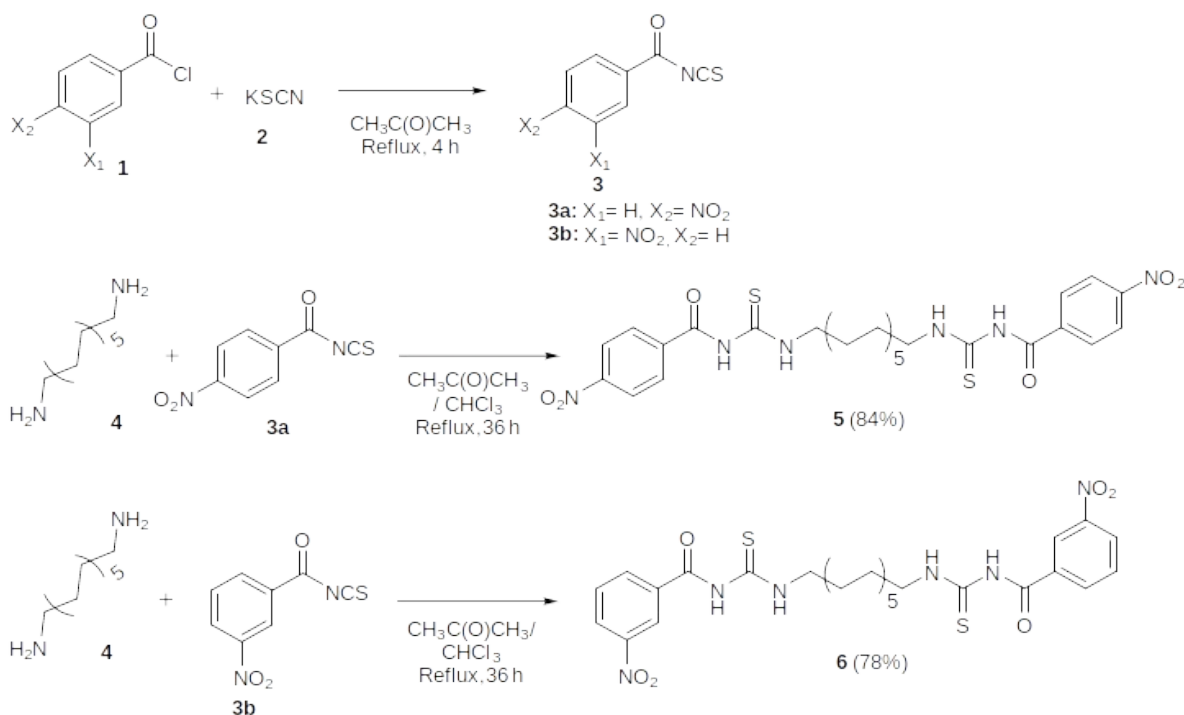
Scheme 1: Synthesis of the bis-acyl thioureas **5**, **6**.

3.2. Acid Dissociation Constants

The pK_a values of bis-acyl thioureas **5** and **6** were determined potentiometrically and spectrophotometrically in a 50% (v/v) DMSO–water hydro-organic solvent system in the presence of 0.1 mol·L^{-1} ionic strength of NaCl and in the acidic medium at 25.0±0.1 °C (**Table 1**). As a result of the calculations of pK_a values with HYPERQUAD from the obtained potentiometric data, two different pK_a values 7.06±0.13, and 12.11±0.06 were determined for **5**, while 6.94±0.11 and 11.17±0.06 were determined for **6** (Table 1). Furthermore, as a result of the calculations of pK_a values with HypSpec from the obtained spectrophotometric data, three different pK_a values as 3.56±0.08, 7.11±0.08, and 12.30±0.08 were determined for **5**, while 3.87±0.01, 7.05±0.01, and 11.82±0.02 were determined for **6** (Table 1).

In studies on the determination of pK_a values of acyl thiourea derivative compounds, potentiometrically, one pK_a value in the range of 9.82–10.19 for each of the benzoylthiourea derivatives in 75:25 (v/v) dioxane–water was reported by Schröder et al. (65). In addition, for each 5,5-diphenylpyrrolidine N-aroylthiourea compound in 30:70 (v/v) acetonitrile–water, potentiometrically two pK_a values, which were in the range of 6.96±0.03 to 7.84±0.04 associated with enol and in the range of 8.29±0.02 to 9.94±0.08 associated with enthiol groups, were reported (66). In other study, for each pyrrolidine N-aroylthioureas in 25:75 (v/v) DMSO–water, potentiometrically two pK_a values, which were in the range of 5.85±0.08 to 6.06±0.06 associated with enol, in the range of 8.37±0.05 to 8.87±0.05 associated with enthiol groups, and in the range of 10.11±0.03 to 11.62±0.03 associated with NH, were reported (67). The synthesized bis-acyl thiourea derivative compounds potentially have eight different pK_a values, the pK_a values of the symmetrical same groups are expected to be very close to each other, and their experimental determination is difficult. The pK_a values of four NH groups, together with two enols and enthiols, can be expected due to protonation in the acidic medium. It can be said that the pK_{a2} value determined as potentiometrically 7.06±0.13 and 6.94±0.11 and spectrophotometrically 7.11±0.08 and 7.05±0.01, respectively for compounds **5** and **6** may be related to the enthiol group in the structure. Similarly, it can be said that the pK_{a3} value determined as potentiometrically 12.11±0.06 and 11.17±0.06 and spectrophotometrically 12.30±0.08 and 11.82±0.02, respectively for compounds **5** and **6** may be related to the NH. It can be said that the pK_{a1} value, which could not be determined potentiometrically for compounds **5** and **6**, but determined as 3.56±0.08 and 3.87±0.01 spectrophotometrically, respectively, may be related to the enol group in the structure. It can be said that the fact that NO_2, which is the electron-withdrawing group, is attached to the phenyl ring increases the acidity of the enol group significantly. Furthermore, when the NO_2 group is attached to the aromatic ring in the para position instead of the meta position, it is seen that the pK_{a1} value decreases, while the pK_{a2} and pK_{a3} values decrease.

Table 1. The Potentiometric and spectrophotometric pK_a values of bis-acyl thioureas **5**, **6** (25.0 ± 0.1 °C, I = 0.1 mol·L^{-1} NaCl, 50% (v/v) DMSO-water)

Ligand		Spectrophotometric pK_a	Potentiometric pK_a
5	pK_{a1}	3.56±0.08	-
	pK_{a2}	7.11±0.08	7.06±0.13
	pK_{a3}	12.30±0.08	12.11±0.06
6	pK_{a1}	3.87±0.01	-
	pK_{a2}	7.05±0.01	6.94±0.11
	pK_{a3}	11.82±0.02	11.17±0.06

While three species formulated as LH_3 ($C_{28}H_{39}N_6O_6S_2^{3+}$), LH_2 ($C_{28}H_{38}N_6O_6S_2^{2+}$), and LH ($C_{28}H_{37}N_6O_6S_2^{+}$) were determined in the calculations performed using the HypSpec program from the spectrophotometric data, two species formulated as LH_2 and LH were determined in the calculations performed using the HYPERQUAD program in the potentiometric data. Deprotonation equilibrium for the ligands is shown in Eq. (1) and deprotonation constants in Eq. (2), omitting charges for simplicity (68). The potentiometric and spectrophotometric distribution curves of bis-acyl thioureas 5, 6 in a 50:50 (v/v) DMSO–water mixture are given in Figure 1.

$$LH_n \rightleftharpoons LH_{n-1}+H \qquad \text{(Eq. 1)}$$
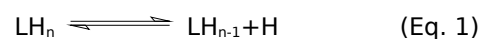
$$K_n = [LH_{n-1}][H]/[LH_n] \qquad \text{(Eq. 2)}$$
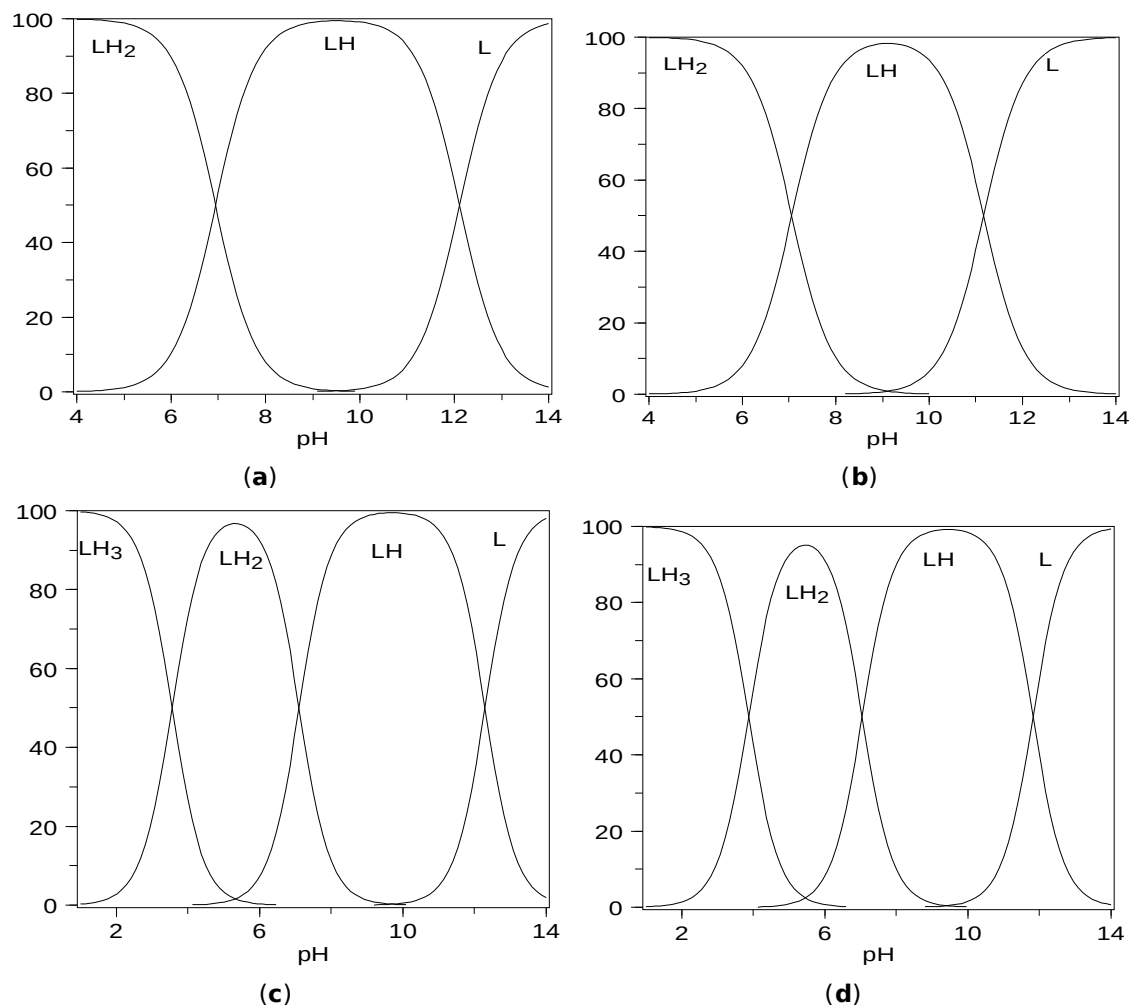
Figure 1: Potentiometric distribution curves [(a) **5**, (b) **6**] and spectrophotometric distribution curves [(c) **5**, (d) **6**] of **5** and **6** (50% (v/v) DMSO-water, 25.0±0.1 °C, I = 0.1 mol·L^{-1} by NaCl).

4. CONCLUSION

The synthesis and characterization of bis-acyl thiourea derivatives **5**, **6**, which may have potential bioactivity and chemosensor properties as well as can be ligands for the coordination of metal ions, were demonstrated. In addition, pK_a values, which carry critical information for future studies on such compounds, were calculated with HYPERQUAD and HypSpec programs using potentiometric and spectrophotometric titration data, respectively.

5. ACKNOWLEDGMENTS

6. REFERENCES

1.   Muhammad M, Khan S, Shehzadi SA, Gul Z, Al-Saidi HM, Waheed Kamran A, Alhumaydhi FA. Recent advances in colorimetric and fluorescent chemosensors based on thiourea derivatives for metallic cations: A review. Dye Pigment. 2022 Sep;205:110477. Available from: <URL>.

2.   Nural Y, Karasu E, Keleş E, Aydıner B, Seferoğlu N, Efeoğlu Ç, Şahin E, Seferoğlu Z. Synthesis of novel acylthioureas bearing naphthoquinone moiety as dual sensor for high-performance naked-eye colorimetric and fluorescence detection of CN− and F− ions and its application in water and food samples. Dye Pigment. 2022 Feb;198:110006. Available from: <URL>.

3.   Mitrea DG, Cîrcu V. Synthesis and characterization of novel acylthiourea compounds used in ions recognition and sensing in organic media. Spectrochim Acta Part A Mol Biomol Spectrosc. 2021 Sep;258:119860. Available from: <URL>.

4.   Khan E, Khan S, Gul Z, Muhammad M. Medicinal Importance, Coordination Chemistry with Selected Metals (Cu, Ag, Au) and Chemosensing of Thiourea Derivatives. A Review. Crit Rev Anal Chem. 2020 Jun;51(8):1–23. Available from: <URL>.

5.   Gemili M, Nural Y, Keleş E, Aydıner B, Seferoğlu N, Şahin E, Sarı H, Seferoğlu Z. Novel 1,4-naphthoquinone N-aroylthioureas: Syntheses, crystal structure, anion recognition properties, DFT studies and determination of acid dissociation constants. J Mol Liq. 2018 Nov;269:920–32. Available from: <URL>.

6.   Huang X, Cao X, Wang W, Zhong H, Cao ZF. Investigation of removal of Ag(I) from aqueous solution by a novel chelating resin containing acyl and thiourea groups. J Dispers Sci Technol. 2019 Apr;40(4):477–86. Available from: <URL>.

7.   Huang X, Cao X, Wang W, Zhong H, Cao Z. Preparation of a novel resin with acyl and thiourea groups and its properties for Cu(II) removal from aqueous solution. J Environ Manage. 2017 Dec;204:264–71. Available from: <URL>.

8.   Zahra U, Saeed A, Abdul Fattah T, Flörke U, Erben MF. Recent trends in chemistry, structure, and various applications of 1-acyl-3-substituted thioureas: a detailed review. RSC Adv. 2022;12(20):12710–45. Available from: <URL>.

9.   Saeed A, Mustafa MN, Zain-ul-Abideen M, Shabir G, Erben MF, Flörke U. Current developments in chemistry, coordination, structure and biological aspects of 1-(acyl/aroyl)-3- (substituted)thioureas: advances Continue. J Sulfur Chem. 2019 May;40(3):312–50. Available from: <URL>.

10.   Nural Y, Gemili M, Seferoglu N, Sahin E, Ulger M, Sari H. Synthesis, crystal structure, DFT studies, acid dissociation constant, and antimicrobial activity of methyl 2-(4-chlorophenyl)-7a-((4-chlorophenyl)carbamothioyl)-1-oxo-5,5-diphenyl-3-thioxo-hexahydro-1H-pyrrolo[1,2-e]imidazole-6-carboxylate. J Mol Struct. 2018 May;1160:375–82. Available from: <URL>.

11.   Nural Y, Gemili M, Yabalak E, Coen LM De, Ulger M. Green synthesis of highly functionalized octahydropyrrolo[3,4-c]pyrrole derivatives using subcritical water, and their anti(myco)bacterial and antifungal activity. ARKIVOC. 2018 Jun;2018(5):51–64. Available from: <URL>.

12.   Arslan B, Binzet G. Synthesis, crystal structure analysis, DFT calculations, antioxidant and antimicrobial activity of N,N-di-2,4-dimethoxybenzyl-N'-2-nitrobenzoylthiourea. J Mol Struct. 2022 Nov;1267:133579. Available from: <URL>.

13.   Erşen D, Ülger M, Mangelinckx S, Gemili M, Şahin E, Nural Y. Synthesis and anti(myco)bacterial activity of novel 5,5-diphenylpyrrolidine N-aroylthiourea derivatives and a functionalized hexahydro-1H-pyrrolo[1,2-c]imidazole. Med Chem Res. 2017 Sep;26(9):2152–60. Available from: <URL>.

14.   Döndaş HA, Nural Y, Duran N, Kilner C. Synthesis, crystal structure and antifungal/antibacterial activity of some novel highly functionalized benzoylaminocarbothioyl pyrrolidines. Turkish J Chem. 2006;30(5):573–83. Available from: <URL>.

15.   Wang H, Zhai ZW, Shi YX, Tan CX, Weng JQ, Han L, Li BJ, Liu XH. Novel Trifluoromethylpyrazole Acyl Thiourea Derivatives: Synthesis, Antifungal Activity and Docking Study. Lett Drug Des Discov. 2019 Jun;16(7):785–91. Available from: <URL>.

16.   Antypenko L, Meyer F, Kholodniak O, Sadykova Z, Jirásková T, Troianova A, Buhaiova V, Cao S, Kovalenko S, Garbe LA, Steffens KG. Novel acyl thiourea derivatives: Synthesis, antifungal activity, gene toxicity, drug-like and molecular docking screening. Arch Pharm (Weinheim). 2019 Feb;352(2):1800275. Available from: <URL>.

17.   Kalaiyarasi A, Haribabu J, Gayathri D, Gomathi K, Bhuvanesh NSP, Karvembu R, Biju VM. Chemosensing, molecular docking and antioxidant studies of 8-aminoquinoline appended acylthiourea derivatives. J Mol Struct. 2019 Jun;1185:450–60. Available from: <URL>.

18.   Arshad N, Saeed A, Perveen F, Ujan R, Farooqi SI, Ali Channar P, Shabir G, El-Seedi HR, Javed A, Yamin M, Bolte M, Hökelek T. Synthesis, X-ray, Hirshfeld surface analysis, exploration of DNA binding, urease enzyme inhibition and anticancer activities of novel adamantane-naphthyl thiourea conjugate. Bioorg Chem. 2021 Apr;109:104707. Available from: <URL>.

19.   Zahra U, Zaib S, Saeed A, Rehman M ur, Shabir G, Alsaab HO, Khan I. New acetylphenol-based acyl thioureas broaden the scope of drug candidates for urease inhibition: synthesis, in vitro screening and in silico analysis. Int J Biol Macromol. 2022 Feb;198:157–67. Available from: <URL>.

20.   Efeoglu C, Yetkin D, Nural Y, Ece A, Seferoğlu Z, Ayaz F. Novel urea-thiourea hybrids bearing 1,4-naphthoquinone moiety: Anti-inflammatory activity on mammalian macrophages by regulating intracellular PI3K pathway, and molecular docking study. J Mol Struct. 2022 Sep;1264:133284. Available from: <URL>.

21.   Ahmed A, Shafique I, Saeed A, Shabir G, Saleem A, Taslimi P, Taskin Tok T, Kirici M, Üç EM, Hashmi MZ. Nimesulide linked acyl thioureas potent carbonic anhydrase I, II and α-glucosidase inhibitors: Design, synthesis and molecular docking studies. Eur J Med Chem Reports. 2022 Dec;6:100082. Available from: <URL>.

22.   Ertano BY, Demir Y, Nural Y, Erdoğan O. Investigation of The Effect of Acylthiourea Derivatives on Diabetes-Associated Enzymes. ChemistrySelect. 2022 Dec;7(46). Available from: <URL>.

23.   Mustafa MN, Saeed A, Channar PA, Larik FA, Zain-ul abideen M, Shabir G, Abbas Q, Hassan M, Raza H, Seo SY. Synthesis, molecular docking and kinetic studies of novel quinolinyl based acyl thioureas as mushroom tyrosinase inhibitors and free radical scavengers. Bioorg Chem. 2019 Sep;90:103063. Available from: <URL>.

24.   Al-Abbasi AA, Tahir MIM, Kayed SF, Kassim MB. Synthesis, characterisation and biological activities of mixed ligand oxovanadium (IV) complexes derived from N , N -diethyl- N ´- para - substituted-benzoylthiourea and hydrotris(3,5-dimethylpyrazolyl)borate. Appl Organomet Chem. 2022 Apr;36(4). Available from: <URL>.

25.   Oyeka EE, Babahan I, Eboma B, Ifeanyieze KJ, Okpareke OC, Coban EP, Özmen A, Coban B, Aksel M, Özdemir N, Groutso TV, Ayogu JI, Yildiz U, Dinçer Bilgin M, Halil Biyik H, Schrage BR, Ziegler CJ, Asegbeloyin JN. Biologically active acylthioureas and their Ni(II) and Cu(II) Complexes: Structural, spectroscopic, anti-proliferative, nucleolytic and antimicrobial studies. Inorganica Chim Acta. 2021 Dec;528:120590. Available from: <URL>.

26.   Le CD, Pham CT, Nguyen HH. Zinc(II) {2}-metallacoronates and {2}-metallacryptates based on dipicolinoylbis(N,N-diethylthiourea): Structures and biological activities. Polyhedron. 2019 Nov;173:114143. Available from: <URL>.

27.   Alharbi W. Advancement and recent trends in seeking less toxic and more active anti-cancer drugs: Insights into thiourea based molecules. Main Gr Chem. 2022 Sep;21(3):885–901. Available from: <URL>.

28.   Al-Riyahee A, Murad D, Shenta A. Electrochemical Studies Of Novel 3,4-Dichloro-N-((5-ChloroPyridin-2-yl)Carbamothioyl)Benzamide Based On Its Complexes With Copper(II), Cobalt(II), Nickel(II) and Zinc(II) ions. Egypt J Chem. 2021 Apr;64(8):4323–41. Available from: <URL>.

29.   Ghazal K, Shoaib S, Khan M, Khan S, Rauf MK, Khan N, Badshah A, Tahir MN, Ali I, Rehman A ur. Synthesis, characterization, X-ray diffraction study, in-vitro cytotoxicity, antibacterial and antifungal activities of nickel(II) and copper(II) complexes with acyl thiourea ligand. J Mol Struct. 2019 Feb;1177:124–30. Available from: <URL>.

30.   Gemili M, Sari H, Ulger M, Sahin E, Nural Y. Pt(II) and Ni(II) complexes of octahydropyrrolo[3,4-c]pyrrole N-benzoylthiourea derivatives: Synthesis, characterization, physical parameters and biological activity. Inorganica Chim Acta. 2017 Jul;463:88–96. Available from: <URL>.

31.   Zhang YM, Wei TB, Xian L, Gao LM. An Efficient Synthesis of Polymethylene-Bis-Aroyl Thiourea Derivatives Under The Condition of Phase-Transfer Catalysis. Phosphorus Sulfur Silicon Relat Elem. 2004 Oct;179(10):2007–13. Available from: <URL>.

32.   Kurt G, Mercimek B. Synthesis and Characterization of N,N'-(propane-1,2 diyldicarbamothioyl)dibenzamide. Molbank. 2008 Nov;2008(3):M578. Available from: <URL>.

33.   Abd Halim AN, Ngaini Z. Synthesis and characterization of halogenated bis(acylthiourea) derivatives and their antibacterial activities. Phosphorus Sulfur Silicon Relat Elem. 2017 Sep;192(9):1012–7. Available from: <URL>.

34.   Abd Halim AN, Ngaini Z. Synthesis and Bacteriostatic Activities of Bis(thiourea) Derivatives with Variable Chain Length. J Chem. 2016;2016:1–7. Available from: <URL>.

35.   Kurt G, Sevgi F, Mercimek B. Synthesis, characterization, and antimicrobial activity of new benzoylthiourea ligands. Chem Pap. 2009 Jan;63(5). Available from: <URL>.

36.   Duan XE, Li R, Tong HB, Li YQ, Bai SD, Guo YJ, Liu DS. Synthesis and structural characterization of electrochemically reversible bisferrocenes containing bis(acyl-thiourea)s: enantiomers and

conformers. New J Chem. 2017;41(9):3333–43. Available from: <URL>.

37. Károlyi BI, Bősze S, Orbán E, Sohár P, Drahos L, Gál E, Csámpai A. Acylated mono-, bis- and tris-Cinchona-Based Amines Containing Ferrocene or Organic Residues: Synthesis, Structure and in Vitro Antitumor Activity on Selected Human Cancer Cell Lines. Molecules. 2012 Feb;17(3):2316–29. Available from: <URL>.

38. Arafa WAA, Ghoneim AA, Mourad AK. N -Naphthoyl Thiourea Derivatives: An Efficient Ultrasonic-Assisted Synthesis, Reaction, and In Vitro Anticancer Evaluations. ACS Omega. 2022 Feb;7(7):6210–22. Available from: <URL>.

39. Maalik A, Hameed S, Bhatti HA, Rauf A, Bukhari SM, Fatima N, Rafique H, Mughal EU, Mumtaz A. Synthesis and Biological Screening of N,N'-bis Disubstituted Adipic Acid Thioureas. Curr Pharm Anal. 2018 Sep;14(6):618–21. Available from: <URL>.

40. Patujo J, Azeem M, Khan M, Muhammad H, Raheel A, Fatima S, Mirza B, Hussain Z, Badshah A. Assessing the biological potential of new symmetrical ferrocene based bisthiourea analogues. Bioorg Chem. 2021 Jan;106:104180. Available from: <URL>.

41. Mumtaz A, Saeed K, Mahmood A, Zaib S, Saeed A, Pelletier J, Sévigny J, Iqbal J. Bisthioureas of pimelic acid and 4-methylsalicylic acid derivatives as selective inhibitors of tissue-nonspecific alkaline phosphatase (TNAP) and intestinal alkaline phosphatase (IAP): Synthesis and molecular docking studies. Bioorg Chem. 2020 Aug;101:103996. Available from: <URL>.

42. Ujan R, Channar PA, Bahadur A, Abbas Q, Shah M, Rashid SG, Iqbal S, Saeed A, Abd-Rabboh HSM, Raza H, Hassan M, Siyal AN, Mahesar PA, Lal B, Channar KA, Khan BA, Nawaz M, Rajoka MSR, et al. Synthesis, kinetics and biological assay of some novel aryl bis-thioureas: A potential drug candidates for Alzheimer's disease. J Mol Struct. 2021 Dec;1246:131136. Available from: <URL>.

43. Koch KR, Hallale O, Bourne SA, Miller J, Bacsa J. Self-assembly of 2:2 metallomacrocyclic complexes of NiII and PdII with 3,3,3′,3′-tetraalkyl-1,1′-isophthaloylbis(thioureas). Crystal and molecular structures of cis-[Pd(L2-S,O)]2 and the adducts of the corresponding NiII complexes: [Ni(L1-S,O)(pyridine)2. J Mol Struct. 2001 Apr;561(1–3):185–96. Available from: <URL>.

44. Schwade VD, Kirsten L, Hagenbach A, Schulz Lang E, Abram U. Indium(III), lead(II), gold(I) and copper(II) complexes with isophthaloylbis(thiourea) ligands. Polyhedron. 2013 May;55:155–61. Available from: <URL>.

45. Nkabyo HA, Barnard I, Koch KR, Luckay RC. Recent advances in the coordination and supramolecular chemistry of monopodal and bipodal acylthiourea-based ligands. Coord Chem Rev. 2021 Jan;427:213588. Available from: <URL>.

46. Selvakumaran N, Bhuvanesh NSP, Karvembu R. Self-assembled Cu (II) and Ni (II) metallamacrocycles formed from 3, 3, 3′, 3′-tetrabenzyl-1, 1′-aroylbis (thiourea) ligands: DNA and protein binding studies, and cytotoxicity of trinuclear complexes. Dalt Trans. 2014;43(43):16395–410. Available from: <URL>.

47. Razak NHA, Tan LL, Hasbullah SA, Heng LY. Reflectance chemosensor based on bis-thiourea derivative as ionophore for copper(II) ion detection. Microchem J. 2020 Mar;153:104460. Available from: <URL>.

48. Hamedan NA, Hasan S, Zaki HM, Alias NZ. Colorimetric chemosensor of symmetrical benzoylthiourea derivatives as for detection of Cu 2+ in aqueous solution. IOP Conf Ser Mater Sci Eng. 2017 Feb;172:012038. Available from: <URL>.

49. Turanov AN, Karandashev VK, Proshin AN. Extraction properties of hexamethylene-1,6-bis[(N-benzoyl)thiourea] in hydrochloric acid solutions. Russ J Inorg Chem. 2006 Dec;51(12):1968–72. Available from: <URL>.

50. Manallack DT. The acid–base profile of a contemporary set of drugs: implications for drug discovery. SAR QSAR Environ Res. 2009 Oct;20(7–8):611–55. Available from: <URL>.

51. Alongi KS, Shields GC. Theoretical Calculations of Acid Dissociation Constants: A Review Article. In: Wheeler RABTAR in CC, editor. Elsevier; 2010. p. 113–38. Available from: <URL>.

52. Nural Y, Gemili M, Ulger M, Sari H, De Coen LM, Sahin E. Synthesis, antimicrobial activity and acid dissociation constants of methyl 5,5-diphenyl-1-(thiazol-2-yl)pyrrolidine-2-carboxylate derivati-ves. Bioorg Med Chem Lett. 2018 Mar;28(5):942–6. Available from: <URL>.

53.   Nural Y, Ozdemir S, Doluca O, Demir B, Yalcin MS, Atabey H, Kanat B, Erat S, Sari H, Seferoglu Z. Synthesis, biological properties, and acid dissociation constant of novel naphthoquinone–triazole hybrids. Bioorg Chem. 2020 Dec;105:104441. Available from: <URL>.

54.   Nural Y, Ozdemir S, Yalcin MS, Demir B, Atabey H, Seferoglu Z, Ece A. New bis- and tetrakis-1,2,3-triazole derivatives: Synthesis, DNA cleavage, molecular docking, antimicrobial, antioxidant activity and acid dissociation constants. Bioorg Med Chem Lett. 2022 Jan;55:128453. Available from: <URL>.

55.   Takács-Novák K, Tam KY. Multiwavelength spectrophotometric determination of acid dissociation constants: Part V: microconstants and tautomeric ratios of diprotic amphoteric drugs. Journal of pharmaceutical and biomedical analysis, 2000 Jan;21(6):1171-1182. Available from: <URL>.

56.   Huang J, Yuan F, Zeng G, Li X, Gu Y, Sh, L, Liu W, Shi, Y. Influence of pH on heavy metal speciation and removal from wastewater using micellar-enhanced ultrafiltration. Chemosphere, 2017 April;173:199-206. Available from: <URL>.

57.   İnci D. Equilibrıum studies on Ni(II) and Cu(II) complexes with 4,7-dİmethyl-1,10-phenanthrolİne and acidic amıno acids in aqueous solution. J Turkish Chem Soc Sect A Chem. 2020 Oct;7(3):775–88. Available from: <URL>.

58.   Türkoğlu G, Berber H, Özkütük M. Spectrophotometric determination of the acidity dissociation constants of symmetric Schiff base derivatives. Gazi Univ J Sci. 2014;27(2):771–83. Available from: <URL>.

59.   Berber H, Ateş NA, Özkütük MY. Synthesis, Characterization And Spectroscoic Studies On Azo-Hydrazone Tautomerism And Acidity Constants Of Certain 4-(Phenyldıazenyl) Benzene-1,3-Diol Derivatives. Anadolu Üniversitesi Bilim Ve Teknol Derg - B Teor Bilim. 2016 Mar;4(1). Available from: <URL>.

60.   Kim H s., Chung TD, Kim H. Voltammetric determination of the pKa of various acids in polar aprotic solvents using 1,4-benzoquinone. J Electroanal Chem. 2001 Feb;498(1–2):209–15. Available from: <URL>.

61.   Doğan A, Başçı NE, Polat MB. Spectrophotometry, potentiometry and HPLC in determination of acidity constant for Cabergoline

and Tadalafil. J Res Pharm. 2019 Feb;23(2):177–86. Available from: <URL>.

62.   Koçak E, Doğan A, Altınöz S, Başçı NE, Çelebier M. Investigating the physicochemical properties of phenazopyridine hydrochloride using high-performance liquid chromatography and UV-Visible spectrophotometry. J Res Pharm. 2018 Jul;22(1):198–205. Available from: <URL>.

63.   Mumcu A, Küçükbay H. Determination of p K a values of some novel benzimidazole salts by using a new approach with 1 H NMR spectroscopy. Magn Reson Chem. 2015 Dec;53(12):1024–30. Available from: <URL>.

64.   Gans P, Sabatini A, Vacca A. Investigation of equilibria in solution. Determination of equilibrium constants with the HYPERQUAD suite of programs. Talanta. 1996 Oct;43(10):1739–53. Available from: <URL>.

65.   Schröder B, Schröder U, Dietze F, Beyer L. Protonation, complexation and thermochemical behaviour of N-benzoylthiocarbamic-O-alkylester anions in solution. Inorg Chem Commun. 2001 Aug;4(8):398–401. Available from: <URL>.

66.   Ersen D, Gemili M, Sarı H, Nural Y. Acid Dissociation Constants of 5,5-Diphenylpyrrolidine N-Aroylthioureas and Stability Constants of their Pt(II) and Ni(II) Complexes in Acetonitrile-Water Hydroorganic Solvent. Celal Bayar Üniversitesi Fen Bilim Derg. 2017 Mar;3(1):125–38. Available from: <URL>.

67.   Nural Y. Synthesis and Determination of Acid Dissociation Constants in Dimethyl Sulfoxide–Water Hydroorganic Solvent of 5,5-Diphenylpyrrolidine N-Aroylthiourea Derivatives. J Turkish Chem Soc Sect A Chem. 2017 Aug;841–54. Available from: <URL>.

68.   Atabey H, Sari H, Al-Obaidi FN. Protonation Equilibria of Carminic Acid and Stability Constants of Its Complexes with Some Divalent Metal Ions in Aqueous Solution. J Solution Chem. 2012 Jun;41(5):793–803. Available from: <URL>.

REVIEW ARTICLE

Differences in Heavy Metals Adsorption on Natural, Modified, and Synthetic Zeolites-A Review

Sebghatullah MUDABER [1] 🆔**, Jenaidullah BATUR** [1*] 🆔

[1]Beijing Key Laboratory for Green Catalysis and Separation and Department of Chemical Engineering, Beijing University of Technology, Beijing 100124, P. R. China

Abstract: This paper presents a comprehensive study of the differences in heavy metal adsorption on natural, modified, and synthetic zeolites. Heavy metal treatment and adsorption are critical issues in today's modern world, and despite advancements in technology, they remain a global challenge. Industrial effluents are a major source of heavy metal pollutants, which have a severe impact on human health and the environment. Therefore, removing heavy metals from contaminated water and wastewater is a necessity. Adsorption is the most commonly used method for removing heavy metals from the environment due to its cost-effectiveness, design, and performance. Among various adsorbents, zeolites are currently considered a suitable method due to their cost-effectiveness, simplicity, and the varying ion-exchange capacity of natural zeolites worldwide for cations such as ammonium and heavy metal ions. The findings of this research could provide useful information for developing efficient and cost-effective methods for the removal of heavy metals from water and wastewater, thus addressing a critical global issue. The outcomes of this research contribute to promoting a green and healthy environment.

1. INTRODUCTION

Heavy metals are commonly defined according to their density; metals with a density higher than 5 $g.cm^{-3}$ are classified as heavy metals (1). According to latest research, it shows that Fe, Pb, Cu, Ni, Cd, and Cr, etc. as heavy metals are the most common pollutants found in industrial wastewater (2) and heavy metals pollution is indicated as one of the most serious problems facing humans and other organisms due to its accumulation in the living organism's and non-biodegradability (3,4). For instance, research on primates has indicated that exposure to lead results in significant behavioral and cognitive deficits like learning ability, memory, adaptability, impairments in activity, and increased distraction, and Pb is known for its high carcinogenic and mutagenic dominance (2,5). Arsenic accumulation in living organisms, including humans, causes skin cancer, and black foot disease (6), and chronic exposure to Cr may produce

several health issues (cancer, hepatic injury, and genetic defects) are reported (7). The recommended dietary intake of zinc, depending upon age and sex, is between 4 and 15 $mg.day^{-1}$. However, intake of excessively large doses of such elements by human, leads to severe damages to the health. Symptoms of zinc toxicity in humans include vomiting, dehydration, electrolyte imbalance, abdominal pain, dizziness, and lack of muscular coordination (8). Heavy metal contaminant exists in many industrial wastewaters, such as metal plating facilities, mining operations, nuclear powerhouse, fertilizer industries, paints and pigments, municipal and storm water run-off, battery and tannery industries (9). Heavy metal pollutants, especially metal ions such as (Fe^{3+}, Cr^{3+}, Cu^{2+}, and Pb^{2+}) are not disposable (10) and their stockpile in living organisms causing various infections that affect the brain nervous system, hematopoietic, and renal diseases. World Health Organization (WHO) recommends exceedingly low

maximal suitable concentrations for the harmful heavy metal cations in daily use drinking water, this recommendation has been welcomed by governments around the world (11). In our ecosystem, there are huge sources of heavy metals that flow with the wastewater streams like batteries, agriculture activities, electroplating, smelting, mining operations, paint, and pigments (4). Technological and industrial promotion is known for their generation of toxic remaining chemicals with the potential to originate numerous infections in the animals and human body. Noteworthiness, the toxic metals are classified among the most concerning compounds in the environment (12), hence to meet increasingly stringent environmental quality and clean life standards, they must be removed from the polluted streams (13). There are various treatment processes available in the literature for metal-polluted waste streams, such as coagulation, chemical precipitation, oxidation of heavy metals, solvent extraction, membrane filtration, electrolytic processes (14), ion exchange (11), precipitation (4), reverse osmosis (15), clotting disambiguation (4), flotation, flocculation (16), electrochemical treatment technologies (12), adsorption and photocatalytic degradation of heavy metals, among these techniques and methods, adsorption as a cost-effective technology, offers flexibility and facile operation and design (14) are frequently in use due it's efficient in removing organic and inorganic contaminants from aqueous environments (17). On the other hand, activated carbon is widely acknowledged as the primary adsorbent for various adsorption processes due to its remarkable properties such as high surface area and superior adsorption capacity. However, its relatively high cost and the requirement for periodic regeneration pose certain challenges. This has prompted the quest for alternative adsorbents that are readily available and cost-effective. As a result, researchers have been actively seeking new adsorbents to replace activated carbon. (18). Zeolites are widely used as adsorbents in the removal of hazardous substances, and as advanced additives or catalysts in construction due to their low cost and high efficiency (19). However, zeolites are considered one of the most prominent types of inorganic cationic exchangers due to their exceptional properties such as high ion exchange capacity, remarkable selectivity, and ability to adapt to various natural environments (2). Ion exchange process is especially used to remove heavy metals and elements leading to hardness

from water and wastewater (20).

This review presents a brief view of the mechanisms of heavy metal sorption on natural, modified, and synthetic zeolites. The major objectives were: Differences in heavy metals sorption on zeolites. Environmental implications of heavy metal removal. The studying of these objectives will provide valuable information about the use of zeolites to treat heavy metals in environmental pollution.

2. NATURAL, MODIFIED, AND SYNTHETIC ZEOLITES

Zeolites are crystalline aluminosilicates with a general formula of $A_{x/n} (SiO_2) (AlO_2)_x \cdot mH_2O$, where A represents a cation (21). These materials have attracted significant attention and have been extensively applied in the energy and environmental industries (22,23,20). As a result, fundamental research on their properties, such as ion exchange, adsorption, and catalysis, has become a key area of interest for the zeolite researchers in different application and synthesis research, such as green chemistry, materials science, green environmental science, and most commonly chemical engineering (24) to developed novel methods to overcome this issue. Highly dealuminated zeolites contain both mesopores and micropores (25), and the pores zeolites' dimensions provide size also suitable shape selectivity for the new guest molecules such as heavy metal ions. The micropores can restrict the diffusion rates of reactant and product molecules due to their configurational regime of diffusion of the zeolite molecules (26). Natural zeolites and synthetic zeolites, which are designated with specific letters that indicate Type A, X, Y, and ZSM, have been extensively studied (27).

The remarkable properties of natural zeolites and their modified forms have revolutionized environmental remediation processes, making them an indispensable tool in mitigating the harmful effects of pollution. These materials have been extensively studied by researchers for their remarkable adsorption capabilities, enabling them to capture a wide range of cations, anions, and molecular species. As a result, they have become highly versatile in various environmental remediation processes such as water and wastewater treatment, soil remediation, and aerial purification.
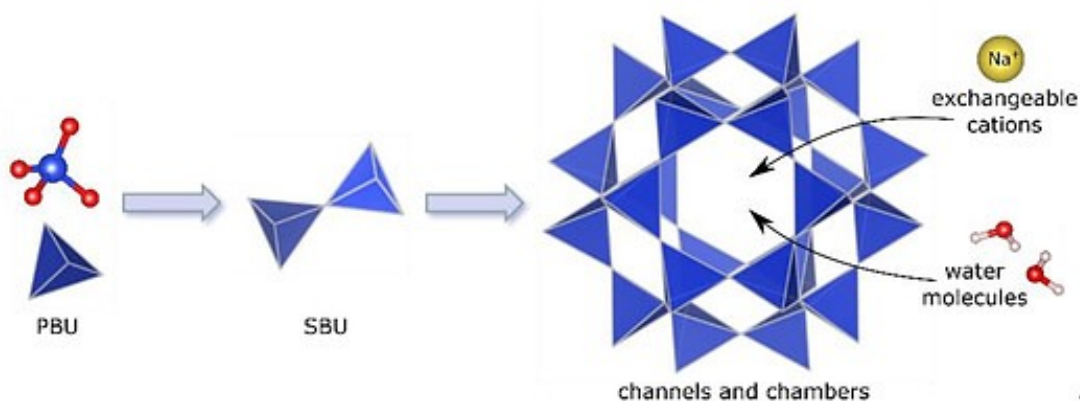
Figure 1: Schematic view of zeolite structure parched from ref (28).

Over the years, researchers have conducted numerous studies on the adsorption efficiencies of natural and synthetic zeolites, as well as their modified forms, in capturing various pollutants. These studies have mainly focused on removing heavy metal cations, including cadmium, lead, nickel, manganese, zinc, chromium, iron, and copper, as well as anionic species such as chromate and arsenate, and organic pollutants like volatile organic compounds (VOCs) such as benzene, toluene, ethyl benzene, and xylene. (24).

The modification of natural zeolites using heavy metals is a promising technique for enhancing their effectiveness in inorganic anion adsorption through surface precipitation. This approach involves the deposition of heavy metal ions onto the surface of natural zeolites to create an effective adsorbent material (29). The abundance of zeolite in nature, along with its low cost, stable structure even in acidic environments, and strong adsorption capacity, have made it an attractive option for industrial wastewater treatment (3, 30, 31). These desirable properties have led to an increase in interest in zeolites (3).

Natural crystalline aluminosilicate minerals include a class of materials named zeolites by the researcher, these natural zeolites materials like CP (clinoptilolite), phillipsite (32), and heulandite originating from alterations of glass-rich volcanic rocks structures that includes fresh or saline water in the molecules. There are also several synthetic and modified with different metal zeolites like ZSM-5, mordenite, and surfactant modified, also can be found alkaline-treated zeolites that can be designed and synthesized in the laboratory to obtain specific and acceptable properties in particular large surface areas with the different pore sizes to promote the application area and diversity (33). However, using natural zeolites, required an activation step to activate the metal side in the zeolite molecules. Natural zeolites show better properties than synthetic ones in commercial separation, it is maybe because synthetic zeolites will synthesize with special conditions and temperatures but natural zeolites form in natural conditions for long period (34).

Zeolite's three-dimensional structure is mainly constructed by $[SiO_4]^{4-}$ and $[AlO_4]^{5-}$ coordination polyhedra (2,3). Zeolites are fascinating minerals that possess unique properties due to their microporous crystalline structure. Their framework is based on repeated units of silicon-oxygen and aluminum-oxygen tetrahedra, and they contain exchangeable alkaline and alkaline-earth metal cations that maintain charge neutrality within the crystal lattice. This characteristic allows zeolites to selectively exchange cations with certain other cations in solutions, such as Pb, Cd, Zi, and Mn. The ion-sieving properties of zeolites are used in various commercial applications, as they can selectively exchange ionic species with diameters small enough to fit through the entry ports of the internal zeolite framework while excluding larger species. This unique feature is particularly useful in industries such as water purification and chemical manufacturing (1). The extensive variation in chemical composition among zeolites necessitates a dependable classification system that is based solely on structural considerations. Framework zeolites, in particular, are constructed from primary building units (TO$_4$ tetrahedra) that are linked together to form a three-dimensional network, with each oxygen atom being shared by two tetrahedra. This sharing coefficient generally ranges from 2 to slightly less than 2. While this process generates numerous potential theoretical networks, only a small number of complex structural units, known as secondary building units (SBUs), have thus far been identified in silicate frameworks. These SBUs consist of a limited number of tetrahedra, typically no more than 16, and have been recognized in only such frameworks (30).

ZSM-5 is a unique and versatile synthetic zeolite that has revolutionized the petroleum industry since its first synthesis in 1975 by Mobil Oil Company. Unlike other naturally occurring zeolites, ZSM-5 has a high silica content and a distinctive pore structure with two different pore systems, which makes it an excellent heterogeneous catalyst for hydrocarbon isomerization reactions. Its chemical formula, $Na_nAl_nSi_{96}-nO_{192} \cdot 16H_2O$, highlights its composition, where the ratio of aluminum to silicon atoms can

vary between 0 to 27. The pore system of ZSM-5 consists of zigzag and straight channels with a hydrophobic tendency, which makes it favorable for adsorbing non-polar molecules such as hydrocarbons. Furthermore, ZSM-5's hydrophobicity and pore size makes it an effective adsorbent for MTBE, a common gasoline additive. ZSM-5 in its raw or modified forms serves primarily as a catalyst and adsorbent, enabling it to find a wide range of applications in the chemical, petrochemical, and environmental industries (33).

CP is the most commonly occurring and abundant known natural zeolite, with significant reserves found in many sedimentary deposits worldwide (4, 33, 35). Its chemical composition is generally represented by the formula $Na_6[(AlO_2)_6(SiO_2)_{30}] \cdot 24H_2O$ (32,61), with a microporous crystal structure typical of alkali such as Na+K>Ca+Mg metals-rich HEU (heulandite) type zeolites with (Si/Al≥4) ratio. Clinoptilolite is also a member of heulandite zeolites that have many common orders, which consists of crystalline Al-silicates characterized by a cage-like microstructure contacted to the atoms by a tetrahedral geometry with three-dimensional type between SiO_4 and AlO_4

network, the order of the bonds is as follow: in this molecules, Si and Al's atoms are at the center of the molecules and oxygen atoms placed at the corners of the molecules of zeolite. The linkage between metals (Al and, Si) with oxygens has made basic tetrahedral geometry units linked through oxygen atoms to form a polyhedral network that constitutes secondary structures of the zeolites (35). Clinoptilolite possesses a two-dimensional channel system comprising three distinct channel types (33), as depicted in Figure 2.

Fe-modified zeolites have been found to exhibit a high capacity for adsorbing heavy metals in solution, effects by some factors: including pH, temperature, and metal concentrations (4). Clinoptilolite, due to its absorption capability for various pollutants, abundance, and relatively low cost, has emerged as an effective metal adsorbent for many water purification applications, especially in the field of removing heavy metals from industrial wastewater (14). Moreover, studies in the works of literature indicate that naturally availed zeolites, CP (clinoptilolite), possess lower adsorption capacities for toxic metals when compared to their synthetic counterparts (36).
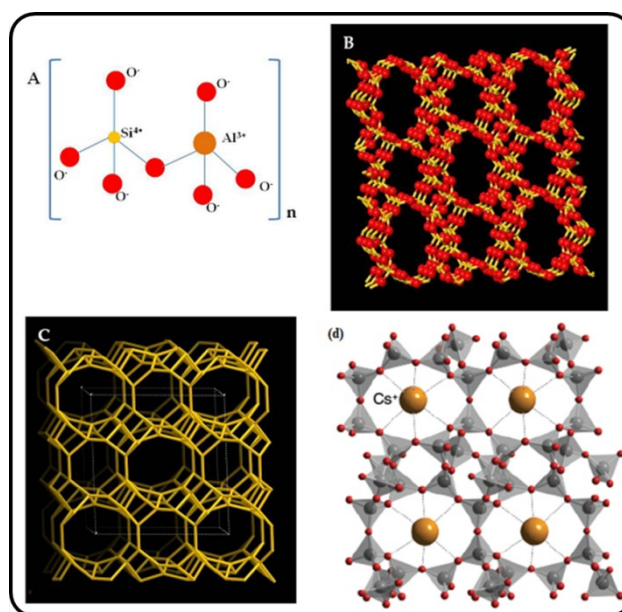
Figure 2: Simplified structure of the (a, b, and, c) (37), CP linked SiO4 tetrahedra and pores with metal cations (e.g., cesium, Cs+) available for ion-exchange (d) (38), that demonstrates the relationship between the trapped cesium ion and the framework.

Zeolites have a wide range of practical uses, including effective chemical sieves, water softeners, and adsorbents. Their unique structural characteristics and adsorbent properties make them particularly well-suited for these applications. The structural cavities and channels of zeolites are capable of hosting a variety of alkaline and alkaline earth cations and water molecules in different complexes. One of the most important applications of zeolites is the removal of heavy metals from drinking water and wastewater, which is typically achieved through a process called ion exchange. In this process, ions such as Na^+, K^+, and Ca^{2+} are

utilized to replace the heavy metal ions in the water. Toxic metals from the solution such as drinking water replace the ion metals that are available in the pores of the zeolite. For the ion exchange process to be successful, several factors must be taken into consideration. These include the concentration and properties of both cations and anions, the temperature and pH of the system, as well as the crystal structure of the zeolite itself. By carefully controlling these variables, we can optimize the ion exchange process and achieve the best possible results (4). To obtain and create hierarchical zeolites, it is important to interconnect

the inherent microspores with other pore systems that play complementary roles within the system. This can be achieved through various routes, such as post-synthesis modification, the use of soft templates in the starting gel, or the formation of composites with macro/mesoporous materials. By combining more than one strategy, it is possible to create macroporous monoliths with specific shapes and functional surfaces formed by the zeolite covering. This approach offers a powerful tool for tailoring the properties of zeolites to meet a wide range of industrial and scientific needs (12, 31).

Researchers have extensively studied the ability of naturally available and synthetic modified clays to conserve harmful chemicals and pathogenic bacteria at named clay surfaces. Zeolites differ from clays in that they typically occur in larger particle sizes, ranging in size from millimeters to greater. Additionally, unlike clays, zeolites do not exhibit shrink-swell behavior. This property makes them highly useful in a variety of applications, such as adsorbents, catalysts, and molecular sieves, where

stability and consistency are critical factors in their effectiveness. (15). Both naturally occurring and synthetic zeolites are highly effective in adsorbing heavy metal cations from contaminated water streams. These metals include but are not limited to Cu^{2+}, Cd^{2+}, Cr^{6+}, Zn^{2+}, Pb^{2+}, and Hg^{2+}. Zeolites can selectively adsorb these metals due to their unique structural characteristics and surface chemistry, making them valuable tools in environmental remediation efforts. They measured the theoretical MAC (maximum adsorption capacities) of zeolite for Cu^{2+}, Cd^{2+}, Cr^{6+}, Zn^{2+}, and Pb^{2+} in seawater to be 3.05, 1.12, 0.32, 13.10, and 6.11 $mg.g^{-1}$, respectively. The addition of zeolite at varying dosages (0.5, 2.0, and 4.0 g L^{-1}) has been found to effectively reduce the bioaccumulation of cadmium. The reduction rate was found to increase with the dosage administered. This demonstrates the potential of zeolites as a cost-effective and efficient solution for reducing the harmful effects of heavy metal bioaccumulation in a variety of environments (24).
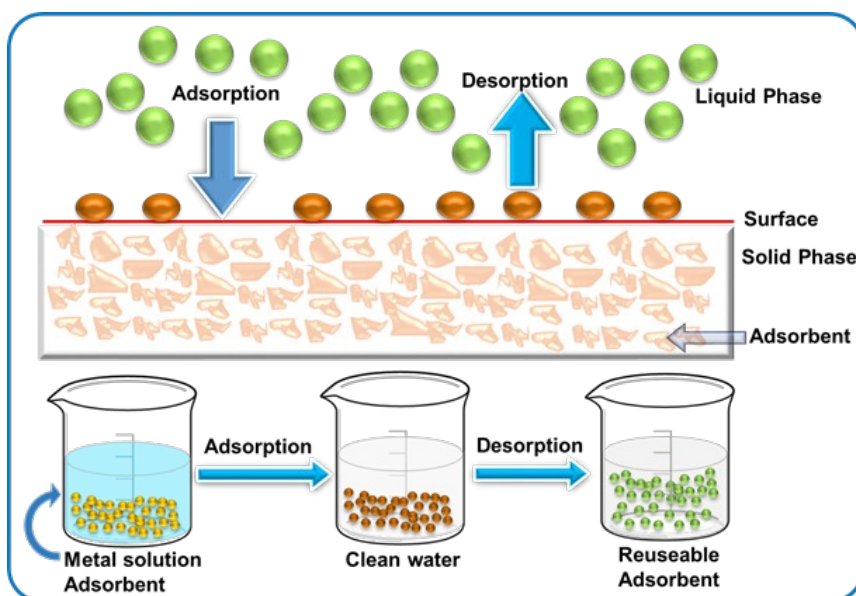
Figure 3: Schematic view of the mechanism of the metal ions adsorb–desorption process in wastewater.

Figure 4 demonstrates that the adsorption rate of NaCl-modified synthetic clinoptilolite for Pb^{2+} is minimally affected by pH, while the adsorption rates for Zn^{2+}, Cd^{2+}, and Cu^{2+} increase with increasing pH and adsorbent dosage. This is due to the high selectivity of clinoptilolite for Pb^{2+} over the other metal cations. At a pH of 2, NaCl-modified synthetic clinoptilolite has a low amount of adsorption for Zn^{2+}, Cd^{2+}, and Cu^{2+}, likely due to the low selectivity of clinoptilolite at low pH and the strong competition from H^+ ions. However, by decreasing the competition from H^+ at higher pH, the amount of adsorption significantly increases. In Figure 5, the removal efficiency of NaCl-modified synthetic clinoptilolite for Zn^{2+}, Pb^{2+}, Cd^{2+}, and Cu^{2+} is shown. The data indicate that the removal efficiency and amount of adsorption are determined by various

factors, such as theoretical adsorption capacity, selectivity, and solid-to-liquid ratio. A high solid-to-liquid ratio leads to higher removal efficiency but lower adsorption due to the increased amount of adsorbent. However, the solid-to-liquid ratio has a lesser effect on the adsorption behavior of clinoptilolite for Pb^{2+} due to its high selectivity. Overall, these results highlight the potential of NaCl-modified synthetic clinoptilolite as an effective adsorbent for removing heavy metals from contaminated water streams (11).

The ratio between Si and Al is the main and important parameter for the properties of zeolites, like hydrophilicity, and cation exchange capacity ph. Zeolites are a diverse group of materials that can be classified based on their Si/Al ratio. As the Si/Al ratio

decreases, zeolites tend to have higher acidity and hydrophobicity, but lower ion exchange capacity. In aqueous solutions, cation exchange occurs through the substitution of Si^{4+} by Al^{3+}, leading to negative charges on the zeolite surface. When these negative charges are balanced by metal ions such as Ni^{2+}, Pb^{2+}, Zn^{2+}, Mn^{2+}, and Cd^{2+} in wastewater, zeolites become effective adsorbents with high cation exchange capacity. In addition, zeolites can become acidic when a proton (H^+) is used to balance the material charge, and the acidity of zeolites is proportional to the Al content and related to the Si/Al ratio. As the Si/Al ratio increases in zeolites, the number of cations that can interact favorably with water decreases. This leads to a reduction in hydrophilicity, making zeolites less water-friendly. However, the isomorphic substitution of Si^{4+} by Al^{3+} offers the opportunity to modify zeolites through the introduction of cations. Metal ions and surfactants can be added to zeolites to enhance their properties and tailor them to specific applications. This modification process can increase the selectivity and efficiency of zeolites for various adsorption and catalytic reactions. Modified zeolites can also exhibit improved stability and durability under harsh conditions. These modifications can expand the range of applications for zeolites and enhance their potential for industrial and environmental applications (33).
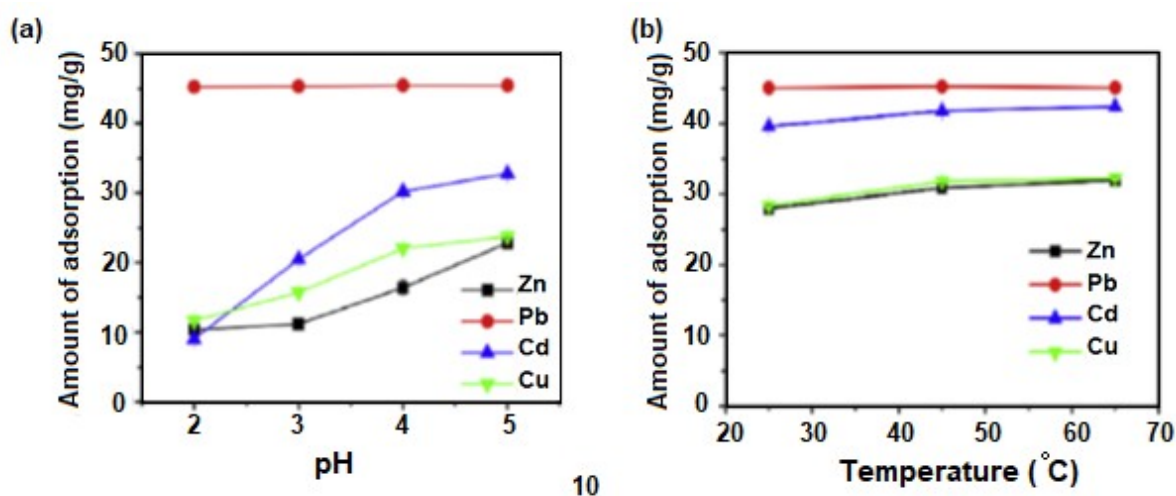
Figure 4: NaCl-modified synthetic-CP adsorption capacity for named metals ion as a function of pH(a) and temperature (b) (8).

Studies have been conducted on the adsorption behavior of four different metal ions, namely Pb^{2+}, Cu^{2+}, Cr^{6+}, and Cd^{2+}, on Fe_3O_4/mesoporous silica. The study showed that the pseudo-second-order model and Langmuir sorption isotherm were followed, with maximum adsorption capacities of 127.24, 125.80, 115.60, and 114.08 $mg.g^{-1}$ for Pb^{2+}, Cu^{2+}, Cr^{6+}, and Cd^{2+} metal ions, respectively. The results revealed that the binding capacity followed the order of $Pb^{2+}> Cu^{2+} > Cr^{6+} > Cd^{2+}$. In addition, the use of $Fe_3O_4/SiO_2/Zr$ Metal-Organic Frameworks showed promising results for the removal of Pb^{2+}, methyl orange, and methylene blue, with adsorption abilities of 102.2, 128, and 219 $mg.g^{-1}$, respectively. The maximum adsorption capacity of 248 $mg.g^{-1}$ was achieved at pH 10 when utilizing Fe_3O_4/silica (0.14:1 mass ratio) for the removal of methylene blue at an equilibrium time of 100 minutes and a temperature of 25 °C. Furthermore, mesoporous γ-Fe_2O_3/silica NCs showed a maximum adsorption capacity of 476 $mg.g^{-1}$. These results suggest that these materials could be effective adsorbents for the removal of heavy metals and dyes from wastewater. The results highlight the potential of Fe_3O_4/mesoporous silica and Fe_3O_4/silica for the removal of heavy metals and dyes from contaminated water. The high adsorption capacity and efficiency of these materials make them attractive candidates for use in wastewater treatment applications. However, further research is needed to investigate the performance of these materials under different operating conditions and in real-world scenarios. (36).

Table 1 and Table 2 summarize the heavy metal (Zn^{2+}, Pb^{2+}, Cd^{2+}, and Cu^{2+} Zn^{2+}, Pb^{2+}, Cd^{2+}, Cu^{2+}, $Ni^{2+,}$ and Cr^{3+}) maximum adsorption capacity in the natural, modified and synthetic zeolite. From the study of Tables 1 and 2, the reaction facilitated under acidic and neutral conditions that are obtained by using Nano Fe-Al zeolite the maximum adsorption capacity (MAC) of Cr (VI) metal ions collected the results show 44.74 $mg.g^{-1}$ at the pH of 3. On the other hand, Cr^{6+} ions removal efficiency at pH < 6 was extremely higher than Cr^{6+} ions removal efficiency at pH > 6, (5). Likewise, the maximum absorption capacity for Pb^{2+}, Cd^{2+}, Cu^{2+}, Ni^{2+}, Co^{2+}, $Mn^{2+,}$ and Cr^{3+} by using natural zeolite is in the following order 159.00 $mg.g^{-1}$, 33.07 $mg.g^{-1}$, 25.76 $mg.g^{-1}$, 2.08 $mg.g^{-1}$, 0.44 $mg.g^{-1}$, 4.00 $mg.g^{-1}$, 5.81

mg.g^{-1}. In the next step by using modified and synthetic zeolite maximum absorption capacity for Pb^{2+}, Cd^{2+}, Cu^{2+}, Ni^{2+}, Co^{2+}, and Cr^{3+} are in the following results were obtained: 228.00 mg.g^{-1}, 129.30 mg.g^{-1}, 101.70 mg.g^{-1}, 132.10 mg.g^{-1}, 41.47 mg.g^{-1}, 83.2 mg.g^{-1}.

It is of utmost importance to perform an in-depth analysis of the isotherm data to formulate a precise equation that effectively represents the results, which can then be utilized for design purposes. The study of adsorption isotherm necessitates the exploration of equilibrium models such as (M-Lan), (M-Fre), (M-D.K. R), and (M-Fre-Iso). The results obtained from the sorption isotherm of natural and modified zeolites are presented in Table 3. The findings reported in Table 3 demonstrate that the removal of Cr^{3+} from metal solutions by Brazilian natural zeolite was accomplished with a high degree of efficiency, achieving removal rates of approximately 96-100%. Additionally, the adsorption isotherms are in alignment with the Freundlich models. Furthermore, an investigation was conducted on the adsorption behavior of natural-CP Greece and synthetic (NaP1) zeolites in the removal of Cr^{3+}. The result was 90% and the adsorption isotherm of these zeolites can be modeled by the Langmuir equation. In the same way, Cd^{2+} removal by modified zeolite (Zeolite A and X) from kaolin was studied and the result was about 99% of the adsorption isotherms of these zeolites were consistent with the (M-Lan), (M-Fre), (M-D.K.R), models. In another study, the Cd^{2+}

removal from wastewater used for industrial application was investigated by applying Brazilian natural scolecite (84–59%), Kardjali natural zeolite (75–905), Greek-CP (90%), NaP1 from CFA (90%) and the above results were obtained. It should be noted that the adsorption isotherms of these zeolites can be modeled in the following order: Freundlich isotherm, Freundlich model, and Langmuir model.

Batch experimental data using zeolite A and X derived from kaolin as the adsorbent has been successfully explained by three adsorption isothermal models, namely (M-Lan), (M-Fre), and (M-D.K. R), for the removal of Cu^{2+}, Pb^{2+}, Ni^{2+}, and Zn^{2+} metals. In contrast, the isothermal data obtained from synthetic zeolite derived from CFA is fully compatible with the Langmuir model. Furthermore, for Cu^{2+} adsorption isothermal data, the Langmuir model with natural clinoptilolite sourced from Turkey, Greece, and Bulgaria is the most effective. Similarly, the adsorption isotherm data for Pb^{2+}, Ni^{2+}, and Zn^{2+} can be best represented by the Langmuir model with natural clinoptilolite from Turkey, Greece, and Turkey, respectively. In recent times, clinoptilolite sourced from Turkey has been utilized to adsorb Co^{2+}, and the adsorption data are consistent with the (M-Lan), (M-Fre), and (M-D.K. R) models. Nonetheless, the adsorption isotherm data can be more precisely explained by the Langmuir model with synthetic NaA zeolite derived from CFA (10).
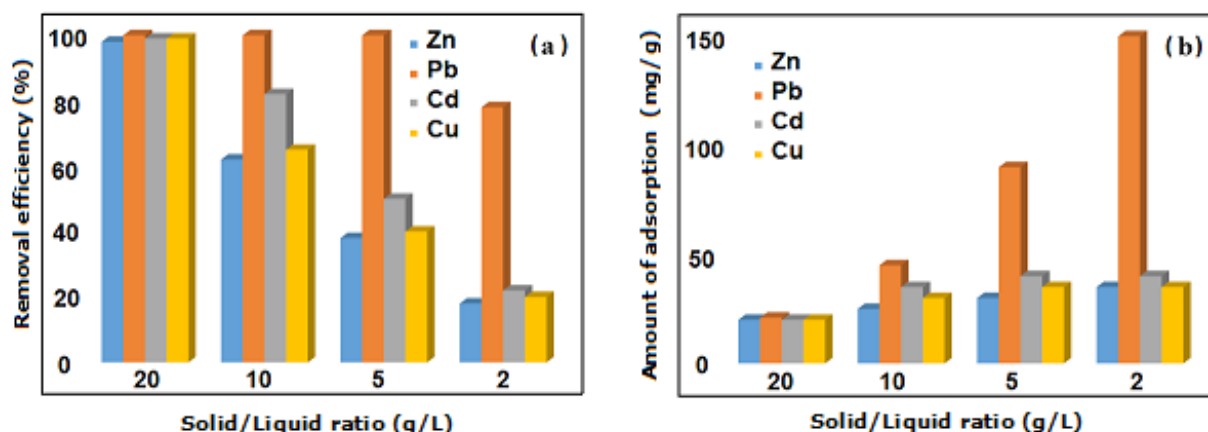
Figure 5: The removal efficiency of NaCl-modified synthetic-CP for Zn(II), Pb(II), Cd(II), and Cu(II) is demonstrated in Figure (a), along with the corresponding amount of adsorption (b), as a function of solid-to-liquid ratio (8).

Table 1. The (MAC) of reported N-Zeolite for Zn^{2+}, Pb^{2+}, Cd^{2+}, Cu^{2+}, Ni^{2+}, and Cr^{3+}.

Zeolite	Metal	MAC (mg.g^{-1}, meq.g^{-1})	Ref
China Na-CP	Zn^{2+}, Pb^{2+}, Cd^{2+}, Cu^{2+}	20.29, 159.00, 30.84, 20.28	(11)
America Na-CP	Zn^{2+}, Pb^{2+}, Cd^{2+}, Cu^{2+}	21.14, 158.70, 33.07, 22.82	
Ukraine Na-CP	Pb^{2+}, Cd^{2+}, Cu^{2+}	≈ 82, ≈ 19, ≈ 21	
Italy Na-CP	Zn^{2+}, Pb^{2+}, Cd^{2+}, Cu^{2+}	8.17, 27.70, 4.22, 25.76	

Slovakia Na-CP	Pb^{2+}, Cd^{2+}, Cu^{2+}	≈ 85, ≈ 36, ≈ 28	
Turkish CP	Pb^{2+}, Zn^{2+}	0.29–0.73, 0.10–0.25	(29)
	Cu^{2+}, Ni^{2+}	0.02–0.22, 0.01–0.17	
Na-CP	Cr^{3+}, Ni^{2+}, Zn^{2+}, Cu^{2+}	0.23, 0.06, 0.10, 0.18	
	Cd^{2+}	0.08	
Scolecite	Pb^{2+}, Cu^{2+}, Zn^{2+}, Ni^{2+}	0.05, 0.13, 0.06, 0.03	
	Co^{2+} Cd^{2+}	0.0078, 0.0032	
Bigadic CP	Pb^{2+}, Zn^{2+}, Cd^{2+}	0.22, 0.73, 0.0053	
Turkish CP	Co^{2+}, Cu^{2+}, Zn^{2+}, Mn^{2+}	0.44, 0.28, 0.27, 0.15	
Brazilian scolecite	Cr^{3+}, Ni^{2+}, Cd^{2+}, Mn^{2+}	5.81, 2.08, 1.78, 4.00	
Sardinian CP	Cu^{2+}, Cd^{2+}, Pb^{2+}	0.34, 0.05–0.19, 0.27–1.20	(39)
	Zn^{2+}	0.10	
CP	Cd^{2+}	0.12–0.18	(40)
Mexican CP	Pb^{2+}	1.40	(41)
Ukraine CP	Pb^{2+}, Cu^{2+}, Ni^{2+}, Cd^{2+}	0.13, 0.40, 0.22, 0.037	(42)
Sardinian CP	Cu^{2+}, Cd^{2+}, Pb^{2+}, Zn^{2+}	0.34,0.05-0.19, 0.27-1.2, 0.1	(43)

1   Maximum adsorption capacity (MAC)

Table 2. The (MAC) of reported (M) and (S) Zeolite for Zn^{2+}, Pb^{2+}, Cd^{2+}, Cu^{2+}, Ni^{2+}, and Cr^{3+}.

Zeolite	*Metal*	*MAC ($mg.g^{-1}$)*	*Reference*
Nano Fe-Al zeolite	Cr^{6+}	44.74	(7)
S-CP	Zn^{2+}, Pb^{2+}, Cd^{2+}, Cu^{2+}	31.74, 181.8, 44.64, 33.76	(11)
NaP1	Cr^{3+}, Cd^{2+}, Cu^{2+}, Zn^{2+}, Ni^{2+}	43.6, 50.8, 50.5, 32.6, 20.1	(10)
Blend of NaX and NaA	Cr^{3+}	71.1	
Blend of NaY and NaP	Cr^{3+}	83.2	
Zeolite X	Cd^{2+}, Zn^{2+}	92.00, 41.00	
NaX +- activated carbon	Cd^{2+}, Cu^{2+}, Pb^{2+}, Ni^{2+}	129.30, 101.70, 2280, 132.10	
Zeolite 4A	Cu^{2+}	39.80-72.00	
Zeolite A	Zn^{2+}, Ni^{2+}	28.60, 24.65	
M-zeolite (NCP-GLU)	Co^{2+}	41.47	
M-zeolite (NCP)	Co^{2+}	19.05	
M-zeolite (MCP-GLU)	Co^{2+}	29.38	
Zeolite nanoparticles	Ni^{2+}	122	(44)

2   Synthetic-Clinoptilolite (S-CP)
3   Maximum adsorption capacity (MAC)
4   Modified (M) and Synthetic (S)

3. NATURAL, MODIFIED, AND SYNTHETIC ZEOLITES ENVIRONMENTAL IMPLICATIONS

In later years, the chemical industry rapidly evolved and significantly improved the conditions and quality of life in our society. Nevertheless, this industrial development has inevitably led to environmental pollution problems. For instance, the debasement of water resources is escalating at an alarming rate owing to the rapid proliferation of an assortment of pollutants emanating from sundry industrial sectors. This is primarily attributable to the commercialization of cutting-edge products and the implementation of innovative transformation technologies and processes (45). Human activities are the primary cause of heavy metal release into terrestrial and aquatic ecosystems. The extraction of mineral deposits containing considerable amounts of sulfide minerals and heavy metals represents a pivotal source of heavy metal contamination in the environment (46). The contamination of sites by both organic and inorganic pollutants is a complex and widespread environmental issue (17). The menace of environmental pollution is widely recognized as one

of the paramount challenges of the contemporary world. It poses a severe threat to human health and ecosystems, with the potential to trigger environmental toxicity and other undesirable outcomes (47).

Toxic metals, such as heavy metals, are considered a high-priority class of pollutants due to their harmful nature. They frequently impede the beneficial use of wastewater for industrial applications and irrigation purposes. This underscores the significance of effective and efficient removal of these pollutants to mitigate their adverse effects on the environment and public health (48). Consequently, heavy metal pollution has attracted widespread concern (49). Land-based sources are a significant contributor to marine ecosystem pollution, with nutrients and pathogens from sewage treatment plants, pesticides from agriculture, metals from mining and smelting activities, traffic, and machinery manufacturing (50), and pharmaceutical industries (51). Protecting the environment and cleaning up water, air, and soil pollution is a matter of utmost importance worldwide, especially in developing countries. However, pollution remediation can be challenging due to four main factors: efficiency, recyclability, environmental safety, and cost-effectiveness. But it is possible to tackle these challenges to ensure a cleaner and healthier environment for ourselves and future generations. Working towards efficient, recyclable, safe, and affordable solutions, can effectively combat pollution and create a better world and environment. (52).

It is meaningful to note that there is no accurate description of what constitutes a heavy metal; however, the literary depiction characterizes it as an innate constituent possessing an elevated atomic mass and a density equivalent to or surpassing 5 g.cm^{-3}, which is minimum five times more elevated than that of aqueous substances. Some of the common heavy metals include Mn, V, Cr, Fe, Co, Ni, Cu, Zn, As, Mo, Ag, Cd, Pb, and Hg (29). The contamination of soil and water is a grave concern, particularly due to its ability to pervade the food chain and amass within the body. Human exposure to heavy metals can occur through the ingestion of contaminated food and water, as well as the inhalation of atmospheric particles laden with heavy metals. Despite the miniscule amounts, the accumulation of heavy metals within the body can trigger a host of medical ailments, such as neurological disorders, hormonal imbalances, cardiovascular failures, renal malfunctions, infertility, hair loss, endocrine disorders, respiratory and gastrointestinal problems, even cancer. A multitude of industrial processes discharges their wastewater into rivers, which eventually results in the deposition and enrichment of river sediments. This, in turn, leads to a heavy metal contamination crisis that necessitates stringent measures. River sediments are often employed to appraise the extent of heavy metal contamination through the utilization of a diverse set of defensive pollution indices. (53).

Table 3. The maximum heavy metals adsorption isotherms of natural, modified, and synthetic Zeolite (7).

Metal ion	Zeolite	Zeolite origin	Metal removal rate (%)	Adsorption isotherms
Cr^{3+}	Natural scolecite	Brazil	100.00–96.00	M-Fre-Iso
Cr^{3+}	CP	Greece	>90.00	M-Lan
Cr^{3+}	NaP1	CFA	>90.00	M-Lan
Cd^{2+}	Zeolite A	Kaolin	>99.00	M-Lan, M-Fre, M-D.K.R
Cd^{2+}	Zeolite X	Kaolin	>99.00	M-Lan, M-Fre, M-D.K.R
Cd^{2+}	Natural scolecite	Brazil	84.00–59.00	M-Fre-Iso
Cd^{2+}	Natural zeolite	Kardjali	75.00–90.00	M-Fre
Cd^{2+}	CP	Greece	>90.00	M-Lan
Cu^{2+}	Zeolite A	Zeolite A	>99.00	M-Lan, M-Fre, M-D.K.R
Cu^{2+}	CP	Turkey	77.96	M-Lan, M-Fre, M-D.K.R
Cu^{2+}	NaOH-M-CP	Bulgaria	95.00	M-Lan
Cu^{2+}	NaX +-activated carbon	CFA		M-Lan
Pb^{2+}	Zeolite X	Kaolin	>99.00	M-Lan, M-Fre, M-D.K.R

Metal	Adsorbent	Source	Removal (%)	Isotherm
Pb^{2+}	Zeolite A	Kaolin	>99.00	M-Lan, M-Fre, M-D.K.R
Pb^{2+}	NaX +-activated carbon	CFA		M-Lan
Zn^{2+}	CP	Turkey	45.96	M-Lan, M-Fre, M-D.K.R
Zn^{2+}	Zeolite A	Kaolin	>99.00	M-Lan, M-Fre, M-D.K.R
Zn^{2+}	CP	Greece	>90.00	M-Lan
Zn^{2+}	NaP1	CFA	>90.00	M-Lan
Ni^{2+}	Zeolite A	Kaolin	>99.00	M-Lan, M-Fre, M-D.K.R
Ni^{2+}	Zeolite X	Kaolin	>99.00	M-Lan, M-Fre, M-D.K.R
Ni^{2+}	Natural scolecite	Brazil	96.00–40.00	M-Fre-Iso
Ni^{2+}	CP	Greece	>90.00	M-Lan
Ni^{2+}	NaP1	CFA	>90.00	M-Lan
Ni^{2+}	NaX +-activated carbon	CFA		M-Lan
Co^{2+}	NaA	CFA		M-Lan
Co^{2+}	CP	Turkey	66.10	M-Lan, M-Fre, M-D.K.R

1 Langmuir (M-Lan), Freundlich (M-Fre), Dubinin Kaganer Radushkevich (M-D.K.R), Freundlich isotherm (M-Fre-Iso)
2 Clinoptilolite (CP), M-CP (Modified- Clinoptilolite)

Marine surface sediments are known to pretense as a sink for harmful metal pollutants, but it's worth noting that these irregularities may not be fixed in sediments. When certain conditions arise due to natural or human-induced causes, such as changes in pH, dissolved oxygen, and redox potential, pollutants can be released back into the water. This can lead to secondary pollution sources, which can have detrimental effects on aquatic environments. It is vital to improving our understanding of heavy metal pollution in coastal regions, particularly in areas like the coastal regions of China that are grappling with significant challenges concerning this issue. Therefore, it is essential to monitor the pollution status of heavy metals in these areas to ensure effective mitigation measures. Removing undesirable metal ions from water systems is an essential task for environmental engineers, but it remains a challenging one. Lead, for example, is a heavy metal that can cause damage to biological systems and is released into the environment from various industrial sources. Removing lead from wastewater is a critical topic that has attracted considerable attention from researchers and policymakers alike.

When heavy metals in sediments or soils transform from stable fractions into susceptible, bioavailable, and mobile forms, they pose a threat to the health of animals and humans. For example, Cd exposure can increase the likelihood of osteoporosis and pulmonary cancer, while chronic dust exposure can lead to peripheral vascular disease. Excessive intake of Pb adversely affects the central nervous system, while Zn may result in infertility and renal disease. Cu can induce depression and Cr may cause tumors in respiratory organs (50). The presence of chromate Cr(VI) and arsenate (As(V)) anions in various sources of water is a prominent issue, as the toxicity of these species can result in death if they are taken over a long period or present in high concentrations (54). Heavy metals such as Cr, Cu, Zn, As, Cd, Pb, and Hg have been listed as priority control pollutants by the United States Environmental Protection Agency (USEPA) because of their potentially harmful, persistent, and irremediable behaviors, and have garnered increasing attention worldwide (50).
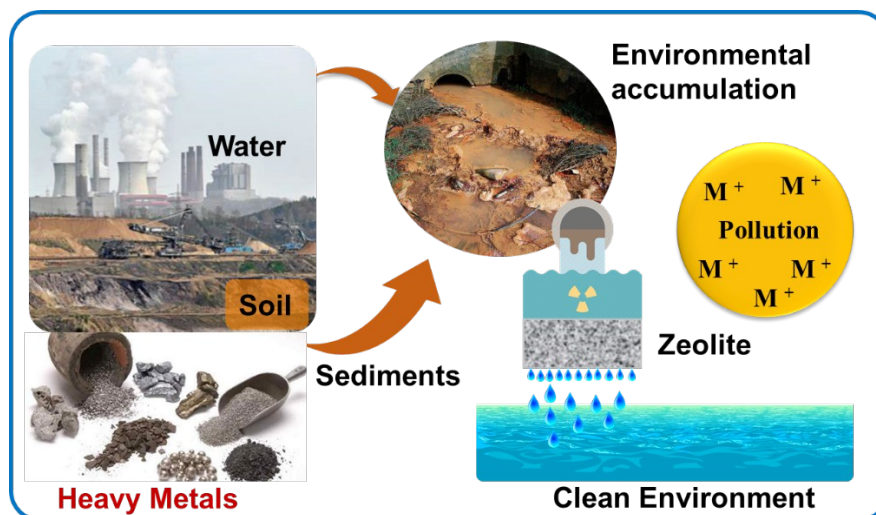
Figure 6: Heavy metal pollution from anthropogenic activities.

Green chemistry, defined as the design of products and processes to prevent or reduce the formation of hazardous chemicals (55), requires the use and development of synthetic reactions based on atomic economy (55). Green chemistry technology has come up as an effective strategy to alleviate venomous by exploiting natural resources for nanomaterial prevarication, lowering operating expenses, reducing environmental impacts, and providing superior biocompatibility, and chemical and thermal stability (56). Green routes are specifically designed to minimize the use and generation of substances that have harmful impacts on both human health and the environment. The goal of these routes is to prioritize the use of non-toxic or less-toxic alternatives and to reduce the overall environmental footprint of the processes involved. By adopting green routes, we can contribute to a more sustainable future for ourselves and the planet (36). As environmental awareness continues to grow, the aquaculture industry is taking proactive steps to mitigate the potential negative impacts of production on surrounding ecosystems. To this end, innovative solutions are being developed to reduce the presence of harmful contaminants in aquaculture waters, particularly in recycling systems and wastewater from aquaculture ponds. One such solution gaining traction is the use of eco-friendly adsorbents, such as natural zeolite minerals. This approach is seen as a promising way to effectively treat contaminated waters and wastewater while minimizing harm to the environment (24). Natural zeolites are aluminosilicate minerals as mentioned above also have porous structures that have high cation-exchange capacity, making them effective adsorbents for heavy metals. They have been used in various applications, including water treatment, gas separation, and catalysis. In the field of aquaculture, natural zeolites are effective in removing heavy metals from contaminated waters and wastewater.

In a study conducted by Hamed et al. (57), natural zeolite was used to remove heavy metals from the wastewater of a fish farm. The results showed that zeolite was able to effectively remove heavy metals,

including Cu, Zn, and Pb, from the wastewater. Another study by Zorpas et al. (58) investigated the use of natural zeolites for the removal of heavy metals from a recirculating aquaculture system. The results showed that the zeolites were able to remove a significant amount of heavy metals from the system, resulting in a reduction of the total dissolved solids and chemical oxygen demand. Overall, the use of natural zeolites as eco-friendly adsorbents is a promising approach for treating contaminated waters and wastewater in aquaculture. It is an effective and sustainable solution that can help mitigate the negative impacts of aquaculture production on the environment.

4. DISCUSSION

There exists a range of methods for purifying heavy metals from contaminated areas, including chemical precipitation, solvent extraction, oxidation, membrane filtration, photocatalytic degradation, and adsorption. The use of these techniques must adhere to the principles of green chemistry, particularly those about economic and environmental considerations. Due to high tax costs, post-treatment issues, and environmental concerns, many of the aforementioned methods are not extensively employed for removing heavy metals.

Zeolites have been identified as potentially valuable adsorbents for heavy metal removal due to their high efficiency, low cost, and eco-friendliness. As the primary inorganic cation exchangers, zeolites offer exceptional ion exchange stowage, selectivity, and compatibility with the natural environment, making them ideal for use in a variety of environmental remediation processes, wastewater treatment, and air purification.

Studies on the adsorption capacity of different zeolite types - including natural, modified, and synthetic - have indicated that natural zeolites can achieve maximum adsorption capacity between 40-100%, while synthetic and modified zeolites can reach up to

90-99%. Adsorption isotherms for metal ions are modeled using Freundlich, Langmuir, or DKR equations, with the maximum adsorption capacity of isotherms reaching about 40-100%. In summary, zeolites are highly effective adsorbents for removing harmful heavy metals from industrial-produced wastewater.

5. CONCLUSION

Heavy metals pose a severe threat to the environment, jeopardizing the health of humans, animals, and plants. Removing these metals from the environment is vital to reduce diseases and creating a green and healthy ecosystem. It also plays an important role in maintaining the balance of the ecosystem and recycling metals that are facing a gradual reduction of mineral resources.

Fortunately, the removal of harmful heavy metals from industrial wastewater provides a valuable and essential solution to environmental pollution challenges. Recent research has found that zeolites are a promising material for heavy metal removal from polluted environments and industrial wastewater. Here are the main points:

1   Among various refining processes, adsorption is a cheap and flexible technology method for the generous removal of organic also inorganic materials. Using zeolite is a suitable method for heavy metal removal as it is cost-effective and straightforward compared to other methods.

2   The adsorption isotherms of several metal ions

6. CONFLICT OF INTEREST

There are no conflicts that need to be reported.

7. REFERENCES

1. Türksoy. R., T. G., Yalçın., E. İ., Türksoy. Ö., Demir. G.Y.,. Removal of heavy metals from textile industry wastewater. *Frontiers in Life Sciences and Related Technologies.* 2021, *2* (2), 44-50. Available from: <DOI>.

2. Motsa, M. M.; Thwala, J. M.; Msagati, T. A. M.; Mamba, B. B. The potential of melt-mixed polypropylene–zeolite blends in the removal of heavy metals from aqueous media. *Physics and Chemistry of the Earth, Parts A/B/C.* 2011, *36* (14), 1178-1188. Available from: <DOI>.

3. El-Azim, H.; Mourad, F. Removal of Heavy Metals Cd (II), Fe (III) and Ni (II), from Aqueous Solutions by Natural (Clinoptilolite) Zeolites and Application to Industrial Wastewater. *Asian Journal of Environment & Ecology* 2018, *7*, 1-13. Available from: <DOI>.

4. Aghazadeh, S.; Safarzadeh, E.; Gharabaghi, M.; Irannajad, M. Modification of natural zeolite for Cu removal from waste waters. *Desalination and Water Treatment* 2016, *57*, 1-8. Available from: <DOI>.

5. World Health, O. *Lead in drinking-water: background document for development of WHO guidelines for drinking-water quality*; WHO/SDE/WSH/03.04/09; World Health Organization., Geneva, 2003. Available from: <URL>.

can best be modeled by M-Fre, M-Lang, or DKR equations. Synthetic and naturally occurring zeolites have successfully adsorbed a wide range of heavy metal Cu, Zn, As, Mo, Ag, Cd, Pb, and Hg from various contaminated water streams.

Zeolites possess a highly desirable microporous crystalline structure that enables them to selectively exchange ionic species based on their size. Due to the size of the entry ports in the internal zeolite framework, only species with diameters that fit through these ports can be exchanged, while larger species are eliminated. This unique property of zeolites, known as ion-sieving, finds widespread application in various commercial fields.

3   The maximum absorption capacity of Pb^{2+}, Cd^{2+}, Cu^{2+}, Ni^{2+}, Co^{2+}, Cr^{3+}, and Cr^{6+} by natural, modified, and synthetic zeolite is in the following order: 228 $mg.g^{-1}$, 129.3 $mg.g^{-1}$, 101.7 $mg.g^{-1}$, 132.1 $mg.g^{-1}$, 41.47 $mg.g^{-1}$, 83.2 $mg.g^{-1}$ and 44.74 $mg.g^{-1}$, respectively.

4   Among the types of zeolites, including natural scolecite, Zeolite A and X, NaX +- activated carbon, modified zeolite (NCP-GLU), and a blend of NaY and NaP, the best type for removing heavy metals with the highest adsorbent capacity is identified.

5   The adsorption isotherms' capacity for removing heavy metals using different types of zeolites ranges from 40-100%. This result indicates that zeolites are excellent adsorbents for removing heavy metals from industrial wastewater.

6. Krauklis, A.; Ozola, R.; Burlakovs, J.; Rugele, K.; Kirillov, K.; Trubaca-Boginska, A.; Rubenis, K.; Stepanova, V.; Klavins, M. FeOOH and Mn_8O10Cl_3 modified zeolites for As(V) removal in aqueous medium. *Journal of Chemical Technology & Biotechnology.* 2017, *92* (8), 1948-1960. Available from: <DOI>.

7. Kong, F.; Zhang, Y.; Wang, H.; Tang, J.; Li, Y.; Wang, S. Removal of Cr(VI) from wastewater by artificial zeolite spheres loaded with nano Fe–Al bimetallic oxide in constructed wetland. *Chemosphere.* 2020, *257*, 127224. Available from: <DOI>.

8. Türkmen, M. Removal of Heavy Metals From Wastewaters by Use of Natural Zeolites. In *Fresenius Environmental Bulletin.* , 2002; Department of Environmental Engineering, Dokuz Eylül University.: Vol. 13, pp 574-580.

9. Dursun, S.; Pala, A. I. Lead pollution removal from water using a natural zeolite. *Journal of International Environmental Application and Science.* 2007, *2*, 11-19.

10. Yuna, Z. Review of the Natural, Modified, and Synthetic Zeolites for Heavy Metals Removal from Wastewater. *Environmental Engineering Science.* 2016, *33* (7), 443-454. Available from: <DOI>.

11. Li, Y.; Bai, P.; Yan, Y.; Yan, W.; Shi, W.; Xu, R. Removal of Zn^{2+}, Pb^{2+}, Cd^{2+}, and Cu2+ from aqueous solution by synthetic clinoptilolite. *Microporous and Mesoporous Materials.* 2019, *273*, 203-211. Available from: <DOI>.

12. Bessa, R. A.; França, A. M. M.; Pereira, A. L. S.; Alexandre, N. P.; Pérez-Page, M.; Holmes, S. M.; Nascimento, R. F.; Rosa, M. F.; Anderson, M. W.; Loiola, A. R. Hierarchical

zeolite based on multiporous zeolite A and bacterial cellulose: An efficient adsorbent of Pb^{2+}. *Microporous and Mesoporous Materials.* 2021, *312*, 110752. Available from: <DOI>.

13. Mirjana Golomeova, A. Z., Krsto Blazev, Boris Krstev, Blagoj Golomeov. Removal of Heavy Metals from Aqueous Solution using Clinoptilolite and Stilbite. *INTERNATIONAL JOURNAL OF ENGINEERING RESEARCH & TECHNOLOGY (IJERT)* . 2014, *03* (11), 1029-1035. Available from: <DOI>.

14. Habeebullah, T.; Munir, S.; Awad, A.; Morsy, E.; Seroji, A.; Mohammed, A. The Interaction between Air Quality and Meteorological Factors in an Arid Environment of Makkah, Saudi Arabia. *International Journal of Environmental Science and Development.* 2014, *6*, 576-580. Available from: <DOI>.

15. Taamneh, Y.; Sharadqah, S. The removal of heavy metals from aqueous solution using natural Jordanian zeolite. *Applied Water Science.* 2017, *7* (4), 2021-2028. Available from: <DOI>.

16. TEKİN, B. a. A., ÜNSAL. Intake of divalent copper and nickel onto natural zeolite from aqueous solutions: a study in mono- and dicomponent systems. *Turkish Journal of Chemistry.* 2022, *46* (4), 1042-1054. Available from:<DOI>.

17. Zhang, Y.; Alessi, D. S.; Chen, N.; Luo, M.; Hao, W.; Alam, M. S.; Flynn, S. L.; Kenney, J. P. L.; Konhauser, K. O.; Ok, Y. S.; et al. Lead (Pb) sorption to hydrophobic and hydrophilic zeolites in the presence and absence of MTBE. *Journal of Hazardous Materials.* 2021, *420*, 126528. Available from: <DOI>.

18. Apreutesei, R.; Catrinescu, C.; Teodosiu, C. Surfactant-Modified Natural Zeolites for Environmental Applications in Water Purification. *Environmental engineering and management journal.* 2008, *7*, 149-161. Available from: <DOI>.

19. Bandura, L.; Panek, R.; Madej, J.; Franus, W. Synthesis of zeolite-carbon composites using high-carbon fly ash and their adsorption abilities towards petroleum substances. *Fuel.* 2021, *283*, 119173. Available from: <DOI>.

20. Zorbay, F.; Arslan, S. Zeolitler ve Kullanım Alanları. *Karaelmas Science and Engineering Journal.* 2012, *2*, 63-68. Available from: <DOI>.

21. Li, Y.; Liang, G.; Chang, L.; Zi, C.; Zhang, Y.; Peng, Z.; Zhao, W. Conversion of biomass ash to different types of zeolites: a review. *Energy Sources, Part A: Recovery, Utilization, and Environmental Effects.* 2019, *43*, 1-14. DOI: 10.1080/15567036.2019.1640316. Polatoglu, I. Chemical behaviour of clinoptilolite rich natural zeolite in aqueous medium. the Graduate School of Engineering and Sciences of
izmir Institute of Technology., Izmir, 2005. Available from: <URL>.

22. Zeng, S.; Wang, R.; Zhang, Z.; Qiu, S. Solventless green synthesis of sodalite zeolite using diatomite as silica source by a microwave heating technique. *Inorganic Chemistry Communications.* 2016, *70*, 168-171. Available from: <DOI>.

23. Wu, Q.; Meng, X.; Gao, X.; Xiao, F.-S. Solvent-Free Synthesis of Zeolites: Mechanism and Utility. *Accounts of chemical research.* 2018, *51* (6), 1396-1403. Available from: <DOI>.

24. Ghasemi, Z.; Sourinejad, I.; Kazemian, H.; Rohani, S. Application of zeolites in aquaculture industry: a review. *Reviews in Aquaculture.* 2018, *10* (1), 75-95. Available from: <DOI>.

25. Davis, M. E. Zeolites from a Materials Chemistry Perspective. *Chemistry of Materials* 2014, *26* (1), 239-245. Available from: <DOI>.

26. Tao, Y.; Kanoh, H.; Abrams, L.; Kaneko, K. Mesopore-Modified Zeolites: Preparation, Characterization, and Applications. *Chemical Reviews.* 2006, *106* (3), 896-910. Available from: <DOI>.

27. Ramos-Guivar, J. A.; Taipe, K.; Schettino, M. A., Jr.; Silva, E.; Morales Torres, M. A.; Passamani, E. C.; Litterst, F. J. Improved Removal Capacity and Equilibrium Time of Maghemite Nanoparticles Growth in Zeolite Type 5A for Pb(II) Adsorption. *Nanomaterials (Basel).* 2020, *10* (9). DOI: 10.3390/nano10091668 From NLM. Ülkü, S. CHEMICAL BEHAVIOUR OF CLINOPTILOLITE RICH NATURAL ZEOLITE IN AQUEOUS MEDIUM. In *Izmir Institute of Technology administrators.*, 2005.

28. Krol, M. M. Natural vs. Synthetic Zeolites. 2020.

29. Wang, S.; Peng, Y. Natural zeolites as effective adsorbents in water and wastewater treatment. *Chemical Engineering Journal.* 2010, *156* (1), 11-24. Available from: <DOI>.

30. Passaglia, E.; Sheppard, R. A. The Crystal Chemistry of Zeolites. *Reviews in Mineralogy and Geochemistry.* 2001, *45* (1), 69-116. Available from: <DOI>. (acccessed 6/14/2023).

31. Batur, J.; Duan, Z.; Jiang, M.; Li, R.; Xie, Y.; Yu, X.-F.; Li, J.-R. Molecular Modification of Zeolites with Cold Atmospheric-Pressure Plasma Jet: A Green and Facile Strategy. *Chemistry of Materials.* 2023, *35* (10), 3867-3879. Available from: <DOI>.

32. Nguyen, M. L., Tanner, C. C. Ammonium Removal From Wastewaters Using Natural New Zealand Zeolites. *New Zealand Journal of Agricultural Research.* 1998, *3* ((41)), 427-446. Available from: <DOI>.

33. Zhang, Y. Characteristics and Mechanisms of Heavy Metal and MTBE Adsorption on Zeolites and Applications in Permeable Reactive Barriers. University of Cambridge, Robinson College 2019.

34. Ozekmekci, M.; Salkic, G.; Fellah, M. F. Use of zeolites for the removal of H2S: A mini-review. *Fuel Processing Technology.* 2015, *139*, 49-60. Available from: <DOI>.

35. Montes Luna, A. d. J.; Castruita de León, G.; García Rodríguez, S. P.; Fuentes López, N. C.; Pérez Camacho, O.; Perera Mercado, Y. A. $Na+/Ca^{2+}$ aqueous ion exchange in natural clinoptilolite zeolite for polymer-zeolite composite membranes production and their $CH_4/CO_2/N_2$ separation performance. *Journal of Natural Gas Science and Engineering.* 2018, *54*, 47-53. Available from: <DOI>.

36. Abdullah, N. H.; Shameli, K.; Abdullah, E. C.; Abdullah, L. C. Solid matrices for fabrication of magnetic iron oxide nanocomposites: Synthesis, properties, and application for the adsorption of heavy metal ions and dyes. *Composites Part B: Engineering* 2019, *162*, 538-568. Available from: <DOI>.

37. Mastinu, A.; Kumar, A.; Maccarinelli, G.; Bonini, S. A.; Premoli, M.; Aria, F.; Gianoncelli, A.; Memo, M. Zeolite Clinoptilolite: Therapeutic Virtues of an Ancient Mineral. *Molecules.* 2019, *24* (8). Available from: <DOI>. From NLM.

38. Kraljević Pavelić, S.; Simović Medica, J.; Gumbarević, D.; Filošević, A.; Pržulj, N.; Pavelić, K. Critical Review on Zeolite Clinoptilolite Safety and Medical Applications in vivo. *Front Pharmacol.* 2018, *9*, 1350. Available from: <DOI>. From NLM.

39. Cincotti, A.; Mameli, A.; Locci, A. M.; Orrú, R.; Cao, G. Heavy Metals Uptake by Sardinian Natural Zeolites: Experiment and Modeling. *Industrial & Engineering Chemistry Research.* 2006, *45*, 1074-1084.

40. Gedik, K.; Imamoglu, I. Affinity of Clinoptilolite-based Zeolites towards Removal of Cd from Aqueous Solutions. *Separation Science and Technology - SEPAR SCI TECHNOL* 2008, *43*, 1191-1207. Available from: <DOI>.

41. Llanes-Monter, M.; Olguín, M.; Solache, M. Lead sorption by a Mexican, clinoptilolite-rich tuff. *Environmental science and pollution research international.* 2007, *14*, 397-403. Available from: <DOI>.

42. Sprynskyy, M.; Buszewski, B.; Terzyk, A. P.; Namieśnik, J. Study of the selection mechanism of heavy metal (Pb^{2+}, Cu^{2+}, Ni^{2+}, and Cd^{2+}) adsorption on clinoptilolite. *Journal of Colloid and Interface Science.* 2006, *304* (1), 21-28. Available from: <DOI>.

43. MUDABER, S. N. B., BATUR. Jenaidullah., . Zeolites as effective adsorbents for heavy metal removal in wastewater treatment of Kabul city-A review. *IAR Journal of Engineering and Technology.* 2023, *4* (2), 20-31. Available from: <DOI>.

44. Yurekli, Y. Removal of heavy metals in wastewater by using zeolite nano-particles impregnated polysulfone membranes. *Journal of Hazardous Materials.* 2016, *309*, 53-64. DOI: https://doi.org/10.1016/j.jhazmat.2016.01.064.

45. Dhaouadi, F.; Sellaoui, L.; Reynel-Ávila, H. E.; Landín-Sandoval, V.; Mendoza-Castillo, D. I.; Jaime-Leal, J. E.; Lima, E. C.; Bonilla-Petriciolet, A.; Lamine, A. B. Adsorption mechanism of Zn^{2+}, Ni^{2+}, Cd^{2+}, and Cu^{2+} ions by carbon-based adsorbents: interpretation of the adsorption isotherms via physical modelling. *Environmental Science and Pollution Research.* 2021, *28* (24), 30943-30954. Available from: <DOI>.

46. Wingenfelder, U.; Hansen, C.; Furrer, G.; Schulin, R. Removal of Heavy Metals from Mine Waters by Natural Zeolites. *Environmental Science & Technology.* 2005, *39* (12), 4606-4613. Available from: <DOI>.

47. Chen, Y.; Liu, Q.; Xu, M.; Wang, Z. Inter-annual variability of heavy metals pollution in surface sediments of Jiangsu coastal region, China: Case study of the Dafeng Port. *Marine Pollution Bulletin.* 2020, *150*, 110720. Available from: <DOI>.

48. Kocaoba, S.; Orhan, Y.; Akyüz, T. Kinetics and equilibrium studies of heavy metal ions removalby use of natural zeolite. *Desalination.* 2007, *214* (1), 1-10. Available from: <DOI>.

49. Javanbakht, V.; Ghoreishi, S. M.; Habibi, N.; Javanbakht, M. A novel magnetic chitosan/clinoptilolite/magnetite nanocomposite for highly efficient removal of Pb(II) ions from aqueous solution. *Powder Technology.* 2016, *302*, 372-383. Available from: <DOI>.

50. Qiao, D.; Wang, G.; Li, X.; Wang, S.; Zhao, Y. Pollution, sources and environmental risk assessment of heavy metals in the surface AMD water, sediments and surface soils around unexploited Rona Cu deposit, Tibet, China. *Chemosphere.* 2020, *248*, 125988. Available from: <DOI>.

51. Nour, H. E.; El-Sorogy, A. S.; Abd El-Wahab, M.; Nouh, E. S.; Mohamaden, M.; Al-Kahtany, K. Contamination and ecological risk assessment of heavy metals pollution from the Shalateen coastal sediments, Red Sea, Egypt. *Marine Pollution Bulletin.* 2019, *144*, 167-172. Available from: <DOI>.

52. Lu, F.; Astruc, D. Nanomaterials for removal of toxic elements from water. *Coordination Chemistry Reviews.* 2018, *356*, 147-164. Available from: <DOI>.

53. Shirani, M.; Afzali, K.; Jahan, S.; Strezov, V.; Soleimani-Sardo, M. Pollution and contamination assessment of heavy metals in the sediments of Jazmurian playa in southeast Iran. *Scientific Reports.* 2020, *10*. Available from: <DOI>.

54. Yıldırım, A.; Mudaber, S.; Öztürk, S. Improved Sustainable Ionic Liquid Catalyzed Production of Symmetrical and Non-Symmetrical Biological Wax Monoesters. *European Journal of Lipid Science and Technology.* 2019, *121* (2), 1800303. Available from: <DOI>.

55. Mudaber, S. Biyolojik vaks mono esterlerin etkin ve yeşil sentezi. Yayınlanmamış yüksek lisans tezi. Bursa Uludağ Üniversitesi, Bursa Turkiye, 2018.

56. Li, R.; Batur, J.; Bian, H.; Wang, Y.-J.; Duan, Z.; Xie, Y.; Li, J.-R. Green and Facile Fabrication of Metal Oxide/Red Phosphorus Composite Catalysts for CO_2 Photoreduction. *ACS Sustainable Chemistry & Engineering* 2022, *10* (26), 8658-8668. Available from: <DOI>.

57. Hamed, M.; Hussein, S.; Salama, A.; Mamoon, A. Use the natural zeolite (clinoptiolite) in removal of ammonia and heavy metals and improving water quality in fish ponds. *Al-Azhar Journal of Agricultural Research* 2022, *47*, 79-88. Available from: <DOI>.

58. Zorpas, A. A.; Pedreño, J. N.; Candel, M. B. A. Heavy metal treatment and removal using natural zeolites from sewage sludge, compost, and agricultural soils: a review. *Arabian Journal of Geosciences.* 2021, *14* (12), 1098. Available from: <DOI>.

Synthesis, Antiproliferative Activity and *In Silico* Studies of Chalcones Derived From 4-(Imidazole-1-yl)Acetophenone

Bedriye Seda Kurşun Aktar[1],* iD **, Abdulraheem Mustafa Ibrahim Al-Karabash[2]** iD **, Ayşe Şahin Yağlıoğlu[3]** iD **, Emine Elçin Oruç Emre[4]** iD

[1]Malatya Turgut Özal University, Yeşilyurt Vocational School, Department of Hair Care and Beauty Services, Malatya, Türkiye.
[2]Çankırı Karatekin University, Faculty of Sciences, Department of Chemistry, Çankırı, Türkiye.
[3]Amasya University, Technical Sciences Vocational School, Department of Chemistry and Chemical Process Technology Department, Amasya, Türkiye.
[4]Gaziantep University, Faculty of Arts and Sciences, Department of Chemistry, Gaziantep, Türkiye.

Abstract: In this study, the synthesis of chalcone compounds (**1**-**11**) derived from 4-(imidazol-1-yl)acetophenone and the structure determination of these compounds by various spectroscopic methods were carried out. The anticancer activities of compounds **1**-**11** were examined against HeLa and PC-3 cancer cells at four different concentrations (100, 50, 25, and 5 µM) using the BrdU ELISA assay. It was determined that all molecules except compounds **1** and **6** in HeLa cancer cells and compounds **2** and **8** against PC-3 cancer cells were more active against HeLa and PC-3 than the standard drug 5-fluorouracil (**5-FU**). The best activity against PC-3 cancer cells was compound **4** (IC$_{50}$: 1.39±0.00 µM). In addition, compound **11** (IC$_{50}$: 1.58±0.01 µM) was found to have the highest activity against HeLa cancer cells. Compound **4** against PC-3 cancer cell and compound **11** against HeLa cancer cell displayed cell selective activity. The ADME properties and drug similarities of the molecules **1**-**11** using the SwissADME software were investigated. According to these properties, compounds **1**-**11** were found to obey Lipinski rules.

Keywords: ADME, Antiproliferative activity, HeLa cell line, *In silico*, PC-3 cell line.

1. INTRODUCTION

The imidazole ring which is a member of the azole family, is a five-membered compound with two nitrogen atoms and acts as both a proton acceptor and a proton donor. It biologically is very important because it can bind to proteins with weak interactions and is widely found in nature. The imidazole ring can be found in many natural molecule's structures such as histidine, histamine and adenine and also in many drugs with various biological activities Figure 1 (1).

Figure 1: The structure of histidine, histamine, and adenine.

Chalcones are an open-chain intermediates used in the synthesis of flavones and aurons (1,3-diphenyl-2-*E*-propen-1-one), which are found in many conjugated forms in nature (2-3). It contains a benzylideneacetophenone scaffold in which two aromatic nuclei are joined by a three-carbon α, β unsaturated carbonyl bridge (4). Chalcones and their derivatives can be synthesized classically by the Claisen-Schmidt reaction, as well as by different catalysts and methods (5-7). Intensive research on drug discovery has led to the formation of a large number of molecules with different pharmacological activities.

Developing, designing, and bringing to market new drug candidates using only conventional procedures is a time-consuming process. Therefore, recently it has come in handy to use computational processes, also known as *in silico* techniques, to screen a large group of molecules and select the most reliable molecule among them. Thus, by evaluating with computational methods, the synthesis and biological activity evaluations of the designed molecules take less time. In addition, it is necessary to examine the ADME (Absorption, Distribution, Metabolism, and Excretion) properties of molecules and other drug similarity properties before they can be used as pharmaceutical drugs. ADME studies in the early stages of drug discovery can help reduce the likelihood of molecules pharmacokinetic failure during clinical phase trials.

Various techniques have been developed to obtain information about the ADME properties of developing molecules. Many of the compounds that were reported to be effective in the past could not be used clinically due to poor pharmacokinetic properties (8). Meanwhile, the use of computer models as an alternative to experimental approaches to predict ADME has gained importance, especially in the early stages of drug discovery (9). SwissAD-ME, developed by the molecular modeling group of the Swiss Bioinformatics Institute, is one of website-based software and plays an important role in the period of computer-aided drug design techniques for the evaluation of ADME studies.

In our previous studies, we determined that chalcones carrying F, CF_3 and OCF_3 groups have high anticancer activity. Therefore, we designed new molecules combining the imidazole ring with aldehydes with fluorine atoms in different positions in this study. Then, the anticancer activities of these compounds against HeLa (Human Uterine Cancer Cell) and PC-3 (human Prostate Cancer Cell) cells were examined, and finally, the ADME properties and other drug similarities of the synthesized molecules were examined using the SwissADME software.

2. EXPERIMENTAL

2.1. Materials and Methods
The used chemicals were provided by Sigma-Aldrich and Merck (USA). Melting points of the compounds were determined with Stuart's melting point SMP30 apparatus. FT-IR spectral analysis was performed on the Perkin Elmer Frontier spectrometer with attenuated total reflection (ATR) apparatus (Waltham, Massachusetts, USA). ^{1}H NMR and ^{13}C

NMR spectral analyses were performed in DMSO-d6 with a Brucker Avance-600 MHz spectrometer (Billerica, MA, USA). Elemental analyses (CHNS) were performed on a VarioMICRO elemental analyzer.

2.2. Procedure for Synthesis of Chalcone Compounds with Imidazole Ring (1-11).
4′-Imidazolacetophenone (0.01 mol) was dissolved in methanol (25 mL). Then, the substituted aromatic aldehyde (0.01 mol) and NaOH (0.01 mol) were added to the 4′-imidazolacetophenone solution. The mixture was stirred at room temperature on a magnetic stirrer for one day. After the reaction was finished, the extraction was done with a mixture of dichloromethane and water (1:1). The solvent was evaporated and the crude material was recrystallized from ethanol to obtain a pure substance (10,11).

(*E*)-1-(4-(1H-imidazol-1-yl)phenyl)-3-(2-fluorophenyl)prop-2-en-1-one (1)
Orange solid; yield: 40%, m.p. 135-136°C. FTIR ν_{max} (cm^{-1}): 2987,2971 (Ar-CH); 1681 (C=O); 1600, 1542, 1459, 1452 (C=C). ^{1}H NMR (600 MHz, DMSO-d6): δ 7.04 (t, 1H, j_1=7.20 Hz, j_2=6.60 Hz), 7.13 (d, 1H, j=8.40 Hz), 7.35-7.32 (m, 1H), 7.47 (t, 1H, j_1=7.80 Hz, j_2=7.80 Hz), 7.89 (d, 1H, j=13.20 Hz, H$_\alpha$), 7,93 (s, 1H), 8.03 (d, 2H, j=6,6 Hz), 8.11 (d, 1H, j=16.80 Hz, H$_\beta$), 8.37 (d, 2H, j=11.40 Hz), 8.42 (s, 1H), 9.83 (s, 1H). Anal. Calcd for $C_{18}H_{13}FN_2O$ (292.31 g/mol). C, 73.96; H, 4.48; N, 9.58. Found: C, 73.97; H, 4.52; N, 9.61 (12).

(*E*)-1-(4-(1H-imidazol-1-yl)phenyl)-3-(3-fluorophenyl)prop-2-en-1-one (2)
White solid; yield: 45%, m.p. 147-149°C. FTIR ν_{max} (cm^{-1}): 2853 (Ar-CH); 1681 (C=O); 1614, 1599, 1489, 1447 (C=C). ^{1}H NMR (600 MHz, DMSO-d6): δ 7.31 (t, 1H, j_1=9.00 Hz, j_2=6.00 Hz), 7.50 (dd, 1H, j_1=8.40 Hz, j_2=8.40 Hz), 7.73 (d, 1H, j=7.80 Hz), 7.79 (d, 1H, j=14.4Hz, H$_\alpha$), 7.91 (d, 2H, j=13.80 Hz, H$_\beta$), 8.05 (d, 2H, j=9.00 Hz), 8.11 (d, 1H, j=13.20 Hz), 8.42 (d, 3H, j=8.40 Hz), 9.81 (s, 1H). ^{13}C NMR (150 MHz, DMSO-d_6): δ 188.27 (C=O); 115.32, 118.07, 120.76, 122.23, 123.55, 126.36, 128.30, 130.90, 130.96, 131.35, 131.40, 135.51, 137.55, 137.81, 143.71. Anal. Calcd for $C_{18}H_{13}FN_2O$ (292.31 g/mol). C, 73.96; H, 4.48; N, 9.58. Found: C, 73.98; H, 4.51; N, 9.63 (12).

(*E*)-1-(4-(1H-imidazol-1-yl)phenyl)-3-(4-fluorophenyl)prop-2-en-1-one (3)
White solid; yield: 36%, m.p. 141-142°C. FTIR ν_{max} (cm^{-1}): 2990, 2920 (Ar-CH); 1668 (C=O); 1597, 1509, 1348 (C=C). ^{1}H NMR (600 MHz, DMSO-d6): δ 7.32 (t, 2H, j_1=9.00 Hz, j_2=8.40 Hz), 7.80 (d, 1H, j_1=15.60 Hz, H$_\alpha$), 7.91 (s, 1H), 7.99 (m, 5H, H$_\beta$, H$_{AR}$), 8.39 (s, 1H), 8.40 (d, 2H, j=9.00 Hz), 9.79 (s, 1H, H). ^{13}C NMR (150 MHz, DMSO-d_6): δ 188.27 (C=O); 116.39, 116.53, 120.85, 122.00, 122.28, 130.87, 132.01, 135.52, 138.08, 138.77, 144.03, 163.20, 164.86. Anal. Calcd for $C_{18}H_{13}FN_2O$ (292.31 g/mol). C, 73.96; H, 4.48; N, 9.58. Found: C, 73.94; H, 4.53; N, 9.62 (12).

(*E*)-1-(4-(1H-imidazol-1-yl)phenyl)-3-(2-(trifluoromethyl)phenyl)prop-2-en-1-one (4)
White solid; yield: 38%, m.p. 245-247 °C. FTIR ν_{max} (cm^{-1}): 3096, 2987 (Ar-CH); 1660 (C=O);

1602, 1573, 1543, 1486 (C=C). ^{1}H NMR (600 MHz, DMSO-d6): δ 7.68 (t, 1H, j_1=7.80 Hz, j_2=7.20 Hz), 7.81 (t, 1H, j_1=7.80 Hz, j_2=7.20 Hz), 7.85 (d, 1H, j=7.80 Hz), 7.90 (s, 1H), 8.01 (d, 1H, j=15.60 Hz, H$_\alpha$), 8.05 (d, 2H, j=7.80 Hz), 8.13 (d, 1H, j=15.00 Hz, H$_\beta$), 8.39 (d, 1H, j=7.80 Hz), 8.42 (d, 2H, j=6.00 Hz), 8.44 (s, 1H), 9.80 (s, 1H). ^{13}C NMR (150 MHz, DMSO d6): δ 188.14 (C=O); 120.83, 122.32, 125.53, 126.26, 126.71, 127.95, 129.42, 131.09, 131.28, 133.02, 133.48, 135.56, 137.57, 138.85, 139.03, 163.30. Anal. Calcd for: $C_{19}H_{13}F_3N_2O$ (342.32 g/mol), C, 66.67; H, 3.83; N, 8.18. Found: C, 66.70; H, 3.85; N, 8.20 (13).

(E)-1-(4-(1H-imidazol-1-yl)phenyl)-3-(3-(trifluoromethyl)phenyl)prop-2-en-1-one (5)
White solid; yield: 34%, m.p. 105-106 °C. FTIR ν_{max} (cm^{-1}): 2971, 2901 (Ar-CH); 1601 (C=O); 1542, 1326 (C=C). ^{1}H NMR (600 MHz, DMSO-d6): δ 7.71 (s, 1H), 7.81 (d, 1H, j=7.80 Hz), 7.86 (d, 1H, j=6.60 Hz), 7.90 (d, 2H, j=12.00 Hz, H$_\alpha$), 7.98 (t, 1H, j_1=7.80 Hz, j_2=12.00 Hz), 8.05 (d, 2H, j=7.80 Hz), 8.21 (d, 1H, j=16.20 Hz, H$_\beta$), 8.37-8.45 (m, 3H), 9.81 (s, 1H). Anal. Calcd for: $C_{19}H_{13}F_3N_2O$ (342.32 g/mol), C, 66.67; H, 3.83; N, 8.18. Found: C, 66.71; H, 3.87; N, 8.22.

(E)-1-(4-(1H-imidazol-1-yl)phenyl)-3-(2-(fluoro-3-(trifluoromethyl)phenyl)prop-2-en-1-one (6)
Yellow solid; yield: 40%, m.p. 208-209 °C. FTIR ν_{max} (cm^{-1}): 3093, 2974 (Ar-CH); 1664 (C=O); 1603, 1544, 1469, 1427 (C=C). ^{1}H NMR (600 MHz, DMSO-d6): δ 7.46 (t, 1H, $j1$=6.00 Hz, $j2$=10.20 Hz), 7.80(d, 1H, j=7.80 Hz), 7.91 (s, 1H), 7.92 (d, 1H, j=16.20 Hz, H$_\alpha$), 8.05 (d, 2H, j=8.40 Hz), 8.14 (d, 1H, j=15.60 Hz, H$_\beta$), 8.41 (s, 1H), 8.42 (d, 2H, j=9.00 Hz), 8.46 (d, 1H, j=7.80 Hz), 9.80 (s, 1H). ^{13}C NMR (150 MHz, DMSO d6): δ 188.40 (C=O); 120.78, 122.19, 124.42,124.89, 125.35, 129.32, 130.25, 130.75, 130.99, 133.58, 135.62, 137.00, 137.72, 139.00,157.45, 162.57. Anal. Calcd for: $C_{19}H_{12}F_4N_2O$ (360.31 g/mol), C, 63.34; H, 3.36; N, 7.77. Found: C, 63.36; H, 3.39; N, 7.81.

E-1-(4-(1H-imidazol-1-yl)phenyl)-3-(2-(fluoro-6-(trifluoromethyl)phenyl)prop-2-en-1-one (7)
White solid; yield: 43%, m.p. 140-141 °C. FTIR ν_{max} (cm^{-1}): 3096, 3057 (Ar-CH); 1660 (C=O); 1602, 1543, 1458 (C=C). ^{1}H NMR (600 MHz, DMSO-d6): δ 7.66-7.71 (m, 1H), 7.72 (d, 1H, j=15.00 Hz, H$_\alpha$), 7.88 (d, 1H, j=11.40 Hz, H$_\beta$), 7.92 (s, 1H), 8.04 (d, 2H, j=7.20 Hz), 8.25 (d, 2H, j=8.40 Hz), 8.30 (d, 2H, j=7.80 Hz), 8.38 (s, 1H), 9.74 (s, 1H) Anal. Calcd for: $C_{19}H_{12}F_4N_2O$ (360.31 g/mol), C, 63.34; H, 3.36; N, 7.77. Found: C, 63.37; H, 3.40; N, 7.82.

E-1-(4-(1H-imidazol-1-yl)phenyl)-3-(4-fluoro-2-(trifluoromethyl)phenyl)prop-2-en-1-one (8)
Yellow solid; yield: 45%, m.p. 149-150 °C. FTIR ν_{max} (cm^{-1}): 3364, 2987 (Ar-CH); 1693 (C=O); 1607, 1544, 1506, 1422 (C=C). ^{1}H NMR (600 MHz, DMSO-d6): δ 7.36 (d, 1H, j=8.40 Hz), 7.83 (d, 1H, j=15.60 Hz, H$_\alpha$), 7.87 (s, 1H), 8.00 (d, 2H, j=9.00 Hz), 8.03 (d, 1H, j=15.60 Hz, H$_\beta$), 8.21 (d, 1H, j=9.00 Hz), 8.23 (s, 1H), 8.37 (s, 1H), 8.41 (d, 2H, j=8.40 Hz), 9.70 (s, 1H). ^{13}C NMR (150 MHz, DMSO d6): δ 188.19 (C=O); 113.84, 120.73, 121.36, 122.16, 122.90, 127.43, 128.01, 128.77, 128.82, 130.91, 134.41, 135.59, 135.80, 138.05, 138.85, 143.78.

Anal. Calcd for: $C_{19}H_{12}F_4N_2O$ (360.31 g/mol), C, 63.34; H, 3.36; N, 7.77. Found: C, 63.35; H, 3.39; N, 7.81.

E-1-(4-(1H-imidazol-1-yl)phenyl)-3-(4-fluoro-3-(trifluoromethyl)phenyl)prop-2-en-1-one (9)
White solid; yield: 50%, m.p. 215-217 °C. FTIR ν_{max} (cm^{-1}): 2987, 2973 (Ar-CH); 1663 (C=O); 1607, 1507, 1423 (C=C). ^{1}H NMR (600 MHz, DMSO-d6): δ 7.37 (d, 1H, j=8.40 Hz), 7.83 (d, 1H, j=15.60 Hz, H$_\alpha$), 7.88 (s, 1H), 8.02 (d, 2H, j=8.40 Hz), 8.05 (s, 1H), 8.40 (d, 1H, j=15.60 Hz, H$_\beta$), 8.41 (s, 2H), 9.74 (s, 1H), 8.21 (d, 1H, j=9.00 Hz), 8.23 (d, 1H, j=8.40 Hz). ^{13}C NMR (150 MHz, DMSO d6): δ 188.17 (C=O); 113.83, 120.65, 121.36, 122.09, 123.26, 124.85, 127.44, 128.05, 130.82, 130.91, 135.59, 135.80, 137.97, 138.91, 143.76, 159.19. Anal. Calcd for: $C_{19}H_{12}F_4N_2O$ (360.31 g/mol), C, 63.34; H, 3.36; N, 7.77. Found: C, 63.40; H, 3.38; N, 7.79.

E-1-(4-(1H-imidazol-1-yl)phenyl)-3-(2-(trifluoromethoxy)phenyl)prop-2-en-1-one (10)
White solid; yield: 80%, m.p. 208-209 °C. FTIR ν_{max} (cm^{-1}): 2970, 2926 (Ar-CH); 1660 (C=O); 1602, 1562, 1543, 1485 (C=C). ^{1}H NMR (600 MHz, DMSO-d6): δ 7.48 (d, 1H, j=8.4Hz), 7.52 (t, 1H, j1=7.20 Hz, j2=7.80 Hz), 7.61 (d, 1H, j=7.80 Hz), 7.90 (d, 2H, j=15.6Hz, H$_\alpha$, H$_{AR}$), 8.07 (d, 2H, j=6.6Hz), 8.16 (d, 1H, j=13.80, H$_\beta$), 8.37 (d, 1H, j=9.6Hz), 8.40 (s, 1H), 8.42 (d, 2H, j=6.6Hz), 9.84 (s, 1H). ^{13}C NMR (150 MHz, DMSO d6): δ 188.09 (C=O); 122.31, 124.98, 127.76, 128.05, 128.54, 129.25, 129.87, 130.71, 130.99, 133.09, 134.39, 136.14, 137.67, 138.96, 147.51, 191.66. Anal. Calcd for: $C_{19}H_{13}F_3N_2O_2$ (358.32 g/mol), C, 63.69; H, 3.66; N, 7.82. Found: C, 63.71; H, 3.69; N, 7.85.

E-1-(4-(1H-imidazol-1-yl)phenyl)-3-(3-(trifluoromethoxy)phenyl)prop-2-en-1-one (11)
White solid; yield: 76%, m.p. 129-130 °C. FTIR ν_{max} (cm^{-1}): 3103, 3065 (Ar-CH); 1659 (C=O); 1603, 1591, 1541, 1485 (C=C). ^{1}H NMR (600 MHz, DMSO-d6): δ 7.47 (d, 1H, j=7.80 Hz), 7.60 (t, 1H, j_1=7.80 Hz, j_2=7.80 Hz), 7.82 (d, 1H, j=15.60 Hz, H$_\alpha$), 7.90 (s, 1H), 7.94 (d, 1H, j=7.80 Hz), 8.03 (d, 2H, j=8.40 Hz), 8.04 (s, 1H), 8.14 (d, 1H, j=15.60 Hz, H$_\beta$), 8.40 (s, 1H), 8.43 (d, 2H, j=8.40 Hz), 9.76 (s, 1H). ^{13}C NMR (150 MHz, DMSO d6): δ 188.27 (C=O); 120.81, 121.59, 122.27, 123.44, 123.93, 128.80, 129.01, 131.00, 131.36, 135.57, 137.51, 137.81, 138.94, 143.33, 149.31. Anal. Calcd for: $C_{19}H_{13}F_3N_2O_2$ (358.32 g/mol), C, 63.69; H, 3.66; N, 7.82. Found: C, 63.72; H, 3.68; N, 7.86.

2.3. Anticancer Activity Studies
2.3.1 Cell culture
HeLa and PC-3 cancer cells were incubated in DMEM medium (37 °C - 5% CO$_2$) for four to five days. Trypan blue solution was used for cell counting. Thoma was taken on a slide and counted under the microscope (14,15).

2.3.2 Microplate experiment design
The cells were seeded into sterile microplates. All procedures were performed in triplicate. 5-Fluorouracil was used as the standard substance and tested at the same concentrations (100, 50, 25,

and 5 μM) as the samples. All wells were completed with the medium and kept in the incubator for 24 hours.

2.3.3. BrdU Cell ELISA cell proliferation assay
The activities of the synthesized compounds were performed using the BrdU Cell Proliferation ELISA Kit (Roche 11 647 229 001, Germany) (14,15).

2.3.4. Determination of IC50 concentration
The IC50 values of the samples were determined with the ED50V10.XLS program.

3. RESULTS AND DISCUSSION

3.1. General Chemistry
Chalcones (**1-11**) with imidazole rings were synthesized by Claisen-Schmidt condensation (Scheme 1). All molecules were scanned in the SciFinder search engine and molecules (**5-11**) were original; molecules (**1-4**) have been synthesized before (**Scheme 1**)(12, 13).
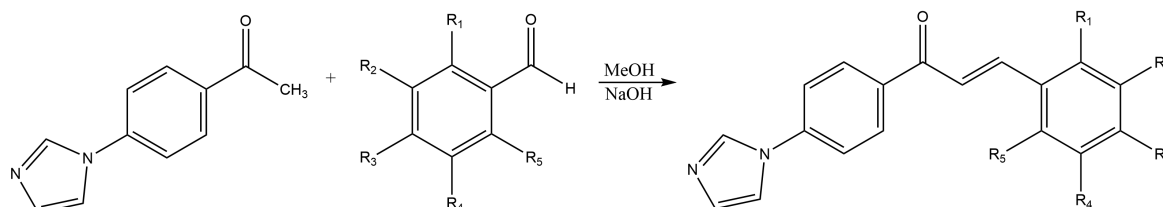
Scheme 1: Synthetic pathway of chalcone compounds with imidazole ring (**1-11**).

Table 1: Functional groups of synthesized (**1-11**) imidazole chalcone compounds.

Compd.	R_1	R_2	R_3	R_4	R_5
1	F	H	H	H	H
2	H	F	H	H	H
3	H	H	F	H	H
4	CF_3	H	H	H	H
5	H	CF_3	H	H	H
6	F	CF_3	H	H	H
7	F	H	H	H	CF_3
8	CF_3	H	F	H	H
9	H	CF_3	F	H	H
10	OCF_3	H	H	H	H
11	H	OCF_3	H	H	H

When the FTIR spectra were examined, aromatic C-H, C=O and C=C stretching bands were detected at 3364-2853 cm^{-1}, 1693-1601 cm^{-1} and 1614-1326 cm^{-1} respectively. The C-F stretching bands was found in the range of 1127-1242 cm^{-1}. When the ^1H and ^{13}C NMR spectra of the synthesized molecules were examined, the chemical shift values of protons and carbons were determined in ppm ranges in accordance with the literature (10,11,16). The biggest proof that chalcone compounds were synthesized, was that they had an olefin structure. AB spin system was observed in the ^1H NMR spectra as it had an olefin structure. The configuration of the molecule was determined by measuring the interaction constant. If the structure was in *cis* configuration, the value of j_{cis} was 7.00-10.00 Hz, if the structure was in *trans* configuration, the value of j_{trans} was 12.00-18.00 Hz (17). AB spin system was observed in all molecules (**1-11**). Determining the *j* values of the molecules between 11.40-16.20 Hz was showed that the synthesized molecules were in the *trans* configuration. Protons at α and β carbon atoms in the chalcone structure were found to resonate in the range of 7.82-8.21 ppm and 7.88-8.40, respectively.

3.2. Anticancer Activity
Anticancer activities of compounds **1-11** against HeLa and PC-3 cancer cells were examined at four different concentrations (100, 50, 25 and 5 μM). The IC_{50} values of compounds **1-11** against HeLa and PC-3 cells were given in Table 2. All compounds except compounds **1** and **6** were observed to have higher activity against HeLa cell than the standard drug **5-FU**. Compounds **10** and **11** were observed to exhibit considerably higher activity against HeLa cells compared to the standard compound. In particular, it was determined that the compounds containing the –OCF_3 group showed high activity. All compounds except compounds **2** and **8** were found to be more active than **5-FU** against PC-3 cancer cells. In particular, compounds **4** and **6** were found to be the most effective compounds against PC-3 cancer cells. It was observed that these two compounds contain -the CF_3 group. Many studies are showing the structure-anticancer activity analysis and showing that the fluoro group has a higher anticancer effect than other substituents. The incorporation of an electron-withdrawing group, such as a fluorine group, into a molecule leads to a marked improvement in anticancer activity (18,19).

Table 2: IC_{50} values of compounds **1**-**11** and **5-FU**.

Compd.	IC$_{50}$	
	HeLa	**PC-3**
1	93.67± 0.50	13.29± 0.05
2	26.44± 0.21	>100
3	17.56± 0.11	22.96± 0.06
4	>100	1.39± 0.00
5	21.02± 0.10	15.60±0.06
6	52.13± 0.31	2.65±0.00
7	24.11± 0.25	20.69±0.05
8	19.97± 0.05	>100
9	25.01± 0.04	41.31±0.24
10	4.27± 0.01	28.60±0.27
11	1.58± 0.01	35.40±0.15
5-FU	40.39± 0.23	50.00±0.22

3.3. SAR Study

When the anticancer activity of the compounds against Hela cell lines were examined, the activities were as follows: **11>10>3>8>5>7>9>2>6>1>4**. It was determined that compounds **10** and **11** carrying the OCF$_3$ group were the most active molecules and that the oxygen atom had a positive effect on the activity. It has been determined that the F atom had the best effect when it was in the 4-position (compound **3**), and its activity decreases when the 2- and 3- positions are changed.

When the anticancer activity of the compounds against PC-3 cell lines were examined, the activities were as follows: **4>6>1>5>7>3>10>11>9>5-FU>2**, **8**. It was determined that the activity was higher in molecules with the F atom in the 2nd position of the phenyl ring. The activity decreased when the fluorine atom was in the 3rd and 4th positions of the phenyl ring. When the compounds carrying CF$_3$ (compound **5,6** and **7**) and OCF$_3$ groups (compound **10** and **11**) were compared, it was determined that the derivatives carrying the CF$_3$ group were more active, while the incorporation of the oxygen atom into the structure had a negative effect on the activity.

3.4. *In silico* ADME Evaluation

In silico studies are web-based according to Lipinski and Weber rules. It was carried out with the SwissADME program (20). The drug similarity properties of compounds **1**-**11** were examined. Molecular weight (MW)<500, mLogP<5; HBA<10; and must comply with rules such as HBD<5. According to these rules, an orally active drug should not have more than one violation. The calculated logP must be less than 5. In the analysis performed, the log P values of compounds **1**-**11** were determined to be less than 5. The molecular weights of the compounds range from 292.31 to 360.31 g/mol. It was determined that compounds **1**-**5** and **10**-**11** could cross the Blood-Brain Barrier (BBB). The synthetic accessibility score of the compounds ranges from 1 (very easy) to 10 (very difficult). The synthetic accessibility of all compounds is in the range of 2.42 to 2.78. The topological polar surface area (TPSA) should be <70 Å2. The topological polar surface area value of all compounds (**1**-**11**) is less than 70 Å^2 (Table 3). Compounds **1**-**11** were found to have drug properties within Lipinski rules. All compounds were found to exhibit high gastrointestinal absorption (GI) (21).

Table 3: *In silico* results of compounds **1**-**11**.

Compd.	Formula	Molecular weight (g/mol)	M LOG P	BBB	GI absorption	TPSA Å^2	Synthetic accessibility	Lipinski
1	$C_{18}H_{13}FN_2O$	292.31	2.76	Yes	High	34.89	2.45	Yes
2	$C_{18}H_{13}FN_2O$	292.31	2.79	Yes	High	34.89	2.44	Yes
3	$C_{18}H_{13}FN_2O$	292.31	2.76	Yes	High	34.89	2.42	Yes
4	$C_{19}H_{13}F_3N_2O$	342.31	2.79	Yes	High	34.89	2.70	Yes
5	$C_{19}H_{13}F_3N_2O$	342.31	2.89	Yes	High	34.89	2.59	Yes
6	$C_{19}H_{12}F_4N_2O$	360.30	2.87	No	High	34.89	2.65	Yes
7	$C_{19}H_{12}F_4N_2O$	360.30	2.89	No	High	34.89	2.78	Yes
8	$C_{19}H_{12}F_4N_2O$	360.30	2.90	No	High	34.89	2.76	Yes
9	$C_{19}H_{12}F_4N_2O$	360.30	2.88	No	High	34.89	2.64	Yes
10	$C_{19}H_{13}F_3N_2O_2$	358.31	3.03	Yes	High	44.12	2.71	Yes
11	$C_{19}H_{13}F_3N_2O_2$	358.31	3.13	Yes	High	44.12	2.59	Yes

Figure 2 : Bioavailability radar of the **1**-**11**. The pink area represents the optimal range for each property (LIPO: Lipophilicity, SIZE: Molecular weight, POLAR: Total Polar Surface Area, INSOLU: Insolubility, INSATU: Instauration, FLEX: Flexibility). (For interpretation of the references to colour in this figure legend, the reader is referred to the web version of this article.).

4. CONCLUSION

A series of chalcones were synthesized and their anticancer activities against Hela and PC3 cell lines were evaluated. In the Hela cell line, the compound **11** is the most active molecule; the most active molecule in the PC-3 cell line is compound **4**. Anticancer activity and *in silico* studies will make important contributions to the development of new active compounds for anticancer and to the pharmaceutical industry in the future.

5. CONFLICT OF INTEREST

The authors declare that they have no conflicts of interest.

6. ACKNOWLEDGMENTS

CRediT authorship contribution statement
Bedriye Seda Kurşun Aktar: Conceptualization, Methodology, Synthesis, Biological analyses, Validation, Formal analysis, Investigation, Writing - original draft, Writing - review & editing, Visualization, Supervision, Project administration, Funding acquisition. Abdulraheem Mustafa Ibrahim AL-KARABASH: synthesis. Emine Elçin Oruç-Emre: Conceptualization, Methodology, Validation, Investigation, Writing - original draft, Writing - review & editing, Funding acquisition. Ayse Şahin Yağlıoğlu: Project administration, Biological

analyses, Writing - original draft, Writing - review & editing, Validation.

7. REFERENCES

1. Alghamdi SS, Suliman RS, Almutairi K, Kahtani K, Aljatli D. Imidazole as a Promising Medicinal Scaffold: Current Status and Future Direction. Drug Des Devel Ther [Internet]. 2021 Jul;15:3289–312. Available from: <URL>.

2. Singh P, Anand A, Kumar V. Recent developments in biological activities of chalcones: A mini review. Eur J Med Chem [Internet]. 2014 Oct 6;85:758–77. Available from: <URL>.

3. Nowakowska Z. A review of anti-infective and anti-inflammatory chalcones. Eur J Med Chem [Internet]. 2007 Feb 1;42(2):125–37. Available from: <URL>.

4. Dimmock JR, Elias DW, Beazely MA, Kandepu NM. Bioactivities of chalcones. Curr Med Chem. 1999;6(12):1125–49.

5. Detsi A, Majdalani M, Kontogiorgis CA, Hadjipavlou-Litina D, Kefalas P. Natural and synthetic 2′-hydroxy-chalcones and aurones: Synthesis, characterization and evaluation of the antioxidant and soybean lipoxygenase inhibitory activity. Bioorg Med Chem [Internet]. 2009 Dec 1;17(23):8073–85. Available from: <URL>.

6. Gürdere MB, Özbek O, Ceylan M. Aluminum chloride–catalyzed C-alkylation of pyrrole and indole with chalcone and bis-chalcone derivatives. Synth Commun [Internet]. 2016 Feb 16;46(4):322–31. Available from: <URL>.

7. Gürdere MB, Aydin A, Yencilek B, Ertürk F, Özbek O, Erkan S, et al. Synthesis, Antiproliferative and Cytotoxic Activities, DNA Binding Features and Molecular Docking Study of Novel Enamine Derivatives. Chem Biodivers [Internet]. 2020 Jul 25;17(7):e2000139. Available from: <URL>.

8. Hay M, Thomas DW, Craighead JL, Economides C, Rosenthal J. Clinical development success rates for investigational drugs. Nat Biotechnol [Internet]. 2014 Jan 9;32(1):40–51. Available from: <URL>.

9. Dahlin JL, Inglese J, Walters MA. Mitigating risk in academic preclinical drug discovery. Nat Rev Drug Discov [Internet]. 2015 Apr 1;14(4):279–94. Available from: <URL>.

10. Oruç Emre EE, Karaküçük İyidoğan A, Şahin Yağlıoğlu A, Demirtaş İ, Kurşun Aktar BS. Synthesis and structure-activity relationship study: Anticancer chalcones derived from 4′-morpholinoacetophenone. Marmara Pharm J [Internet]. 2017 Oct 3;21(4):949–60. Available from: <URL>.

11. Kurşun Aktar BS, Oruç-Emre EE, Demirtaş I, Yaglioglu AS, Guler C, Adem S, et al. Synthesis of novel fluorinated chalcones derived from 4′-morpholinoacetophenone and their antiproliferative effects. J Mol Struct [Internet]. 2017 Dec 5;1149:632–9. Available from: <URL>.

12. Mathew B, Baek SC, Thomas Parambi DG, Lee JP, Mathew GE, Jayanthi S, et al. Potent and highly selective dual-targeting monoamine oxidase-B inhibitors: Fluorinated chalcones of morpholine versus imidazole. Arch Pharm (Weinheim) [Internet]. 2019 Apr 21;352(4):1800309. Available from: <URL>.

13. Rao GE, Rahaman SA, Rani AP. Synthesis, characterization and biological evolution of nitrogenous heterocyclic ring containing chalcones. Int J Pharm Sci Rev Res [Internet]. 2017;43(2):200–7. Available from: <URL>.

14. Sahin Yaglioglu A, Yaglioglu MS, Tosyalıoglu N, Adem S, Demirtas I. Chemical profiling, in vitro biological activities and Pearson correlation between chemical profiling and anticancer activities of four Abies species from Turkey. South African J Bot [Internet]. 2022 Dec 1;151:600–13. Available from: <URL>.

15. Sahin Yaglioglu A, Eser F, Yaglioglu MS, Demirtas I. The antiproliferative and antioxidant activities of the essential oils of Juniperus species from Turkey. Flavour Fragr J [Internet]. 2020 Sep 2;35(5):511–23. Available from: <URL>.

16. Sıcak Y, Kekeçmuhammed H, Karaküçük İyidoğan A, Taşkın Tok T, Oruç Emre EE, Öztürk M. Chalcones bearing nitrogen-containing heterocyclics as multi-targeted inhibitors: Design, synthesis, biological evaluation and molecular docking studies. J Mol Recognit [Internet]. 2023 Jul 5;36(7):e3020. Available from: <URL>.

17. Balcı M. Nuclear Magnetic Resonance Spectroscopy. Education Publishing House; 2020. 464 p, Ankara.

18. Zhang S, Luo Y, He L-Q, Liu Z-J, Jiang A-Q, Yang Y-H, et al. Synthesis, biological evaluation, and molecular docking studies of novel 1,3,4-oxadiazole derivatives possessing benzotriazole moiety as FAK inhibitors with anticancer activity. Bioorg Med Chem [Internet]. 2013 Jul 1;21(13):3723–9. Available from: <URL>.

19. Zhou S, Ren J, Liu M, Ren L, Liu Y, Gong P. Design, synthesis and pharmacological evaluation of 6,7-disubstituted-4-phenoxyquinoline derivatives as potential antitumor agents. Bioorg Chem [Internet]. 2014 Dec 1;57:30–42. Available from: <URL>.

20. Daina A, Michielin O, Zoete V. SwissADME: a free web tool to evaluate pharmacokinetics, drug-likeness and medicinal chemistry friendliness of small molecules. Sci Rep [Internet]. 2017 Mar 3;7(1):42717. Available from: <URL>.

21. Sicak Y. Design and antiproliferative and antioxidant activities of furan-based thiosemicarbazides and 1,2,4-triazoles: their structure-activity relationship and SwissADME predictions. Med Chem Res [Internet]. 2021 Aug 15;30(8):1557–68. Available from: <URL>.